For JES CB review
Comments to d0-run2eb-034@fnal.gov

DØ Note 5382
August 24, 2007
Version 1.0

Jet Energy Scale Determination at DØ Run II (final p17 version)

This note describes the determination of the Final p17 Jet Energy Scale corrections for data and MC.

List of changes with respect to v0.9

- Sect. 10.1: added a paragragh indicating that, due to the (data quality-related) instability of the $k_{\rm O}^{\rm ZS}/k_{\rm R}^{\rm ZS}$ correction derived in the unsuppressed ZB overlay MC, and how close it appears to be to the correction based on the suppressed ZB overlay MC, the parameterizations corresponding to the latter have been adopted. Small discrepancies are being covered with an additional uncertainty. Relevant plots are included in Appendix F1.

- Sect. 14.2: updated Figs. 82 and 83 using a special γ+jet forward MC sample to increase statistics for $|\eta_{\rm jet}^{\rm det}| > 2.0$. Added a paragraph on the direct closure in MC using a consistent event selection with that used to derive the individual subcorrections (plots are included in Appendix I1). Also added a paragraph on the dependence of the direct closure on the $\Delta\mathcal{R}$ matching criterion between the reconstructed and particle jets (plots are included in Appendix I2).

- Sect. 14.3: added a paragraph on the more traditional closure method based on the ΔS observable, with plots included in Appendix I5.

List of changes with respect to v0.8

- As indicated in v0.8, there are issues with large weight fluctuations in the unsuppressed ZB overlay γ+jet MC and potential problems with data quality of the overlay which make rather difficult to perform reliable fits for $k_{\rm O}^{\rm ZS}/k_{\rm R}^{\rm ZS}$. However, despite the significant differences of the individual $k_{\rm O}^{\rm ZS}$ and $k_{\rm R}^{\rm ZS}$ corrections between unsuppressed and suppressed cases, the ratio $k_{\rm O}^{\rm ZS}/k_{\rm R}^{\rm ZS}$ appears numerically very close (within $\sim 0.5\%$ or better) to the one for the suppressed case. Therefore, for data JES we are currently using the parameterizations of $k_{\rm O}^{\rm ZS}/k_{\rm R}^{\rm ZS}$ from the suppressed ZB overlay MC. Plots of $k_{\rm O}^{\rm ZS}$, $k_{\rm R}^{\rm ZS}$ and $k_{\rm O}^{\rm ZS}/k_{\rm R}^{\rm ZS}$ for the unsuppressed ZB overlay case have not been updated in this version of the note.

- Sect. 8.3.1: updated high-energy extrapolation of MPF response using a wider grid scan of parameters in MC to ensure the global minimum in well contained within the table. Using as default the interpolated cubic-log fit parameters from the table. Result basically numerically identical to previous iterations.

- Added Sect. 12 providing an overview of the QCD-specific JES corrections and four-momentum calibration procedure. Closure tests for these QCD-specific corrections have not been finalized yet and therefore are not included in this version of note.

- Sect. 13: updated summary plots od data and MC γ+jet JES corrections and uncertainties. Changes in central corrections for data result from switching to the new $k_{\rm O}^{\rm ZS}/k_{\rm R}^{\rm ZS}$ correction derived in suppressed ZB overlay MC. Included summary plots of data and MC QCD-specific JES corrections for $\mathcal{R}_{\rm cone} = 0.7$ jets.

- Sect. 14: added preliminary closure tests for γ+jet JES in data. Additional information also included in Appendix I.

List of changes with respect to v0.7

- Sects. 6 and 10.1: found an inconsistenty in the event selection and rederived $k_{\rm O}^{\rm ZS}$, $k_{\rm R}^{\rm ZS}$ and $k_{\rm O}^{\rm ZS}/k_{\rm R}^{\rm ZS}$ for the suppressed ZB overlay case. The largest numerical effect was in $k_{\rm O}^{\rm ZS}$. As a result $k_{\rm O}^{\rm ZS}/k_{\rm R}^{\rm ZS}$ is closer to 1. The corrections for the unsuppressed case also have to rederived, but there are some technical issues with large weight fluctuations and concerns about data quality of the unsuppressed ZB overlay which still need to be resolved. The expectation is that $k_{\rm O}^{\rm ZS}/k_{\rm R}^{\rm ZS}$ will also become closer to 1. For the unsuppressed ZB case, the plots shown in this version of the note are still the old ones (same as in v0.7).

- Sect. 9.4: added systematic uncertainty for high-energy extrapolation in dijets. Updated statistical uncertainty from the global fit, where the statistical uncertainties for γ+jet and dijet are scaled separately by their $\sqrt{\chi^2/ndf}$ for those $\eta_{\rm jet}^{\rm det}$ bins with $\chi^2/ndf > 1$ (in v0.7 it was done using the common $\sqrt{\chi^2/ndf}$ of the combined fit).

- Sect. 11: updated showering correction in data (changed fit range from $\Delta\mathcal{R} < 2.5$ to $\Delta\mathcal{R} < 2.0$, increased MC template statistics for $|\eta_{\rm jet}^{\rm det}| > 2.0$ and dropped measurements with too low statistics either in data or in the MC templates). Changes in the central value are very small (per-mill level in general). Included discussion on the checks performed and the conclusion reached regarding the observed discrepancy between data and fitted profiles. Updated accordingly the systematic uncertainty.
- Sect. 13: updated summary plots for data and MC corrections and uncertainties. Only changes made in central corrections result from refit of the showering correction. Changes in uncertainties result from the above updates.

List of changes with respect to v0.6

- Sect. 8: updated breakdown of photon energy scale uncertainty (overall uncertainty remains the same).
- Sect. 9: added discussion in Sect. 9.2.6 on the assumptions made in the global fit and their validation using the full simulation. In Sect. 9.4 increased the statistical uncertainty from the global fit by $\sqrt{\chi^2/ndf}$ for those $\eta_{\rm jet}^{\rm det}$ bins with $\chi^2/ndf > 1$. Updated summary plots of uncertainties accordingly.
- Sect. 13: added Sect. 13.1, including a brief discussion on the procedure to map $E_{\rm jet}^{\rm meas}$ to E' in order to evaluate the JES subcorrections. Updated summary plots for data and MC corrections and uncertainties. No changes made in central corrections and updates to uncertainties almost invisible.

List of changes with respect to v0.5

- Sect. 8: updates related to the new photon energy scale and its new uncertainty (photon correction plots, response fit, response error plots). New high energy extrapolation fit with new table in parameters (A, B, C) that reflects the update of photon energy scale. First proposal how to treat correlations for central jet response (not yet implemented in jetcorr).
- Sect. 9: updated relative response correction in data using the new photon energy scale correction. All data-related plots have been updated, including internal closure tests and systematic uncertainties. Relevant plots were updated as well in Appendix E.
- Sect. 10.2: redid global fit including higher statistics points for $|\eta_{\rm jet}^{\rm det}| > 2.0$ and a more careful evaluation of the statistical uncertainty. Parameterized systematic uncertainty due to single pion response scaling and updated plots summarizinsg systematic uncertainties. Relevant plots were updated as well in Appendix F.
- Sect. 11: implemented a more correct estimate of the statistical uncertainty. Completed systematic uncertainties. Relevant plots were updated as well in Appendix G.
- Sect. 13: updated summary plots for data and MC corrections and uncertainties. Uncertainties essentially complete (see caveats in that section).
- Sect. 14: added this section including preliminary closure tests of the MC corrections.

List of changes with respect to v0.4

- Sect. 6: found a bug in the offset table in jetcorr, which implied the NP contribution was actually coming from MB events with 0 PVs, instead of ZB events with LM veto and 0 PVs. After correcting the bug had to rederive the $k_{\rm O}^{\rm ZS}$ bias correction. The following plots were updated accordingly: Figs. 1, 3 in Sect. 6 and Figs. 90-93 in Appendix B.
- Sect. 8.3.1: updated high energy extrapolation and added justification for the currently assumed 1.5% prior in the C parameter of the single pion scaling factor.
- Sect. 8.4: completed high energy extrapolation response systematics and updated photon energy scale uncertainty.

- Appendix D2: "temporary" increase in photon energy scale uncertainty.
- Sect. 10.1: after fixing bug in offset, had to rederive $k_{\mathrm{O}}^{\mathrm{ZS}}/k_{\mathrm{R}}^{\mathrm{ZS}}$ plots and systematics. The following plots were updated accordingly: Figs. **??**, **??** in Sect. 10.1 and Figs. 165-168 in Appendix F.
- Sect. 9: included results on relative response correction and related uncertainties in MC. All plots are included in Appendix E2.
- Sect. 10.2: updated topology bias correction and corresponding plots in Appendix F2. A minor inconsistency was found in the calculation of the true jet response (see Eq. 9), which should be the ratio of averages instead of the average of ratio. Added discussion on systematic uncertainty due to signle pion response. Plots summarizing uncertainties still need to be updated for the statistical uncertainty of the new global fit and the systematic from the single pion response.
- Appendix F: included plots (Figs. 175 and 176) which will be used to assign a systematic uncertainty due to the difference between data and MC in the single pion response.
- Sect. 11: included plots with global fit to showering correction as well as several systematic uncertainties.
- Appendix G: added appendix to include additional plots on showering correction.
- Sect. 13: updated summary plots for data corrections and included plots for MC corrections. Still some uncertainties missing (see caveats in that section).

Contents

1. INTRODUCTION

2. DØ DETECTOR

2.1. Calorimeters

2.2. Calorimeter Calibration

3. STANDARD OBJECTS RECONSTRUCTION AND IDENTIFICATION

This section describes the procedures used to reconstruct and identify the basic objects required to determine the jet energy scale corrections.

3.1. Primary Vertex

The first step is the reconstruction of vertices from prompt tracks along the z direction. These vertices, referred to as "primary vertices" (PV), are used to indicate the presence, as well as location along the z axis, of one or several $p\bar{p}$ inelastic collisions in a given event. The Tevatron luminous region is approximately Gaussian, centered at $z \simeq 0$ cm and has an RMS of approximately 30 cm. Therefore, a significant fraction of $p\bar{p}$ inelastic collisions can take place at z positions considerably displaced from the center of the detector, and it would be important to reconstruct the corresponding primary vertices with high efficiency

The reconstruction of primary vertices involves three steps: track selection, vertex fitting, and vertex selection. Tracks are selected with at least 2 SMT hits, $p_T \geq 0.5$ GeV, and transverse impact parameter significance with respect to the beam position smaller than 3. Starting from the track with highest p_T, the tracks are clustered along the z-direction. Tracks are added to the first track if they are within 2 cm in z. By constraining all tracks in a cluster to a common vertex, the track parameters and vertex position is recalculated using a Kalman Filter technique [1]. The algorithm is repeatedly applied to the remaining tracks to build a list of PV candidates.

The presence of multiple interactions during the hard-scatter collision typically leads to several PVs reconstructed in the event. For each reconstructed PV, the probability that it originates from a soft $p\bar{p}$ inelastic interaction ("minimum bias probability") is computed making use of a template of the distribution of $\log_{10}(p_T)$ from the associated tracks. The PV with the lowest minimum bias probability is chosen as the hard-scatter PV. To ensure that a hard-scatter PV of good quality is selected, it is required to be reconstructed from at least three tracks, and have $|z_{\rm PV}| \leq 50$ cm.

3.2. Calorimeter Objects

The jet energy calibration procedure entirely relies on calorimeter objects (photons, jets and missing transverse energy), which are reconstructed starting from the individual calorimeter cells. This section presents a discussion on the calorimeter cell selection procedure, as well as the reconstruction and identification algorithms used for the relevant calorimeter objects.

3.2.1. Calorimeter Cells Selection

The DØ calorimeter is comprised of a large number of cells, each of which is subject to electronic noise, as well as to signals from uranium decay ("uranium noise"). The average of the pedestal distribution is defined as zero in the hardware, therefore a cell can have positive or negative energy. Such distribution is asymmetric around zero, with a larger tail on the positive side. In order to limit the amount of information to be processed, a cell is read out only if the absolute value of its energy is larger than a certain threshold, usually given in units of the RMS of the pedestal distribution ($\sigma_{\rm ped}$). This threshold is set in the hardware to $1.5\sigma_{\rm ped}$ and is referred to as "online zero suppression". Due to the asymmetry of the

pedestal distribution, this zero suppression results in a net positive average cell energy, even in absence of a particle flux.

If the threshold above which a cell is considered for further reconstruction is low (e.g. $2\sigma_{\rm ped}$), the fraction of cells with energy mostly originating from noise ("noise cells") is still rather large. On the other hand, if the threshold is increased too much, a significant amount of energy from a true signal is missed. DØ uses the so called "T42" algorithm [2] to identify possible signal cells with a higher threshold while keeping lower energy cells only if they are nearby. The concept is based on the idea that in a finely grained calorimeter, isolated low-energy cells are likely to originate from noise. Thus, cells with negative energy are rejected, and cells with positive energy above $2.5\sigma_{\rm ped}$ are considered only if they are neighbor to a cell with an energy of at least $4\sigma_{\rm ped}$. "Neighborhood" is defined in 3D space, and a cell can have up to nine neighbors. The T42 algorithm leads to a better rejection of noise cells, and hence to better jet energy and missing transverse energy resolution. In the rest of this paper we will refer to "zero suppression" as the combined effect of the hardware and T42 thresholds.

A calorimeter cell not only carries energy information, it also has a direction, which is calculated from the cell's position in the detector and the reconstructed hard-scatter PV. Given the cell's energy and direction, the cell transverse energy is computed assuming it is a massless object.

3.2.2. Electromagnetic Clusters

Electromagnetic clusters are formed from seed towers in the electromagnetic calorimeter which have $p_T > 500$ MeV. Neighboring towers are added if they have $p_T > 50$ MeV and if they are within $\Delta\mathcal{R} < 0.3$ of the seed tower in the central region of the detector, or within a cone radius of 10 cm in the third layer of the EM calorimeter in the end caps. Such preclusters are used as starting points for the final clusters if their energy exceeds 1 GeV. Any EM tower within $\Delta\mathcal{R} < 0.4$ is added, and the center of the final cluster is defined by the energy weighted mean of its cells in the third layer of the EM calorimeter.

3.2.3. Jets

Jets resulting from the hard interaction usually involve a large number of particles, which in turn deposit energy in numerous calorimeter cells. The reconstruction of jets, either from stable particles or calorimeter towers, involves a clustering algorithm to assign particles or calorimeter towers to jets. In this paper we focus on jets clustered using the so-called Run II Midpoint algorithm [3], which belongs to the class of fixed-cone algorithms. The jet centroid is defined as $(y_{\rm jet}, \phi_{\rm jet})$, and objects are clustered if their distance relative to the jet axis, $\Delta\mathcal{R} = \sqrt{(y - y_{\rm jet})^2 + (\phi - \phi_{\rm jet})^2} < \mathcal{R}_{\rm cone}$, where $\mathcal{R}_{\rm cone}$ is the cone radius. Jet energy scale corrections and uncertainties have been determined for $\mathcal{R}_{\rm cone} = 0.5$ and 0.7.

The jet reconstruction procedure involves a number of steps. First, pseudo-projective calorimeter towers ($\Delta\eta \times \Delta\phi = 0.1 \times 0.1$) are reconstructed by adding the four-momentum of the calorimeter cells above threshold they contain, treating each cell as massless. The momentum of each cell is defined with respect to the interaction vertex, as reconstructed by the tracking system. As a result, calorimeter towers are massive. In a second step, the calorimeter towers with $p_T \geq 1$ GeV are used as seeds to find pre-clusters, which are formed by adding neighboring towers within $\Delta\mathcal{R} < 0.3$ of the seed towers. The pre-clustering step is used to reduce the number of seeds passed to the main algorithm, in order to keep the analysis computationally feasible. A cone of radius $\mathcal{R}_{\rm cone}$ is formed around each pre-cluster,

centered at its centroid, and a new jet center is computed using the E-scheme:

$$\mathbf{p}_{\rm jet} = (E_{\rm jet}, \vec{p}_{\rm jet}) = \sum_i (E_{\rm i}, \vec{p}_{\rm i}) \,, \tag{1}$$

$$y_{\rm jet} = \frac{1}{2} \ln \left(\frac{E_{\rm jet} + p_{z\rm jet}}{E_{\rm jet} - p_{z\rm jet}} \right) , \tag{2}$$

$$\phi_{\rm jet} = \tan^{-1} \left(\frac{p_{y\rm jet}}{p_{x\rm jet}} \right) , \tag{3}$$

$$p_{T\rm jet} = \sqrt{p_{x\rm jet}^2 + p_{y\rm jet}^2}, \tag{4}$$

where the sums are over all towers contained in the cone. This procedure is repeated iteratively for each of the seeds, always using the E-scheme, until the jet center is stable. Stable solutions are called proto-jets. The sensitivity to soft radiation is reduced by the addition of midpoints between pairs of proto-jets and repeating the iterative procedure for these midpoint seeds. The last step of the algorithm involves splitting and merging to treat overlapping proto-jets, i.e. proto-jets separated by a distance $\Delta\mathcal{R} < 2\mathcal{R}_{\rm cone}$. Overlapping proto-jets are merged into a single jet if more than 50% of the p_T of the lower-energy jet is contained in the overlap region. Otherwise, the energy of each cell in the overlap region is assigned to the nearest jet. Finally, the jet four-momentum is recomputed using the E-scheme and jets with $p_T < 6$ GeV are discarded.

The jet algorithm described above can also be applied to stable particles in MC events. Stable particles are defined as those having a lifetime long enough to not decay within the DØ detector volume. All stable particles produced in the interaction are considered, including not only the ones from the hard scattering process, but also from the underlying events. The exception are muons and neutrinos, which are not included. Jets clustered from the list of considered stable particles (particle jets) are used to define the *particle level* jet energy. The goal of the jet energy scale calibration procedure is to correct calorimeter jets to the particle level.

3.2.4. Missing Transverse Energy

The missing energy in the transverse direction is defined by its components in x and y:

$$\not\!\!E_x = -p_x^{\rm meas} \quad \text{and} \quad \not\!\!E_y = -p_y^{\rm meas},$$

where $p_{x,y}^{\rm meas}$ are the components of the visible transverse momentum, computed from calorimeter and ICD cells that pass the T42 selection:

$$p_{x,y}^{\rm vis} = \sum_{\rm cells} p_{x,y\rm i}.$$

The missing E_T needs to be adjusted for energy scale corrections that are applied to reconstructed electromagnetic objects. For the determination of the jet energy scale corrections, only the corrections of electromagnetic objects that pass the photon identification criteria described in Sect. 3.3 are subtracted:

$$\not\!\!E_{x,y}^{\rm corr} = \not\!\!E_{x,y} - \sum_{i \in \rm photons} \left(E_{x,y\rm i}^{\rm corrected} - E_{x,y\rm i}^{\rm uncorrected} \right) .$$

3.3. Photon Identification Criteria

Clusters in the electromagnetic calorimeter are identified as photons if they pass the following selection criteria:

- the object is an isolated electromagnetic cluster with or without an associated track,
- the object must be reconstructed either in the central region ($|\eta_{\rm det}| < 1$) or in the endcap regions ($1.5 < |\eta_{\rm det}| < 2.5$), and must be in the fiducial regions of the detector (objects near intermodule boundaries are excluded),
- the fraction EMF of energy deposited in the electromagnetic part of the calorimeter must be greater than 0.96,
- the probability to have a spatially matched track must be less than 0.1%,
- the calorimeter isolation of the photon candidate in the ring $\Delta\mathcal{R} \in [0.2, 0.4]$ must be less than 0.07,
- the cluster width squared in $r \times \phi$ in the third layer of the EM calorimeter must be less than 14 cm^2.
- the scalar sum of the transverse momenta of all tracks with $\Delta\mathcal{R} \in [0.05, 0.7]$ around the photon candidate must be less than 1 GeV. Tracks are considered if their transverse momentum exceeds 0.4 GeV, and if their distance of closest approach in z to the vertex is less than 1 cm.
- two variables constructed from energy depositions in the preshower detector are used to discriminate against wide clusters and photons from neutral pions:
  - the squared difference between the preshower position in ϕ and the position in the third layer of the cluster in the EM calorimeter, weighted by the energy depositions (in GeV) in strips of the preshower detector must be less than 0.003, and
  - the squared difference between the preshower position in ϕ and the position in the third layer of the cluster in the EM calorimeter, weighted by the energy depositions squared (in GeV^2) in strips of the preshower detector must be less than 0.0015.

This set of criteria is further referred to as a tight photon selection or simply as tight photon. For the purpose of background studies, namely the contamination from dijet events where one of the jets is misidentified as photon, additional two sets with less stringent criteria are considered. Loose photon selection is the same as the tight one but no cut on the scalar sum of transverse momenta of associated tracks is applied, as well as no information from the preshower detector is used. Medium selection is also based on the tight one but the cut on the scalar sum of transverse momenta of associated tracks is released to 2 GeV and outer radius of the hollow cone set to 0.4.

3.4. Jet Identification Criteria

Jets are identified from reconstructed calorimeter objects according to the following selection criteria:

- The fraction energy deposited in the electromagnetic part of the calorimeter (EMF) must be greater than 0.05 and less than 0.95. Jets in the forward region ($\left|\eta_{\text{jet}}^{\text{det}}\right| > 2.5$) must satisfy EMF > 0.04.
- The fraction of energy in the coarse hadronic calorimeter (CHF) must be less than 0.44 for jets in $\left|\eta_{\text{jet}}^{\text{det}}\right| < 0.8$, less than 0.46 for jets in the endcap region $1.5 < \left|\eta_{\text{jet}}^{\text{det}}\right| < 2.5$, and less than 0.4 for all other jets. Jets in the region $0.85 < \left|\eta_{\text{jet}}^{\text{det}}\right| < 1.25$ are allowed to have CHF < 0.6 is at the same time the number of cells that contain 90% of the jet energy is less than 20. This cut is aimed at removing jets dominated by noise originating in the coarse hadronic calorimeter.
- The jet must be confirmed by level 1 trigger information. This cut is defined by the ratio

$$L1_{\text{ratio}} = \frac{p_T^{\text{from L1 readout}}}{p_T^{\text{from precision readout}}},$$

  where $p_T^{\text{from precision readout}}$ is the vector sum from a jet's tower p_Ts from the precision readout, excluding the coarse hadronic layers and $p_T^{\text{from L1 readout}}$ is the scalar $p_T$sum in a cone of radius $\Delta\mathcal{R} = 0.5$ from the 100 most energetic L1 towers in the event. A jet must satisfy

  - $L1_{\text{ratio}} > 0.5$, or
  - $L1_{\text{ratio}} > 0.35$ and $p_T < 15$ GeV and $1.4 < \left|\eta_{\text{jet}}^{\text{det}}\right|$ (end cap), or
  - $L1_{\text{ratio}} > 0.1$ and $p_T < 15$ GeV and $3.0 < \left|\eta_{\text{jet}}^{\text{det}}\right|$ (forward)
  - $L1_{\text{ratio}} > 0.2$ and $p_T \geq 15$ GeV and $3.0 < \left|\eta_{\text{jet}}^{\text{det}}\right|$ (forward).

4. OVERVIEW OF THE JET ENERGY SCALE CORRECTION PROCEDURE

The goal of the jet energy scale correction is to relate, on average, the jet energy measured in the detector to the energy of the final state particle jet. The particle jet energy $E_{\rm jet}^{\rm ptcl}$ can be obtained from the measured jet energy $E_{\rm jet}^{\rm meas}$ via the following relation:

$$E_{\rm jet}^{\rm ptcl} = \frac{E_{\rm jet}^{\rm meas} - E_{\rm O}}{R_{\rm jet} S_{\rm jet}} \tag{5}$$

where:

- $E_{\rm O}$ represents an offset energy, which includes contributions from noise (both electronic and from radioactive decay of the uranium absorber), additional $p\bar{p}$ interactions and previous crossings (pile-up). The physics underlying event, defined as the energy contributed by spectators to the hard interaction, is considered as part of the high-p_T event and therefore not subtracted. The offset energy depends on the jet cone radius ($\mathcal{R}_{\rm cone}$), jet detector pseudorapidity ($\eta_{\rm jet}^{\rm det}$), number of reconstructed primary vertices ($n_{\rm PV}$) and instantaneous luminosity (L). *(The definition of $\eta_{\rm jet}^{\rm det}$ is: "one tenth of the E_T-weighted jet position in the calorimeter". In practice:* $0.1 \times {\rm TMBJet : detEta()}$*.)*
- $R_{\rm jet}$ represents the energy response of the calorimeter to particle jets, which is smaller than unity, due to energy lost in material before the calorimeter as well as uninstrumented regions between modules, the lower response of the calorimeter to hadrons as compared to electrons or photons, and module-to-module inhomogeneities. The jet response is a function of jet energy. It also depends on $\mathcal{R}_{\rm cone}$, since particles near the jet core have higher energy and thus higher response than particles near the jet boundary, and $\eta_{\rm jet}^{\rm det}$, due to the non-uniformity of the calorimeter response, especially in the ICR.
- $S_{\rm jet}$ represents a correction for the fraction of energy deposited outside the jet cone from particles belonging to the particle jet, as a result of the development of showers in the calorimeter and the finite calorimeter cell size (detector showering). It also corrects for the fraction of energy deposited inside the jet cone from particles not belonging to the particle jet. Typically the net correction is smaller than unity. It depends strongly on $\mathcal{R}_{\rm cone}$ and $\eta_{\rm jet}^{\rm det}$, and only mildly on jet energy.

It should be pointed out that the terms in Eq. 5 refer to the true values of the corrections. In practice, the offset, response and showering corrections that are measured represent only estimators of the true corrections, and thus are affected by a number of biases which need to be explicitly corrected for, in order to ensure the particle jet energy is recovered.

4.1. True Corrections

Let us first examine the definition of the *true corrections* discussed in the previous section. The particle jet energy is defined as the sum of energies of all stable particles belonging to the particle jet:

$$E_{\rm jet}^{\rm ptcl} = \sum_{\rm i \in ptcljet} E_{\rm i}. \tag{6}$$

The measured jet energy receives contributions from particles both inside and outside the particle jet, as well as offset energy:

$$E_{\rm jet}^{\rm meas} = \sum_{\rm i\in ptcljet} E_{\rm i}^{\rm meas} S_{\rm i} + \sum_{\rm i\notin ptcljet} E_{\rm i}^{\rm meas} S_{\rm i} + E_{\rm O} \tag{7}$$

where $E_{\rm i}^{\rm meas}$ is the visible calorimeter energy from particle i and $S_{\rm i}$ is the fraction of such energy contained within the calorimeter jet cone. Therefore, the *true offset* correction is defined as the energy $E_{\rm O}$ such that:

$$E_{\rm jet}^{\rm meas} - E_{\rm O} = \sum_{\rm i\in ptcljet} E_{\rm i}^{\rm meas} S_{\rm i} + \sum_{\rm i\notin ptcljet} E_{\rm i}^{\rm meas} S_{\rm i}. \tag{8}$$

It should be noted that $E_{\rm O}$ includes also the extra energy that gets above the cell threshold, and thus becomes visible, as a result of the combined effect of the offset and jet energy added to each cell. Or, in other words, after subtracting the *true offset*, the resulting energy is that inside the calorimeter jet cone in absence of any noise, pile-up or multiple interaction effects.

The *true response* correction is intuitively defined as the ratio of visible energy for particles from the particle jet (which includes energy contributions beyond the calorimeter jet cone boundary), to the incident particle jet energy (given by Eq. 6):

$$R_{\rm jet} = \frac{\sum_{\rm i\in ptcljet} E_{\rm i}^{\rm meas}}{E_{\rm jet}^{\rm ptcl}}. \tag{9}$$

In order to satisfy Eq. 5, the *true showering* correction is necessarily defined as:

$$S_{\rm jet} = \frac{\sum_{\rm i\in ptcljet} E_{\rm i}^{\rm meas} S_{\rm i} + \sum_{\rm i\notin ptcljet} E_{\rm i}^{\rm meas} S_{\rm i}}{\sum_{\rm i\in ptcljet} E_{\rm i}^{\rm meas}} \tag{10}$$

and represents a correction from the visible energy inside the calorimeter jet cone, resulting from particles both inside and outside the particle jet, to the total (i.e. regardless of the jet cone) visible energy resulting from the particle jet.

4.2. Estimated Corrections

As already indicated, the jet offset, response and showering corrections can be estimated in data, and are represented by $\hat{E}_{\rm O}$, $\hat{R}_{\rm jet}$ and $\hat{S}_{\rm jet}$. A priori, the corrected jet energy would be given by Eq. 5, with the *true corrections* replaced by the *estimated corrections*:

$$E_{\rm jet}^{\rm corr} = \frac{E_{\rm jet}^{\rm meas} - \hat{E}_{\rm O}}{\hat{R}_{\rm jet}\hat{S}_{\rm jet}}. \tag{11}$$

But because the estimated corrections suffer from a number of biases, the corrected jet energy as given by Eq. 11 can differ by several percent from $E_{\rm jet}^{\rm ptcl}$. Suitable bias corrections are derived in Monte Carlo (MC) to correct on average the estimated corrections to the true ones.

Therefore, the final corrected jet energy is given by the modified expression:

$$E_{\mathrm{jet}}^{\mathrm{corr}} = \frac{(E_{\mathrm{jet}}^{\mathrm{meas}} - \hat{E}_{\mathrm{O}})k_{\mathrm{O}}}{\hat{R}_{\mathrm{jet}}k_{\mathrm{R}}\hat{S}_{\mathrm{jet}}} \tag{12}$$

where k_{O} and k_{R} represent the required bias corrections to offset and response, respectively. As will be discussed in Sect. 11, $\hat{S}_{\mathrm{jet}}$ is a-priori an unbiased estimator of the *true showering* correction, and no bias correction is required.

After these corrections, Eq. 12 should provide on average the correct energy of the particle jet.

5. DATA AND MONTE CARLO SAMPLES

This section gives an overview of the different data and MC samples used to determine the jet energy scale corrections.

5.1. Data Samples

Different data samples are required, either to deterrmine, or to validate the jet energy scale corrections. The following samples are used:

- **Minimum bias (MB)**: This sample is collected using the so-called "minimum bias trigger", which requires hits in the north and south luminosity counters, signaling the presence of a $p\bar{p}$ inelastic collision. It is used to measure the contribution from multiple interactions to the offset energy (see Sect. 6).
- **Zero bias (ZB)**: This sample is collected during beam crossings but without any trigger requirement, hence the name "zero bias". It is used to measure the contribution from noise and pile-up to the offset energy (see Sect. 6).
- **γ+jet**: This sample is collected using triggers requiring an isolated electromagnetic cluster with different transverse momentum threshold. It is used to measure the calorimeter response to a jet (see Sect. 8), intercalibrate the calorimeter response as a function of jet pseudorapidity (see Sect. 9), and determine the showering correction (see Sect. 11).
- **Dijet**: This sample is collected using triggers that require at least one jet with transverse momentum $p_{T\text{jet}} > 15$, 25, 45, 65, 95 and 125 GeV. It is used, together with the γ+jet sample described above, to intercalibrate the calorimeter response as a function of jet pseudorapidity (see Sect. 9).

These samples have been extracted from the complete Run IIa dataset, which corresponds to an integrated luminosity of approximately 1 fb^{-1}.

5.2. Monte Carlo Samples

Since jet energy scale corrections must be determined for MC separately, the following samples have been generated using PYTHIA 6.323 [4] with CTEQ6L1 [6] parton distribution functions:

- **γ+jet**: This sample includes $2 \to 2$ direct photon production processes ($p\bar{p} \to q\gamma + X$ and $p\bar{p} \to \gamma g + X$) and has been generated at different thresholds for the transverse momentum of the outgoing partons: $\hat{p}_T > 5$, 10, 20, 40, 80, 160, 320 and 640 GeV.
- **Dijet**: This sample includes the inclusive $2 \to 2$ parton processes ($p\bar{p} \to q\bar{q} + X$, $p\bar{p} \to qg + X$ and $p\bar{p} \to gg + X$) and has been generated in different bins for the transverse momentum of the outgoing partons: $\hat{p}_T$: 5-10, 10-20, 20-40, 40-80, 80-160, 160-320 and >320 GeV.
- **Dijet (γ-like)**: This sample includes the inclusive $2 \to 2$ parton processes ($p\bar{p} \to q\bar{q}+X$, $p\bar{p} \to qg+X$ and $p\bar{p} \to gg+X$) and has been generated in different bins for the transverse momentum of the outgoing partons: $\hat{p}_T$: 5-10, 10-20, 20-30, 30-40, 40-60, 60-80, 80-120,

120-1600 and 160-320 GeV. A number of cuts on the generated particles are applied in order to enrich the sample in jets faking photons. This sample is mainly used to study and correct for the dijet background contamination in the γ+jet sample in data.

(The generator-level selection cuts follow the procedure discussed in Sect. 4.1 of Ref. [7]. A large QCD dijet sample had been used to select EM-like jets satisfying rather loose requirements (EMF$\geq$ 0.90, iso$\leq$ 0.15). By studying the particle-level properties of those jets, the following variables [7] where used to enrich the content of EM-like jets:

- *minimum p_T of the electron or photon in a cone of $\mathcal{R}_{\rm cone} < 0.2$ (R02) around the EM cluster's centroid: 0.05*`CKIN(3)` *(`CKIN(3)` represents the minimum $\hat{p}_T$ for the inclusive $2 \rightarrow 2$ parton process defined in the rest frame of the hard interaction);*
- *minimum fraction of the scalar sum of p_T of all particles in R02 contributed by electrons/photons: 0.5;*
- *maximum fraction of the scalar sum of p_T of all particles in R02 contributed by hadrons: 0.4;*
- *maximum p_T of the most energetic hadron in R02: 14 GeV.*

Since the actual photon selection used for the JES determination is significantly tighter than EMF$\geq$ 0.90, iso$\leq$ 0.15, no significant biases are expected in the preselected QCD dijet sample using the above cuts. This was explicitly confirmed by finding good agreement in the estimated sample purity from a EM-like enriched QCD dijet MC sample using the above cuts, and from a large inclusive (unbiased) QCD dijet MC sample [8].)

PYTHIA is used to compute the leading order (in QCD) matrix elements for each of the above samples, as well as simulate the underlying event. For the latter, which includes the contribution from beam remants and multiple parton interactions, only phenomenological models exist. We use the so-called "PYTHIA TUNE A" [9], which was optimized to describe CDF Run I data. Fragmentation, hadronization and particle decays are also handled by PYTHIA.

After generation, events are processed through the GEANT [10] based simulation of the DØ Run II detector. In order to achieve a more realistic simulation of noise, pile-up and multiple interactions, the digitized signals from zero bias (ZB) data events are overlaid on the MC. The default MC production at DØ has used overlaid ZB events with the symmetric $1.5\sigma_{\rm ped}$ zero-suppression cut applied at the calorimeter cell level ("suppressed ZB overlay"). In order to study the impact of this approximation, additional γ+jet and dijet samples have been generated without ZB overlay ("no ZB overlay"), as well as with ZB overlay without the $1.5\sigma_{\rm ped}$ zero-suppression cut ("unsuppressed ZB overlay"). Finally, the events are processed through the same reconstruction program as for real data.

(Unfortunately, the ZB samples used for MC overlay do not span the full run range in data, but are typically restricted to relatively short data taking periods. Furthermore, the overlay sample not always contain a luminosity spectrum representative of the full Run IIa dataset. To illustrate these points, Fig. 86 in Appendix A presents a comparison of the distributions of run number, instantaneous luminosity and primary vertex multiplicity for selected γ+jet events (following Sect. 8.1, except for the cut on $n_{\rm PV}$, which is relaxed to $n_{\rm PV} \geq 1$) in data, MC with unsuppressed ZB overlay and MC with suppressed ZB overlay. As it can be appreciated, the unsuppressed ZB overlay sample, which is used to derive some of the corrections for the data JES, provides a sufficiently realistic description of the luminosity profile in data.)

For each of the above samples, events generated in different $\hat{p}_T$ bins are properly weighed and combined to yield physical spectra.

5.3. Data Quality Requirements

TO BE FILLED IN.

6. OFFSET CORRECTION

The $p\bar{p}$ inelastic collisions can be classified as non-diffractive, single-diffractive and double-diffractive. A high-p_T interaction involves the break-up of both proton and antiproton, and therefore belongs to the category of non-diffractive $p\bar{p}$ collisions.

The goal of the offset correction is to subtract the energy not associated with the high-p_T interaction. The energy resulting from soft interactions involving the spectator partons that constituted the colliding proton and antiproton (underlying event), is considered to be part of the high-p_T interaction, and is therefore not subtracted out. *(This is in contrast with the Preliminary p17 JES, where the underlying event contribution was included as part of the offset correction. The justification for this change in procedure is twofold. First, it is not possible to consistently define the particle level without underlying event, since the underlying event tuning in* PYTHIA *involves adjusting parameters related to initial state radiation. Therefore, switching off the underlying event effectively changes the physics. Second, the underlying event is process-dependent, i.e. depends on which partons participated in the high-p_T interaction, at which scale, etc, and a-priori can not be measured in a control samples such as e.g. MB events. Fig. 96 in Appendix B illustrates this point by comparing the offset energy in events with exactly one primary vertex reconstructed, between MB events from data, and $Z \to \nu\bar{\nu}$ MC including ZB overlay. The offset energy in this case is dominated by the underlying event contribution, and it is found to be substantially higher in a hard-scatter event such as $Z \to \nu\bar{\nu}$.)* The excess energy to be subtracted out include contributions from electronic noise, uranium noise, pile-up and additional $p\bar{p}$ collisions (multiple interactions) within the same bunch crossing. Each of these contributions is briefly discusssed below.

In absence of beam crossings, the average energy per cell is not zero due to radiation from uranium decay and electronic noise. The electronic calibration corrects the average to zero, but the energy distribution is a-priori non-symmetric. Furthermore, as discussed in Sect. 3.2.1, cells with negative energy or with positive energy between $2.5\sigma_{\rm ped}$ and $4\sigma_{\rm ped}$ but no neighbor above $4\sigma_{\rm ped}$, are considered empty and not used for the reconstruction of calorimeter objects. Therefore, a net positive contribution of offset energy due to noise is expected.

The shaping time of the calorimeter preamplifier is longer than the bunch crossing time of 396 ns, so it is possible that the signal of interest may be formed on top of a signal from a previous bunch crossing. This causes an improper determination of the baseline to be subtracted electronically from the signal we are interested in. This effect is called pile-up, and depends on the instantaneous luminosity from previous bunch crossings, as well as the location of the present bunch crossing with respect to the beginning of the superbunch.

A crossing triggered as a high-p_T event can be modeled as the sum of one hard parton scattering and a ZB event at the same luminosity. Since only inelastic $p\bar{p}$ collisions can deposit significant energy in the detector, we disregard the elastic interactions that may take place during the ZB event. The number of additional $p\bar{p}$ inelastic interactions during the ZB event follows a Poisson distribution with average given by $\sigma_{\rm inel}\mathcal{L}_{\rm bunch}$, where $\sigma_{\rm inel}$ is the total $p\bar{p}$ inelastic cross section and $\mathcal{L}_{\rm bunch}$ is the integrated luminosity of the colliding bunch.

The contribution from noise, pile-up and multiple interactions is estimated using ZB and MB data samples, which are described in next section. This estimate, however, can differ substantially from the *true offset energy* (see Sect. 4.1), due to the different impact of zero suppression inside the jet as compared to the ZB and MB data samples. Such effect can only be estimated in MC and is also corrected for. In this sense, the offset correction, not only

subtracts the energy not associated with the high-p_T collision, but also the energy associated with the high-p_T collision that becomes visible as a result of the added offset energy in each calorimeter cell.

6.1. Sample Selection

As already discussed, the offset correction is defined to include only contributions from noise, pile-up and multiple interactions, which are estimated using samples of ZB and MB events.

Minimum bias events are collected at a rate of approximately 0.5 Hz, based on the MB trigger. The MB trigger requires a simultaneous hit in the north and south Luminosity Monitors (LM), signaling the presence of an inelastic $p\bar{p}$ interaction. This sample is dominated by soft interactions and is used to estimate the contribution from multiple interactions to the offset energy.

Zero bias events are collected at a rate of approximately 0.5 Hz, corresponding to beam crossings and without any trigger requirement. Therefore, they represent a truly unbiased measurement of the energy in the calorimeter regardless of the nature of the $p\bar{p}$ interaction. By selecting events which did not fire the MB trigger (LM veto) or have any primary vertices reconstructed, this sample can be depleted on multiple interactions, and thus be used to estimate the contribution from noise and pile-up to the offset energy.

Both samples are selected applying a modified version of the data quality requirements (see Sect. 5.3), where events with bad muon runs are not excluded. In order to avoid biases in the determination of the offset energy, cells with large occupancy ($> 40\%$) in a given run are excluded.

(For a more detailed discussion on triggers and event selection see Appendix 1.)

6.2. Method

The average offset energy is estimated for each calorimeter ring in $i\eta$ (summing over all towers in $i\phi$), and as a function of n_{PV} and L, by adding the estimated contributions from noise and pile-up (NP), and multiple interactions (MI):

$$\hat{E}_{\mathrm{O}}^{\mathrm{ring}}(i\eta, n_{\mathrm{PV}}, L) = \hat{E}_{\mathrm{NP}}^{\mathrm{ring}}(i\eta, L) + \hat{E}_{\mathrm{MI}}^{\mathrm{ring}}(i\eta, n_{\mathrm{PV}}, L). \tag{13}$$

The NP contribution is expected to depend on L via the pile-up component. The MI contribution is mainly dependent on n_{PV}, assuming that every additional interaction contributes a reconstructed primary vertex in the event. It is also parameterized as a function of L in order to take into account a possible luminosity dependence of the primary vertex reconstruction efficiency. The primary vertex reconstruction algorithm was described in Sect. 3.1. In order to maximize the efficiency to identify multiple interactions, no cuts on minimum track multiplicity per vertex or $|z_{\mathrm{PV}}|$ are applied.

6.2.1. Noise and Pile-up

The average energy per $i\eta$ ring due to noise and pile-up, $\hat{E}_{\mathrm{NP}}^{\mathrm{ring}}$, is measured in ZB events by requiring a LM veto. Since the luminosity monitor is not 100% efficient, we additionally exclude events with any primary vertices reconstructed. The average energy for each $i\eta$ ring is parameterized as a function of L. Fig. 1 shows the average energy density per $i\eta$ ring for three different values of L. Dividing the energy by the ring area allows to better visualize the

$i\eta$ dependence, since for $|i\eta| > 32$ towers are larger in size. The bump in the $|i\eta|$=8-15 range corresponds to the poorly instrumented ICR, where the noise fluctuations are amplified by the large weight factors applied to convert ADC counts to GeV.

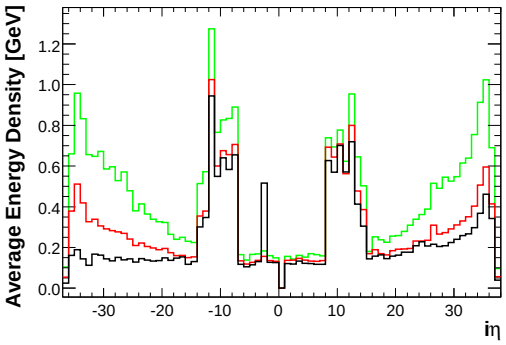

FIG. 1: Average energy density per $i\eta$ ring in ZB events selected as discussed in the text. Lines with different color correspond to a different L: 0.1×10^{32} cm^{2}s^{-1} (black), 0.5×10^{32} cm^{2}s^{-1} (red) and 1.2×10^{32} cm^{2}s^{-1} (green).

6.2.2. Multiple Interactions

The average energy per $i\eta$ ring due to multiple interactions, $\hat{E}^{\rm ring}_{\rm MI}$, is estimated from the average energy per ring measured in MB events, $\hat{E}^{\rm ring}_{\rm MB}$. The latter is parameterized as a function of $n_{\rm PV}$ and L. For every $i\eta$ and L bin, the average MB energy is measured as a function of $n_{\rm PV}$, for $n_{\rm PV} = 1 - 6$. Figure 2(left) shows the average energy per $i\eta$ ring as a function of $n_{\rm PV}$ for MB events collected at high luminosity ($L = 1.6 \times 10^{32}$ cm^{2}s^{-1}). As it can be appreciated, the $n_{\rm PV}$-dependence can be reasonably well described by a linear function. Therefore, a linear fit is performed and the result from the function used for any value of $n_{\rm PV}$. Fig. 2(right) shows the average energy density per $i\eta$ ring for MB events with different $n_{\rm PV}$, and corresponding to $L = 0.2 \times 10^{32}$ cm^{2}s^{-1}.

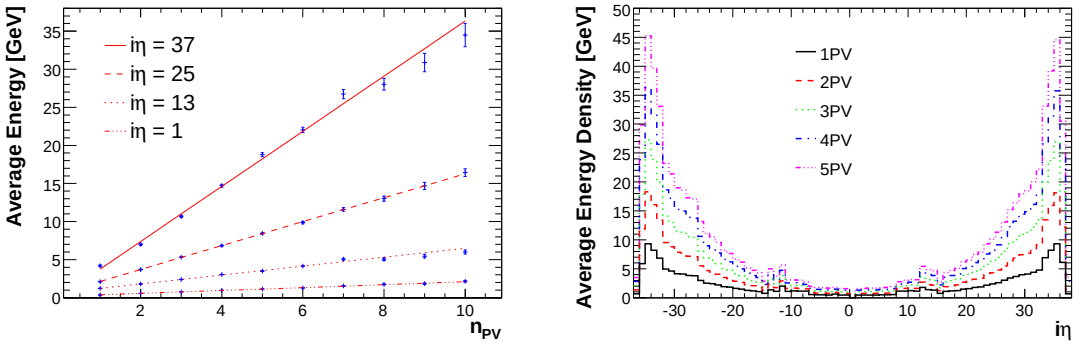

FIG. 2: Left: Average MB energy as a function of $n_{\rm PV}$ for different $i\eta$ rings. Right: Average MB energy density per $i\eta$ ring as a function of $n_{\rm PV}$.

Given an event with $n_{\rm PV}$ reconstructed primary vertices, we assume the total number of additional interactions is $n_{\rm PV}$-1. Therefore, we define the average energy per $i\eta$ ring due to multiple interactions as the difference between the MB energy for events with $n_{\rm PV}$ primary

vertices and the MB energy for events with exactly one primary vertex:

$$\hat{E}^{\rm ring}_{\rm MI}(i\eta, n_{\rm PV}, L) = \hat{E}^{\rm ring}_{\rm MB}(i\eta, n_{\rm PV}, L) - \hat{E}^{\rm ring}_{\rm MB}(i\eta, n_{\rm PV} = 1, L). \quad (14)$$

6.2.3. Total Jet Offset Energy

The estimated total offset energy for a jet takes into account the average energy per ring within the jet area, assuming the jet is a circle in (y, ϕ) space with radius $\mathcal{R}_{\rm cone}$. Therefore, this is an average correction that does not take into account the different shape of individual jets. The estimated total offset energy (appearing e.g. in Eq. 11) is given by:

$$\hat{E}_{\rm O}(\eta^{\rm det}_{\rm jet}, n_{\rm PV}, L) = \sum_{i\eta \in \mathcal{R}_{\rm cone}} \hat{E}^{\rm ring}_{\rm O}(i\eta, n_{\rm PV}, L) f^{\rm tower}(i\eta, \eta^{\rm det}_{\rm jet}), \quad (15)$$

where $\hat{E}^{\rm ring}_{\rm O}$ is given by Eq. 13 and $f^{\rm tower}$ represents the fraction of towers in a particular $i\eta$ ring which are within the jet cone.

6.3. Results

Figure 3 shows the estimated jet offset energy as a function of $\eta^{\rm det}_{\rm jet}$, for events with up to five primary vertices reconstructed. This estimate has been obtained using Eq. 15, separately for jets with $\mathcal{R}_{\rm cone} = 0.7$ and 0.5, and assuming $L = 0.3 \times 10^{32}$ cm^{2}s^{-1}, which represents the average instantaneous luminosity of the MB sample. As it can be appreciated, the offset energy for $\mathcal{R}_{\rm cone} = 0.5$ jets is roughly a factor of two smaller than for $\mathcal{R}_{\rm cone} = 0.7$ jets, in good agreement with the naive expectation based on the ratio of areas.

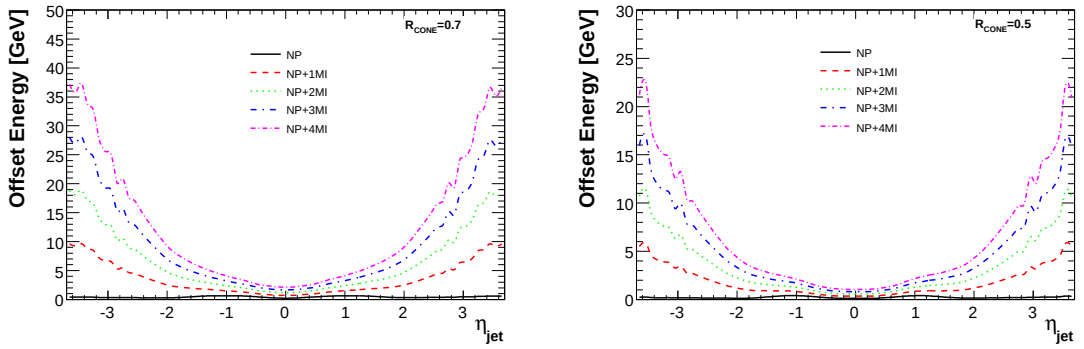

FIG. 3: Estimated total jet offset energy (in GeV) as a function of $\eta^{\rm det}_{\rm jet}$, for jets with $\mathcal{R}_{\rm cone} = 0.7$(left) and $\mathcal{R}_{\rm cone} = 0.5$(right). The different lines show the prediction for NP only ($n_{\rm PV} = 1$), as well as NP and MI ($n_{\rm PV} > 1$).

6.4. Zero-Suppression Bias Correction

As already indicated in Sect. 4.2, the total offset energy estimated from MB and ZB events can differ substantially from the true offset energy inside the jet. This is so because the calorimeter cells inside the jet already contain energy from the hard interaction and are therefore more likely to be above the zero-suppression threshold. As a result, the actual

offset energy deposited inside the jet is higher than what can be predicted based on the lower occupancy MB and ZB events. Such bias is expected to increase with jet energy.

Therefore, it is necessary to derive an average correction factor from the offset-corrected jet energy, to the actual jet energy in absence of noise, pile-up and multiple interactions. This correction factor can only be estimated in MC, by comparing the measured jet energy from the same high-p_T events processed with and without offset energy added.

For this purpose, we consider the same γ+jet MC events processed in three ways (see Sect. 5.2):

1. without ZB overlay: i.e. no offset energy from noise, pile-up and multiple interactions. This provides the reference level to correct to.

2. with (zero)suppressed ZB overlay: the derived correction factor will be applicable to the jet energy scale calibration in MC since, as explained in Sect. 5.2, the standard MC production at DØ used (zero)suppressed ZB overlay.

3. with (zero-)unsuppressed ZB overlay: the derived correction factor will be applicable to the jet energy scale calibration in data since that provides the most realistic description of the per-cell energy spectrum arising from noise, pileup and multiple interactions.

In order to derive such correction, the first step is to identify a set of back-to-back γ+jet events in the sample without ZB overlay. Such events are selected by requiring exactly one photon and one reconstructed jet satisfying $\Delta\phi(\gamma, \text{jet}) > 3.0$ rad. Next, each of the events in the selected set without ZB overlay is located within the samples with ZB overlay (both suppressed and unsuppressed), thus resulting in three subsets of events with common partonic origin but different overlay. Furthermore, only events where a reconstructed jet in the case of ZB overlay is matched within $\Delta\mathcal{R} < \mathcal{R}_{\text{cone}}/2$ with the only existing jet in the case of no ZB overlay, are kept. These subsets of common events are then used to compute the bias correction factor, defined as:

$$k_{\text{O}}^{\text{ZS}} = \frac{E_{\text{jet}}^{\text{meas,noZB}}}{E_{\text{jet}}^{\text{meas}} - \hat{E}_{\text{O}}}, \tag{16}$$

where the numerator is the average jet energy in the sample without ZB overlay, and the denominator is the average jet energy (of the matched jet) after offset correction in the sample with (zero-suppressed or zero-unsuppressed, as appropriate) ZB overlay. This correction is measured separately for $\mathcal{R}_{\text{cone}} = 0.7$ and 0.5 jets, in 0.4-wide bins of $\left|\eta_{\text{jet}}^{\text{det}}\right|$, and as a function of E', where E' represents an estimator of the true jet energy based on the measured photon p_T and the jet pseudo-rapidity (see Sect. 7.1.2). The correction factor is found to depend on the primary vertex multiplicity. The central value of the correction is estimated for the average n_{PV} of the sample, which corresponds to 1.5 (suppressed ZB overlay) and 1.8 (unsuppressed ZB overlay).

Figure 4 presents examples of the k_{O}^{ZS} correction factor for $\mathcal{R}_{\text{cone}} = 0.7$ jets for the suppressed ZB overlay case. The correction factor is shown for two different $\left|\eta_{\text{jet}}^{\text{det}}\right|$ bins and as a function of p'_T, defined as $E'/\cosh(\left(\eta_{\text{jet}}^{\text{det}}\right)_{\text{cob}})$, where $\left(\eta_{\text{jet}}^{\text{det}}\right)_{\text{cob}}$ stands for the value of $\eta_{\text{jet}}^{\text{det}}$ at the center of the bin. The different symbols correspond to different primary vertex multiplicity in the event. As it can be appreciated, the correction can be a few percent in magnitude, and differs by about 1-2% between the case of suppressed and unsuppressed ZB overlay. *(A complete set of plots can be found in Figs. 88-91 in Appendix B.)*

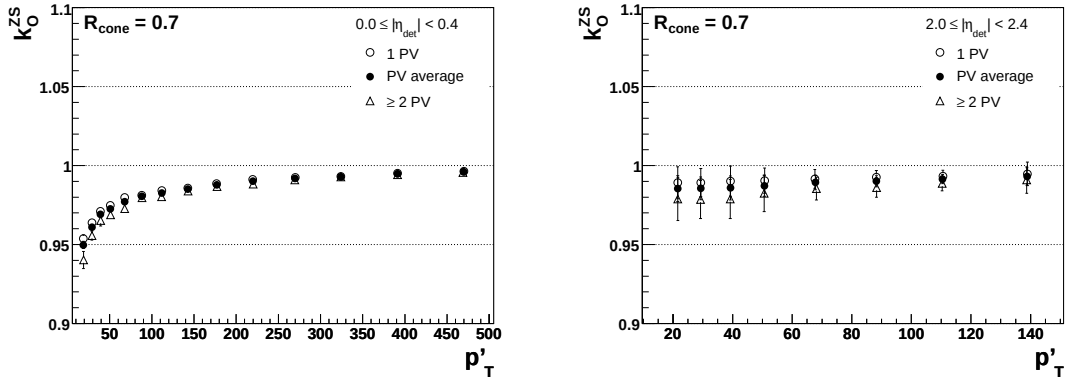

FIG. 4: Examples of $k_{\rm O}^{\rm ZS}$ correction factor for $\mathcal{R}_{\rm cone} = 0.7$ jets in the suppressed ZB overlay case. The different symbols correspond to different primary vertex multiplicity in the event.

6.5. Uncertainties

The offset correction measurement in data as given by Eq. 15 has a very high statistical precision, and the detailed parameterization in terms of $\eta_{\rm jet}^{\rm det}$, $n_{\rm PV}$ and L results in negligible systematic uncertainties. Such correction is found to be stable as a function of time to better than 5%, which is conservatively assigned as a systematic uncertainty. *(See Fig. 87 in Appendix B. This is believed to be a very conservative systematic uncertainty since the deviation from the nominal correction extreme analyses at DØ, i.e. using a very different trigger list mixture, might have is expected to be well below* 5%*.)*

Therefore, the uncertainties in the offset correction are completely dominated by the uncertainties in the $k_{\rm O}^{\rm ZS}$ correction factor. These uncertainties are illustrated in Fig. 5 for $\mathcal{R}_{\rm cone} = 0.7$ jets with $\left|\eta_{\rm jet}^{\rm det}\right| = 0.0$ and 2.0 in the suppressed ZB overlay case. *(A full set of plots for* $\mathcal{R}_{\rm cone} = 0.7$ *and 0.5 in the suppressed(unsuppressed) ZB overlay case are presented in Figs. 92 and 93 (Figs. 94 and 95) in Appendix B, respectively.)* The two main sources of systematic uncertainty are discussed below.

As shown in Fig. 4, there a non-negligible $n_{\rm PV}$-dependence which is currently not parameterized. The central value of the $k_{\rm O}^{\rm ZS}$ correction factor is estimated for the average $n_{\rm PV}$ in the MC samples with ZB overlay: $< n_{\rm PV} >= 1.5$ (suppressed) and $< n_{\rm PV} >= 1.8$ (unsuppressed). However, different physics analysis might have a different $< n_{\rm PV} >$ depending on the triggers and prescales involved. The corresponding systematic uncertainty is estimated as half of the difference in the value of $k_{\rm O}^{\rm ZS}$ for the case of $n_{\rm PV} = 1$ and the case of $n_{\rm PV} \geq 2$. For $n_{\rm PV} \geq 2$ the average $n_{\rm PV}$ is: $< n_{\rm PV} >= 2.3$ (suppressed) and $< n_{\rm PV} >= 2.6$ (unsuppressed). This is a conservative choice which should cover all relevant Run IIa physics analyses. For example, the heavily prescaled low p_T jet trigger `JT_15TT` has $< n_{\rm PV} >= 1.6$, while the unprescaled high p_T jet trigger `JT_125TT` has $< n_{\rm PV} >= 2.2$.

An additional source of systematic uncertainty on $k_{\rm O}^{\rm ZS}$ is related to the choice of $\Delta\mathcal{R}$ matching criteria between jets in the samples with and without ZB overlay. To estimate such uncertainty, the matching criterion in $\Delta\mathcal{R}$ is varied by ± 0.1 with respect to the nominal $\mathcal{R}_{\rm cone}/2$ and the correction factor estimated. The assigned systematic uncertainty is half of the difference between $k_{\rm O}^{\rm ZS}$ for both extremes.

(We have studied the dependence of the estimated offset on the z position of the selected primary vertex ($z_{\rm PV}$*) in the event. It should be pointed out that the leading dependence is*

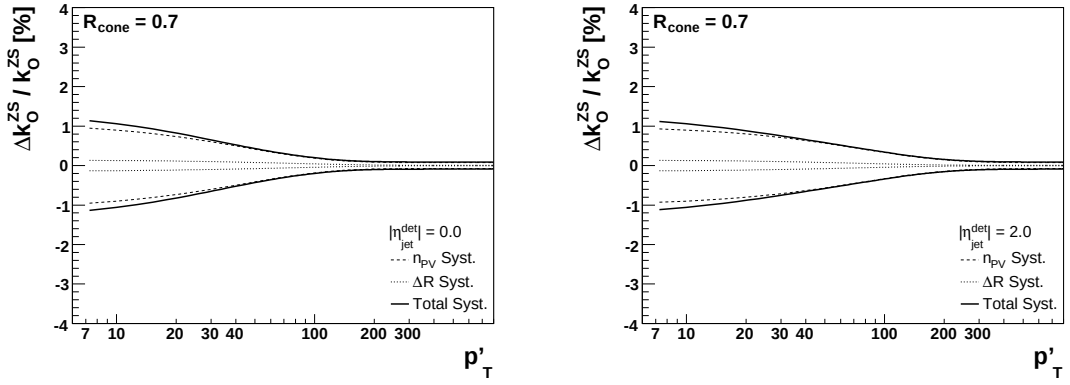

FIG. 5: Example of systematic uncertainties on the $k_{\rm O}^{\rm ZS}$ correction factor vs p'_T for $\mathcal{R}_{\rm cone} = 0.7$ jets in the suppressed ZB overlay case. Different plots correspond to different values of $\eta_{\rm jet}^{\rm det}$.

expected to be related to the underlying event corresponding to the hard-scatter. To illustrate this, the total offset energy as a function of $i\eta$ has been measured in MC for $Z \to \nu\bar{\nu}$ events with ZB overlay in the case of $n_{\rm PV} = 1$ (i.e. consisting only of the underlying event, noise and pileup). Such energy has been measured in three different intervals of $z_{\rm PV}$: $[-60, -30]$, $[-30, +30]$ and $[+30, +60]$ cm. This exercise has also been done for MB events in data with $n_{\rm PV} = 1$, which are already known not to be a good representation of the energy from the underlying event in hard-scatter process. In any case, it is useful to compare the result to that in $Z \to \nu\bar{\nu}$ MC. Fig. 97 in Appendix B shows the ratios of the measurements in the individual $z_{\rm PV}$ intervals to the average measurement (inclusive over $z_{\rm PV}$). As it can be appreciated, for both $Z \to \nu\bar{\nu}$ MC and MB data events, there is a north-south asymmetry depending on $z_{\rm PV}$: in the case of $z_{\rm PV}$ in the $[-60, -30]$ cm interval, the estimated deviation from the average is approximately $-(15-20)\%$ for $i\eta < -16$ and $+(15-20)\%$ for $i\eta > +16$. The sign of the effect is reversed in the case of $z_{\rm PV}$ in the $[+30, +60]$ cm interval. The fact that the energy in the calorimeter endcap closest to the hard-scatter primary vertex is smaller than in the opposite side, although at first sight looks counter-intuitive, can easily be understood. The key point is to remember that the p_T spectrum of particles from the underlying event is approximately flat in rapidity, which means that the energy spectrum is very forward-peaked. Therefore, for an event with $z_{\rm PV}$ in the $[-60, -30]$ cm interval, a forward positive $i\eta$ tower will receive more energy than its negative $i\eta$ counterpart.)

(At this point, it is worth pointing out that such direct effect is of no relevance to us since the offset correction does not subtract the underlying event. Nevertheless, we can examine any residual dependence in the MI contribution that could arise e.g. from a modified impact on the zero-suppression depending on $z_{\rm PV}$ for the hard-scatter. We have measured the MI contribution (see Eq. 14) from MB data event for the case of $n_{\rm PV} = 2$,4 and 6 (i.e. corresponding to 1,3 and 5 additional interactions, respectively). In this case the selected primary vertex plays the role of the "underlying event" from the hard-scatter, and the measurement is performed again in three different intervals of $z_{\rm PV}$: $[-60, -30]$, $[-30, +30]$ and $[+30, +60]$ cm. The corresponding plots can be found in Fig. 98 in Appendix B. As expected, the asymmetry persists but its magnitude is smaller ($\sim 6\%$ for 1 MI) and decreases with increased primary vertex multiplicity ($\sim 3\%$ for 5 MI). In any case, since no physics analysis we know of is sensitive to this kind of asymmetry, we are not currently assigning a systematic uncertainty.)

7. OVERVIEW OF THE RESPONSE CORRECTION

The response correction is numerically the largest correction in the jet energy scale calibration procedure, since it accounts for a number of rather sizable instrumental effects that distort the jet energy measurement. First, particles emerging from the hard interaction interact with the material before the calorimeter and lose a fraction of their energy, which can be rather significant for the lowest momentum particles. Furthermore, charged particles bend in the magnetic field and, depending on their p_T, can possibly never reach the calorimeter (e.g. central tracks with $p_T < 0.3$ GeV) or deposit their energy in calorimeter cells far away from the jet axis, and thus not be clustered by the jet algorithm. Most particles reaching the calorimeter (except for muons and neutrinos, which constitute a very small fraction of the jet energy) are completely absorbed and their deposited energy is transformed into a visible signal. The DØ calorimeter is non-compensating, which implies it has a higher and more linear response to electromagnetic particles ($e^{\pm}, \gamma$) than to hadrons ($e/h > 1$). The energy dependence of the calorimeter response to hadrons is nearly logarithmic as a result of the slow rise of the fraction of π^0's as a function of the incident hadron energy during the hadronic shower development, in combination with the non-compensating nature of the calorimeter [11]. Zero suppression can also significantly contribute to the non-linearity of response to hadrons, especially at low momentum. Finally, module-to-module inhomogeneities or poorly instrumented regions of the calorimeter (e.g. the ICR) can result in significant distortions to the measured jet energy.

Some of these instrumental effects (e.g. the calorimeter response to hadrons) are very difficult to model accurately enough in the MC simulation. As a result, data and MC have different response to jets, which require this correction to be determined separately for data and MC. While in MC it is a-priori possible to compute exactly the response correction by comparing the measured jet energy to the particle jet energy, this information is not available in data. The so-called Missing E_T Projection Fraction (MPF) method [12] was developed to measure the calorimeter response to jets in data. We make use of this method to measure the jet response in both, data and MC. Applying the MPF method to MC, where the true jet response can a-priori be known, allows to study the biases of the method and develop suitable correction procedures to be applied to data. In the next sections we give an overview of the MPF method, followed by a discussion on the expected biases and the corresponding corrections. Finally, we present the strategy to measure the jet response correction.

7.1. Missing E_T Projection Fraction Method

Let us consider a two-body process X+jet, where $X(= \gamma, Z$ or jet) is referred to as the "tag object", and the jet is the "probe object" whose response we are interested in estimating. As we will see, the MPF method can be used to estimate the calorimeter response of the probe jet relative to the response of the tag object. This fact will be exploited to intercalibrate the response of different calorimeter regions. In case the absolute response of the tag object is known, it will then be possible to estimate the absolute response of the probe jet.

At the particle level, the transverse momenta of the tag object ($\vec{p}_{T\mathrm{tag}}$) and of the hadronic recoil ($\vec{p}_{T\mathrm{recoil}}$) are balanced:

$$\vec{p}_{T\mathrm{tag}} + \vec{p}_{T\mathrm{recoil}} = 0. \tag{17}$$

Please note that the probe jet is part of the hadronic recoil but may not constitute all of it. As already discussed, in a real calorimeter the response of the tag object (R_{tag}) and of

the hadronic recoil (R_{recoil}) might be different (an obvious case is when the tag object is a photon), which results in a transverse momentum imbalance as measured by the calorimeter:

$$\vec{p}_{T\text{tag}}^{\,\text{meas}} + \vec{p}_{T\text{recoil}}^{\,\text{meas}} = -\vec{\not{E}}_T^{\,\text{meas}}, \tag{18}$$

where $\vec{p}_{T\text{tag}}^{\,\text{meas}} = R_{\text{tag}}\vec{p}_{T\text{tag}}$ is the measured transverse momentum of the tag object, $\vec{p}_{T\text{recoil}}^{\,\text{meas}} = R_{\text{recoil}}\vec{p}_{T\text{recoil}}$ is the measured transverse momentum of the hadronic recoil, and $\vec{\not{E}}_T^{\,\text{meas}}$ is the measured $\not{E}_T$ in the event (see Sect. 3.2.4).

From Eqs. 17 and 18 it is possible to derive the following expression:

$$\frac{R_{\text{recoil}}}{R_{\text{tag}}} = 1 + \frac{\vec{\not{E}}_T^{\,\text{meas}} \cdot \vec{n}_{T\text{tag}}}{p_{T\text{tag}}^{\text{meas}}}, \tag{19}$$

which shows that the response of the hadronic recoil relative to the response of the tag object can be estimated from the projection of $\vec{\not{E}}_T$ onto the tag object direction in the transverse plane ($\vec{n}_{T\text{tag}}$) and $p_{T\text{tag}}^{\text{meas}}$.

In the ideal case where the probe jet is identical to the hadronic recoil, then we can replace in Eq. 19 R_{recoil} by R_{jet}. However, among other effects, the presence of additional jets in the event (some of which might not even be reconstructed), make this idealized situation impossible to achieve in practice. By requiring exactly two reconstructed objects (tag and probe) back-to-back in azimuth, it will be possible to improve the approximation that $R_{\text{jet}} \simeq R_{\text{recoil}}$. However, as we will see, residual effects at the percent level will remain which we will need to correct for. Therefore, to avoid confusion with the true response of the particle jet (R_{jet}), we will refer to the jet response estimated with the MPF method as $R_{\text{MPF}}^{\text{sample}}$, where the superscript will be used to indicate which sample has been used to estimate it. The latter information is important since the MPF response is an event-wide quantity and therefore depends on the actual sample used (via e.g. the parton flavor composition, color flow, etc) as well as the corrections applied to the tag object p_T, which are also propagated to $\not{E}_T$.

7.1.1. Resolution Bias

As we have seen, Eq. 19 attributes the average $\not{E}_T$ imbalance in the event to differences in calorimeter response between the tag and probe objects. Therefore, for a precise determination it is important to eliminate any sources of $\not{E}_T$ imbalance which are unrelated to calorimeter response.

In particular, when measuring $R_{\text{recoil}}/R_{\text{tag}}$ in bins of $p_{T\text{tag}}^{\text{meas}}$, there is the possibility of a significant imbalance purely arising from resolution effects, which must then be corrected for. The dominant effect arises from the finite calorimeter energy resolution coupled with a steeply falling p_T spectrum. In this case, each $p_{T\text{tag}}^{\text{meas}}$ bin tends to contain on average more upward fluctuations from lower p_T than lower fluctuations from higher p_T. As a result, there is positive bias in the average $p_{T\text{tag}}^{\text{meas}}$ which translates into an artificial source of $\not{E}_T$ imbalance in the event. We refer to this effect as "resolution bias".

Fortunately, this bias can be precisely estimated if the tag object p_T spectrum and p_T resolution are known. For the sake of simplicity, let us assume a exponentially falling p_T spectrum, $f(p_T) \propto \exp(-\alpha p_T)$, and a Gaussian p_T resolution. In this case, the measured relative p_T imbalance can be estimated as:

$$\Delta p_T/p_T \simeq -\alpha(\sigma_{p_T}/p_T)^2 p_T, \tag{20}$$

where α is typically $\simeq 0.05-0.1$ for dijet events, and σ_{p_T}/p_T ranges from $\simeq 0.02$ for photons to $\simeq 0.05-0.30$ for jets.

Therefore, the expected resolution bias in the transverse momentum of the tag photon in γ+jet events is much smaller than 1% and can thus be neglected. In contrast, the expected resolution bias in the transverse momentum of the tag jet in dijet events can be as large as $3-15\%$ and will need to be explicitly corrected for. In order to evaluate this correction, the simplified expression in Eq. 20 is not used, but instead a detailed numerical calculation is performed taking into account the measured p_T spectrum in data dijet events as a function of $\eta_{\rm jet}^{\rm det}$ and a precise measurement of the jet energy resolution for a jet in the central calorimeter. Such correction procedure has been validated in MC and verified to work to within $\sim 0.5-1.0\%$. *(See Appendix C for a detailed discussion.)*

7.1.2. Absolute MPF Response

The absolute MPF jet response can be estimated from Eq. 19 using γ+jet events assuming the EM energy scale energy corrections have corrected the measured photon transverse momentum ($p_{T\gamma}^{\rm meas}$) to the particle level. In this case $R_\gamma = 1$ and Eq. 19 can be rewritten as:

$$R_{\rm MPF}^{\gamma^{\rm meas}+{\rm jet}} = 1 + \frac{\vec{\not{E}}_T^{\ \rm meas} \cdot \vec{n}_{T\gamma}}{p_{T\gamma}^{meas}}. \tag{21}$$

The most important dependence of the jet response we are interested in is jet energy. Unfortunately, as discussed in Sect. 7.1.1, the poor jet energy resolution will cause a bias in the estimated jet response when binning in terms of the measured probe jet energy. Therefore, in order to measure the energy dependence of the jet response with minimal impact from resolution effects, we use the E' energy estimator, defined as:

$$E' = p_{T\gamma}^{\rm meas}\cosh(\eta_{\rm jet}), \tag{22}$$

where $\eta_{\rm jet}$ is the jet pseudorapidity with respect to the reconstructed hard-scatter primary vertex in the event. The E' variable is strongly correlated with the particle level jet energy, since it is calculated using the photon transverse momentum and the jet direction, quantities which are measured more precisely than the jet energy itself. The energy dependence of the jet response is well described by a quadratic logarithmic function:

$$R(E') = p_0 + p_1\log(E'/E_0) + p_2\log^2(E'/E_0), \tag{23}$$

where $E_0 = 100$ GeV and p_i $(i = 0, 1, 2)$ are free parameters to be determined.

A detailed discussion on the measurement of the absolute response for jets in the central calorimeter region will be given in Sect. 8.

7.1.3. Relative MPF Response Versus Pseudorapidity

The MPF method applied to dijet events, with the tag jet well contained inside the central calorimeter ($\left|\eta_{\rm jet}^{\rm det}\right| < 0.4$ or CC) and the probe jet anywhere in the detector ($\eta_{\rm jet}^{\rm det}$), can be used to derive a relative correction factor relative to the CC response, used to intercalibrate the jet response versus $\eta_{\rm jet}^{\rm det}$.

In this case, the MPF response of a probe jet located at $\eta_{\rm jet}^{\rm det}$ relative to the response of the tag CC jet is defined as:

$$R^{\text{dijet}}_{\text{relMPF},\eta} = 1 + \frac{\vec{\not{E}}_T^{\text{ meas}} \cdot \vec{n}_{TCC}}{p_{TCC}^{\text{meas,off corr}}} \tag{24}$$

where $\vec{\not{E}}_T^{\text{ meas}}$ is the measured (uncorrected) $\not{E}_T$, $\vec{n}_{TCC}$ is the unit vector in the transverse plane pointing in the direction of the tag jet, and $p_{TCC}^{\text{meas,off corr}}$ is the measured transverse momentum of the tag jet corrected by offset. According to Eq. 19, this observable can indeed be interpreted as:

$$R^{\text{dijet}}_{\text{relMPF},\eta} \simeq \frac{R^{\text{dijet}}_{\text{MPF},\eta}}{R^{\text{dijet}}_{\text{MPF,CC}}}, \tag{25}$$

where $R^{\text{dijet}}_{\text{MPF},\eta}(R^{\text{dijet}}_{\text{MPF,CC}})$ denotes the MPF response of the probe(tag) jet. It is important to realize that in dijet events with a central-forward configuration, the forward jet has on average a higher energy than the central jet. As a result, $R^{\text{dijet}}_{\text{relMPF},\eta}$ is not expected to be equal to one even for a perfectly uniform calorimeter. Also, following the discussion in Sect. 7.1.1, resolution effects will cause the measured $R^{\text{dijet}}_{\text{relMPF},\eta}$ to deviate from one even in the case of two back-to-back central jets. These and other important considerations will be discussed in detail in Sect. 9.

7.2. MPF Response Biases

As already discussed in the previous section, an estimate of the absolute jet response can be obtained by applying the MPF method to selected γ+jet events, so that $\hat{R}_{\text{jet}} = R_{\text{MPF}}^{\gamma^{\text{meas}}+\text{jet}}$. It was also suggested that the MPF response is not an unbiased estimator of the true jet response and that explicit bias corrections are required. These corrections are estimated using MC which, despite the fact that it does not correctly predict the absolute jet response, it is expected to predict relative changes more reliably. The nature of these biases and how the corresponding corrections are determined is discussed below:

1. The selected γ+jet sample in data suffers from a non-negligible background contamination (especially at low p_T) from dijet events, where one of the jets is misidentified as a photon. In these background events there is a certain amount of hadronic energy around the misidentified photon that is undetected, and thus the measured photon p_T is too low resulting in a positive bias to R_{MPF}. On the other hand, even for pure γ+jet events, the measured photon p_T is overestimated with respect to the true (particle-level) photon p_T, which results in a negative bias to R_{MPF}. A correction factor, k^{γ}_{R}, is derived in MC to correct the measured MPF response of the mixture (signal+background) sample ($R^{\text{mixture}}_{\text{MPF}}$) to that of a pure γ+jet sample with the photon at the particle level ($R^{\gamma+\text{jet}}_{\text{MPF}}$):

$$k^{\gamma}_{\text{R}} = \frac{R^{\gamma+\text{jet}}_{\text{MPF}}}{R^{\text{mixture}}_{\text{MPF}}}. \tag{26}$$

   This correction is only very mildly dependent of $\mathcal{R}_{\text{cone}}$, and it is parameterized as a function of E' and $\eta^{\text{det}}_{\text{jet}}$.

2. Due to the different effect of zero suppression inside and outside the jet, the presence of offset energy in the event introduces a $\not{E}_T$ imbalance in the direction opposite to the

jet, which results in a positive bias to $R_{\rm MPF}$. A corresponding correction factor, $k_{\rm R}^{\rm ZS}$, is determined in γ+jet MC, by comparing the MPF response (using the particle-level photon) in the case of ZB overlay to no ZB overlay (i.e. no offset energy):

$$k_{\rm R}^{\rm ZS} = \frac{R_{\rm MPF}^{\gamma+{\rm jet,noZB}}}{R_{\rm MPF}^{\gamma+{\rm jet}}}. \tag{27}$$

This correction is estimated for $\mathcal{R}_{\rm cone} = 0.7$ and 0.5, and it is parameterized as a function of E' and $\eta_{\rm jet}^{\rm det}$. For each $\mathcal{R}_{\rm cone}$, it is determined separately for the case of suppressed and unsuppressed ZB overlay, making such correction applicable to MC and data jet energy calibrations, respectively. This bias is highly correlated with the corresponding bias on offset (see Sect. 6.4), and thus there is a large cancellation between $k_{\rm R}^{\rm ZS}$ and $k_{\rm O}^{\rm ZS}$ which has been verified numerically on full MC. However, the cancellation is not complete and both, $k_{\rm R}^{\rm ZS}$ and $k_{\rm O}^{\rm ZS}$, corrections are considered separately.

3. Finally, the MPF method provides an estimate of the response to the recoil against the photon, which can differ significantly from the *true jet response*, especially for forward jets. Such bias also depends sensitively on the topological cuts applied to select the γ+jet sample. A corresponding correction factor, $k_{\rm R}^{\rm topo}$, is determined in γ+jet MC without ZB overlay, and it is defined as the ratio of the *true jet response* (given by Eq. 9) to the MPF response (using the particle-level photon):

$$k_{\rm R}^{\rm topo} = \frac{R_{\rm jet}}{R_{\rm MPF}^{\gamma+{\rm jet,noZB}}}. \tag{28}$$

This correction is estimated for $\mathcal{R}_{\rm cone} = 0.7$ and 0.5, and it is parameterized as a function of E' and $\eta_{\rm jet}^{\rm det}$.

Finally, the total correction to the estimated jet response in Eq. 12 is given by:

$$k_{\rm R} = k_{\rm R}^{\gamma} k_{\rm R}^{\rm ZS} k_{\rm R}^{\rm topo}. \tag{29}$$

7.3. Outline of the True Response Estimation Procedure

Here we give a brief outline of the procedure used to estimate the true jet response, which will be discussed in detail in Sects. 8-10.

The first step is to estimate the MPF response for a CC jet in a pure sample of γ+jet events with the photon corrected to the particle level: $R_{\rm MPF,CC}^{\gamma+{\rm jet}}$. This is straightforward in the case of MC, since there is no dijet background contamination and the MPF response can be computed using the particle-level photon on an event by event basis. In the case of data, the MPF response for the selected γ+jet sample ($R_{\rm MPF,CC}^{\rm mixture}$) is computed, and then corrected for the effect of background and photon energy scale via $R_{\rm MPF,CC}^{\gamma+{\rm jet}} = R_{\rm MPF,CC}^{\rm mixture} k_{\rm R,CC}^{\gamma}$. In both, data and MC, the estimated $R_{\rm MPF,CC}^{\gamma+{\rm jet}}$ is then parameterized as a function of E' using the functional form given in Eq. 23. A discussion of this measurement and the related uncertainties is the main topic of Sect. 8.

In a second step, a correction $F_{\eta}^{\gamma+{\rm jet}}$ is determined to intercalibrate the MPF response in $\eta_{\rm jet}^{\rm det}$ with respect to the central calorimeter. This η-dependent correction is defined such that it satisfies:

$$R_{{\rm MPF},\eta}^{\gamma+{\rm jet}} = R_{\rm MPF,CC}^{\gamma+{\rm jet}} F_{\eta}^{\gamma+{\rm jet}}. \tag{30}$$

By combining selected γ+jet and dijet events it is posible to determine $F_\eta^{\gamma+\text{jet}}$ with high resolution in $\eta_{\text{jet}}^{\text{det}}$, and over a wide energy range. Combining the measurements in γ+jet and dijet events is not trivial since there are differences arising, among others, from the different parton flavor composition. In addition, in the case of data it is necessary to correct for the effect of the dijet background contamination in the γ+jet sample. A detailed discussion of the procedure used, the estimated correction and related uncertainties is given in Sect. 9.

Finally, the true response for a jet with detector pseudorapidity $\eta_{\text{jet}}^{\text{det}}$ is computed as:

$$R_{\text{jet},\eta} = R_{\text{MPF,CC}}^{\gamma+\text{jet}} F_\eta^{\gamma+\text{jet}} k_{\text{R},\eta}^{\text{ZS}} k_{\text{R},\eta}^{\text{topo}}, \tag{31}$$

where $k_{\text{R},\eta}^{\text{ZS}}$ and $k_{\text{R},\eta}^{\text{topo}}$ are the bias correction factors described above. These correction factors are presented in Sect. 10.

8. ABSOLUTE MPF RESPONSE CORRECTION

This chapter describes the determination of response correction for central calorimeter jets using the Missing E_T Projection Fraction method as described in the previous chapter. Central response provides the absolute scale for jet energy calibration. Forward jets are then calibrated with respect to this scale.

8.1. Sample Selection

The sample of γ+jet candidate events in data is collected by a set of triggers requiring at least one electromagnetic cluster with transverse momentum above certain threshold. *(See Table 10 in Appendix D.)* For the determination of the absolute response correction in MC, we use the γ+jet MC samples described in Sect. 5.2.

Further selection criteria are applied in order to extract a subset of events with suitable characteristics for the measurement of the jet response via the MPF method. These requirements are:

- Events with no reconstructed primary vertex or with more than two primary vertices are rejected. The main primary vertex associated with the hard interaction must satisfy the vertex selection criteria discussed in Sect. 3.1.
- Exactly one photon candidate with measured transverse momentum $p_{T\gamma}^{\rm meas} > 7$ GeV, satisfying the tight photon identification criteria (see Sect. 3.3). Such photon must be in the central calorimeter: $|\eta_\gamma^{\rm det}| < 1$.
- In order to avoid a possible bias caused by a jet triggering the event, we require $p_{T\gamma}^{\rm meas}$ to be in the high efficiency range of the particular trigger used to collect the event. In addition, we require a matching within $\Delta\mathcal{R} < 0.4$ between the photon candidate and the electromagnetic trigger tower at Level 1. This is not required in MC.
- Exactly one reconstructed jet (with $\mathcal{R}_{\rm cone} = 0.7$ or 0.5, as appropriate) satisfying the jet selection criteria described in Sect. 3.4. We refer to this jet as the "probe jet". No additional jet is allowed in the event, except if it matches the photon candidate within $\Delta\mathcal{R} < 0.2$, since the photon candidate can be also be reconstructed as a jet.
- The probe jet must have $\left|\eta_{\rm jet}^{\rm det}\right| < 0.4$, so that its core is well contained inside the central calorimeter.
- The photon and jet are required to be back-to-back in the $r-\phi$ plane, i.e. the difference of their azimuthal angle, $\Delta\phi(\gamma, {\rm jet})$, should be larger than 3.0 radians.
- Events with cosmic muon candidates are rejected. This is not required in MC.
- To further eliminate cosmics and other physics backgrounds, the following set of cuts on $\not\!\!E_T$ is applied depending on $p_{T\gamma}^{\rm meas}$:

$$\begin{aligned}
\not\!\!E_T &< 2.0\, p_{T\gamma}^{\rm meas} \text{ for } p_{T\gamma}^{\rm meas} < 15 \text{ GeV},\\
\not\!\!E_T &< 1.2\, p_{T\gamma}^{\rm meas} \text{ for } 15 < p_{T\gamma}^{\rm meas} < 25 \text{ GeV},\\
\not\!\!E_T &< 1.1\, p_{T\gamma}^{\rm meas} \text{ for } 25 < p_{T\gamma}^{\rm meas} < 50 \text{ GeV, and}\\
\not\!\!E_T &< 0.9\, p_{T\gamma}^{\rm meas} \text{ for } p_{T\gamma}^{\rm meas} > 50 \text{ GeV}.
\end{aligned}$$

The selected γ+jet events in data are affected by two types of backgrounds, physics and instrumental, which are discussed below.

8.1.1. Physics Backgrounds

The physics backgrounds are defined to include processes with one or more real electromagnetic clusters: $Z/\gamma^* \to e^+e^-$, $W(\to e\nu)$+jet and di-photon production. In the case of $Z/\gamma^* \to e^+e^-$, with one of the electrons misidentified as a photon, and the other electron misidentified as a jet, the measured MPF response is expected to be close to one. In the case of $W(\to e\nu)$+jet, with the electron misidentified as a photon, the neutrino will contribute additional $\not\!\!E_T$ in the jet hemisphere, thus reducing the measured MPF response. The combination of track veto (part of the photon identification criteria), stringent cut on $\Delta\phi(\gamma, \text{jet})$ and $\not\!\!E_T$ cuts reduce the contribution from the above processes to negligible levels. The expected bias on the MPF response was studied in MC and was estimated to be below 0.1%. *(See Fig. 111 in Appendix D.)*

8.1.2. Instrumental Background

The selected γ+jet sample in data suffers from a significant contamination of QCD dijet events, where one of the jets fluctuates to a leading π^0 (with $\pi^0 \to \gamma\gamma$) and thus is misidentified as a photon. The probability for a jet to be misidentified as a photon depends on the photon identification criteria but is typically very small. Nevertheless, this background contamination remains sizable, particularly at low $p_{T\gamma}^{\text{meas}}$, owing the large rate for QCD dijet production, with a cross section about three orders of magnitude larger than that for direct γ+jet production.

Figure 6 illustrates the estimated purity of the selected γ+jet sample as a function of E', separately for the three different photon identification criteria (loose, medium and tight) described in Sect. 3.3. *(Purity fits were performed simultaneously as a function of E' and $\eta_{\text{jet}}^{\text{det}}$. What is plotted in Fig. 6 are the fitted functions for $\eta_{\text{jet}}^{\text{det}} = 0$. The fitted purity and total uncertainty for the tight photon selection in the different $\eta_{\text{jet}}^{\text{det}}$ bins are shown in Fig. 118 in Appendix D.)* As it can be appreciated, the purity depends significantly on the photon identification criteria and improves for higher E'.

The purity was estimated using the γ+jet and dijet(γ-like) MC samples described in Sect. 5.2. Two methods were developed to estimate the sample purity: a template fit using the scalar sum of the transverse momenta of all tracks in a hollow cone of $0.05 < \Delta\mathcal{R} < 0.7$ within the direction of photon candidate (see Sect. 3.3), and the determination using directly MC leading-order cross section and selection efficinecy predictions for signal and background. The template fit method provides a more direct measurement of the sample purity. However it suffers from large uncertainties due to limited statistics in both data and MC samples. The second method provides smaller uncertainties however it relies on leading-order cross sections which may be quite different from true ones, especially for forward jets. Therefore it was used to determine only the shape of the purity dependence on E' and jet pseudorapidity, whereas the template fit estimate fixes the overall scale. A suitable uncertainty on the ratio of signal to background cross sections was chosen to cover for the differencies between both methods. An additional source of systematic uncertainty on the sample purity arises from uncertainties in the description of the fragmentation process in PYTHIA. This uncertainty was extracted from Ref. [15]. *(More detailed information about the purity determination of the γ + jet sample can be found in Appendix D1.)*

The presence of this instrumental background leads to a positive bias in the measured MPF response, since the "photon" is usually surrounded by hadronic activity resulting from the fragmentation of the original parton. This effect can be suppressed by using more stringent photon identification criteria, but it can not be completely eliminated. Therefore, we will explicitly correct the measured MPF response for this effect.

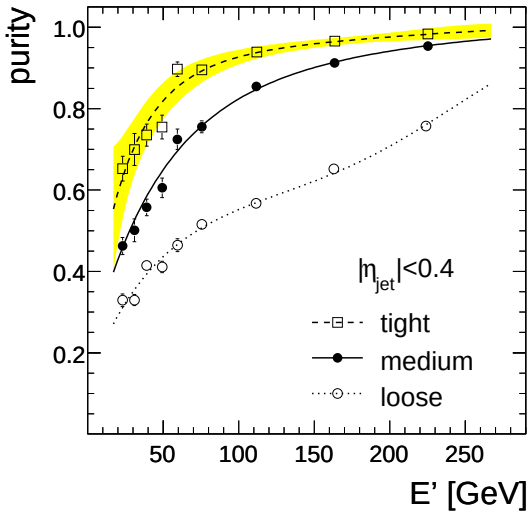

FIG. 6: Estimated purity of the selected $\gamma+$jet sample in data for $\left|\eta_{\rm jet}^{\rm det}\right| < 0.4$ and as a function of E'. The different curves correspond to different photon identification criteria: tight (dashed), medium (solid) and loose (dotted). Also shown is the total uncertainty band for the purity corresponding to the tight criteria. *(The points represent the estimates based by LO MC cross sections for signal and background scaled to match template-fit based purities, see an explanation in Appendix D1. In practice, only the loose photon points had to be scaled since the jets are central ($\eta_{jet} = 0$).)*

8.2. Method

The measurement of the absolute MPF response was discussed in Sect. 7.1.2. The goal is to estimate the MPF response for pure γ+jet events with the photon at the particle level. In the case of MC, this is achieved by using a modified version of Eq. 21:

$$R_{\rm MPF,CC}^{\gamma+{\rm jet,MC}} = 1 + \frac{\vec{\not{E}}_T^{\ \rm corr} \cdot \vec{n}_{T\gamma}}{p_{T\gamma}}, \tag{32}$$

where, on an event-by-event basis, the particle level photon transverse momentum, $p_{T\gamma}$, is used instead of $p_{T\gamma}^{\rm meas}$, and $\not{E}_T$ is corrected accordingly: $\vec{\not{E}}_T^{\ \rm corr} = \vec{\not{E}}_T^{\ \rm meas} + \vec{p}_{T\gamma}^{\rm meas} - \vec{p}_{T\gamma}$. In the case of data, the application of Eq. 21 results in a measurement of the MPF response which is affected by the bias in $p_{T\gamma}^{\rm meas}$, as well as the presence of the dijet background. We refer to this response measurement as $R_{\rm MPF,CC}^{\rm mixture}$. Following the discussion in Sect. 7.2, this measurement in data will be corrected by a suitable average correction, $k_{\rm R}^{\gamma}$, such that the desired MPF response measurement is obtained:

$$R_{\rm MPF,CC}^{\gamma+{\rm jet,data}} = R_{\rm MPF,CC}^{\rm mixture} k_{\rm R,CC}^{\gamma}. \tag{33}$$

The determination of the $k_{\rm R}^{\gamma}$ correction factor will be discussed in Sect. 8.2.1. After this correction, both data and MC measurements can be treated identically. The MPF response

is measured as a function of E', and fitted using the parameterization given in Eq. 23. Results are presented in Sect. 8.3.

8.2.1. Photon Corrections

As already discussed, the MPF response measurement in data must be corrected for the bias caused by the dijet contamination, as well as the fact that the reconstructed photon p_T is not at the particle level even for pure γ+jet events. Such corrections are determined using the same MC samples used to estimate the purity in Sect. 8.1.2. Since these biases are related to a miscalibration of the transverse momentum in the photon hemisphere and thus are independent of the jet algorithm, they are derived for $\mathcal{R}_{\rm cone} = 0.7$ jets and applied also to the measurement of the MPF response for $\mathcal{R}_{\rm cone} = 0.5$ jets.

In general, the measured MPF response in the selected γ+jet sample with a jet at $\eta_{\rm jet}^{\rm det}$ can be expressed as a linear combination of the MPF responses for γ+jet signal and dijet background, weighted by the respective fractions:

$$R_{{\rm MPF},\eta}^{\rm mixture} = \rho_\eta R_{{\rm MPF},\eta}^{\gamma^{\rm meas}+{\rm jet}} + (1-\rho_\eta) R_{{\rm MPF},\eta}^{\rm dijet}, \tag{34}$$

where both MPF responses are with respect to the measured photon p_T, and ρ_η is the sample purity (see e.g. Fig. 6). The relative difference between the MPF response of the mixture sample and the MPF response of the pure sample is given by:

$$c_{{\rm bckg},\eta} \equiv \frac{R_{{\rm MPF},\eta}^{\rm mixture}}{R_{{\rm MPF},\eta}^{\gamma^{\rm meas}+{\rm jet}}} - 1 = (1-\rho_\eta)\left(\frac{R_{{\rm MPF},\eta}^{\rm dijet}}{R_{{\rm MPF},\eta}^{\gamma^{\rm meas}+{\rm jet}}} - 1\right). \tag{35}$$

Fig. 7 compares $R_{\rm MPF,CC}^{\rm dijet}$ and $R_{\rm MPF,CC}^{\gamma^{\rm meas}+{\rm jet}}$ in the central calorimeter as predicted by the MC, for loose, medium and tight photon identification criteria. The fits of the relative differences in response appearing in the right side of Eq. 35 are represented by solid lines. The shaded regions shown around the solid lines correspond to the statistical error of the fit. *(To reduce the uncertainty due to the limited statistics of the dijet MC sample, the cut on the azimuthal angle between photon and jet was relaxed to $\Delta\phi > 2.8$ rad.)*

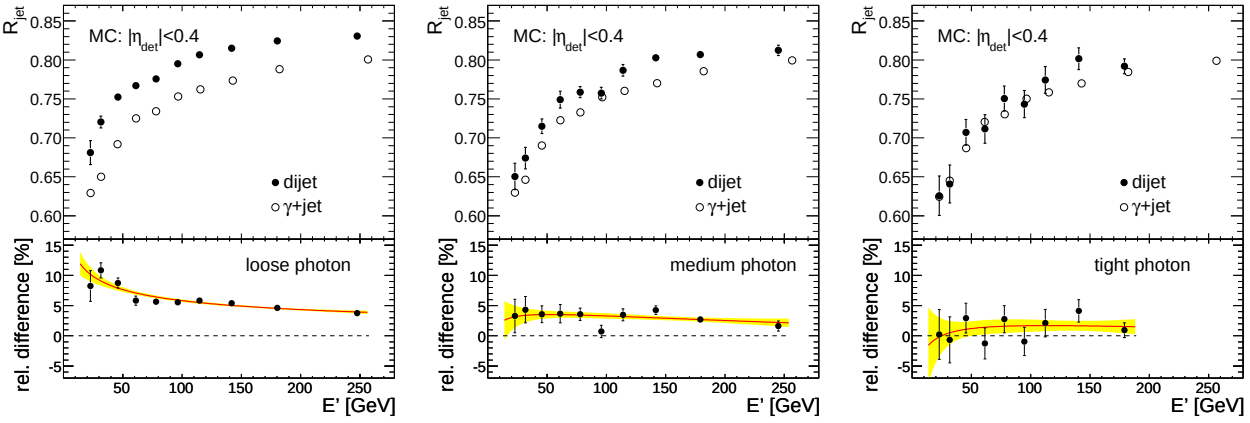

FIG. 7: Comparison of MPF response between signal γ+jet and dijet MC samples, for different photon identification criteria: loose (left), medium (center) and tight (right).

As it can be appreciated, the additional hadronic activity around the misidentified photon in the dijet sample reduces the $\not\!\!E_T$ in the direction of jet, thus increasing the measured

MPF response relative to that for the γ+jet sample. This effect is sizable for the loose photon identification criteria. Instead, the tight photon criteria effectively suppresses this additional hadronic activity, yielding a MPF response for the dijet sample which is $\leq 2\%$ larger than for the signal sample. In order to cover for potential imperfections in the MC simulations, an additional 1% systematic uncertainty was assigned to the relative difference between the response in the γ + jet and background dijet samples. This conservative choice covers for half of the background correction in case of the default tight photon selection. The final background correction $c_{\rm bckg}$ is shown as the dashed lines in Fig. 8 for the different photon identification criteria. The shaded areas around the dashed lines represent the total uncertainty on $c_{\rm bckg}$ from progagating the uncertainties on the different terms entering Eq. 35.

The second correction is related to the calibration of the photon energy scale. As discussed in Sect. 2.2, the absolute energy calibration of the electromagnetic calorimeter is obtained using electrons from $\mathrm{Z} \to \mathrm{e}^+\mathrm{e}^-$ decays. Corrections for the energy loss of electrons in the material in front of the calorimeter as a function of $\eta^{\rm det}$ and p_T are derived in MC and applied to electromagnetic objects in data. However, photons interact less with the material than electrons, and as a result the electron energy scale correction overcorrects the photon p_T relative to the particle level. This effect is particularly sizable at low p_T.

The relative difference between the MPF response of a pure γ+jet sample using the measured photon p_T, $R_{\rm MPF,CC}^{\gamma^{\rm meas}+{\rm jet}}$, and using the particle-level photon p_T, $R_{\rm MPF,CC}^{\gamma+{\rm jet}}$:

$$c_{scale} \equiv 1 - \frac{R_{\rm MPF,CC}^{\gamma+{\rm jet}}}{R_{\rm MPF,CC}^{\gamma^{\rm meas}+{\rm jet}}} \tag{36}$$

can be estimated in MC *(See Fig. 112 in Appendix D for additional information).* Photon interactions with material in front of calorimeter are not described with sufficient precision in the standard MC. The photon energy scale factor c_{scale}, represented in Fig. 8 by a dotted line, was therefore corrected for the difference in the reconstructed photon energy between the standard and a more detailed MC simulation *(See Appendix D2).*

Being directly related to the photon energy scale, this correction factor is independent of $\eta_{\rm jet}^{\rm det}$. The dashed area indicates the total uncertainty, which is discussed in Sect. 8.4. *(A more detailed discussion on the determination on photon energy scale uncertainty is then given in Appendix D2.)* As it can be appreciated, the correction is approximately -2% at $E' \sim 20$ GeV and it is slowly rising with the photon energy. This correction includes a -0.6% shift, unrelated to the photon energy scale, required to match the electron energy scales between data and MC. The dependence of this correction on the photon identification criteria is very small. *(See Fig. 116 in Appendix D for additional information.)*

Finally, the total correction $k_{\rm R}^{\gamma}$ in Eq. 33 can be expressed in terms of the background correction $c_{\rm bckg}$ and the photon energy scale correction c_{scale} as:

$$k_{{\rm R},\eta}^{\gamma} = \frac{1 - c_{\rm scale}}{1 + c_{{\rm bckg},\eta}} \approx 1 - \left(c_{\rm scale} + c_{{\rm bckg},\eta}\right). \tag{37}$$

The sum $c_{\rm scale} + c_{{\rm bckg},\eta}$ for $\eta_{\rm jet}^{\rm det} = 0$ is shown in Fig. 8 as a thick solid line, and represents the relative size of the total photon correction. The thin solid lines represent the total uncertainty, which is calculated by propagation of the corresponding uncertainties on the background and photon energy scale corrections.

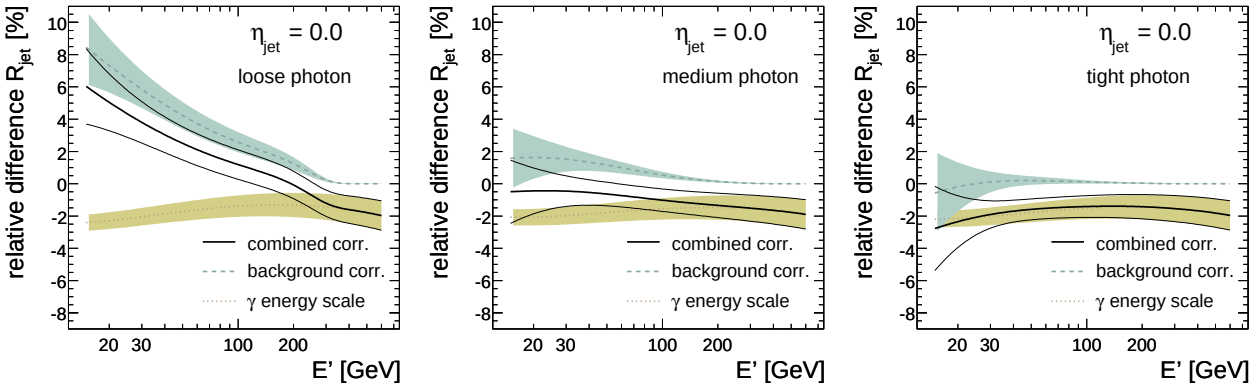

FIG. 8: Estimated photon corrections for the MPF response measurement in data: background (dashed), photon energy scale (dotted) and total (solid). Different plots correspond to different photon identification criteria: loose (left), medium (center) and tight (right).

8.3. Results

The estimated MPF response as a function of E' for $\mathcal{R}_{\rm cone} = 0.7$ jets is shown in Fig. 9 for MC (left) and data (right). *(Plots corresponding to* $\mathcal{R}_{\rm cone} = 0.5$ *can be found in Fig. 113 in Appendix D.)* In the case of MC, the MPF response is directly obtained using Eq. 32. In the case of data, the MPF response for the mixture sample is first computed using Eq. 21 and then corrected using Eq. 33. In both data and MC, the tight photon identification criteria have been used. An exception is the last point at $E' \sim 320$ GeV in data, which uses the loose photon criteria in order to increase the statistics and thus help reduce the uncertainty from extrapolation of the MPF response to higher energies. At such high E', the purity for the loose photon criteria is sufficiently high that the required background correction is $< 0.5\%$. Since jets do not enter directly the calculation of the MPF response, the dependence on $\mathcal{R}_{\rm cone}$ is expected to be very small. In fact, the MPF response for $\mathcal{R}_{\rm cone} = 0.5$ is about 0.5% higher at $E' \sim 100$ GeV than for $\mathcal{R}_{\rm cone} = 0.7$, in both data and MC. The measured MPF response is fitted using the parameterization in Eq. 23, and the fitted parameters are summarized in Table. 1.

Type	$\mathcal{R}_{\rm cone}$	p_0	p_1	p_2
MC	0.7	0.75336 ± 0.00068	0.05688 ± 0.00106	-0.00781 ± 0.00070
MC	0.5	0.75741 ± 0.00063	0.05760 ± 0.00098	-0.00944 ± 0.00067
data	0.7	0.7294 ± 0.0015	0.0761 ± 0.0033	-0.0134 ± 0.0027
data	0.5	0.7350 ± 0.0015	0.0766 ± 0.0034	-0.0155 ± 0.0028

TABLE 1: Fitted parameters for the MPF response parameterization given in Eq. 23.

(In general, the response follows the quadratic-logarithmic dependence quite well. However, there is a residual structure at $E' \sim 40 - 50$ *GeV of the order* $\pm 1\%$ *which is not present in MC and whose origin is currently not understood. Nevertheless, the shape distortion is within the claimed systematic uncertainty on the photon energy scale and it could possibly be explained by the difference of the real photon energy scale and the one obtained from MC. The following potential sources were investigated and ruled out: trigger bias, bias due to* $\not\!\!E_T$ *cut and* W*+jet contamination. None of them was found to be responsible for the apparent*

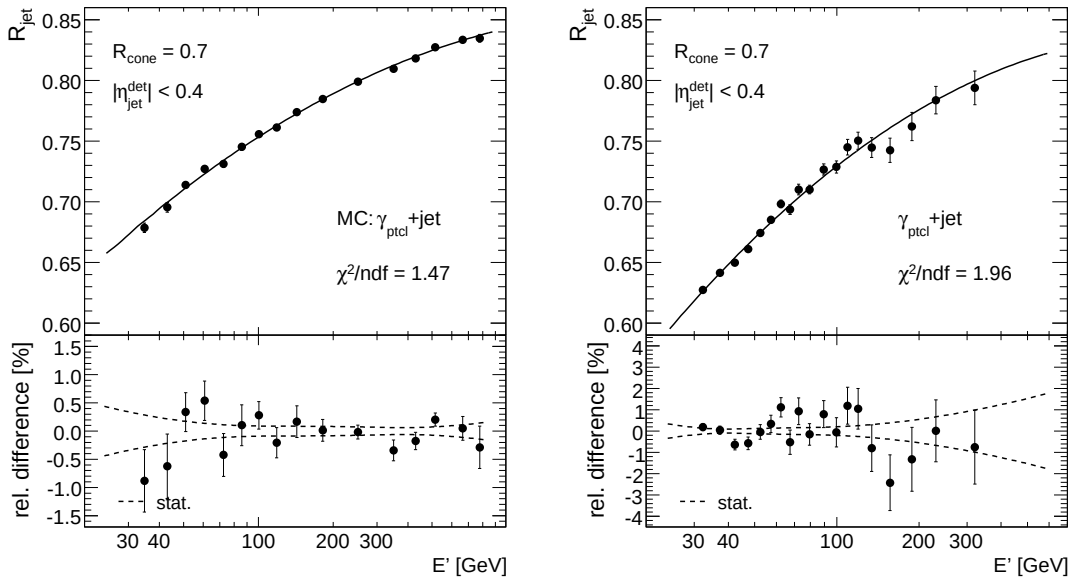

FIG. 9: Absolute MPF response for $\mathcal{R}_{\rm cone} = 0.7$ jets in MC (left) and data (right) as a function of E'. The solid line indicates the fit to the function in Eq. 23. The lower plots show the relative difference of the points with respect the fitted function, along with the statistical uncertainty from the fit (dashed line).

deviation from the quadratic-logarithmic fit at $E' \sim 40-50$ GeV. A possible trigger bias was studied by increasing the values of p_T thresholds for the selected triggers. The cut on $\not\!\!E_T$ for $p_{T\gamma} > 50$ GeV was found to affect only the highest E' bins as intended, and the effect of the cut is below 0.2% at $E' \sim 50$ GeV. MC studies suggest that the W+jet contamination is negligible. This was further confirmed in data by releasing and tightening the cut on the spatial track-match probability. Varying the cut from 10^{-6} up to 0.1 did not lead to any significant change in response at $E' \sim 50$ GeV.)

8.3.1. High Energy Extrapolation

To further reduce the MPF response uncertainty at high energies, a dedicated MC was developed. In this MC, the cell-level energy deposited by hadrons is scaled down in order to reproduce the jet response measured in data. The scaling factor depends on the true hadron energy $E_{\rm h}$ and is defined as $k(E_{\rm h}; A, B) = R(E_{\rm h}; A, B)/R_\pi^{\rm MC}(E_{\rm h})$, where $R_\pi^{\rm MC}$ is the single pion response measured in MC, parameterized as $R_\pi^{\rm MC}(E) = c_2\left[1 - a_2\,(E/E_0)^{m_2-1}\right]$, with $E_0 = 0.75\,{\rm GeV}$, $a_2 = 0.588$, $m_2 = 0.456$, and $c_2 = 0.870$. The chosen functional form was developed in Ref. [16], and has been shown to describe reasonably well available test beam data in the $\sim 10-375$ GeV range. The numerator of the scale factor would ideally represent the single pion response in data, and it is assumed to have the same functional form, but with modified parameters: $R(E) = c_1\left[1 - a_1\,(E/E_0)^{m_1-1}\right]$, with $a_1 = A \cdot a_2$, $m_1 = m_2 + B$, and $c_1 = C \cdot c_2$ and where (A, B, C) are coefficients to be determined. In case the single pion response in MC agrees with that in data, then $(A, B, C) = (1, 0, 1)$. While interpreting the scale factor in terms of a single pion response ratio is useful to choose a more physical energy parameterization, it is important to realize that it is simply serving the purpose of a well-motivated calibration procedure for the jet response in MC, and that the numerator, evaluated at the estimated (A, B, C) does not a-priori have to precisely agree with measurements of isolated pion response in data. As an example, a possible source of

discrepancy would be the different impact of zero suppression on the response for isolated pions as compared to pions inside jets.

The C parameter parameterizes the difference between the single pion response in data and MC for pion energies asymptotically going to infinity, i.e. in the region where the single pion response should match that for electrons. In this sense, the C parameter can be interpreted as a possible miscalibration between MC and data. The calorimeter calibration procedure used in data and MC results in an expected value of $C = 1$, to which a conservative 1.5% systematic uncertainty is assigned. *(This can be verified by comparing the reconstructed $Z \to e^+e^-$ invariant mass distribution from the uncorrected (i.e. before energy-loss and absolute electron energy scale corrections) calorimeter cluster energies in data and MC. See Appendix D3a.)*

The procedure to estimate (A, B, C) is described next. For a given choice of (A, B, C), the $\not\!\!E_T$ is recomputed and a new MPF response as a function of E' is derived in γ+jet MC without ZB overlay. *(Technically it is not possible to calculate the expected jet response for arbitrary values of (A, B, C). Rather than this we generated a set of MC samples scaning the grid from $A = 1.4 - 2.1$ in $\Delta A = 0.1$ steps, $B = -0.2 - 0$ in $\Delta B = 0.05$ steps, and $C = 0.95 - 1.05$ in $\Delta C = 0.05$ steps. The observed responses were then parametrized by cubic logarithmic fits for each generated point from the grid. The cubic term gives the fit more freedom than the quadratic logarithmic one. This is important for the fitting procedure, otherwise the fit without constrain on C would give, under the assumption of unambiguous mapping between (A, B, C) and the individual quadratic logarithmic fit parameters, exactly the same result as the standard quadratic logarithmic fit. In order to estimate the response for an arbitrary set of parameters (A, B, C), the cubic logarithmic fit parameters were then determined from the grid table using linear interpolation. As a second option, the cubic logarithmic fit parameters were also parametrized as quadratic functions of parameters (A, B, C). This case lead to the same results as the linear interpolation, both in terms of jet response and its error.)* The resulting new MC prediction, $R_{\rm MPF}^{\gamma+{\rm jet,noZB}}(A, B, C)$, corresponds to the scaled MPF response in absence of the zero-suppression bias (see Sect. 10.1), and therefore it must be divided by k_R^{ZS} in order to implement such effect. Then, a χ^2 fit is performed between the calibrated response in MC, $R_{\rm MPF}^{\gamma+{\rm jet,noZB}}(A, B, C)/k_R^{ZS}$, and the corrected (by photon energy scale and background) MPF response measurements in data shown in Fig. 9. The χ^2 is modified by adding a penalty term, $[(C - 1)/0.015]^2$, which constraints $C = 1$ within the assigned 1.5% uncertainty. In this fit, (A, B, C) are left floating. The estimated parameters $(\hat{A}, \hat{B}, \hat{C})$ determine the central value for the response and the covariance matrix is used to estimate the uncertainty.

The result of such fit in case of $\mathcal{R}_{\rm cone} = 0.7$ jet in data is presented in Fig. 10. The result of the fit is in good agreement with the quadratic logarithmic fit but it has significantly smaller uncertainty at high energy. At $E' = 600\,{\rm GeV}$, the statistical uncertainty is $\sim 0.4\%$. *(A similar result, in terms of MPF response, was obtained with a 2-parameter fit, where C was fixed to $C = 1$. Plots showing the fits in the $C = 1$ and unconstrained-C scenarios can be found in Fig. 123 in Appendix D3. As can be seen from the second plot, the jet response measurements themselves determine the parameter C to be consistent with one within 2.6% precision, wich results in slighly higher error of $\sim 1\%$ on response at $E' = 600\,{\rm GeV}$ as compared to the constrained case. In this sense, the a-priori knowledge on $C = 1 \pm 0.015$ helps to reduce the uncertainty on response at high energies.)*

The improvement results from the fact the MC-based prediction has a more solid physics foundation: it includes the energy-dependence of the quark and gluon fractions in γ+jet events, the fragmentation differences between quark and gluons, etc, relevant to predict the

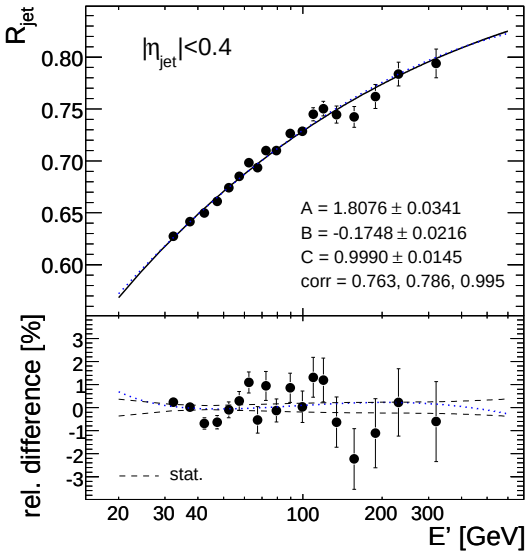

FIG. 10: Fitted MPF response measurement in data for $\mathcal{R}_{\rm cone} = 0.7$ jets using MC with parametrized single pion response. The dotted line represents the result of the quadratic logarithmic fit from Fig. 9.

gluon-dominated response at high energy. The distribution of pion energies in a jet evolves very slowly with jet energy. *(See Fig. 124 in Appendix D3.)* Less than 9% of pions in a 500 GeV jet has energy above 30 GeV. The average pion energy is $\sim$ 11GeV, which is still in the region where the single pion response is quite well determined from the jet response measurements available in data. A discussion of the systematic uncertainties related to this MC-based prediction is given in Sect. 8.4.

(Fig. 130 in Appendix D3 compares the derived single pion response corresponding to the fitted (A, B, C) parameters to the first preliminary direct measurements based on selected isolated tracks in minimum bias data (see Appendix D3b for more details on this measurement). The preliminary nature of the direct measurements in data must be stressed: issues related to possible trigger biases still need to be understood, as well as implement a more refined noise/background subtraction procedure. Measurements at low energy are significantly affected by noise, whereas measurements above $15 - 20$ GeV can suffer from a non-negligible electron contamination. Both effects would result in a positive bias to the estimated single pion response. Nevertheless, although not directly comparable, it is encouraging that two completely different approaches give a qualitatively similar answer. In the a-priori most robust region for the direct measurement ($\sim 5-10$) GeV, the agreement is excellent. In order to calculate the uncertainty on the fitted single pion response, a MC method was used in which we randomly generated (A, B, C) parameters to follow $L(A, B, C) = \exp(-(\chi^2 - \chi^2_{min})/2)$ distribution. We then determined the distribution of single pion responses at particular energies and from these distributions we computed the most probable values and the errors. The same procedure was adopted for the case of jet response. The result was identical with the fit from Fig. 10, both in terms of mean value and the errors.)

8.4. Uncertainties

In the case of the MPF response measurement in MC, the only uncertainty results from the statistical error of the fit, shown as the dashed line in Fig. 9(left).

The main sources of uncertainty in the MPF response measurement in data are shown in

Fig. 11 for $\mathcal{R}_{\rm cone} = 0.7$ jets. The uncertainties for $\mathcal{R}_{\rm cone} = 0.5$ jets are almost identical except the statistical error and the errors connected with the high energy extrapolation procedure which was performed only for cone 0.7 jets. They include the statistical uncertainty of the fit, the uncertainty on the photon energy scale, the uncertainty on the correction for the dijet background contamination, the uncertainty on high energy extrapolation and an uncertainty to account for the stability versus time of response *(See Appendix D4 for a discussion on the time-dependence of response. STILL NEED TO INCLUDE THIS UNCERTAINTY IN THE PLOTS, but it is already implemented in jetcorr. In the central region, it is anyway quite small, 0.1%, and it will not change the picture.)*.

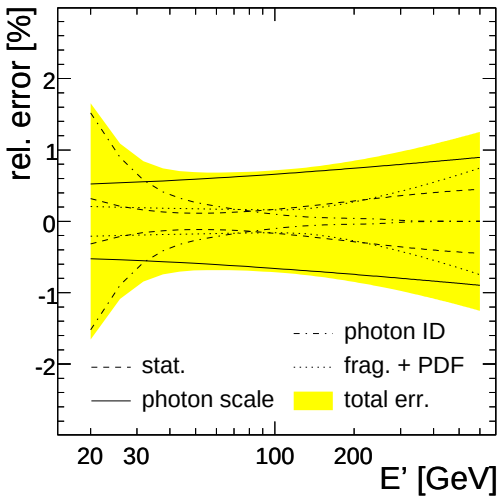

FIG. 11: Relative uncertainties on the MPF response measurement in data for $\mathcal{R}_{\rm cone} = 0.7$ jets.

As it can be appreciated, the main source of uncertainty is the photon energy scale in almost entire range of accessible energies. At high energies, the uncertainties related to the high energy extrapolation also contribute but they are still below the photon energy scale uncertainty. The statistical uncertainty, shown as the dashed curve in Fig. 11, is estimated taking into account the full covariance matrix from the fit. At low jet energies below 30 GeV, the uncertainty due to the dijet background correction becomes a dominant one.

The uncertainty on the photon energy scale correction, shown as the solid curve in Fig. 11, has two main contributions, which are added in quadrature. *(See Fig. 114 in Appendix D. More detailed information on the photon energy scale is provided in Appendix D2.)* The first contribution is the uncertainty on the determination of the absolute electron energy scale, which has been estimated to be 0.5% using the $Z \to ee$ mass peak. *(J. Stark, private communication.)* The second contribution is related to uncertainties in the MC description of the relative energy scale between photons and electrons, as a result of the different interaction with matter. It consists of two parts: one is related with the knowledge of material in front of calorimeter and the second one is related with the uncertainties in the simulation of photon-initiated showers in the material. The best estimate of additional material in front of the solenoid with respect to the detector simulation is $\sim 0.28X_0$. The effect of material was studied using MC with additional $0.17X_0$ and $0.36X_0$ material. The two cases are very conservative estimates already ruled out by the data *(J. Stark, private communication.)*. The uncertainty on the photon energy scale due to the material knowledge was estimated as

$1/\sqrt{12}$ of the full difference in the photon scale between the two extreme choices of additional material ($0.17X_0$ and $0.36X_0$). In addition, there is an uncertainty on the photon scale related to the accuracy of the detailed GEANT-based simulation of photon-initiated electromagnetic showers. While comparisons between data and MC on electron showers from J/Ψ and Z decays suggest the simulation is sufficiently accurate *(J. Stark, private communication.)*, the corresponding systematic uncertainty for photons is difficult to quantify. Currently, this uncertainty is conservatively estimated as $\sim$ 40% larger than the uncertainty due to the material description.

The uncertainty on the dijet background correction, shown as the dotted line in Fig. 11 is related to the uncertainty on $c_{\rm bckg}$ (see blue band in Fig. 8(right)), which has two components added in quadrature: purity and relative response between γ+jet and dijet MC events. *(See Fig. 115 in Appendix D.)* Ideally, the corrected MPF response in data should be independent of the photon identification criteria, despite the large differences in purity among them. Fig. 12 compares the MPF response in data for the different photon criteria, before (left) and after (right) the background correction. The observed residual differences after full correction are consistent with the assigned systematic uncertainty. Part of the observed difference between medium and tight criteria is unrelated to the background and can already be observed in pure γ+jet MC with the photon at the particle level. *(See Fig. 116 in Appendix D.)* This effect is believed to be caused by distortions in the hadronic activity in the photon hemisphere, which propagate to $\not\!\!E_T$, as a result of tightening the photon isolation. Such effect will be corrected later on by the topology bias correction (see Sect. 10.2), and therefore it does not represent an additional source of systematic uncertainty.

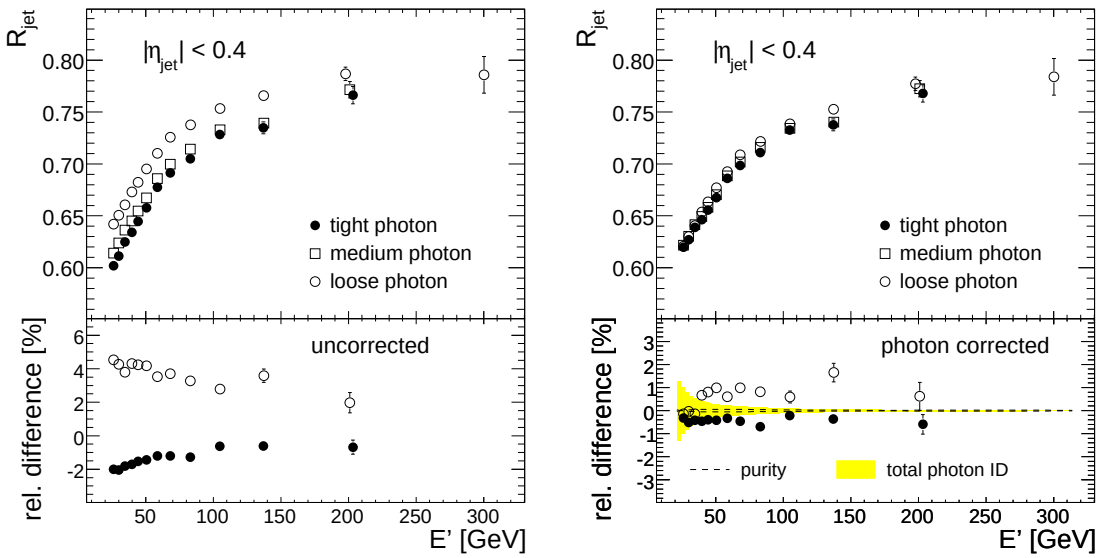

FIG. 12: Comparison of the MPF response in data for different photon identification criteria, before (left) and after (right) background corrections. The relative difference shown in the lower plots is with respect to the response for the medium photon criteria. The shaded region represents the total assigned systematic uncertainty for the dijet background correction in case of tight photon selection.

Finally, regarding the high energy extrapolation uncertainty, in addition to the statistical uncertainty from the fit in data discussed in Sect. 8.3.1, the following two sources of systematic uncertainty were considered: parton distribution functions (PDFs) and fragmentation model. The uncertainties are related to the dependence of the predicted hadron spectra at high energy on the parton flavor of jets as well as the modeling of the fragmen-

tation. *(Figure 125 in Appendix D3 summarizes the uncertainties affecting the high energy extrapolation of response.)*

It is well known that the different fragmentation of quarks and gluons result in differences in the spectra of hadrons within the jet, which in turn lead to a difference in jet response. Indeed, the jet response at $E' = 600$ GeV in $\gamma+q$ events is $\sim 2\%$ higher than for $\gamma+g$ events, as predicted using the full MC with the tuned single pion response. The predicted parton flavor content in high energy γ+jet events depends on the relative weight of the $q\bar{q}$ vs qg initial state, which is determined by the PDFs. The limited knowledge of the gluon PDF at high x results in an uncertainty in the parton flavor of the jet which must be taken into account. This uncertainty is estimated using CTEQ6.1M. The quark-jet fraction was calculated in PYTHIA for each of the individual 40 sets of PDFs and the resulting PDF uncertainty was calculated according to the CTEQ group prescription. The estimated quark-jet fraction at $E' \sim 600\,\text{GeV}$ is 0.1 ± 0.1. *(See Fig. 126 in Appendix D3.)* Given a particular prediction for the quark-jet fraction as a function of energy and the individual responses for $\gamma + q$ and $\gamma + g$ events, the corresponding jet response can be estimated. For example, the estimated difference between quark- and gluon-jet responses is about 2% at $E' = 600\,\text{GeV}$, so the 10% uncertainty on the quark-jet fraction translates into a 0.2% uncertainty on response. *(Figure 127 in Appendix D3 compares the MPF response in CC for γ+quark versus γ+gluon events in MC without ZB overlay, with the single pion response scaled down in order to better match the jet response in data.)* The uncertainty stays on the same level even at low energies where the smaller uncertainty on the quark-jet fraction is compensated by the increase in the difference between quark- and gluon-jet responses. *(See dash-dotted line in Fig. 125 in Appendix D3).*

The systematic uncertainty due to fragmentation is estimated by comparing the predicted jet response for the Lund model, implemented in PYTHIA, and the cluster model, implemented in HERWIG. The two models can lead to different hadron spectra inside the jet, and thus a different predicted response at high energy. This systematic uncertainty is estimated in particle-level MC by computing the jet response after applying to each hadron a realistic response function. For a more consistent comparison of the fragmentation model effect, the soft underlying event was switched off. Since precise measurements of the jet response in data exist for E' in the 40-100 GeV range, the predicted jet responses as a function of E' for PYTHIA and HERWIG are internormalized in the 40-100 GeV E' range, and the difference for $E' > 100$ GeV is assigned as the systematic uncertainty. This uncertainty is $\sim 0.8\%$ at $E' = 600$ GeV and decreases linearly to zero at $E' = 100$ GeV. *(See Fig. 128 in Appendix D3. Following the procedure discussed above, the fragmentation uncertainty was determined as the difference in response (right plot in Fig. 128) with respect to the constant line fit (left plot in Fig. 128) in the 40-100 GeV E' range.)*

8.4.1. Correlations

Preliminary proposal, how to treat correlations in the response uncertainty, is discussed in this section. All sources of error on absolute normalization are listed in Table 2 together with the proposal how to treat the correlation in jet energy. The errors were divided into two classes: fully correlated and fully uncorrelated. If the error has some partial correlation or if the correlation is not known, the source was clasified as fully uncorrelated.

Full error matrix of the statistical error is known and the correlation in energy can be provided. Giving the size of the error (0.4% out of full 1.3% error at $E' = 600\,\text{GeV}$) it is probably not worth. The proposal is to treat the statistical error as fully uncorrelated in

Source	rel. uncertainty			correlation in E
	20 GeV	100 GeV	600 GeV	
stat.	0.3%	0.3%	0.4%	treat as fully uncorrelated
electron scale	0.5%	0.5%	0.5%	fully correlated
material	0.1%	0.2%	0.5%	fully correlated
photonic shower	0.2%	0.3%	0.7%	treat as fully uncorrelated
purity	$< 0.1\%$	$< 0.1\%$	$< 0.1\%$	treat as fully correlated
R_{jet} for EM-like jets	1.5%	0.2%	$< 0.1\%$	treat as fully uncorrelated
fragmentation	0%	0%	0.8%	treat as fully correlated
PDF	0.2%	0.2%	0.2%	treat as fully uncorrelated
time stability	0.1%	0.1%	0.1%	fully correlated

TABLE 2: Sources of uncertainty on jet response and the correlation of the error in jet energy.

energy. Electron scale fixes the absolute energy normalization. The error therefore gives full correlation both in terms of jet energy and the pseudorapidity. Material uncertainties are treated as fully correlated. Remaining photon energy scale uncertainties has probably significant cross-correlation in energy as well, however these are not know. Therefore they are treated as fully uncorrelated. Error on purity is negligible and it is treated as fully correlated. The dominant uncertainty in photon identification correction is due to limitted statistics of the dijet background MC which is used to determine the difference in response between dijet background and $\gamma+$jet signal. Due to statistical nature of the uncertainty, the dijet response error is treated as fully uncorrelated. Fragmentation uncertainty was derived as a difference between too models. Such error gives full correlation across jet energy. Correlation in PDF uncertainty can be computed using CTEQ6.1M error machinery. However, due to small size, it is not worth and the error is treated as fully uncorrelated. Last source, the time stability, is naturally fully correlated in energy.

Fig. 13 shows the size of fully correlated (solid line) and uncorrelated (dashed line) errors. For most of the energies, both types of errors contributes equally. Only at low energies of $E' < 30\,\mathrm{GeV}$, the uncorrelated errors dominate.

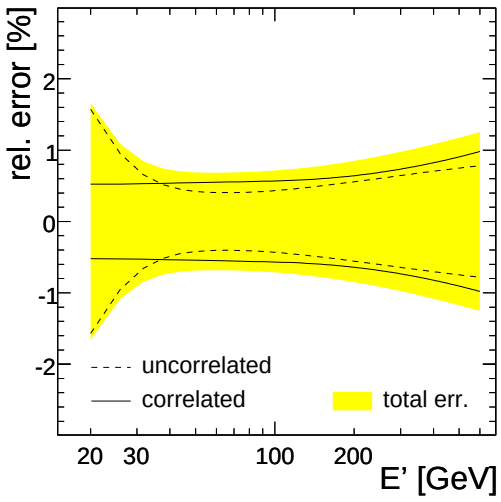

FIG. 13: Fully correlated (solid lines) and uncorrelated (dashed lines) part of the error on central calorimeter jet response.

9. RELATIVE MPF RESPONSE CORRECTION

Even after calibration, the DØ calorimeter exhibits a non-uniform response to jets as a function of $\eta_{\rm jet}^{\rm det}$. The jet response is rather uniform within the CC cryostat. However, in data (MC) the EC response is $\sim 15\%$ (10%) lower than the CC response. Another important contribution to this non-uniformity arises from the poorly instrumented inter-cryostat region ($0.8 < \left|\eta_{\rm jet}^{\rm det}\right| < 1.6$). As discussed in Sect. 2.1, in this region a substantial amount of energy is lost in the solenoid, cryostat walls, module end-plates and support structures. In particular, the $0.8 < \left|\eta_{\rm jet}^{\rm det}\right| < 1.2$ region presents the largest deviation in energy dependence of response with respect to the central calorimeter, due to the limited sampling of the jet energy and significant losses in dead material. In the $1.2 < \left|\eta_{\rm jet}^{\rm det}\right| < 1.4$ region, the system lacks electromagnetic calorimetry and the total depth drops below six interaction lengths. The goal of the relative MPF response correction is to make the MPF response uniform versus $\eta_{\rm jet}^{\rm det}$ and identical to the CC response. As already indicated, different calorimeter regions have different energy dependence of response, therefore this correction is not only a function of $\eta_{\rm jet}^{\rm det}$, but also energy.

The relative MPF response correction is estimated using samples of γ+jet and dijet events. The former allows a direct and consistent derivation of the MPF response relative to the central calorimeter (see Sect. 8). The latter brings the additional statistics required to measure this correction in fine bins of $\eta_{\rm jet}^{\rm det}$ and up to much higher energies than the γ+jet sample can reach. By contrasting and combining these two different physics samples, we attempt to reduce as much as possible both statistical and systematic uncertainties.

9.1. Sample Selection

The selection of γ+jet events is identical to that used for the absolute response measurement (see Sect. 8.1), except that the probe jet is not restricted to the central calorimeter.

Dijet events in data are collected using single jet triggers that require at least one jet with transverse momentum $p_{T\rm jet} > 15$, 25, 45, 65, 95 and 125 GeV. For the determination of the relative MPF response correction in MC, we use the dijet MC samples described in Sect. 5.2. The selection of dijet events closely follows the γ+jet selection, with one of the jets effectively playing the role of the photon. It includes the following requirements:

- Events with no reconstructed primary vertex or with more than two primary vertices are rejected. The main primary vertex associated with the hard interaction must satisfy the vertex selection criteria discussed in Sect. 3.1.

- Exactly two reconstructed jets (with $\mathcal{R}_{\rm cone} = 0.7$ or 0.5, as appropriate) satisfying the jet selection criteria described in Sect. 3.4. No jet which does not satisfy those criteria is allowed in the event.

- At least one of the jets has $\left|\eta_{\rm jet}^{\rm det}\right| < 0.4$, so that its core is well contained inside the central calorimeter. Such jet is referred to as "tag" whereas the other jet is referred to as "probe". If both jets have $\left|\eta_{\rm jet}^{\rm det}\right| < 0.4$ both possibilities for "tag" and "probe" assignments are considered.

- In order to avoid a trigger bias, the uncorrected transverse momentum of the tag jet in each jet trigger sample is required to be above a given threshold. Such lower threshold is also used as upper threshold for the previous (i.e. lower p_T) jet trigger, in order to ensure the statistical independence of the different samples. *(See Table 13 in Appendix E.*

The offline threshold cut is applied on the CC jet raw p_T after offset subtraction, and corresponds to the 98% efficiency point of the jet trigger turn on curve. No evidence of a trigger bias is observed.) This cut is not required in MC.

- The jets are required to be back-to-back in the $r-\phi$ plane, i.e. the difference of their azimuthal angle, $\Delta\phi(\text{jet}_{\text{probe}}, \text{jet}_{\text{tag}})$, should be larger than 3.0 radians.
- Events with cosmic muon candidates are rejected. This is not required in MC.
- To further eliminate cosmics, the ratio of missing E_T over leading jet p_T is required to be $\not\!\!E_T/p_{T\text{leading}-\text{jet}} < 0.7$.

9.2. Method

As discussed in Sect 7.3, the relative MPF response correction is designed to calibrate the jet response in a given calorimeter region to the jet response in the central calorimeter at the same energy.

This correction is evaluated up to $\left|\eta_{\text{jet}}^{\text{det}}\right| < 3.6$, using rather fine binning in $\eta_{\text{jet}}^{\text{det}}$, depending on the calorimeter region. In the case of data, the binning used is: 0.1 ($\left|\eta_{\text{jet}}^{\text{det}}\right| \leq 1.0$), 0.05 ($1.0 < \left|\eta_{\text{jet}}^{\text{det}}\right| \leq 1.8$), 0.1 ($1.8 < \left|\eta_{\text{jet}}^{\text{det}}\right| \leq 2.0$), 0.2 ($2.0 < \left|\eta_{\text{jet}}^{\text{det}}\right| \leq 2.4$) and 0.4 ($2.4 < \left|\eta_{\text{jet}}^{\text{det}}\right| \leq 3.6$). The binning used in MC is identical, except in the $1.0 < \left|\eta_{\text{jet}}^{\text{det}}\right| \leq 1.8$ region, where it is increased to 0.1. In the case of data, the correction is evaluated separately for negative and positive $\eta_{\text{jet}}^{\text{det}}$, whereas for MC, symmetry is assumed and the correction is evaluated in bins of $\left|\eta_{\text{jet}}^{\text{det}}\right|$.

9.2.1. The p'_T Variable

Although E' is the natural variable to parameterize the energy dependence of response (see Eq. 23), it is useful to examine the expected $\eta_{\text{jet}}^{\text{det}}$ dependence at fixed p_T assuming a uniform calorimeter. For this purpose, the p'_T variable is introduced, defined as:

$$p'_T \equiv \frac{E'}{\cosh(\eta_{\text{jet}}^{\text{det}})}, \tag{38}$$

where, in the case of γ+jet events, E' is given by Eq. 22. In terms of p'_T, Eq. 23 can be rewritten as: s

$$R(\eta_{\text{jet}}^{\text{det}}; p'_T) = \hat{p}_0(p'_T) + \hat{p}_1(p'_T)\log\left(\cosh\left(\eta_{\text{jet}}^{\text{det}}\right)\right) + \hat{p}_2(p'_T)\log^2\left(\cosh\left(\eta_{\text{jet}}^{\text{det}}\right)\right), \tag{39}$$

with

$$\begin{aligned} \hat{p}_0(p'_T) &= p_0 + p_1\log(p'_T/E_0) + p_2\log^2(p'_T/E_0), \\ \hat{p}_1(p'_T) &= p_1 + 2p_2\log(p'_T/E_0), \\ \hat{p}_2(p'_T) &= p_2. \end{aligned} \tag{40}$$

As we will see below, p'_T is the variable in terms of which the relative MPF response correction is estimated, which will later be mapped to, and fitted as a function of, E'.

9.2.2. Procedure in the γ+jet Sample

The procedure to determine the relative MPF response correction in the γ+jet sample is as follows:

1. For each p'_T bin, the MPF response $R_{\mathrm{MPF},\eta}$ is estimated in the different $\eta^{\mathrm{det}}_{\mathrm{jet}}$ bins. As discussed in Sect. 8.2, in the case of data, the presence of dijet background and imperfect calibration of the photon energy scale leads to $R_{\mathrm{MPF},\eta} = R^{\mathrm{mixture}}_{\mathrm{MPF},\eta}$, whereas in the case of MC, the measured MPF response is for a pure γ+jet sample with the photon at the particle level and thus $R_{\mathrm{MPF},\eta} = R^{\gamma+\mathrm{jet}}_{\mathrm{MPF},\eta}$.

2. Restricted to the $\eta^{\mathrm{det}}_{\mathrm{jet}}$ bins within $\left|\eta^{\mathrm{det}}_{\mathrm{jet}}\right| < 0.4$ and, for each p'_T bin, the $R_{\mathrm{MPF},\eta}$ measurements are fitted with the expected $\eta^{\mathrm{det}}_{\mathrm{jet}}$ dependence for the CC response using the following expression (see Eqs. 39, 40):

$$p_3|_{p'_T} R^{\gamma+\mathrm{jet}}_{\mathrm{MPF,CC}}(\eta^{\mathrm{det}}_{\mathrm{jet}}; p'_T), \tag{41}$$

   where the p_i $(i = 0, 1, 2)$ coefficients inside the $R^{\gamma+\mathrm{jet}}_{\mathrm{MPF,CC}}$ parameterization are the coefficients for the CC response shown in Table 1, and $p_3|_{p'_T}$ is a free parameter to be determined. In the case of data, the measured $R_{\mathrm{MPF},\eta}$ points are first corrected by $k^{\gamma}_{\mathrm{R,CC}}$. The purpose of this step is to determine any residual correction (i.e. p_3) required to ensure that the relative MPF response will be on average one within $\left|\eta^{\mathrm{det}}_{\mathrm{jet}}\right| < 0.4$. Both in data and MC, p_3 is found to be one on average, as expected.

3. Next, the relative MPF response correction in a given $(p'_T, \eta^{\mathrm{det}}_{\mathrm{jet}})$ bin is computed as:

$$\frac{R_{\mathrm{MPF},\eta}|_{p'_T}}{p_3|_{p'_T} R^{\gamma+\mathrm{jet}}_{\mathrm{MPF,CC}}(\eta^{\mathrm{det}}_{\mathrm{jet}}; p'_T)}. \tag{42}$$

   In the case of data, the numerator still corresponds to the MPF response for the mixture sample. Therefore, even in CC, this ratio is slightly smaller than one. The reason for not applying the photon correction at this point will become evident from the discussion in Sect. 9.2.5. As it will be shown in Sect. 9.2.6, such correction will eventually be taken into account as part of the global fit to the full set of measurements.

4. Finally, the correction measured in each (p'_T,$\eta^{\mathrm{det}}_{\mathrm{jet}}$) bin is mapped to the corresponding (E',$\eta^{\mathrm{det}}_{\mathrm{jet}}$) bin. The solid circles in Fig. 14 illustrate the measured correction (Eq. 42) as a function of E' in two different $\eta^{\mathrm{det}}_{\mathrm{jet}}$ bins.

The relative MPF response correction in the γ+jet sample, extracted from the above measurements following the procedure discussed in Sect. 9.2.6, will be denoted as $F^{\gamma+\mathrm{jet}}_{\eta}$.

9.2.3. Procedure in the Dijet Sample

The procedure to determine the relative MPF response correction in the dijet sample is as follows:

1. For each $\eta^{\mathrm{det}}_{\mathrm{jet}}$ bin, the average relative MPF response $R^{\mathrm{dijet}}_{\mathrm{relMPF},\eta}$ (see Eq. 24) is computed in bins of $p'_{T\mathrm{CC}}$, defined as:

$$p'_{T\mathrm{CC}} = \frac{p^{\mathrm{meas,off\ corr}}_{T\mathrm{CC}} \cosh(\eta_{\mathrm{jet}})}{\cosh(\eta^{\mathrm{det}}_{\mathrm{jet}})}, \tag{43}$$

   where $p^{\mathrm{meas,off\ corr}}_{T\mathrm{CC}}$ if the measured transverse momentum of the tag jet corrected by offset.

2. Next, $R^{\rm dijet}_{{\rm relMPF},\eta}$ and $p^{\rm meas,off\ corr}_{TCC}$ are corrected in each p'_{TCC} and $\eta^{\rm det}_{\rm jet}$ bin by the estimated resolution bias (see Sect. C):

$$R^{\rm dijet,corr}_{{\rm relMPF},\eta} = R^{\rm dijet}_{{\rm relMPF},\eta}(1+\frac{\delta p^{\rm meas}_T}{p^{\rm meas}_T})^{-1},$$
$$p^{\rm meas,corr}_{TCC} = p^{\rm meas,off\ corr}_{TCC}(1+\frac{\delta p^{\rm meas}_T}{p^{\rm meas}_T}), \quad (44)$$

and the E' variable in dijets is defined as:

$$E' = \frac{p^{\rm meas,corr}_{TCC}}{R^{\gamma+{\rm jet}}_{\rm MPF,CC}(p^{\rm meas,corr}_{TCC})}\cosh(\eta_{\rm jet}). \quad (45)$$

The variable p'_T is then defined as in Eq. 38.

3. As in the case of γ+jet, any residual correction required to ensure that the relative MPF response correction is on average one within $\left|\eta^{\rm det}_{\rm jet}\right| < 0.4$, is estimated. Restricted to the $\eta^{\rm det}_{\rm jet}$ bins within $\left|\eta^{\rm det}_{\rm jet}\right| < 0.4$ and, for each p'_T bin, the $R^{\rm dijet,corr}_{{\rm relMPF},\eta}$ measurements are fitted with the expected $\eta^{\rm det}_{\rm jet}$ dependence for the CC response using the following expression:

$$p_3|_{p'_T}\frac{R^{\gamma+{\rm jet}}_{\rm MPF,CC}(\eta^{\rm det}_{\rm jet};p'_T)}{R^{\gamma+{\rm jet}}_{\rm MPF,CC}(\eta^{\rm det}_{\rm jet}=0;p'_T)}, \quad (46)$$

where $p_3|_{p'_T}$ is a free parameter to be determined and

$$\frac{R^{\gamma+{\rm jet}}_{\rm MPF,CC}(\eta^{\rm det}_{\rm jet};p'_T)}{R^{\gamma+{\rm jet}}_{\rm MPF,CC}(\eta^{\rm det}_{\rm jet}=0;p'_T)} = 1+\frac{\hat{p}_1(p'_T)}{\hat{p}_0(p'_T)}\log\left(\cosh(\eta^{\rm det}_{\rm jet})\right)+\frac{\hat{p}_2(p'_T)}{\hat{p}_0(p'_T)}\log^2\left(\cosh(\eta^{\rm det}_{\rm jet})\right). \quad (47)$$

In the above expression the functions $\hat{p}_i(p'_T)$ $(i=0,1,2)$ are given by Eq. 40, with the p_i $(i=0,1,2)$ coefficients from Table 1. The fitted p_3 is consistent with one within $< 0.5\%$, which indicates the resolution bias correction in CC is working satisfactorily. Nevertheless, this small residual is corrected for.

4. Next, the relative MPF response correction in a given $(p'_T,\eta^{\rm det}_{\rm jet})$ bin is computed as:

$$R^{\rm dijet,corr}_{{\rm relMPF},\eta}|_{p'_T}\frac{R^{\gamma+{\rm jet}}_{\rm MPF,CC}(\eta^{\rm det}_{\rm jet}=0;p'_T)}{p_3|_{p'_T}R^{\gamma+{\rm jet}}_{\rm MPF,CC}(\eta^{\rm det}_{\rm jet};p'_T)}. \quad (48)$$

5. Finally, the correction measured in each $(p'_T,\eta^{\rm det}_{\rm jet})$ bin is mapped to the corresponding $(E',\eta^{\rm det}_{\rm jet})$ bin. The open circles in Fig. 14 illustrate the measured correction (Eq. 48) as a function of E' in two different $\eta^{\rm det}_{\rm jet}$ bins.

The relative MPF response correction in the dijet sample, extracted from the above measurements following the procedure discussed in Sect. 9.2.6, will be denoted as $F^{\rm dijet}_\eta$.

9.2.4. Sample Dependence of the Relative MPF Response

As illustrated in Fig. 14, the measured correction is significantly different between the γ+jet and dijet samples. In order to consistently determine the relative MPF response correction

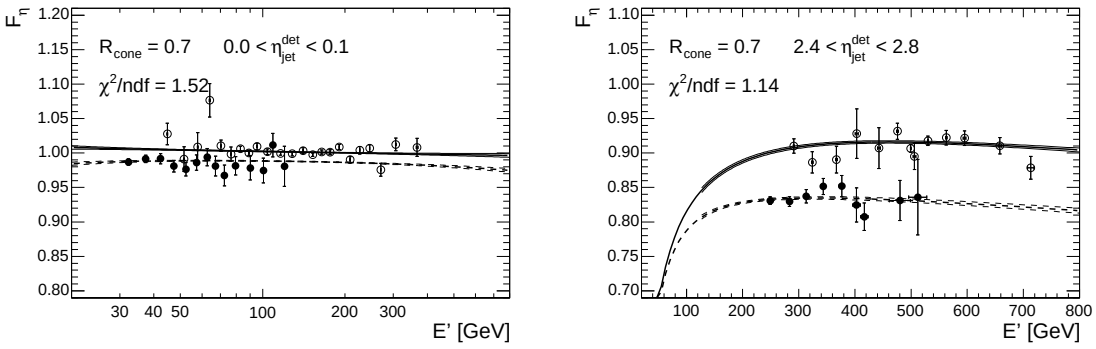

FIG. 14: Relative MPF response correction for $\mathcal{R}_{\rm cone} = 0.7$ jet in data as a function of E' and for two different $\eta_{\rm jet}^{\rm det}$ bins: $0 < \eta_{\rm jet}^{\rm det} < 0.1$ (left) and $2.4 < \eta_{\rm jet}^{\rm det} < 2.8$ (right). The solid (open) circles represent the measurements in the γ+jet (dijet) sample. The lines shown represent the result from the global fit discussed in Sect. 9.2.6.

from the combination of these measurements, it is important to understand the nature of these discrepancies.

One of the important considerations in the γ+jet sample is the presence of the dijet contamination and the fact that the photon energy is not at the particle level. As indicated in Sect. 9.2.2, the numerator of Eq. 42 is affected by this bias which, as in the case of the absolute MPF response (see Sect. 8.2.1), must be corrected for. This is the main reason for the discrepancy between γ+jet and dijet measurements for central jets, illustrated in Fig. 14(left). However, this bias is also expected to depend on $\eta_{\rm jet}^{\rm det}$. The dependence on $\eta_{\rm jet}^{\rm det}$ of the photon corrections is discussed in Sect. 9.2.5. The actual procedure used to incorporate this correction in the determination of $F_\eta^{\gamma+{\rm jet}}$ will be discussed in Sect. 9.2.6.

The main contribution to the discrepancy between both set of measurements, particularly at high $\eta_{\rm jet}^{\rm det}$ (see e.g. Fig. 14(right)), originates from the different parton flavor composition of the γ+jet and dijet samples. Whereas the leading jet in γ+jet events is dominatly quark-originated at low energy and gluon-originated at high energy, the dijet sample has the opposite behavior. On the other hand, the different fragmentation between quarks and gluons results in a lower expected response for gluon jets, owing to their softer spectrum of particles. Thus, neglecting a rapidity dependence of the parton-level composition of the jets (actually present in the γ+jet sample), the expectation in a uniform calorimeter would be that the response for the forward (i.e. high energy) jets relative to the response for central jets is larger in the dijet sample than in the γ+jet sample: i.e. $F_\eta^{\rm dijet}/F_\eta^{\gamma+{\rm jet}} \geq 1$. Furthermore, in a given $\eta_{\rm jet}^{\rm det}$ bin, this ratio is found to be nearly independent of E' over the range where both samples overlap. We therefore define the "dijet-to-γ+jet scale factor" SF_η as:

$$SF_\eta \equiv \frac{F_\eta^{\rm dijet}(E')}{F_\eta^{\gamma+{\rm jet}}(E')}, \tag{49}$$

which will be key to combine both sets of measurements in Sect. 9.2.6. It should be noted that, by definition, $SF_\eta = 1$ for $\eta_{\rm jet}^{\rm det} = 0$.

9.2.5. Pseudo-Rapidity Dependence of the Photon Corrections

The photon corrections for selected γ+jet events in data in case of the jet in the central calorimeter were discussed in Sect. 8.2.1. For a jet at a given $\eta_{\rm jet}^{\rm det}$, the correction is also given by Eq. 37, where the only η-dependent terms are the expected sample purity ρ_η and the ratio $R_{{\rm MPF},\eta}^{\rm dijet}/R_{{\rm MPF},\eta}^{\gamma^{\rm meas}+{\rm jet}}$ in $c_{{\rm bckg},\eta}$ (see Eq. 35). In the case of ρ_η, it is parameterized as a function of E' and $\eta_{\rm jet}^{\rm det}$ using MC. *(The fitted purity and total uncertainty for the tight photon selection in the different $\eta_{\rm jet}^{\rm det}$ bins are shown in Fig. 118 in Appendix D.)* In the case of $R_{{\rm MPF},\eta}^{\rm dijet}/R_{{\rm MPF},\eta}^{\gamma^{\rm meas}+{\rm jet}}$, the limited MC statistics does not allow for a very robust determination as a function of $\eta_{\rm jet}^{\rm det}$, and a different approach is followed which, in addition to statistical stability, will also bring the benefit of a reduced MC dependence.

Under the assumption that the response of the recoil against the central tag object in dijet events is independent on whether such object is a jet or a misidentified photon, it is possible to derive the following expression:

$$\frac{R_{{\rm MPF},\eta}^{\rm dijet}(E')}{R_{{\rm MPF},\eta}^{\gamma^{\rm meas}+{\rm jet}}(E')} = SF_\eta \frac{R_{{\rm MPF,CC}}^{\rm dijet}(p'_T)}{R_{{\rm MPF,CC}}^{\gamma^{\rm meas}+{\rm jet}}(p'_T)}, \tag{50}$$

where $R_{{\rm MPF,CC}}^{\rm dijet}/R_{{\rm MPF,CC}}^{\gamma^{\rm meas}+{\rm jet}}$ is estimated in MC (see Fig. 7) and SF_η (see Eq. 49) is determined from a simultaneous fit to the $F_\eta^{\rm dijet}$ and $F_\eta^{\gamma+{\rm jet}}$ measurements. The validity of this approximation has been verified in MC by comparing in different $\eta_{\rm jet}^{\rm det}$ bins the measured $R_{{\rm MPF},\eta}^{\rm dijet}/R_{{\rm MPF},\eta}^{\gamma^{\rm meas}+{\rm jet}}$ to the prediction given by Eq. 50. *(See Figs. 132, 133 and 134 in Appendix E for a comparison in MC between observation and the prediction given by Eq. 50 for the loose, medium and tight photon identification criteria, respectively. The preliminary parameterization used for SF_η is:*

$$SF_\eta = 1 + 0.02138 \log\left(\cosh(\eta_{\rm jet}^{\rm det})\right) - 0.0009987 \log^2\left(\cosh(\eta_{\rm jet}^{\rm det})\right), \tag{51}$$

which was obtained from the global fit in the determination of the relative MPF response correction in MC.)

9.2.6. Global Fit to γ+jet and Dijet Samples

In a particular $\eta_{\rm jet}^{\rm det}$ bin, the relative MPF response correction in the γ+jet sample is defined as:

$$F_\eta^{\gamma+{\rm jet}}(E';\{p_{i,\eta}\}) = \frac{R_{{\rm MPF},\eta}^{\gamma+{\rm jet}}(E';\{p_{i,\eta}\})}{R_{{\rm MPF,CC}}^{\gamma+{\rm jet}}(E')} = \frac{p_{0,\eta} + p_{1,\eta}\log(E'/E_0) + p_{2,\eta}\log^2(E'/E_0)}{R_{{\rm MPF,CC}}^{\gamma+{\rm jet}}(E')}, \tag{52}$$

where $R_{{\rm MPF,CC}}^{\gamma+{\rm jet}}(E')$ is fixed to the parameterization determined in Sect. 8, and $p_{i,\eta}$ ($i = 0, 1, 2$) are coefficients to be estimated from the measurements. Please note that these coefficients correspond to the MPF response for the pure γ+jet sample with the photon at the particle level (i.e. after photon corrections) whereas, as indicated in Sect. 9.2.2, the measurements in the γ+jet sample do not have the photon corrections applied. This is taken into account during the fit discussed below.

Following Eq. 49, the relative MPF response correction in the dijet sample is defined as:

$$F_\eta^{\rm dijet}(E';\{p_{i,\eta}\}, SF_\eta) = SF_\eta F_\eta^{\gamma+{\rm jet}}(E';\{p_{i,\eta}\}) \tag{53}$$

with the additional SF_η coefficient to be determined.

Therefore, in each $\eta^{\rm det}_{\rm jet}$ bin, a total of four parameters (p_0, p_1, p_2, SF_η) are required to define $F^{\gamma+{\rm jet}}_\eta$ and $F^{\rm dijet}_\eta$. These parameters can be estimated from a simultaneous fit to the measurements in the γ+jet and dijet samples (see e.g. Fig. 14). The fitting function used is given by:

$$F_\eta(E';\{p_{i,\eta}\},SF_\eta) = \begin{cases} F^{\gamma+{\rm jet}}_\eta(E';\{p_{i,\eta}\})/k^\gamma_{{\rm R},\eta}(E';SF_\eta) & \text{if } \gamma\text{+jet,} \\ F^{\rm dijet}_\eta(E';\{p_{i,\eta}\},SF_\eta) & \text{if dijet,} \end{cases} \tag{54}$$

where $k^\gamma_{{\rm R},\eta}$ takes into account the fact that the γ+jet measurements are uncorrected, and the correction depends (via Eqs. 37 and 50) on the actual SF_η being estimated. This allows to reduce the MC dependence of the photon corrections applied to the data measurements.

Following the discussion above, given the 66 $\eta^{\rm det}_{\rm jet}$ bins used in data, a total of 264 parameters would have to be determined. The very fine $\eta^{\rm det}_{\rm jet}$ binning has the advantage of an accurate determination of the relative MPF response correction in regions where the energy dependence changes quickly with $\eta^{\rm det}_{\rm jet}$ (e.g. in the ICR). On the other hand, the limited available statitistics in each of the bins can introduce potentially large fluctuations in the fitted parameters. In order to avoid this problem and ensure a smooth parameterization of the relative MPF response correction in the $(E', \eta^{\rm det}_{\rm jet})$ plane, each of the four parameters (p_0, p_1, p_2, SF_η) are expressed as suitable functions of $\eta^{\rm det}_{\rm jet}$ (see e.g. Fig. 15), whose coefficients now become the actual parameters to be determined. For instance, SF_η is found to be well described by the following parameterization:

$$SF_\eta = 1 + b\log\left(\cosh(\eta^{\rm det}_{\rm jet})\right) + c\log^2\left(\cosh(\eta^{\rm det}_{\rm jet})\right). \tag{55}$$

Through this procedure, the total number of free parameters in data is reduced from 264 to 55, which are determined from a global fit to approximately 1900 available measurements in the $(E', \eta^{\rm det}_{\rm jet})$ plane. In general, good quality fits are obtained through this procedure, typically with $\chi^2/ndf \sim 1.2$.

At this point it is appropriate to stress that one of the main motivations to perform a global fit combining measurements in the γ+jet and dijet samples is to reduce the uncertainty from extrapolation of the relative response correction to the highest energies. Such global fit involves the assumption that the energy dependence of the relative response corrections in both samples is the same, but they can differ by up to a ($\eta^{\rm det}_{\rm jet}$-dependent) constant factor. Furthermore, it is assumed that in any $\eta^{\rm det}_{\rm jet}$ region the jet response can be well described by a quadratic logarithmic function (see Eq. 23). Both assumptions have been validated using the full simulation. One of the most stringent tests performed in the MC attempts to reproduce the procedure followed in data: γ+jet measurements are considered in the $p'_T < 200$ GeV range, whereas dijet measurements are used for $p^{\rm meas}_{T\rm jet} > 50$ GeV. The global fit procedure is performed and the resulting extrapolated relative response correction for γ+jet is compared to the actual available MC measurements (not used in the fit) up to $p'_T \sim 600$ GeV. In general good agreement is found between the high energy prediction and the direct measurements, thus yielding confidence in the procedure and its application to data. *(See Figure 151 in Appendix E2 for a comparison of the residual between the extrapolated relative response correction in γ+jet MC (using a restricted set of measurements analogous to data) and the actual available high-energy relative response measurements not used in the global fit. The different plots shown correspond for the actual fine (typically 0.1-wide) $\eta^{\rm det}_{\rm jet}$ bins used in the global fit, where the reduced statistical power of the dijet MC relative to the γ+jet MC (in contrast with data, where dijets completely dominate the high-energy behavior) and possibly*

the rigidity of the global fit may sometimes cause a deviation in the prediction with respect to the actual measurements (see in particular plot corresponding to $1.0 < \left|\eta_{\rm jet}^{\rm det}\right| < 1.1$*). However, when averaged over wider bins, these localized imperfections of the global fit tend to become unimportant. For instance, as it will be discussed in Sect. 9.4, the closure tests in 0.4-wide* $\eta_{\rm jet}^{\rm det}$ *bins, from which a residual systematic uncertainty is obtained, also include those high-energy measurements not used in the global fit, and agreement within the quoted residual uncertainty is observed.)*

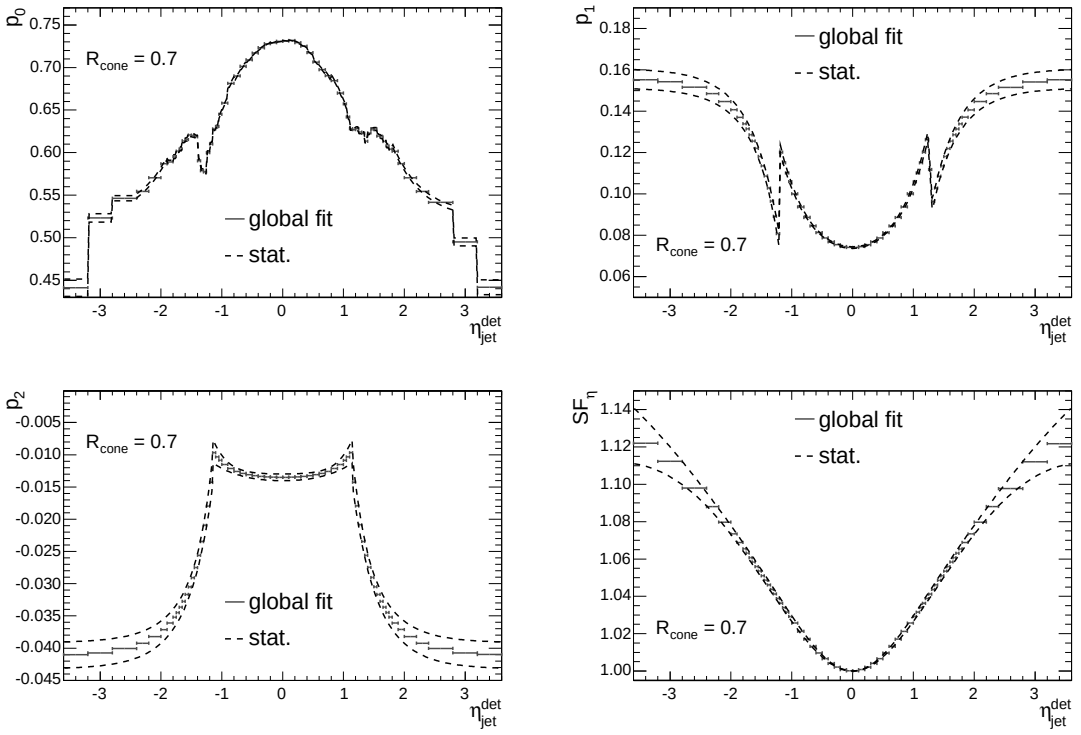

FIG. 15: Parameterizations for (p_0, p_1, p_2, SF_η) resulting from the global fit to the relative MPF response measurements in data for $\mathcal{R}_{\rm cone} = 0.7$ jets. The dashed lines illustrate the statistical uncertainty band.

9.3. Results

Following the fitting procedure discussed in Sect. 9.2.6, the relative response corrections for γ+jet (see Eq. 52) and dijet (see Eq. 53) are simultaneously estimated as smooth functions in the $(E', \eta_{\rm jet}^{\rm det})$ plane.

Figure 14 shows an example of the global fit in data for $\mathcal{R}_{\rm cone} = 0.7$ jets in two different $\eta_{\rm jet}^{\rm det}$ bins. *(A larger set of plots for different* $\eta_{\rm jet}^{\rm det}$ *bins for* $\mathcal{R}_{\rm cone} = 0.7$ *and* 0.5 *can be found in Figs. 135 and 136, respectively, in Appendix E1. The corresponding plots for* $\mathcal{R}_{\rm cone} = 0.7$ *and* 0.5 *in MC can be found, respectively, in Figs. 145 and 146 in Appendix E2.)* The resulting functional form for the (p_0, p_1, p_2, SF_η) parameters is shown in Fig. 15. *(The result corresponding to* $\mathcal{R}_{\rm cone} = 0.5$ *jets in data can be found in Fig. 137 in Appendix E1. The corresponding plots for* $\mathcal{R}_{\rm cone} = 0.7$ *and* 0.5 *in MC can be found, respectively, in Figs. 147 and 148 in Appendix E2.)* Finally, Fig. 16 presents the final relative MPF response correction in data for $\mathcal{R}_{\rm cone} = 0.7$ jets as a function of $\eta_{\rm jet}^{\rm det}$, and for different values of E'. This figure illustrates the non-uniform response of the calorimeter as a function of $\eta_{\rm jet}^{\rm det}$. A uniform

calorimeter would have a measured correction identical to one, independent to E' and $\eta_{\rm jet}^{\rm det}$. The measured correction for $\mathcal{R}_{\rm cone} = 0.5$ jets is very similar. *(The result corresponding to $\mathcal{R}_{\rm cone} = 0.5$ jets in data can be found in Fig. 138 in Appendix E. The corresponding plots for $\mathcal{R}_{\rm cone} = 0.7$ and 0.5 in MC can be found, respectively, in Figs. 149 and 150 in Appendix E2.)*

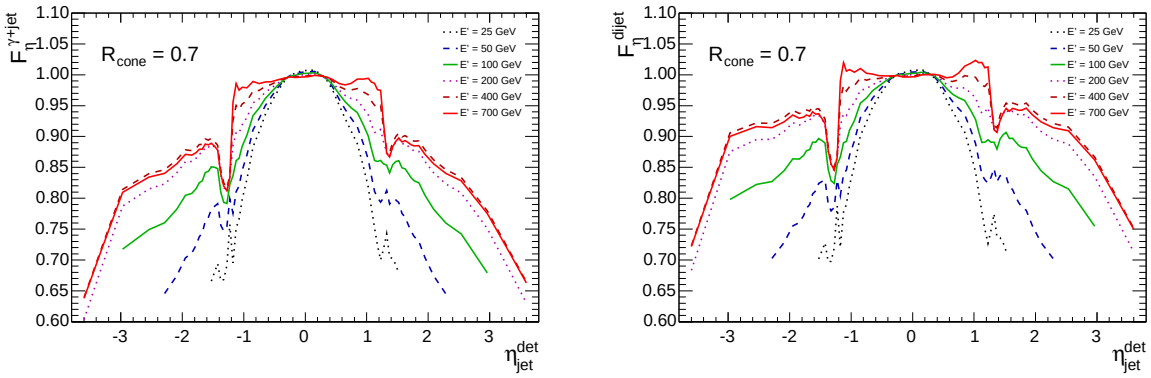

FIG. 16: Relative MPF response correction in data for $\mathcal{R}_{\rm cone} = 0.7$ jets as a function of $\eta_{\rm jet}^{\rm det}$ and separately for γ+jet (left) and dijet (right). The different lines correspond to particular values of E'.

9.4. Uncertainties

The uncertainties on the relative MPF response correction in data for $\mathcal{R}_{\rm cone} = 0.7$ jet are shown in Fig. 17 as a function of $\eta_{\rm jet}^{\rm det}$, separately for γ+jet and dijet. *(A summary of the uncertainties for $\mathcal{R}_{\rm cone} = 0.5$ jets in data can be found in Fig. 139 in Appendix E1. The corresponding plots for $\mathcal{R}_{\rm cone} = 0.7$ and 0.5 in MC can be found, respectively, in Figs. 153 and 154 in Appendix E2.)* They include the statistical uncertainty from the global fit, as well as the following systematic uncertainties: average residual and background correction in the case of γ+jet, and average residual, resolution bias correction and high-energy extrapolation in the case of dijet. These systematic uncertainties are explained in mode detail below. The total uncertainty is obtained by adding in quadrature these three individual contributions, whose magnitudes are different for $F_\eta^{\gamma+\rm jet}$ and $F_\eta^{\rm dijet}$.

The statistical uncertainty is computed by error propagation on Eq. 54 using the full covariance matrix from the global fit. For those $\eta_{\rm jet}^{\rm det}$ bins where $\chi^2/ndf > 1$, the statistical uncertainty has been increased by $\sqrt{\chi^2/ndf}$. In Fig. 17 it is shown for $p'_T = 50$ GeV, since for this low value of p'_T it can be displayed in the whole $\eta_{\rm jet}^{\rm det}$ range. As it can be appreciated, this uncertainty is typically smaller than 0.5%, except for $\left|\eta_{\rm jet}^{\rm det}\right| > 2.8$, where it becomes $\geq 1\%$ as a result of the limited available statistics. The energy dependence of this uncertainty is rather mild since, owing to the nature of the global fit, it is constrained at low p_T by the γ+jet measurements and at high p_T by the dijet measurements.

Ideally, the estimated relative MPF response correction would result in a uniform MPF response as a function of $\eta_{\rm jet}^{\rm det}$, and identical to the CC response (see Eq. 30). However, limitations in the quality of, and/or approximations made in, the global fit may lead to deviations from this ideal behavior. In order to verify the performance of this correction, suitable observables are defined for γ+jet and dijet, which are evaluated as a function of E' in 0.4-wide bins of $\left|\eta_{\rm jet}^{\rm det}\right|$. In case the correction works perfectly, these observables should be identical to one and independent of energy. *(These observables are defined as follows. In the*

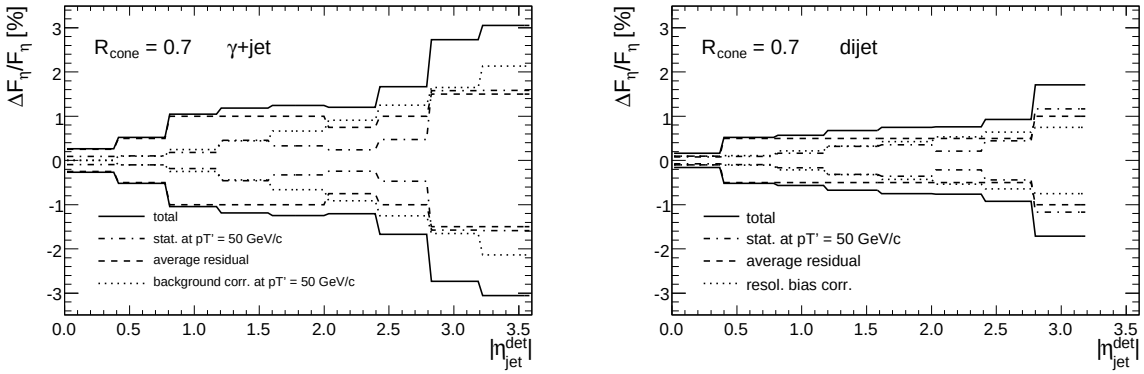

FIG. 17: Uncertainties on the relative MPF response correction in data for $\mathcal{R}_{\rm cone} = 0.7$ jets, as a function of $|\eta^{\rm det}_{\rm jet}|$ and separately for γ+jet (left) and dijet (right). The solid line shows the total uncertainty, resulting from the sum in quadrature of the individual contributions: statistical (dashed-dotted), average residual (dashed) and background correction (dotted).

case of γ+jet:

$$f^{\gamma+\rm jet}_{\rm closure} = \frac{< R^{\rm mixture}_{{\rm MPF},\eta} k^{\gamma}_{{\rm R},\eta} >}{< R^{\gamma+\rm jet}_{\rm MPF,CC} F^{\gamma+\rm jet}_{\eta} >} \tag{56}$$

where the numerator is the average MPF response measured in data, which needs to be corrected with the photon corrections, and the denominator is the average MPF response as returned by jetcorr. In the case of dijet:

$$f^{\rm dijet}_{\rm closure} =< R^{\rm dijet,corr}_{{\rm relMPF},\eta} > \frac{R^{\gamma+\rm jet}_{\rm MPF,CC}(p'_T)}{R^{\gamma+\rm jet}_{\rm MPF,CC}(E')} \tag{57}$$

where $< R^{\rm dijet,corr}_{{\rm relMPF},\eta} >$ is the average relative MPF response (given by Eq. 24) but with the probe jet corrected by the measured $F^{\rm dijet}_{\eta}$ and propagated to $\not\!\!E_T$:

$$\vec{\not\!\!E}_T{}^{\rm corr} = \vec{\not\!\!E}_T + \left(1 - \frac{1}{F^{\rm dijet}_{\eta}}\right) \vec{p}_T^{\rm \,meas,off\ corr}. \tag{58}$$

) By fitting a constant to the estimated closure observable versus E' in each wide $|\eta^{\rm det}_{\rm jet}|$ bin, the average residual from one is determined. In general, residuals smaller than 1% over the available energy range are found, owing to the physical energy parameterization used during the global fit. *(Summary plots of residuals for $\mathcal{R}_{\rm cone} = 0.7$ jets in data can be found in Figs. 140 and 141 in Appendix E1, respectively for γ+jet and dijet events. Summary plots of residuals for $\mathcal{R}_{\rm cone} = 0.5$ jets in data can be found in Figs. 142 and 143 in Appendix E1, respectively for γ+jet and dijet events. Summary plots of residuals for $\mathcal{R}_{\rm cone} = 0.7$ jets in MC can be found in Figs. 155 and 156 in Appendix E2, respectively for γ+jet and dijet events. Summary plots of residuals for $\mathcal{R}_{\rm cone} = 0.5$ jets in MC can be found in Figs. 157 and 158 in Appendix E2, respectively for γ+jet and dijet events.)* The assigned systematic uncertainty for $\mathcal{R}_{\rm cone} = 0.7$ jets in data as a function of $|\eta^{\rm det}_{\rm jet}|$ is displayed by the dashed line in Fig. 17. The uncertainties corresponding to $\mathcal{R}_{\rm cone} = 0.5$ jets are rather similar.

Finally, in the case of the relative MPF response in γ+jet, a systematic uncertainty is assigned to cover for possible imperfections in the background correction as a function of

$\eta_{\rm jet}^{\rm det}$ (see Eq. 37). Ideally, the corrected absolute MPF response would be independent of the photon selection criteria. In practice, inaccuracies in the predicted η-dependence of the photon purity or the ratio between the MPF response for dijet and γ+jet events, would result in a measured relative MPF response which is dependent on the photon identification criteria. *(The plots comparing the corrected absolute response for loose, medium and tight criteria can be found in Fig. 144 in Appendix E.)* Such systematic uncertainty is estimated following the procedure discussed in Sect. 8.4. In order to avoid double-counting when propagating this uncertainty in Eq. 30, we must subtract in quadrature the 0.5% assigned uncertainty to the CC MPF response. The remaining assigned uncertainty is displayed as the dotted line in Fig. 17.

In the case of relative MPF response in dijet, the need for a resolution bias correction contributes a systematic uncertainty related to the precision of such correction as estimated in MC, as well as its sensitivity to the assumed jet energy resolution and tag jet spectrum in data. The assigned systematic uncertainty is $\sim 0.75\%$ at $\eta_{\rm jet}^{\rm det} \sim 3.0$ and decreases linearly towards a minimum of 0.1% at $\eta_{\rm jet}^{\rm det} = 0$. *(See Appendix C for a more detailed discussion.)* A robust prediction for the relative MPF response correction in dijet at the highest p_T is relevant for measurements such as the inclusive jet cross section. Direct measurements in data are available up to e.g. $p_T \sim 350(150)$ GeV for $0.4 < \left|\eta_{\rm jet}^{\rm det}\right| < 0.8$ ($2.0 < \left|\eta_{\rm jet}^{\rm det}\right| < 2.4$), which results in a rather precise extrapolation to higher p_T given the logarithmic dependence of response as a function of energy. The validity of such extrapolation can be tested in MC, by performing the global fit procedure using samples of γ+jet and dijet events in a similar energy range as available in data, and comparing the predicted relative response correction for dijets at high p_T with actual available measurements. While no evidence of a systematic effect is observed, a maximum systematic uncertainty of 1% is assigned for $E' \sim 800$ GeV, decreasing linearly to zero at the typical E' where sufficiently precise measurements are available in data in each $\left|\eta_{\rm jet}^{\rm det}\right|$ bin. *(See Fig. 152 in Appendix 2. It should be pointed out that restricting the energy range for γ+jet and dijet MC to that in data, due to the limited available MC statistics and large weight fluctuations, results in a somewhat unstable global fit which can show artificially large systematic differences between prediction and the high-energy measurements (not used in the fit). This limitation is not present in data, owing to the much higher statistical power of the dijet measurements. In order to reduce this problem, the global fit for this MC test is performed in 0.2-wide $\left|\eta_{\rm jet}^{\rm det}\right|$ bins.)*

10. MPF RESPONSE BIAS CORRECTIONS

As already discussed in Sect. 7.2, the MPF response determination suffers from three main biases that need to be corrected in order to recover the true jet response. The first bias affects the response measurement in data only, and it is related to the improper calibration of the measured photon p_T as well as the presence of dijet background contamination in the selected γ+jet sample. The correction for this bias was discussed in Sect. 8.2.1. This section presents the correction for the other two biases, which affect the determination of response in both data and MC.

10.1. Zero-Suppression Bias Correction

As already indicated in Sect. 7.2, the absolute MPF response determination in γ+jet events is biased due to a $\not\!\!E_T$ imbalance caused by a different effect of zero-suppression on the offset energy deposited inside the jet compared to the offset energy deposited outside the jet. Indeed, the offset energy deposited in cells inside the jet is more likely to become visible since those cells already contain energy from the hard interaction and may be above the zero-suppression threshold. As a result, the $\not\!\!E_T$ in the direction of the jet is reduced, thus artificially increasing the estimated MPF response.

This bias is of the same nature as the bias in the estimated offset energy discussed in Sect. 6.4. Similarly, a correction factor for the MPF response is estimated in MC making use of a γ+jet sample where the same events are processed with both, unsuppressed and suppressed, ZB overlay and without ZB overlay (see Sect. 5.2). The three samples are selected requiring exactly the same cuts as in Sect. 8.1, except that the jet is not restricted to be in the central calorimeter only. Then, the comparison of the MPF response in the sample with unsuppressed (suppressed) ZB overlay, $R_{\rm MPF}^{\gamma+{\rm jet}}$, to that in the sample without ZB overlay, $R_{\rm MPF}^{\gamma+{\rm jet,noZB}}$, will result in the correction factor used for jet energy calibration in data (MC). Such correction factor is defined in Eq. 27 and it is measured in different $\left|\eta_{\rm jet}^{\rm det}\right|$ bins and as a function of p'_T (defined as in Sect. 6.4).

An example of the response correction factor for $\mathcal{R}_{\rm cone} = 0.7$ jets in the case of suppressed ZB overlay is shown in Fig. 18. The correction factor for $\mathcal{R}_{\rm cone} = 0.5$ jets is almost identical. *(A complete set of plots can be found in Figs. 159-162 in Appendix F.)*

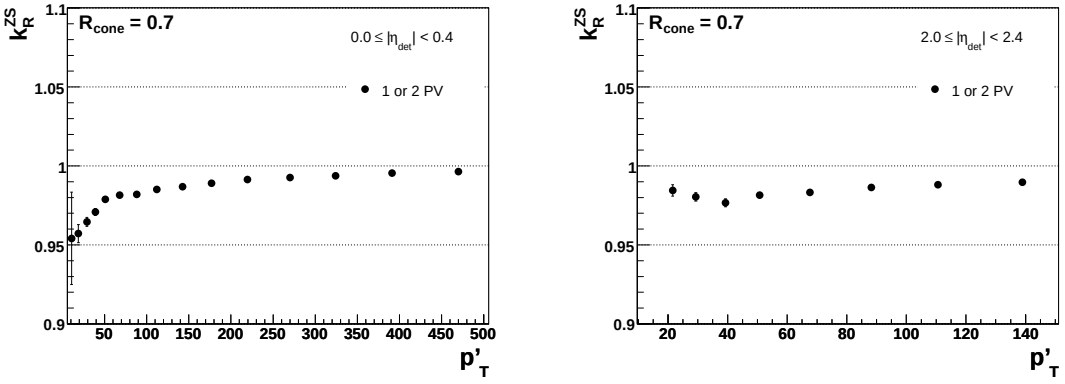

FIG. 18: Examples of $k_{\rm R}^{\rm ZS}$ correction factor for $\mathcal{R}_{\rm cone} = 0.7$ jets in the suppressed ZB overlay case. Different plots correspond to different $\left|\eta_{\rm jet}^{\rm det}\right|$ bins.

The effect of zero suppression on response is correlated with the zero suppression effect on offset discussed in Sect. 6.4. They are both of the same sign and similar magnitude (compare e.g. Figs. 4 and 18) and therefore there is a large, although not perfect, cancellation in the ratio k_O^{ZS}/k_R^{ZS} appearing in Eq. 12. Technically, it is convenient to parameterize the k_O^{ZS}/k_R^{ZS} ratio instead of the individual contributions. An example of this ratio is shown in Fig. 19 for $\mathcal{R}_{\rm cone} = 0.7$ jets in the suppressed ZB overlay case. *(A complete set of plots can be found in Figs. 163-166 in Appendix F1.)* The magnitude of this bias is typically smaller than 1%, except for $\left|\eta_{\rm jet}^{\rm det}\right| > 3.0$, where it can be as large as $2-3\%$.

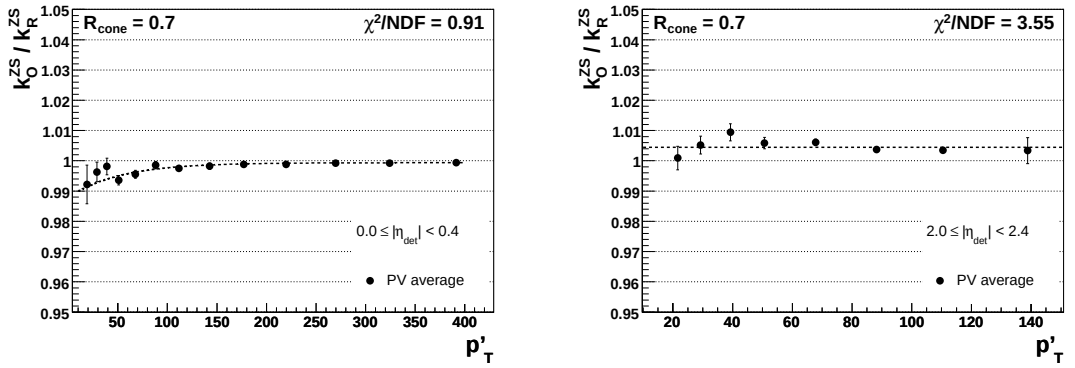

FIG. 19: Examples of $k_{\rm O}^{\rm ZS}/k_{\rm R}^{\rm ZS}$ correction factor for $\mathcal{R}_{\rm cone} = 0.7$ jets in the suppressed ZB overlay case. Different plots correspond to different $\left|\eta_{\rm jet}^{\rm det}\right|$ bins.

Owing to the almost perfect cancellation of the k_O^{ZS} and k_R^{ZS} bias corrections, many systematic uncertainties also cancel. One example is the systematic uncertainty related to the fact that these corrections are derived in MC, which predicts a $\sim 10\%$ higher jet response data. Such uncertainty could be assessed by comparing the predicted correction for a particular value of E' with that for a reduced E', $E'_{red} = E' R_{data}(E')/R_{MC}(E')$, which would more closely correspond to the actual expected visible energy in data. Given the fact the E'_{red} is not expected to differ more than 10% from E', and the very small dependence of k_O^{ZS}/k_R^{ZS} on E', this uncertainty is expected to be negligible. *(Another example is a possible difference in the offset energy, with respect to the Run IIa average, during the limited run range corresponding to the unsuppressed ZB overlay sample used in MC. Figure 87 shows a stability of the offset energy versus time of better than 5%, which eliminates this concern.)* Therefore, the dominant contributions result from those systematic uncertainties affecting almost exclusively k_O^{ZS} (see Sect. 6.5), as well as the statistical uncertainty on k_O^{ZS}/k_R^{ZS} from limited MC statistics. These uncertainties are illustrated in Fig. 20 for $\mathcal{R}_{\rm cone} = 0.7$ jets with $\left|\eta_{\rm jet}^{\rm det}\right| = 0.0$ and 2.0 in the suppressed ZB overlay case. *(A full set of plots are presented in Figs. 167-170 in Appendix F1.)*

(There are issues with large weight fluctuations in the unsuppressed ZB overlay γ+jet MC and potential problems with data quality of the overlay which make rather difficult to perform reliable fits for $k_{\rm O}^{\rm ZS}/k_{\rm R}^{\rm ZS}$. However, despite the significant differences of the individual $k_{\rm O}^{\rm ZS}$ and $k_{\rm R}^{\rm ZS}$ corrections between unsuppressed and suppressed cases, the ratio $k_{\rm O}^{\rm ZS}/k_{\rm R}^{\rm ZS}$ appears numerically very close (typically within $\sim 0.5\%$ or better) to the one for the suppressed case. Therefore, for data JES we are currently using the parameterizations of $k_{\rm O}^{\rm ZS}/k_{\rm R}^{\rm ZS}$ from the suppressed ZB overlay MC. This is illustrated in Figs. 165-166 in Appendix F1, where the (jumpy) unsuppressed ZB overlay measurements are compared to the suppressed ZB overlay fit. An additional uncertainty is assigned to cover for the observed systematic

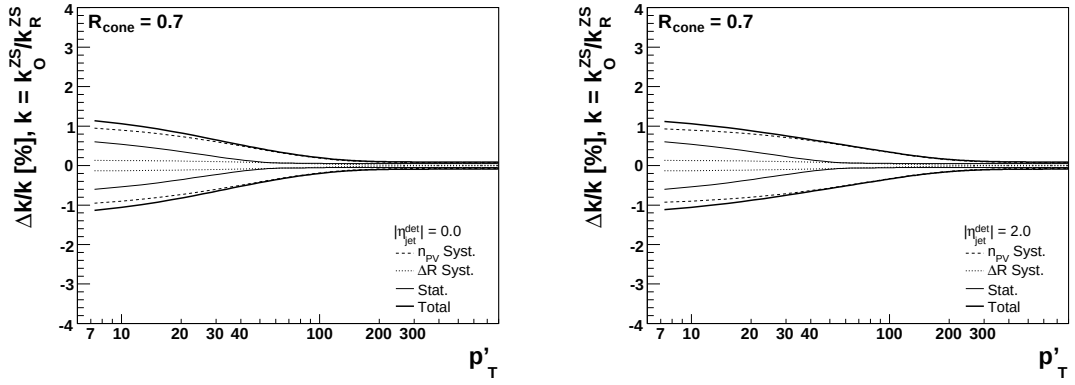

FIG. 20: Example of relative uncertainties on the $k_{\rm O}^{\rm ZS}/k_{\rm R}^{\rm ZS}$ correction factor vs p'_T for $\mathcal{R}_{\rm cone} = 0.7$ jets in the suppressed ZB overlay case. Different plots correspond to different values of $\eta_{\rm jet}^{\rm det}$.

discrepancies, shown as the outer dashed lines. Such uncertainty is currently being included into the statistical uncertainty. The total uncertainty assigned is illustrated in Figs. 169-170 in Appendix F1.)

10.2. Topology Bias Correction

After applying the above two bias corrections, the MPF response provides an estimate of the response to the hadronic recoil against the particle-level photon, which can be different from the true jet response. There are a number of physics and intrumental effects which can contribute to this difference, each of them yielding contributions of a-priori different sign that could partly cancel each other. The goal of the bias correction discussed in this section is to correct for the net effect of all these contributions.

An example of physics-related bias is the fact that, despite the stringent γ+jet selection requiring exactly one jet and $\Delta\phi(\gamma, \text{jet}) > 3.0$ rad., the presence of additional soft radiation below the 6 GeV jet reconstruction threshold can spoil the p_T balance between the jet and the photon. Depending on whether such radiation populates the photon or jet hemispheres, the estimasted MPF response can be higher or lower than the true jet response. Another example is the fact that, owing to the shrinkage of the rapidity space, especially for forward jets, the hadronic recoil can be significantly larger in physical space than the reconstructed jet. Since the particles outside the jet cone are of lower energy than in the jet core, the estimated MPF response is a-priori lower than the actual response to the jet. This difference is also enhanced by the larger effect of zero suppression on low calorimeter energy deposits. Finally, the MPF method relies on p_T balance and therefore is a-priori more suitable for jet p_T, rather than energy, calibration. The difference between jet p_T and energy calibration is largest for low energy jets, where jet mass effects can be sizable. Also, the MPF method can absorb instrumental effects unrelated to energy calibration such as e.g, the rapidity bias in the ICR.

The net bias correction factor, denoted by $k_{\rm R}^{\rm topo}$, is estimated in γ+jet MC without ZB overlay, selected using the same criteria as for the absolute response measurement (see Sect. 8.1). As indicated in Eq. 28, it is defined as the ratio of the true jet response (see Eq. 9) and the MPF response with respect to the particle-level photon (see Eq. 32). The true jet response is estimated as the ratio of the average visible energy in the calorimeter from

particles belonging to the particle jet matching the reconstructed jet within $\Delta\mathcal{R} < \mathcal{R}_{\rm cone}/2$, to the average particle jet energy. This correction factor is measured separately for $\mathcal{R}_{\rm cone} = 0.7$ and 0.5 jets, in different $\left|\eta^{\rm det}_{\rm jet}\right|$ bins and as a function of p'_T (defined as in Sect. 6.4). Fig. 21 shows a comparison of the $k^{\rm topo}_{\rm R}$ correction for $\mathcal{R}_{\rm cone} = 0.7$ and 0.5 jets with $\left|\eta^{\rm det}_{\rm jet}\right| < 0.4$. *(A complete set of plots can be found in Figs. 171 and 172 in Appendix F).*

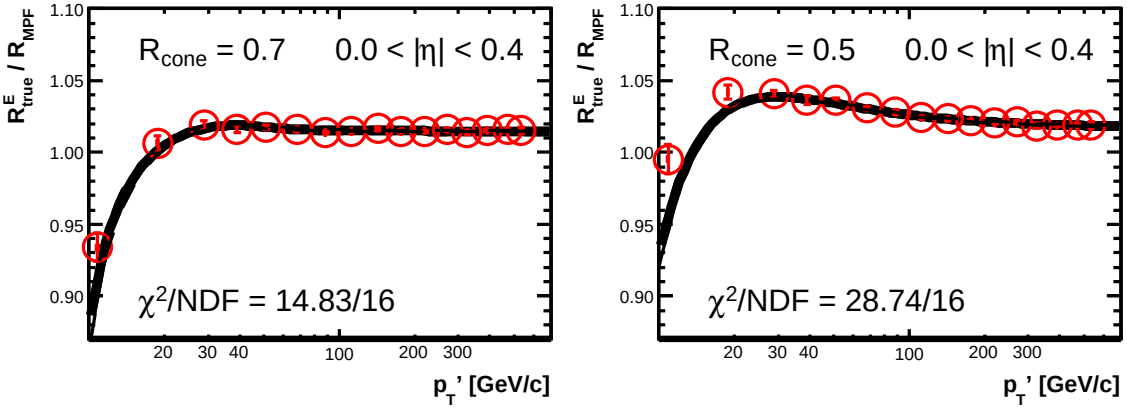

FIG. 21: Example of the topology bias correction for $\mathcal{R}_{\rm cone} = 0.7$ (left) and $\mathcal{R}_{\rm cone} = 0.5$ (right) jets with $\left|\eta^{\rm det}_{\rm jet}\right| < 0.4$.

Figure 22 illustrates the relative uncertainties on the $k^{\rm topo}_{\rm R}$ correction factor for $\mathcal{R}_{\rm cone} = 0.7$ jets for two different values of $\eta^{\rm det}_{\rm jet}$. *(A complete set of plots can be found in Figs. 173 and 174 in Appendix F).* The list of uncertainties includes the statistical error from the fit in MC, varying the matching criterion between the reconstructed and particle jets ($\Delta\mathcal{R} = \mathcal{R}_{\rm cone}/2 \pm 0.1$), varying the hadron response and varying the physics model. The latter, discussed in more detail below, constitutes the largest source of systematic uncertainty, particularly in the forward region. *(See Appendix F2b for a detailed discussion.)*

The difference in response for hadrons between data and MC could possibly affect the size of the topology bias correction, and therefore results in a systematic uncertainty in the case of the correction for data. Such uncertainty is estimated by comparing the topology bias correction for the standard γ+jet MC to the correction from a special γ+jet MC where the single pion response has been scaled in order to achieve agreement in the jet response between data and MC (see Sect. 8.3.1). The difference is $\leq 0.5\%$ for central jets and $\sim 1-2\%$ for forward jets, which is assigned as a systematic uncertainty. *(See Figs. 175 and 176 in Appendix Fa.)*

The particle-level p_T balance in γ+jet event can be mainly spoiled by parton showering from hard-scatter partons (initial and final state radiation) or by additional soft radiation caused by parton spectator interactions (soft underlying event). Both processes are modeled in an approximate way in general purpose MC event generators such as PYTHIA and HERWIG [5]. Both generators incorporate the leading order matrix elements for the simulated hard process followed by the leading-logarithmic approximation of partonic shower. The soft underlying event, as well as fragmentation, are based on empirical models tuned to data. Unfortunately, the soft-underlying event in HERWIG has not been tuned to Tevatron data, and therefore HERWIG has not been used in this study.

Three sets of PYTHIA parameters, so-called Tune A, Tune B and Tune DWT, have been compared. Tune A and B were tuned to the CDF Run I data [9]. Tune A allows for more initial state radiation than Tune B. Consequently, the contribution of soft underlying event

is smaller in Tune A than in Tune B. Run II data slightly favor Tune A which is used as a default setting for the full MC simulation of the DØ detector response. DØ Run II data on dijet azimuthal decorrelations [17] show lack of initial state radiation in Tune B while there is too much radiation in Tune A. The so-called Tune DWT [18] has been developed to provide an improved description of this observable.

A parameterized simulation of the detector response has been used to compare the predicted topology bias in PYTHIA Tune A, Tune B and Tune DWT. The systematic uncertainty due to physics modeling has been estimated as the maximum observed difference with respect to PYTHIA Tune A. *(Since then, fully simulated samples of Tune DW γ+jet MC in the forward region have become available. While somewhat statistics-limited, the preliminary comparison of the topology bias correction from the Tune A and Tune DW fully simulated samples (see Fig. 181 in Appendix Fb) is found to be within the systematic uncertainty band shown in Fig. 173, which confidence in this estimate based on the parameterized simulation.)*

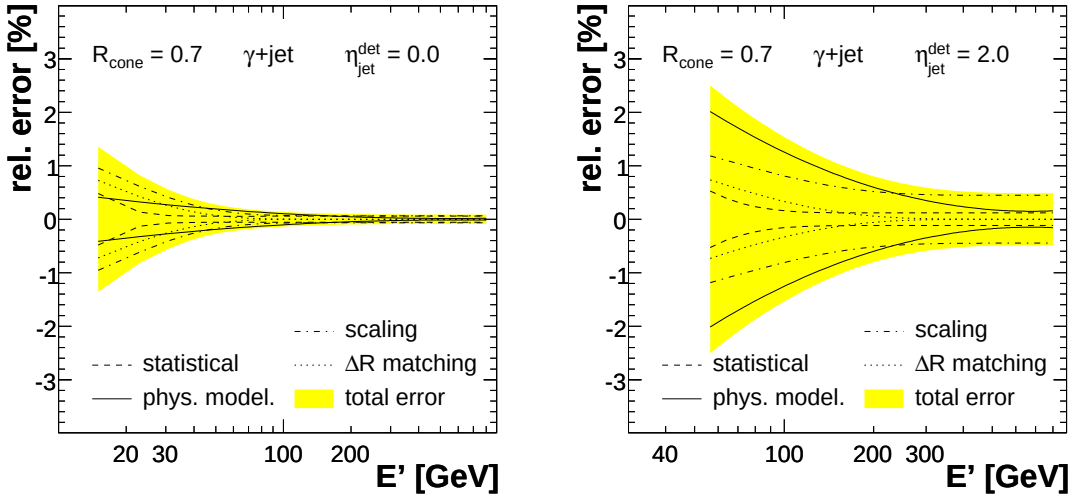

FIG. 22: Example of relative uncertainties on the $k_{\mathrm{R}}^{\mathrm{topo}}$ correction factor vs p'_T for $\mathcal{R}_{\mathrm{cone}} = 0.7$ jets. Different plots correspond to different values of $\eta_{\mathrm{jet}}^{\mathrm{det}}$.

11. SHOWERING CORRECTION

(A more detailed discussion on the showering correction, including a complete set of plots can be found in Ref. [23]. The plots shown in this section still need to be brought to publication level.)

After the offset and full set of response corrections discussed in Sects. 6 and 8-10, the corrected jet energy does not yet correspond to the particle-jet energy. Indeed, after offset subtraction, not all the energy contained inside the jet cone originates from particles belonging to the particle jet, so the response correction can not possibly recover the original particle jet energy. Because of effects such as the shower development as a result of interactions with the detector material, the granularity and pseudo-projective arrangement of the calorimeter towers, as well as the bending of low momentum charged tracks in the magnetic field, particles not belonging to the particle jet (e.g. from the underlying event) may contribute energy inside the jet cone. The same instrumental effects also cause some of the energy originated from particles belonging to the particle jet to leak outside the jet cone. Therefore, the so-called "showering correction" is required in order to compensate for the net energy flow through the jet cone boundary. Such a correction must be defined in a way consistent with respect to the rest of corrections, in order to ensure that the particle jet energy is recovered. The definition of this showering correction is given in Eq. 10 in Sect. 4.1, and we refer to it as the "true showering correction".

11.1. Method

The showering correction is determined both in data and MC using γ+jet events selected using the same criteria as for the absolute response measurement (see Sect. 8.1), with the exception that the probe jet is not restricted to be in the central calorimeter. The procedures to estimate the showering correction in data and MC are different. In the case of MC, it is possible to directly obtain an unbiased estimator of the "true showering correction". In contrast, in the case of data an observable sensitive to the jet showering must be defined, resulting in an a-priori biased estimator of the showering correction that must be calibrated. Sections 11.1.1 and 11.1.2 below present an overview of both procedures.

The showering correction is estimated separately for $\mathcal{R}_{\rm cone} = 0.7$ and 0.5 jets, in different 0.4-wide bins of $\left|\eta_{\rm jet}^{\rm det}\right|$ (up to $\left|\eta_{\rm jet}^{\rm det}\right| < 3.6$) and as a function of p'_T (defined as in Sect. 6.4).

11.1.1. Monte Carlo Method

In the case of MC, the showering correction is estimated in simulated γ+jet events without ZB overlay (i.e. offset energy). Owing to the detailed information available in the simulation regarding the amount of energy deposited in each calorimeter cell by each particle, it is possible to directly estimate the "true showering correction" according to Eq. 10. In absence of offset effects, the numerator of the showering correction in Eq. 10 represents the uncorrected jet energy as determined by the jet algorithm. The denominator is estimated by adding the visible energy in the calorimeter cells from the particles originating, either directly or as daughters of particles originating, from the particle jet. Therefore, the measurement of the true showering correction in MC requires a spatial matching between the calorimeter probe jet and the particle jet which, for consistency with the rest of corrections, is required to be within $\Delta\mathcal{R} < \mathcal{R}_{\rm cone}/2$.

11.1.2. Template-Based Method

The measurement of the showering correction in data is based on examining the energy distribution in the calorimeter in annuli of increasing radius $\Delta\mathcal{R}(y,\phi)$ with respect to the jet axis. We refer to such distribution as the "jet energy profile". Such energy distribution is obtained by combining cells into towers following exactly the same procedure as the jet algorithm (see Sect. 3.2.3), and then adding the energy from all towers within a particular $\Delta\mathcal{R}$ annulus.

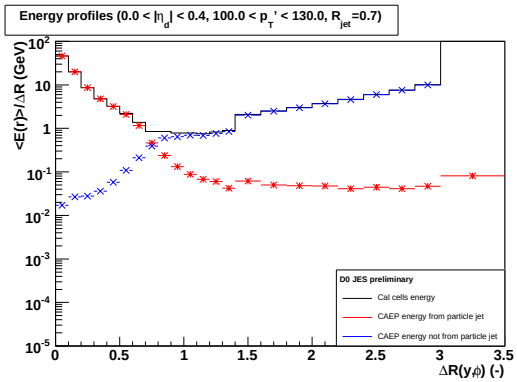

FIG. 23: Example of the jet energy profile for jets with $100 < p'_T < 130$ GeV and $\left|\eta^{\rm det}_{\rm jet}\right| < 0.4$ in γ+jet MC without ZB overlay. Shown in red (blue) are the contributions from particles (not) belonging to the particle jet matching the reconstructed probe jet.

Figure 23 shows an example of the jet energy profile for central jets in γ+jet MC without ZB overlay. *(See Figs. 182 and 183 in Appendix G1 for additional examples.)* Exploiting the available MC information, it is possible to compute the energy profiles corresponding to the particles belonging to the particle jet matching the reconstructed jet ("particle-jet profile") and the rest of the particles ("not-particle-jet profile"). The latter receives contributions from the underlying event as well as particles resulting from large-angle gluon radiation during the parton shower evolution. This figure allows to visualize the need for the showering correction. The integral of the total jet profile up to $\Delta\mathcal{R} < \mathcal{R}_{\rm cone}$, $E^{\rm meas}_{\rm jet}$, represents the uncorrected jet energy as reconstructed by the jet algorithm, which receives contributions from both particle-jet and not-particle-jet profiles: $E^{\rm meas}_{\rm jet} = E^{{\rm meas}(\Delta\mathcal{R}<\mathcal{R}_{\rm cone})}_{\rm ptclj} + E^{{\rm meas}(\Delta\mathcal{R}<\mathcal{R}_{\rm cone})}_{\rm not-ptclj}$. On the other hand, the integral of the particle-jet profile up to infinity, $E^{\rm meas}_{\rm ptclj}$, represents the total visible energy from the particle jet, a small fraction of which is deposited beyond the jet cone boundary. The ratio of both integrals represents an estimator of the "true showering correction", denoted by $\hat{S}_{\rm jet}$:

$$\hat{S}_{\rm jet} = \frac{E^{\rm meas}_{\rm jet}}{E^{\rm meas}_{\rm ptclj}} = \frac{E^{{\rm meas}(\Delta\mathcal{R}<\mathcal{R}_{\rm cone})}_{\rm ptclj}}{E^{\rm meas}_{\rm ptclj}} + \frac{E^{{\rm meas}(\Delta\mathcal{R}<\mathcal{R}_{\rm cone})}_{\rm not-ptclj}}{E^{\rm meas}_{\rm ptclj}}. \tag{59}$$

The distinct spatial distribution of energy around the jet centroid for each of these two contributions, as shown in Fig. 23, suggests that the showering correction could be estimated from a fit to the total jet profile, using templates for the particle-jet and not-particle-jet profiles extracted from MC. Indeed, this requires that the MC provides a good enough description of the jet profile. This includes proper modeling, not only of the physics, but also of instrumental effects. Regarding the physics description, the γ+jet MC samples used

are generated using PYTHIA Tune A [9], which has been verified to successfully describe the jet shapes in inclusive jet production [24]. The level of agreement observed in this measurement confirms this is also the case in γ+jet events.

Therefore, this is the procedure that will be used to estimate the showering correction in data. In practice, it is necessary to include in addition a template describing the offset energy profile. Such an offset template is estimated in γ+jet MC by subtracting from each template in the sample including unsuppressed ZB overlay, the corresponding template in the sample without ZB overlay. *(See Figs. 184 and 185 in Appendix G2 for some examples.)* This allows to properly take into account distortions to the template shape related to the interplay between zero-suppression and the presence of offset energy. Since the overlay in MC is based on ZB data events, the estimated offset profile is expected to closely match the one present in data. Finally, since the energy scale is different between data and MC, two global factors, α and β, are allowed to respectively rescale the particle-jet and not-particle jet profiles, whereas the well-determined offset profile is kept fixed. In addition, the scale factor β effectively allows to correct for a possible disagreement between data and MC on the absolute magnitude of the underlying event contribution. The α and β scale factors are estimated by performing a χ^2 fit of the observed jet profile in data (up to $\Delta\mathcal{R} = 2.0$) to a linear combination of the three templates, where α and β are the parameters to be estimated. *(Only measurements where both data and MC template profiles have a number of equivalent events greater than 100 are considered. This ensures that uncertainties in the energy profile are correct enough to obtain a robust template fit. This requirement is relaxed to 50 in the* $3.2 < \left|\eta_{\rm jet}^{\rm det}\right| < 3.6$ *bin in order to obtain a minimum of one measurement in data.)* The estimated showering correction is then given by:

$$\hat{S}_{\rm jet} = \frac{E_{\rm ptclj}^{{\rm meas}(\Delta\mathcal{R}<\mathcal{R}_{\rm cone}),{\rm MC}}}{E_{\rm ptclj}^{\rm meas,MC}} + \frac{\hat{\beta}}{\hat{\alpha}}\frac{E_{\rm not-ptclj}^{{\rm meas}(\Delta\mathcal{R}<\mathcal{R}_{\rm cone}),{\rm MC}}}{E_{\rm ptclj}^{\rm meas,MC}}, \tag{60}$$

where $E_{\rm ptclj}^{\rm meas,MC}$, $E_{\rm ptclj}^{{\rm meas}(\Delta\mathcal{R}<\mathcal{R}_{\rm cone}),{\rm MC}}$ and $E_{\rm not-ptclj}^{{\rm meas}(\Delta\mathcal{R}<\mathcal{R}_{\rm cone}),{\rm MC}}$ are estimated from the particle-jet and not-particle-jet MC templates, and $\hat{\alpha}$ and $\hat{\beta}$ are the estimated scale factors from the fit.

The procedure has been validated in full MC, where the estimated showering correction is found to very closely match the "true showering correction" estimated following the procedure described in Sect. 11.1.1. Small biases (typically $\leq 0.5\%$) are corrected for to ensure a properly calibrated estimator in data. *(Figures 186 and 187 in Appendix G3 illustrate the template fitting procedure in γ+jet MC with unsuppressed ZB overlay. As expected, the fit returns $\hat{\alpha} = \hat{\beta} = 1$ and the template-based showering correction can be estimated using Eq. 60. The ratio of the true showering correction (see Sect. 11.1.1) and the template-based correction defines the calibration factor to be applied to data, shown in Figs. 188 and 189 in Appendix G4. As it can be appreciated, such calibration factor is very close to 1, which demonstrates the template-based method provides an almost unbiased estimator of the true showering correction. Since the* p'_T *and* $\left|\eta_{\rm jet}^{\rm det}\right|$ *binning used in MC is identical to that used in data, measurements in data are corrected point-by-point using these factors before being parameterized using a smooth function.)*

Figure 24 compares the measured jet profile to the fitted one in data for jets with $80 < p'_T < 100$ GeV in the central ($\left|\eta_{\rm jet}^{\rm det}\right| < 0.4$) and forward ($2.0 < \left|\eta_{\rm jet}^{\rm det}\right| < 2.4$) regions. In general, reasonably good quality fits are found in a wide kinematic range, which suggests a good MC description of the jet energy profile. However, in some instances (e.g. Fig. 24(left)),

discrepancies between the data and fitted energy profiles are observed, particularly near $\mathcal{R}_{\rm cone}$. A corresponding systematic uncertainty will be assigned. *(Figures 190 and 191 in Appendix G3 provide additional examples of template fits in data.)*

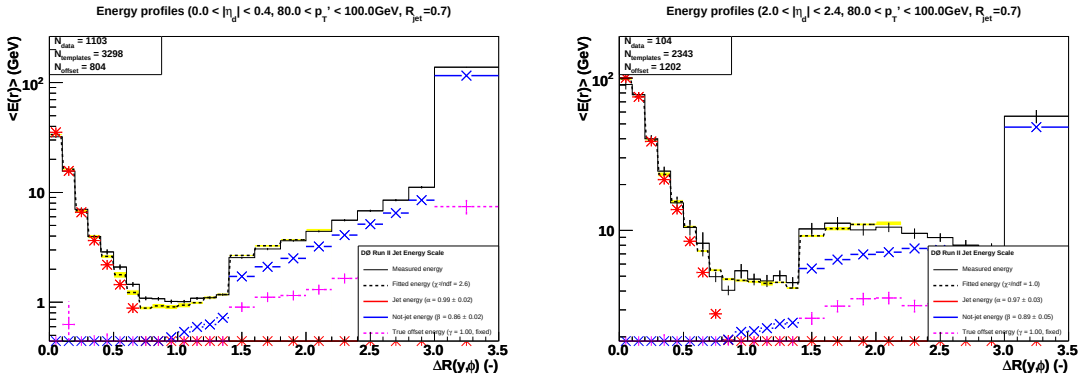

FIG. 24: Comparison of the measured jet profile in γ+jet data to the fitted jet profile for jets with $80 < p'_T < 100$ GeV in two different $\left|\eta^{\rm det}_{\rm jet}\right|$ regions.

(In fact, as pointed out during the CB review, the agreement between data and fitted profiles is less than perfect in particular in the $\left|\eta^{\rm det}_{\rm jet}\right| < 0.4$ *and* $0.4 < \left|\eta^{\rm det}_{\rm jet}\right| < 0.8$ *bins for* $p'_T < 100$ *GeV. A number of studies have been performed to try to understand the source of the problem and assess whether an additional systematic uncertainty is required. These systematic checks are summarized in Appendix G8.)*

11.2. Results

Figure 25 presents the estimated showering corrections for $\mathcal{R}_{\rm cone} = 0.7$ jets in MC, as a function of p'_T and for different $\eta^{\rm det}_{\rm jet}$ bins. Also shown is the result of a smooth parameterization of the correction as a function of $(p'_T, \eta^{\rm det}_{\rm jet})$. *(Figure 192 in Appendix G6 presents the showering correction for* $\mathcal{R}_{\rm cone} = 0.5$ *jets in MC.)*

The (bias-corrected) showering corrections in data is presented in Figure 26 for $\mathcal{R}_{\rm cone} = 0.7$ jets. Except for $p'_T < 30$ GeV, where dijet background contamination effects in data and data-to-MC differences in jet reconstruction efficienty and energy resolution dominate, a reasonably good agreement between the showering correction in data and MC is observed. This motivates parameterizing the correction in data using the same energy dependence as observed in MC. *(Figure 193 in Appendix G7 presents the showering correction for* $\mathcal{R}_{\rm cone} = 0.5$ *jets in data.)*

11.3. Uncertainties

In the case of MC, the uncertainties on the showering correction are limited to the statistical uncertainty from the fit, which is very small. In the case of data, several additional systematic uncertainties need to be considered. Figure 27 illustrates the relative uncertainties on the showering correction for $\mathcal{R}_{\rm cone} = 0.7$ jets in data for two different values of $\eta^{\rm det}_{\rm jet}$. *(A complete set of plots can be found in Figs. 203 and 204 in Appendix G9).*

In addition to the statistical uncertainty from the fit to the measurements, the following systematic uncertainties have been considered:

- Limited MC statistics in the templates: already included in the statistical uncertainty

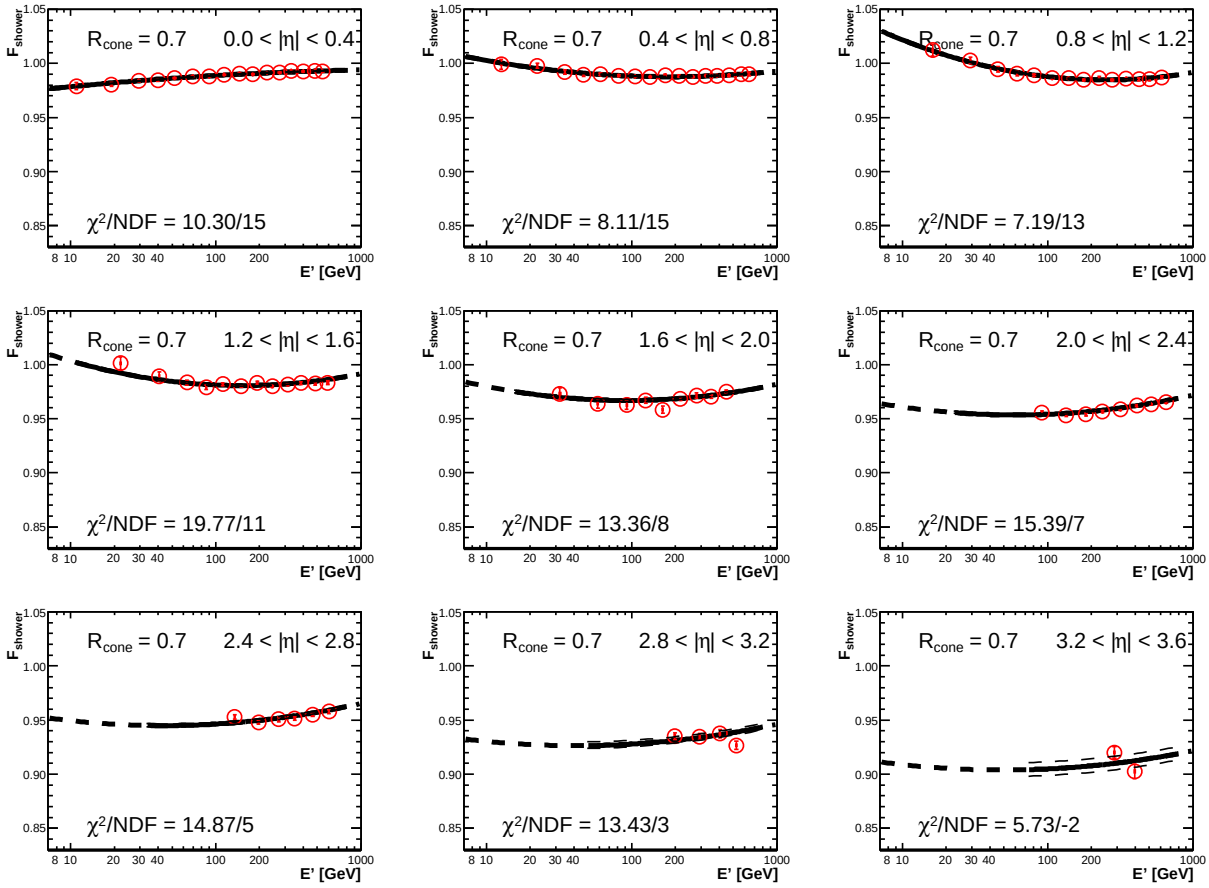

FIG. 25: Showering correction for $\mathcal{R}_{\rm cone} = 0.7$ jets in MC, as a function of p'_T and for different $\eta^{\rm det}_{\rm jet}$ bins. The solid line represents the result of a smooth parameterization of the correction as a function of $(p'_T, \eta^{\rm det}_{\rm jet})$.

from the template fit;

- Dijet background contamination in the γ+jet sample in data: such a contamination would mainly result in a modification of the average parton flavor composition of the jets, thus slightly distorting the jet profile shape. This uncertainty has been estimated in MC by comparing the template-based showering correction estimated from fitting jet profiles corresponding to pure γ+jet MC and from γ+jet plus EM+jet MC mixed in the expected sample purity in data (see Fig. 118 in Appendix D1). In both cases, the templates used were obtained from pure γ+jet MC, in complete analogy to how the showering correction is estimated in data. Figures 205 and 206 in Appendix G10 illustrate the relative difference in the estimated showering correction with respect to the nominal (pure γ+jet sample). The yellow band represents the currently assigned uncertainty.

- $\Delta\mathcal{R}$ matching: the arbitrary choice of $\Delta\mathcal{R} = \mathcal{R}_{\rm cone}/2$ in the particle jet to reconstructed jet matching when building the profiles results in a source of systematic uncertainty, as the distortion to the profiles (properly calibrated in MC) might be different between data and MC. The data is refitted with MC templates that have been obtained by varying the matching criterion $\Delta\mathcal{R} = \mathcal{R}_{\rm cone}/2 \pm 0.1$ and the relative difference used to assess a systematic uncertainty. Figures 207 and 208 in Appendix G11 illustrate

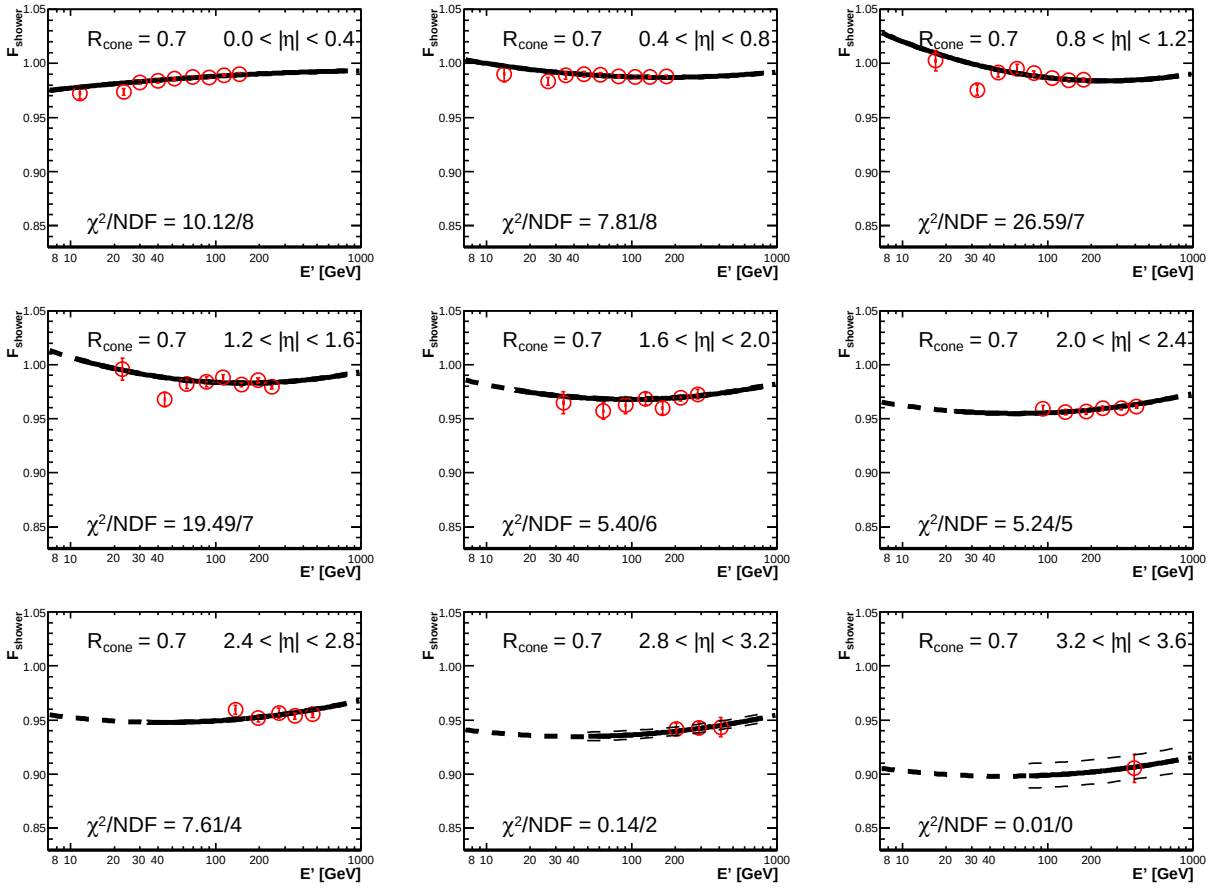

FIG. 26: Showering correction for $\mathcal{R}_{\rm cone} = 0.7$ jets in data, as a function of p'_T and for different $\eta^{\rm det}_{\rm jet}$ bins. The solid line represents the result of a smooth parameterization of the correction as a function of $(p'_T, \eta^{\rm det}_{\rm jet})$.

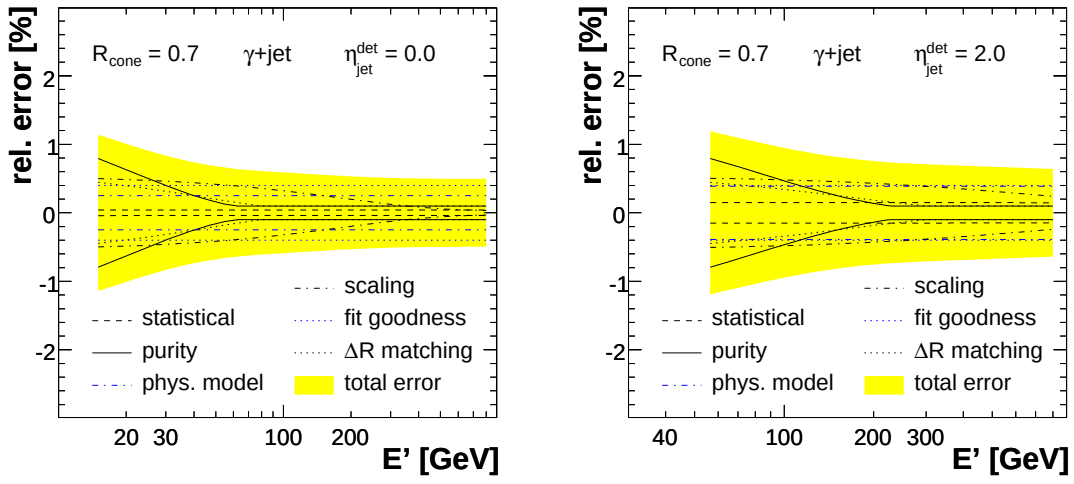

FIG. 27: Example of relative uncertainties on the showering correction vs p'_T for $\mathcal{R}_{\rm cone} = 0.7$ jets in data. Different plots correspond to different values of $\eta^{\rm det}_{\rm jet}$.

the relative difference in the estimated showering correction in data with respect to

the nominal. The yellow band represents the currently assigned uncertainty. Please note that there is some double-counting with respect to the uncertainty due to dijet contamination quoted above since varying the $\Delta\mathcal{R}$ matching also goes in the direction of probing the jet flavor composition, as gluon-originated particle jets will be less well matched to the reconstructed jet.

- Difference between data and MC in single pion response: this can cause a distortion in the particle-jet and not-particle-jet profiles used in the template method and therefore introduce a bias in the measurement in data. The reduced single pion response in data is expected to mainly result in suppressed tails (and not so much the core) of the particle-jet and not-particle-jet profiles with respect to the MC prediction. Therefore, the fitted scale factors would be essentiall unaffected, but the estimated showering correction could still be biased. In this scenario, this systematic uncertainty can be estimated from the true showering correction (since it so closely relates to the template-based showering). In order to evaluate it, the true showering has been compared between γ+jet MC with and without the single pion response scaled down (see Figures 209 and 210 in Appendix G12 respectively for $\mathcal{R}_{\rm cone} = 0.7$ and 0.5 jets.). As it can be appreciated, the effect is typically $\leq 0.5\%$.

- Physics model: the description of the underlying event (the main contribution to the not-particle-jet profile) is based on phenomenological models tuned to Tevatron Run I and Run II data. A different tune for the underlying event in PYTHIA, Tune DW [18], has been used to generate fully simulated samples of γ+jet MC. *(These samples have been generated in the forwad region, $\left|\eta_{\rm jet}^{\rm det}\right| > 2.0$, in order to ensure there is enough statistics in the a-priori most sensitive region.)* The difference in the true showering correction between Tune A and Tune DW is in the permille-level, which indicates the distortion to the not-particle-jet profile is very small. The assigned systematic uncertainty is 0.5% for $\eta_{\rm jet}^{\rm det} = 3.6$, linearly decreasing to 0.25% for $\eta_{\rm jet}^{\rm det} = 0.0$. *(See Figs. 211 and 212 in Appendix G13.)*

- Goodness of fit: as already indicated, there are instances where the template fit to the data jet energy profile is of poor quality (see e.g. Fig. 24(left)). Typically, an excess of energy is found in the data near $\mathcal{R}_{\rm cone}$, which is not reproduced by the fitted MC template. Studies in MC showed that a significant fraction of the discrepancy could be related to the dijet background contamination, for which a systematic uncertainty has already been assigned. However, potential inaccuracies in the simulation such as in the hadronic shower development, zero-suppression effects near $\mathcal{R}_{\rm cone}$, etc, could also be responsible for this discrepancy. A number of studies have been performed to try to identify the likely cause for this discrepancy, but these effects are very difficult to isolate and quantify. Nevertheless, by splitting the observed excess energy between the particle-jet and not-particle-jet profiles, it is possible to estimate the impact on the showering correction. *(See Appendix G8 for a discussion on the studies performed.)* As a result of these studies, a conservative 0.4% systematic uncertainty has been assigned.

Finally, it should be pointed out that this showering correction is strictly speaking applicable only to jets with a parton flavor composition similar to that in the γ+jet sample. In the case of dijet events, the parton flavor composition can be rather different (especially at the lowest and highest p_T) than for γ+jet. We have compared the true jet showering in γ+jet and dijet MC and we will likely provide a residual correction. The size of the effect for $\mathcal{R}_{\rm cone} = 0.7$ jets is typically $\leq 0.5\%$ for $\left|\eta_{\rm jet}^{\rm det}\right| < 0.4$ and $\sim 1.0\%$ for $2.0 < \left|\eta_{\rm jet}^{\rm det}\right| < 2.4$.

12. QCD-SPECIFIC CORRECTIONS

The jet energy calibration corrections derived so far are designed to correct the energy of jets with a flavor composition similar to that in the γ+jet sample to the particle level. Furthermore, these corrections are not guaranteed to properly calibrate to the particle level the rest of the jet four-momentum components. These caveats do not represent significant limitations for any physics measurements relying on the comparison of observables betwen data and MC (e.g. top mass measurement), which represent the bulk of DØ's physics program. Rather than on the absolute energy scale, these measurements depend on the relative data-to-MC intercalibration. Therefore, as long as MC is biased in the same way as data, the measurements can still be carried out in an unbiased way.

However, most of the QCD physics program is based on the direct comparison with theory of observables in data after unfolding of experimental effects. These measurements fully depend on the absolute energy calibration of jets in data. As discussed previously, the different flavor composition of jets in QCD multijet as compared to γ+jet production, will require a dedicated jet energy calibration to be derived for this sample. Furthermore, many of the observables considered involve components of the four-momentum other than energy, which are also required to be properly calibrated to the particle level. A prime example is the measurement of the inclusive jet differential p_T spectrum in bins of jet rapidity, which depends on the calibration of jet p_T and y, or the measurement of the dijet mass spectum, which requires calibration of the full jet four-momentum.

This section presents a discussion on the strategy to calibrate the jet four-momentum in the QCD dijet sample. These corrections are determined only for $\mathcal{R}_{\text{cone}} = 0.7$ jets.

12.1. Jet Energy Calibration

In order to understand what modifications are required to properly calibrate jet energies in the case of the QCD dijet sample, it is useful to start from the expression of the corrected energy in case of the γ+jet sample, making explicit the different subcorrections and at which energy they are evaluated. Therefore, given a jet with detector pseudorapidity $\eta_{\text{jet}}^{\text{det}}$, the corrected jet energy is given by (following Eqs. 12 and 31):

$$E_{\text{jet}}^{\text{corr}} = \frac{(E_{\text{jet}}^{\text{meas}} - E_{\text{O},\eta})}{R_{\text{MPF,CC}}^{\gamma+\text{jet}} F_{\eta}^{\gamma+\text{jet}} \left(k_{\text{R},\eta}^{\text{topo},\gamma+\text{jet}}\right)^{\text{MC}} S_{\text{jet},\eta}^{\gamma+\text{jet}}} \left(\frac{k_{\text{O},\eta}^{\text{ZS}}}{k_{\text{R},\eta}^{\text{ZS}}}\right)^{\text{MC}}, \tag{61}$$

where all subcorrections which are expected to be sample-dependent are denoted with the superscript "γ+jet", and those which have been determined in MC include the superscript "MC". All subcorrections are evaluated at the estimated E' for the jet (see Sect. 13.1).

In the case of jet energy calibration for the QCD dijet sample, it would a-priori appear necessary to redetermine every sample-dependent subcorrection above. In fact, the relative MPF response correction (F_{η}^{dijet}) was already determined in Sect. 9 and is therefore available. While the showering correction could in principle be directly estimated from QCD dijet data following a similar approach to that used in Sect. 11, the absolute MPF response correction can not be estimated for QCD dijet events. By carefully taking into account the meaning of each of the subcorrections, it can be demonstrated that the energy for jets from QCD dijet events can be properly calibrated using the following modified formula:

$$E_{\rm jet}^{\rm corr} = \frac{(E_{\rm jet}^{\rm meas} - E_{{\rm O},\eta})}{R_{\rm MPF,CC}^{\gamma+{\rm jet}} F_\eta^{\rm dijet} \left(k_{{\rm R},\eta}^{{\rm topo},\gamma+{\rm jet}}\right)^{\rm MC} \left(\frac{R_{\rm jet,CC}^{\rm dijet}}{R_{\rm jet,CC}^{\gamma+{\rm jet}}}\right)^{\rm MC} \left(S_{{\rm jet},\eta}^{\rm dijet}\right)^{\rm MC}} \left(\frac{k_{{\rm O},\eta}^{\rm ZS}}{k_{{\rm R},\eta}^{\rm ZS}}\right)^{\rm MC}, \qquad (62)$$

where the main difference is the replacement of $S_{{\rm jet},\eta}^{\gamma+{\rm jet}}$ with $S_{{\rm jet},\eta}^{\rm dijet}$ (also evaluated at E'), and the addition of the correction factor $R_{\rm jet,CC}^{\gamma+{\rm jet}}/R_{\rm jet,CC}^{\rm dijet}$, defined as the ratio of true jet responses in CC betwen γ+jet and dijet events which, in contrast with the rest of subcorrections, must be evaluated at p_T'. *(In the next update will likely include an appendix with the algebra that shows how we get to the above expression.)*

Please note that these two additional corrections are being evaluated in MC, for both data and MC jet energy calibration. In the case of $S_{{\rm jet},\eta}^{\rm dijet}$, this is justified by the good agreement obtained between the direct measurements of $S_{{\rm jet},\eta}^{\gamma+{\rm jet}}$ in data and MC (compare Figs. 25 and 26 in Sect. 11.2). The different jet flavor composition between QCD dijet and γ+jet events results in typically $\leq 1\%$ differences in the true showering correction (see Fig. 213 in Appendix H). Nevertheless, this correction is explicitly parameterized.

In contrast, there is a significant difference in true jet response for central jets between γ+jet and dijet events as predicted by MC, as it can be appreciated in Fig. 28(left). Furthermore, owing to the different single pion response in data and MC, such ratio is also estimated for data using MC with a tuned single pion response (see Sect. 8.3.1). As shown in Fig. 28(right), there is indeed a significant difference between both ratios, which must be taken into account for precision QCD measurements.

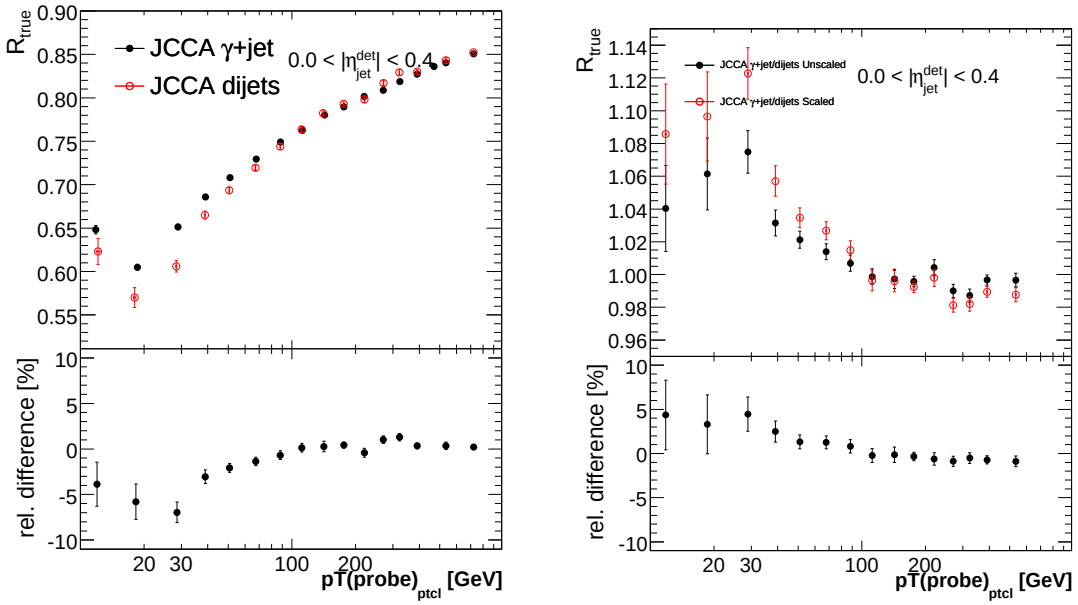

FIG. 28: Left: ratio of true jet response for jets with $|\eta_{\rm jet}^{\rm det}| < 0.4$ from γ+jet and dijet MC events as a function of particle-jet p_T. Right: comparison between the true jet response ratio as predicted by default MC ("unscaled") and by a special MC with a tuned single pion response ("scaled").

12.2. Jet p_T Calibration

Monte Carlo predicts that jet rapidity and mass are both biased, which implies that a single calibration factor can not simultaneously correct jet energy and p_T. Therefore, a explicit calibration procedure for jet p_T is required. Fortunately, we can heavily rely on available subcorrections from energy calibration. In fact, the corrected jet p_T can be estimated according to the following expression:

$$p_{T\text{jet}}^{\text{corr}} = \frac{(p_{T\text{jet}}^{\text{meas}} - p_{TO,\eta})}{R_{\text{MPF,CC}}^{\gamma+\text{jet}} F_\eta^{\text{dijet}} \left(k_{\text{R},\eta}^{\text{topo,pT},\gamma+\text{jet}}\right)^{\text{MC}} \left(\frac{R_{\text{jet,CC}}^{\text{dijet}}}{R_{\text{jet,CC}}^{\gamma+\text{jet}}}\right)^{\text{MC}} \left(S_{\text{jet},\eta}^{\text{pT,dijet}}\right)^{\text{MC}}} \left(\frac{k_{\text{O,pT},\eta}^{\text{ZS}}}{k_{\text{R},\eta}^{\text{ZS}}}\right)^{\text{MC}}, \quad (63)$$

where $p_{TO,\eta}$ stands for the offset p_T correction, $k_{\text{O,pT},\eta}^{\text{ZS}}$ is the zero-suppression bias correction to the estimated offset p_T, $k_{\text{R},\eta}^{\text{topo,pT},\gamma+\text{jet}}$ is the p_T-based topology bias correction to MPF response and $S_{\text{jet},\eta}^{\text{pT,dijet}}$ is the true showering correction to p_T.

Since only the offset energy correction has been explicitly measured, we therefore make the following approximation:

$$(p_{T\text{jet}}^{\text{meas}} - p_{TO,\eta}) k_{\text{O,pT},\eta}^{\text{ZS}} \simeq \frac{p_{T\text{jet}}^{\text{meas}}}{E_{\text{jet}}^{\text{meas}}} (E_{\text{jet}}^{\text{meas}} - E_{\text{O},\eta}) k_{\text{O},\eta}^{\text{ZS}}, \quad (64)$$

which is expected to be accurate enough in the kinematic range of interest of QCD measurements (typically $p_{T\text{jet}}^{\text{corr}} > 50$ GeV). *(We still need to quantify how precise this approximation is.)*

Similarly to Eq. 28, the p_T-based topology bias correction to MPF response is defined as:

$$k_{\text{R},\eta}^{\text{topo,pT},\gamma+\text{jet}} = \frac{R_{\text{jet}}^{\text{pT},\gamma+\text{jet}}}{R_{\text{MPF}}^{\gamma+\text{jet,noZB}}} \quad (65)$$

where $R_{\text{jet}}^{\text{pT},\gamma+\text{jet}}$ is the p_T-based true jet response (recall Eq. 9 for the definition of (energy-based) true jet response):

$$R_{\text{jet}}^{\text{pT}} = \frac{|\sum_{\text{i}\in\text{ptcljet}} \vec{p}_{T\text{i}}^{\text{meas}}|}{p_{T\text{jet}}^{\text{ptcl}}}. \quad (66)$$

This correction is closer to one than in the case of energy, which indicates that the MPF method is more suitable for calibration of jet p_T than for calibration of jet energy. *(See Fig. 214 in Appendix H for a complete set of plots for $\mathcal{R}_{\text{cone}} = 0.7$ jets.)*

Finally, the true showering correction to p_T is defined similarly to the (energy-based) true showering correction (see Eq. 10):

$$S_{\text{jet}}^{\text{pT}} = \frac{|\sum_{\text{i}\in\text{ptcljet}} \vec{p}_{T\text{i}}^{\text{meas}} S_{\text{i}} + \sum_{\text{i}\notin\text{ptcljet}} \vec{p}_{T\text{i}}^{\text{meas}} S_{\text{i}}|}{|\sum_{\text{i}\in\text{ptcljet}} \vec{p}_{T\text{i}}^{\text{meas}}|}. \quad (67)$$

As expected, the net p_T flow through the jet cone boundary is smaller than the net energy flow, as shown in Fig. 215 in Appendix H. Such correction is explicitly parameterized for QCD dijet MC.

12.3. Jet Rapidity Calibration

As already indicated above, Monte Carlo predicts a bias in the reconstructed jet rapidity with respect to the particle level. As shown in Fig. 29, the jet rapidity is generally biased towards the central calorimeter, with the largest deviations observed in the ICR. While not fully understood, the main two reasons for this bias are expected to be: (i) instrumental effects in the ICR, which would be responsible for the large bias near $y_{\rm jet}^{\rm ptcl} \sim 1.5$ and (ii) jet algorithm-related effects, which would cause the increase of the bias towards EC. *(Regarding (ii), apparently a similar effect was observed when comparing the DØ Run I cone algorithm and the the Snowmass algorithm, which calculated four-vector variables similarly to the Run II cone algorithm.)* Since currently there is no reliable experimental handle in data regarding this bias, it is currently being estimated in MC. The rapidity bias $\Delta y_{\rm jet} = y_{\rm jet}^{\rm meas} - y_{\rm jet}^{\rm ptcl}$ is parameterized with a smooth 2D function versus $(p_{T\rm jet}^{\rm ptcl}, y_{\rm jet}^{\rm meas})$. The actual measurement is performed in bins of $(p_{T\rm jet}^{\rm ptcl}, y_{\rm jet}^{\rm ptcl})$ to avoid a resolution bias, and then it is remapped to $(p_{T\rm jet}^{\rm ptcl}, y_{\rm jet}^{\rm meas})$. The corrected jet rapidity is then given by:

$$y_{\rm jet}^{\rm corr} = y_{\rm jet}^{\rm meas} - \Delta y_{\rm jet} \tag{68}$$

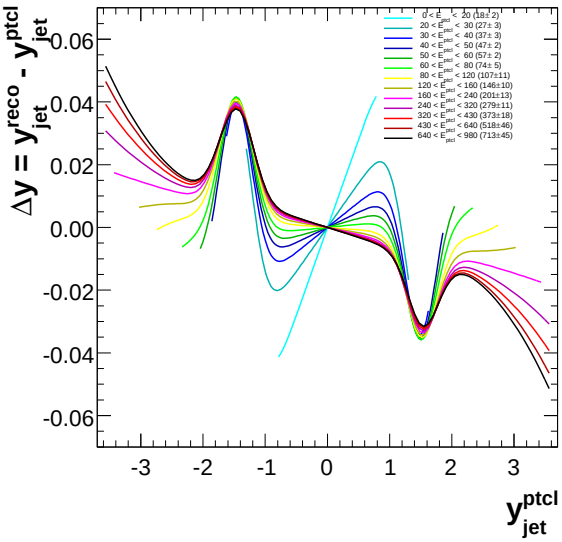

FIG. 29: Rapidity bias vs particle-jet rapidity as predicted by QCD dijets MC for $\mathcal{R}_{\rm cone} = 0.7$ jets in different particle-jet energy bins.

12.4. Four-Momentum Correction

The calibrated jet four-momentum $P_{\rm jet}^{\mu,\rm corr}$ is given by:

$$P_{\rm jet}^{\mu,\rm corr} = (E_{\rm jet}^{\rm corr}, p_{T\rm jet}^{\rm corr} \cos\phi_{\rm jet}^{\rm corr}, p_{T\rm jet}^{\rm corr} \sin\phi_{\rm jet}^{\rm corr}, p_{z\rm jet}^{\rm corr}), \tag{69}$$

were $E_{\rm jet}^{\rm corr}$ and $p_{T\rm jet}^{\rm corr}$ are defined, respectively, in Eqs. 62 and 63. The measured jet azimuthal angle is assumed to be unbiased, and thus $\phi_{\rm jet}^{\rm corr} = \phi_{\rm jet}^{\rm meas}$. Finally, given the calibrated jet energy and rapidity (see Eq. 68):

$$p_{z\rm jet}^{\rm corr} = E_{\rm jet}^{\rm corr} \frac{\exp(2y_{\rm jet}^{\rm corr}) - 1}{\exp(2y_{\rm jet}^{\rm corr}) + 1}. \tag{70}$$

13. SUMMARY OF CORRECTIONS AND UNCERTAINTIES

This section just provides a snapshot of the preliminary corrections and uncertainties for data and MC currently implemented in jetcorr (v07-02-58).

Summary plots of corrections and uncertainties are shown below for both data and MC. The JES correction factors k_{JES} are obtained from the measured offset E_0, response R_{jet} and showering R_{cone} sub-corrections using the following relation:

$$k_{\rm JES} = \frac{E^{\rm ptcl}_{\rm jet}}{E^{\rm meas}_{\rm jet}} = k_{\rm O}k_{\rm R}k_{\rm S}, \tag{71}$$

$$k_{\rm O} = \frac{E^{\rm meas}_{\rm jet} - E_{\rm O}}{E^{\rm meas}_{\rm jet}}, \tag{72}$$

$$k_{\rm R} = \frac{1}{R_{jet}}, \tag{73}$$

$$k_{\rm S} = \frac{1}{S_{jet}}. \tag{74}$$

13.1. $E^{\rm meas}_{\rm jet}$ to E' mapping

The individual subcorrections discussed in previous sections have all been parameterized as a function of the E' variable, which then becomes the variable in terms of which they must be evaluated. Given the uncorrected jet energy ($E^{\rm meas}_{\rm jet}$), this is accomplished by solving the following equation for E':

$$E^{\rm meas}_{\rm jet} - \hat{E}_{\rm O} = E' \frac{R^{\gamma+{\rm jet}}_{\rm MPF}(E')k^{\rm topo}_{\rm R}(E')S_{\rm jet}(E')}{(k^{\rm ZS}_{\rm O}/k^{\rm ZS}_{\rm R})(E')} S^{\rm phys}_{\rm jet}(E'), \tag{75}$$

where $S^{\rm phys}_{\rm jet} = E^{\rm ptcl}_{\rm jet}/E'$ is estimated in γ+jet MC as a function of E' and $\eta^{\rm det}_{\rm jet}$, separately for $\mathcal{R}_{\rm cone} = 0.7$ and 0.5 jets. Please note that $S^{\rm phys}_{\rm jet}$ is the required correction in order to replace the E' factor in the right hand side of Eq. 75 by $E^{\rm ptcl}_{\rm jet}$, thus making this expression consistent since the individual subcorrections are designed to correct the measured jet energy to the particle-jet level. The term $S^{\rm phys}_{\rm jet}$ is interpreted as the fraction of energy lost from out-of-cone radiation (physics showering), since it compares the particle-jet energy to E', the estimated energy of the parton recoiling against the photon in an ideal $2 \to 2$ process. As expected, $S^{\rm phys}_{\rm jet} < 1$, particularly for $\mathcal{R}_{\rm cone} = 0.5$ and/or forward jets, where values as low as $0.85 - 0.9$ can be reached. Since the different subcorrections are typically logarithmic in energy, a precision of $\leq 5\%$ in this mapping from $E^{\rm meas}_{\rm jet}$ to E' is sufficient.

Figure 30(31) shows the estimated $S^{\rm phys}_{\rm jet}$ correction as a function of p'_T (defined as in Sect. 6.4) for selected γ+jet MC events with a $\mathcal{R}_{\rm cone} = 0.7(0.5)$ calorimeter jet in different $\left|\eta^{\rm det}_{\rm jet}\right|$ regions. The increase in $S^{\rm phys}_{\rm jet}$ for $p'_T < 30$ GeV is still under investigation but it is believed to be caused by biases due to the event selection and/or 6 GeV reconstruction threshold for particle jets. Therefore, it is not explicitly parameterized. In order to verify how precisely this mapping works, the estimated E' inside jetcorr ($E'_{\rm jetcorr}$) via Eq. 75 is compared to the true E' in γ+jet MC. As it can be appreciated in Figs. 32 and 33, the mapping is precise to the $\leq 3\%$ level for non low-E_T biased jets (i.e. $p'_T \geq 30$ GeV) over the

full $\eta_{\rm jet}^{\rm det}$ range.

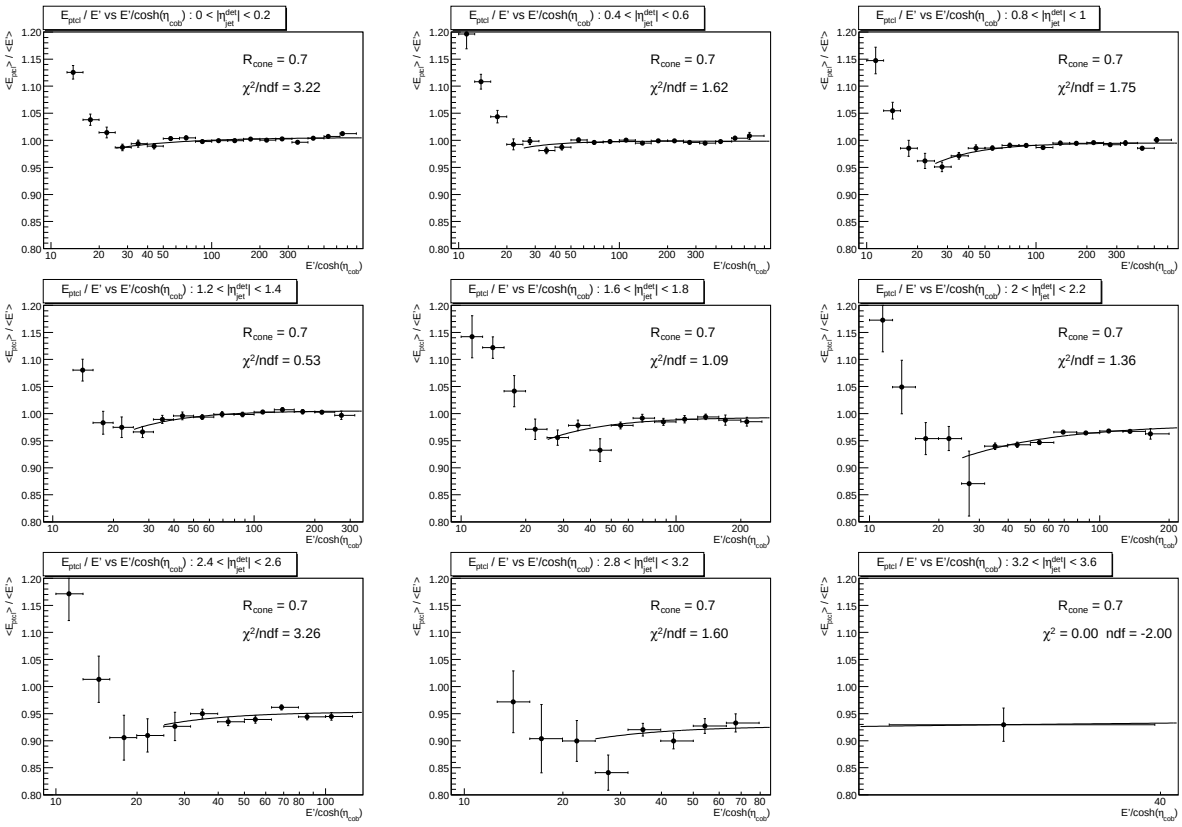

FIG. 30: Estimated $S_{\rm jet}^{\rm phys}$ correction factor in selected γ+jet MC events for $\mathcal{R}_{\rm cone} = 0.7$ jets in different $\left|\eta_{\rm jet}^{\rm det}\right|$ regions.

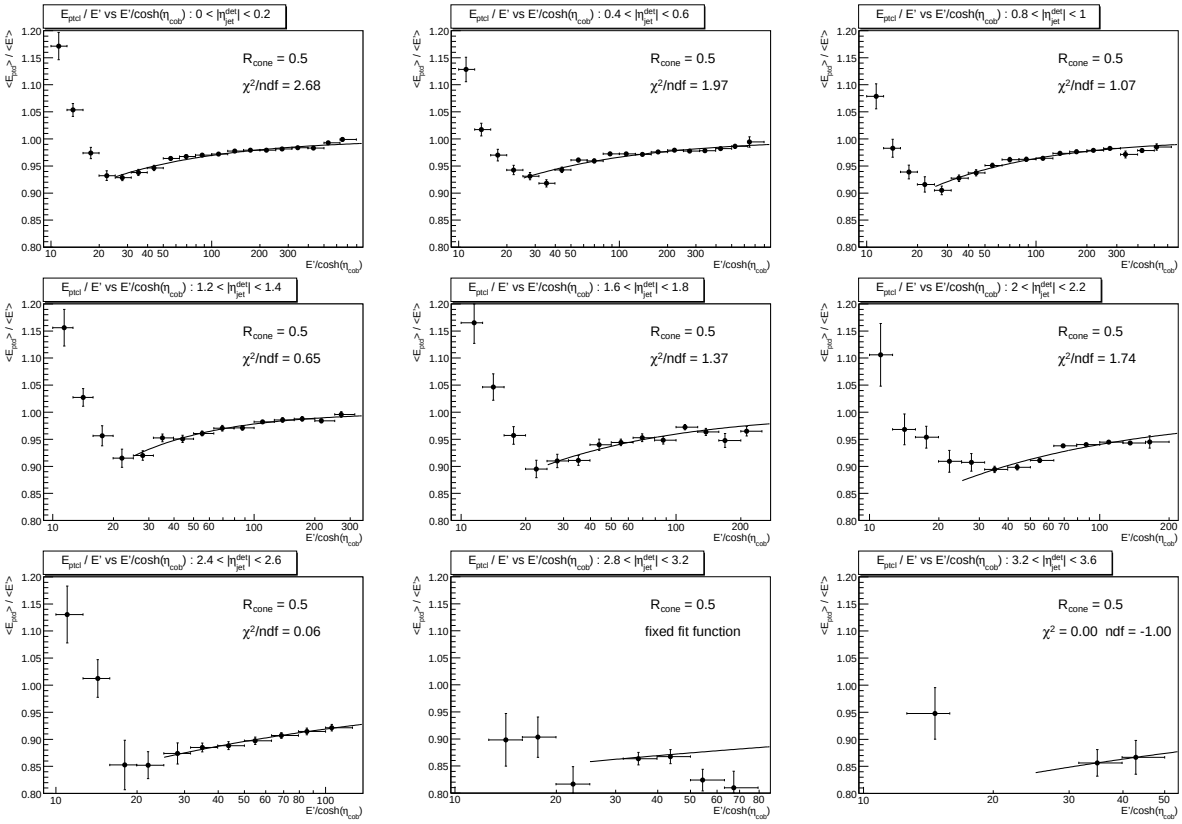

FIG. 31: Estimated $S_{\rm jet}^{\rm phys}$ correction factor in selected γ+jet MC events for $\mathcal{R}_{\rm cone} = 0.5$ jets in different $\left|\eta_{\rm jet}^{\rm det}\right|$ regions.

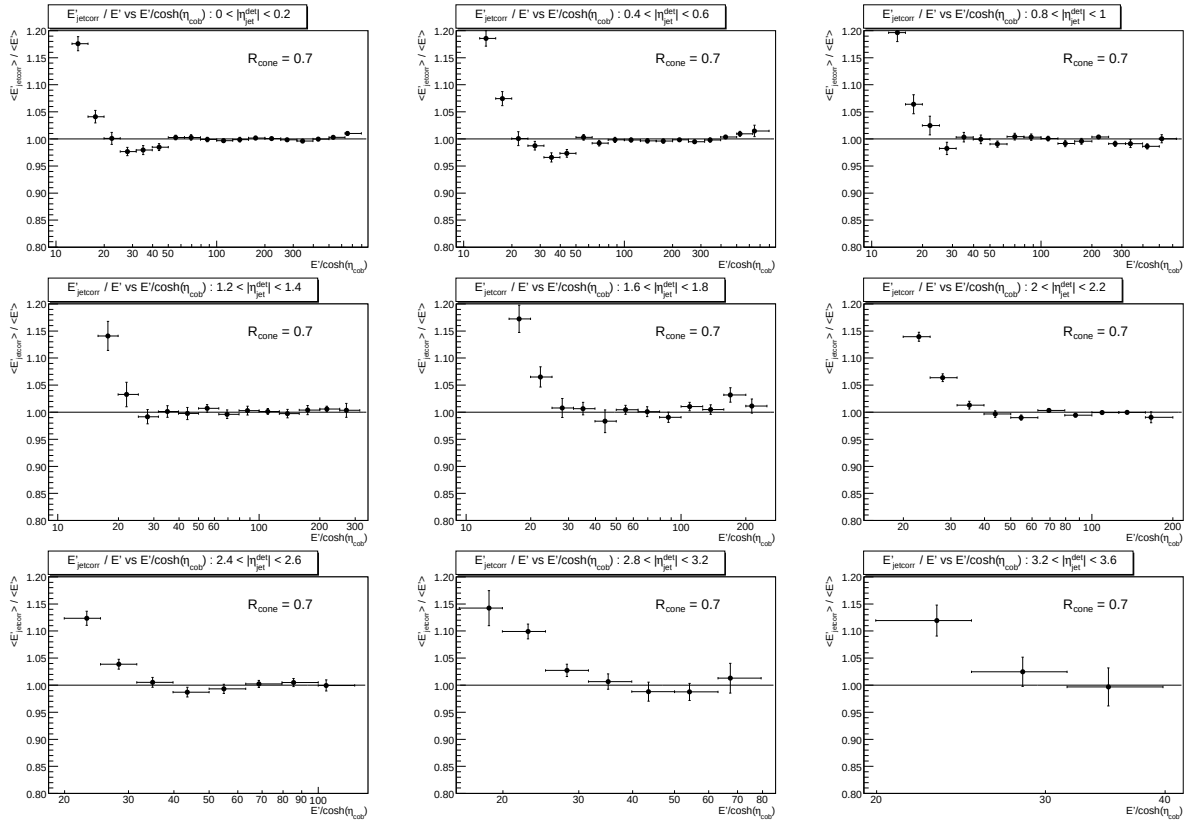

FIG. 32: Ratio of E'_{jetcorr} (estimated using Eq. 75) and the true event E' in selected γ+jet MC events for $\mathcal{R}_{\text{cone}} = 0.7$ jets in different $\left|\eta_{\text{jet}}^{\text{det}}\right|$ regions.

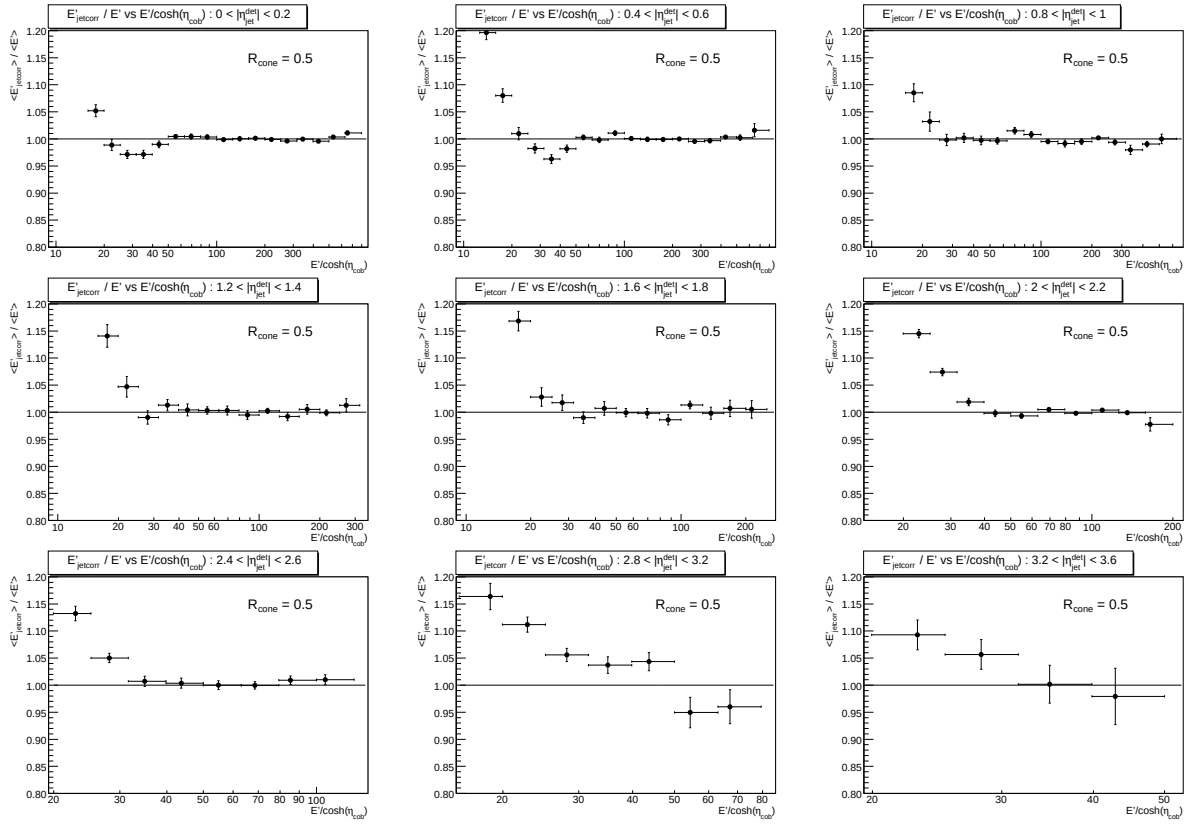

FIG. 33: Ratio of E'_{jetcorr} (estimated using Eq. 75) and the true event E' in selected γ+jet MC events for $\mathcal{R}_{\text{cone}} = 0.5$ jets in different $\left|\eta_{\text{jet}}^{\text{det}}\right|$ regions.

13.2. γ+jet Corrections and Uncertainties

13.2.1. Data $\mathcal{R}_{\rm cone} = 0.7$

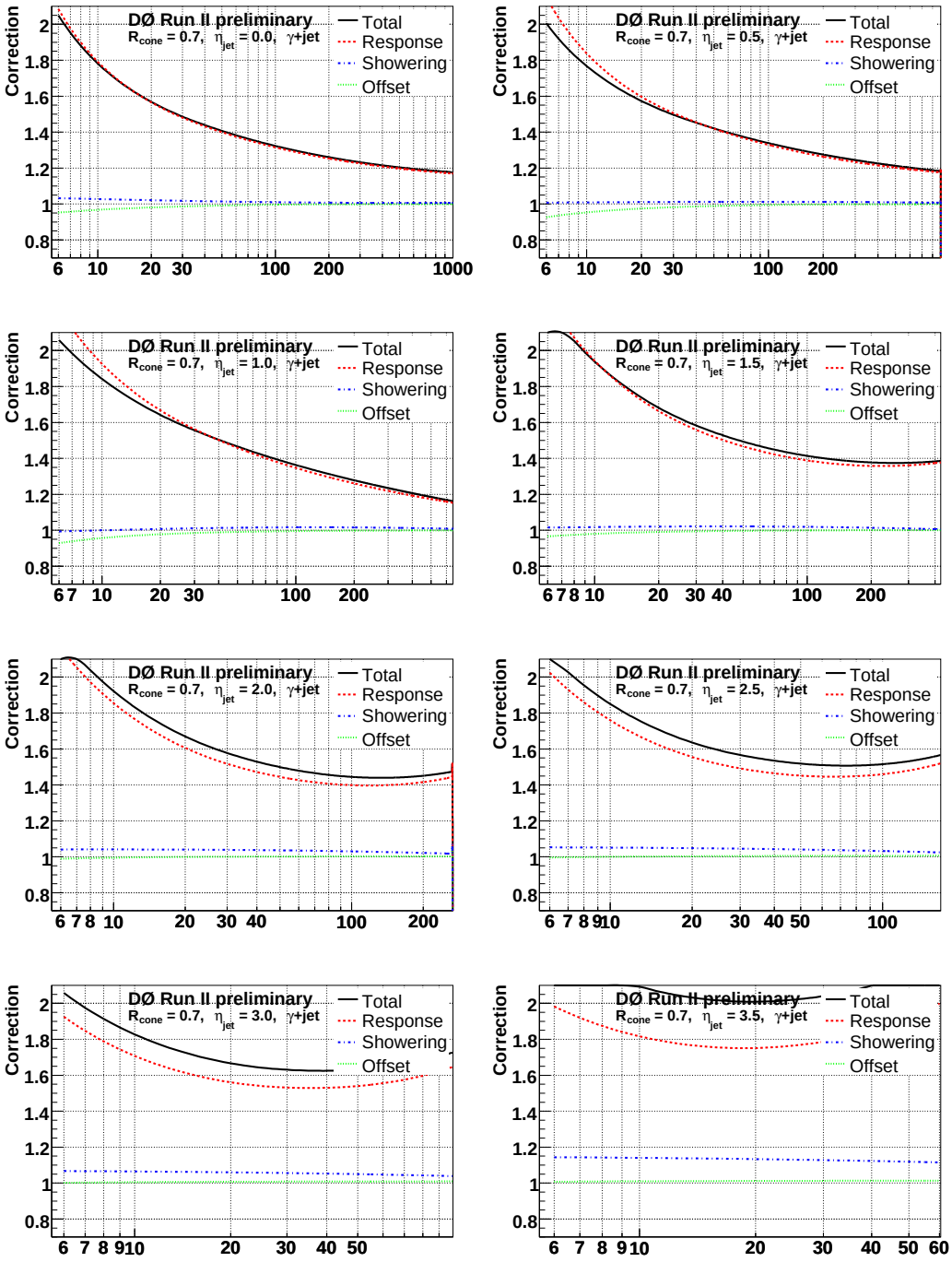

FIG. 34: Jet energy scale corrections in data for $\mathcal{R}_{\rm cone} = 0.7$ as a function of $E_{T,\rm jet}^{\rm meas}$ for different $\eta_{\rm jet}^{\rm det}$ values (from left to right and top to bottom: $\eta_{\rm jet}^{\rm det} = 0.0$, 0.5, 1.0, 1.5, 2.0, 2.5, 3.0 and 3.5).

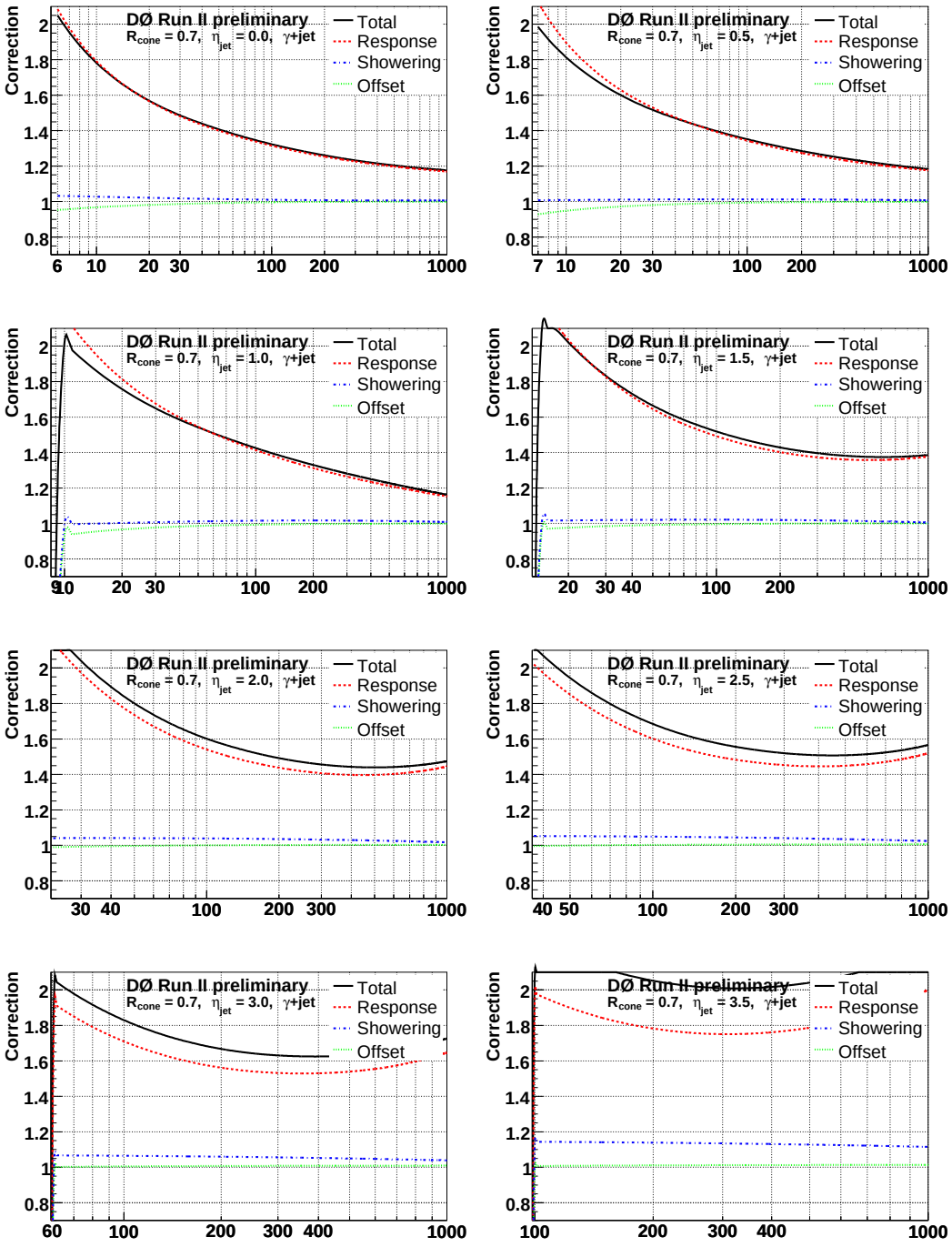

FIG. 35: Jet energy scale corrections in data for $\mathcal{R}_{\rm cone} = 0.7$ as a function of $E_{\rm jet}^{\rm meas}$ for different $\eta_{\rm jet}^{\rm det}$ values (from left to right and top to bottom: $\eta_{\rm jet}^{\rm det} = 0.0$, 0.5, 1.0, 1.5, 2.0, 2.5, 3.0 and 3.5).

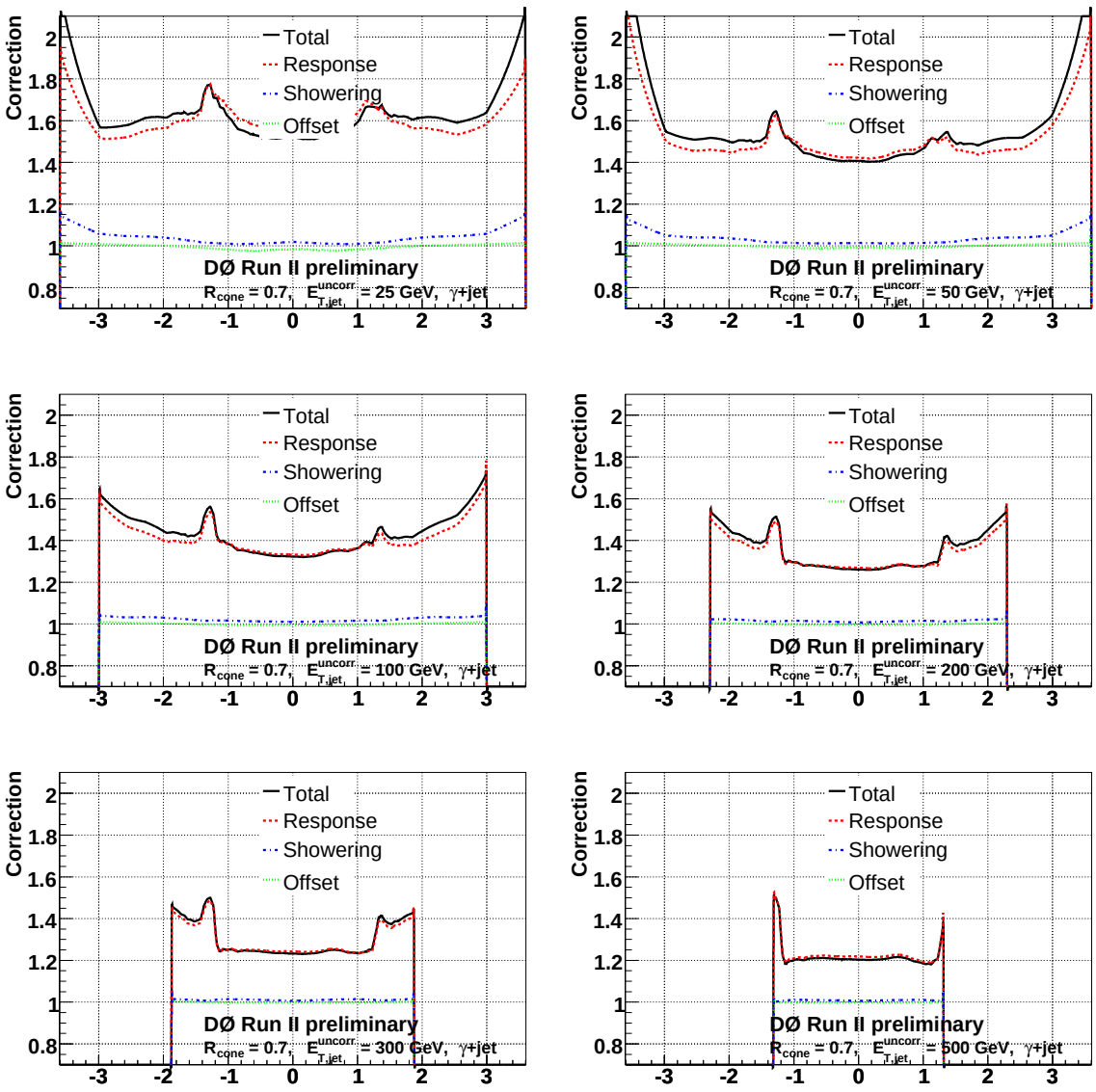

FIG. 36: Jet energy scale corrections in data for $\mathcal{R}_{\rm cone} = 0.7$ as a function of $\eta^{\rm det}_{\rm jet}$ for different $E^{\rm meas}_{T,\rm jet}$ values (from left to right and top to bottom: $E^{\rm meas}_{T,\rm jet} = 25$, 50, 100, 200, 300 and 500 GeV).

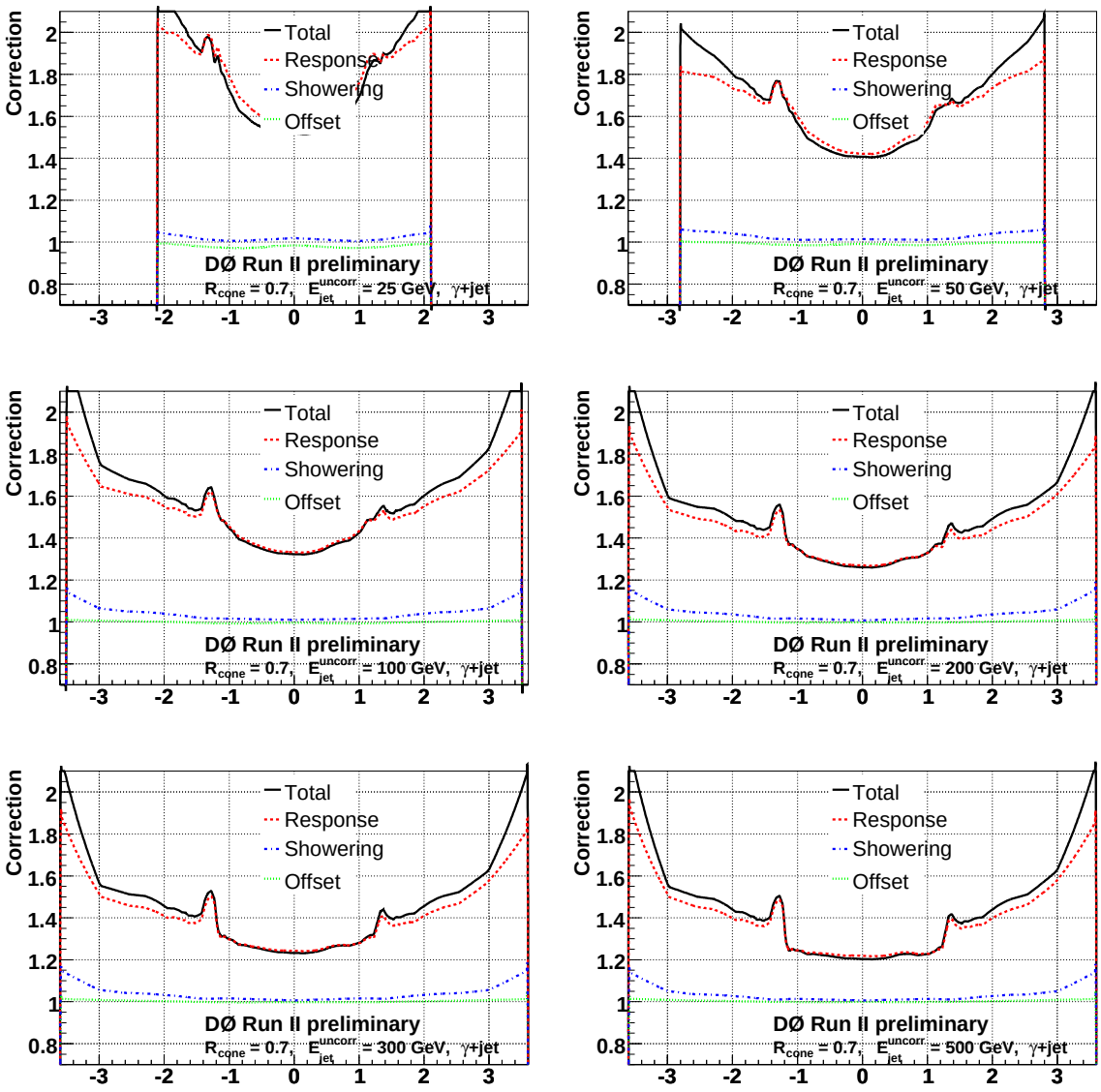

FIG. 37: Jet energy scale corrections in data for $\mathcal{R}_{\rm cone} = 0.7$ as a function of $\eta_{\rm jet}^{\rm det}$ for different $E_{\rm jet}^{\rm meas}$ values (from left to right and top to bottom: $E_{\rm jet}^{\rm meas} = 25$, 50, 100, 200, 300 and 500 GeV).

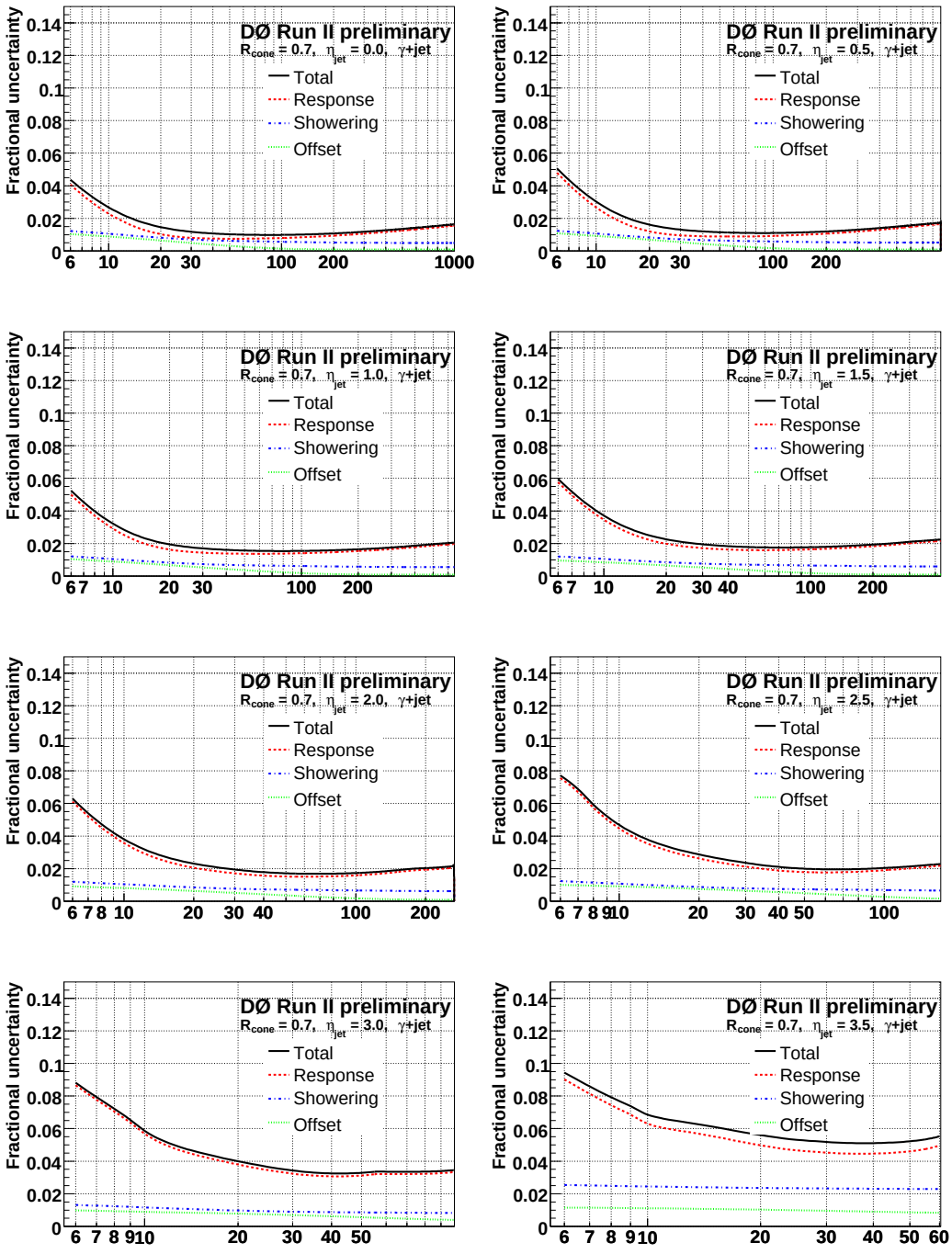

FIG. 38: Relative jet energy scale uncertainties in data for $\mathcal{R}_{\rm cone} = 0.7$ as a function of $E_{T,\rm jet}^{\rm meas}$ for different $\eta_{\rm jet}^{\rm det}$ values (from left to right and top to bottom: $\eta_{\rm jet}^{\rm det} = 0.0$, 0.5, 1.0, 1.5, 2.0, 2.5, 3.0 and 3.5).

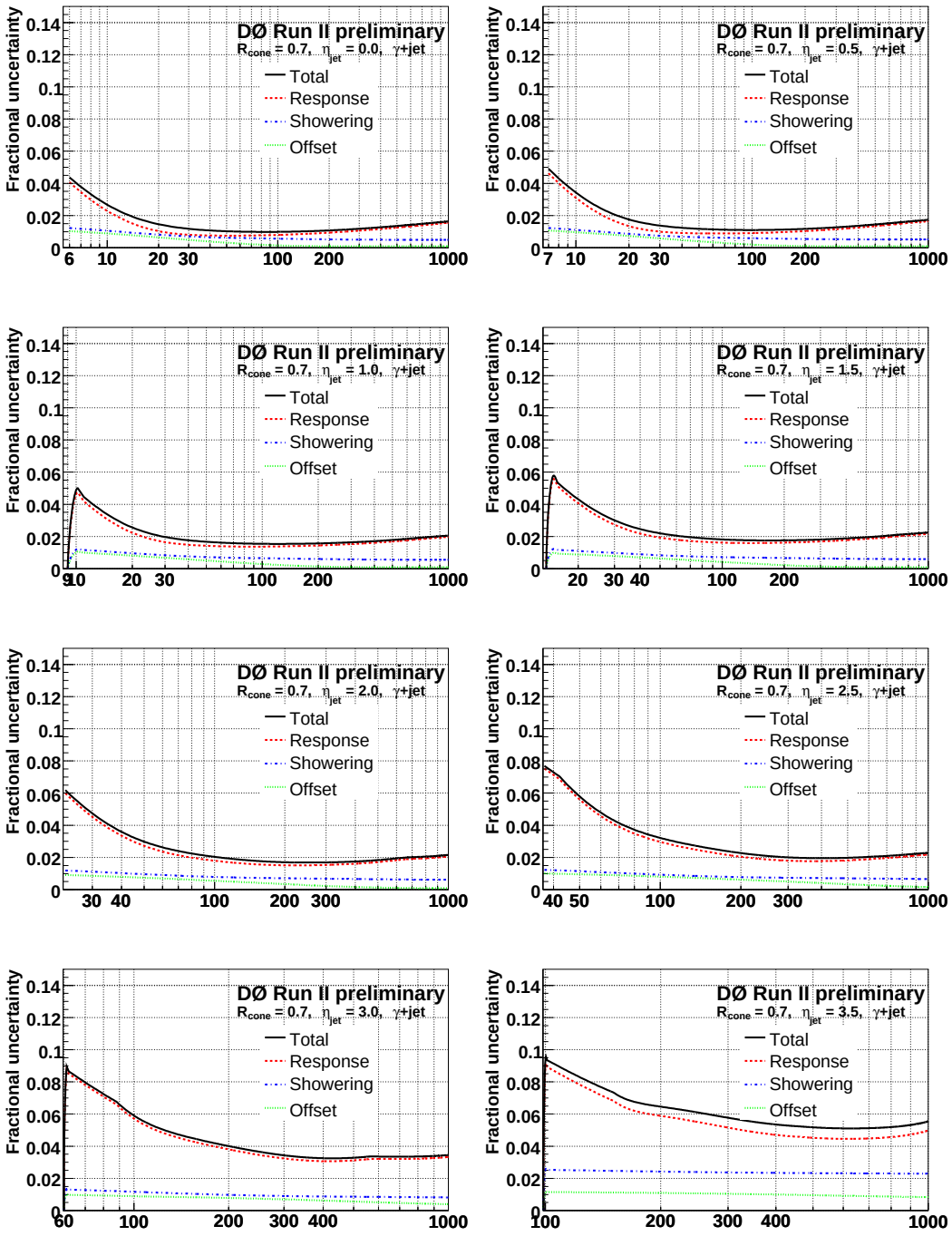

FIG. 39: Relative jet energy scale uncertainties in data for $\mathcal{R}_{\rm cone} = 0.7$ as a function of $E_{\rm jet}^{\rm meas}$ for different $\eta_{\rm jet}^{\rm det}$ values (from left to right and top to bottom: $\eta_{\rm jet}^{\rm det} = 0.0$, 0.5, 1.0, 1.5, 2.0, 2.5, 3.0 and 3.5).

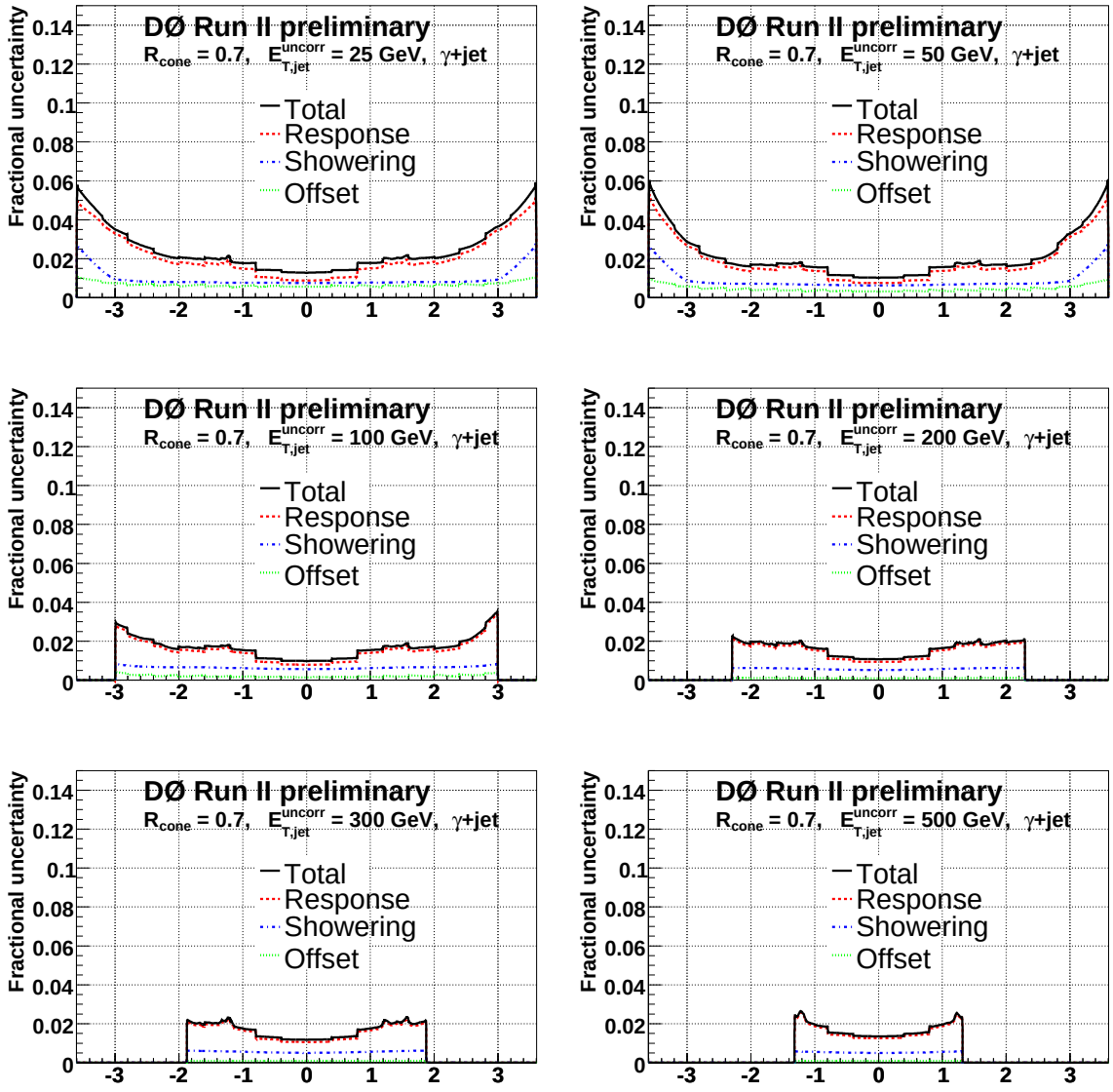

FIG. 40: Relative jet energy scale uncertainties in data for $\mathcal{R}_{\rm cone} = 0.7$ as a function of $\eta_{\rm jet}^{\rm det}$ for different $E_{T,\rm jet}^{\rm meas}$ values (from left to right and top to bottom: $E_{T,\rm jet}^{\rm meas} = 25$, 50, 100, 200, 300 and 500 GeV).

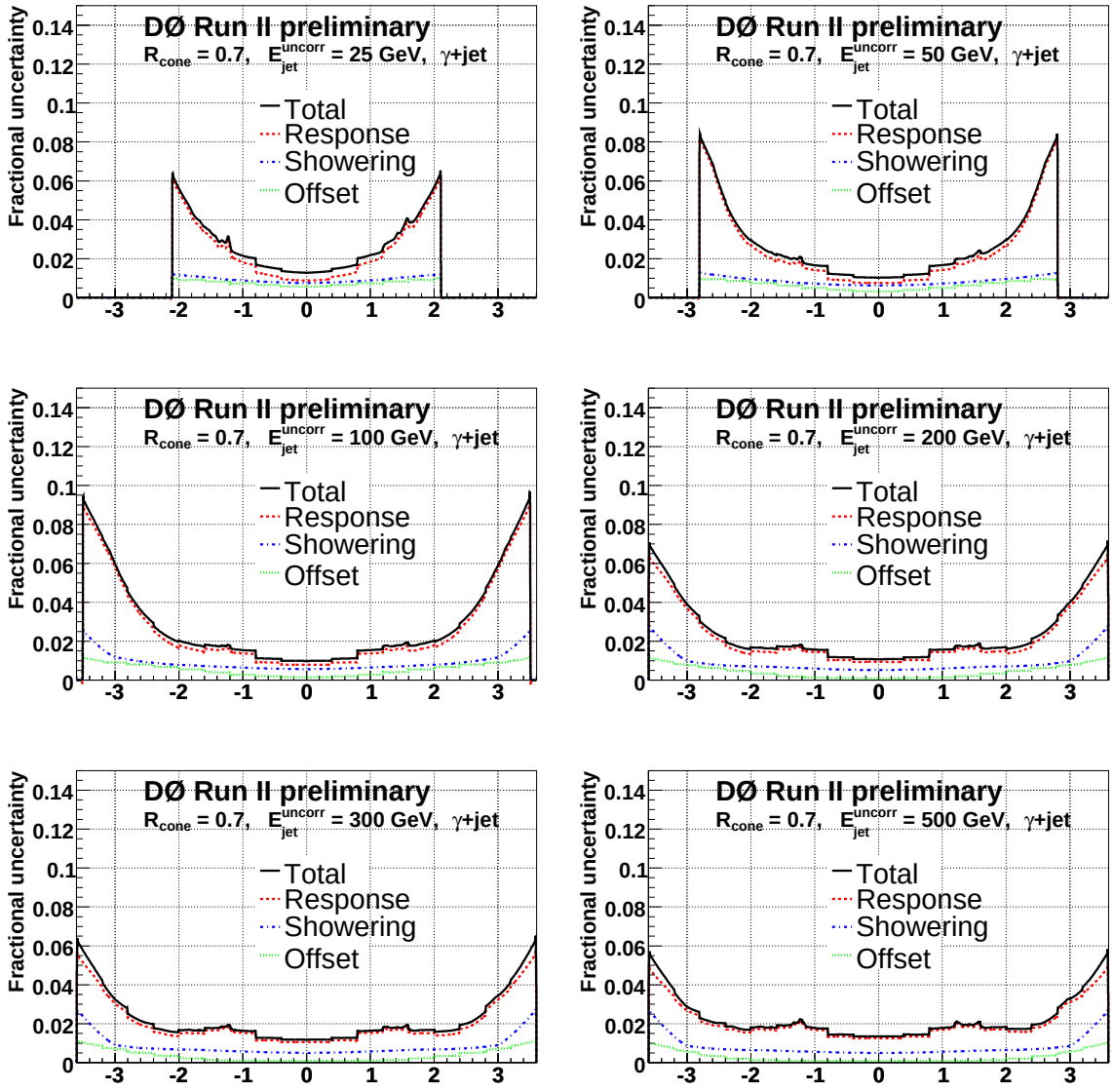

FIG. 41: Relative jet energy scale uncertainties in data for $\mathcal{R}_{\rm cone} = 0.7$ as a function of $\eta_{\rm jet}^{\rm det}$ for different $E_{\rm jet}^{\rm meas}$ values (from left to right and top to bottom: $E_{\rm jet}^{\rm meas} = 25$, 50, 100, 200, 300 and 500 GeV).

13.2.2. *Data* $\mathcal{R}_{\rm cone} = 0.5$

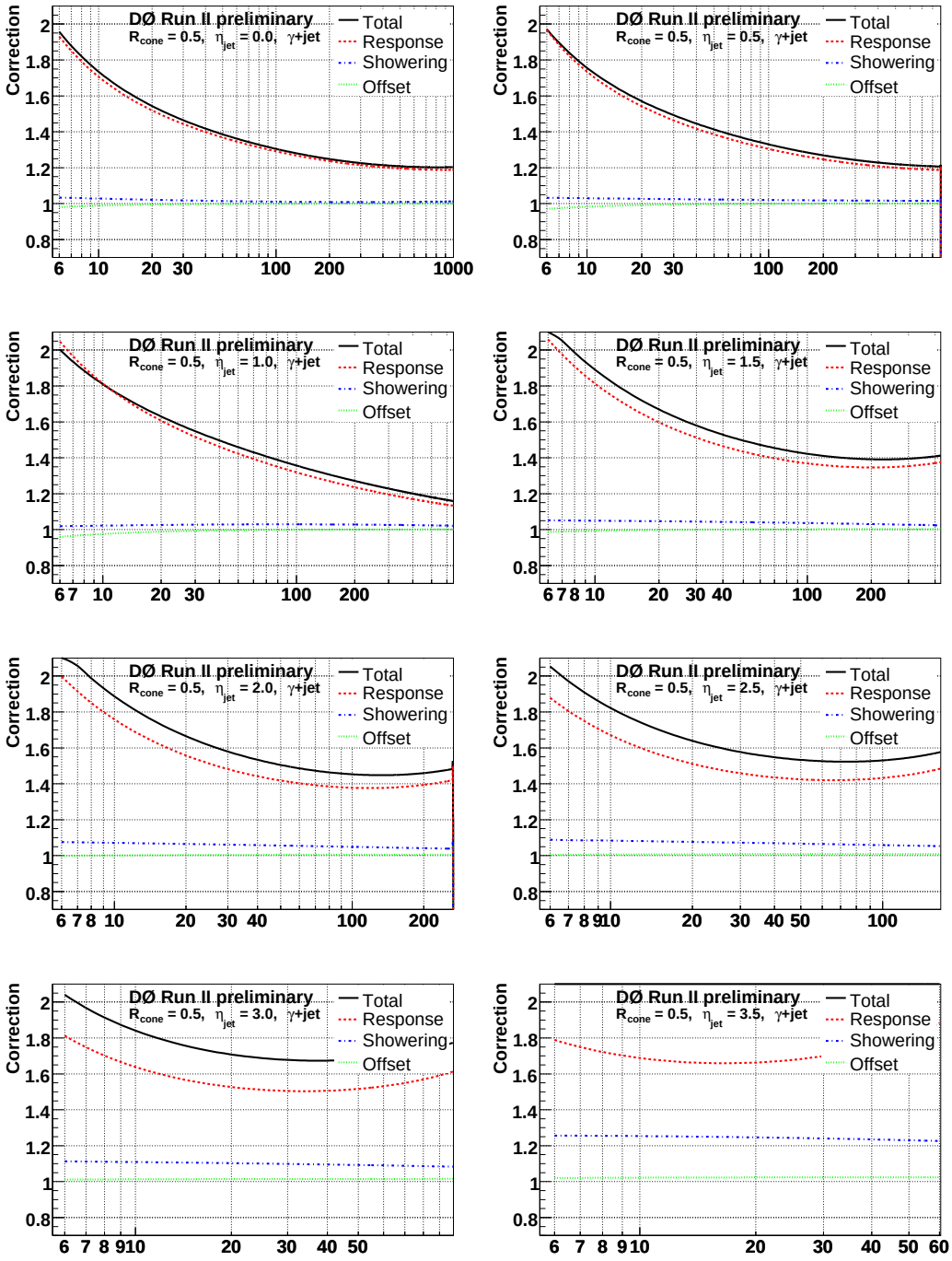

FIG. 42: Jet energy scale corrections in data for $\mathcal{R}_{\rm cone} = 0.5$ as a function of $E_{T,\rm jet}^{\rm meas}$ for different $\eta_{\rm jet}^{\rm det}$ values (from left to right and top to bottom: $\eta_{\rm jet}^{\rm det} = 0.0$, 0.5, 1.0, 1.5, 2.0, 2.5, 3.0 and 3.5).

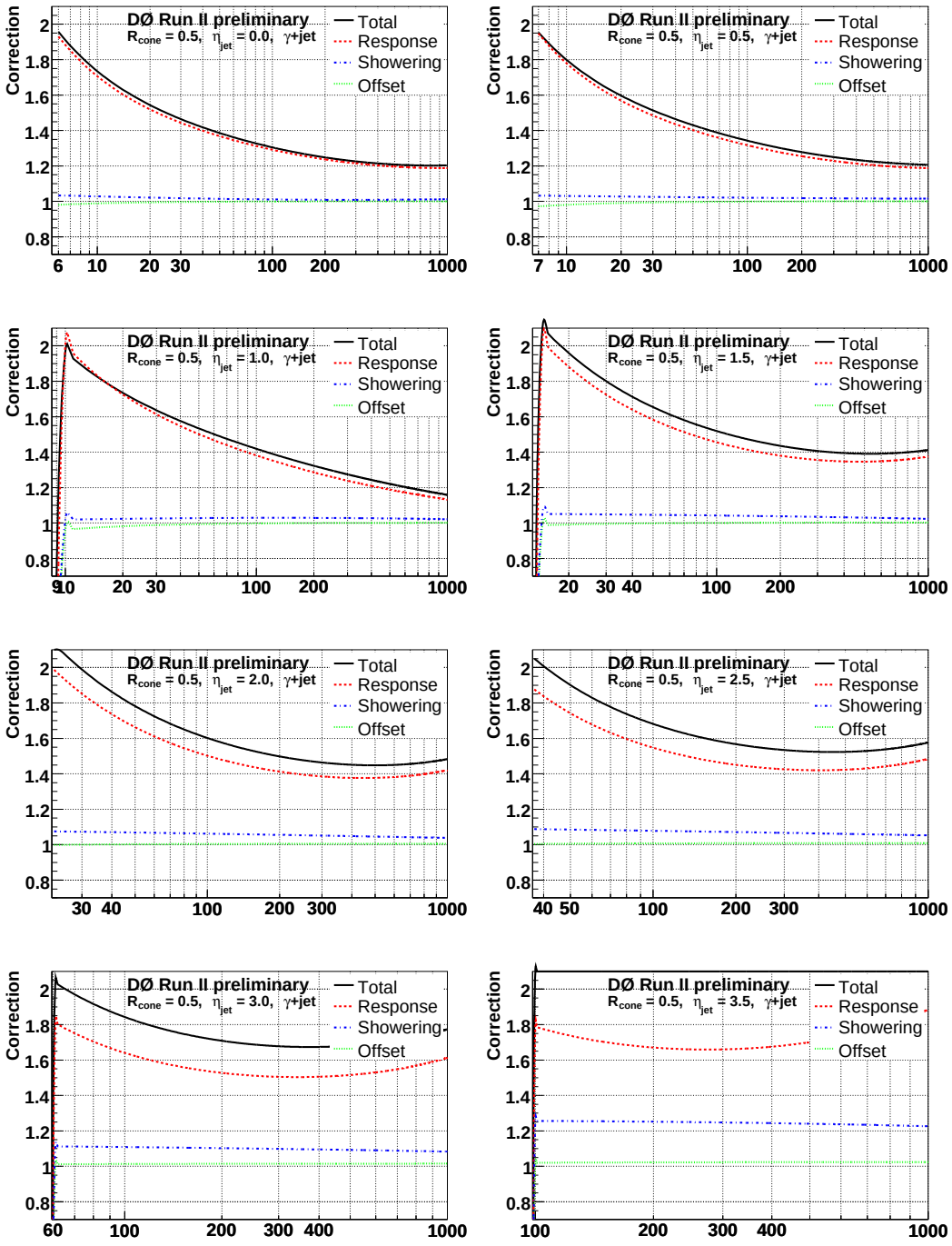

FIG. 43: Jet energy scale corrections in data for $\mathcal{R}_{\rm cone} = 0.5$ as a function of $E_{\rm jet}^{\rm meas}$ for different $\eta_{\rm jet}^{\rm det}$ values (from left to right and top to bottom: $\eta_{\rm jet}^{\rm det} = 0.0$, 0.5, 1.0, 1.5, 2.0, 2.5, 3.0 and 3.5).

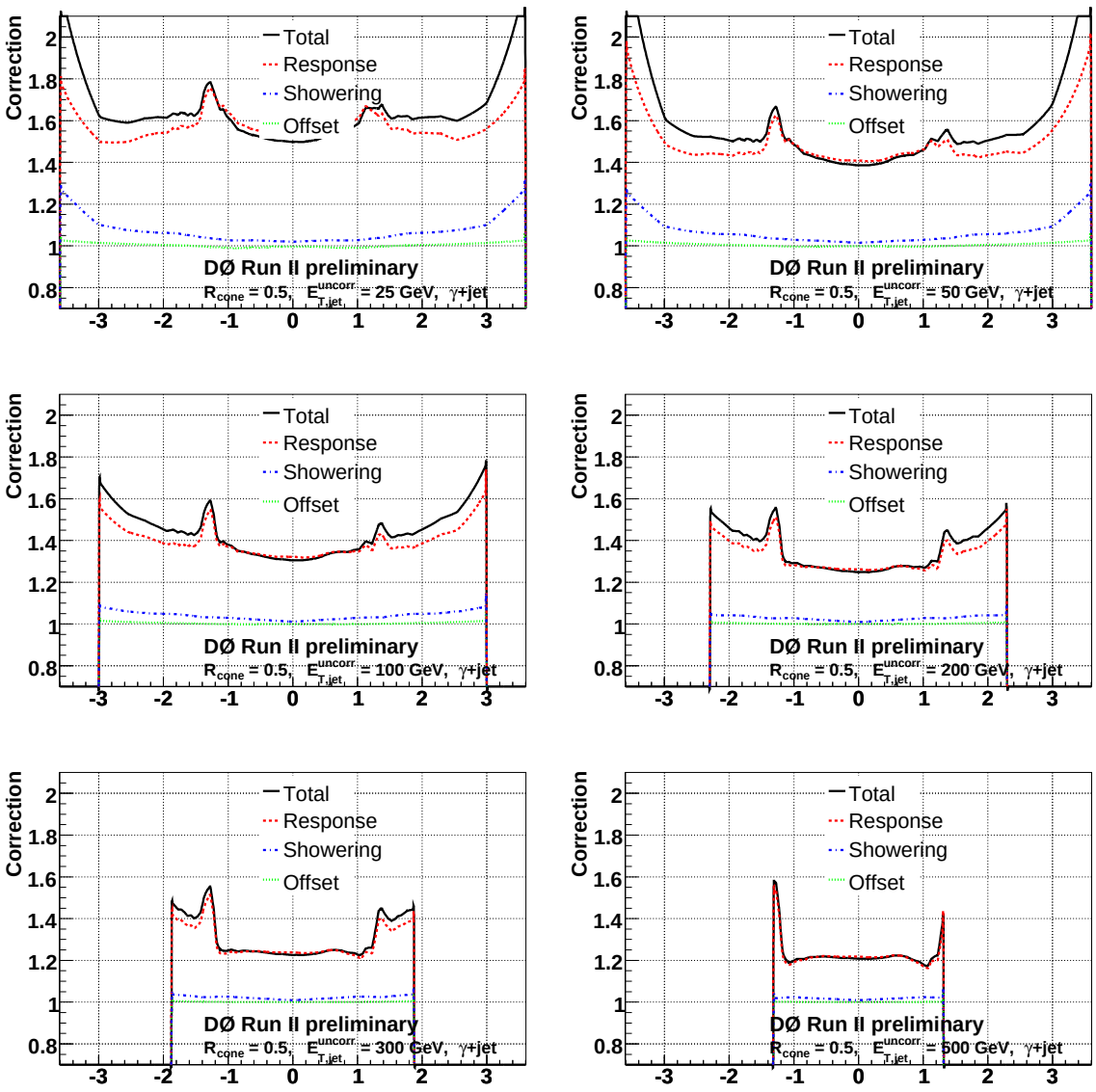

FIG. 44: Jet energy scale corrections in data for $\mathcal{R}_{\rm cone} = 0.5$ as a function of $\eta^{\rm det}_{\rm jet}$ for different $E^{\rm meas}_{T,{\rm jet}}$ values (from left to right and top to bottom: $E^{\rm meas}_{T,{\rm jet}} = 25$, 50, 100, 200, 300 and 500 GeV).

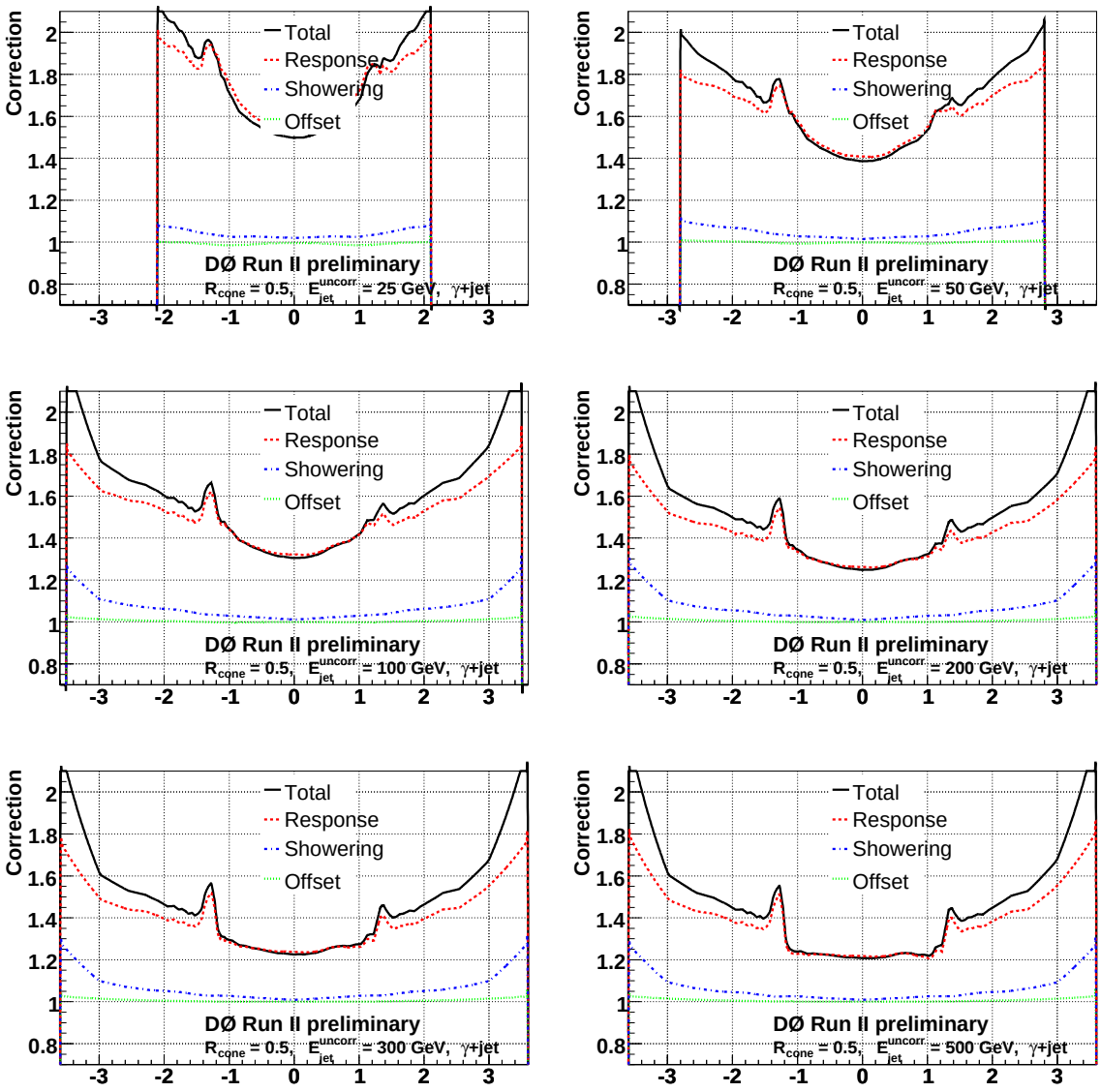

FIG. 45: Jet energy scale corrections in data for $\mathcal{R}_{\rm cone} = 0.5$ as a function of $\eta_{\rm jet}^{\rm det}$ for different $E_{\rm jet}^{\rm meas}$ values (from left to right and top to bottom: $E_{\rm jet}^{\rm meas} = 25$, 50, 100, 200, 300 and 500 GeV).

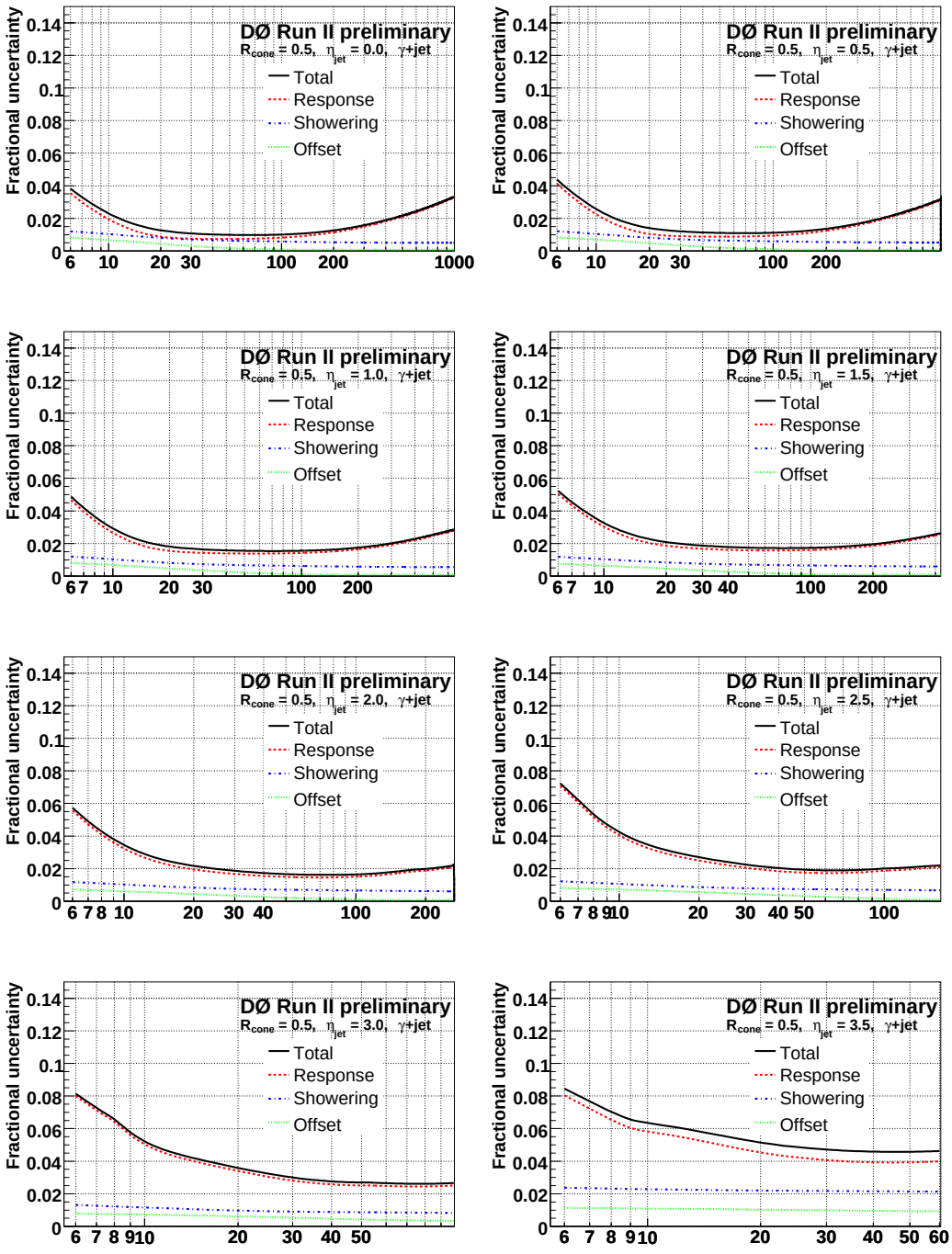

FIG. 46: Relative jet energy scale uncertainties in data for $\mathcal{R}_{\rm cone} = 0.5$ as a function of $E_{T,\rm jet}^{\rm meas}$ for different $\eta_{\rm jet}^{\rm det}$ values (from left to right and top to bottom: $\eta_{\rm jet}^{\rm det} = 0.0$, 0.5, 1.0, 1.5, 2.0, 2.5, 3.0 and 3.5).

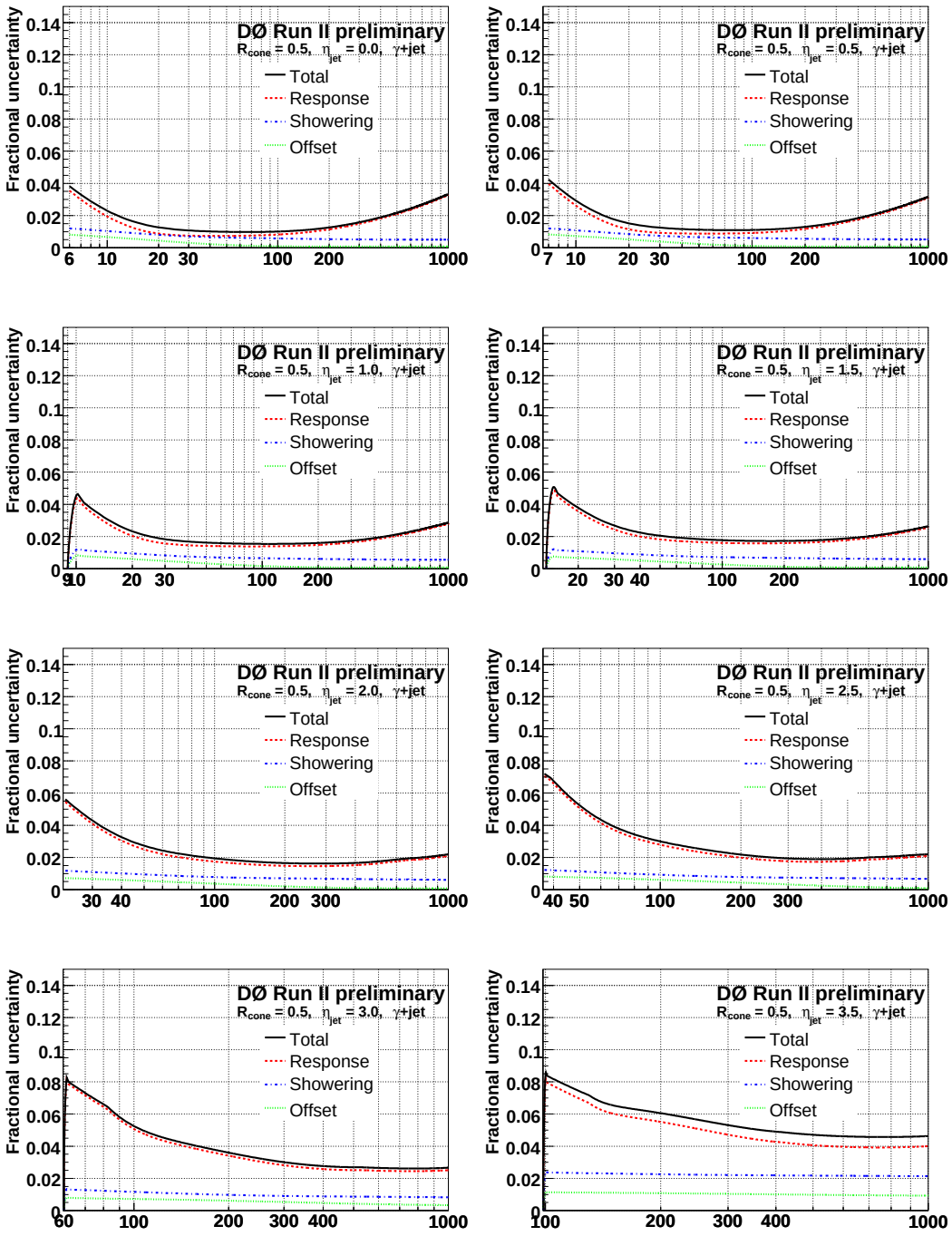

FIG. 47: Relative jet energy scale uncertainties in data for $\mathcal{R}_{\rm cone} = 0.5$ as a function of $E_{\rm jet}^{\rm meas}$ for different $\eta_{\rm jet}^{\rm det}$ values (from left to right and top to bottom: $\eta_{\rm jet}^{\rm det} = 0.0$, 0.5, 1.0, 1.5, 2.0, 2.5, 3.0 and 3.5).

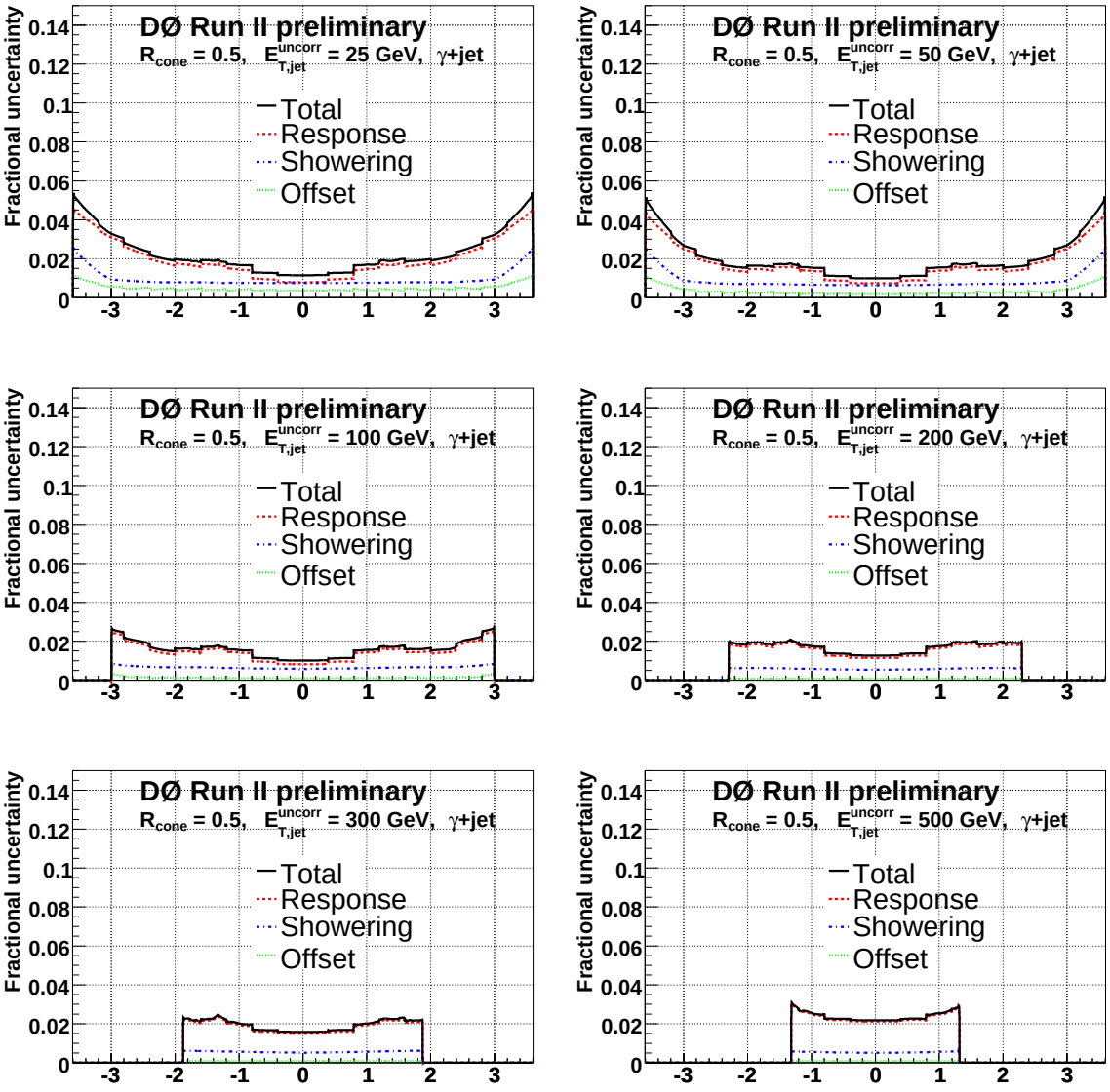

FIG. 48: Relative jet energy scale uncertainties in data for $\mathcal{R}_{\rm cone} = 0.5$ as a function of $\eta_{\rm jet}^{\rm det}$ for different $E_{T,\rm jet}^{\rm meas}$ values (from left to right and top to bottom: $E_{T,\rm jet}^{\rm meas} = 25$, 50, 100, 200, 300 and 500 GeV).

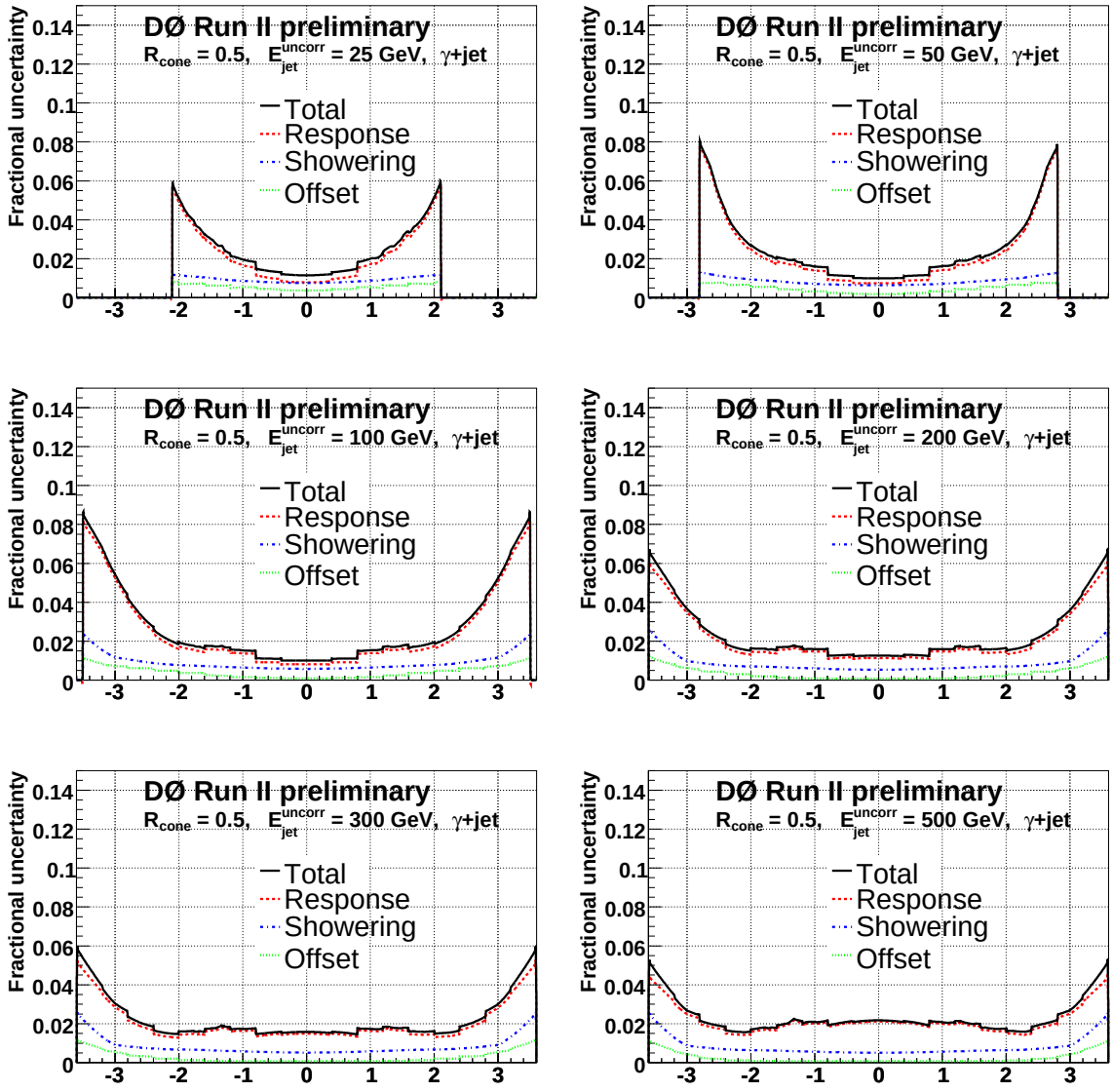

FIG. 49: Relative jet energy scale uncertainties in data for $\mathcal{R}_{\rm cone} = 0.5$ as a function of $\eta_{\rm jet}^{\rm det}$ for different $E_{\rm jet}^{\rm meas}$ values (from left to right and top to bottom: $E_{\rm jet}^{\rm meas} = 25$, 50, 100, 200, 300 and 500 GeV).

13.2.3. MC $\mathcal{R}_{\rm cone} = 0.7$

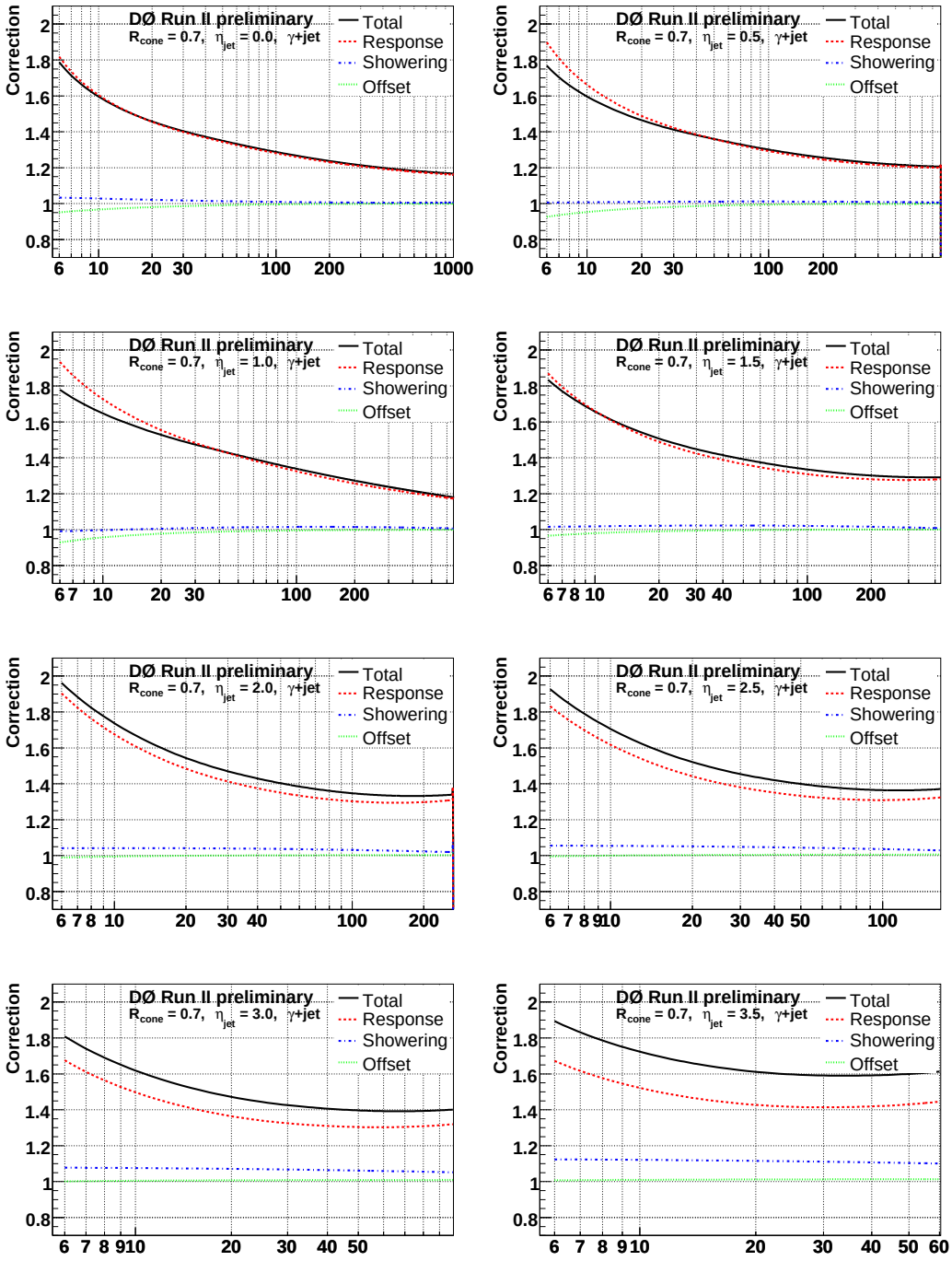

FIG. 50: Jet energy scale corrections in MC for $\mathcal{R}_{\rm cone} = 0.7$ as a function of $E_{T,\rm jet}^{\rm meas}$ for different $\eta_{\rm jet}^{\rm det}$ values (from left to right and top to bottom: $\eta_{\rm jet}^{\rm det} = 0.0$, 0.5, 1.0, 1.5, 2.0, 2.5, 3.0 and 3.5).

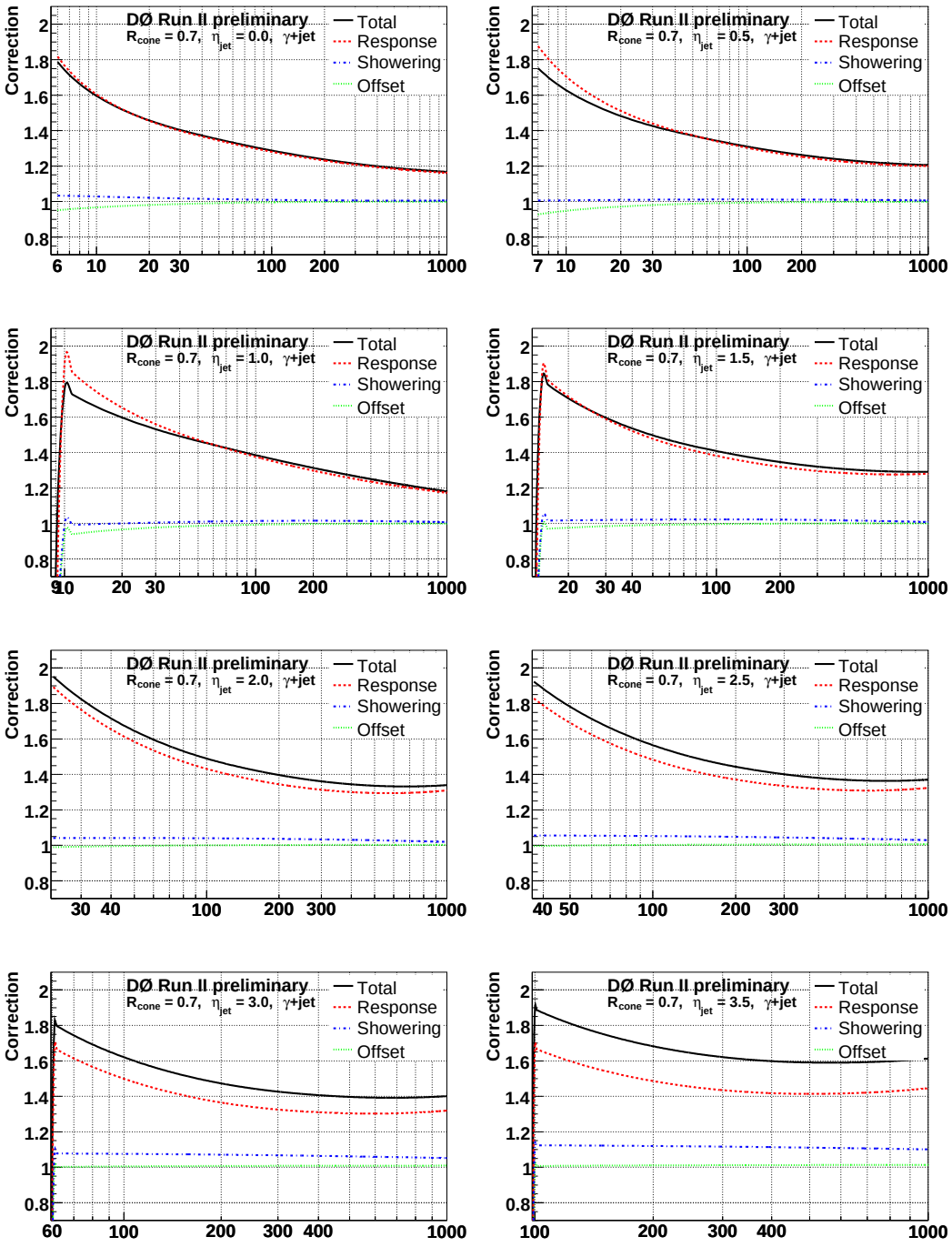

FIG. 51: Jet energy scale corrections in MC for $\mathcal{R}_{\rm cone} = 0.7$ as a function of $E_{\rm jet}^{\rm meas}$ for different $\eta_{\rm jet}^{\rm det}$ values (from left to right and top to bottom: $\eta_{\rm jet}^{\rm det} = 0.0$, 0.5, 1.0, 1.5, 2.0, 2.5, 3.0 and 3.5).

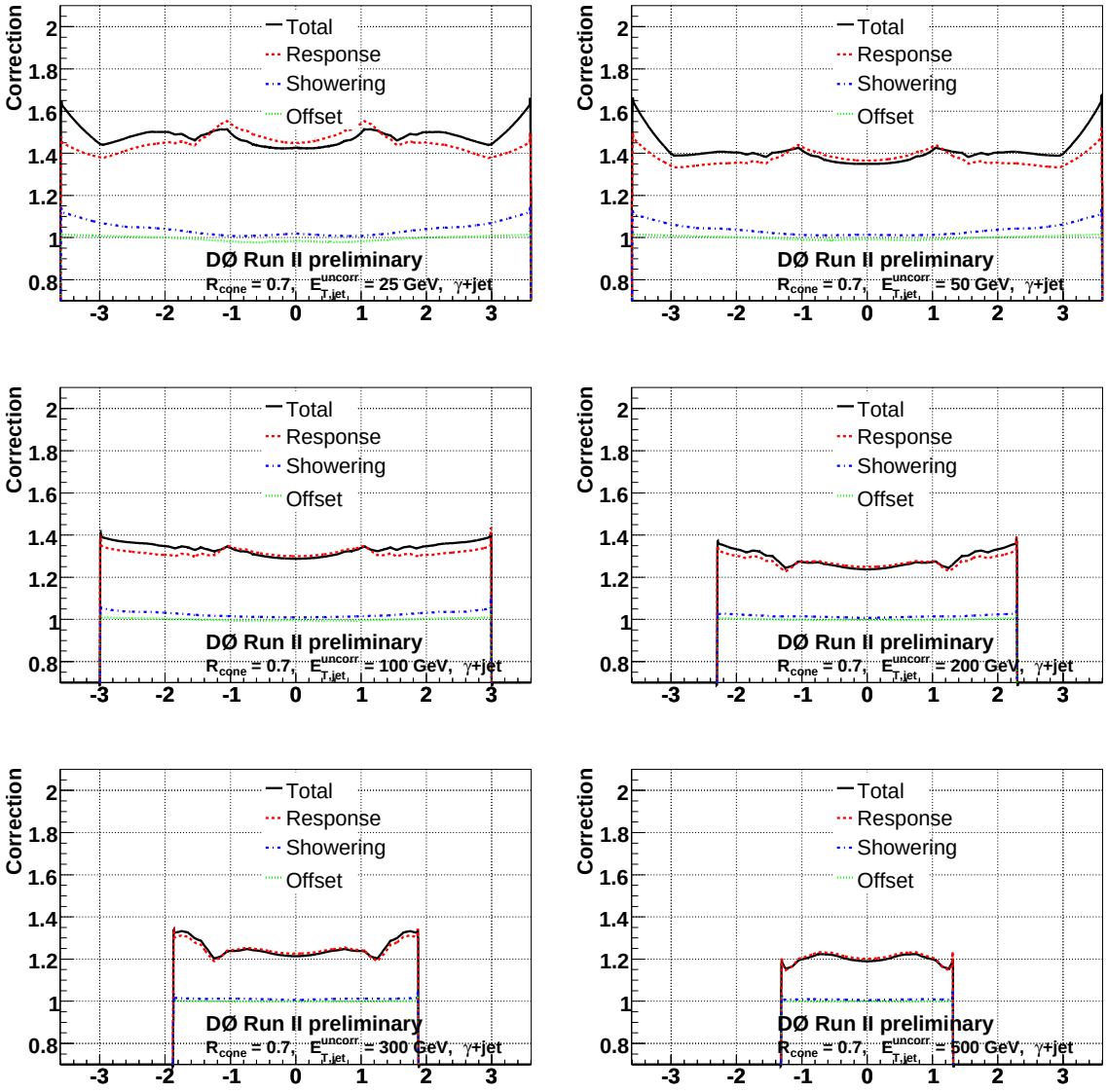

FIG. 52: Jet energy scale corrections in MC for $\mathcal{R}_{\rm cone} = 0.7$ as a function of $\eta_{\rm jet}^{\rm det}$ for different $E_{T,\rm jet}^{\rm meas}$ values (from left to right and top to bottom: $E_{T,\rm jet}^{\rm meas} = 25$, 50, 100, 200, 300 and 500 GeV).

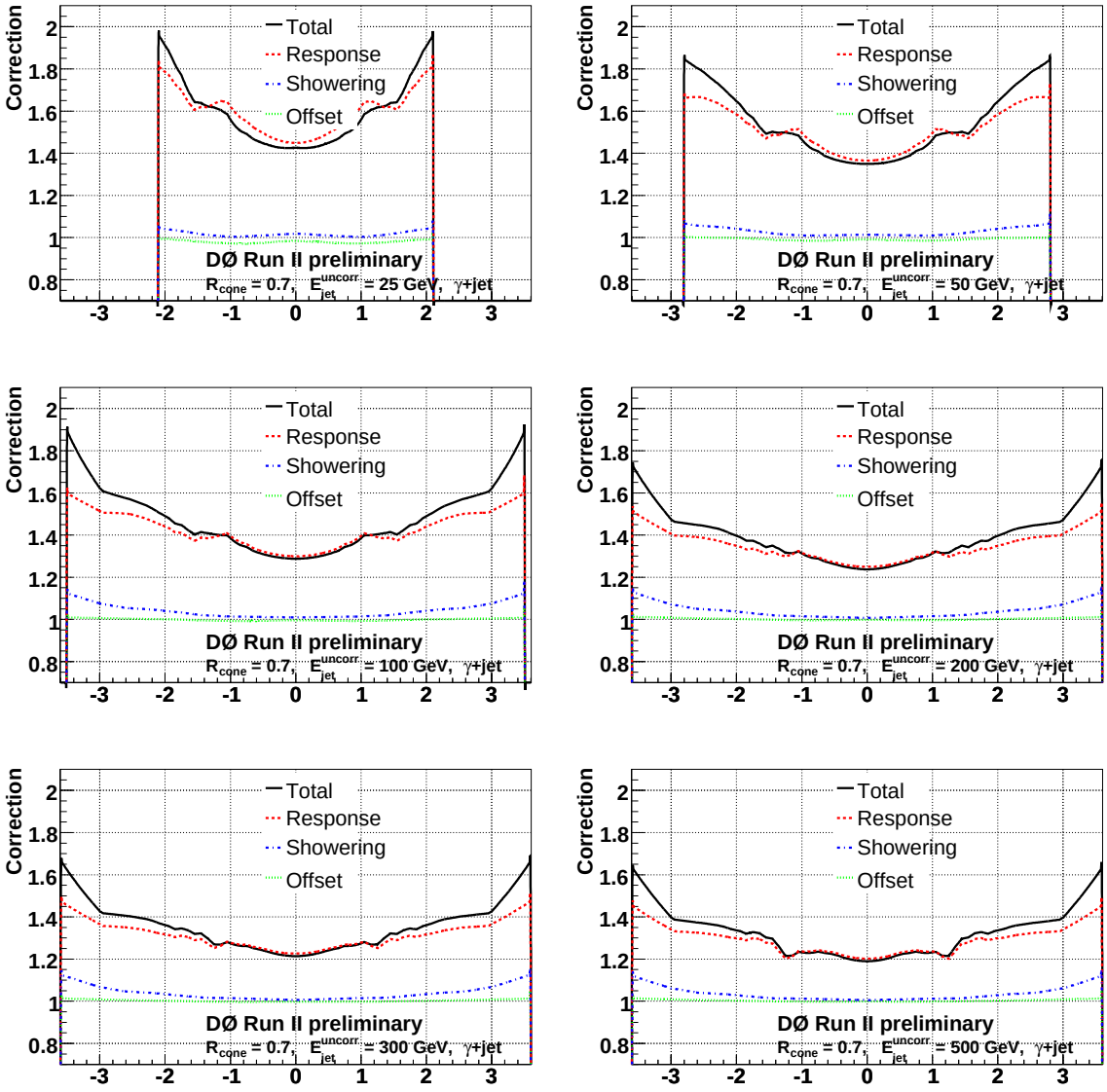

FIG. 53: Jet energy scale corrections in MC for $\mathcal{R}_{\rm cone} = 0.7$ as a function of $\eta_{\rm jet}^{\rm det}$ for different $E_{\rm jet}^{\rm meas}$ values (from left to right and top to bottom: $E_{\rm jet}^{\rm meas} = 25$, 50, 100, 200, 300 and 500 GeV).

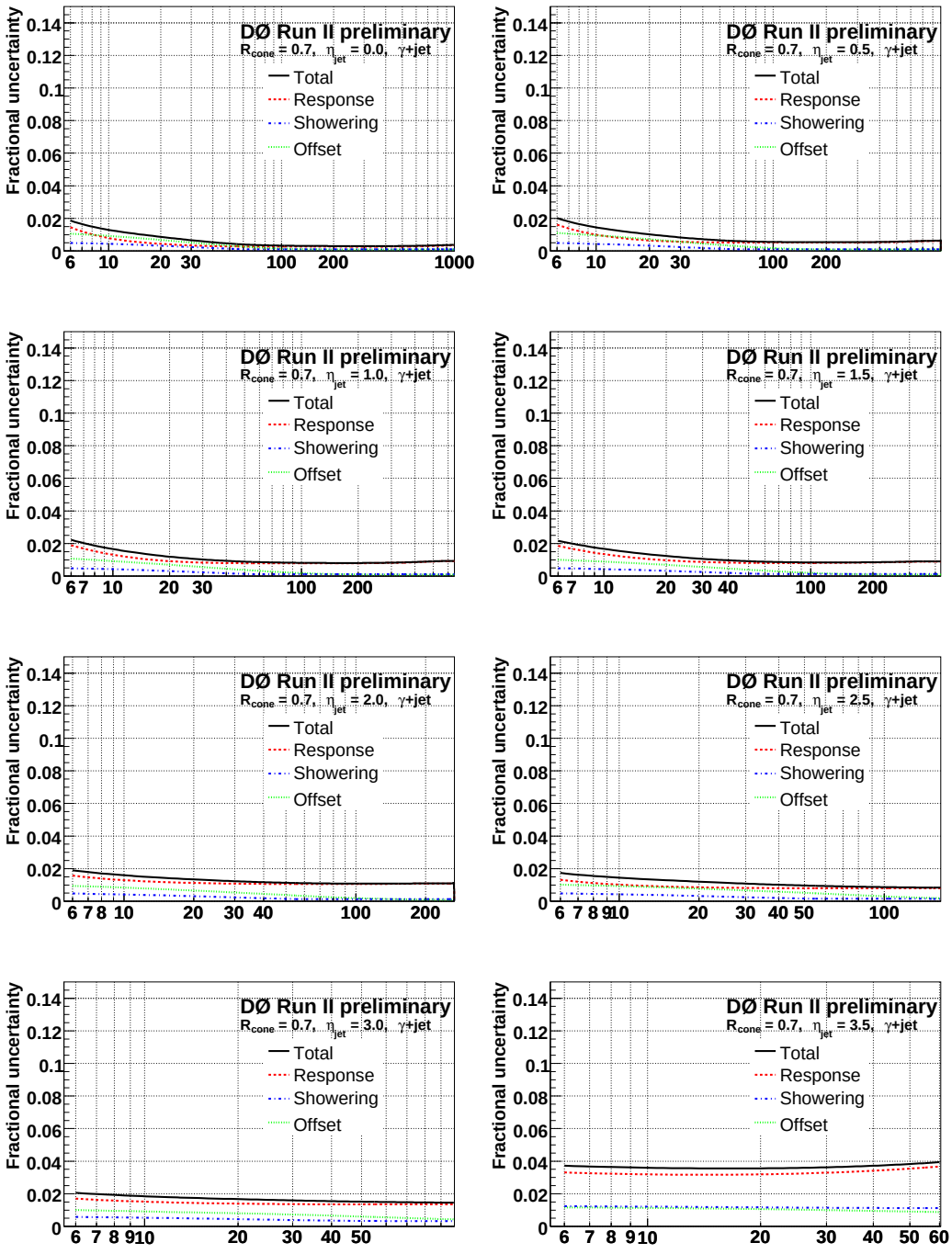

FIG. 54: Relative jet energy scale uncertainties in MC for $\mathcal{R}_{\rm cone} = 0.7$ as a function of $E_{T,\rm jet}^{\rm meas}$ for different $\eta_{\rm jet}^{\rm det}$ values (from left to right and top to bottom: $\eta_{\rm jet}^{\rm det} = 0.0$, 0.5, 1.0, 1.5, 2.0, 2.5, 3.0 and 3.5).

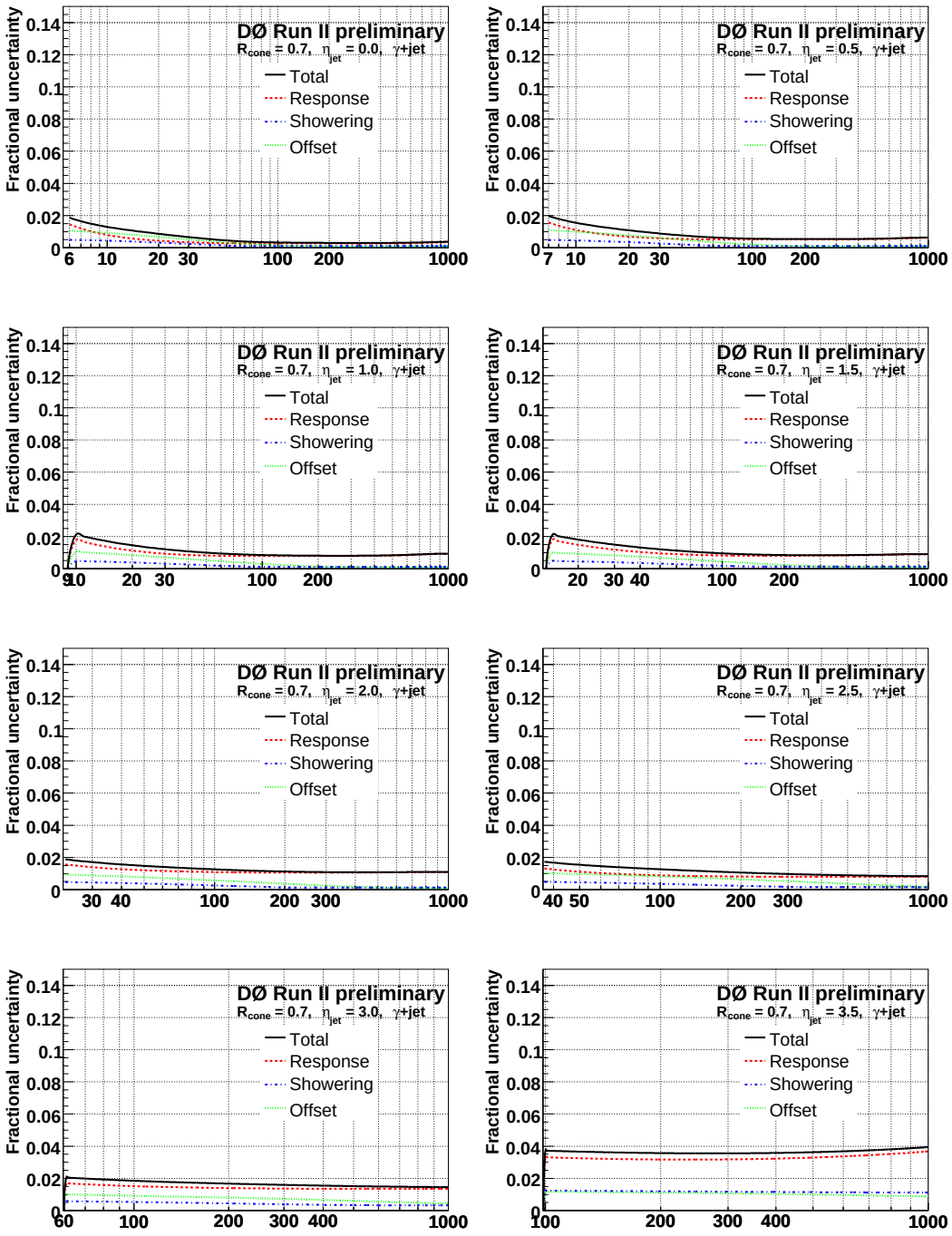

FIG. 55: Relative jet energy scale uncertainties in MC for $\mathcal{R}_{\rm cone} = 0.7$ as a function of $E_{\rm jet}^{\rm meas}$ for different $\eta_{\rm jet}^{\rm det}$ values (from left to right and top to bottom: $\eta_{\rm jet}^{\rm det} = 0.0$, 0.5, 1.0, 1.5, 2.0, 2.5, 3.0 and 3.5).

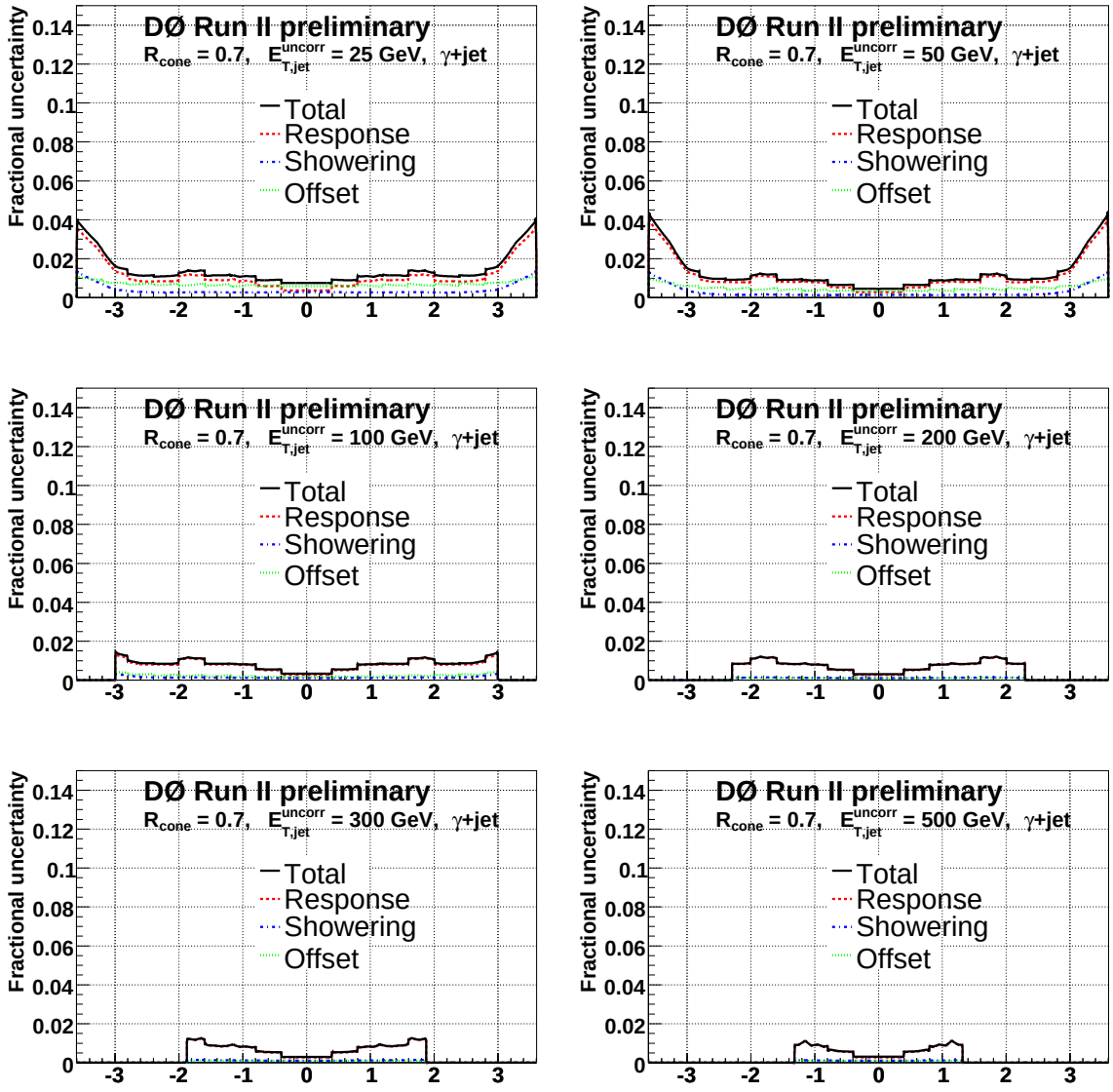

FIG. 56: Relative jet energy scale uncertainties in MC for $\mathcal{R}_{\rm cone} = 0.7$ as a function of $\eta_{\rm jet}^{\rm det}$ for different $E_{T,\rm jet}^{\rm meas}$ values (from left to right and top to bottom: $E_{T,\rm jet}^{\rm meas} = 25$, 50, 100, 200, 300 and 500 GeV).

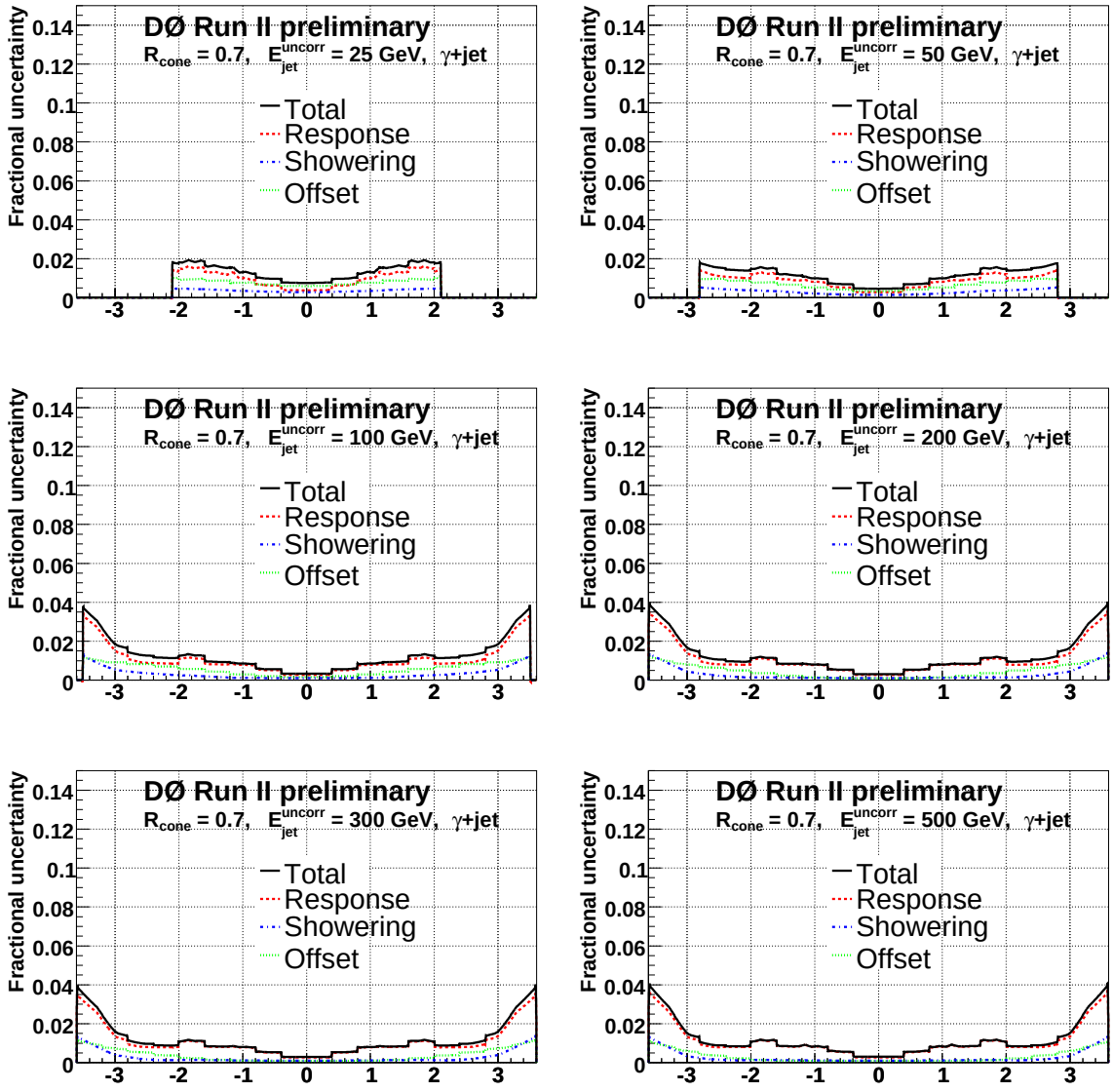

FIG. 57: Relative jet energy scale uncertainties in MC for $\mathcal{R}_{\rm cone} = 0.7$ as a function of $\eta_{\rm jet}^{\rm det}$ for different $E_{\rm jet}^{\rm meas}$ values (from left to right and top to bottom: $E_{\rm jet}^{\rm meas} = 25$, 50, 100, 200, 300 and 500 GeV).

13.2.4. MC $\mathcal{R}_{\rm cone} = 0.5$

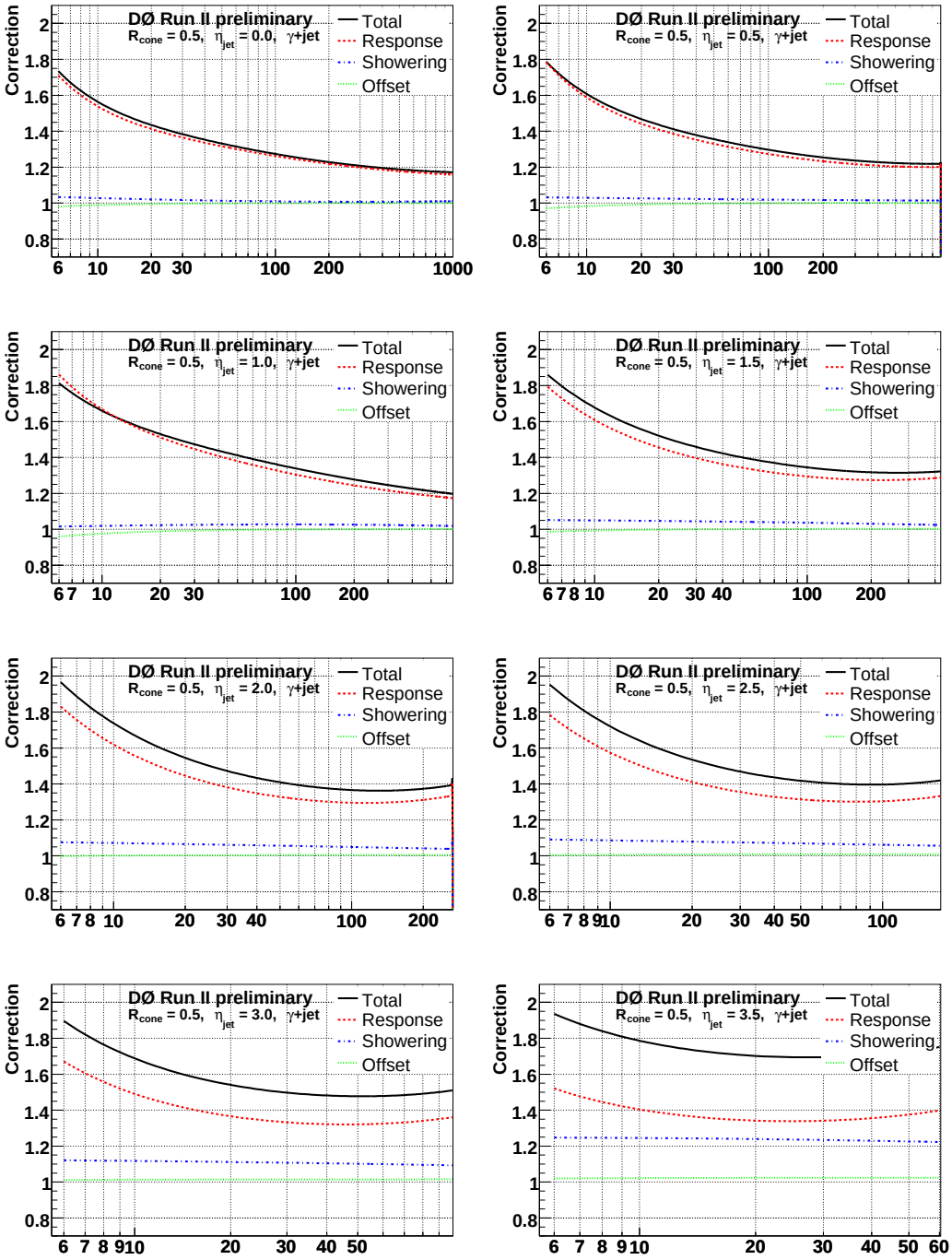

FIG. 58: Jet energy scale corrections in MC for $\mathcal{R}_{\rm cone} = 0.5$ as a function of $E_{T,\rm jet}^{\rm meas}$ for different $\eta_{\rm jet}^{\rm det}$ values (from left to right and top to bottom: $\eta_{\rm jet}^{\rm det} = 0.0$, 0.5, 1.0, 1.5, 2.0, 2.5, 3.0 and 3.5).

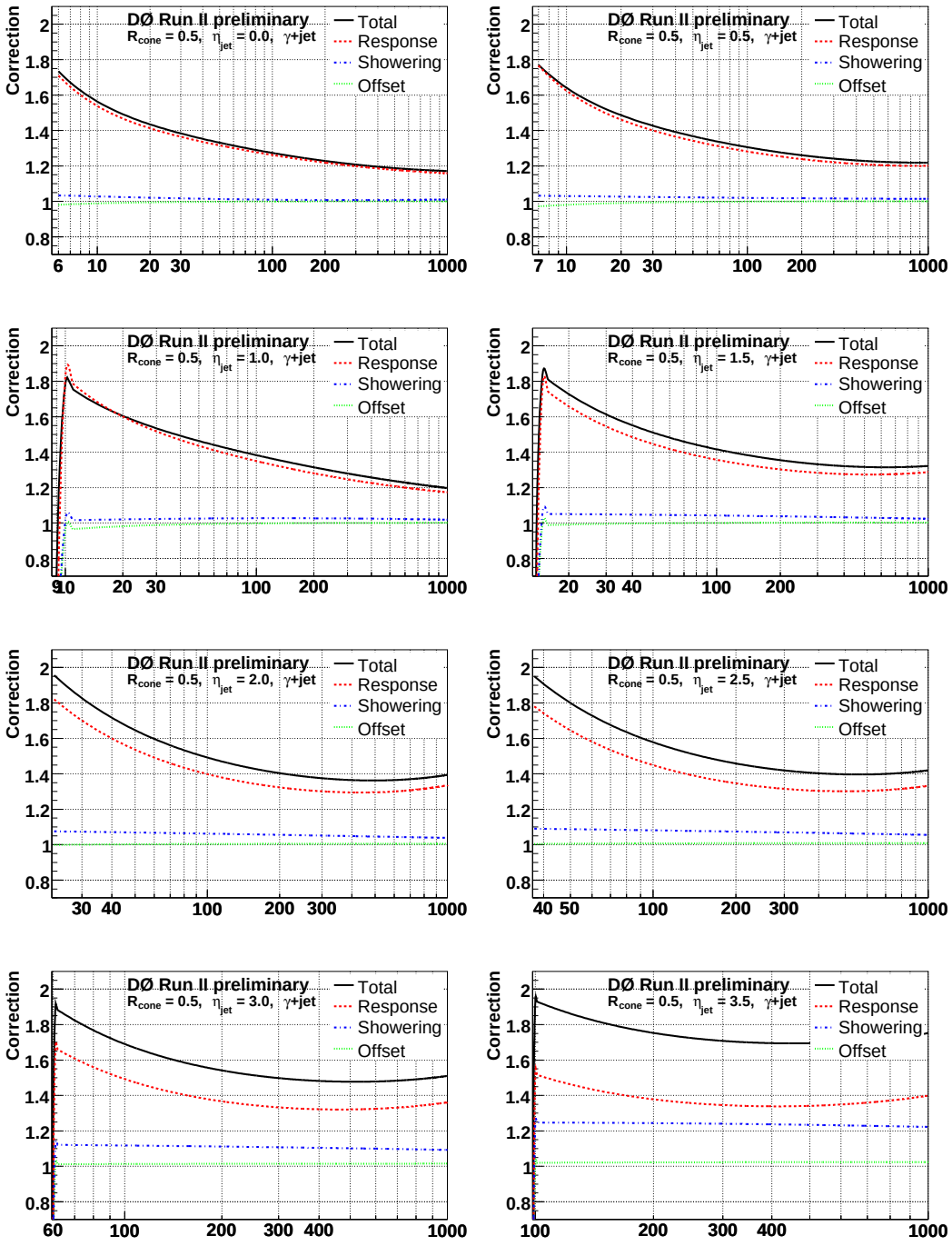

FIG. 59: Jet energy scale corrections in MC for $\mathcal{R}_{\rm cone} = 0.5$ as a function of $E_{\rm jet}^{\rm meas}$ for different $\eta_{\rm jet}^{\rm det}$ values (from left to right and top to bottom: $\eta_{\rm jet}^{\rm det} = 0.0$, 0.5, 1.0, 1.5, 2.0, 2.5, 3.0 and 3.5).

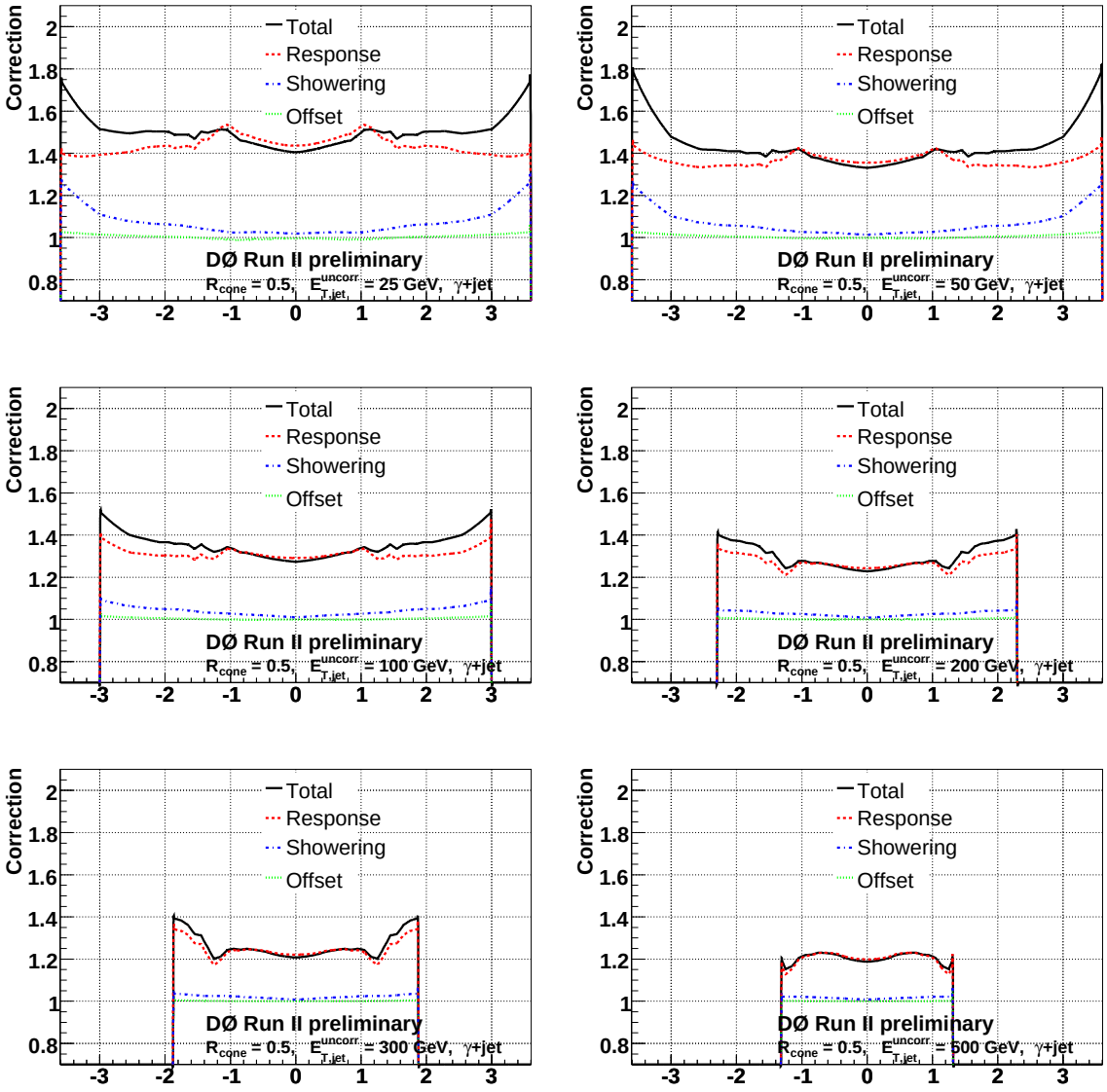

FIG. 60: Jet energy scale corrections in MC for $\mathcal{R}_{\rm cone} = 0.5$ as a function of $\eta_{\rm jet}^{\rm det}$ for different $E_{T,\rm jet}^{\rm meas}$ values (from left to right and top to bottom: $E_{T,\rm jet}^{\rm meas} = 25$, 50, 100, 200, 300 and 500 GeV).

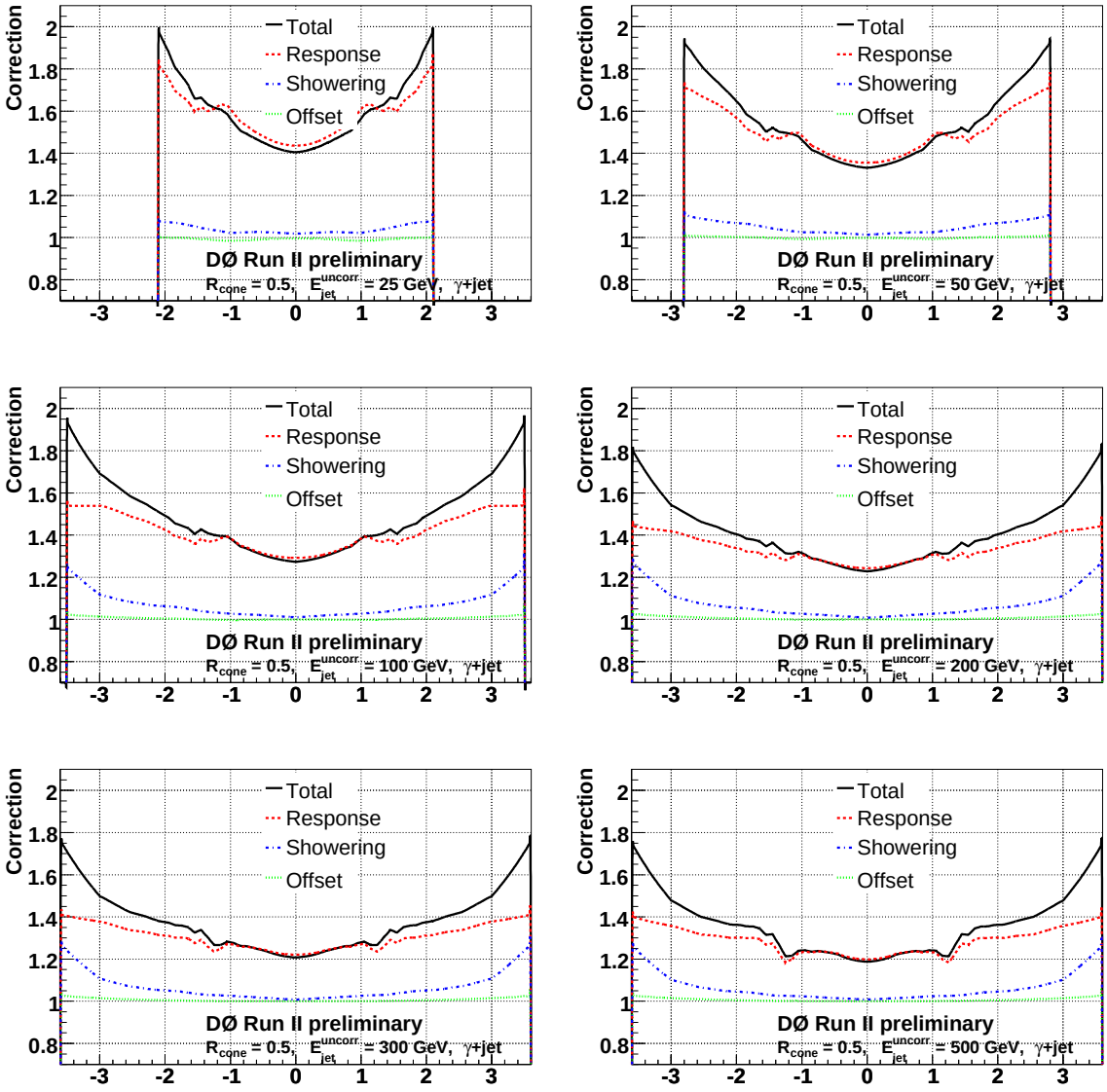

FIG. 61: Jet energy scale corrections in MC for $\mathcal{R}_{\rm cone} = 0.5$ as a function of $\eta_{\rm jet}^{\rm det}$ for different $E_{\rm jet}^{\rm meas}$ values (from left to right and top to bottom: $E_{\rm jet}^{\rm meas}$ = 25, 50, 100, 200, 300 and 500 GeV).

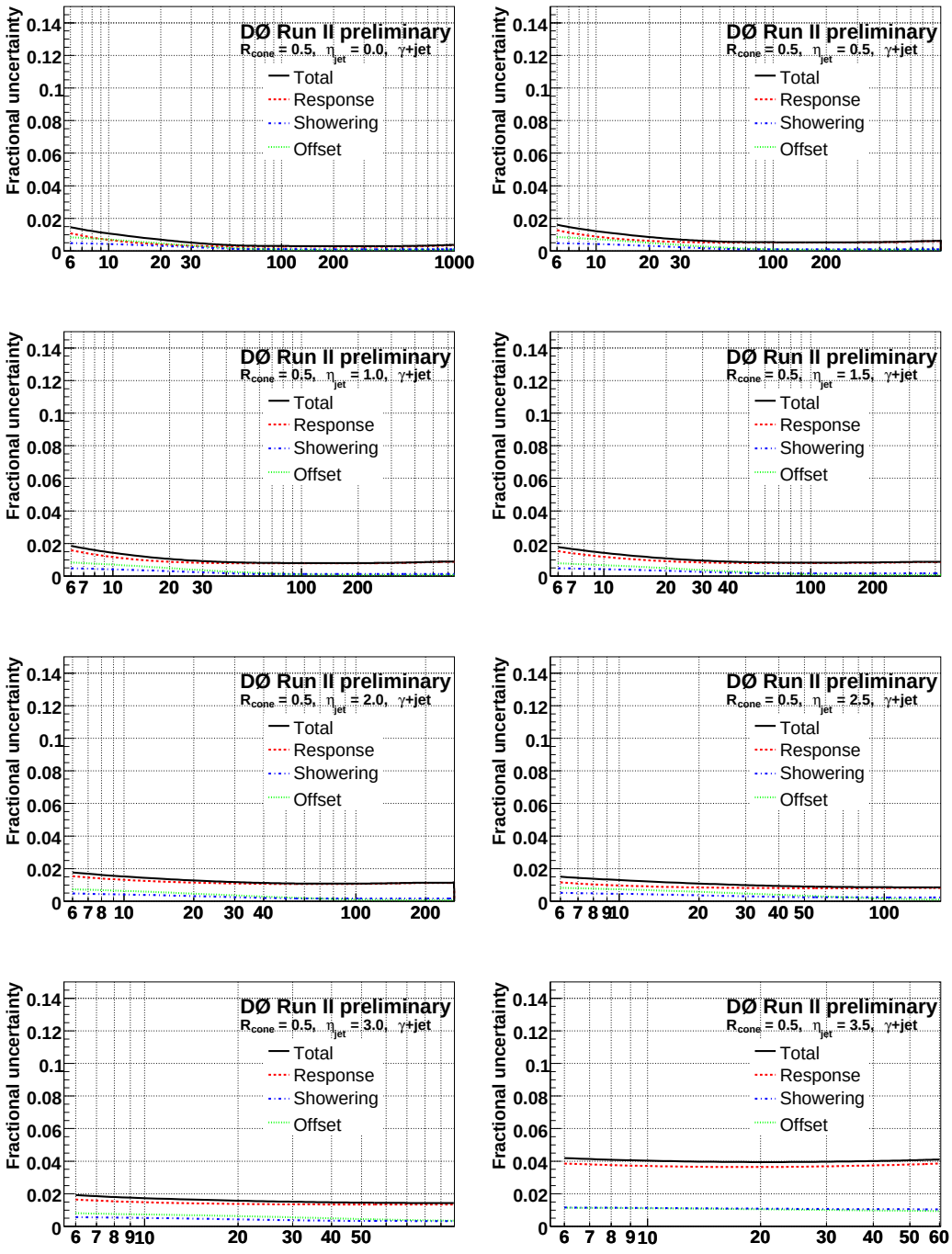

FIG. 62: Relative jet energy scale uncertainties in MC for $\mathcal{R}_{\rm cone} = 0.5$ as a function of $E_{T,\rm jet}^{\rm meas}$ for different $\eta_{\rm jet}^{\rm det}$ values (from left to right and top to bottom: $\eta_{\rm jet}^{\rm det} = 0.0$, 0.5, 1.0, 1.5, 2.0, 2.5, 3.0 and 3.5).

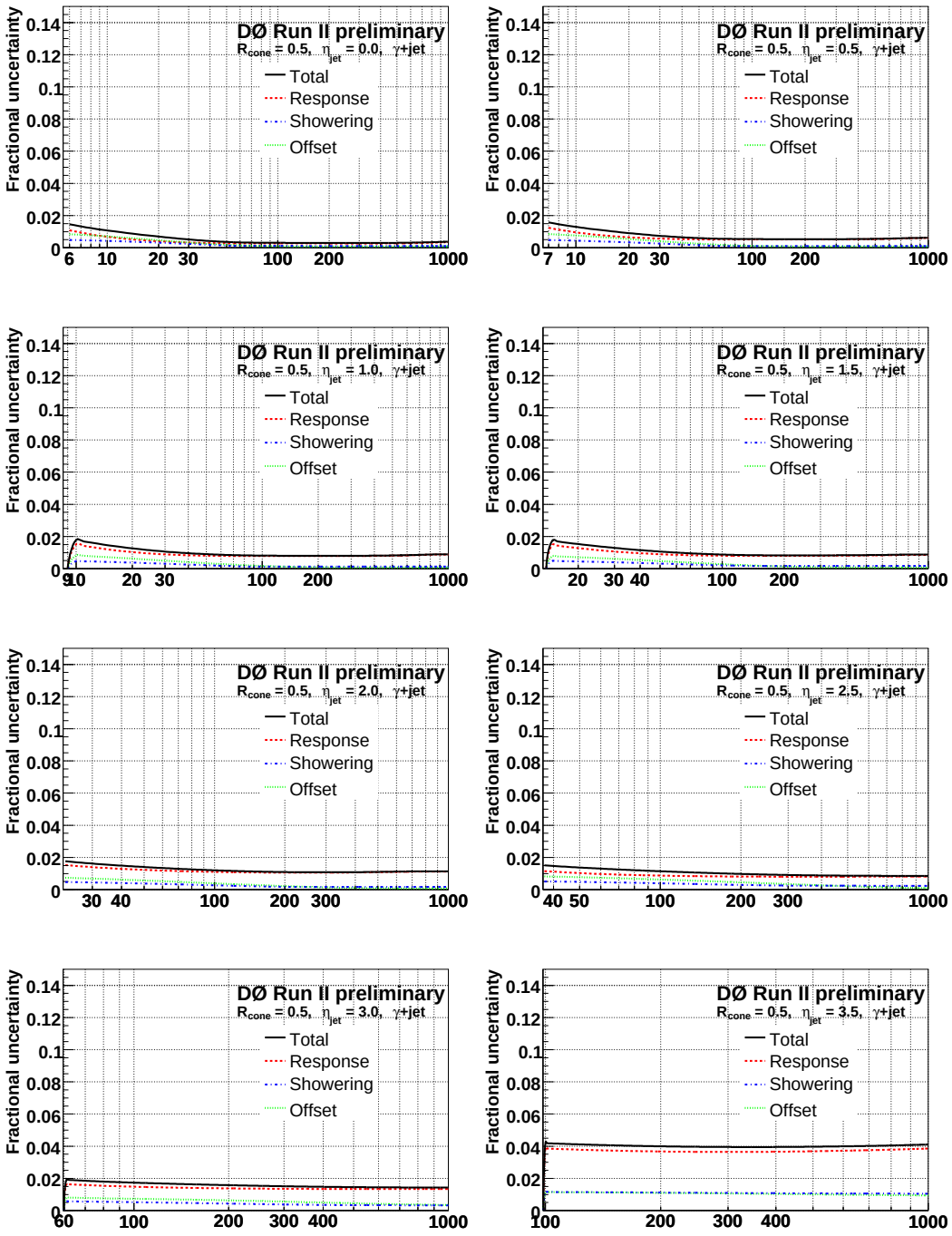

FIG. 63: Relative jet energy scale uncertainties in MC for $\mathcal{R}_{\rm cone} = 0.5$ as a function of $E_{\rm jet}^{\rm meas}$ for different $\eta_{\rm jet}^{\rm det}$ values (from left to right and top to bottom: $\eta_{\rm jet}^{\rm det} = 0.0$, 0.5, 1.0, 1.5, 2.0, 2.5, 3.0 and 3.5).

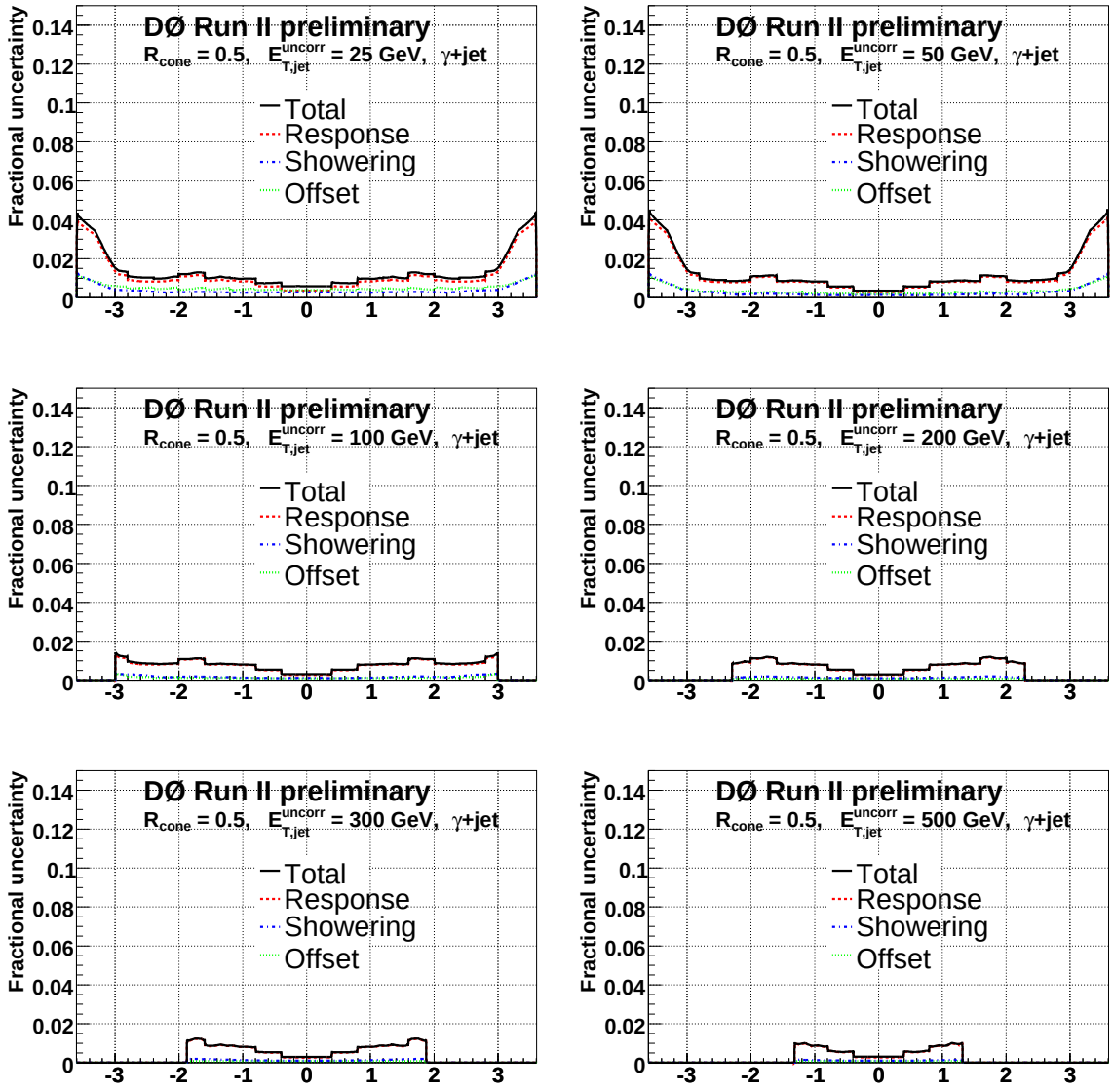

FIG. 64: Relative jet energy scale uncertainties in MC for $\mathcal{R}_{\rm cone} = 0.5$ as a function of $\eta_{\rm jet}^{\rm det}$ for different $E_{T,\rm jet}^{\rm meas}$ values (from left to right and top to bottom: $E_{T,\rm jet}^{\rm meas} = 25$, 50, 100, 200, 300 and 500 GeV).

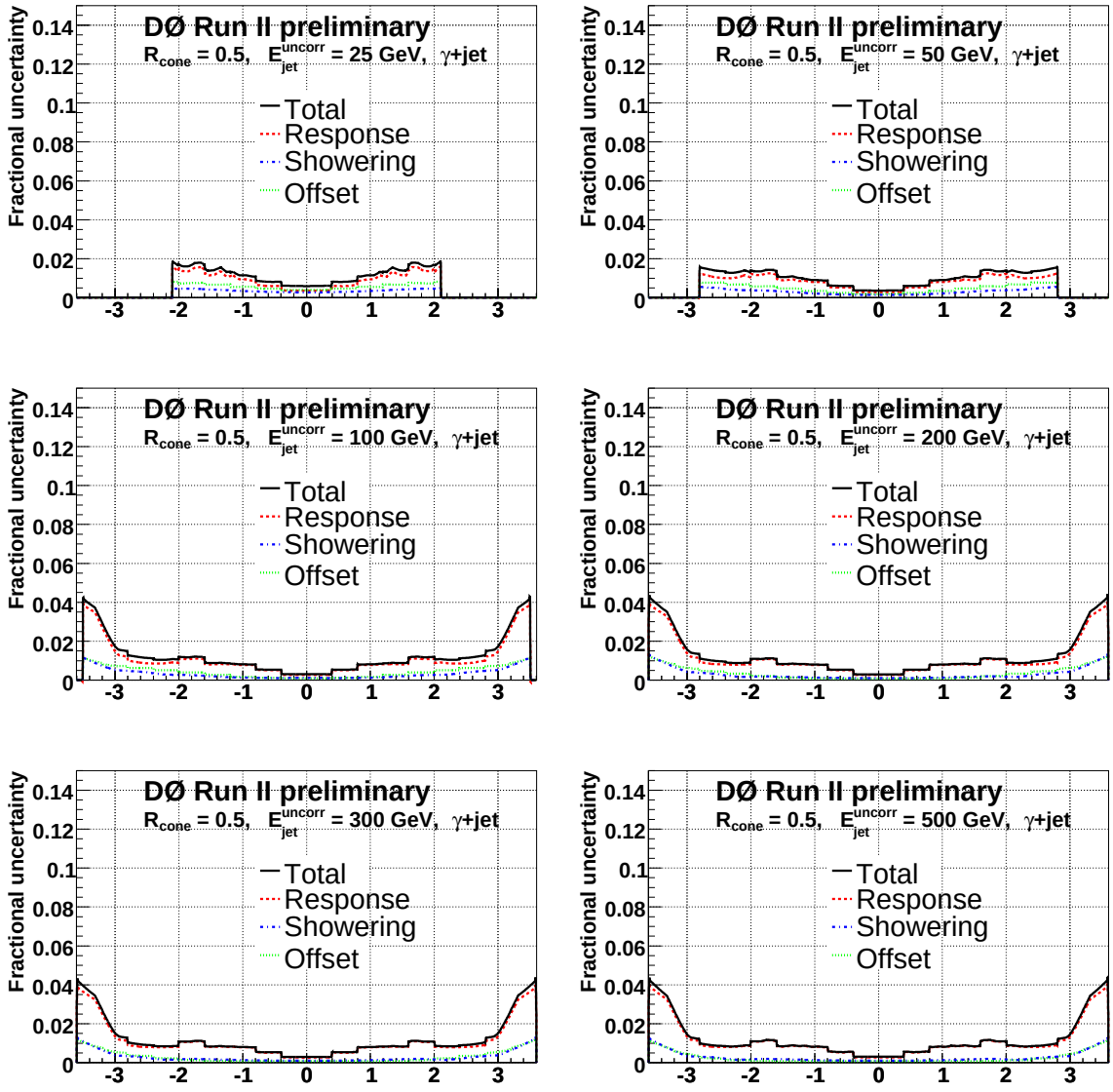

FIG. 65: Relative jet energy scale uncertainties in MC for $\mathcal{R}_{\rm cone} = 0.5$ as a function of $\eta_{\rm jet}^{\rm det}$ for different $E_{\rm jet}^{\rm meas}$ values (from left to right and top to bottom: $E_{\rm jet}^{\rm meas} = 25$, 50, 100, 200, 300 and 500 GeV).

13.3. QCD-Specific Corrections and Uncertainties

13.3.1. Data $\mathcal{R}_{\rm cone} = 0.7$

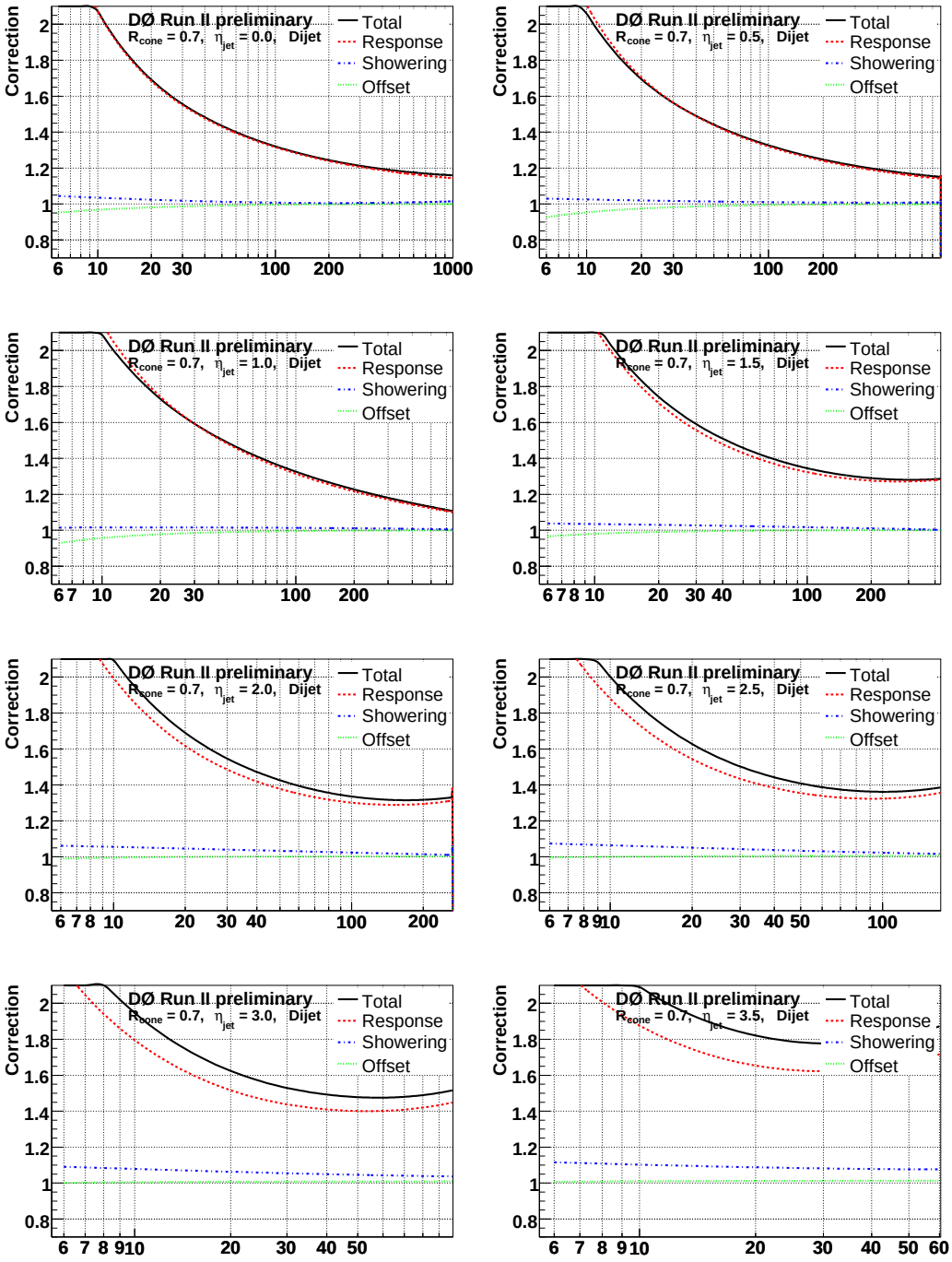

FIG. 66: Jet energy scale corrections in data for $\mathcal{R}_{\rm cone} = 0.7$ as a function of $E_{T,\rm jet}^{\rm meas}$ for different $\eta_{\rm jet}^{\rm det}$ values (from left to right and top to bottom: $\eta_{\rm jet}^{\rm det} = 0.0$, 0.5, 1.0, 1.5, 2.0, 2.5, 3.0 and 3.5).

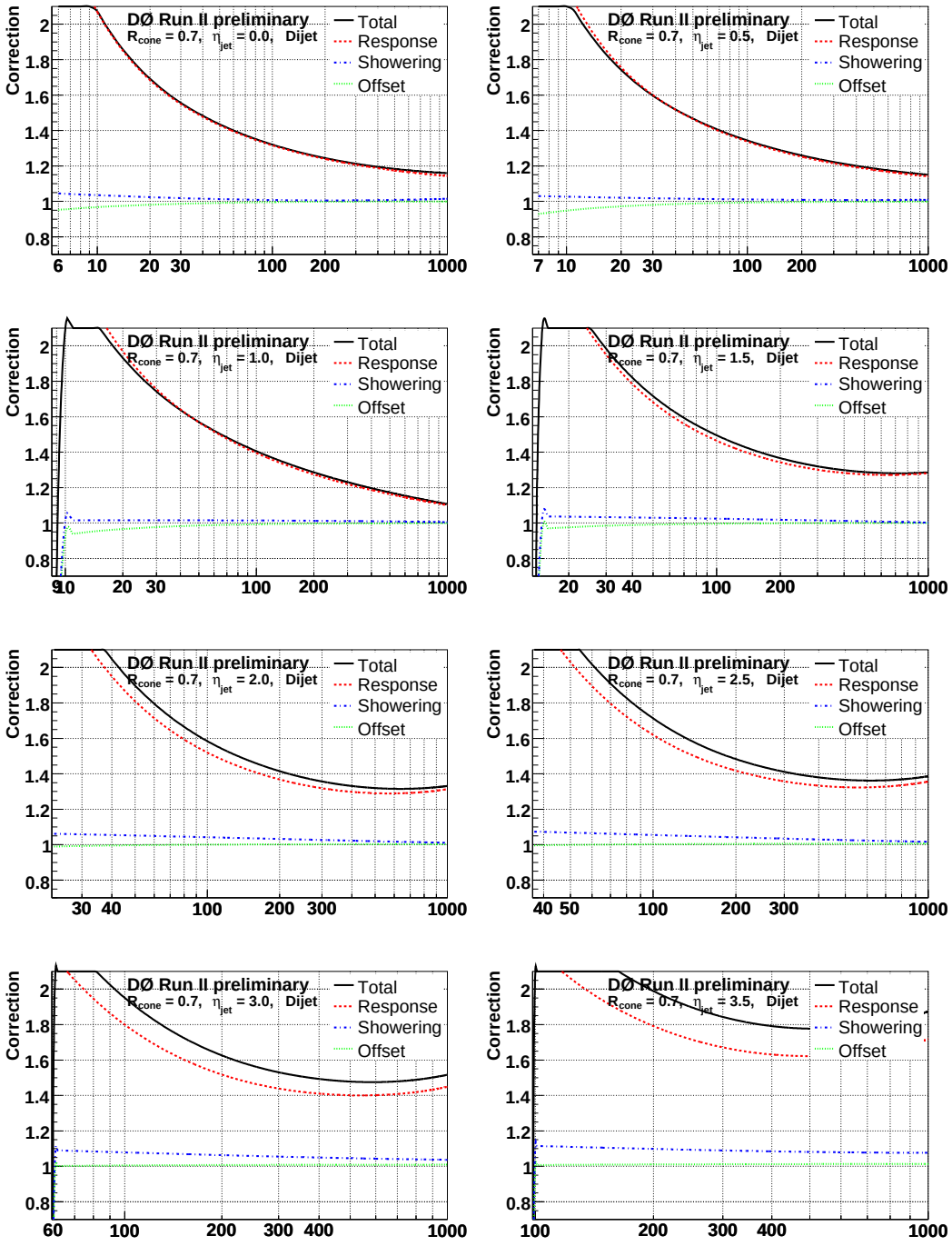

FIG. 67: Jet energy scale corrections in data for $\mathcal{R}_{\rm cone} = 0.7$ as a function of $E_{\rm jet}^{\rm meas}$ for different $\eta_{\rm jet}^{\rm det}$ values (from left to right and top to bottom: $\eta_{\rm jet}^{\rm det} = 0.0$, 0.5, 1.0, 1.5, 2.0, 2.5, 3.0 and 3.5).

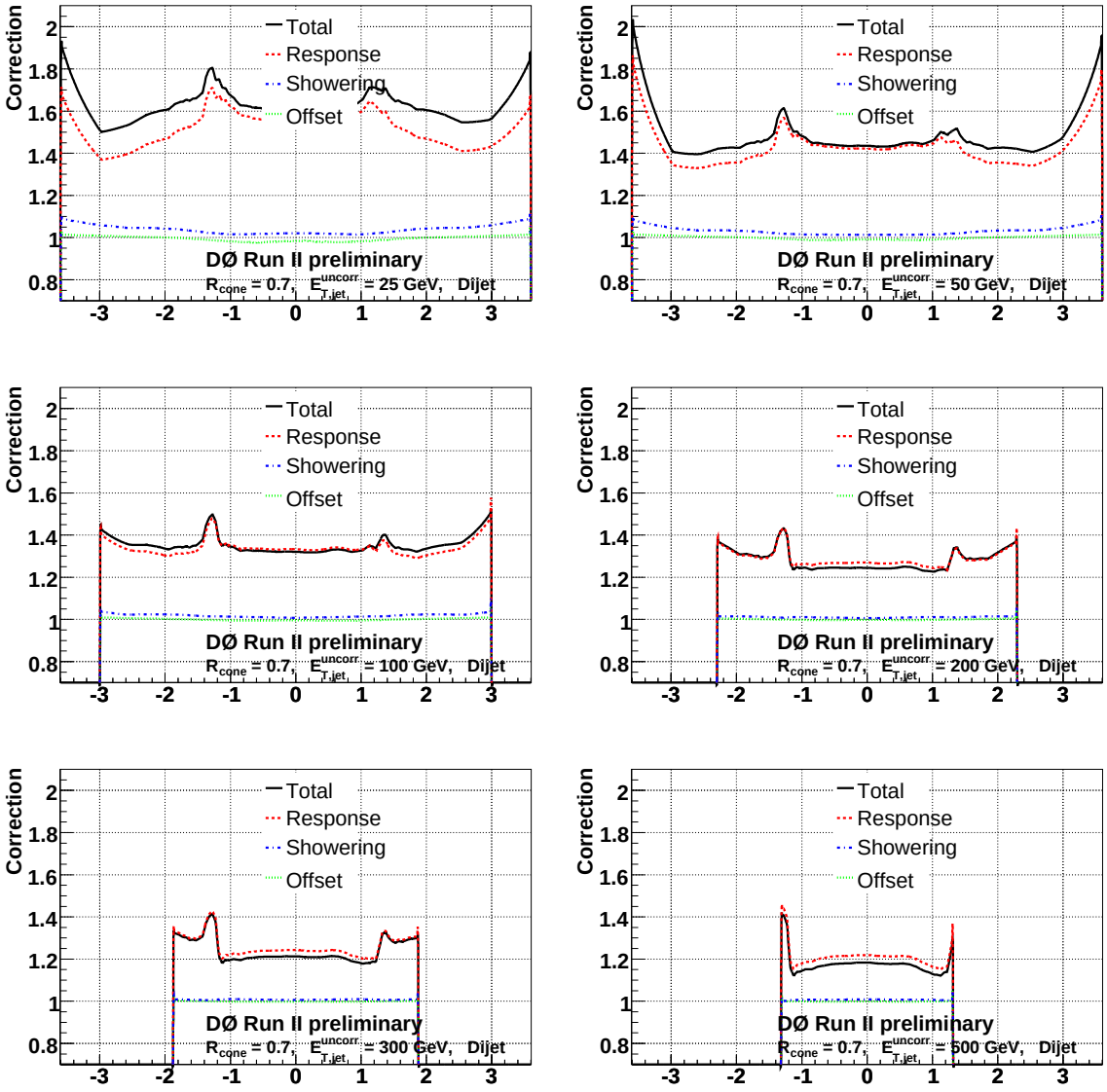

FIG. 68: Jet energy scale corrections in data for $\mathcal{R}_{\rm cone} = 0.7$ as a function of $\eta_{\rm jet}^{\rm det}$ for different $E_{T,\rm jet}^{\rm meas}$ values (from left to right and top to bottom: $E_{T,\rm jet}^{\rm meas} = 25$, 50, 100, 200, 300 and 500 GeV).

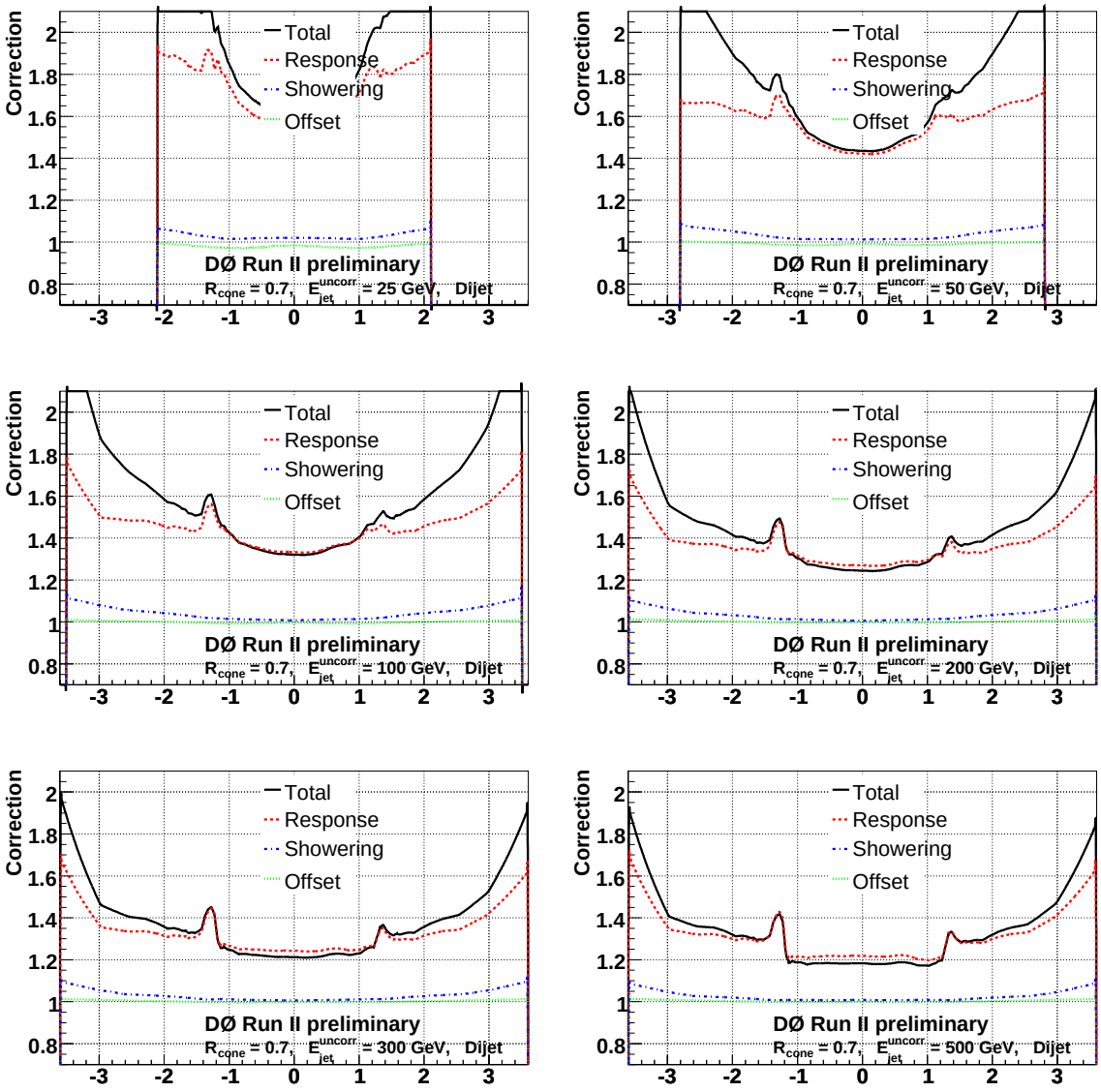

FIG. 69: Jet energy scale corrections in data for $\mathcal{R}_{\rm cone} = 0.7$ as a function of $\eta_{\rm jet}^{\rm det}$ for different $E_{\rm jet}^{\rm meas}$ values (from left to right and top to bottom: $E_{\rm jet}^{\rm meas} = 25$, 50, 100, 200, 300 and 500 GeV).

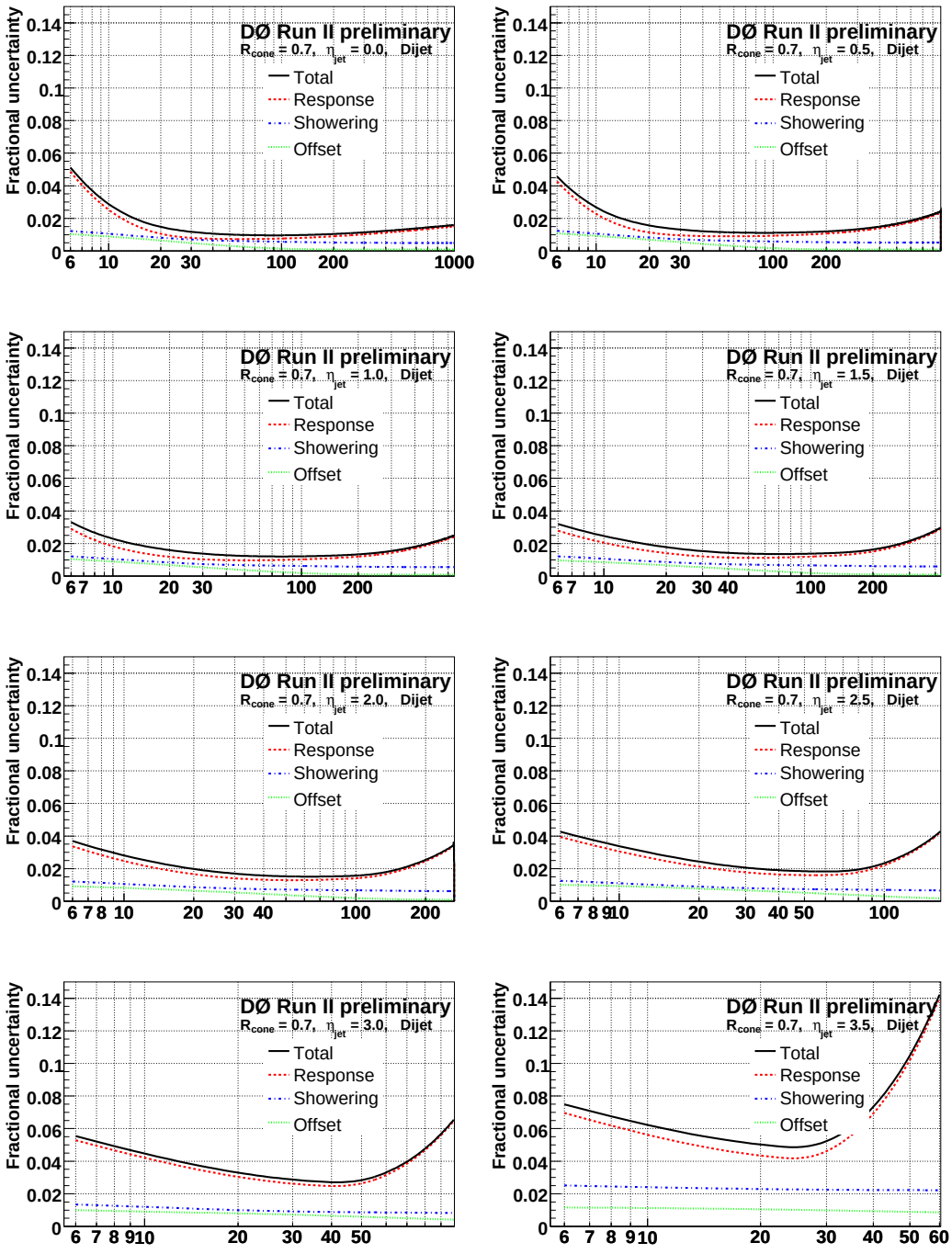

FIG. 70: Relative jet energy scale uncertainties in data for $\mathcal{R}_{\rm cone} = 0.7$ as a function of $E_{T,\rm jet}^{\rm meas}$ for different $\eta_{\rm jet}^{\rm det}$ values (from left to right and top to bottom: $\eta_{\rm jet}^{\rm det} = 0.0$, 0.5, 1.0, 1.5, 2.0, 2.5, 3.0 and 3.5).

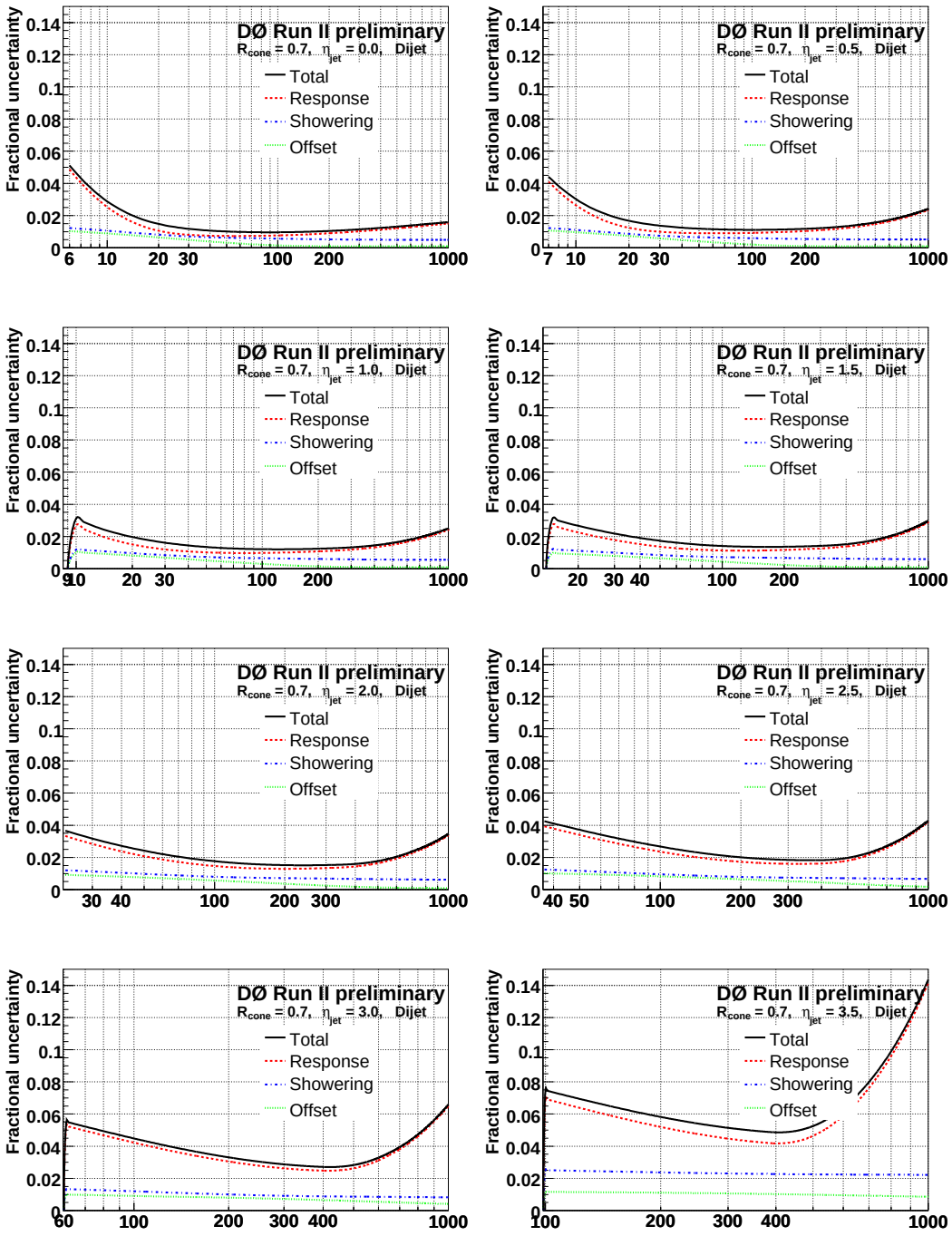

FIG. 71: Relative jet energy scale uncertainties in data for $\mathcal{R}_{\rm cone} = 0.7$ as a function of $E_{\rm jet}^{\rm meas}$ for different $\eta_{\rm jet}^{\rm det}$ values (from left to right and top to bottom: $\eta_{\rm jet}^{\rm det} = 0.0$, 0.5, 1.0, 1.5, 2.0, 2.5, 3.0 and 3.5).

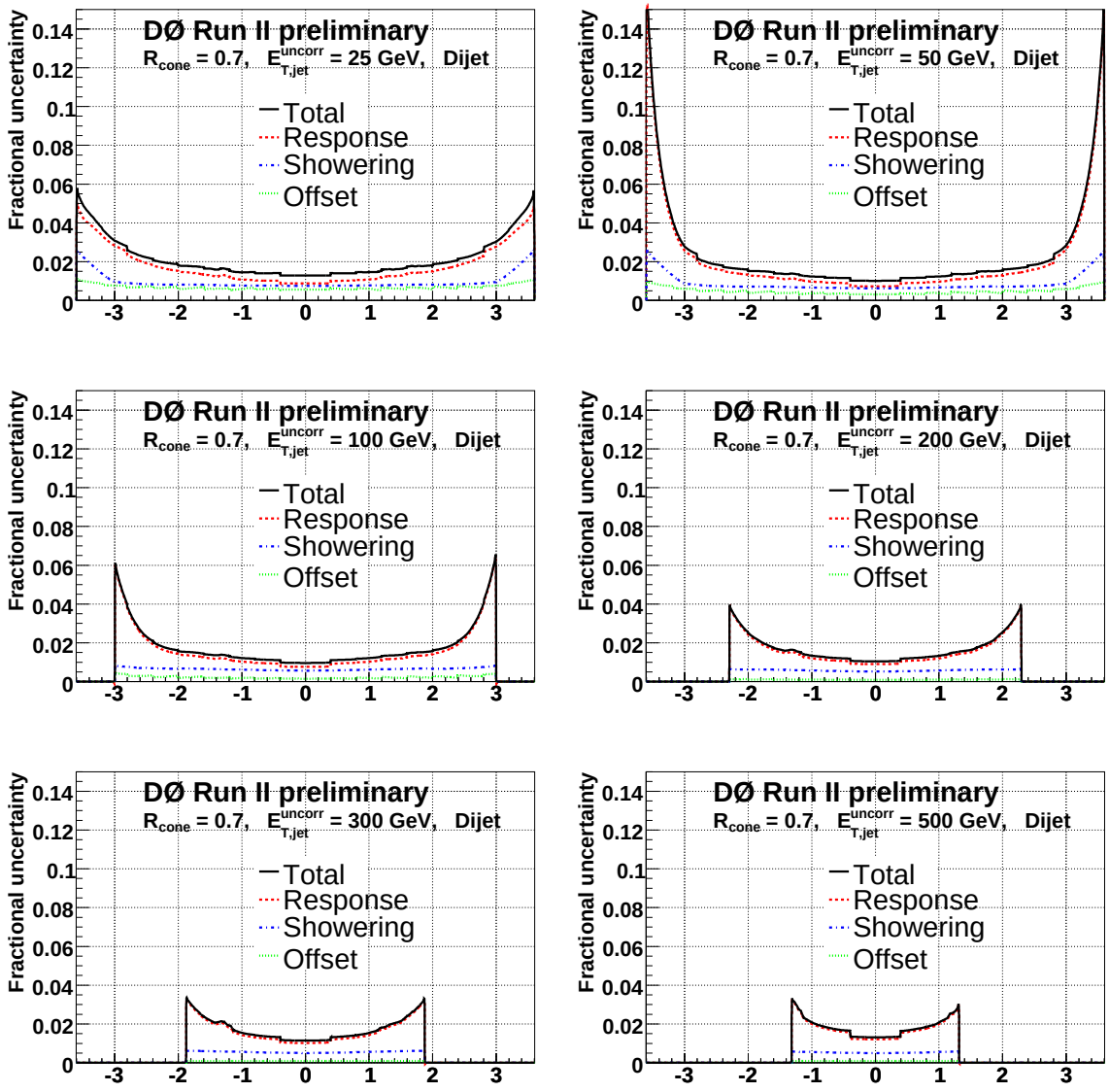

FIG. 72: Relative jet energy scale uncertainties in data for $\mathcal{R}_{\rm cone} = 0.7$ as a function of $\eta_{\rm jet}^{\rm det}$ for different $E_{T,\rm jet}^{\rm meas}$ values (from left to right and top to bottom: $E_{T,\rm jet}^{\rm meas} = 25$, 50, 100, 200, 300 and 500 GeV).

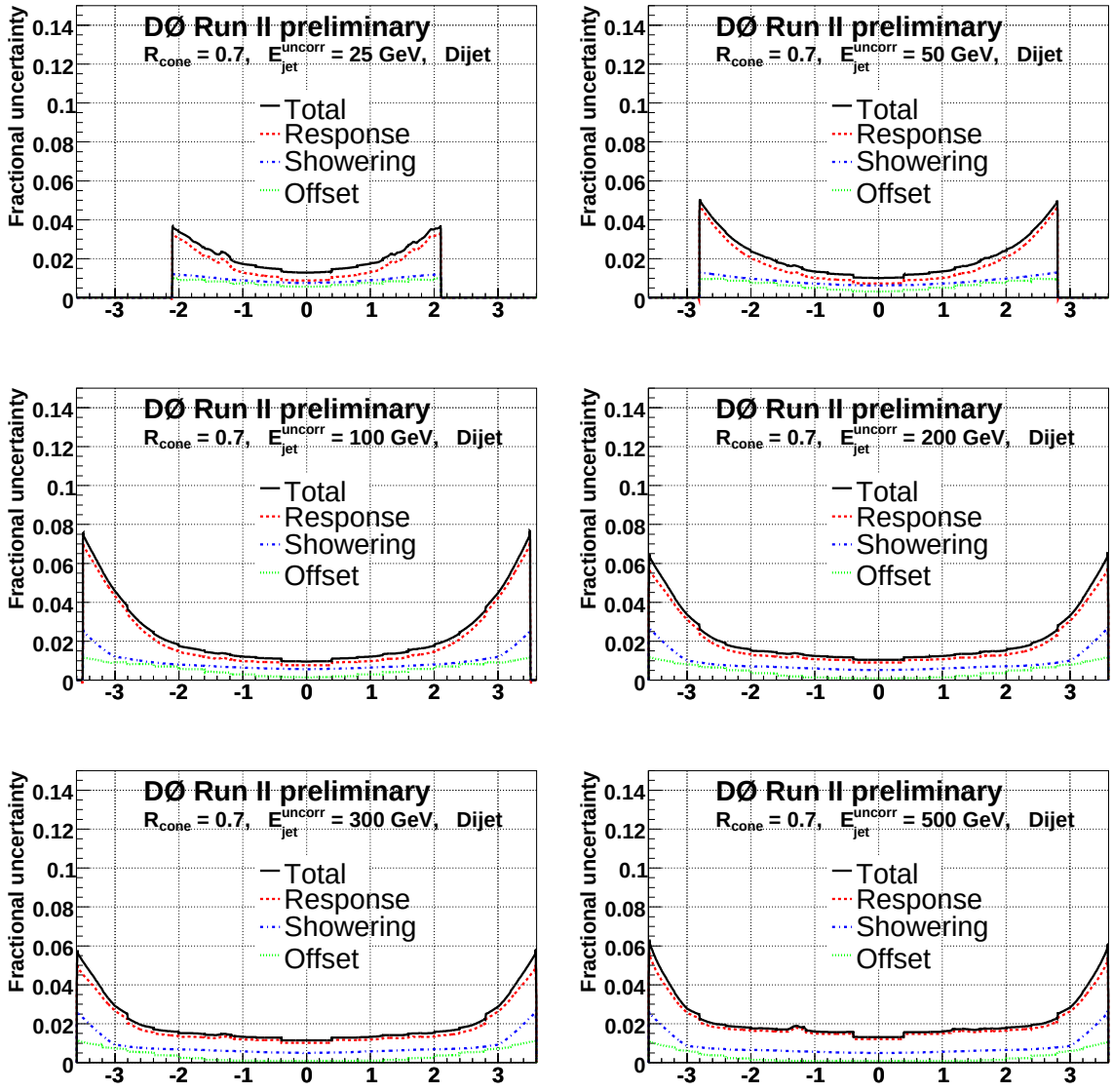

FIG. 73: Relative jet energy scale uncertainties in data for $\mathcal{R}_{\rm cone} = 0.7$ as a function of $\eta_{\rm jet}^{\rm det}$ for different $E_{\rm jet}^{\rm meas}$ values (from left to right and top to bottom: $E_{\rm jet}^{\rm meas} = 25$, 50, 100, 200, 300 and 500 GeV).

13.3.2. MC $\mathcal{R}_{\rm cone} = 0.7$

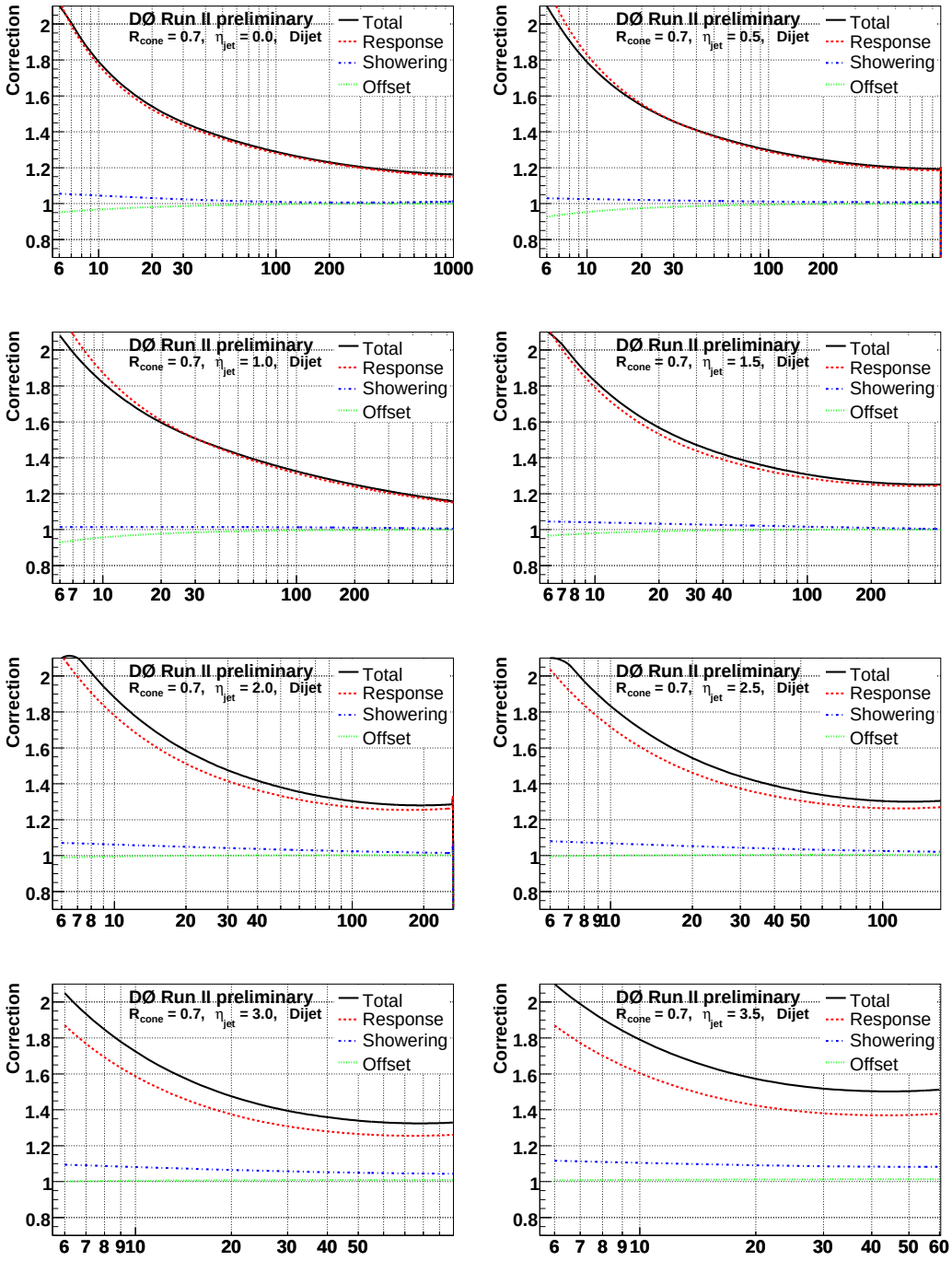

FIG. 74: Jet energy scale corrections in MC for $\mathcal{R}_{\rm cone} = 0.7$ as a function of $E_{T,\rm jet}^{\rm meas}$ for different $\eta_{\rm jet}^{\rm det}$ values (from left to right and top to bottom: $\eta_{\rm jet}^{\rm det} = 0.0$, 0.5, 1.0, 1.5, 2.0, 2.5, 3.0 and 3.5).

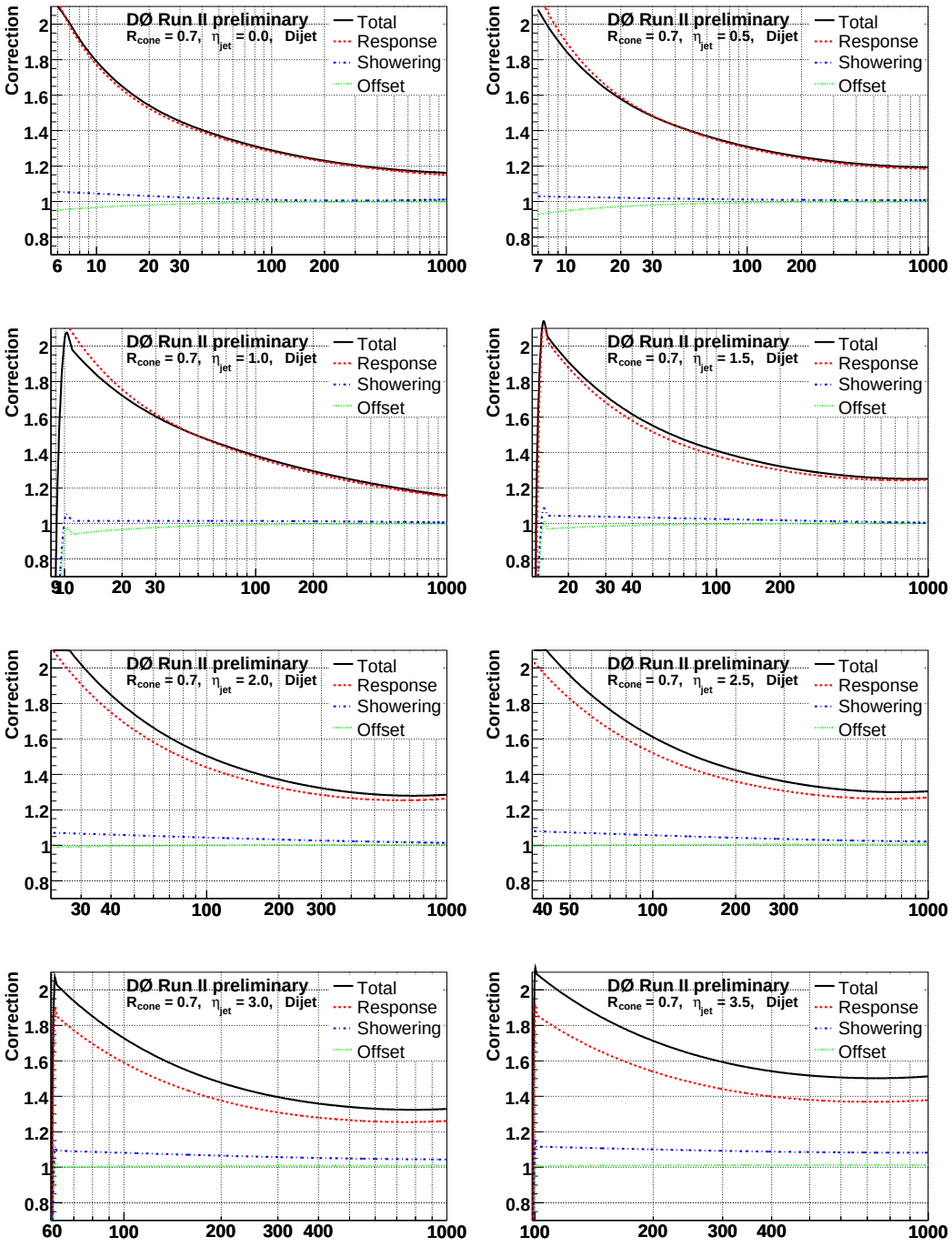

FIG. 75: Jet energy scale corrections in MC for $\mathcal{R}_{\rm cone} = 0.7$ as a function of $E_{\rm jet}^{\rm meas}$ for different $\eta_{\rm jet}^{\rm det}$ values (from left to right and top to bottom: $\eta_{\rm jet}^{\rm det} = 0.0$, 0.5, 1.0, 1.5, 2.0, 2.5, 3.0 and 3.5).

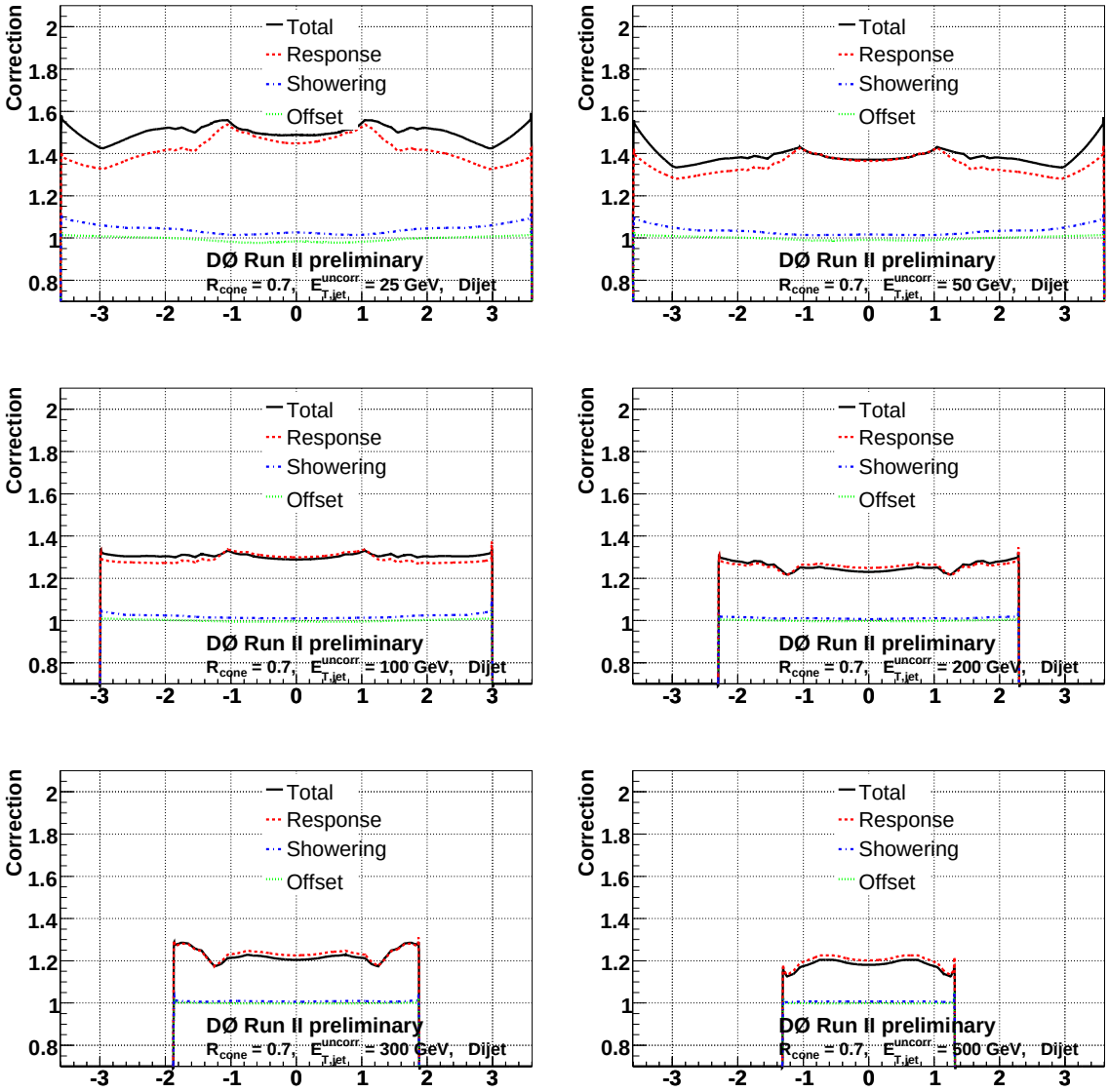

FIG. 76: Jet energy scale corrections in MC for $\mathcal{R}_{\rm cone} = 0.7$ as a function of $\eta_{\rm jet}^{\rm det}$ for different $E_{T,\rm jet}^{\rm meas}$ values (from left to right and top to bottom: $E_{T,\rm jet}^{\rm meas} = 25$, 50, 100, 200, 300 and 500 GeV).

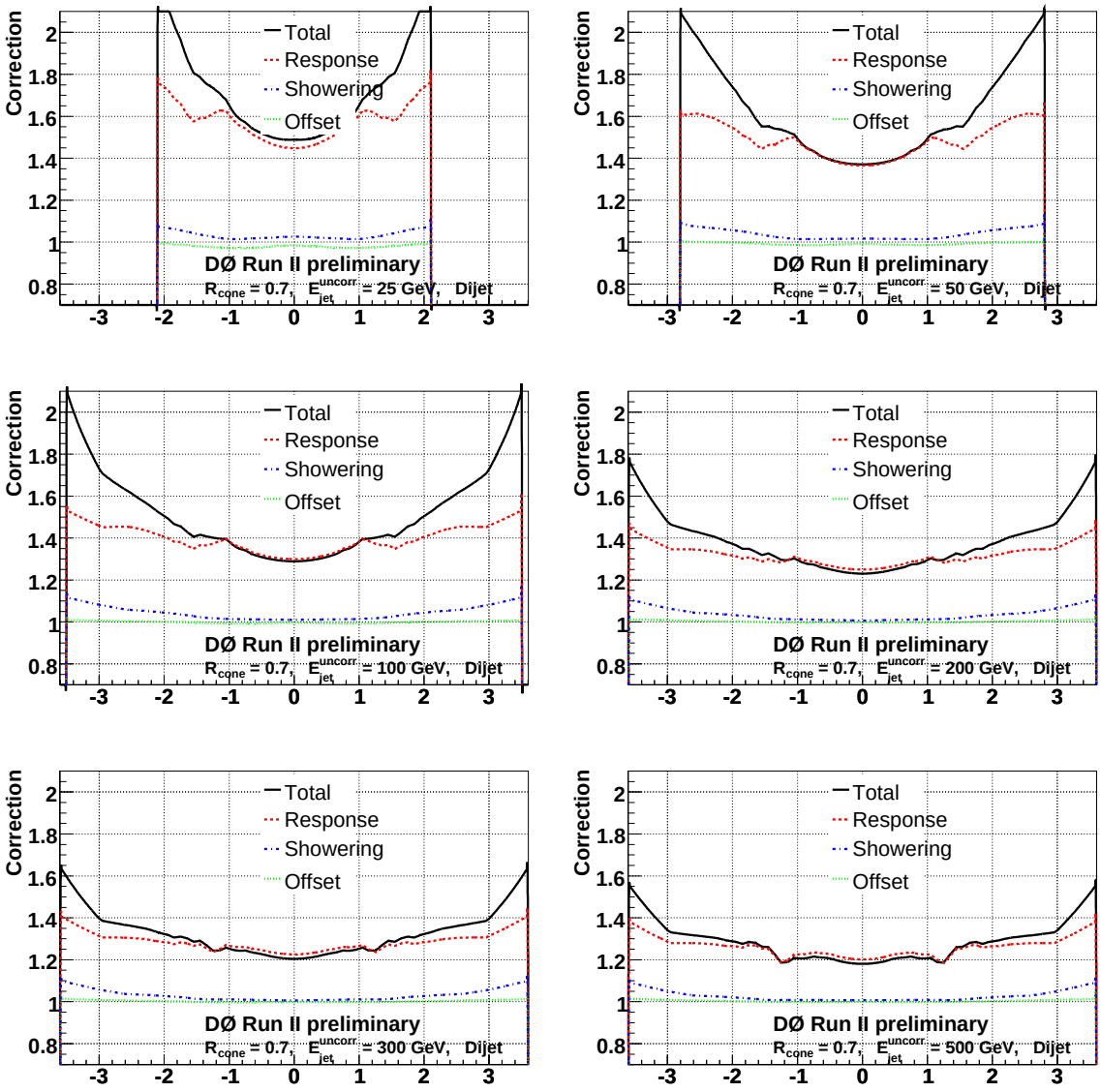

FIG. 77: Jet energy scale corrections in MC for $\mathcal{R}_{\rm cone} = 0.7$ as a function of $\eta_{\rm jet}^{\rm det}$ for different $E_{\rm jet}^{\rm meas}$ values (from left to right and top to bottom: $E_{\rm jet}^{\rm meas} = 25$, 50, 100, 200, 300 and 500 GeV).

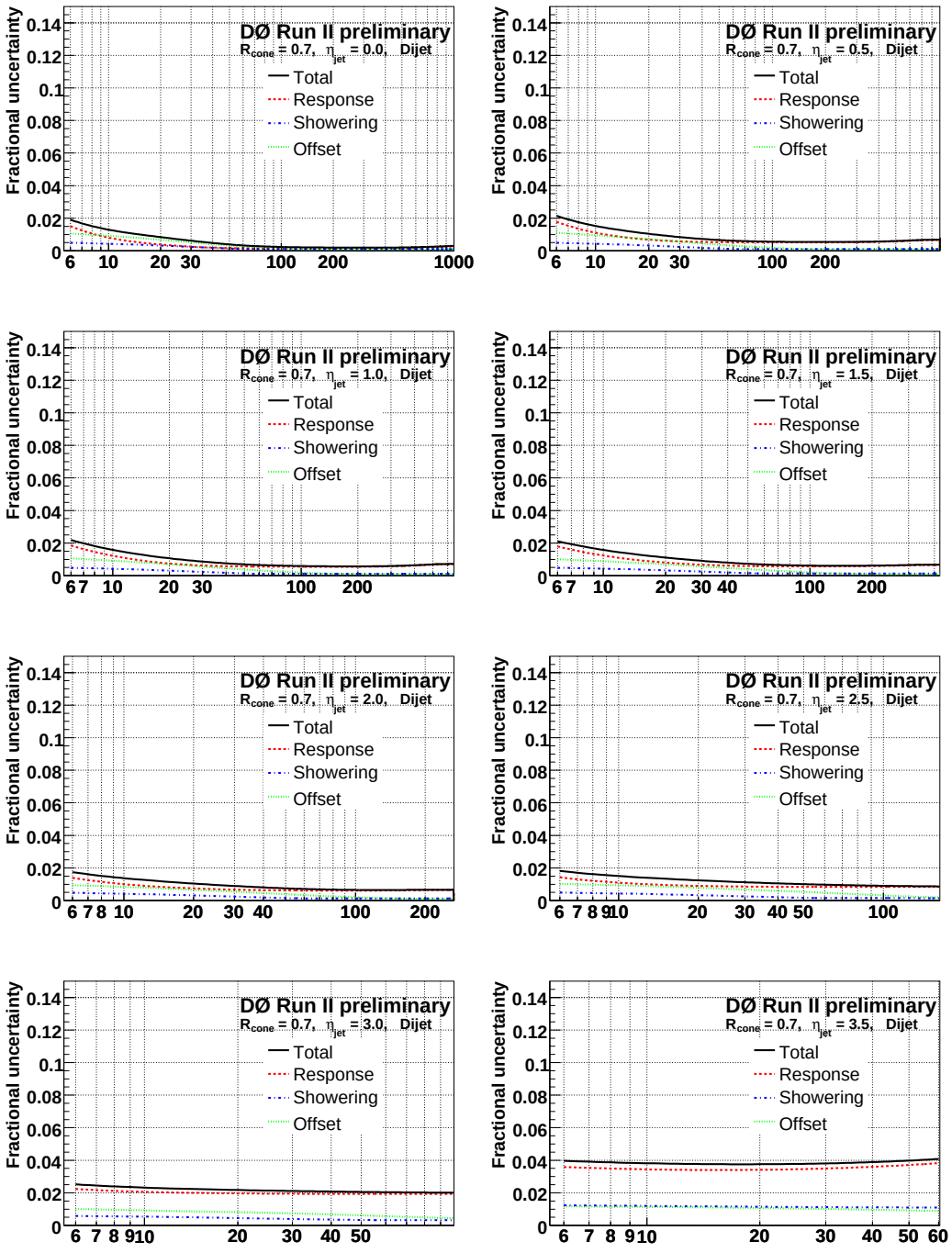

FIG. 78: Relative jet energy scale uncertainties in MC for $\mathcal{R}_{\rm cone} = 0.7$ as a function of $E_{T,\rm jet}^{\rm meas}$ for different $\eta_{\rm jet}^{\rm det}$ values (from left to right and top to bottom: $\eta_{\rm jet}^{\rm det} = 0.0$, 0.5, 1.0, 1.5, 2.0, 2.5, 3.0 and 3.5).

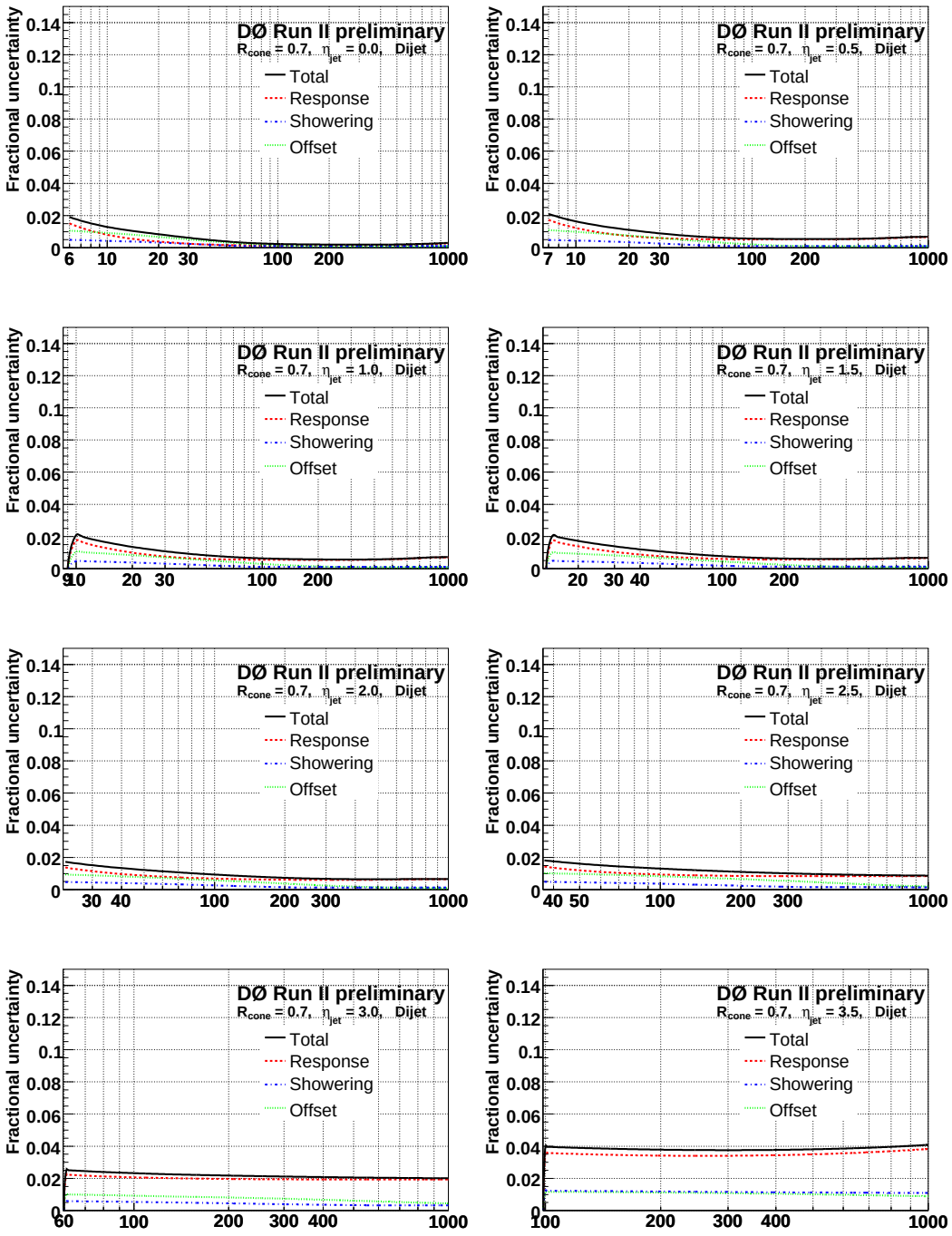

FIG. 79: Relative jet energy scale uncertainties in MC for $\mathcal{R}_{\rm cone} = 0.7$ as a function of $E_{\rm jet}^{\rm meas}$ for different $\eta_{\rm jet}^{\rm det}$ values (from left to right and top to bottom: $\eta_{\rm jet}^{\rm det} = 0.0$, 0.5, 1.0, 1.5, 2.0, 2.5, 3.0 and 3.5).

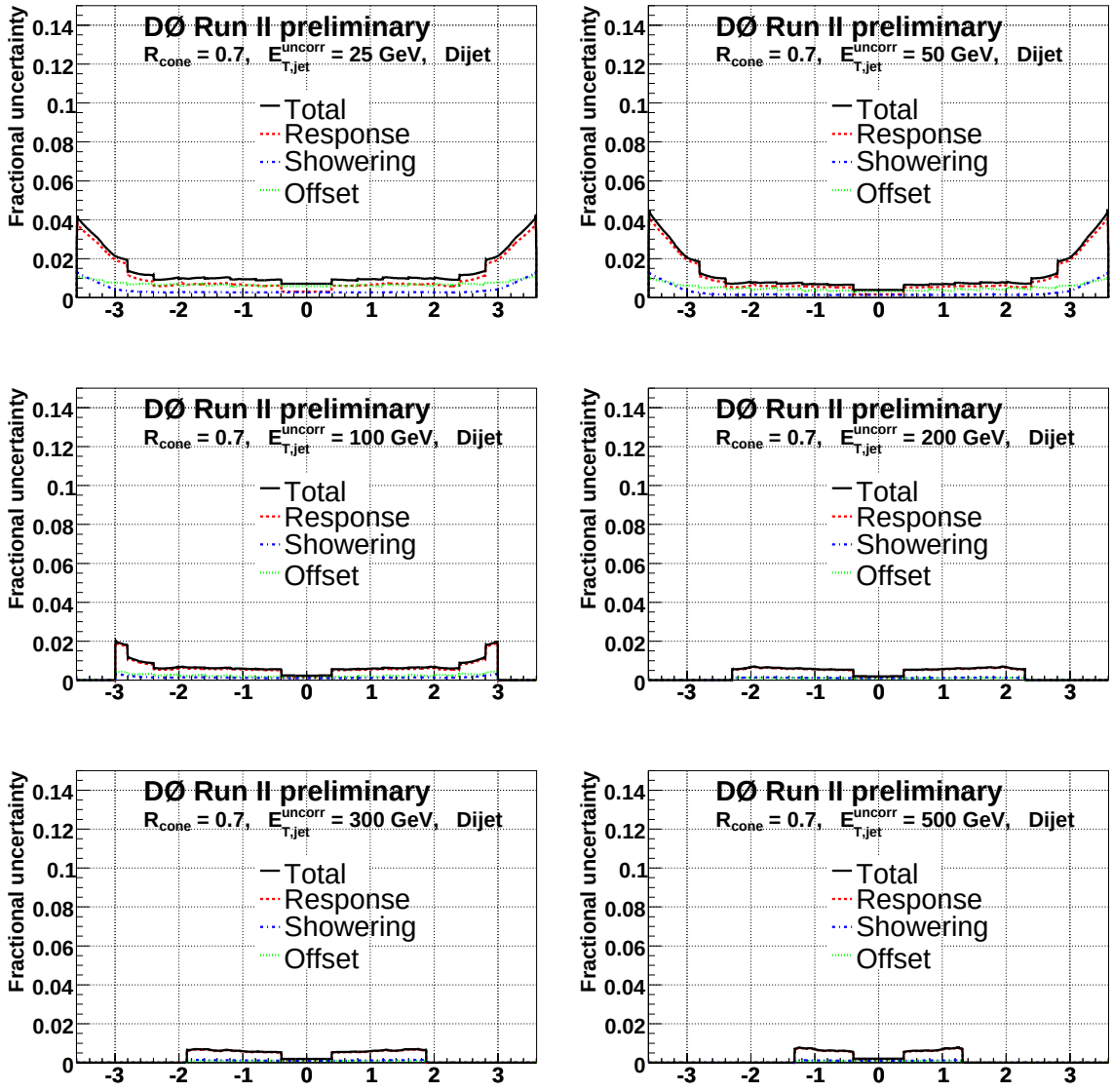

FIG. 80: Relative jet energy scale uncertainties in MC for $\mathcal{R}_{\rm cone} = 0.7$ as a function of $\eta_{\rm jet}^{\rm det}$ for different $E_{T,\rm jet}^{\rm meas}$ values (from left to right and top to bottom: $E_{T,\rm jet}^{\rm meas} = 25$, 50, 100, 200, 300 and 500 GeV).

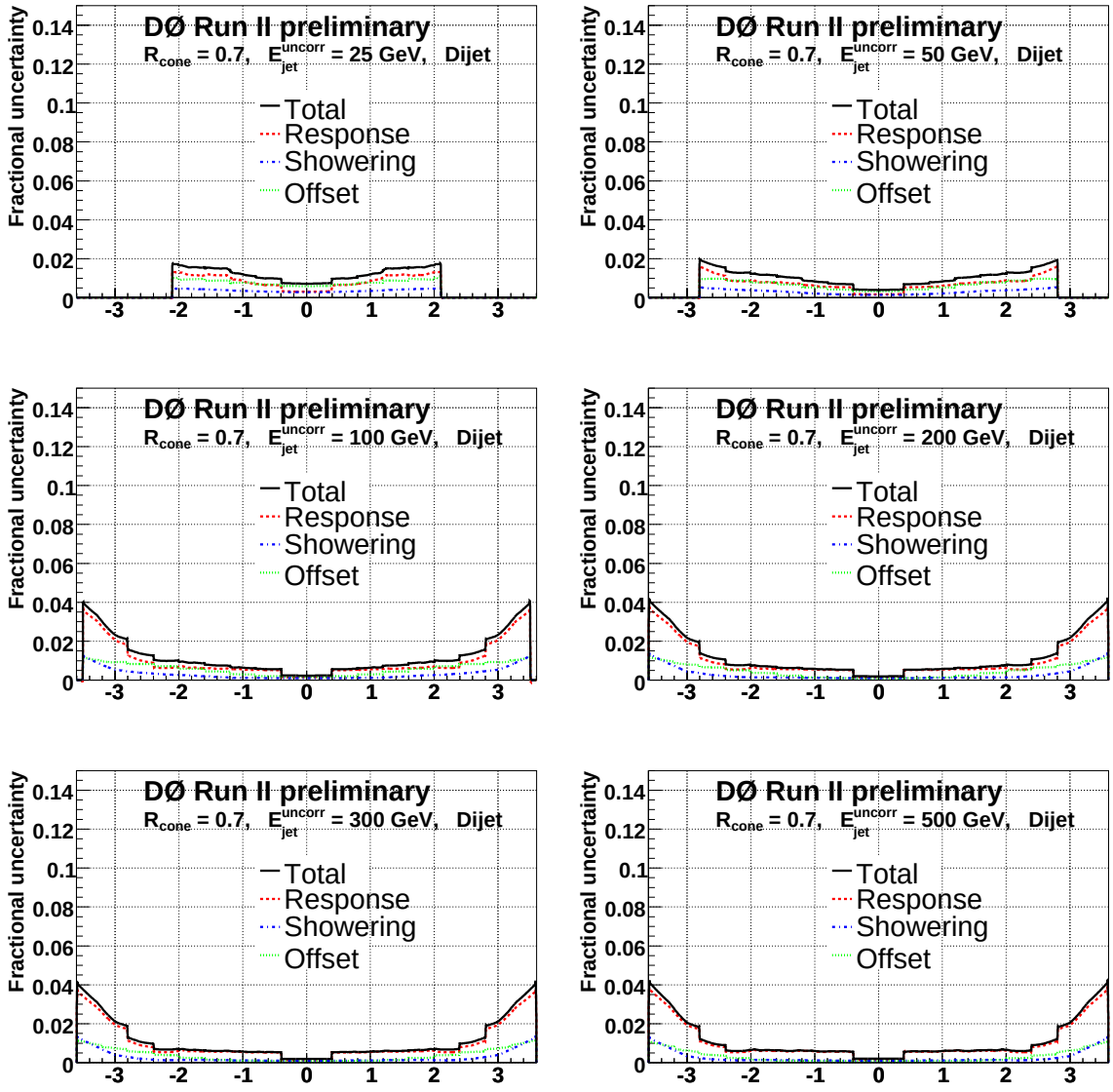

FIG. 81: Relative jet energy scale uncertainties in MC for $\mathcal{R}_{\rm cone} = 0.7$ as a function of $\eta_{\rm jet}^{\rm det}$ for different $E_{\rm jet}^{\rm meas}$ values (from left to right and top to bottom: $E_{\rm jet}^{\rm meas} = 25$, 50, 100, 200, 300 and 500 GeV).

14. CLOSURE TESTS

This section presents preliminary results on the validation of the jet energy scale corrections and their assigned uncertainties. These validation tests are referred to as "closure tests", and their goal is to assess whether the corrections are calibrating jet energy back to the particle level within the quoted total uncertainties. Even in such case, it is not guaranteed that the rest of 4-momentum components (e.g. p_T) are automatically calibrated as well. The need for a full 4-momentum calibration (never provided in the past) is being investigated and will be quantified in the near future. For the moment, this section will only discuss closure tests in the context of energy calibration.

In order to assess whether closure of the corrections is achieved, observables able to probe the relationship between the (calibrated) calorimeter- and particle-jet energies must be defined. In the case of MC, as it will be discussed in Sect. 14.2, this can be rather straightforward. In the case of data, the connection is not so direct and effects unrelated to jet energy calibration (e.g. background contamination, photon energy scale, physics showering, etc) must be properly accounted for.

14.1. Sample Selection

Since closure tests are mainly designed to probe the absolute energy scale calibration, a natural physics sample to use is γ+jet. The event selection used for closure tests closely follows that used for the absolute response measurement (see Sect. 8.1), except that no upper cuts on primary vertex or jet multiplicity are applied. By considering events with $n_{\rm PV} \geq 1$, we enforce consistency with the determination of the $k_{\rm O}^{\rm ZS}$ correction, which was estimated for the inclusive ($n_{\rm PV} \geq 1$) sample. The reasons for the ≥ 1 jets requirement are twofold. First, by not removing events with extra jets we minimize biases to the actual average offset in the sample, since some of those jets will likely arise from additional interactions. Second, we attempt to avoid introducing different biases in the event selection in data and MC arising e.g. from differences in the jet reconstruction efficiency.

Closure tests are performed separately for $\mathcal{R}_{\rm cone} = 0.7$ and 0.5 jets, in different 0.4-wide bins of $\left|\eta_{\rm jet}^{\rm det}\right|$ (up to $\left|\eta_{\rm jet}^{\rm det}\right| < 3.6$) and as a function of p'_T (defined as in Sect. 6.4).

In order to reduce the effect from the low E_T bias (not explicitly corrected for), an additional cut of $p_{T\gamma}$ >30 GeV is applied. However, it must be kept in mind that the effectiveness of such cut is limited since ≥ 1 jets are allowed in the sample. Furthermore, even for events with exactly one jet, the low E_T bias near/in the ICR is still present above 30 GeV. Therefore, some deviations at low p'_T will be observed in the closure variable which are believed to arise from the uncorrected low E_T bias.

14.2. Direct Closure Tests in MC

In the case of MC, the availability of the particle jet information allows to define a "direct" closure variable:

$$\mathcal{D} = \frac{< E_{\rm jet}^{\rm corr} >}{< E_{\rm jet}^{\rm ptcl} >}, \tag{76}$$

where $E_{\rm jet}^{\rm corr}$ is the corrected jet energy (see Eq. 12) and $E_{\rm jet}^{\rm ptcl}$ is the energy of the closest particle jet matching the reconstructed jet within $\Delta\mathcal{R} < \mathcal{R}_{\rm cone}/2$. The averages in Eq. 76

are taken for the set of events within the particular $(p'_T, |\eta^{\rm det}_{\rm jet}|)$ bin under consideration.

Figures 82 and 83 present, respectively, a summary of closure tests for $\mathcal{R}_{\rm cone} = 0.7$ and 0.5 jets in MC. The jet energy scale corrections have been evaluated using the internally remapped E'. The rise observed at low p'_T is believed to arise from the low E_T bias, as discussed in Sect. 14.1. Taking this into consideration, in general closure is achieved within the claimed $0.5 - 1\%$ uncertainties. Some of the trends observed are consistent with known limitations of the individual subcorrections (e.g. the slope in the $0.8 < |\eta^{\rm det}_{\rm jet}| < 1.2$ region arises from the relative response correction, for which a residual systematic uncertainty had already been assigned).

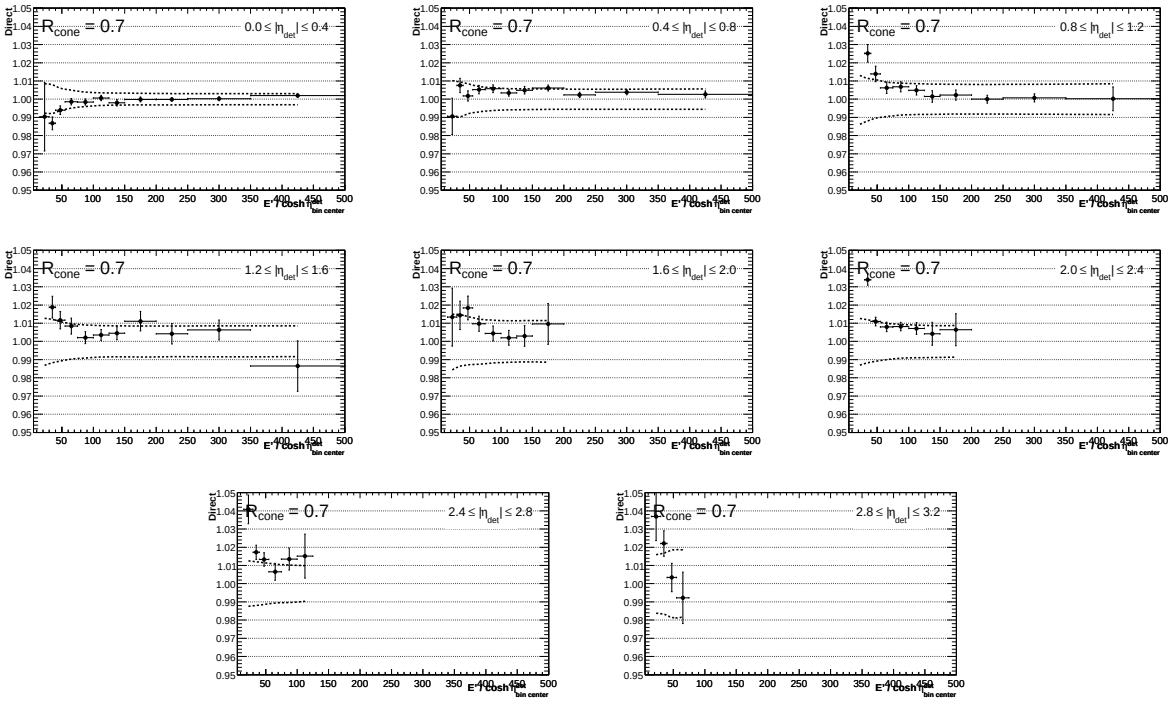

FIG. 82: Closure test for $\mathcal{R}_{\rm cone} = 0.7$ jets in MC as a function of p'_T and in different $|\eta^{\rm det}_{\rm jet}|$ bins. The points correspond to the value of the direct closure variable (see Eq. 76) and the dashed line represents the total jet energy scale uncertainty.

(The systematic uncertainty on the direct closure in MC from varying the $\Delta\mathcal{R}$ matching criterion between the reconstructed and particle jets by $\Delta\mathcal{R} = \mathcal{R}_{\rm cone}/2 \pm 0.1$ is shown in Fig. 218 and 219 in Appendix I2, respectively for $\mathcal{R}_{\rm cone} = 0.7$ and 0.5 jets. As it can be appreciated, the dependence is $\leq 0.1\%$ and probably consistent with statistical fluctuations. We therefore conclude that such systematic uncertainty on closure can be neglected.)

(As discussed in Sect. 14.1, the event selection used for the direct closure in MC is not fully consistent with that used to derive the individual subcorrections. The main inconsistency is in the jet multiplicity cut. The consistent selection to perform this closure test should require exactly one jet in the sample without ZB overlay, and then allow ≥ 1 jets for the selected events when ZB overlay is added. Closure plots using this consistent selection are shown in Appendix I1. Closure is slightly improved in some $\eta^{\rm det}_{\rm jet}$ bins (e.g. 0.4-0.8 and 0.8-1.2), with some of the features attributed to the low ET bias still present, and no real changes to the final conclusion.)

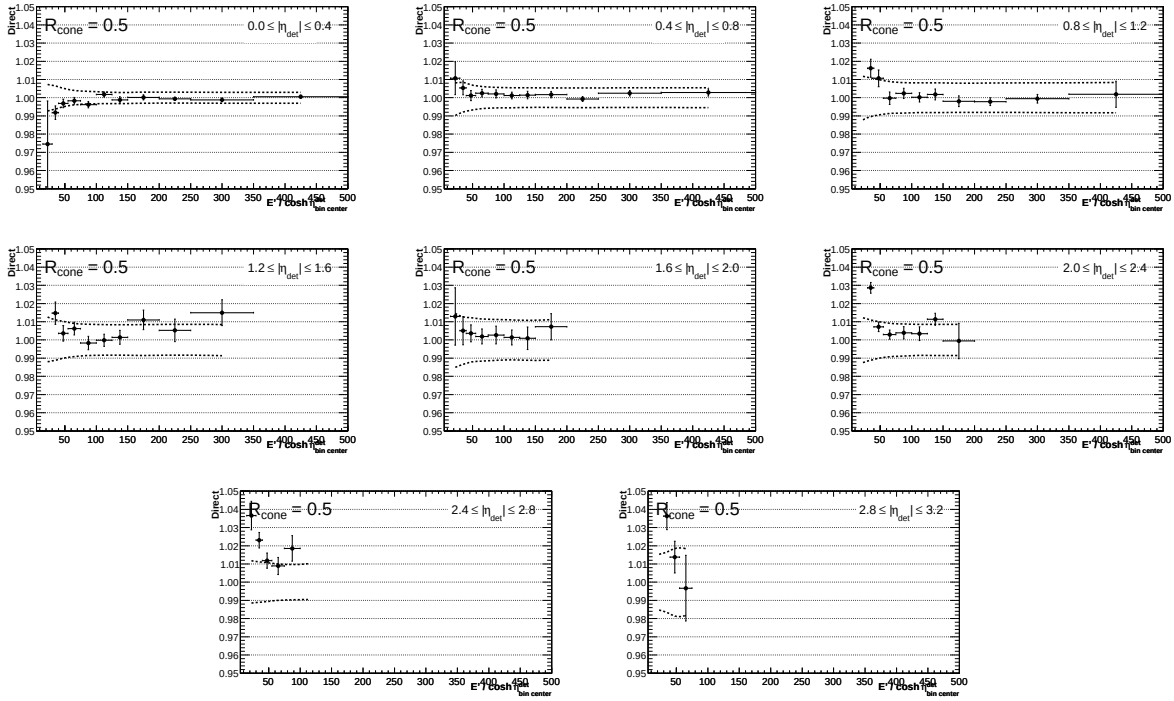

FIG. 83: Closure test for $\mathcal{R}_{\rm cone} = 0.5$ jets in MC as a function of p'_T and in different $\left|\eta^{\rm det}_{\rm jet}\right|$ bins. The points correspond to the value of the direct closure variable (see Eq. 76) and the dashed line represents the total jet energy scale uncertainty.

14.3. Closure Tests in Data

In contrast with MC, in the case of data there is no possibility to directly check the absolute energy calibration, as no information regarding particle jets is available. Therefore, closure tests are based on the comparison of the corrected jet energies between data and MC. Provided the jet energy calibration works properly in MC (see Sect. 14.2), it would then possible to relate the relative data-to-MC intercalibration to absolute calibration in data.

As in the case of the direct closure in MC, we use γ+jet events (see Sect. 14.1). The closure observable is defined as the ratio of the average corrected jet energies between data and MC ($< E^{\rm corr,Data}_{\rm jet} > / < E^{\rm corr,MC}_{\rm jet} >$), computed as a function of p'_T in different $\left|\eta^{\rm det}_{\rm jet}\right|$ regions.

Since the goal of the closure tests is to validate the jet energy calibration in pure γ+jet events, it is very important to properly account for any differences between data and MC which could possibly result in biases in the closure observable.

The most relevant effect is related to the presence of QCD dijet background in data. Since the closure observable does not directly involve the reconstructed photon p_T, the main difference results from the flavor composition of the jet. As already discussed, jets from QCD background are gluon-dominated, whereas jets from γ+jet signal are quark-dominated, and there can be up to 8% difference in response at low p_T (see Fig. 127 in Appendix D3). In order to account for this bias, data is not compared to pure γ+jet MC, but rather to a mixture of γ+jet and QCD dijet (γ-like) MC, combined using the estimated sample purity. This allows to correct for the leading difference between data and MC. However, given the smallness of the jet energy calibration uncertainties, residual sub-leading differences remain which must be corrected for. In particular, while the application of the jet energy calibration corrections

would in principle precisely intercalibrate jets from γ+jet events between data and MC, it is not guaranteed that the gluon-dominated jets from the QCD background will automatically be intercalibrated. This is the consequence of the different single pion response between data and MC, which results in a few-percent lower jet energies for the QCD background events in data than predicted by MC. Unless corrected, this would introduce a small bias in the data-to-MC closure tests. This residual miscalibration of the QCD background can be estimated from special MC samples using a single pion response tuned to data. A corresponding correction factor is derived and used to further correct the jet energies in the QCD dijet (γ-like) MC. The largest correction is for central jets, reaching -4% at $p_T \sim 30$ GeV and quickly decreasing towards 0% at $p_T \sim 100$ GeV. Forward jets have a harder energy spectrum of hadrons, and the residual correction is negligible. Please note that the net effect on the closure observable is suppressed by $(1-\rho)$, where ρ is the expected sample purity. Therefore, a -4% correction at $p_T \sim 30$ GeV for central jets in QCD dijet (γ-like) MC only translates into a $\sim 4\%(1-0.7) = 1.2\%$ upward shift in the data-to-MC closure observable. *(See Appendix I3 for more details.)* Finally, we also correct the measured photon energy in MC in order to ensure it is on the same scale as in data. *(This includes a +0.6% constant shift required to equalize the electron energy scale, plus a p_T-dependent correction (see Fig. 122 in Appendix D2) required to equalize the photon energy scale.)* As already indicated, such correction enters the closure test indirectly, via the binning of the closure variable in terms of E'.

Figure 84 presents the results of relative data-to-MC closure for $\mathcal{R}_{\rm cone} = 0.7$ jets as a function of p'_T and in different $\left|\eta^{\rm det}_{\rm jet}\right|$ bins. The corresponding plots for $\mathcal{R}_{\rm cone} = 0.5$ jets are shown in Figure 85. Since a-priori jet energy calibration uncertainties for data and MC are largely uncorrelated, the uncertainty on the closure observable is defined as the sum in quadrature of data and MC uncertainties. This uncertainty is represented in Figs. 84 and 85 by the dashed line. In general, data and MC appear intercalibrated within the estimated uncertainties. Please note that no systematic uncertainties on the closure method itself have been included.

(Figures 221 and 222 in Appendix I4 compare the data-to-MC closure in three different MC scenarios: signal only (left row), background only (middle row) and mixture (right row). While only the mixture MC scenario is the one to be considered to draw conclusions regarding data-to-MC closure, the other plots are useful to assess the impact of the QCD background on the closure observable. In particular, the background-only plots show that the data/MC ratio is typically smaller than one, which indicates that the dominant effect of the background is not so much via the smaller response of gluon-dominated jets (which would make the data/MC ratio go in the opposite direction), but rather the higher effective partonic energies (as compared to γ+jet) selected for a given E' bin, owing to the energy lost in the photon hemisphere even for the tight criteria. The background-only plots also illustrate the limited available statistics for the QCD dijet (γ-like) MC which, when combined with the γ+jet signal MC, can cause significant fluctuations in the mixture plots. We are currently generating additional statistics of the QCD dijet (γ-like) MC to try to improve the statistical stability of the closure results.)

(A closure observable that traditionally has been used is the p_T balance between the reconstructed photon and the corrected jet in selected back-to-back γ+jets event: $\Delta S = p^{\rm corr}_{T\rm jet}/p^{\rm meas}_{T\gamma} - 1$. Please note that this is no longer the closure observable of choice for us, as we would like to directly check energy calibration. Even for perfectly calibrated jets, $\Delta S < 0$ due to the physics out-of-cone radiation not included in the particle jet. This effect is larger for smaller cone size jets. For consistency with the energy calibration plots (Figs. 84-85), the

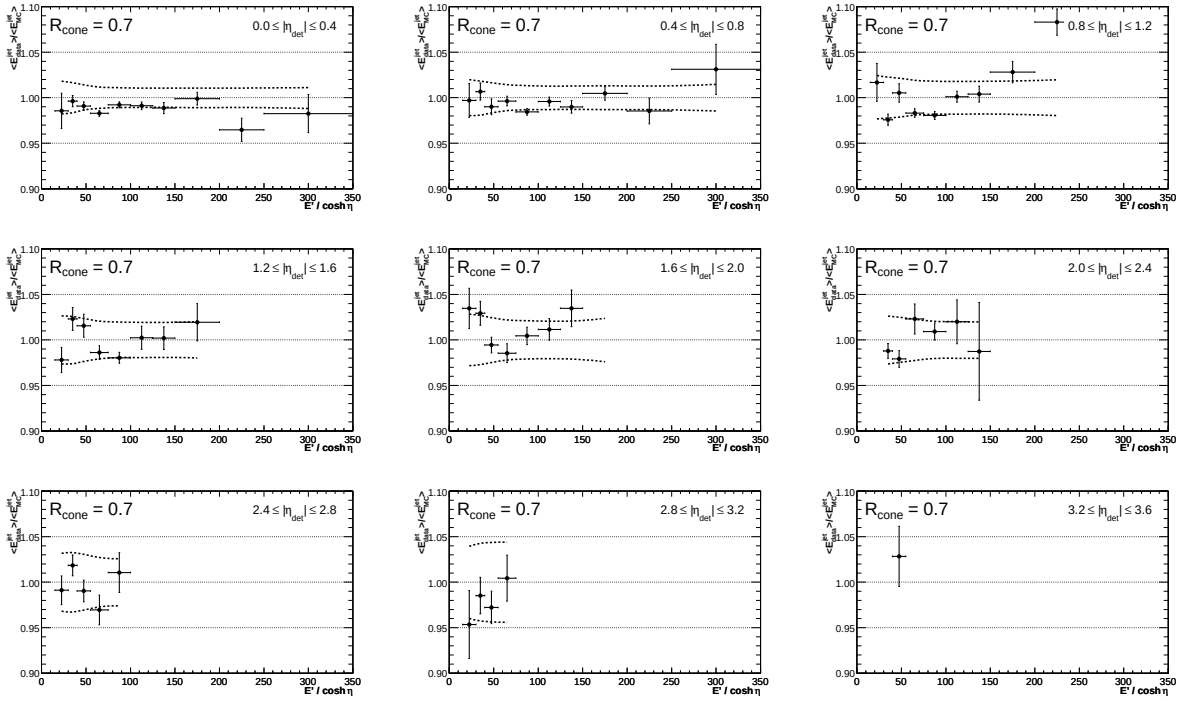

FIG. 84: Relative data-to-MC closure test for $\mathcal{R}_{\text{cone}} = 0.7$ jets as a function of p'_T and in different $\left|\eta_{\text{jet}}^{\text{det}}\right|$ bins. The points correspond to the value of the closure variable whereas the dashed line represents the total jet energy scale uncertainty.

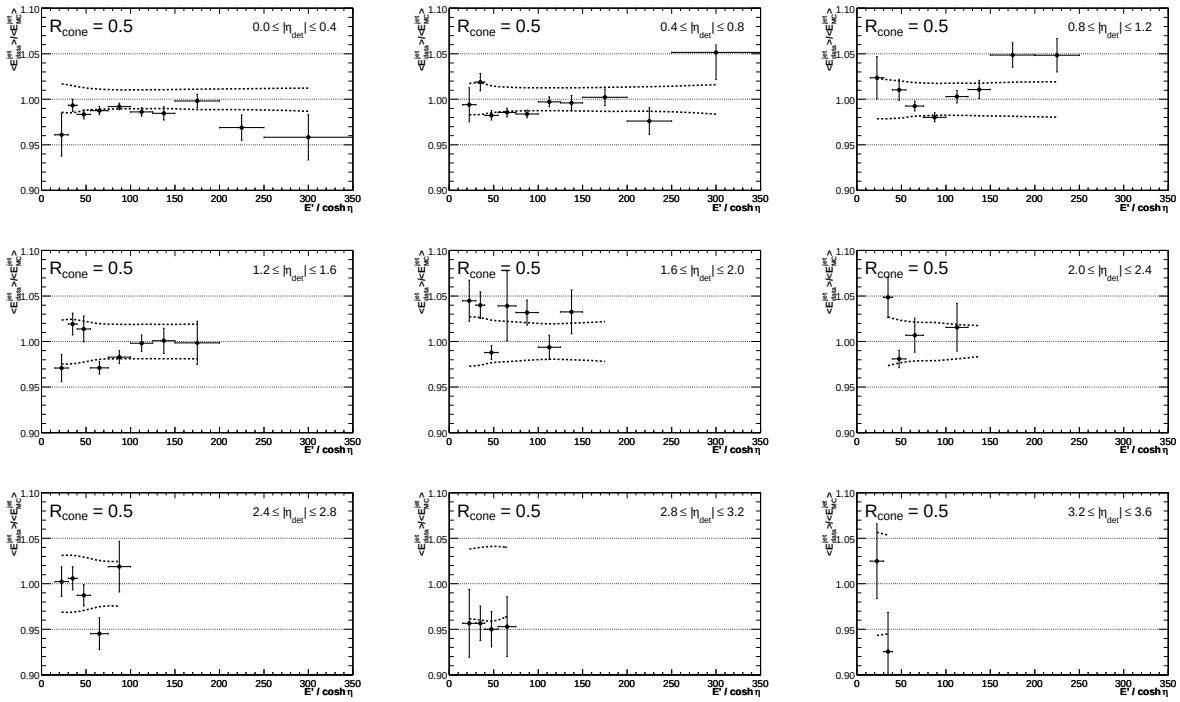

FIG. 85: Relative data-to-MC closure test for $\mathcal{R}_{\text{cone}} = 0.5$ jets as a function of p'_T and in different $\left|\eta_{\text{jet}}^{\text{det}}\right|$ bins. The points correspond to the value of the closure variable whereas the dashed line represents the total jet energy scale uncertainty.

ΔS closure observable is estimated using the same event selection and corrections to MC. Figures 223-226 in Appendix I5 present the ΔS observable as a function of $p_{T\gamma}^{\text{meas}}$ for data, mixture MC, and their difference.)

15. CONCLUSIONS

APPENDIX A: DATA AND MONTE CARLO SAMPLES

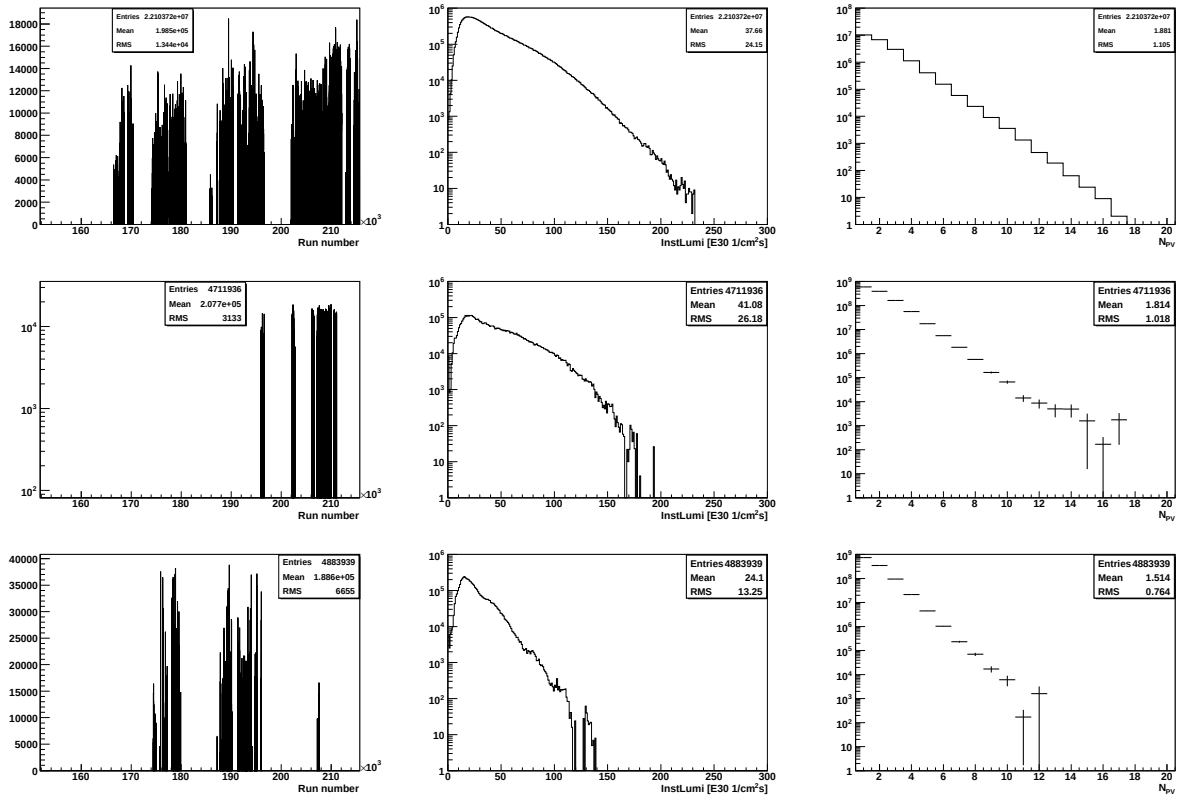

FIG. 86: Distributions of run number, instantaneous luminosity and primary vertex multiplicity for selected γ+jet events in data (upper row), MC with unsuppressed ZB overlay (middle row) and MC with suppressed ZB overlay (lower row). In the case of MC, the run number and instantaneous luminosity shown correspond to the ZB overlay event from data.

APPENDIX B: OFFSET CORRECTION

1. Sample Selection

The dataset used for this measurement is the whole Run IIa CSG ZBMB skim (`d0reco` versions p17.09.01 and p17.09.03), containing approximately 54M events. Such skim contains both ZB and MB events defined, respectively, as events firing the ZB and MB triggers (see Table 3).

ZB triggers	MB triggers
zero_bias	min_bias
zero_bias_NCU	min_bias_NCU
zero_bias^2	min_bias_nim_NCU
zero_bias_NCU^2	min_bias_nim_ncu

TABLE 3: List of ZB and MB triggers considered.

The ZB trigger only makes the requirement that there is a $p\bar{p}$ crossing. The MB trigger requires a hit in the Luminosity Monitor (LM), signaling the presence of a non-elastic interaction. Luminosity Monitor veto (LM veto) is the requirement of not having a L1AndOr term 'fastz' or 'fastz_VME'.

The standard data quality selection (using `caf_dq` and `dq_def` version 2006_05_04) is applied, but modified so that bad muon runs are not excluded. In contrast with the previous version of the jet energy scale corrections, events containing NADA cells are not excluded, as they are considered for physics analyses.

In order to avoid biases in the determination of the offset energy, cells with large occupancy ($> 40\%$) in a given run are excluded. Unfortunately, it is not possible to consider each run separately. Therefore, only if 1000 consecutive events in the sample have the same run number, they are consider for removal of high occupancy cells. This assumes that the ZBMB CSG skim is not segmented much. Following this approach we remove approximately 3000 cells in the sample.

2. Bias Correction

(CAVEAT: plots on the $k_{\mathrm{O}}^{\mathrm{ZS}}$ correction factor and its uncertainties for the unsuppressed ZB overlay case have not been updated yet.)

This section presents a complete set of plots corresponding to the $k_{\mathrm{O}}^{\mathrm{ZS}}$ correction factors, separately for $\mathcal{R}_{\mathrm{cone}} = 0.7$ and 0.5 jets, and for the suppressed and unsuppressed ZB overlay cases. Figure 88(89) shows the $k_{\mathrm{O}}^{\mathrm{ZS}}$ correction factors for $\mathcal{R}_{\mathrm{cone}} = 0.7(0.5)$ jets in the case of suppressed ZB overlay, for different $\left|\eta_{\mathrm{jet}}^{\mathrm{det}}\right|$ bins and as a function of p'_T (defined as $E'/\cosh(\langle\eta_{\mathrm{jet}}^{\mathrm{det}}\rangle)$). Figure 90(91) shows the $k_{\mathrm{O}}^{\mathrm{ZS}}$ correction factors for $\mathcal{R}_{\mathrm{cone}} = 0.7(0.5)$ jets in the case of unsuppressed ZB overlay, for different $\left|\eta_{\mathrm{jet}}^{\mathrm{det}}\right|$ bins and as a function of p'_T (defined as $E'/\cosh(\langle\eta_{\mathrm{jet}}^{\mathrm{det}}\rangle)$). The different symbols correspond to different primary vertex multiplicity in the event.

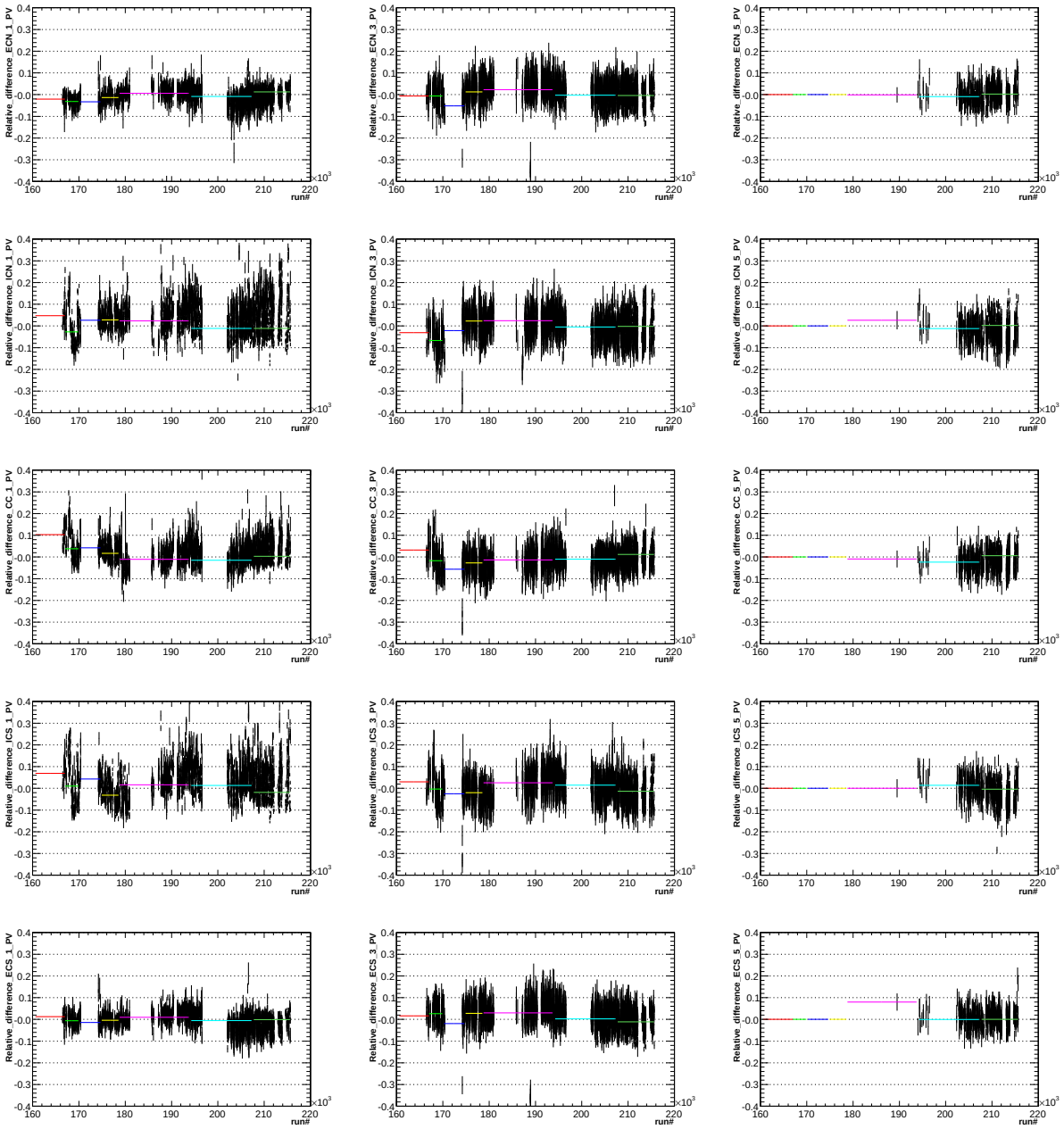

FIG. 87: Relative difference of the minimu bias energy with respect to the Run IIa average as a function of run number for different detector regions; from top to bottom: ECN ($-36 \leq i\eta < -16$), ICN ($-16 \leq i\eta < -8$), CC ($-8 \leq i\eta \leq +8$), ICS ($+8 < i\eta \leq +16$) and ECS ($+16 < i\eta \leq +36$). Different rows correspond to different primary vertex multiplicity: $n_{\rm PV} = 1$ (left), $n_{\rm PV} = 3$ (middle) and $n_{\rm PV} = 5$ (right). Shown in colors are the averages over different trigger lists version, from $v8$ (lower run numbers) to $v14$ (higher run numbers).

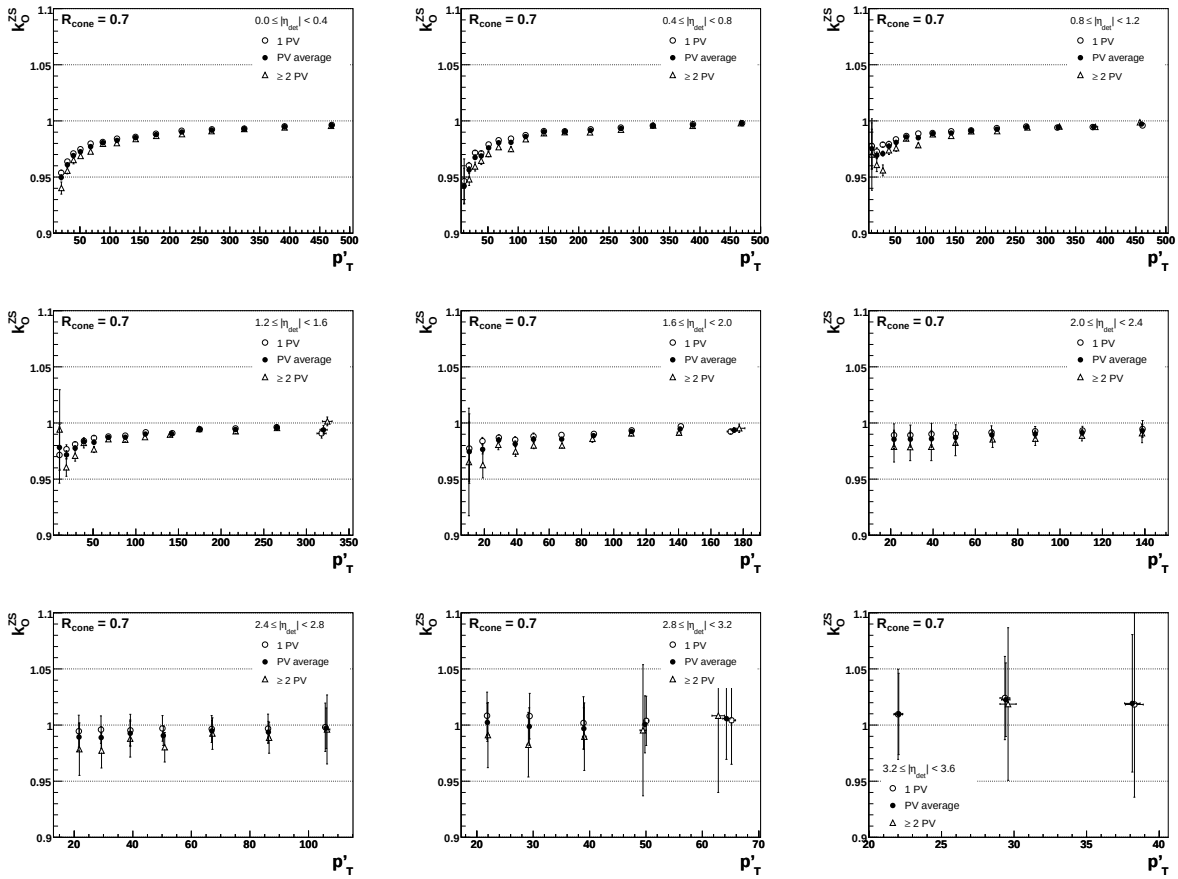

FIG. 88: $k_{\mathrm{O}}^{\mathrm{ZS}}$ correction factor vs p'_T for $\mathcal{R}_{\mathrm{cone}} = 0.7$ jets in the suppressed ZB overlay case. Different plots correspond to different $\left|\eta_{\mathrm{jet}}^{\mathrm{det}}\right|$ bins and the different symbols in each plot correspond to different primary vertex multiplicity in the event.

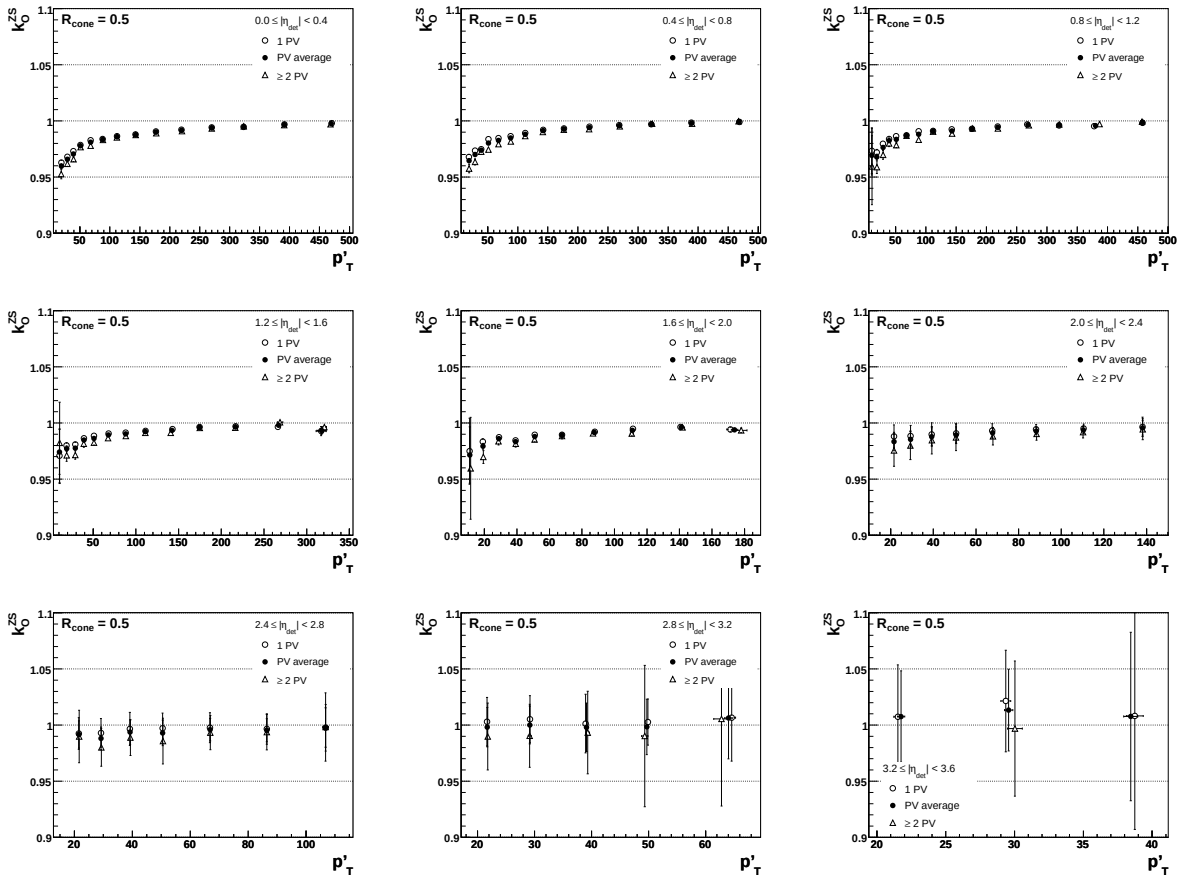

FIG. 89: $k_{\mathrm{O}}^{\mathrm{ZS}}$ correction factor vs p'_T for $\mathcal{R}_{\mathrm{cone}} = 0.5$ jets in the suppressed ZB overlay case. Different plots correspond to different $\left|\eta_{\mathrm{jet}}^{\mathrm{det}}\right|$ bins and the different symbols in each plot correspond to different primary vertex multiplicity in the event.

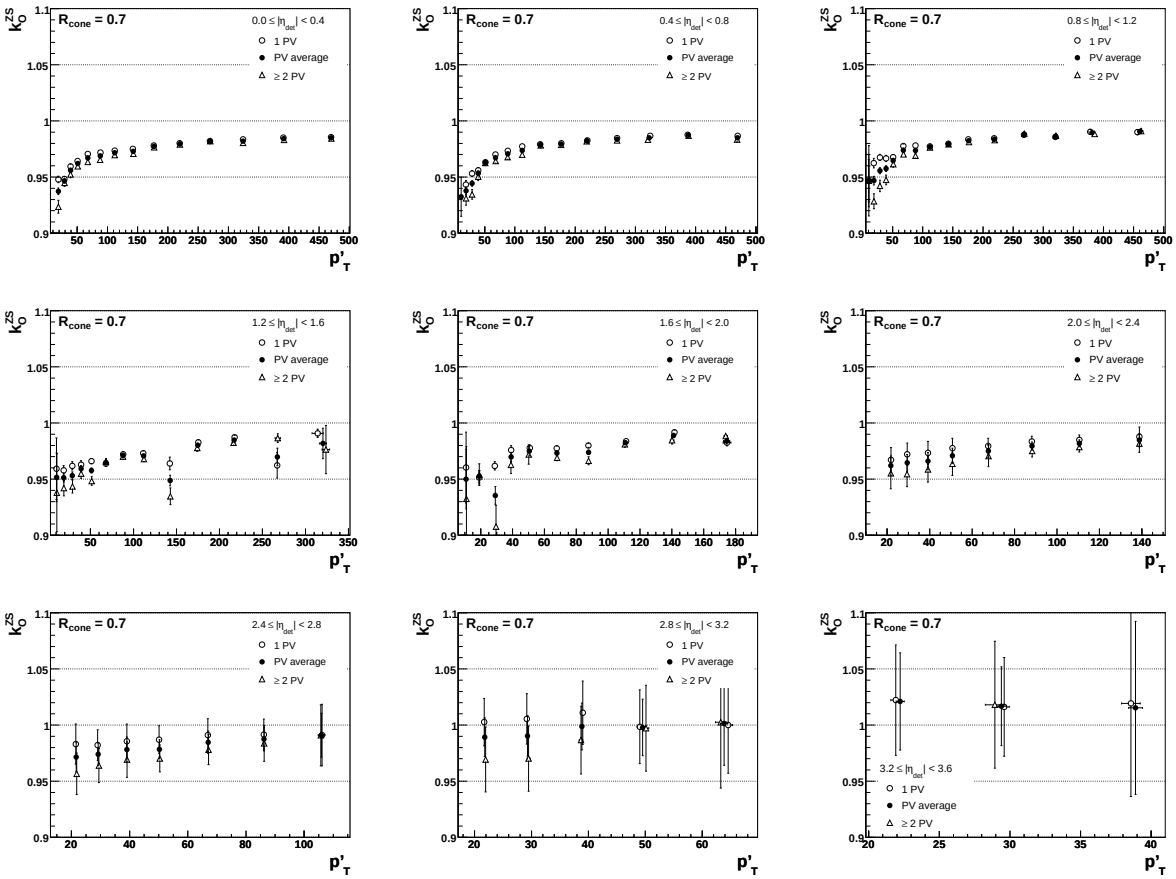

FIG. 90: $k_{\mathrm{O}}^{\mathrm{ZS}}$ correction factor vs p'_T for $\mathcal{R}_{\mathrm{cone}} = 0.7$ jets in the unsuppressed ZB overlay case. Different plots correspond to different $\left|\eta_{\mathrm{jet}}^{\mathrm{det}}\right|$ bins and the different symbols in each plot correspond to different primary vertex multiplicity in the event.

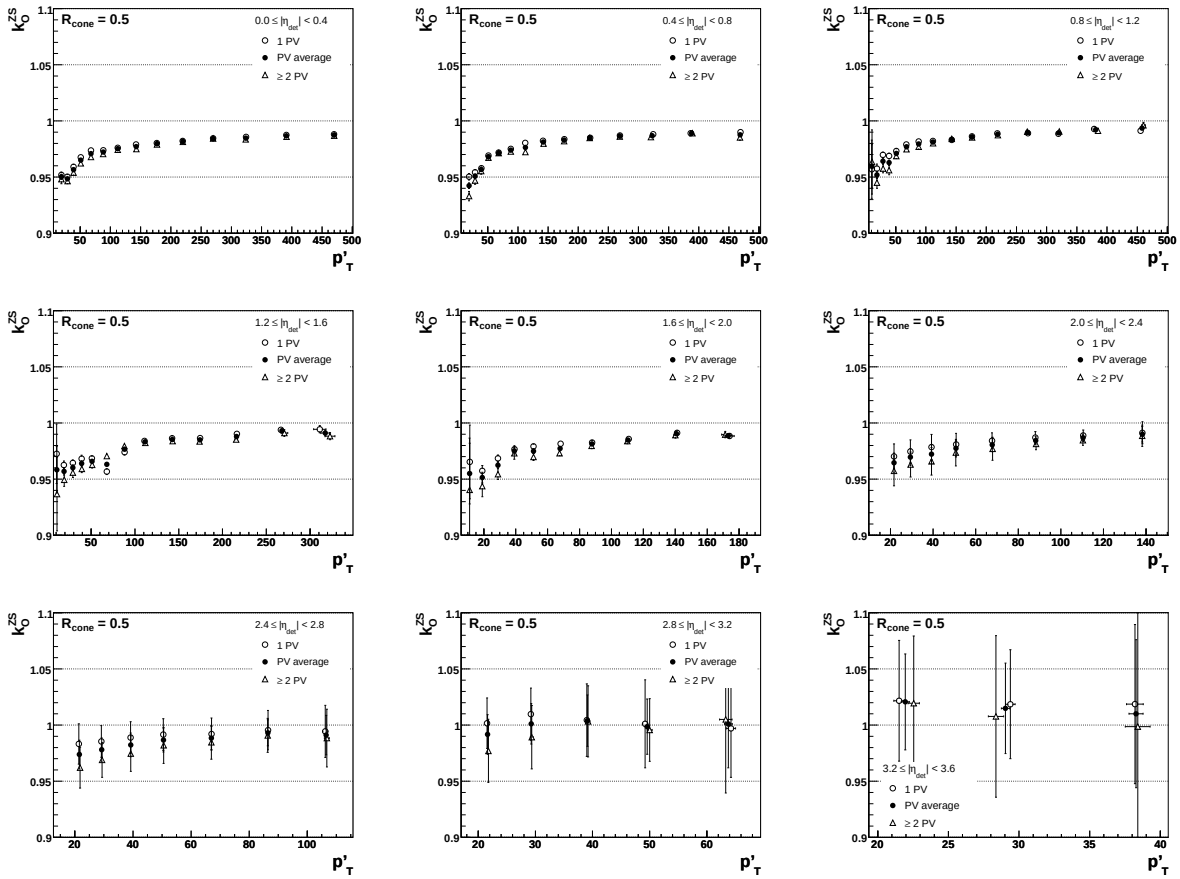

FIG. 91: $k_{\mathrm{O}}^{\mathrm{ZS}}$ correction factor vs p'_T for $\mathcal{R}_{\mathrm{cone}} = 0.5$ jets in the unsuppressed ZB overlay case. Different plots correspond to different $\left|\eta_{\mathrm{jet}}^{\mathrm{det}}\right|$ bins and the different symbols in each plot correspond to different primary vertex multiplicity in the event.

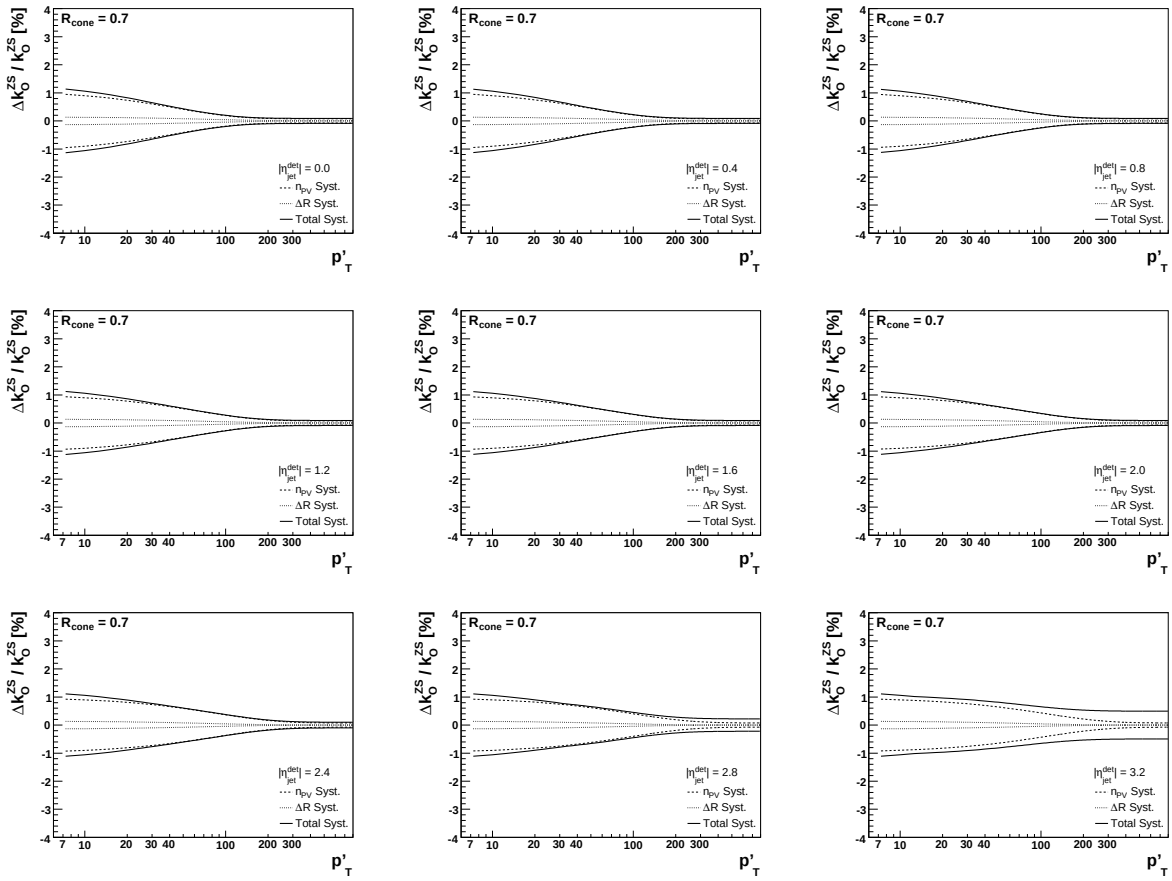

FIG. 92: Systematic uncertainties on the $k_{\mathrm{O}}^{\mathrm{ZS}}$ correction factor vs p'_T for $\mathcal{R}_{\mathrm{cone}} = 0.7$ jets in the suppressed ZB overlay case. Different plots correspond to different values of $\eta_{\mathrm{jet}}^{\mathrm{det}}$.

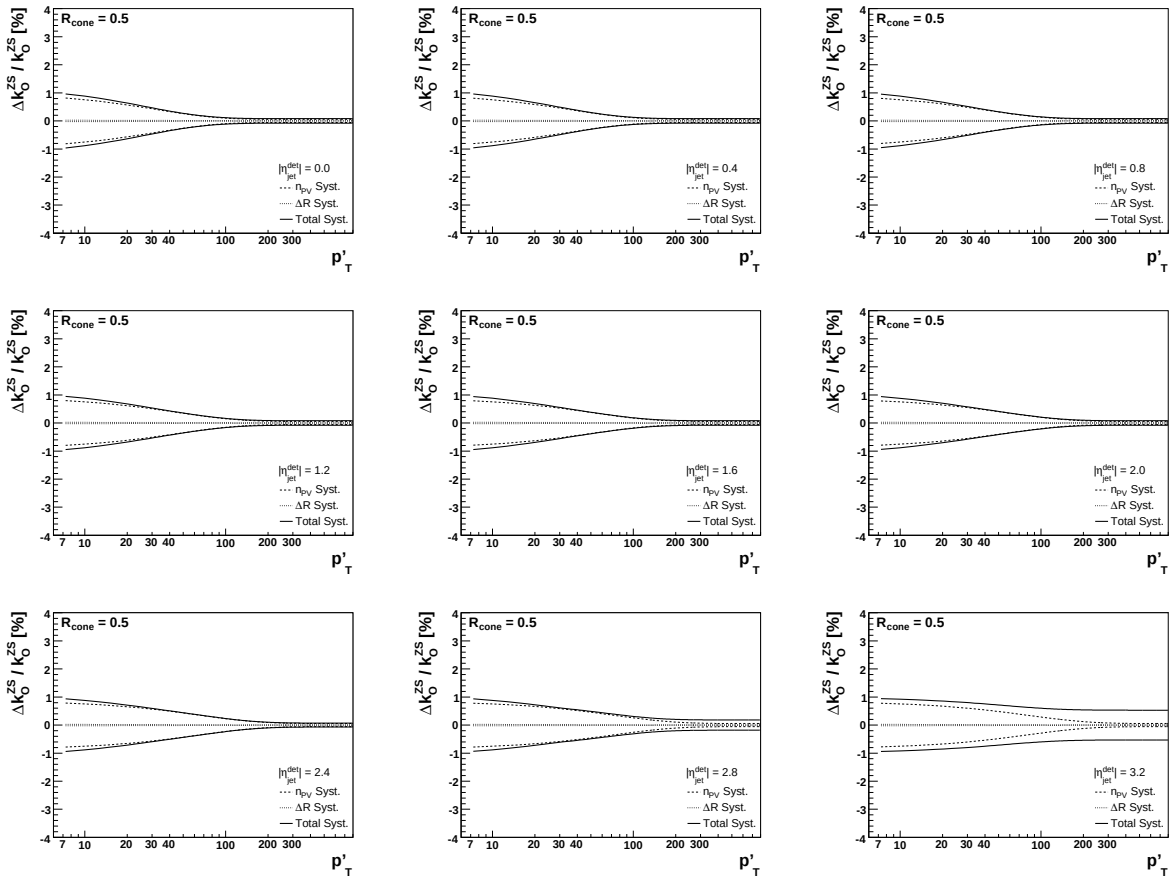

FIG. 93: Systematic uncertainties on the $k_{\mathrm{O}}^{\mathrm{ZS}}$ correction factor vs p'_T for $\mathcal{R}_{\mathrm{cone}} = 0.5$ jets in the suppressed ZB overlay case. Different plots correspond to different values of $\eta_{\mathrm{jet}}^{\mathrm{det}}$.

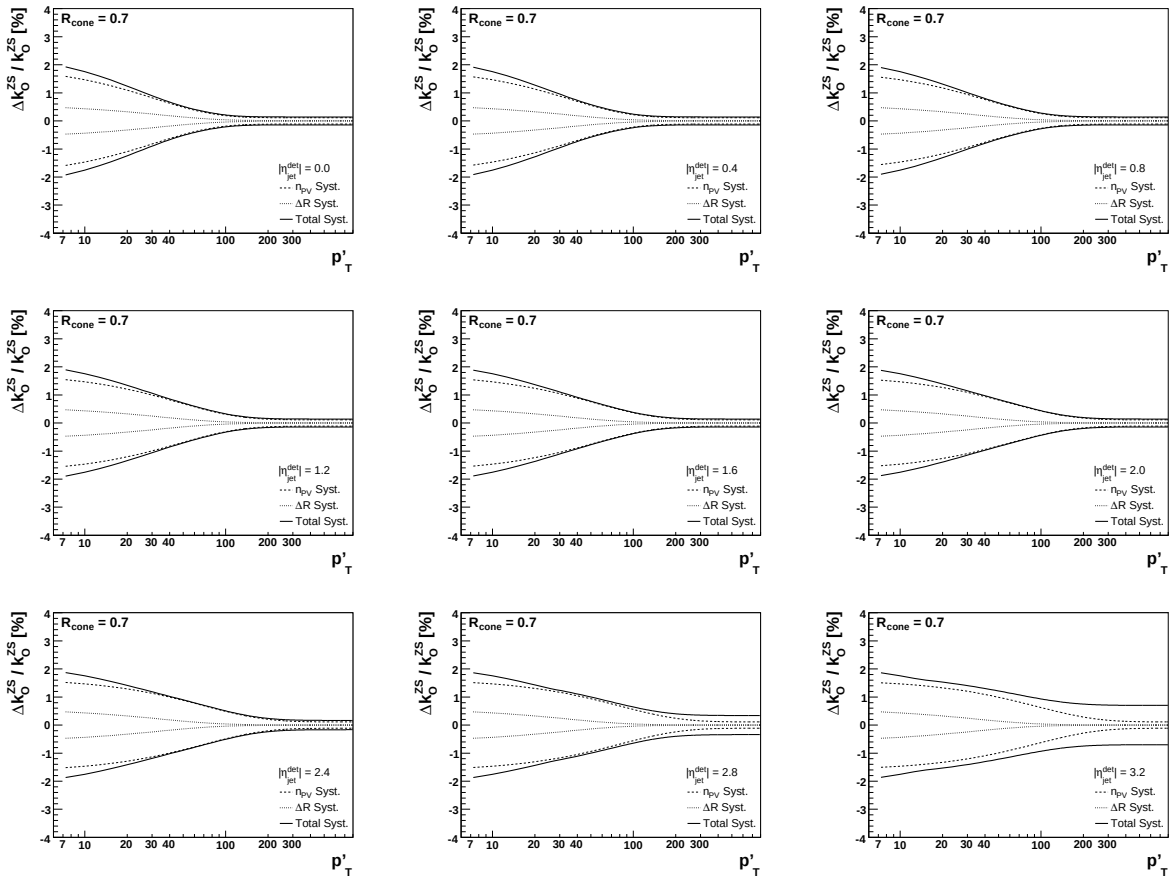

FIG. 94: Systematic uncertainties on the $k_{\mathrm{O}}^{\mathrm{ZS}}$ correction factor vs p_T' for $\mathcal{R}_{\mathrm{cone}} = 0.7$ jets in the unsuppressed ZB overlay case. Different plots correspond to different values of $\eta_{\mathrm{jet}}^{\mathrm{det}}$.

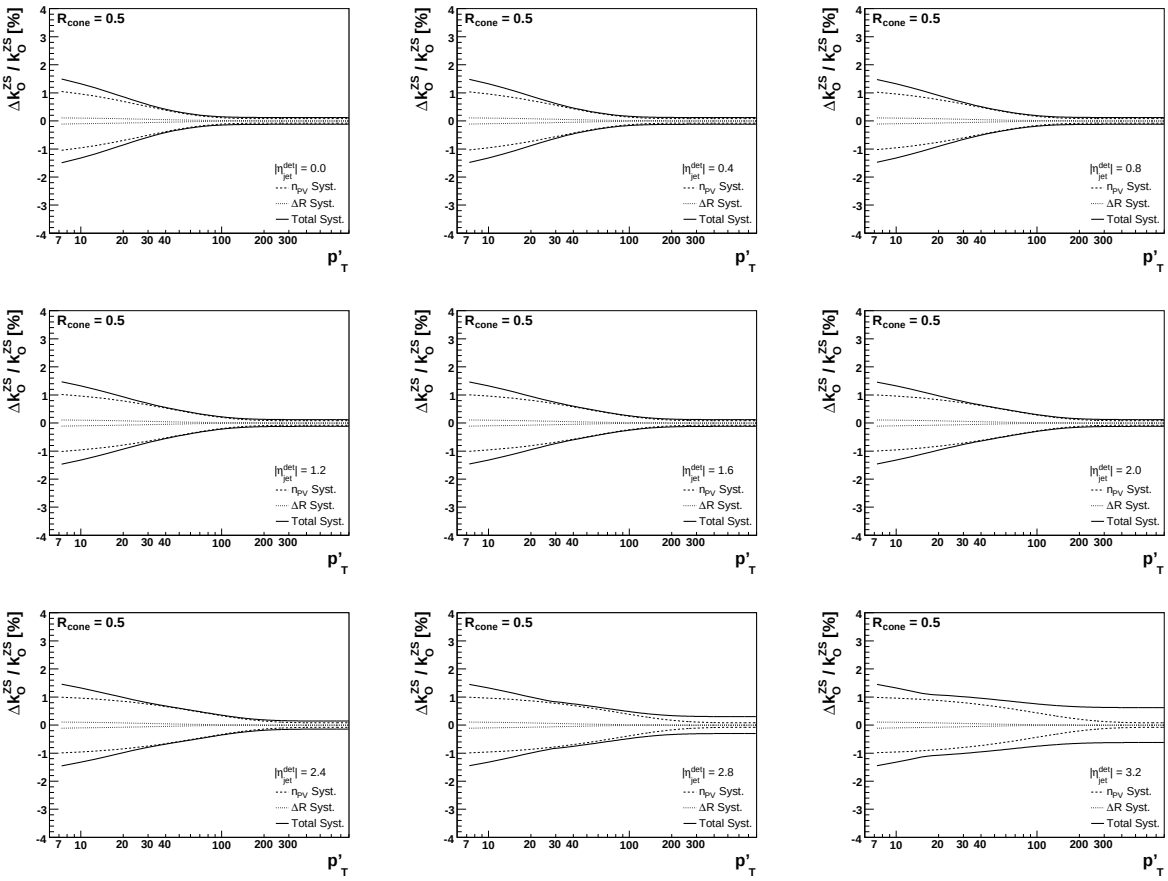

FIG. 95: Systematic uncertainties on the $k_{\mathrm{O}}^{\mathrm{ZS}}$ correction factor vs p_T' for $\mathcal{R}_{\mathrm{cone}} = 0.5$ jets in the unsuppressed ZB overlay case. Different plots correspond to different values of $\eta_{\mathrm{jet}}^{\mathrm{det}}$.

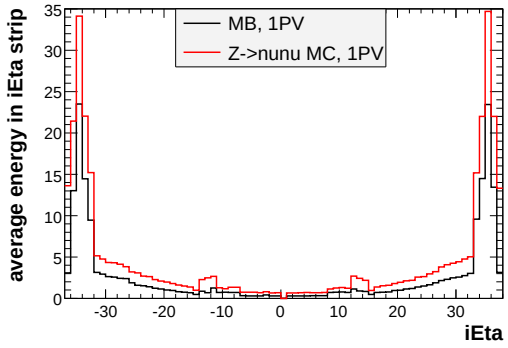

FIG. 96: Comparison between the offset energy as a function of $i\eta$ for MB events in data (black), and $Z \to \nu\bar{\nu}$ MC with ZB overlay (red). The offset energy is dominated by the underlying event contribution, which appears to be more energetic in the case of $Z \to \nu\bar{\nu}$ events.

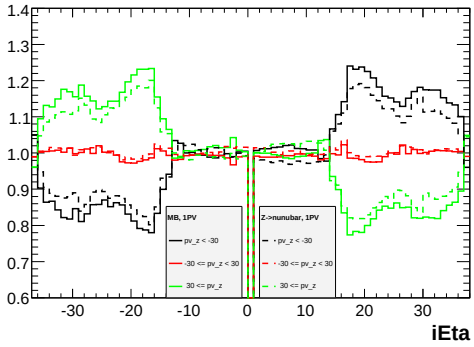

FIG. 97: Dependence of the offset energy vs $i\eta$ on z_{PV} for MB data events (solid) and $Z \to \nu\bar{\nu}$ MC events (dashed), computed for the following three intervals: $[-60, -30]$, $[-30, +30]$ and $[+30, +60]$ cm. Shown is the ratio of the measured offset energy in a particular z_{PV} interval to the average measurement (inclusive over z_{PV}).

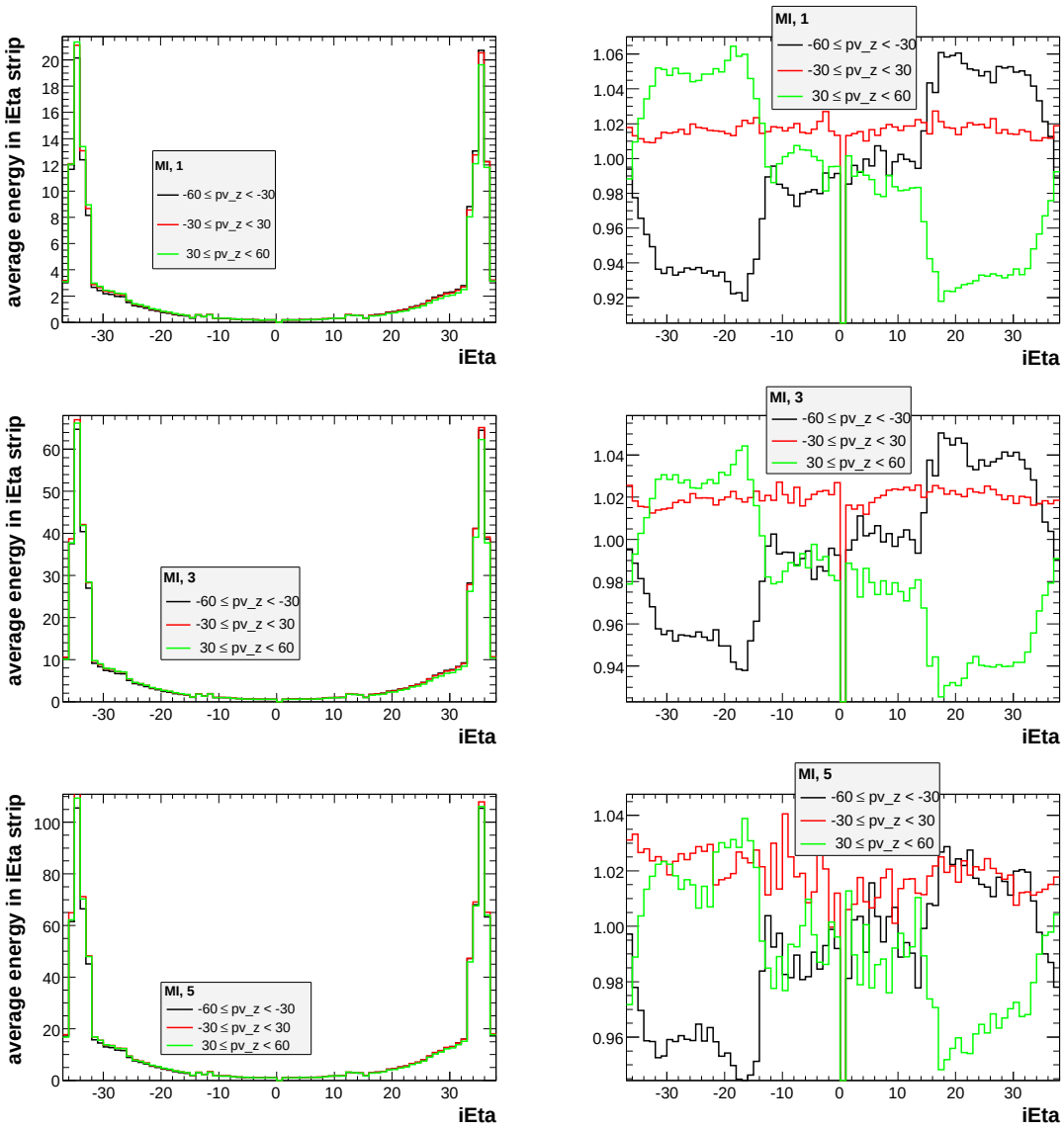

FIG. 98: Dependence of the MI offset contribution on z_{PV}, computed for the following three intervals: $[-60,-30]$, $[-30,+30]$ and $[+30,+60]$ cm, and separately for 1 MI (upper plots), 3 MI (middle plots) and 5 MI (lower plots). Left plots show the average energy per $i\eta$ ring whereas right plots illustrate the ratio with respect to the average in each $i\eta$ ring.

APPENDIX C: RESOLUTION BIAS CORRECTION

When binning a steeply falling spectrum in terms of a poorly measured variable, such as jet $p_T^{\rm meas}$, a shift with respect to the true value $p_T^{\rm ptcl}$ is observed. We call this effect "resolution bias". The resolution bias is closely related to the observed cross section increase of a smeared $p_T^{\rm meas}$ spectrum with respect to the true $p_T^{\rm ptcl}$ spectrum [13]. The increase for the smeared cross section is observed because the number of events migrating from higher and lower $p_T^{\rm ptcl}$ into the bin of $p_T^{\rm meas}$ outweigh the number of events migrating out of the bin (equally often to higher and lower p_T). The resolution bias arises because the events migrating into the bin from lower $p_T^{\rm ptcl}$ far outweigh the number of events migrating in from higher $p_T^{\rm ptcl}$ where the cross section is smaller.

1. Resolution Bias in a Simplified Case

We can study the impact of the resolution bias by looking at a simple case where the p_T cross section is exponentially falling, $f(p_T^{\rm ptcl}) = N_0 \exp(-\alpha p_T)$, the resolution is gaussian, $g(p_T^{\rm ptcl}, p_T^{\rm meas}) = \exp(-\frac{(p_T^{\rm meas}-p_T^{\rm ptcl})^2}{2\sigma^2})/\sqrt{2\pi}\sigma$, and further $\sigma = const$ (so that we can carry out the integrations analytically) and the jet energy has been corrected by jet energy scale:

$$< p_T^{\rm ptcl} > (p_T^{\rm meas}) = \frac{\int_0^\infty f(x) g(p_T^{\rm meas} - x) x dx}{\int_0^\infty f(x) g(p_T^{\rm meas} - x) dx} \tag{C1}$$

$$\approx \frac{\int_{-\infty}^\infty N_0 \exp(-\alpha x) \frac{1}{\sqrt{2\pi}\sigma} \exp(-\frac{(p_T^{\rm meas}-x)}{2\sigma^2}) x dx}{\int_{-\infty}^\infty N_0 \exp(-\alpha x) \frac{1}{\sqrt{2\pi}\sigma} \exp(-\frac{(p_T^{\rm meas}-x)}{2\sigma^2}) dx} = -\alpha\sigma^2 + p_T^{\rm meas} \tag{C2}$$

$$\Rightarrow \delta p_T/p_T = \frac{(< p_T^{\rm meas} > - < p_T^{\rm ptcl} >)(p_T^{\rm meas})}{p_T} = \alpha(\frac{\sigma}{p_T})^2 p_T \quad (> 0) \tag{C3}$$

$$F(p_T^{\rm meas}) = \int_0^\infty f(x) g(p_T^{\rm meas} - x) dx$$

$$\approx \int_{-\infty}^\infty N_0 e^{-\alpha p_T} \frac{1}{\sqrt{2\pi}\sigma} e^{-\frac{(p_T^{\rm meas}-x)^2}{2\sigma^2}} dx = N_0 e^{-\alpha(p_T^{\rm meas} - \alpha\sigma^2)} \tag{C4}$$

$$= f(p_T^{\rm meas} - \delta p_T) = f(< p_T^{\rm ptcl} >) \tag{C5}$$

The only approximations made above are in extending the limit of integration. The function F gives the observed smeared p_T spectrum, the δp_T shift between the true and observed average $< p_T >$.

The shift in measured response relative to the true response R is directly related to the

shift in p_T (again, for simplicity and analytical solvability, we consider $R = const$)

$$< R > (p_T^{\rm meas}) = \frac{\int_0^\infty f(x) g(p_T^{\rm meas} - x) \frac{Rx}{p_T^{\rm meas}} dx}{\int_0^\infty f(x) g(p_T^{\rm meas} - x) dx} \quad \text{(C6)}$$

$$\approx \frac{\int_{-\infty}^\infty N_0 \exp(-\alpha x) \frac{1}{\sqrt{2\pi}\sigma} \exp(-\frac{(p_T^{\rm meas} - x)}{2\sigma^2}) \frac{Rx}{p_T^{\rm meas}} dx}{\int_{-\infty}^\infty N_0 \exp(-\alpha x) \frac{1}{\sqrt{2\pi}\sigma} \exp(-\frac{(p_T^{\rm meas} - x)}{2\sigma^2}) dx} \quad \text{(C7)}$$

$$= R \frac{< p_T^{\rm ptcl} >}{p_T^{\rm meas}} = R \left(1 + \frac{\delta p_T^{\rm meas}}{p_T^{\rm meas}} \right) \quad \text{(C8)}$$

$$\Rightarrow R = < R > (p_T^{\rm meas}) \left(1 + \frac{\delta p_T^{\rm meas}}{p_T^{\rm meas}} \right)^{-1} . \quad \text{(C9)}$$

2. Resolution Bias in JES

In the Jet Energy Scale context we want to correct for the resolution bias effect in tag+probe dijet topologies, where we have tag jet in CC ($|\eta_{\rm det}^{jet}| < 0.4$), there are exactly two jets ($n_{jet} = 2$) and the angle between the tag and probe jet is $\Delta\phi > 3.0$. The cross section will depend on both p_T and $\eta_{\rm det}^{jet}$ of the tag and probe jets, on the topological cuts and on the cut on additional jets. Furthermore, the jet p_T resolution is dependent on both p_T and $\eta_{\rm det}$. In this case we can write a more elaborate 2D function for $f(p_T^{tag}, p_T^{probe}, \eta_{\rm det}^{tag}, \eta_{\rm det}^{jet})$, use parameterized $\sigma_{p_T}(p_T, \eta_{\rm det})$ for both jets and integrate the equations numerically.

However, we don't know the jet p_T resolutions in the forward region very well and the p_T measurement of the forward jets is also rather uncertain (in the JES context we can only assume we know the JES in CC). We therefore assume that the tag and probe jet have the same (particle level) p_T, and bin in terms of the (uncorrected) central (tag) jet's p_T so that we are only sensitive to the well known jet p_T resolution in the central calorimeter. The relative response can also be corrected using Eq. C9:

$$R_{\rm relMPF}^{\rm corr} = < R_{\rm relMPF} > (p_T^{\rm meas}) \left(1 + \frac{\delta p_T^{\rm meas}}{p_T^{\rm meas}} \right)^{-1} . \quad \text{(C10)}$$

The expected bias in the uncorrected tag jet p_T, $\delta p_T^{\rm meas}$, is given by:

$$\delta p_T^{\rm meas}(p_T^{\rm meas}, \eta_{\rm det}^{probe}) = \frac{\int_0^\infty dx f(x, \eta_{\rm det}^{probe}) g(x R_{\rm CC}(x), p_T^{\rm meas}) x R_{\rm CC}(x)}{\int_0^\infty dx f(x, \eta_{\rm det}^{probe}) g(x R_{\rm CC}(x), p_T^{\rm meas})} - p_T^{\rm meas}, \quad \text{(C11)}$$

where f represents the particle-level spectrum of the tag jet after full event selection (i.e. in particular it depends on $\eta_{\rm det}^{probe}$), and g represents a Gaussian function that includes the (detector and possibibly physics) smearing effect that leads to the resolution bias. Therefore, spectrum and resolution are the two key ingredients that, in this simple formalism, need to be determined. These subjects will be covered in the next two sections.

But before starting such discussion, it is important to realize that, when we have two jets in CC, we know that a properly working resolution bias correction should yield $R_{\rm relMPF,CC}^{\rm corr} = 1$. This is additional information that we can use for a first evaluation of the performance of the resolution bias correction, even in absence of knowledge of the true (unbiased) relative response. In case a small residual is observed, it is possible to explicitly correct for it (see

Eq. 48). The relative response of central-central topologies is the so-called "p_3-term", which ideally should be identical to one. Looking back at Eq. C3 we notice that any problems in our calculation of the resolution bias in a fixed bin of p_T could be assigned to either α or σ. The σ is not rapidity dependent so if we correct by the residual in the resolution bias correction for all η bins at same p_T, we can enforce the correct effective resolution. Little care is needed, because the residual could also be due to α that can have η dependent uncertainty. In any case, the residuals in CC will give some indication of how well the method is working.

3. Determination of the Tag Jet p_T Spectrum

In order to obtain the most accurate possible resolution bias correction in data, the tag jet p_T spectrum should be extracted directly from data.

The data for the cross section parametrizations fits is the same as used for response measurements. The data was selected from single jet triggers using the thresholds listed in Table 4. Small discontinuities in the fit between triggers JT_65TT and JT_95TT, and JT_95TT and JT_125TT were identified to come from relative inefficiency of the cuts $n_{vtx} \leq 2$ and $n_{\text{jets}} = 2$. The former is the dominant one, as Minimum bias vertices produce observable jets only about 10% of the time (13.6% of Minimum Bias events contain at least one jet). This effect was observed because different s ingle jet triggers have different average instantaneous luminosities. The applied correction factors are listed in Table 4. No other luminosity or trigger dependent inefficiencies have been identified.

TABLE 4: Single jet trigger thresholds in corrected p_T and trigger-dependent cut efficiencies.

Trigger	JT_15TT	JT_25TT_NG	JT_45TT	JT_65TT	JT_95TT	JT_125TT
Threshold (GeV/c)	40	55	75	105	175	230
$n_{vtx} \leq 2$ efficiency	0.886	0.886	0.876	0.868	0.778	0.699
$n_{\text{jets}} = 2$ efficiency	0.967	0.967	0.967	0.966	0.958	0.955

The cross section parametrization (see Eq. C13) is a commonly used 4-parameter ansatz for inclusive jet cross section unsmearing[13]. We assume it is a useful functional form also for exclusive dijet cross section with a $\Delta\phi > 3.0$ cut, and we explicitly allow the parameters to vary versus η. As it will be shown, such ansatz does indeed describe well the spectrum in data.

$$\begin{aligned} f(p_T,\eta) \;=\; & N_0(\eta)\left(\frac{p_T}{100\ \text{GeV/c}}\right)^{-\alpha(\eta)}\left(\left(1-\frac{2p_T}{\sqrt{s}}\right)\left(1-\frac{2p_T\cosh(\eta)}{\sqrt{s}}\right)\right)^{\beta(\eta)/2} \\ & \cdot\exp\left(-\gamma(\eta)\frac{p_T}{100\ \text{GeV/c}}\right) \end{aligned} \tag{C12}$$

To get the best available parameters N_0, α, β and γ for f, we fit the smeared cross section to data in narrow $\eta_{\text{det}}^{probe}$ bins. Note that because of the finite bin size in p_T and η the above equations are integrated over p_T and $\eta_{\text{det}}^{probe}$ for each bin to get the best possible agreement. The parameters of f are constrained to be in the following ranges to limit fluctuations:

$$\begin{aligned} N_0(\eta) &\in [0.2, 1.4], \\ \alpha(\eta) &\in [3.5, 5.0] \\ \beta(\eta) &\in [6.5, 11.5] \\ \gamma(\eta) &= 0. \end{aligned}$$

The fitted values of the parameter are given in Table 5. Figures 99a)-c) show the triple differential yield in data, parametrized and smeared ansatz fit, and the ratio of the two, respectively. Overall, the smeared parametrization follows data generally to within a few percent. Figures 101 and 3 show the fits in the original 0.1 η slices and combined 0.6 η slices, respectively.

The same procedure was applied to dijet MC, selected in the same way as in data. The fitted values of the parameter are given in Table 6. Figures 100a)-c) show the triple differential yield in data, parametrized and smeared ansatz fit, and the ratio of the two, respectively. In MC it is possible to directly measure the particle-level p_T spectrum of the tag jet, which is found to be in good agreement with the spectrum derived by unsmearing the measured CC jet p_T spectrum. This effectively validates the procedure used in data to derive the spectrum.

Figure 104 compares the estimated CC jet p_T spectra in data and MC in different 0.1-wide $\eta_{\text{jet}}^{\text{det}}$ bins. The MC spectrum is sufficiently close to the one in data that the MC can be used to study the performance of the resolution bias correction.

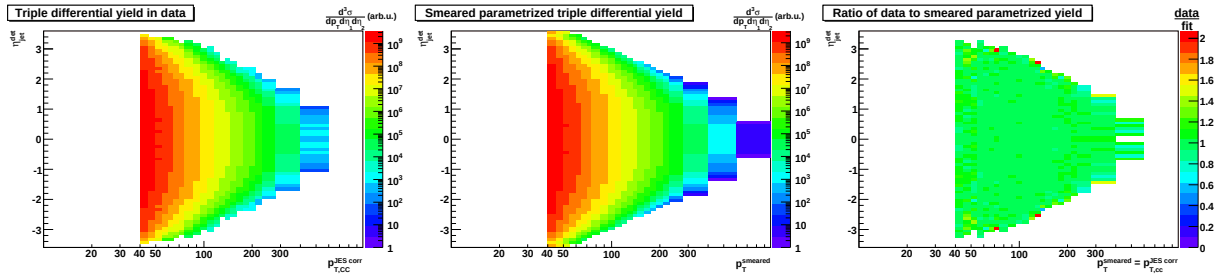

(a) (b) (c)

FIG. 99: (a) Triple differential yield in data. (b) Smeared parametrized yield. (c) Ratio of data to smeared fit.

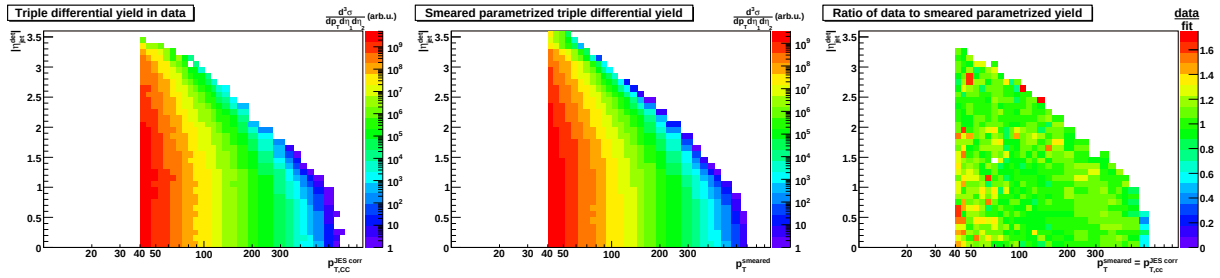

(a) (b) (c)

FIG. 100: (a) Triple differential yield in Monte Carlo. (b) Smeared parametrized yield for Monte Carlo. (c) Ratio of Monte Carlo to smeared fit.

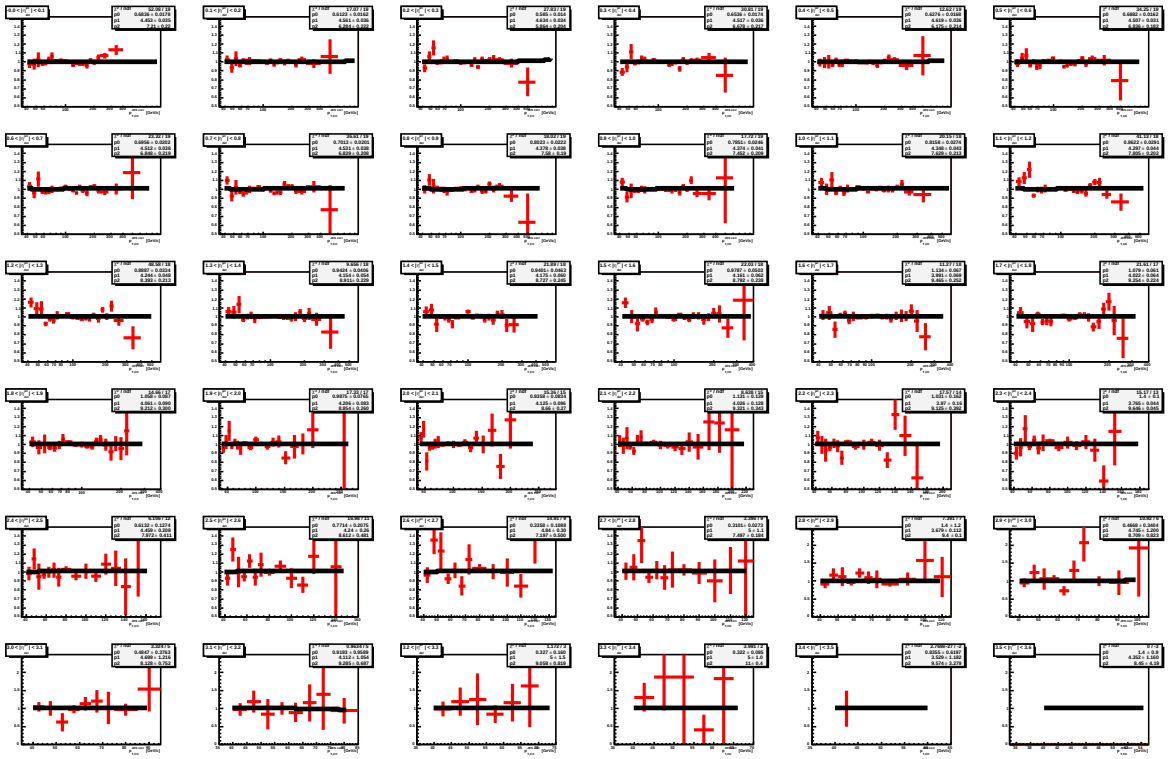

FIG. 101: Ratio of data to smeared fit in 0.1 slices of $|\eta|$.

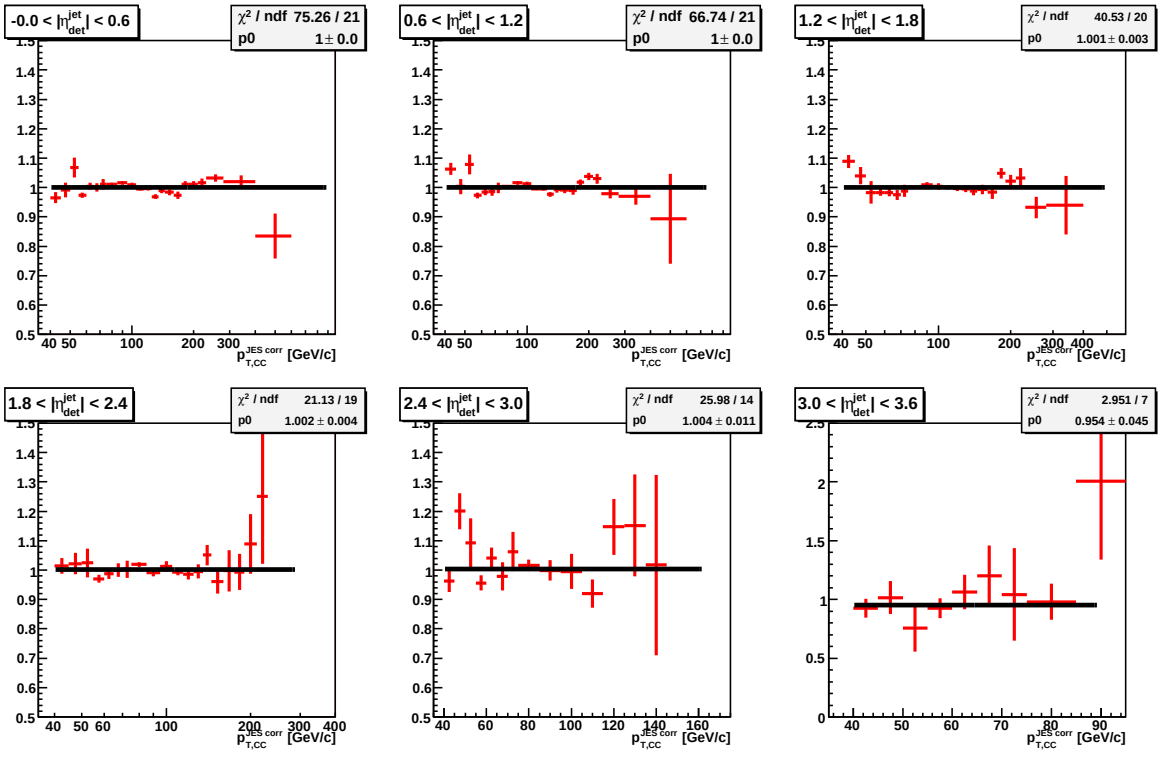

FIG. 102: Ratio of data to smeared ansatz in 0.6 wide bins of $|\eta|$. The ansatz parametrization is the same as shown by black line in Fig. 101.

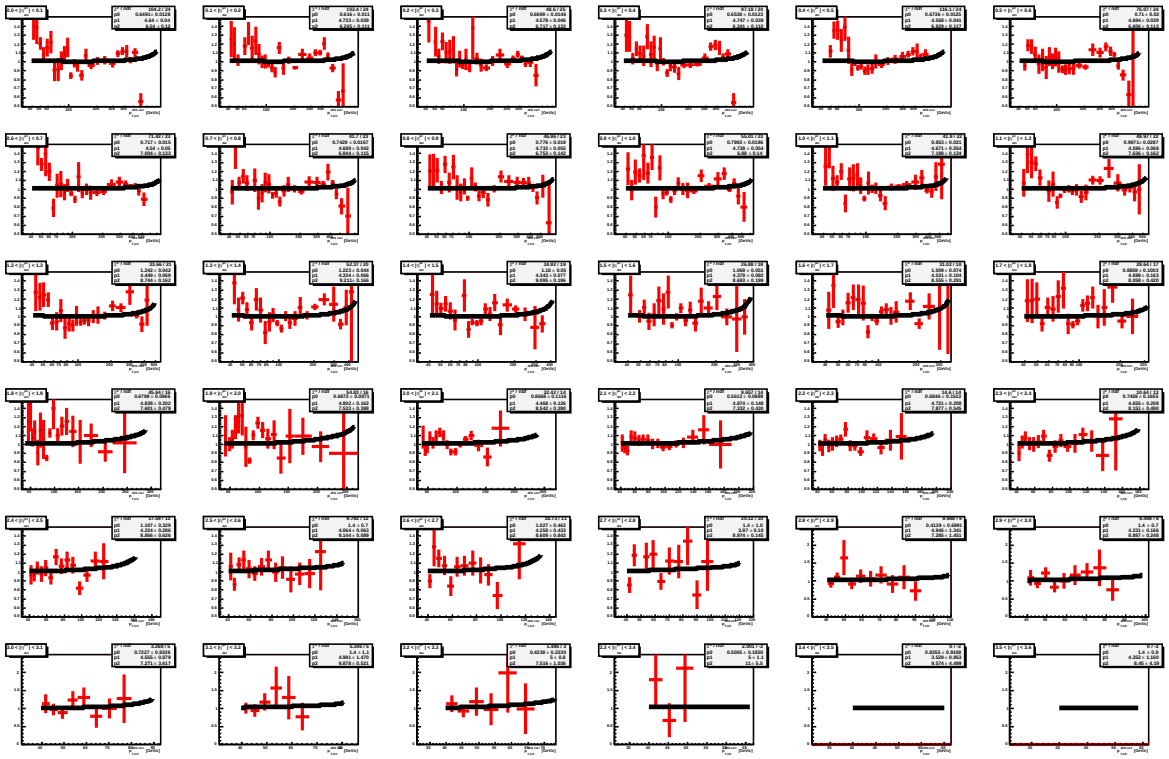

FIG. 103: Ratio of Monte Carlo to smeared fit in 0.1 slices of $|\eta|$.

TABLE 5: Ansatz fit parameters for data.

N_0	α	β	γ	η	χ^2/NDF
0.6836563	4.453286	7.211165	0	0.05	52.11 / 19
0.6124591	4.560942	6.287521	0	0.15	17.07 / 19
0.5857235	4.632584	5.875834	0	0.25	27.97 / 19
0.6536109	4.516571	6.678273	0	0.35	30.80 / 19
0.6278949	4.617992	6.180567	0	0.45	12.63 / 19
0.6882774	4.50741	6.837075	0	0.55	34.25 / 19
0.695628	4.511879	6.848656	0	0.65	23.32 / 19
0.7013213	4.531299	6.839531	0	0.75	36.61 / 19
0.8024391	4.37748	7.580573	0	0.85	18.03 / 19
0.7851927	4.373577	7.452855	0	0.95	17.73 / 19
0.8158817	4.347649	7.629652	0	1.05	20.15 / 18
0.8622991	4.296781	7.805914	0	1.15	41.14 / 18
0.8888393	4.24424	8.393455	0	1.25	48.60 / 18
0.9425215	4.154221	8.912243	0	1.35	9.66 / 18
0.940156	4.174545	8.726916	0	1.45	21.89 / 18
0.9788228	4.161434	8.792968	0	1.55	22.03 / 18
1.13432	3.991106	9.465566	0	1.65	11.27 / 18
1.079181	4.021478	9.254095	0	1.75	21.62 / 17
1.057924	4.060831	9.211733	0	1.85	14.66 / 17
0.9875835	4.2063	8.853892	0	1.95	17.33 / 17
0.9359376	4.124781	8.660468	0	2.05	15.36 / 15
1.1306	4.025869	9.321325	0	2.15	8.64 / 15
1.031142	3.970251	9.125261	0	2.25	17.57 / 14
1.4	3.765208	9.645524	0	2.35	15.17 / 13
0.6132436	4.459144	7.972039	0	2.45	6.11 / 12
0.7716595	4.240003	8.6129	0	2.55	16.98 / 11
0.3359198	4.839354	7.198276	0	2.65	14.91 / 9
0.3100833	5	7.497462	0	2.75	3.40 / 9
1.4	3.679016	9.39969	0	2.85	7.39 / 7
0.4673572	4.743869	8.710738	0	2.95	10.92 / 6
0.4853033	4.698148	8.130165	0	3.05	3.32 / 5
0.8842289	4.13521	9.234966	0	3.15	0.96 / 5
0.3270369	5	9.057752	0	3.25	1.17 / 3
0.3219701	5	11	0	3.35	3.99 / 2
0.8354663	3.528514	9.574143	0	3.45	0.00 / -2
1.399999	4.351956	8.44956	0	3.55	0.00 / -3

TABLE 6: Ansatz fit parameters for Monte Carlo.

N_0	α	β	γ	η	χ^2/NDF
0.6490511	4.639538	6.539661	0	0.05	104.17 / 24
0.6159873	4.732832	6.265371	0	0.15	103.42 / 24
0.6698998	4.578335	6.717456	0	0.25	48.60 / 25
0.6538077	4.747196	6.340882	0	0.35	97.18 / 24
0.6736126	4.568402	6.828947	0	0.45	116.14 / 24
0.710049	4.693926	6.606061	0	0.55	76.07 / 24
0.7170035	4.539886	7.003674	0	0.65	71.42 / 23
0.7429112	4.688989	6.843537	0	0.75	41.70 / 23
0.77603	4.732106	6.752988	0	0.85	46.96 / 23
0.799257	4.738215	6.879669	0	0.95	55.01 / 23
0.8529813	4.671058	7.198185	0	1.05	41.90 / 22
0.9971348	4.595942	7.635634	0	1.15	49.97 / 22
1.242363	4.44893	8.744128	0	1.25	33.66 / 21
1.223076	4.334253	9.211323	0	1.35	52.37 / 20
1.180017	4.342625	9.09457	0	1.45	34.92 / 19
1.06856	4.379092	8.693147	0	1.55	26.88 / 18
1.009147	4.530758	8.555175	0	1.65	31.02 / 18
0.8859498	4.697677	8.058257	0	1.75	28.64 / 17
0.6799456	4.838146	7.600759	0	1.85	45.64 / 16
0.6872908	4.802201	7.533066	0	1.95	54.83 / 16
0.8667667	4.467811	8.542125	0	2.05	32.42 / 14
0.5613206	4.873928	7.332042	0	2.15	9.66 / 14
0.6845933	4.721373	7.876692	0	2.25	14.60 / 14
0.7459188	4.655051	8.151001	0	2.35	10.64 / 13
1.106554	4.223864	8.866196	0	2.45	17.59 / 12
1.4	4.063853	9.143907	0	2.55	9.79 / 12
1.02702	4.258173	8.608926	0	2.65	18.73 / 11
1.4	3.969822	8.974385	0	2.75	20.12 / 10
0.4139054	4.945502	7.285188	0	2.85	9.99 / 9
1.4	4.230621	8.887286	0	2.95	8.41 / 8
0.7227319	4.554558	7.271105	0	3.05	3.27 / 5
1.4	4.991151	9.878103	0	3.15	5.35 / 5
0.4237578	5	7.515608	0	3.25	1.49 / 3
0.5004573	5	11	0	3.35	2.00 / -2
0.8354663	3.528514	9.574143	0	3.45	0.00 / -3
1.399999	4.351956	8.44956	0	3.55	0.00 / -3

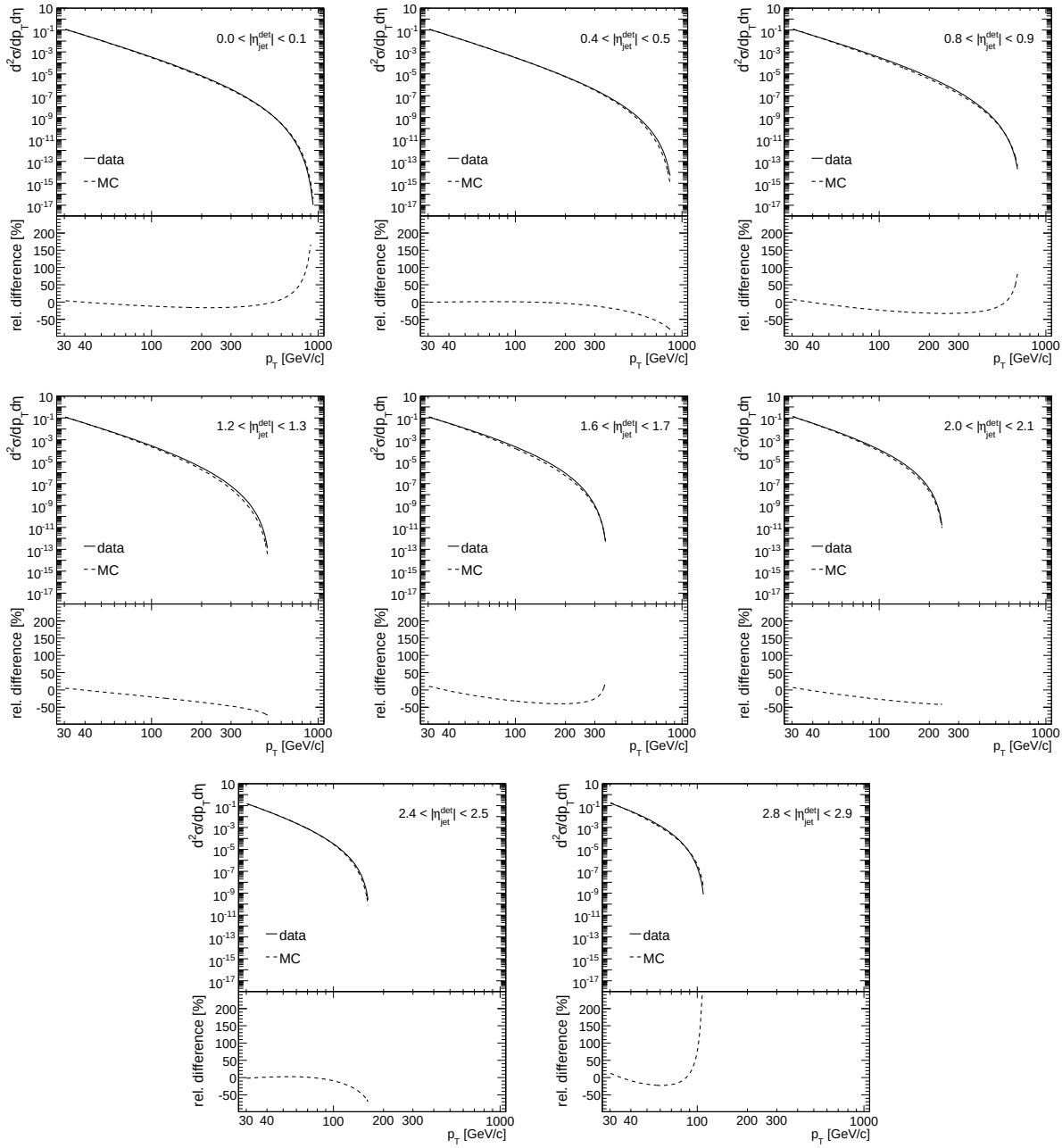

FIG. 104: Comparison between estimated CC jet p_T spectra in data and MC.

4. Choice of Jet Energy Resolution

As shown in Eq. C11, in order to compute the resolution bias correction, the particle-level p_T spectrum must be smeared with the (assumed) Gaussian resolution corresponding to the measured central jet p_T, which is typically parameterized as:

$$\sigma = \sqrt{N^2 + S^2 p_T + C^2 p_T^2}. \tag{C13}$$

The resolution parameters N, S and C are determined from JES-corrected jets using the so-called "Asymmetry Method" [14]. This results in the so-called "raw resolution" ($\sigma_{\rm raw}$). In order to obtain the detector-level jet p_T resolution (a.k.a. "corrected resolution", $\sigma_{\rm corr}$), the physics smearing resulting from soft radiation below the jet reconstruction threshold and particle-level imbalance must be unfolded:

$$\sigma_{\rm corr} = \sqrt{(\sigma_{\rm raw} K_{\rm soft})^2 - \sigma_{\rm MC}^2} \tag{C14}$$

Table 7 summarizes the estimated resolution parameters corresponding to $\sigma_{\rm raw}$ for both data and MC. The soft radiation correction ($K_{\rm soft}$) is parameterized as $K_{\rm soft} = 1 - \exp(-a_0 - a_1 p_T)$, with the a_i sumamrized in Table 8. The particle-level imbalance contribution is estimated in particle-level MC and is also parameterized using Eq. C13. The parameters are shown in Table 9.

TABLE 7: Fit parameters for raw jet resolution in CC with $p_{T,soft}^{cut} = 6$ GeV/c. No soft radiation or particle level imbalance corrections have been applied.

Parameter	Value in data	Value in MC (reco)
N (GeV)	2.135±0.669	3.787±0.721
S ($\sqrt{\rm GeV}$)	1.052±0.031	0.816±0.053
C	0.027±0.006	0.045±0.003

TABLE 8: Soft radiation correction parameters in CC

Parameter	Value in data	Value in MC
a_0	2.137	1.873
a_1 (GeV^{-1})	0.0081	0.0079

TABLE 9: Fit parameters for particle-level imbalance correction in CC.

Parameter	Value in MC
N (GeV)	1.286
S ($\sqrt{\rm GeV}$)	0.388
C	0.021

However, given the approximations made in the resolution bias correction formula (e.g. that both reconstructed jets correspond to the same particle-level p_T, something which we know cannot hold exactly), it is not a-priori obvious which resolution, whether "raw", "corrected", or maybe even some "partly-corrected" version of it, should be used. Fortunately, we have the "p_3-term" to provide some guidance: the best resolution choice

would yield a "p_3-term" closest to one. Furthermore, as discussed below, we can use MC to compare several scenarios of assumed resolutions with the unbiased relative response and thus pick the least unbiased approach. The three scenarios we will consider are: $\sigma_{\rm raw}$, $\sigma_{\rm corr}$ and the intermediate, partly corrected only by soft-radiation, $\sigma_{\rm part} = \sigma_{\rm raw} K_{\rm soft}$.

Finally, the chosen resolution, regardless of the degree of correction, must be degraded back to the raw jet p_T-level, which is what enters Eq. C11. The reason is that the above resolution(s) has been estimated on JES-corrected jets, which is known to yield an improved relative jet p_T resolution. This is because in a given bin of $p_T^{\rm ptcl}$ the non-constant, rising response corrects low fluctuations up more and high fluctuations less than the mean response. This way both ends of the distribution get closer to the average and resolution improves. The required correction ($\sim 10\%$) can be analytically estimated using a parameterization of the CC jet response as:

$$\frac{\sigma}{p_T} \to \frac{\sigma}{p_T}\left(1 + \frac{R'_{\rm CC}(p_T)p_T}{R_{\rm CC}(p_T)}\right) \tag{C15}$$

5. Resolution Bias Correction Studies in MC

An advantage of using MC is that it is possible to measure the unbiased η-dependent corrections directly binning in terms of the particle-level p_T, either $p_{T,\rm CC}^{\rm ptcl}$ or $< p_T^{\rm ptcl} >$. The latter is expected to be less affected by "physics smearing" (soft radiation and particle-level imbalance), and therefore it is considered as the default method to obtain the "true" η-dependent corrections. This allows to compare the estimated η-dependent corrections after resolution bias with the true ones, and then determine to what precision the method is working. It also allows to decide which resolution to use based on checking which one yields the smallest possible bias.

In the case of $< p_T^{\rm ptcl} >$ binning it is necessary to apply the so-called "2nd resolution bias correction". NEED EXPLANATION. Figure 105 compares the p_3-term before and after the "2nd resolution bias correction', showing it is consistent with one in the latter case.

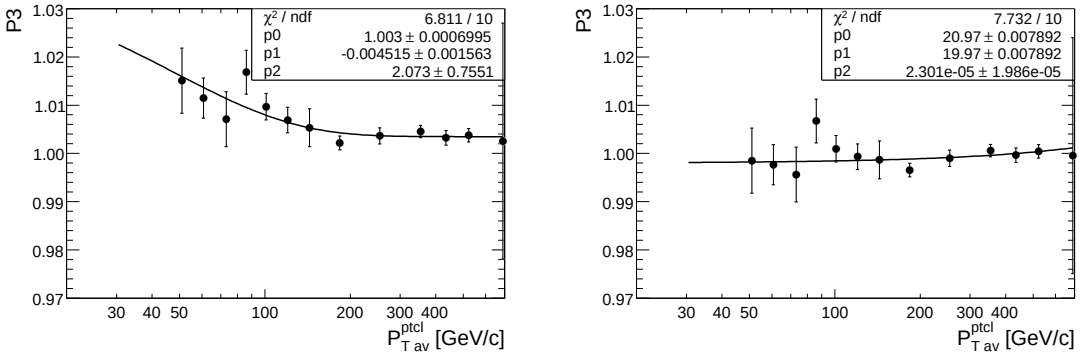

FIG. 105: Comparison of p_3-term in the case of $< p_T^{\rm ptcl} >$-binning before (left) and after (right) "2nd resolution bias correction".

As discussed in the previous section, in the realistic case of binning in terms of $p_{T,\rm CC}^{\rm meas}$, a choice needs to be made regarding which jet energy resolution (corrected, partly corrected or raw) to use. Given a well-known MC spectrum, we can check which resolution brings the p_3-term closest to one. Fig. 106 compares the estimated p_3-term in each case, showing that the raw(corrected) resolution leads to a over(under)correction in the resolution bias

whereas the partly-corrected resolution gives the best performance. An exponential fit to the points will be used to correct any small residual effects. The choice of the partly-corrected resolution can be further confirmed by verifying that the estimated η-dependent corrections are in general closest to the true ones in all $\eta_{\rm jet}^{\rm det}$ bins. The comparison between the "true" η-dependent corrections (based on $< p_T^{\rm ptcl} >$ binning) and the estimated ones from the $p_{T,\rm CC}^{\rm meas}$ binning for different choices of the jet energy resolution is presented in Fig. 107. This comparison validates the resolution bias correction (based on the partly-corrected resolution) to a precision $\leq 0.5\%$.

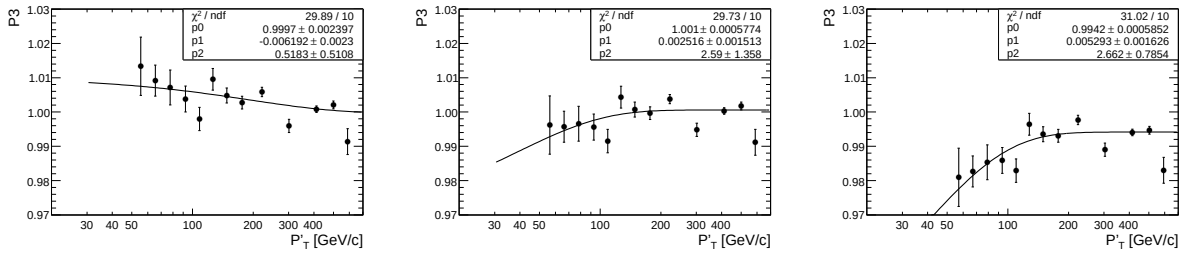

FIG. 106: p_3-term in MC in the case of $p_{T,\rm CC}^{\rm meas}$-binning for $\sigma_{\rm raw}$ (left), $\sigma_{\rm part}$ (center) and $\sigma_{\rm corr}$ (right)

.

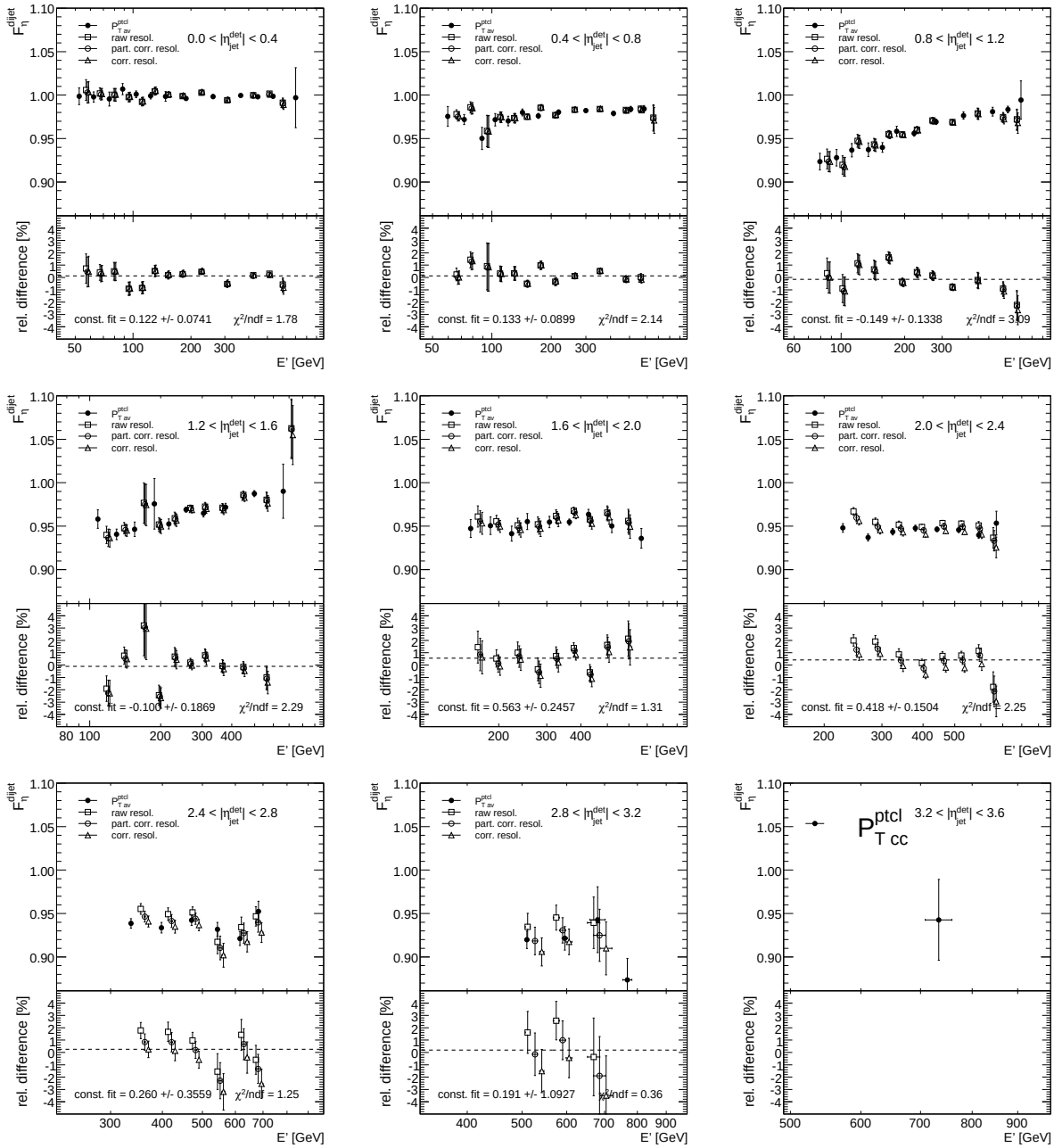

FIG. 107: Comparison between the true relative response corrections and the estimated ones based on $p_{T,\mathrm{CC}}^{\mathrm{meas}}$ binning for different choices of the jet energy resolution. The bottom plots show the relative differences with respect to the true answer, and the dashed line represents a average fitted bias for the favored case of the partly-corrected resolution.

6. Resolution Bias Correction in Data

Figure 108 illustrates the magnitude of the resolution bias correction in data, for different values of $p_T^{\rm meas}$ and as a function of $\eta_{\rm det}^{probe}$.

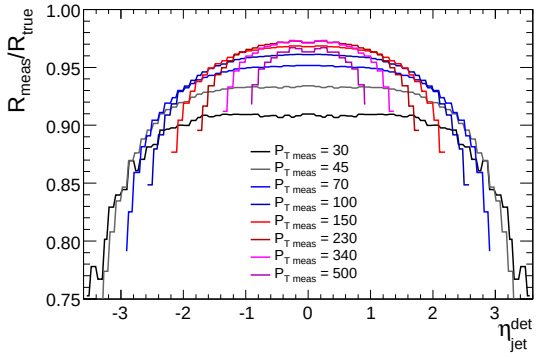

FIG. 108: Resolution bias correction in data for different values of $p_T^{\rm meas}$ as a function of $\eta_{\rm det}^{probe}$.

Figure 109 compares the p_3-term in data for the three different choices of resolution (using the data spectrum). The conclusion obtained in the previous section is confirmed in data, where also the p_3-term is closest to one for the case of the partly-corrected resolution.

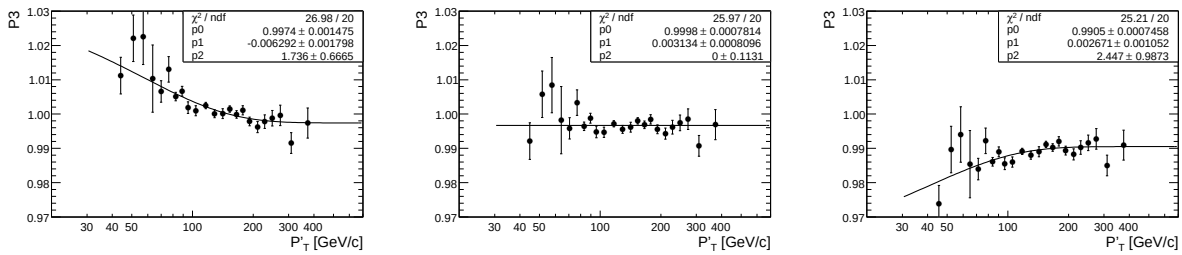

FIG. 109: p_3-term in data in the case of $p_{T,\rm CC}^{\rm meas}$-binning for $\sigma_{\rm raw}$ (left), $\sigma_{\rm part}$ (center) and $\sigma_{\rm corr}$ (right)

Figure 110 illustrates the dependence of the measured relative response correction in dijets for the three choices of resolution in the resolution bias correction (using the data-derived spectrum), and for the case of using the MC-derived spectrum and the partly-corrected resolution. The bottom plots show the relative difference with respect to the nominal case: data-derived spectrum and partly-corrected resolution. The dashed lines represent the total systematic uncertainty assigned to the resolution bias correction. It is taken as 0.75% in the $2.8 < \eta_{\rm jet}^{\rm det} < 3.2$ bin and made decrease linearly towards zero at $\eta_{\rm jet}^{\rm det} = 0$. If the extrapolated systematic is $< 0.1\%$, a constant 0.1% is taken. Such uncertainty is expected to cover for the internal closure of the method (as studied in MC in the previous section), as well as any small uncertanties related to the determination of the spectrum and/or resolutions.

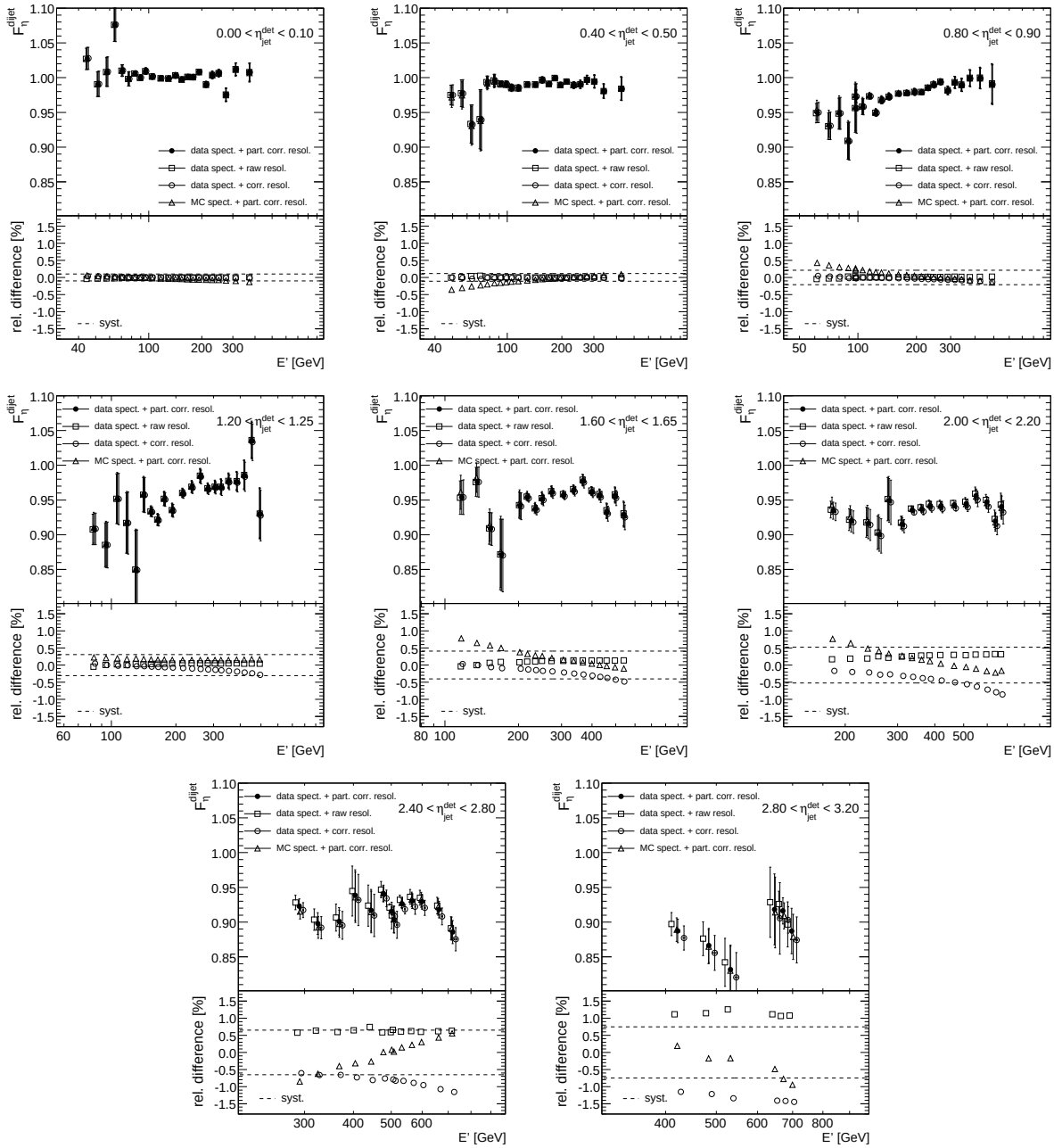

FIG. 110: Comparison of the relative response in dijets data for different scenarios of the resolution bias correction. The bottom plots show the relative difference with respect to the nominal one, i.e. data spectrum+partly-corrected resolution. The dashed lines represent the assigned systematic uncertainty to the resolution bias correction in data.

APPENDIX D: ABSOLUTE MPF RESPONSE CORRECTION

Trigger	L3 threshold [GeV]	turn-on point [GeV]
EM5	5	6
CEM5	5	6
CEM6	6	7
EM9	9	10
EM12	12	15
EM15	15	19
EM_LO_SH	7	10
EM_HI_SH	20	25
E1_SHT20	20	24
E1_SHT22	22	28
E1_SHT25	25	30
E1_SH30	30	37
E1_SH35	35	50

TABLE 10: List of single EM triggers used for collection of the $\gamma + \text{jet}$ sample.

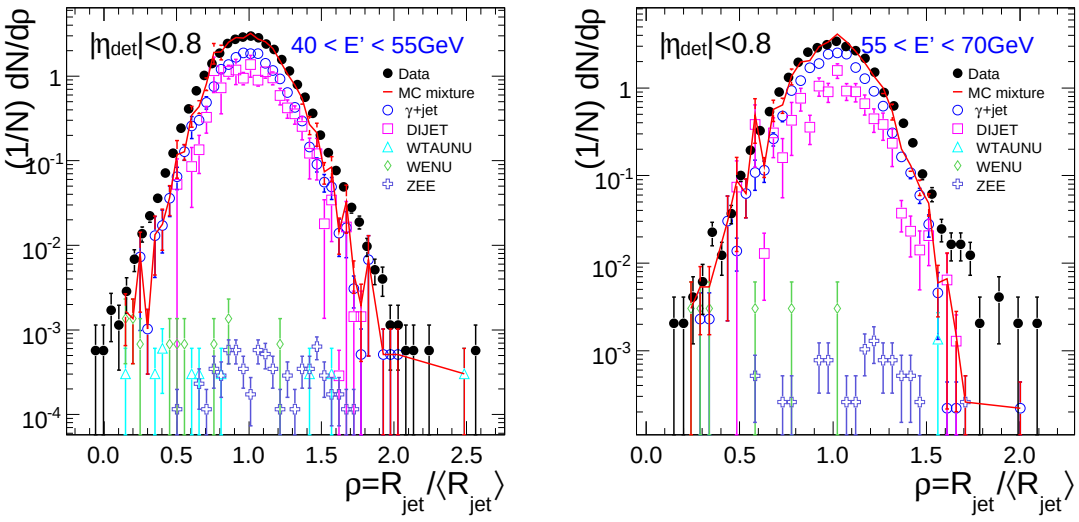

FIG. 111: Comparison of the MPF response distributions in data and MC for central jets in two E' bins. The relative contributions from the different processes in MC were calculated using the cross sections from PYTHIA. In order to better compare the data and Monte Carlo distributions, the MPF response has been normalized to have mean equal to one.

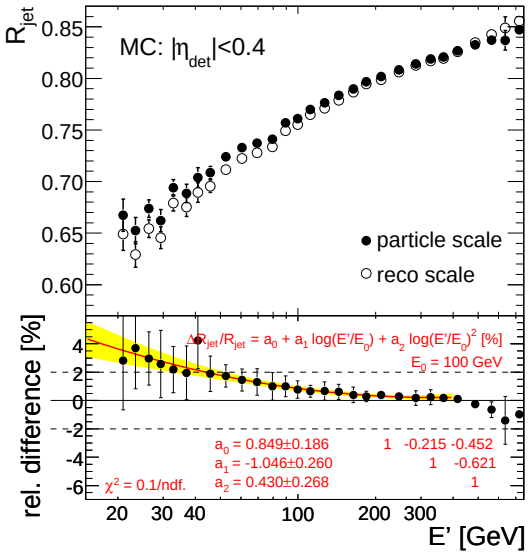

FIG. 112: Difference in MC response derived from the reconstructed photon (open circles) and from the particle-level photon p_T (full circles).

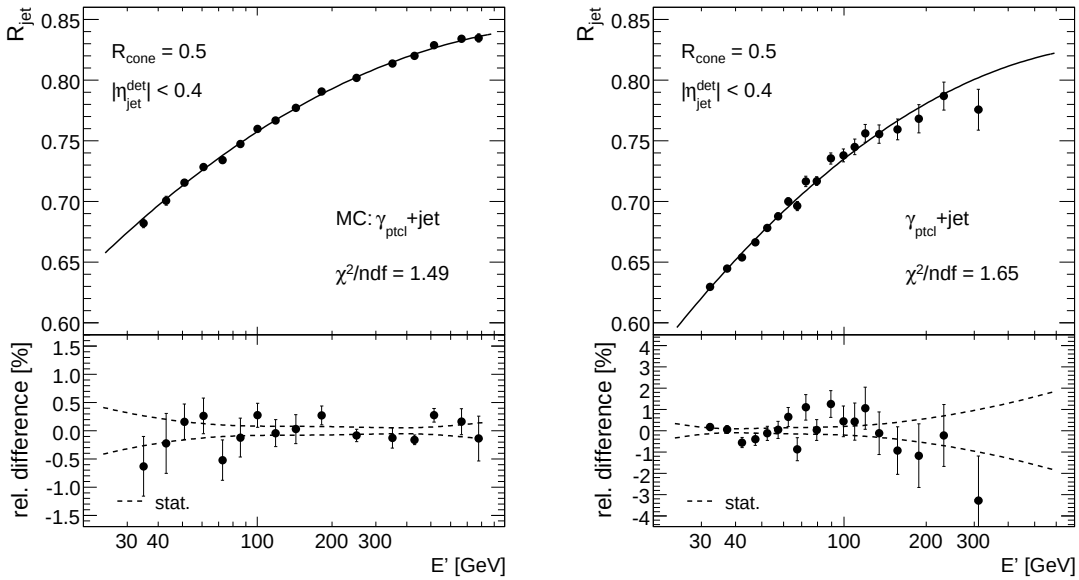

FIG. 113: Absolute MPF response for $\mathcal{R}_{\rm cone} = 0.5$ jets in MC (left) and data (right) as a function of E'. The solid line indicates the fit to the function in Eq. 23. The lower plots show the relative difference of the points with respect the fitted function.

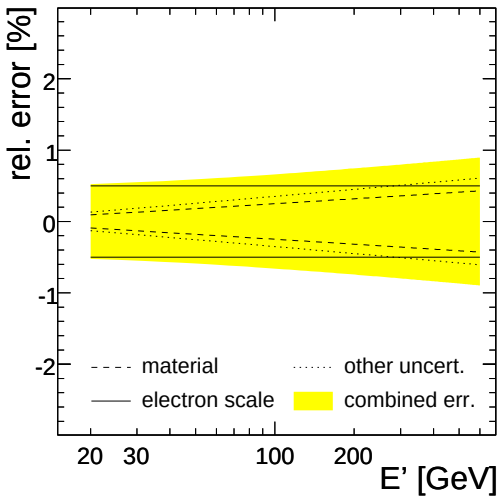

FIG. 114: Response uncertainty due to photon energy calibration. Individual contributions are: electron scale uncertainty (solid line), uncertainty due to knowledge of material in front of calorimeter (dashed line) and an estimate of remaining uncertainties on relative electron-photon energy scale (dotted line).

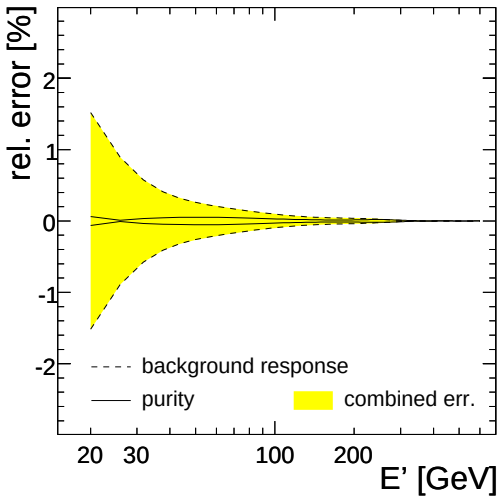

FIG. 115: Response uncertainty due to the background correction. Individual contributions are: purity error (solid line), and error on difference in response for $\gamma + \text{jet}$ and dijet background samples (solid line).

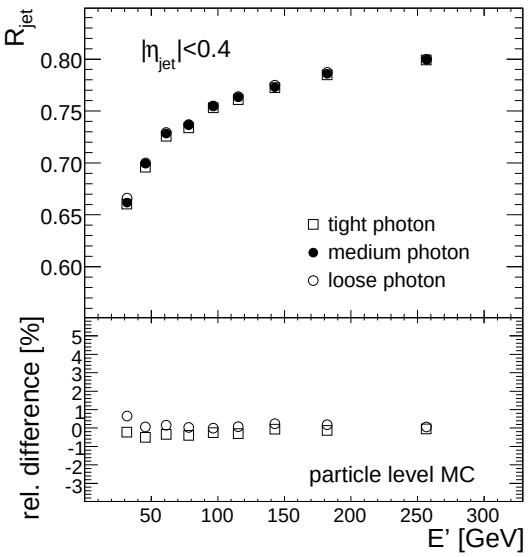

FIG. 116: Comparison of the MPF response derived in MC using the particle-level photon p_T for tight, medium, and loose photon criteria. The relative difference in the bottom part of plot is with respect to the medium photon response.

1. Sample Purity Estimation

As was discussed in Sect. 8.1.2, the selected γ + jet sample suffers from a contamination of QCD dijet events. Here, we provide more detailed information about the method and results of purity estimation.

The sample purity was estimated using the γ+jet and dijet(γ-like) MC samples described in Sect. 5.2. Two methods were developed to estimate the purity: template fit using the scalar sum of the transverse momenta of all tracks in the hollow cone of $0.05 < \Delta\mathcal{R} < 0.7$ within the direction of photon candidate (for more detailed definition see Sect. 3.3), and purity determination using directly MC leading-order cross section predictions for signal and background.

In the template fit method, the purity is estimated as the fraction of signal events extracted from a fit to the hollow cone track variable distribution in data, using normalized templates of such distribution from signal and background MC. An example of the distribution of the hollow cone track variable ($HC07$) for MC signal, MC dijet background, and data is given in Fig. 117. In general, the MC provides a very good decription of the $HC07$ variable, which was the reason why this variable was used in the template fit. This was not the case of calorimeter based variables, such as the number of cells assigned to the photon candidate cluster in the first layer of electromagnetic calorimeter, or the fractional energy of cluster deposited in this first layer.

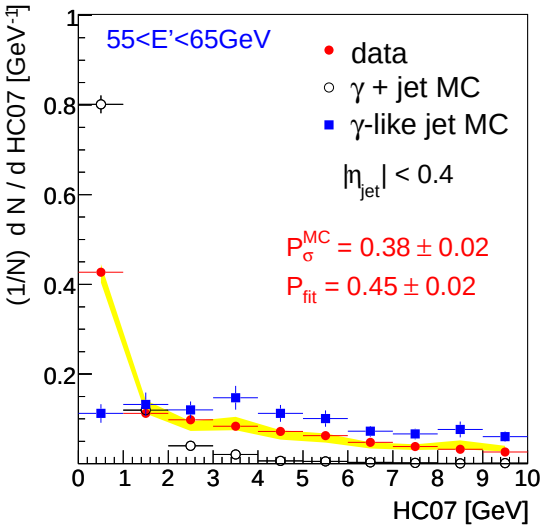

FIG. 117: Distribution of the $HC07$ variable in data (red circles), compared to the result of the template fit (shaded histogram). Shown also are the templates for signal (open circles) and background (blue squares), normalized to the fitted fractions. P_{fit} and P_{MC} stand, respectively, for the fitted and estimated (using MC cross sections) sample purities.

The template fit cannot be performed in the case of tight photon definition, because only photon candidates with $HC07 < 1$ GeV are accepted. In that case, the result of template fit P_{med} for medium photons was used and the tight photon purity P_{tight} was estimated from counting the number of expected events with $HC07 < 1$ GeV for the signal and background

in MC :

$$P_{tight} = \frac{P_m S^{(1)}_{med}}{P_{med} S^{(1)}_{med} + (1 - P_{med}) B^{(1)}_{med}} \tag{D1}$$

where $S^{(1)}_{med}$ and $B^{(1)}_{med}$ are fractional number of events with $HC07 < 1\,\mathrm{GeV}$ for medium photon selection seen observed in MC signal, resp. MC background. The template fit method provides us with more direct measurement of the purity. However it suffers from large errors due to limited statistics in data and MC.

The second method provides smaller statistical uncertainties, but relies on leading-order cross sections which may be quite different from true ones, especially for forward jets. To take advantage of the smaller statistical uncertainties, the global purity fit was performed on the purities derived from this second method. But then, the signal over background ratio S/B was scaled to match the purity from the template method. In other words, the shape of the purity dependence on photon p_T and jet direction η is determined from MC LO cross sections, and the overall scale is then fixed with the results of the template fit method.

The results of the purity fits for all three photon definitions are summarized in Figs. 118-120. In case of loose, the scaling factor between MC cross section and template based purities was found to be

$$F_{loose} = 1.4 + 0.1234\,\eta^2_{jet}\,, \tag{D2}$$

and the systematic error on S/B ratio ($F^{sys}_{loose} = 0.3 + 0.1234\,\eta^2_{jet}$) was chosen to cover for the difference in purities from the two methods. In case of medium and tight photon selections, the LO cross section based estimates follow quite closely the template fit purities and no scaling is needed in the central region:

$$F_{tight,medium} = 1.0 + 0.1234\,\eta^2_{jet}\,, \tag{D3}$$

Systematic error on S/B was parametrized as $F^{sys}_{medium,tight} = 0.2 + 0.1234\,\eta^2_{jet}$ and it covers for the differences between the two methods. An additional source of systematic uncertainty on the sample purity arises from uncertainties in the fragmentation description in PYTHIA. This uncertainty was extracted from Ref. [15].

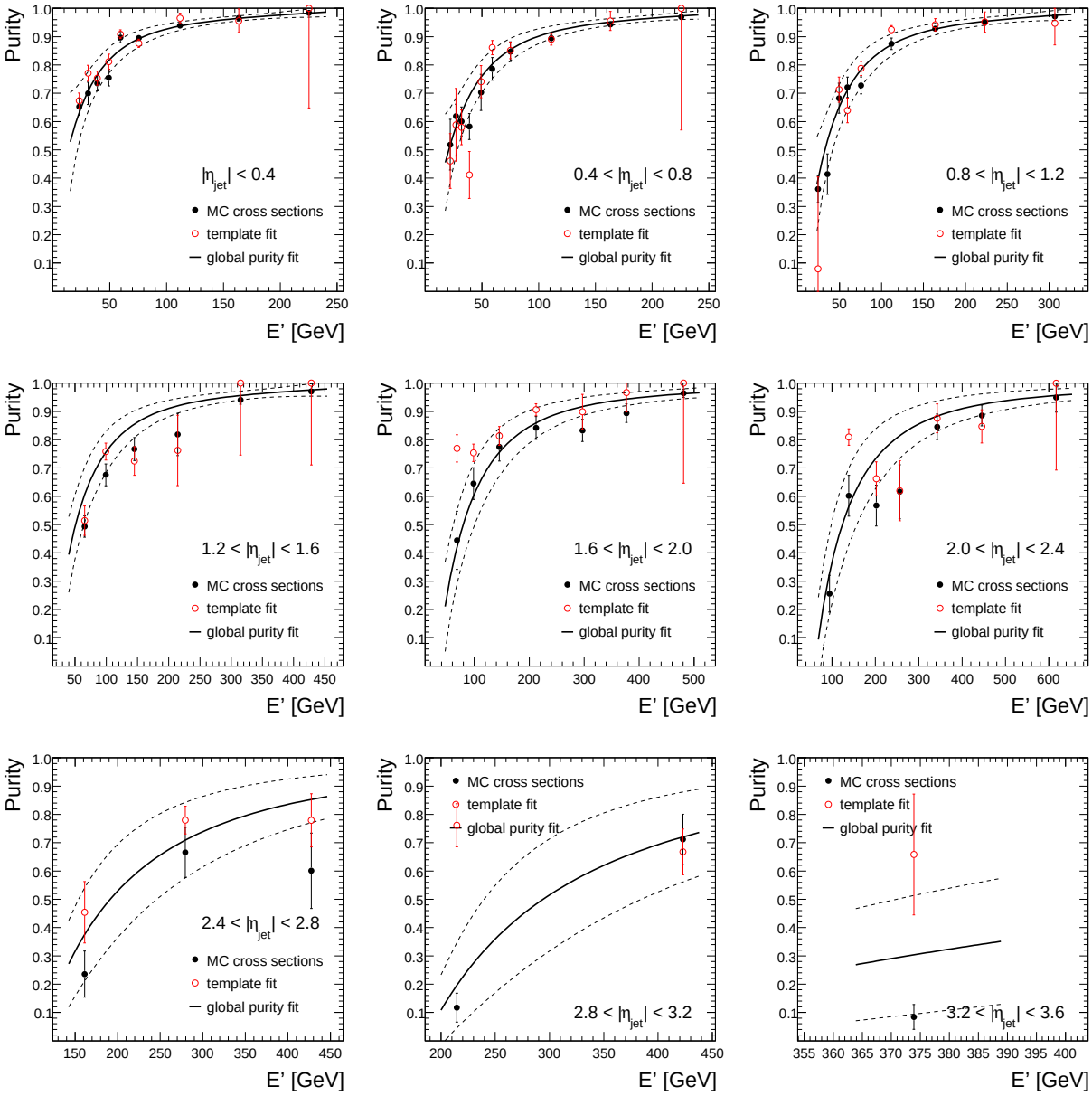

FIG. 118: Purity fit for the tight photon selection. Dashed lines represent estimated total uncertainties on purity.

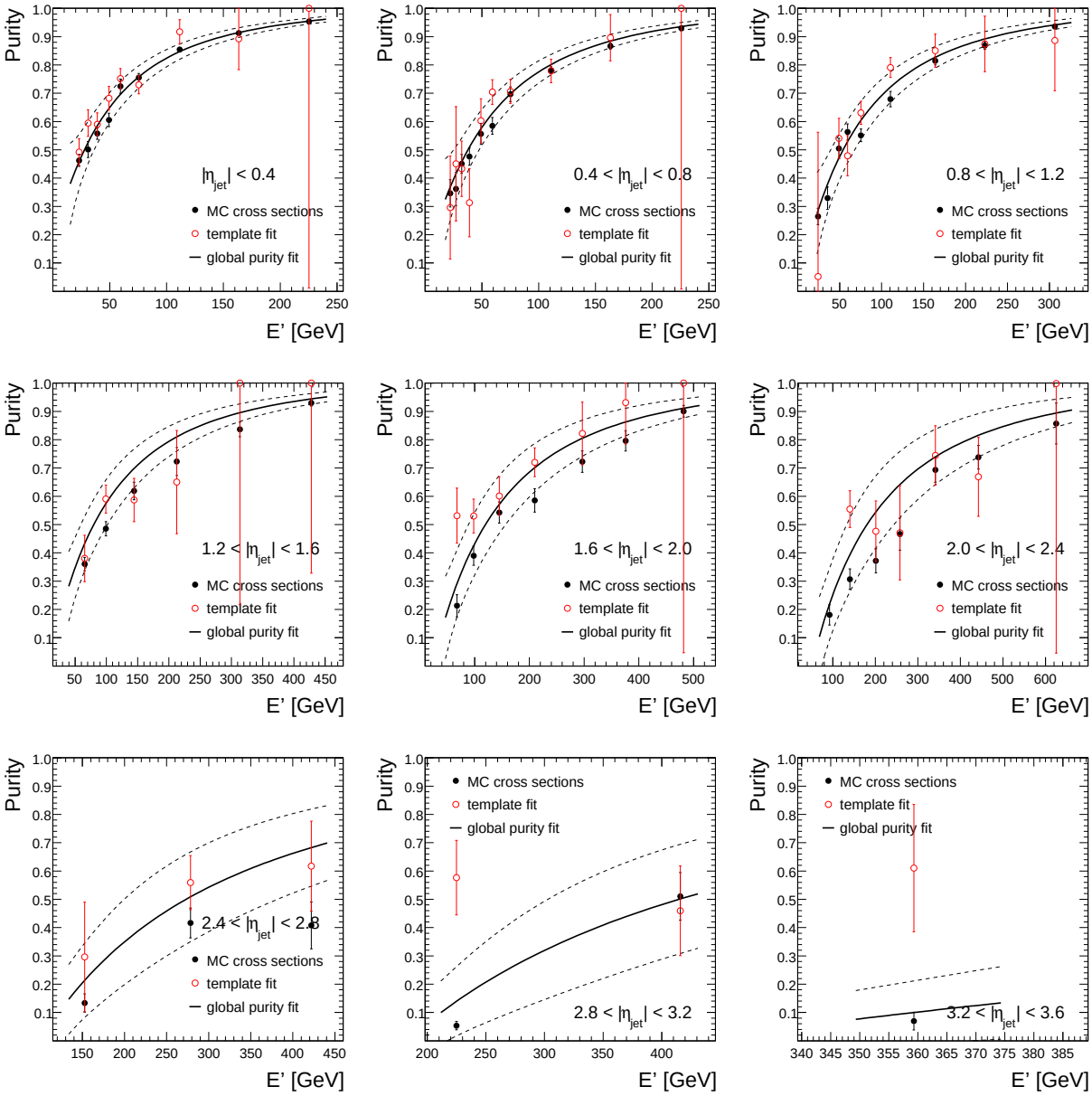

FIG. 119: Purity fit for the medium photon selection. Dashed lines represent estimated total uncertainties on purity.

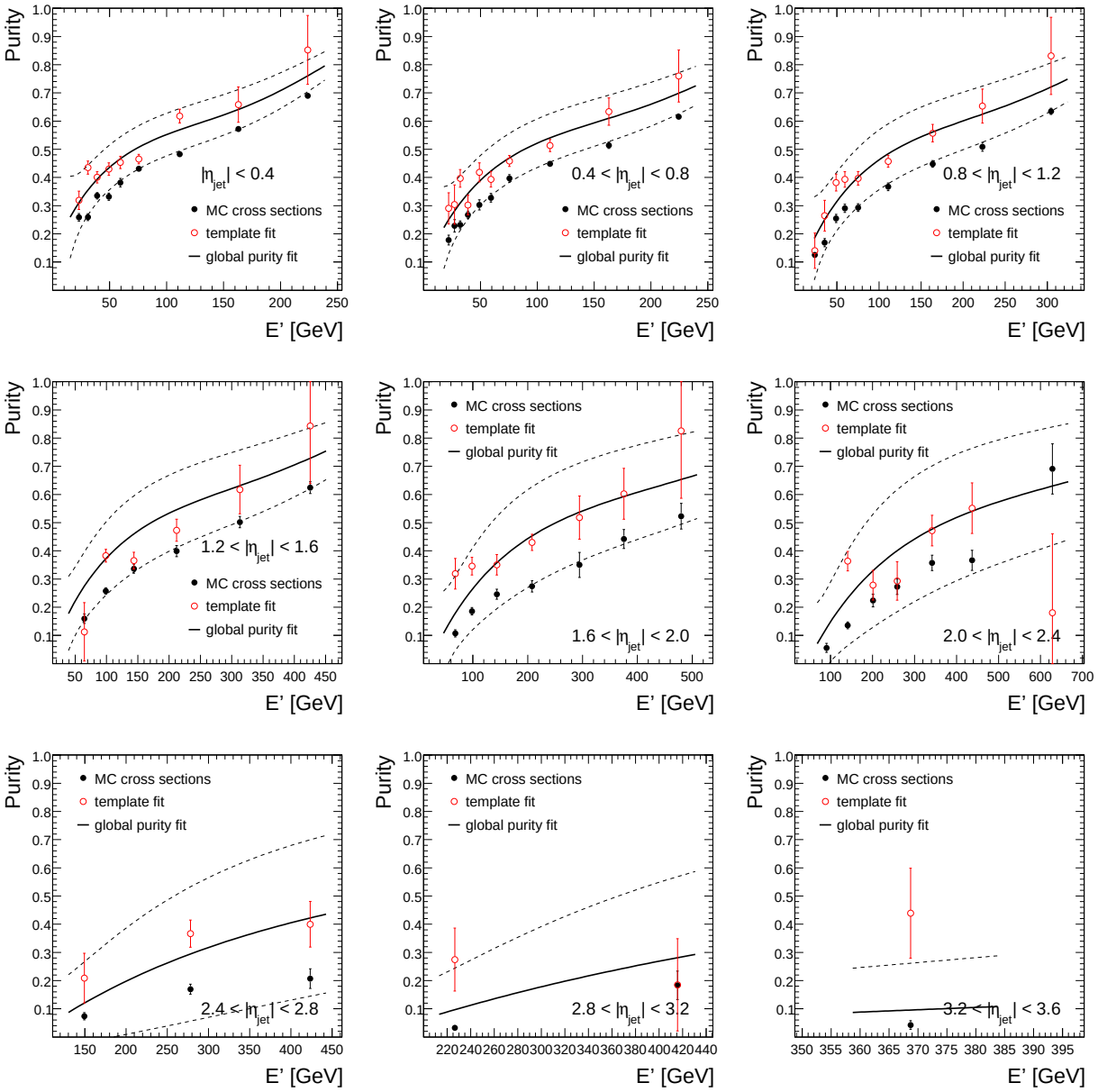

FIG. 120: Purity fit for the loose photon selection. Dashed lines represent estimated total uncertainties on purity.

2. Systematic Uncertainty on Photon Energy Scale

As discussed in Sect. 8.2, the measurement of the MPF response in data involves corrections for the dijet background contamination as well as the photon energy scale. The latter is defined for a pure sample of γ+jet events and relates the measured to the particle-level photon p_T. Such correction is required due to the fact that the absolute electron energy scale derived in $Z \to e^+e^-$ events, while suitable to correct 45 GeV electrons to the particle level, results in an overcorrection for photons (see Fig. 8). This is the result of the fact that photons interact less with material than electrons.

Such correction can only be estimated in MC, and therefore a systematic uncertainty must be assigned to account for how well the MC may describe the data. Unfortunately, the standard p17 MC used for generation of the γ+jet samples is known to suffer from significant flaws in d0gstar regarding both, the description of electromagnetic showers, as well as the description of the amount of material in front of the calorimeter [19]. Fortunately, significant effort by the W mass group as resulted in major improvements in both. In particular, the W mass group has developed a special version of d0gstar including modifications to GEANT (updated bremsstrahlung and photon cross sections look-up tables, and adjusted parameters for particle tracking) [20], as well as including additional material before the solenoid (best estimate: $\sim 0.28X_0$ [21]. Such improvements have been validated by the resulting good MC description of the longitudinal energy deposition in the calorimeter for electrons from Z and J/Ψ decays as a function of the angles of incidence. This allows to use such improved MC as a close enough representation of data that the systematic uncertainty on the photon energy scale for the standard p17 MC can be assessed.

In order to estimate this uncertainty, samples of single electron and photons have been generated for different scenarios:

1. "Default": standard p17 d0gstar;
2. "W mass set": improved p17 d0gstar including only updates to photon cross sections and particle tracking parameters;
3. "W mass set $+0.17X_0$": as 2), but including $0.17X_0$ of fudge material;
4. "W mass set $+0.36X_0$": as 3), but including $0.38X_0$ of fudge material.

The "truth" is expected to lie between 3) and 4), whereas 1) represents the default used for evaluation of the photon energy scale correction.

Such samples have been generated for different energies (electrons: E_e=15, 25, 45, 85 and 135 GeV; E_γ=15, 25, 45, 85, 135 and 285 GeV), requiring $\left|\eta^{\rm det}\right| < 1.1$ and using a realistic $z_{\rm PV}$ distribution. These samples have been reconstructed with the standard p17 d0reco, which includes corrections for energy loss and absolute electron energy scale based on the standard p17 d0gstar (this is also what is being done in data).

Figure 121 presents a comparison of the reconstructed and particle-level electron/photon energies as a function of the reconstructed energy, in the different scenarios. As expected, only electrons corresponding to scenario 1) have a corrected energy consistent with the particle level. Photons in scenario 1) appear overcorrected with respect to the particle level, and such correction is exactly the standard photon energy scale correction applied to the measurement of response in data. As it can be appreciated, the improved d0gstar in scenarios 2)-4) predicts an increase in the visible electron energy of $\sim 5-7\%$, and as a result the default p17 d0reco corrections does not bring electrons to the particle level. A similar shift is also observed for photons.

The photon energy scale corrections in scenarios 2)-4) are defined as the difference between the reconstructed and particle-level photon energies *after* the absolute electron energy scale correction. Such calibration is simulated here by shifting all points by the observed deviation from the particle-level for 45 GeV electrons in each of the scenarios. Fig. 122 presents the difference in the photon energy scale correction in scenarios 1) and 3) (full circles) and in scenarios 1) and 4) (open circles). The average (stars) correspond to the difference for the case of $0.28X_0$ of fudge material, which is the expected value from data (determined with very high precision). As it can be appreciated, there is an energy-dependent difference which we choose to correct for. Therefore, the dashed curve represents the additional correction factor applied to the photon energy scale correction derived from the standard MC. The uncertainty assigned is the full difference with respect to the extremes of fudge material ($0.17X_0$ and $0.36X_0$). In addition, a 0.5% uncertainty due to the electron energy scale is added in quadrature. The total assigned uncertainty is shown in Fig. 114.

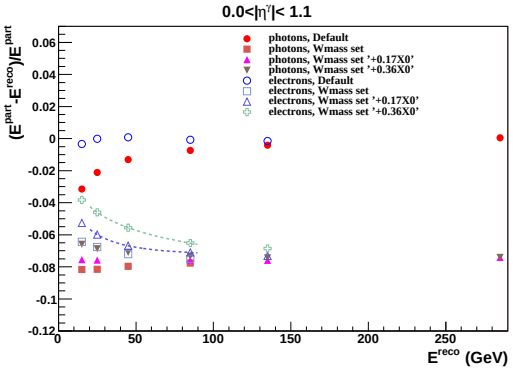

FIG. 121: Relative difference between reconstructed and particle-level energies for electrons and photons generated with different versions of d0gstar, and reconstructed with the standard p17 d0reco.

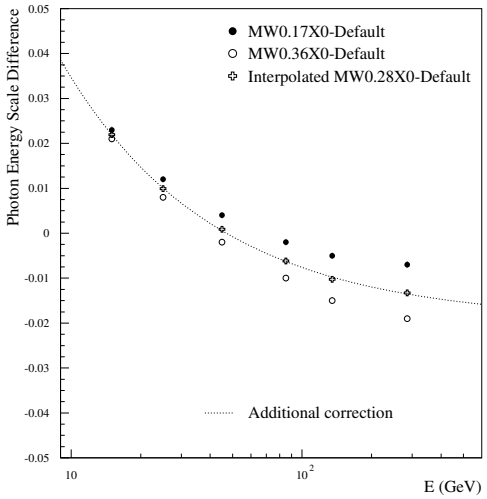

FIG. 122: Comparison of the photon energy scale between the default and the improved versions of d0gstar. See text for a discussion on the different symbols and lines shown.

3. High Energy Extrapolation of Response

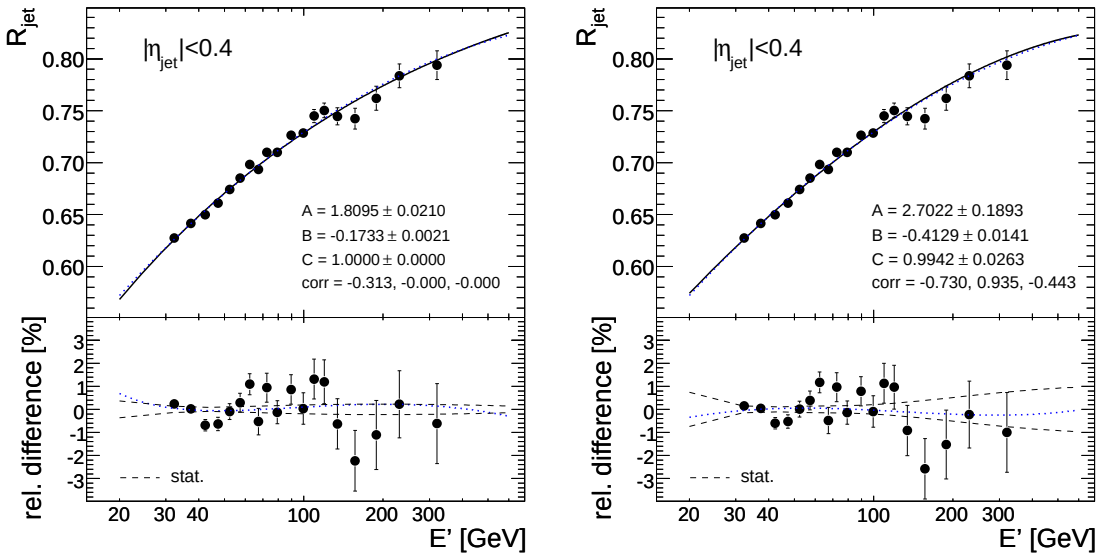

FIG. 123: Fitted MPF response measurement in data for $\mathcal{R}_{\text{cone}} = 0.7$ jets using MC with parametrized single pion response in two different scenarios: $C = 1$ (left) and C unconstrained (right). The dotted line represents the result of the quadratic logarithmic fit from Fig. 9. In case of the unconstrained fit, the quadratic dependence of the cubic logarithmic fit parameter on parameters (A, B, C) was used. This choice was made due to fact that found minimum is outside of the grid range and the quadratic parametrization is more reliable in this region.

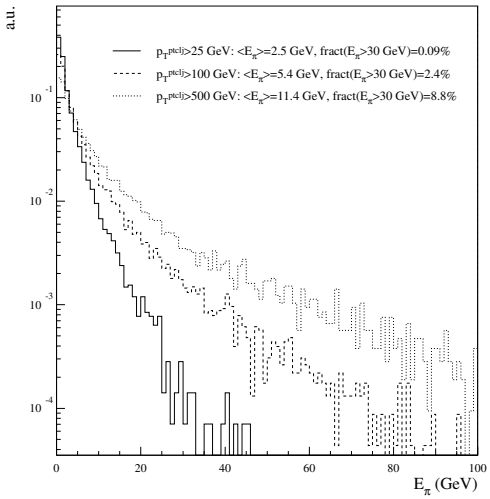

FIG. 124: The energy distribution of pions in a jet.

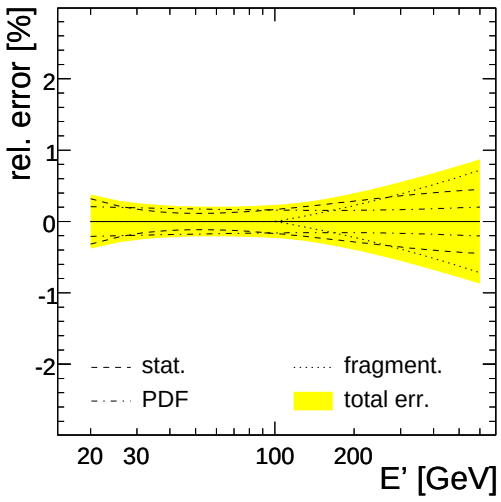

FIG. 125: Individual sources of uncertainties in high energy extrapolation for response of cone 0.7 jets in data.

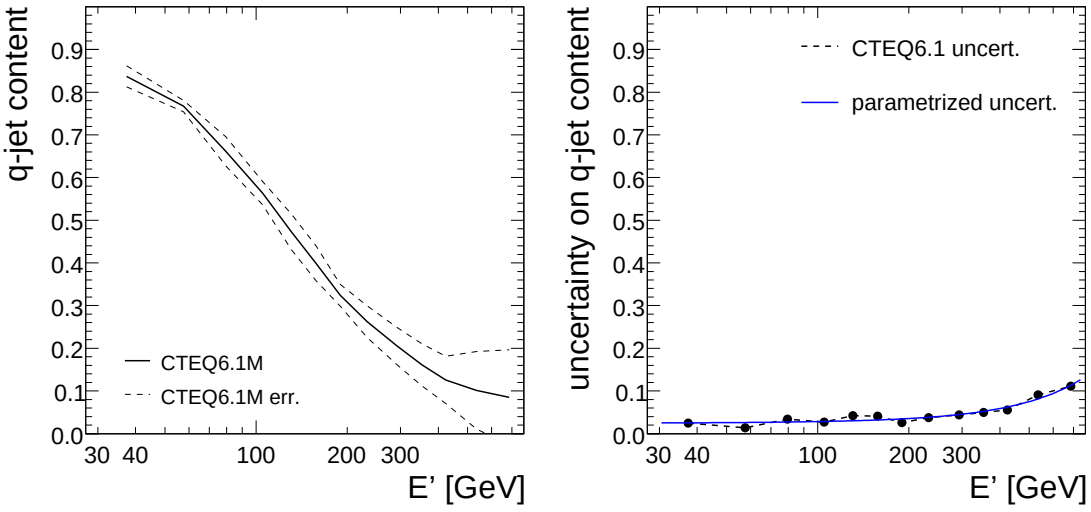

FIG. 126: Left: quark jet fraction and its uncertainty for $\gamma +$ jet sample with central rapidity jets ($|\eta| < 0.4$) estimated by PYTHIA for CTEQ6.1M. Right: uncertainty on quark jet fraction. Solid line represents the quadratic fit used in the calculation of the corresponding uncertainty on jet response.

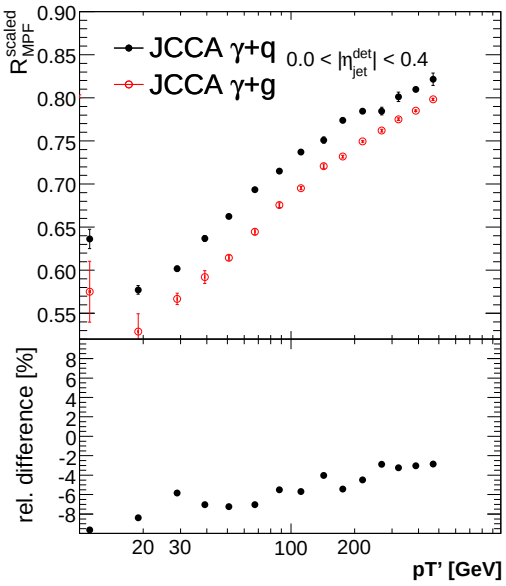

FIG. 127: Comparison of the MPF response in CC for γ+quark versus γ+gluon events in MC without ZB overlay, and using a scaled single pion response to better represent the expected difference in data.

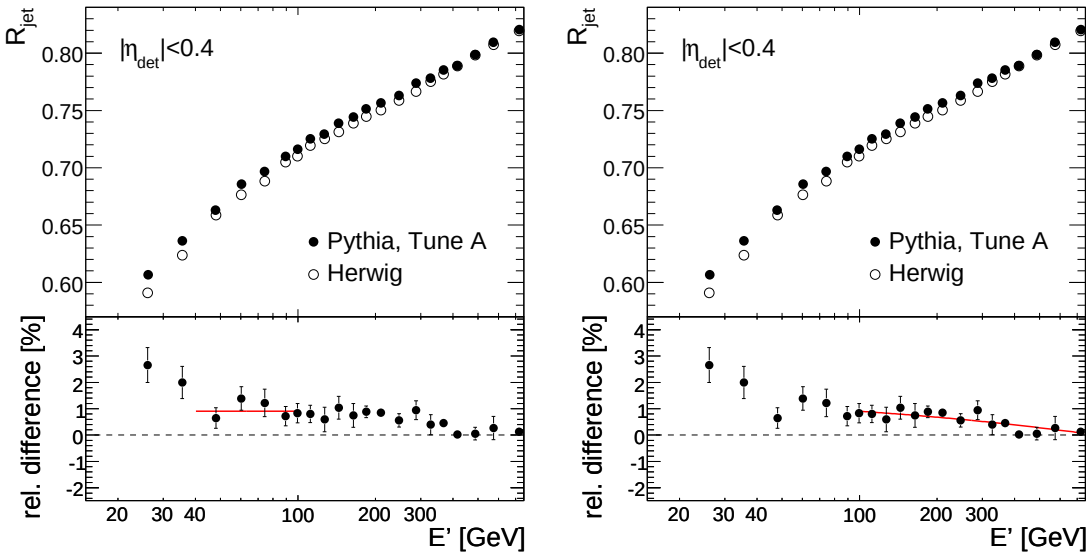

FIG. 128: Difference response for PYTHIA Tune A and HERWIG in particle level MC with tuned pion response. Soft underlying event simulation was swtiched off. Solid line in the left plot represents the fit to the difference for E' between $40 - 100$ GeV, and for $E' > 100$ GeV in the right plot.

a. *Comparison of Uncorrected Z Mass Peak in Data and MC*

After the calibration procedure, the absolute energy scale of the calorimeters in data and MC are expected to be very close. This can be verified by comparing the reconstructed $Z \to e^+e^-$ peak from the uncorrected (i.e. before energy-loss and absolute electron energy scale corrections) calorimeter cluster energies in data and MC. Events are selected in data (2EMHigtpT skim) and MC (p17.09.01 ALPGEN) using the following criteria:

- good primary vertex (≥ 3 tracks and $|z_{\rm PV}| < 60$ cm);
- exactly two EM objects;
- both EM objects are in CC and in fiducial regions, and satisfy the following criteria: $HMX7 < 12$, $Iso < 0.15$ and $EMF > 0.9$;
- at least one EM object has a track match;
- M_{ee} window cut: 91.2 ± 15.0 GeV.

Figure 129 compares the reconstructed $Z \to e^+e^-$ invariant mass distribution between data and MC, before (left) and after (right) energy-loss and absolute electron energy scale corrections. By definition, the full set of corrections bring the $Z \to e^+e^-$ peak in excellent agreement between data and MC (in the case of MC, oversmearing of the electron energies is also included in order to match the width of the distribution in data). However, what we are mostly interested in is the difference in scales before the corrections (left plot), which is found to be within 1%. This result motivates the (conservative) choice of a 1.5% uncertainty on the C paramter as a constraint in the determination of the high energy extrapolation of response discussed in Sect. 8.3.1.

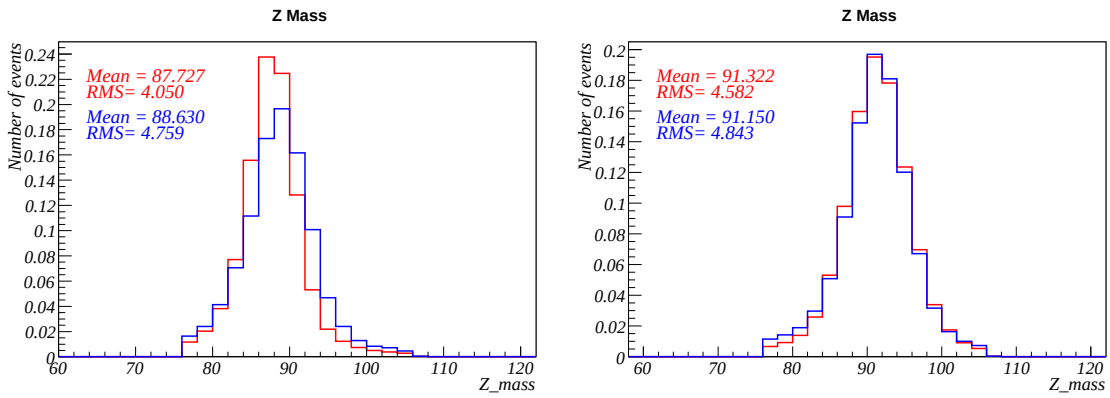

FIG. 129: Comparion of the $Z \to e^+e^-$ invariant mass distribution between data and MC: before (left) and after (right) energy-loss and electron energy scale corrections. The MC distribution in the right plot also includes oversmearing of the electron energies.

b. Isolated Pion Response Measurement

(This writeup has been kindly provided by Krisztian Peters.)

The isolated pion response was determined from data that was collected during normal physics running. We used Minimum Bias and Zero Bias events below 6 GeV in the central calorimeter region. Above 6 GeV the data was collected with a tracking-based trigger for isolated tracks with a threshold at $p_T > 5$ GeV: TIS(1,5.). Data with the TIS(1,5.) trigger was collected in early 2006 and 6.3 million events have been recorded.

Previous to this measurement, the pion shower characteristics and response were studied in MC. The effects that drive shower shapes and overall response normalization have been identified. These include dead material in front of the calorimeter, magnetic field effects, noise, integration time, back-scattering and zero suppression. They mainly result in a rapid decrease of the response at small pion energies.

In the MC it was also studied how to select isolated pions in the data in an unbiased way. Main backgrounds to this measurement are two-fold: overlap energy contribution in the calorimeter from (mainly) neutral particles and the fact that isolated charged tracks are not always due to pions. The neutral overlap has later to be subtracted from the response. The fact that single tracks are also due to protons/anti-protons and kaons has a negligible effect as was shown by MC studies. At higher energies there is however a significant electron and muon contamination from W decays. In order to reduce this background we vetoed on loose electrons and on tracks that matched a hit in any of the muon detector segments. No precise estimate of/nor correction for the residual electron/muon contamination as a function of energy is yet available.

For the response measurement we sort events in bins of track energy, compute the event-by-event response in each bin and take the average value of this distribution. In this analysis we required basic track quality conditions (like minimum number of hits, etc.) to ensure a reliable energy measurement from the tracking. In order to significantly reduce the background from charged particles, no other tracks were allowed within a cone of $\Delta\mathcal{R} < 1.0$. In the example presented here, the isolation for the TIS(1,5.) sample was relaxed to $\Delta\mathcal{R} < 0.7$ to enhance statistics at higher energies. This result agrees with the one obtained with the higher isolation. Finally, we also veto on events where the energy measured by the CAL is more than twice the energy measured by the tracker. We know from MC studies that the response of charged pions does not exceed this threshold, thus we can safely interpret these events as events with an additional contribution from a high energy π^0 or γ overlap or as instrumental background.

The main background from the neutral energy overlap is not removed by the above cut. These are mainly low energy photons and neutrons. From MC studies we know that pion showers contain almost their entire energy within a cone of $\Delta\mathcal{R} = 0.5$. In the present analysis we estimate the background contribution from the hollow cone $0.5 - 0.7$ around the isolated pion. This energy contribution is normalized to the area of the other cone sizes and is subtracted from their energy response. As a cross check the same background subtraction was determined from the hollow cone $0.4 - 0.5$ giving comparable results. One should note that the applied background subtraction removes the calorimeter electronics noise as well, which is a substantial fraction of the response in the lower energy domain. Fig.130 shows the result of the isolated pion response measurement in the central calorimeter for $|\eta| < 0.4$ compared to the estimated one from the jet response calibration procedure in MC discussed in Sect. 8.3.1.

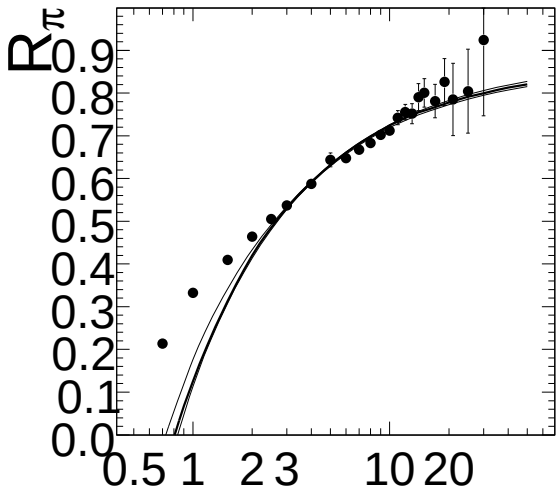

FIG. 130: Comparison of single pion response derived from data (full cicrles) and from the fit to the jet response (thick solid line represents the most probable value, thin lines then correspond to the 67% probability region).

4. Time Dependence of MPF Response

In this section we examine the time dependence of the MPF response and assess a systematic uncertainty to cover for the possible shifts in the average correction different analyses might have depending on the run range considered.

Figure 131 shows the relative difference of the MPF response as a function of trigger list version (v8 through v14) with respect to the Run IIa average. This relative difference is computed in different 0.4-wide $\eta_{\rm jet}^{\rm det}$ bins and in different p'_T bins to explore a possible energy dependece. The event selection and procedure followed is identical to that discussed in Sect. 8, with the exception of the photon ID criteria, which is set to "loose" in order to increase statistics.

As it can be appreciated, the MPF response is in general stable within $\leq 1\%$ for the central calorimeter, and in general in all calorimeter regions for trigger list versions v12-v14 (which constitutes typically $\sim 85-90\%$ of the total Run IIa sample used by physics analyses). However, significant deviations (up to 8%) with respect to the Run IIa average can be observed in earlier trigger list versions, and in particular in the $-1.6 < \eta_{\rm jet}^{\rm det} < -1.2$ region during trigger list versions v10 and v11. These deviations are found to be basically energy independent. In the following, the higher statistics measurement for $p'_T > 30$ GeV will be used to assess a systematic uncertainty. The concern is that, depending on the distribution of integrated luminosity among trigger list versions, a given analysis might require a slightly different average response than the one provided from the γ+jet sample.

In order to estimate such uncertainty, we have collected information on the integrated luminosity used per trigger list version for a number of physics analyses based on the Run IIa sample (see Table 11). Based on this information, and the estimated relative shifts shown in Fig. 131, the expected deviation in the average response for each of the analyses is computed, and summarized in Table 12. Also shown is the assigned systematic uncertainty.

Physics Analysis		$\mathcal{L}$(pb^{-1}) per Trigger List Version						
		v8	v9	v10	v11	v12	v13	v14
NP	W'	3.1	24.6	10.1	64.0	230.0	400.0	330.0
	Jets+MET	0.0	0.0	0.0	62.5	226.8	373.3	329.5
TOP	μ+jets	5.6	24.8	10.7	65.2	230.9	299.7	234.4
	e+jets	4.9	24.7	9.8	62.8	227.1	349.1	234.1
	alljets (3JT)	11.8	11.8	11.8	64.3	200.9	371.0	333.0
	$e\mu$	5.8	24.8	10.8	65.2	231.0	375.6	333.0
	ee	25.0	24.8	10.8	65.2	231.0	346.5	332.9
QCD	3-jet	42.6	47.9	21.4	79.3	268.1	463.6	416.9
	incl. jet (JT_8TT)	0.0	0.0	0.0	0.0	0.0068	0.0111	0.0029
	incl. jet (JT_15TT)	0.0	0.0	0.0	0.0	0.037	0.049	0.013
	incl. jet (JT_25TT)	0.0	0.0	0.0	0.0	0.38	0.61	0.53
	incl. jet (JT_45TT)	0.0	0.0	0.0	0.0	3.76	9.42	3.96
	incl. jet (JT_65TT)	0.0	0.0	0.0	0.0	29.8	40.0	3.38
	incl. jet (JT_95TT)	0.0	0.0	0.0	0.0	88.6	280.0	137.4
	incl. jet (JT_125TT)	0.0	0.0	0.0	0.0	91.6	375.1	236.2
HIGGS	single EM	26.6	24.8	10.8	65.9	231.0	378.3	234.6

TABLE 11: Integrated luminosity (pb^{-1}) as a function of trigger list version for different physics analyses based on the Run IIa data sample.

$\eta_{\text{jet}}^{\text{det}}$ Bin	Max. Deviation	Min. Deviation	Assigned Syst. Uncertainty
$[-3.6, -3.2)$	$+0.74\%$	-0.20%	$\pm 1.00\%$
$[-3.2, -2.8)$	$+0.44\%$	$+0.05\%$	$\pm 0.50\%$
$[-2.8, -2.4)$	$+0.27\%$	-0.23%	$\pm 0.50\%$
$[-2.4, -2.0)$	$+0.03\%$	-0.26%	$\pm 0.25\%$
$[-2.0, -1.6)$	$+0.03\%$	-0.23%	$\pm 0.25\%$
$[-1.6, -1.2)$	$+0.39\%$	-0.80%	$\pm 0.75\%$
$[-1.2, -0.8)$	$+0.16\%$	-0.46%	$\pm 0.50\%$
$[-0.8, -0.4)$	$+0.05\%$	-0.03%	$\pm 0.10\%$
$[-0.4, +0.0)$	$+0.08\%$	-0.01%	$\pm 0.10\%$
$[+0.0, +0.4]$	$+0.08\%$	-0.02%	$\pm 0.10\%$
$(+0.4, +0.8]$	$+0.05\%$	-0.03%	$\pm 0.10\%$
$(+0.8, +1.2]$	$+0.25\%$	-0.18%	$\pm 0.50\%$
$(+1.2, +1.6]$	$+0.60\%$	-0.40%	$\pm 0.75\%$
$(+1.6, +2.0]$	$+0.22\%$	-0.19%	$\pm 0.25\%$
$(+2.0, +2.4]$	$+0.24\%$	-0.23%	$\pm 0.25\%$
$(+2.4, +2.8]$	$+0.35\%$	-0.31%	$\pm 0.50\%$
$(+2.8, +3.2]$	$+0.08\%$	-0.42%	$\pm 0.50\%$
$(+3.2, +3.6]$	$+0.06\%$	-1.01%	$\pm 1.00\%$

TABLE 12: Maximum and minimum deviations from the Run IIa average response expected within the list of physics analyses in Table 11. The rightmost column summarizes the assigned systematic uncertainty per detector region.

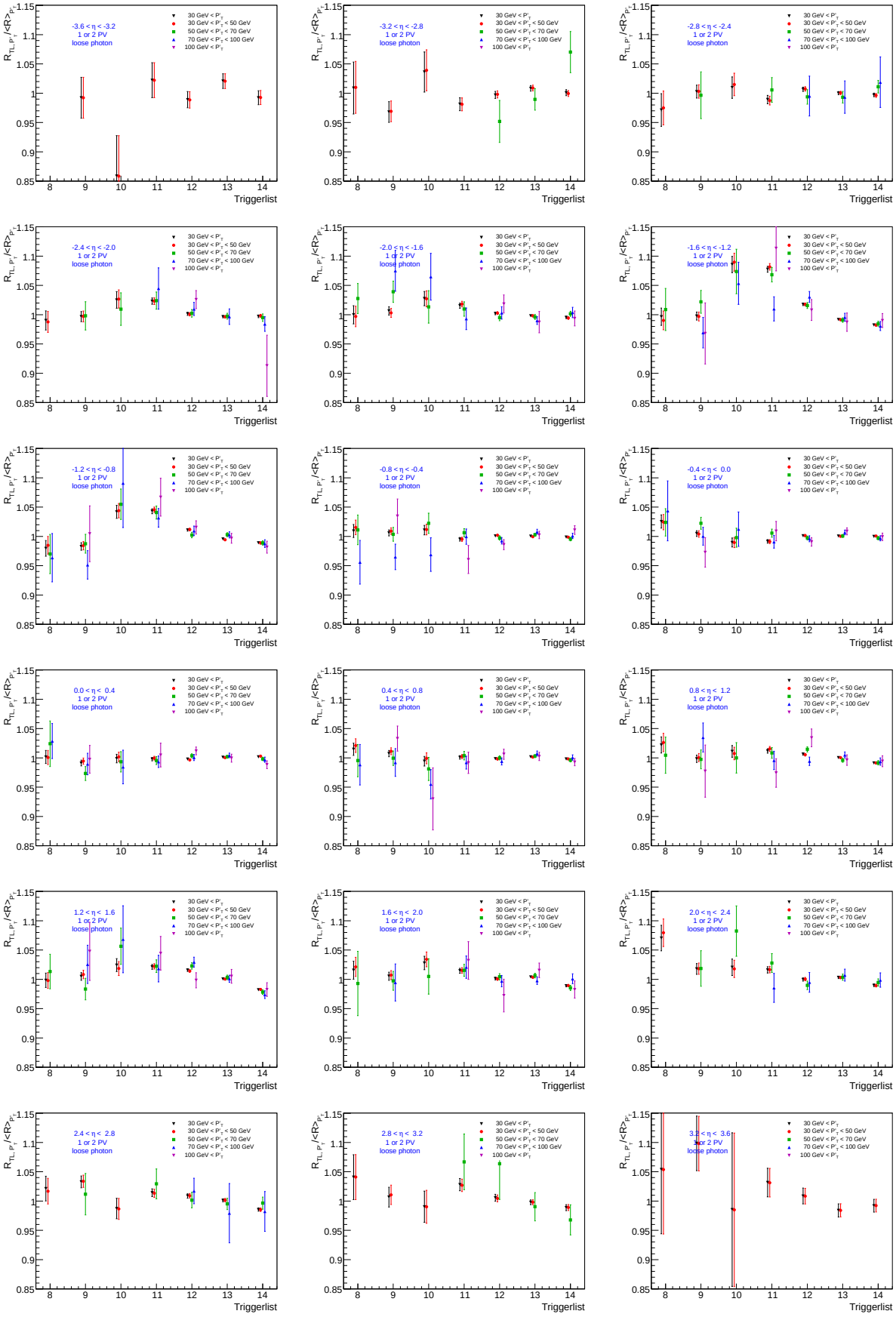

FIG. 131: Relative difference of the MPF response with respect to the Run IIa average, as a function of trigger list version. Different plots correspond to different calorimeter regions.

APPENDIX E: RELATIVE MPF RESPONSE CORRECTION

Trigger	L3 threshold [GeV]	offline cut [GeV]
JT_15TT	15	28
JT_25TT_NG	25	51
JT_45TT	45	57
JT_65TT	65	81
JT_95TT	95	110
JT_125TT	125	145

TABLE 13: List of single jet triggers used for collection of the dijet sample.

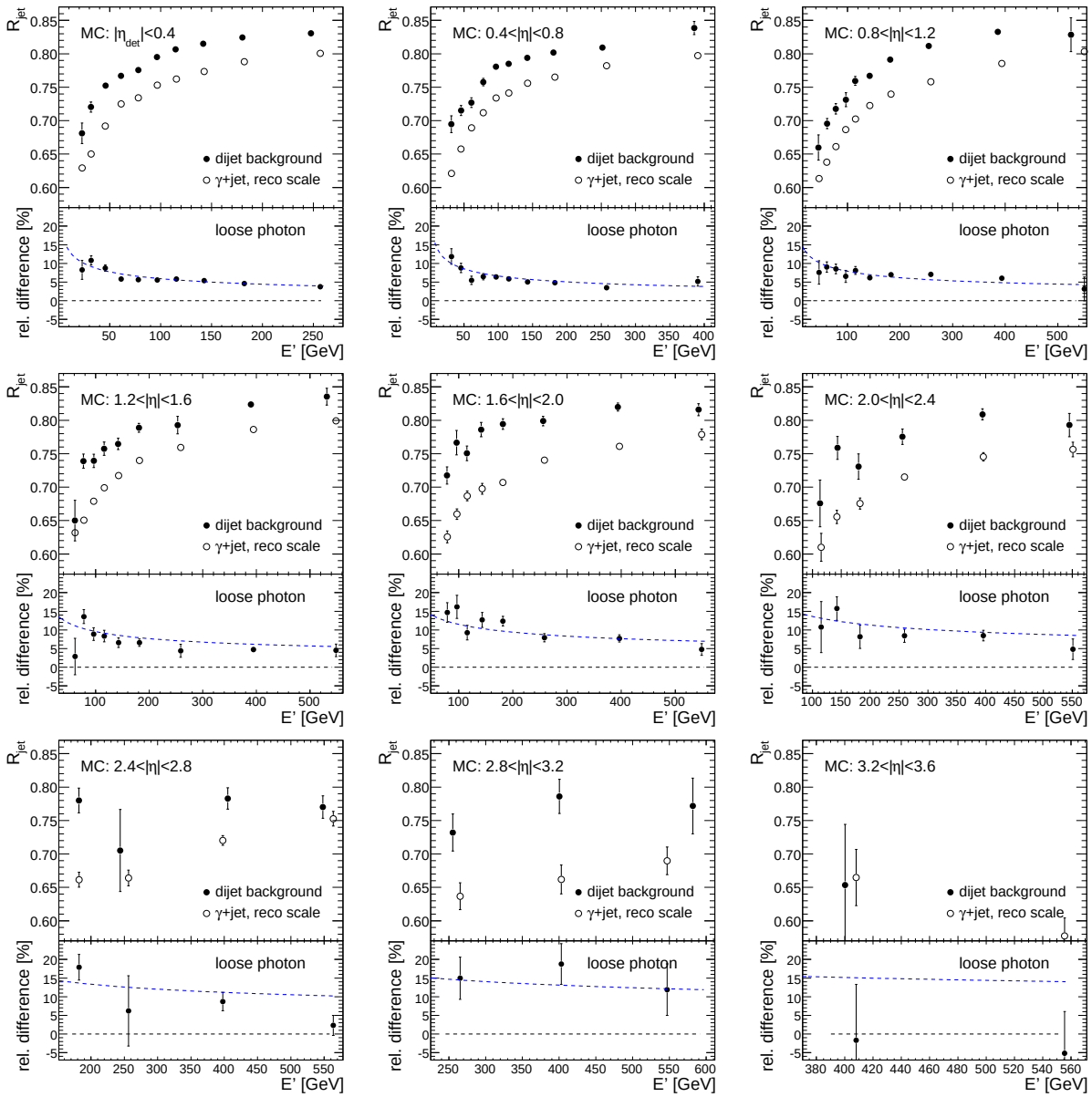

FIG. 132: Comparison of the MPF response for selected γ+jet candidate events (using the loose photon identification criteria) in dijet and γ+jet MC, for different $\left|\eta_{\rm jet}^{\rm det}\right|$ bins. The lower part of each plot compares the relative difference of the signal and background responses to the prediction (dashed line) given by Eq. 50, where SF_η was estimated during the η-intercalibration procedure.

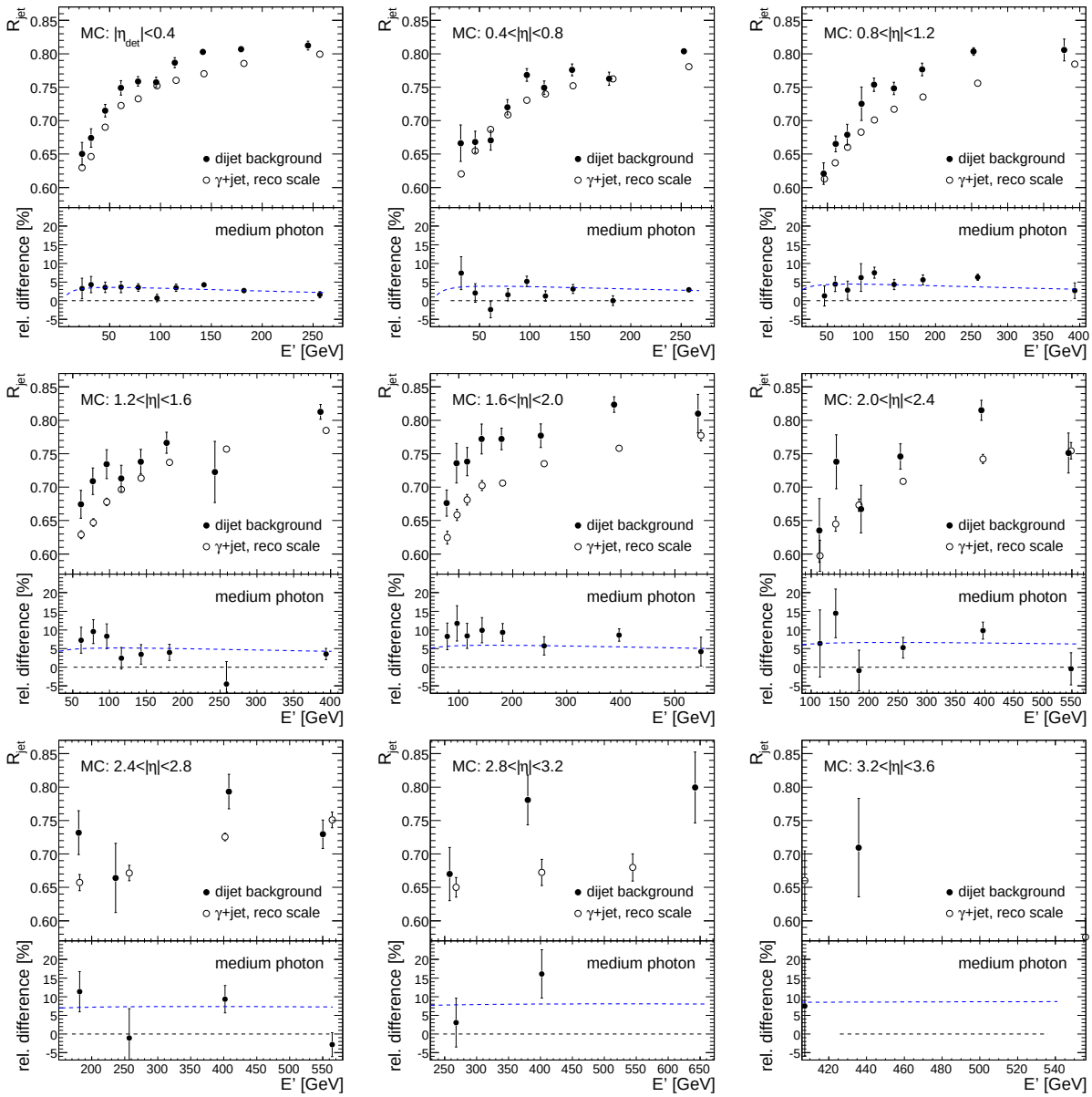

FIG. 133: Comparison of the MPF response for selected γ+jet candidate events (using the medium photon identification criteria) in dijet and γ+jet MC, for different $\left|\eta_{\rm jet}^{\rm det}\right|$ bins. The lower part of each plot compares the relative difference of the signal and background responses to the prediction (dashed line) given by Eq. 50, where SF_η was estimated during the η-intercalibration procedure.

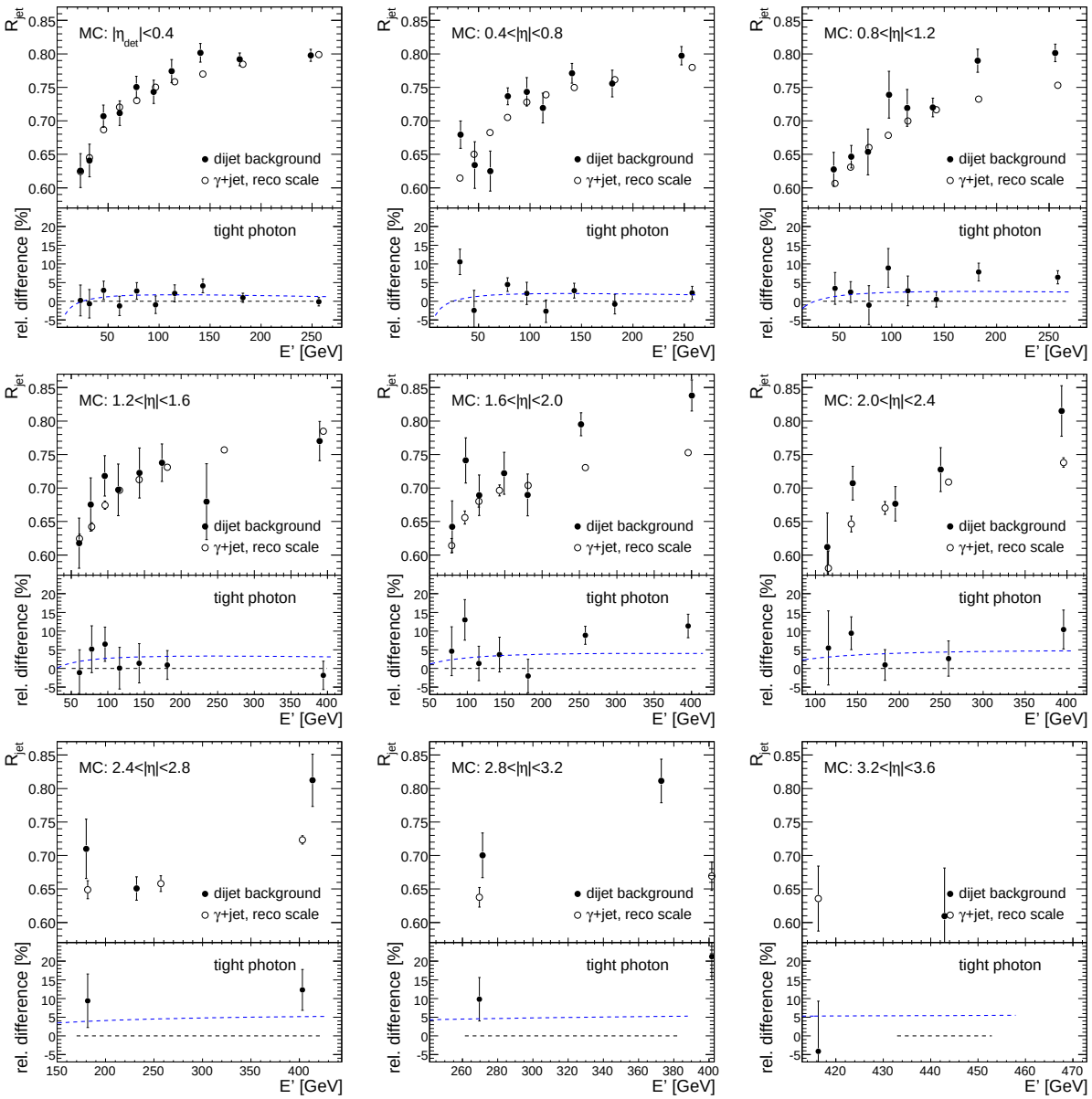

FIG. 134: Comparison of the MPF response for selected γ+jet candidate events (using the tight photon identification criteria) in dijet and γ+jet MC, for different $\left|\eta_{\rm jet}^{\rm det}\right|$ bins. The lower part of each plot compares the relative difference of the signal and background responses to the prediction (dashed line) given by Eq. 50, where SF_η was estimated during the η-intercalibration procedure.

1. Relative MPF Response Correction in Data

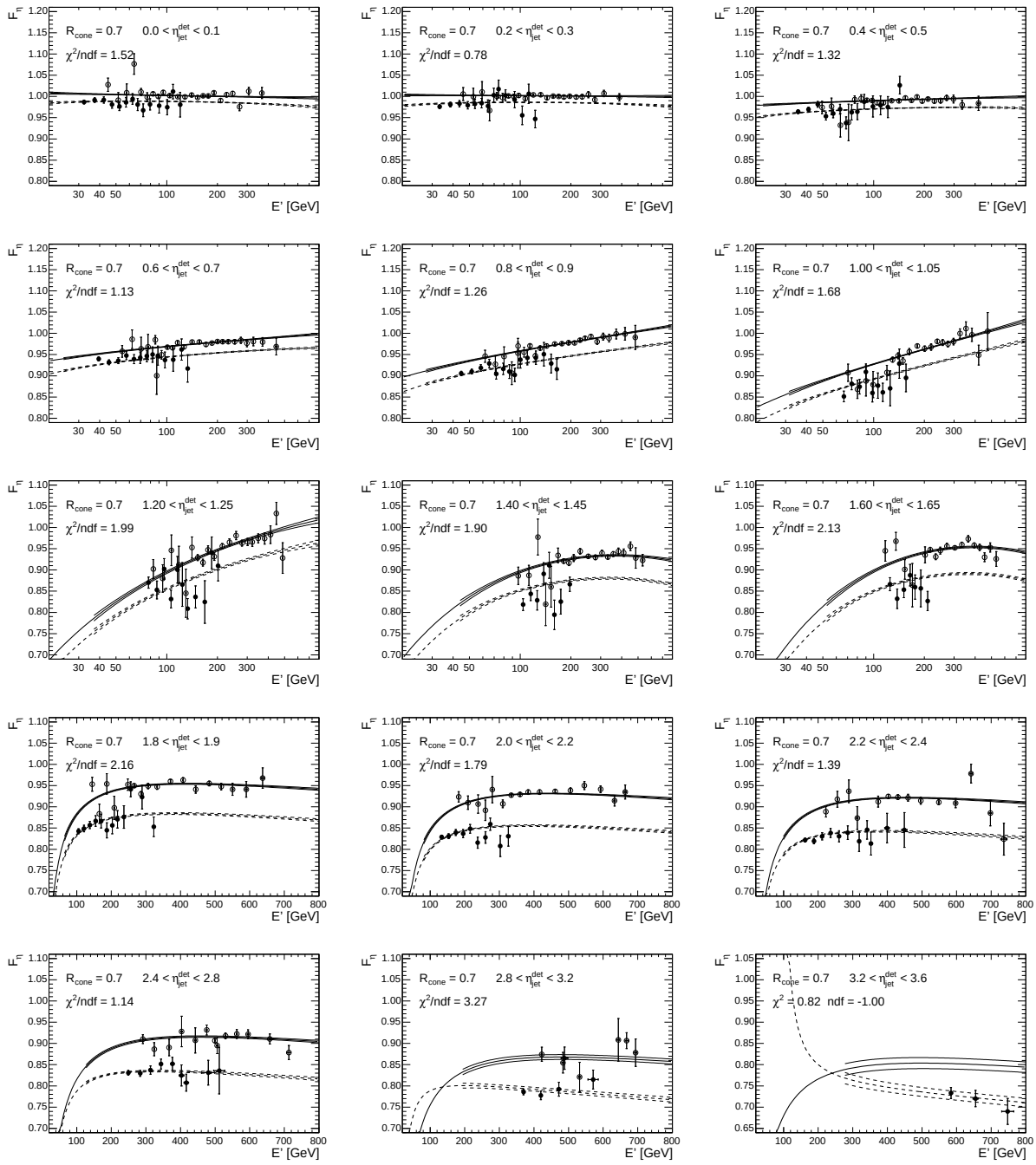

FIG. 135: Relative MPF response correction for $\mathcal{R}_{\rm cone} = 0.7$ jet in data as a function of E' and for different $\eta_{\rm jet}^{\rm det}$ bins. The solid (open) circles represent the measurements in the γ+jet (dijet) sample. The lines shown represent the result from the global fit discussed in Sect. 9.2.6.

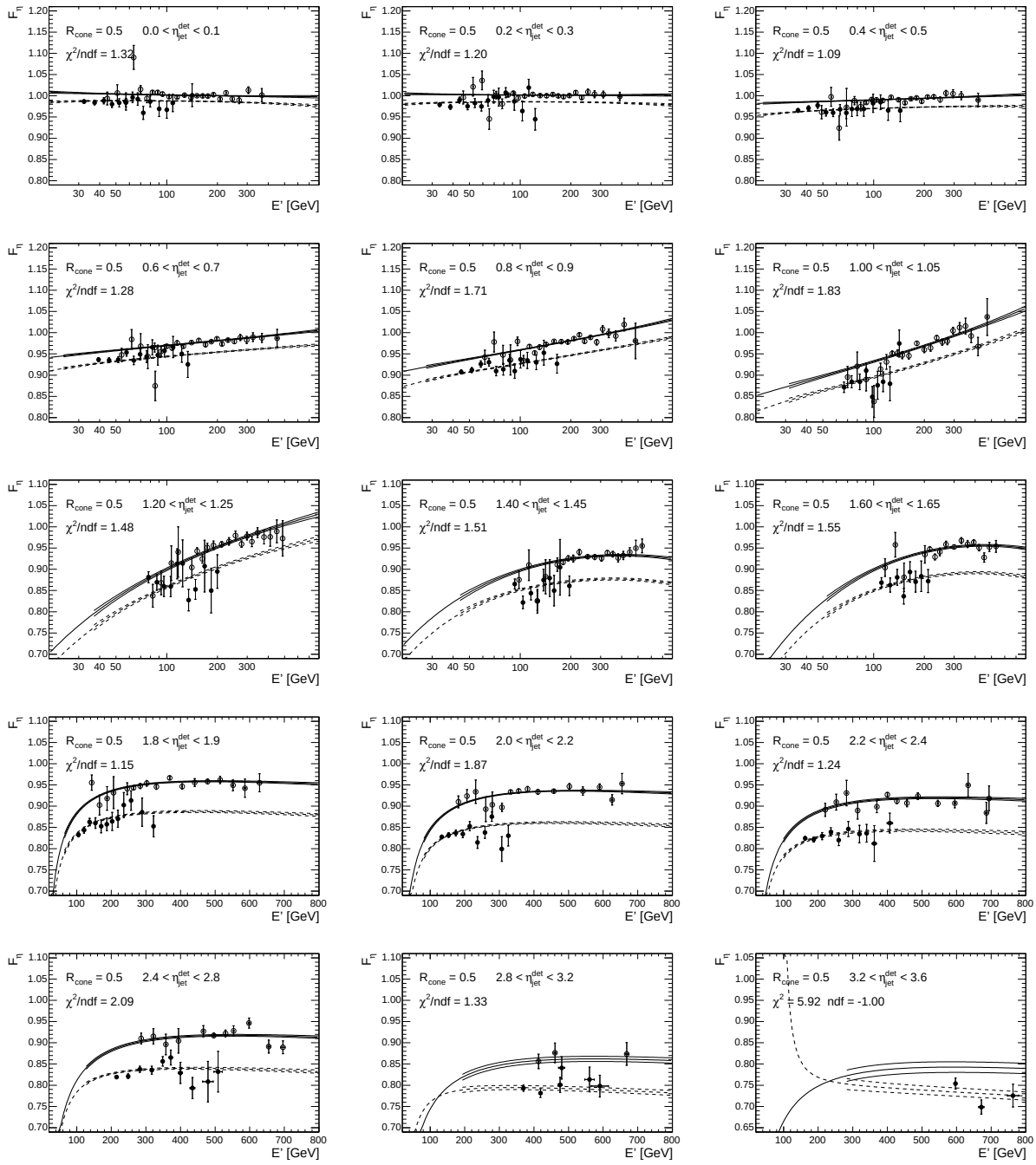

FIG. 136: Relative MPF response correction for $\mathcal{R}_{\rm cone} = 0.5$ jet in data as a function of E' and for different $\eta_{\rm jet}^{\rm det}$ bins. The solid (open) circles represent the measurements in the γ+jet (dijet) sample. The lines shown represent the result from the global fit discussed in Sect. 9.2.6.

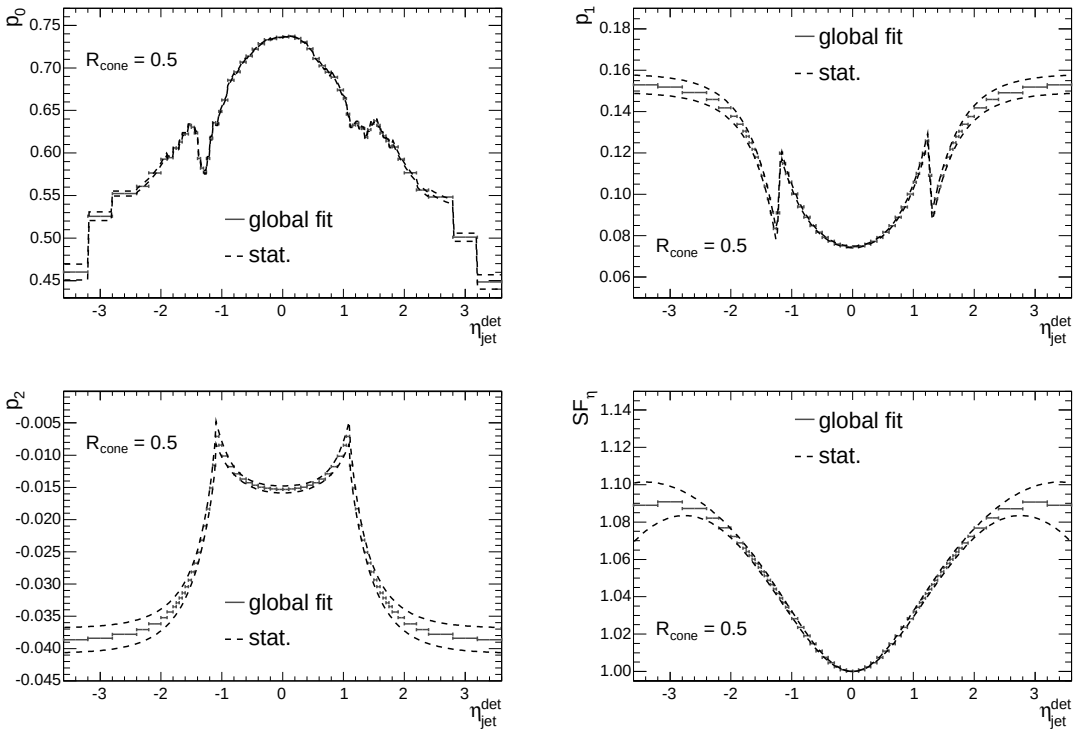

FIG. 137: Parameterizations for (p_0, p_1, p_2, SF_η) resulting from the global fit to the relative MPF response measurements in data for $\mathcal{R}_{\rm cone} = 0.5$ jets. The dashed lines illustrate the statistical uncertainty band.

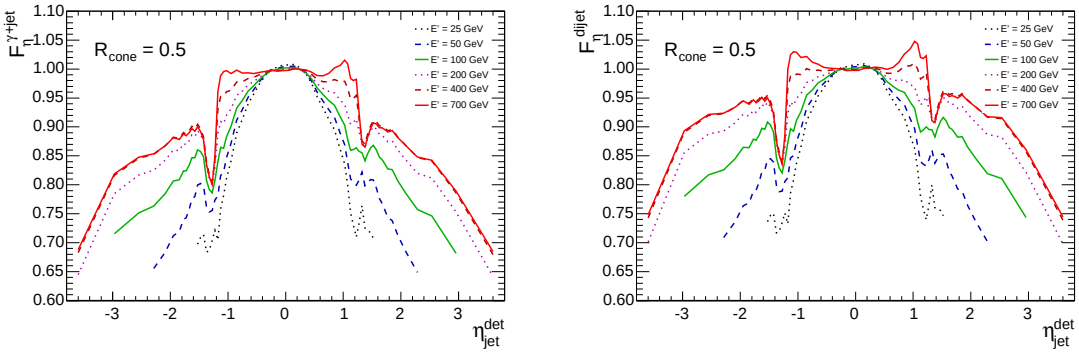

FIG. 138: Relative MPF response correction in data for $\mathcal{R}_{\rm cone} = 0.5$ jets as a function of $\eta_{\rm jet}^{\rm det}$ and separately for γ+jet (left) and dijet (right). The different lines correspond to particular values of E'.

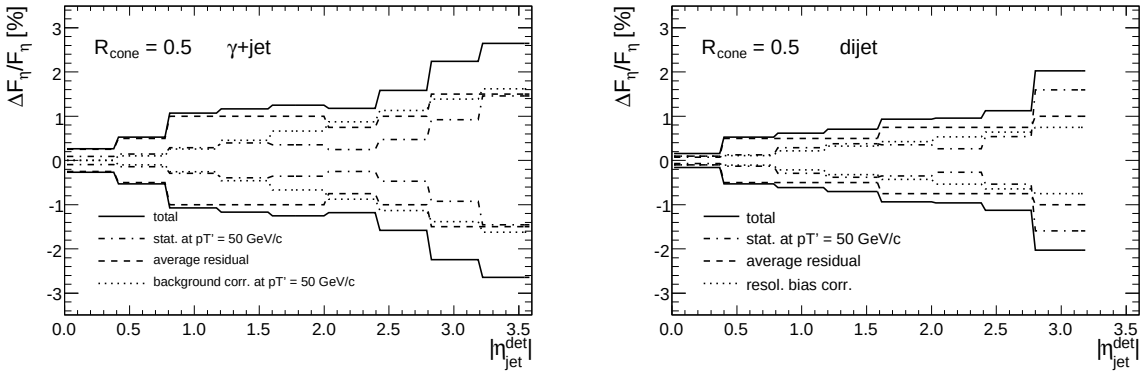

FIG. 139: Uncertainties on the relative MPF response correction in data for $\mathcal{R}_{\rm cone} = 0.5$ jets, as a function of $|\eta^{\rm det}_{\rm jet}|$ and separately for γ+jet (left) and dijet (right). The solid line shows the total uncertainty, resulting from the sum in quadrature of the individual contributions: statistical (dashed-dotted), average residual (dashed) and background correction (dotted).

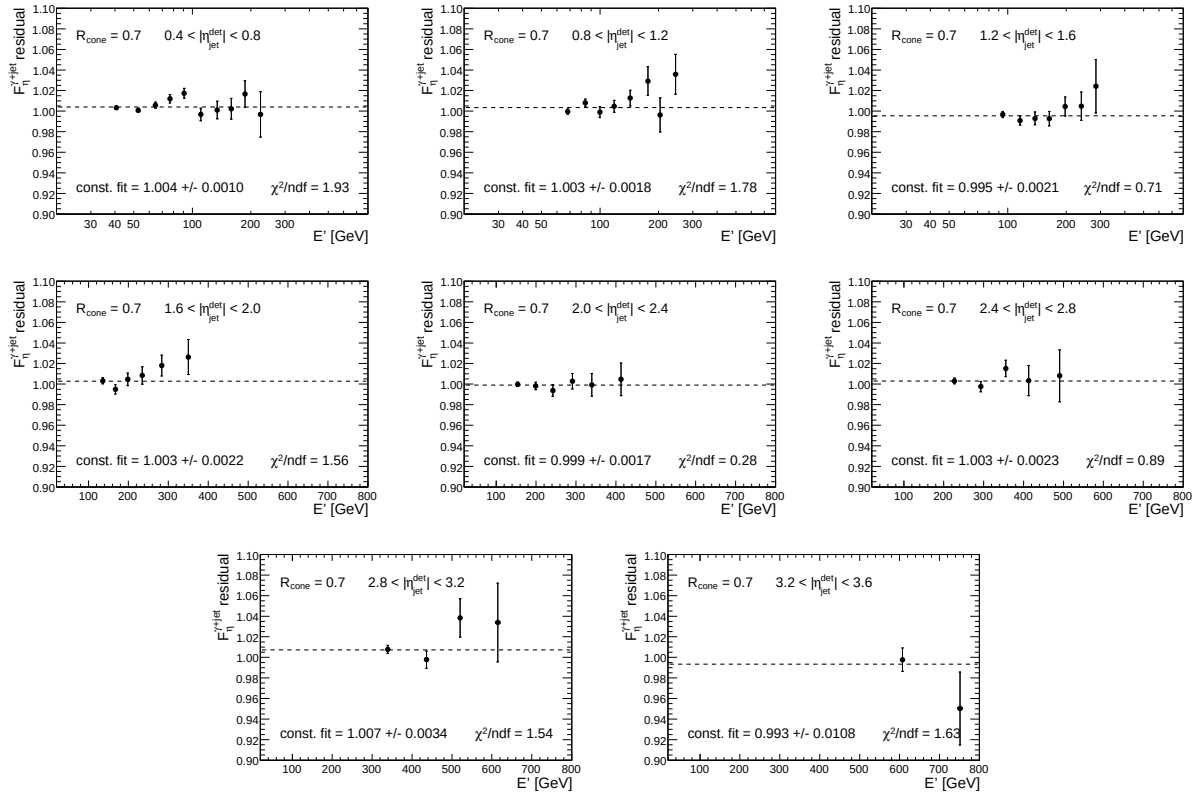

FIG. 140: Residuals of the relative MPF response corrections in γ+jet data for $\mathcal{R}_{\rm cone} = 0.7$ jets. Shown as a dashed line is the result of a constant fit to the measured closure observable as a function of E'.

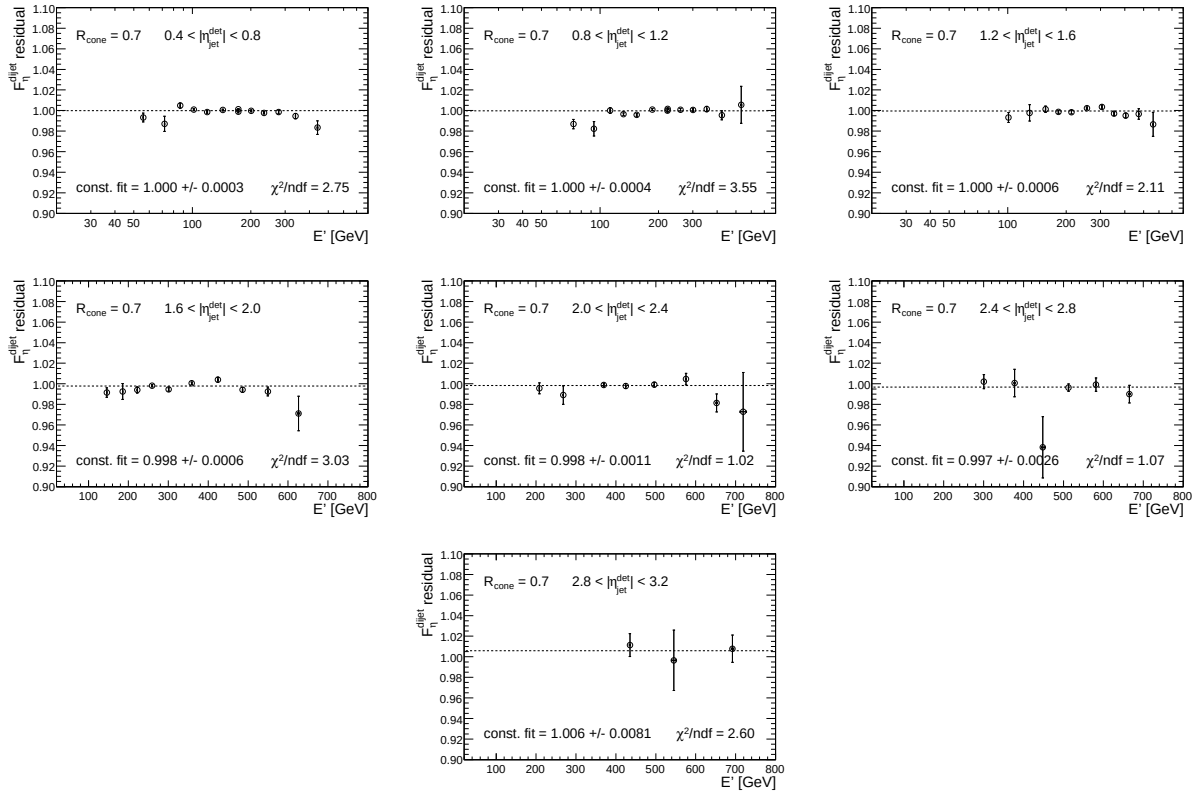

FIG. 141: Residuals of the relative MPF response corrections in dijet data for $\mathcal{R}_{\rm cone} = 0.7$ jets. Shown as a dashed line is the result of a constant fit to the measured closure observable as a function of E'.

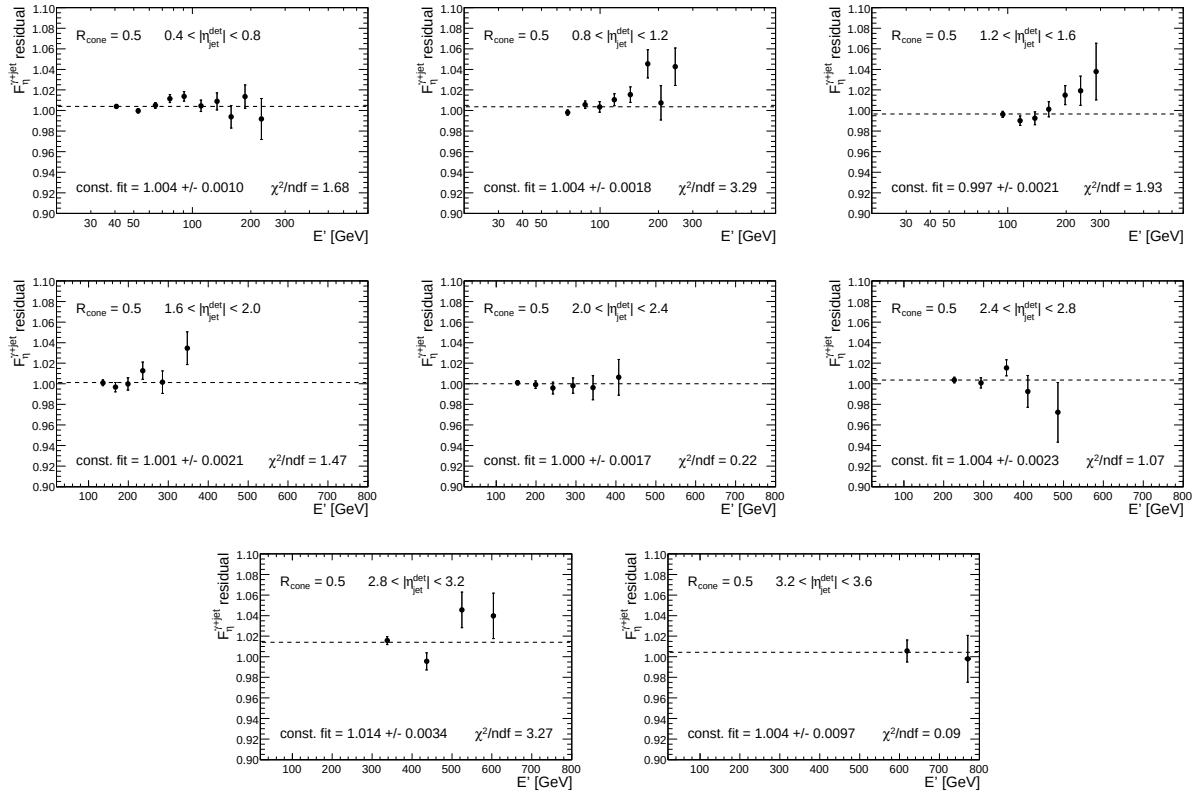

FIG. 142: Residuals of the relative MPF response corrections in γ+jet data for $\mathcal{R}_{\text{cone}} = 0.5$ jets. Shown as a dashed line is the result of a constant fit to the measured closure observable as a function of E'.

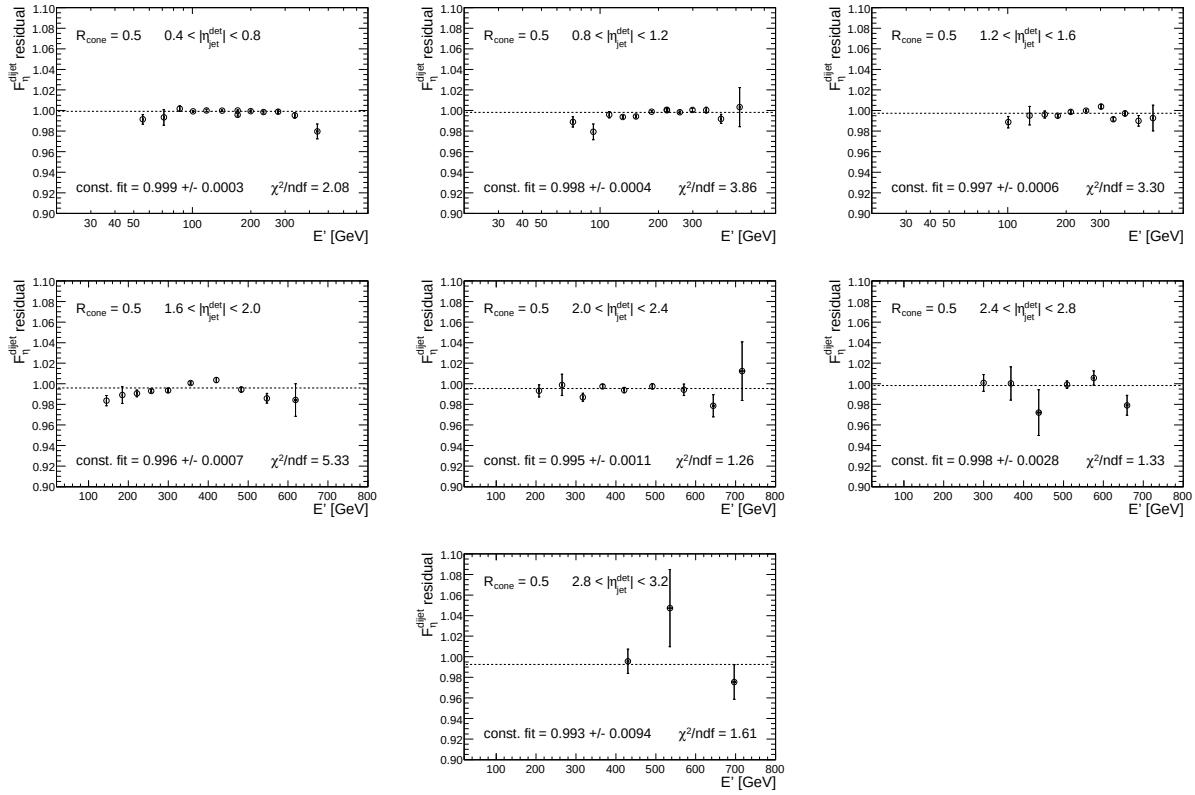

FIG. 143: Residuals of the relative MPF response corrections in dijet data for $\mathcal{R}_{\rm cone} = 0.5$ jets. Shown as a dashed line is the result of a constant fit to the measured closure observable as a function of E'.

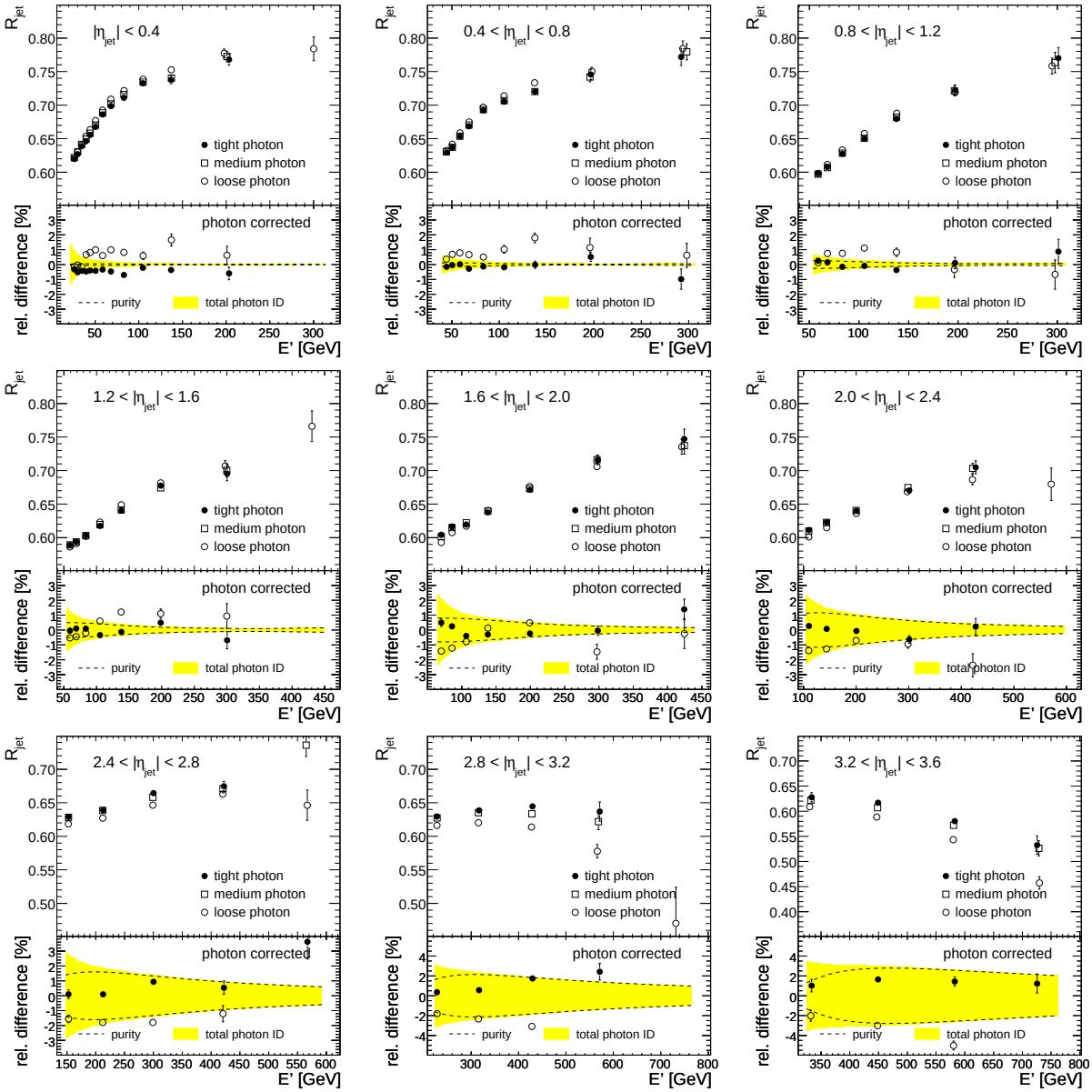

FIG. 144: Comparison between the corrected MPF response in γ+jet data for $\mathcal{R}_{\rm cone} = 0.7$ jets corresponding to loose, medium and tight photon criteria. The lower plots show the relative difference with respect to the medium criteria and the dashed lines illustrate the assigned systematic uncertainty. The shaded regions represent the asigned systematic error for the dijet background correction in case of tight photon selection. The dashed lines show the contribution to this error due to uncertainty on purity determination.

2. Relative MPF Response Correction in MC

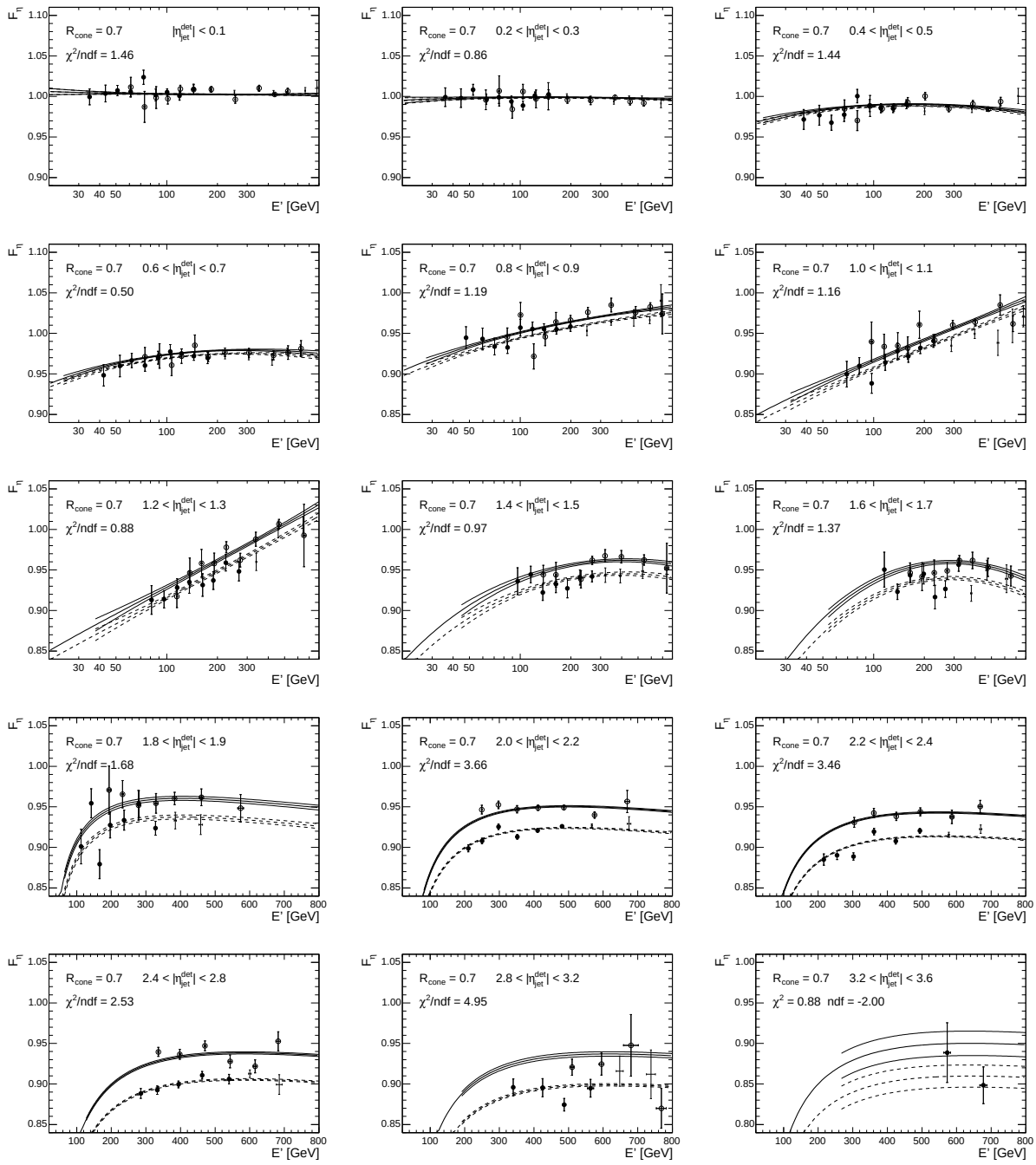

FIG. 145: Relative MPF response correction for $\mathcal{R}_{\rm cone} = 0.7$ jet in MC as a function of E' and for different $\eta^{\rm det}_{\rm jet}$ bins. The solid (open) circles represent the measurements in the γ+jet (dijet) sample. The lines shown represent the result from the global fit discussed in Sect. 9.2.6.

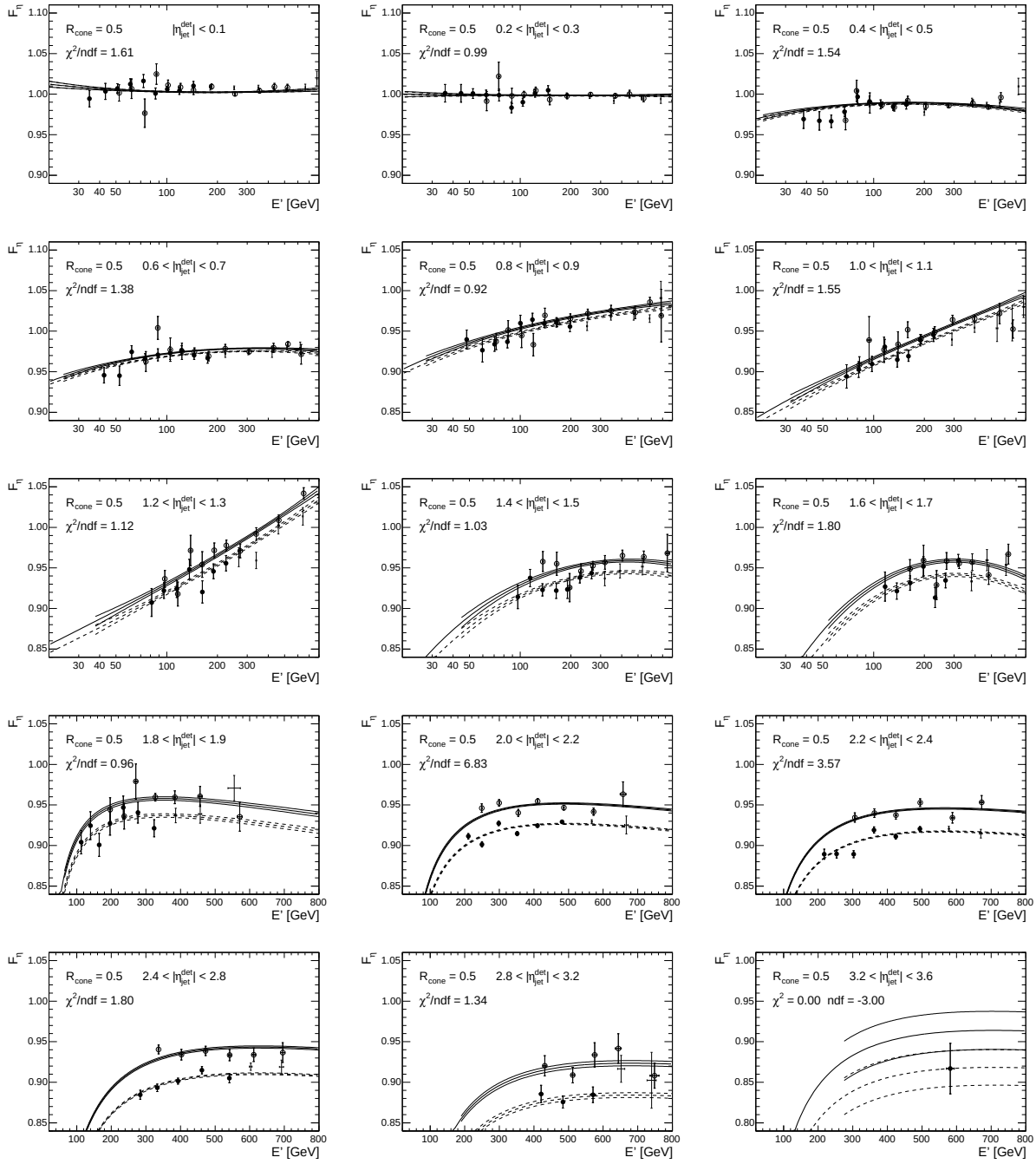

FIG. 146: Relative MPF response correction for $\mathcal{R}_{\rm cone} = 0.5$ jet in MC as a function of E' and for different $\eta_{\rm jet}^{\rm det}$ bins. The solid (open) circles represent the measurements in the γ+jet (dijet) sample. The lines shown represent the result from the global fit discussed in Sect. 9.2.6.

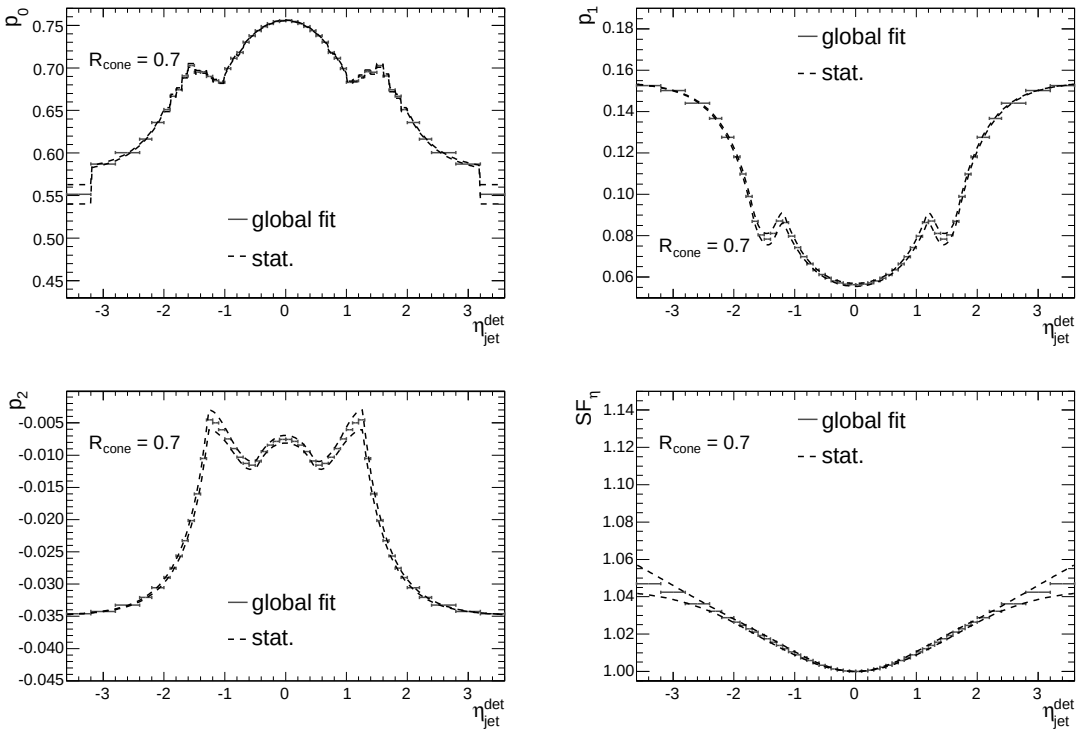

FIG. 147: Parameterizations for (p_0, p_1, p_2, SF_η) resulting from the global fit to the relative MPF response measurements in MC for $\mathcal{R}_{\rm cone} = 0.7$ jets. The dashed lines illustrate the statistical uncertainty band.

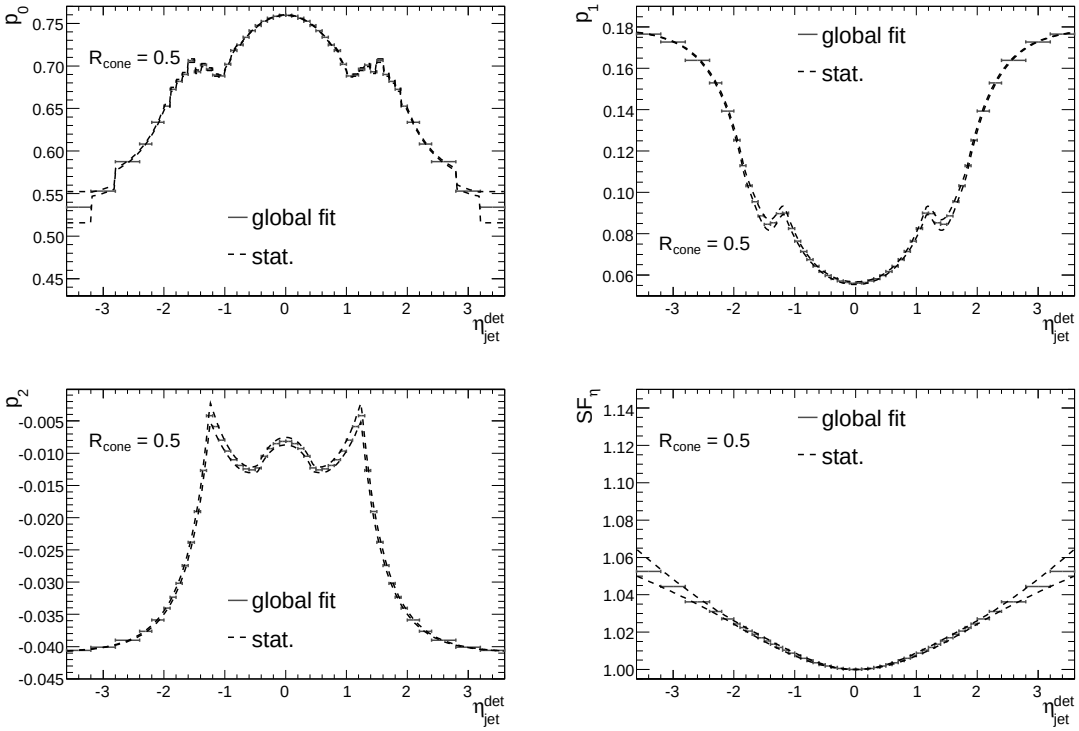

FIG. 148: Parameterizations for (p_0, p_1, p_2, SF_η) resulting from the global fit to the relative MPF response measurements in MC for $\mathcal{R}_{\rm cone} = 0.5$ jets. The dashed lines illustrate the statistical uncertainty band.

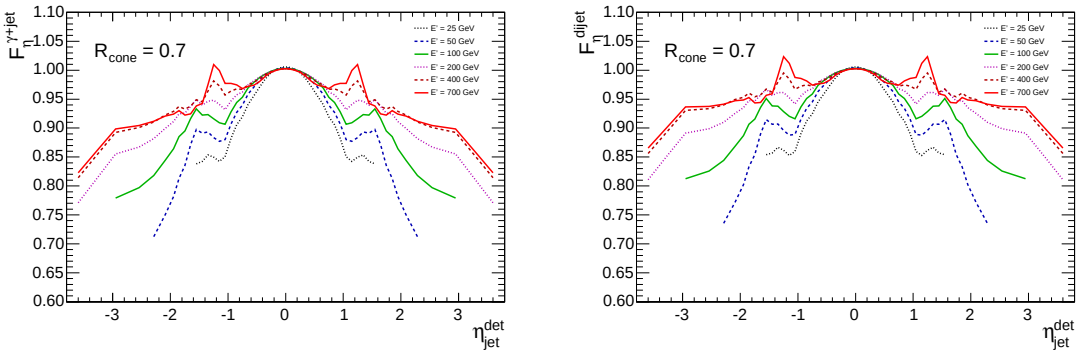

FIG. 149: Relative MPF response correction in MC for $\mathcal{R}_{\text{cone}} = 0.7$ jets as a function of $\eta_{\text{jet}}^{\text{det}}$ and separately for γ+jet (left) and dijet (right). The different lines correspond to particular values of E'.

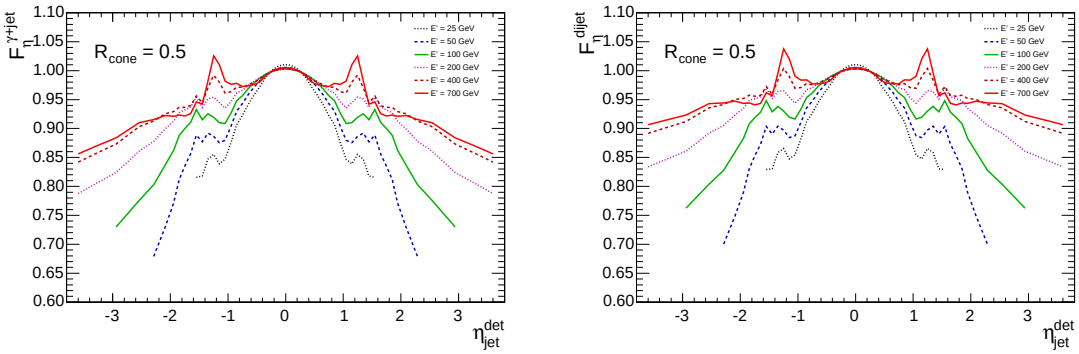

FIG. 150: Relative MPF response correction in MC for $\mathcal{R}_{\text{cone}} = 0.5$ jets as a function of $\eta_{\text{jet}}^{\text{det}}$ and separately for γ+jet (left) and dijet (right). The different lines correspond to particular values of E'.

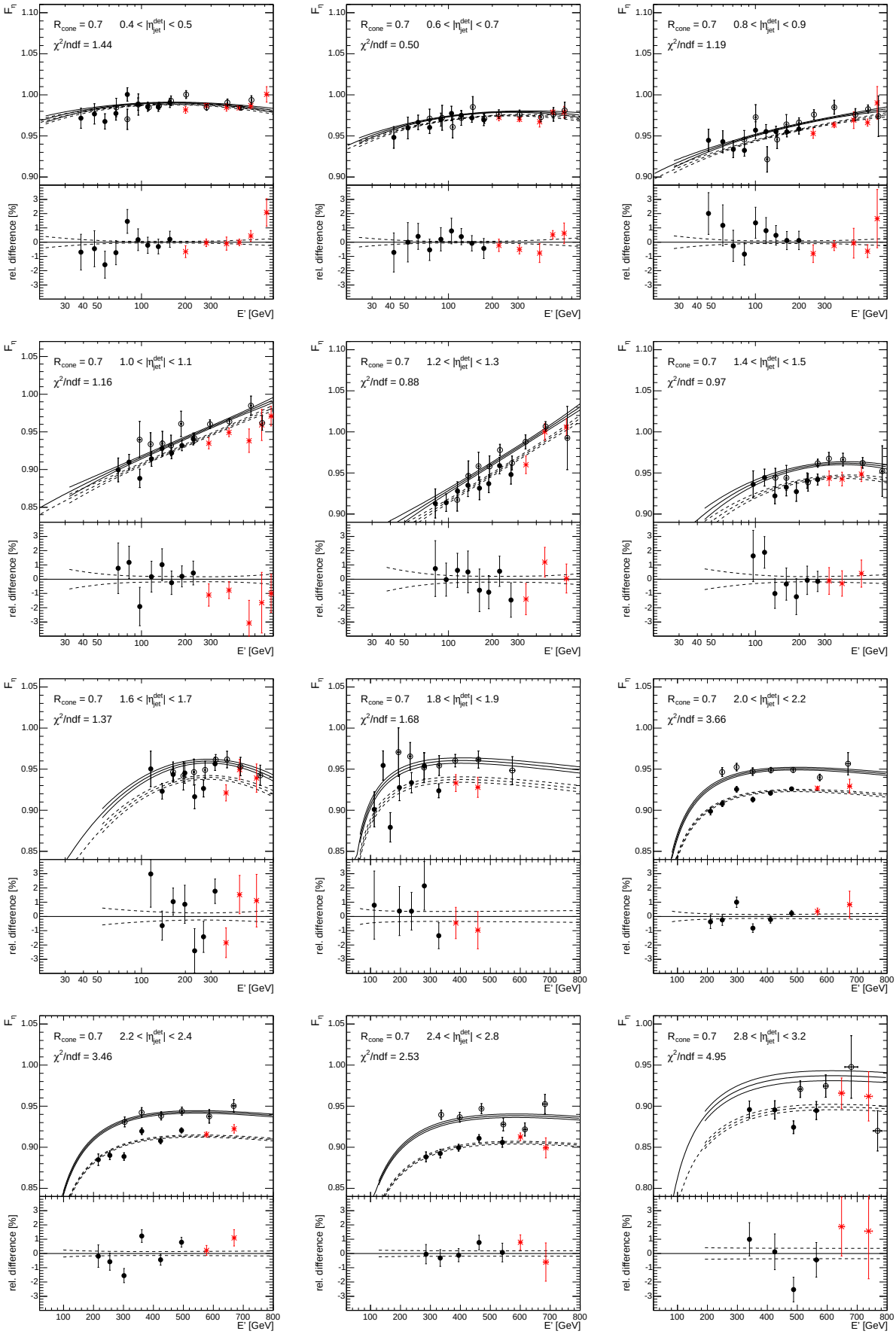

FIG. 151: Relative MPF response correction for $\mathcal{R}_{\rm cone} = 0.7$ jet in MC as a function of E' and for different $\eta_{\rm jet}^{\rm det}$ bins. The solid (open) circles represent the measurements in the γ+jet (dijet) sample used in the global fit (solid and dashed lines). The red stars correspond to the high-energy measurements in.the γ+jet sample not used in the global fit.

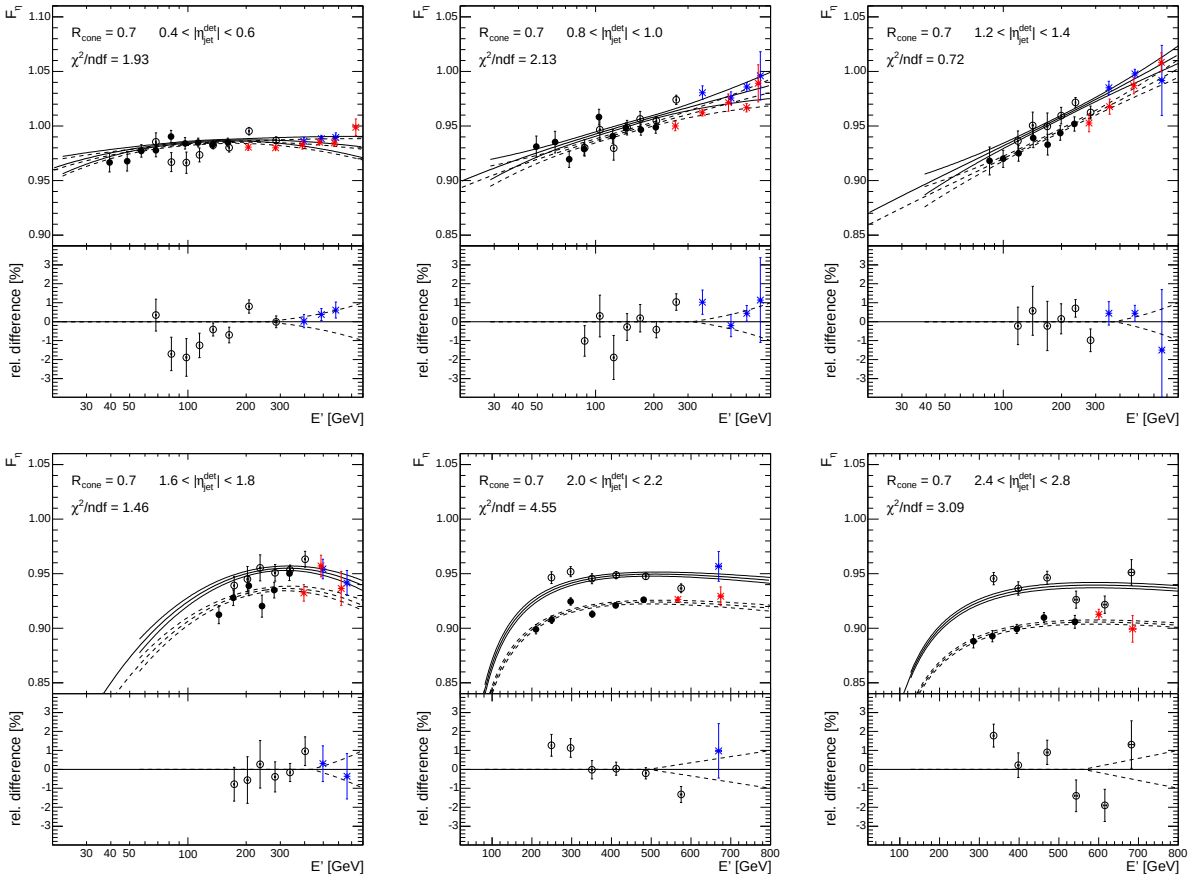

FIG. 152: Relative MPF response correction for $\mathcal{R}_{\rm cone} = 0.7$ jet in MC as a function of E' and for different $\eta_{\rm jet}^{\rm det}$ bins. The solid (open) circles represent the measurements in the γ+jet (dijet) sample used in the global fit (solid and dashed lines). The red (blue) stars correspond to the high-energy measurements in.the γ+jet (dijet) sample not used in the global fit. The lower plots present the relative difference between the relative MPF response prediction and actual measurements for dijets, along with the assigned systematic uncertainty for high-energy extrapolation (dashed lines).

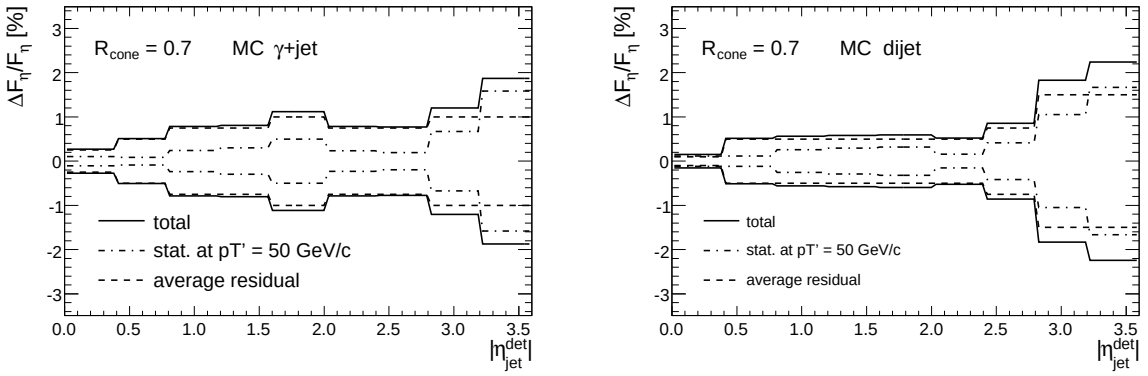

FIG. 153: Uncertainties on the relative MPF response correction in MC for $\mathcal{R}_{\rm cone} = 0.7$ jets, as a function of $|\eta_{\rm jet}^{\rm det}|$ and separately for γ+jet (left) and dijet (right). The solid line shows the total uncertainty, resulting from the sum in quadrature of the individual contributions: statistical (dashed-dotted) and average residual (dashed).

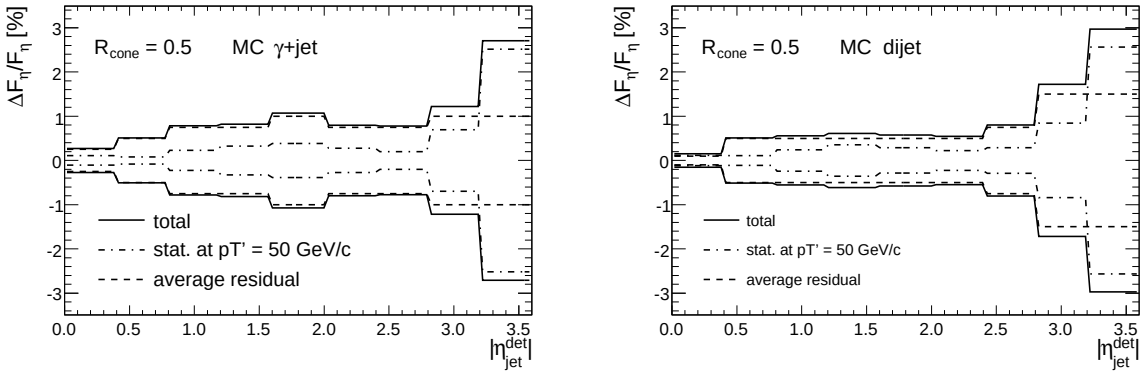

FIG. 154: Uncertainties on the relative MPF response correction in MC for $\mathcal{R}_{\rm cone} = 0.5$ jets, as a function of $|\eta^{\rm det}_{\rm jet}|$ and separately for γ+jet (left) and dijet (right). The solid line shows the total uncertainty, resulting from the sum in quadrature of the individual contributions: statistical (dashed-dotted) and average residual (dashed).

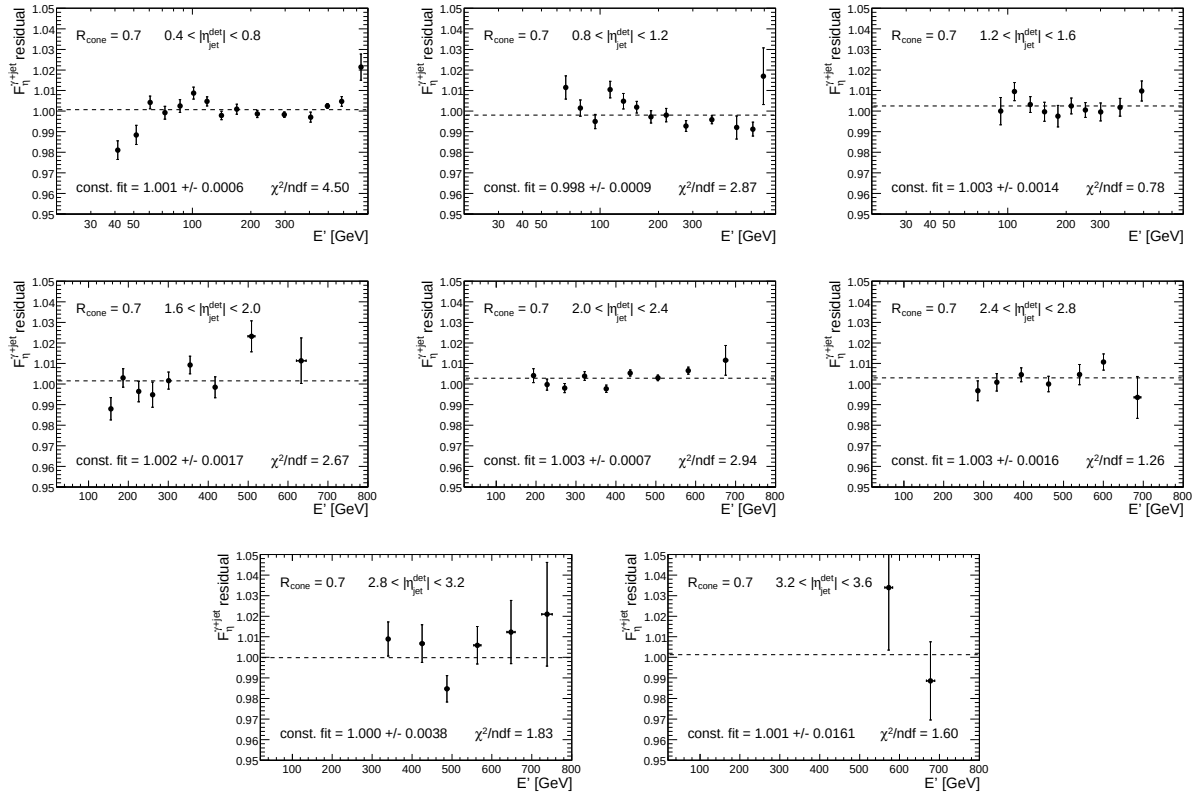

FIG. 155: Residuals of the relative MPF response corrections in γ+jet MC for $\mathcal{R}_{\rm cone} = 0.7$ jets. Shown as a dashed line is the result of a constant fit to the measured closure observable as a function of E'.

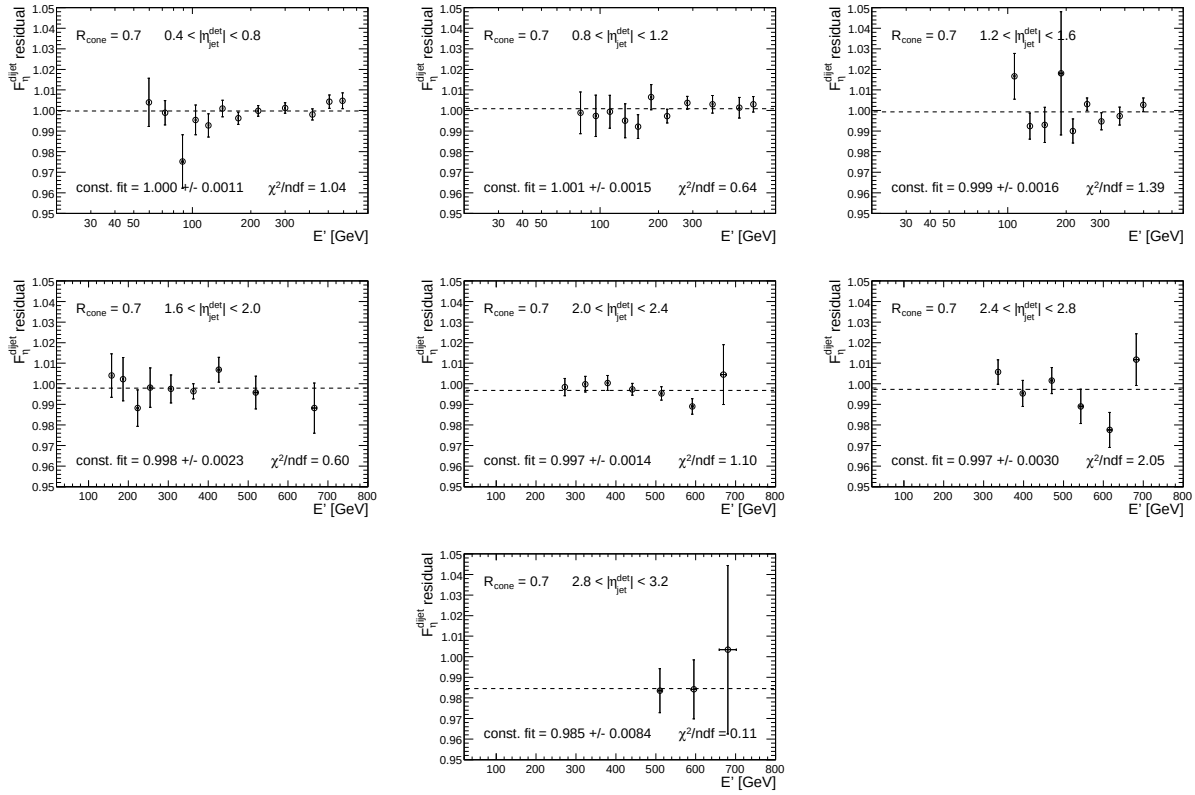

FIG. 156: Residuals of the relative MPF response corrections in dijet MC for $\mathcal{R}_{\rm cone} = 0.7$ jets. Shown as a dashed line is the result of a constant fit to the measured closure observable as a function of E'.

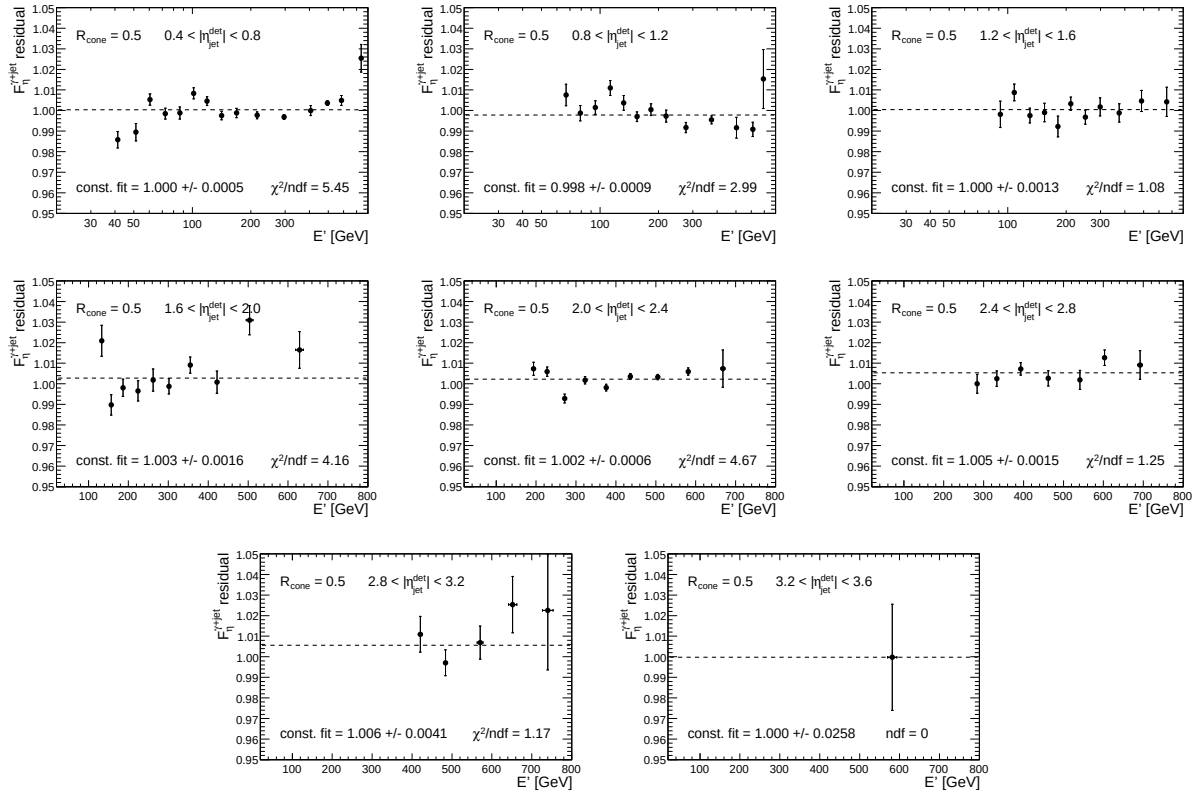

FIG. 157: Residuals of the relative MPF response corrections in γ+jet MC for $\mathcal{R}_{\rm cone} = 0.5$ jets. Shown as a dashed line is the result of a constant fit to the measured closure observable as a function of E'.

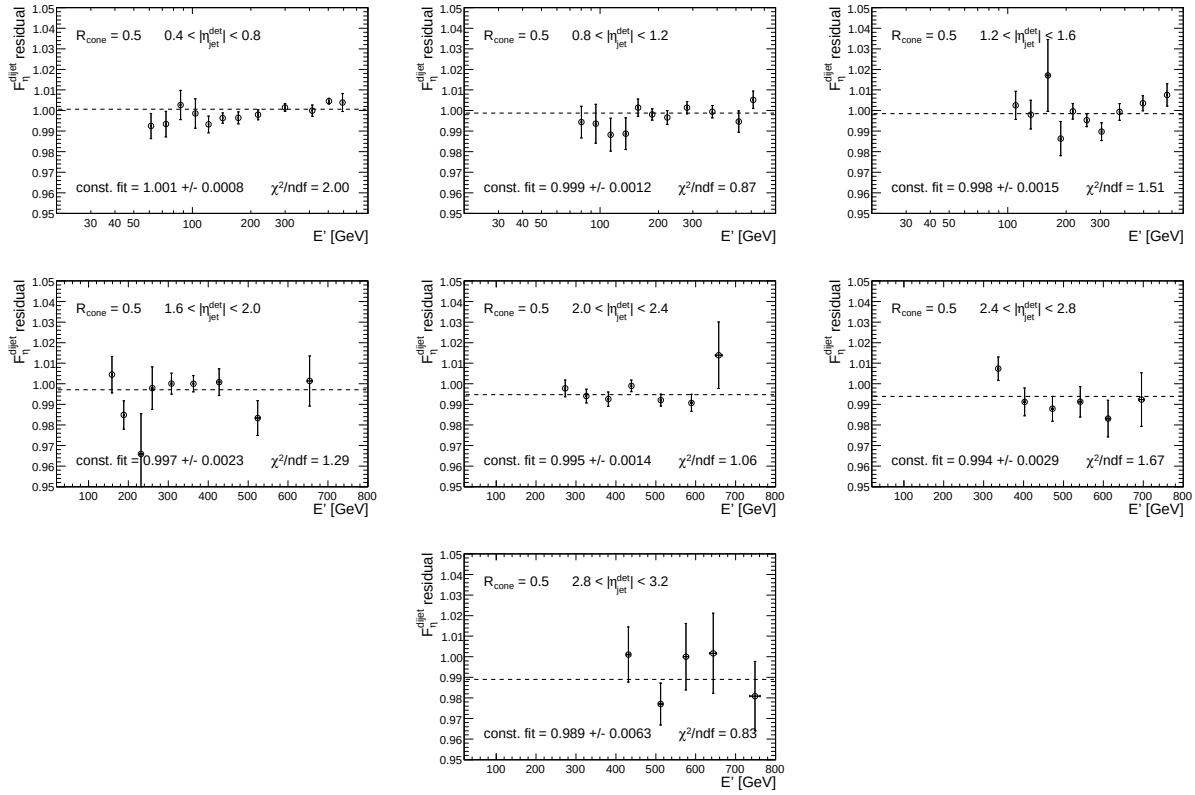

FIG. 158: Residuals of the relative MPF response corrections in dijet MC for $\mathcal{R}_{\rm cone} = 0.5$ jets. Shown as a dashed line is the result of a constant fit to the measured closure observable as a function of E'.

APPENDIX F: MPF RESPONSE BIAS CORRECTIONS

1. Zero-Suppression Bias Correction

(CAVEAT: plots on the $k_{\mathrm{R}}^{\mathrm{ZS}}$ correction factor for the unsuppressed ZB overlay case have not been updated yet.)

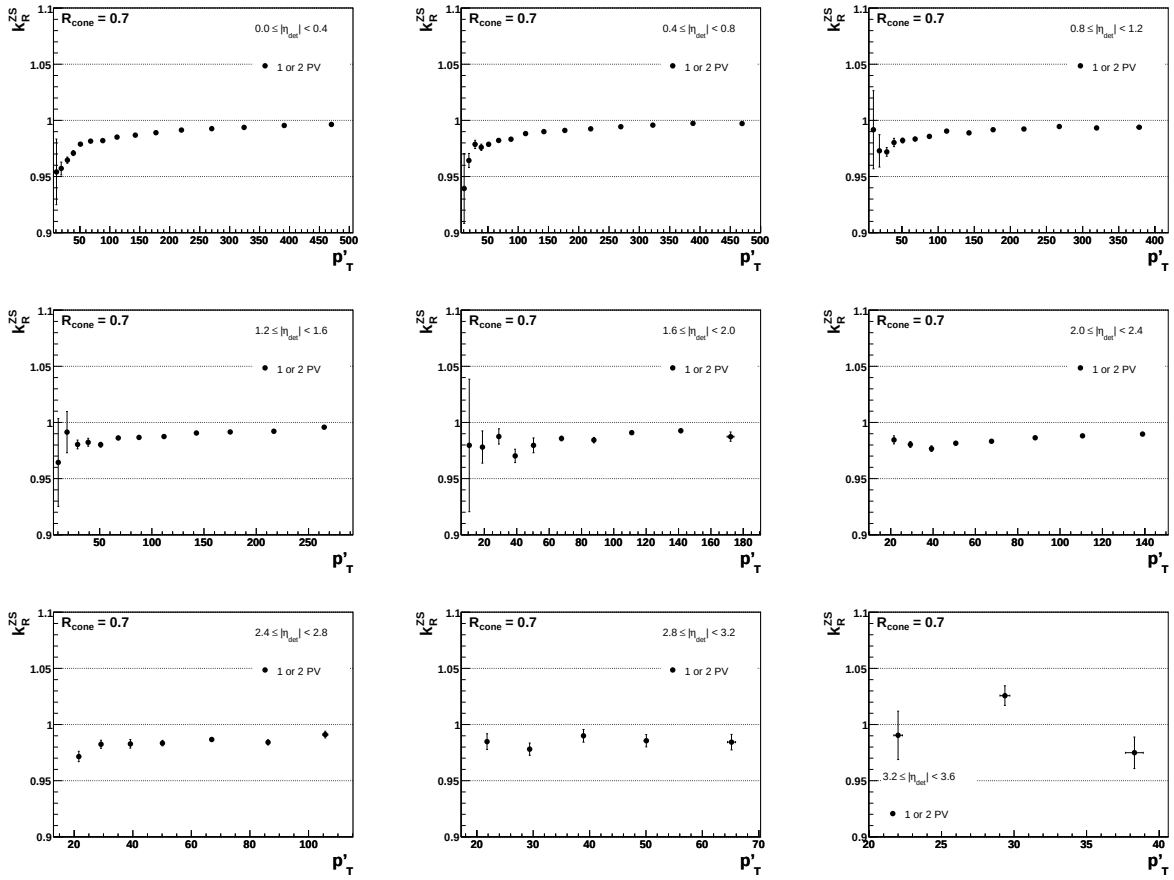

FIG. 159: $k_{\mathrm{R}}^{\mathrm{ZS}}$ correction factor vs p'_T for $\mathcal{R}_{\mathrm{cone}} = 0.7$ jets in the suppressed ZB overlay case. Different plots correspond to different $\left|\eta_{\mathrm{jet}}^{\mathrm{det}}\right|$ bins.

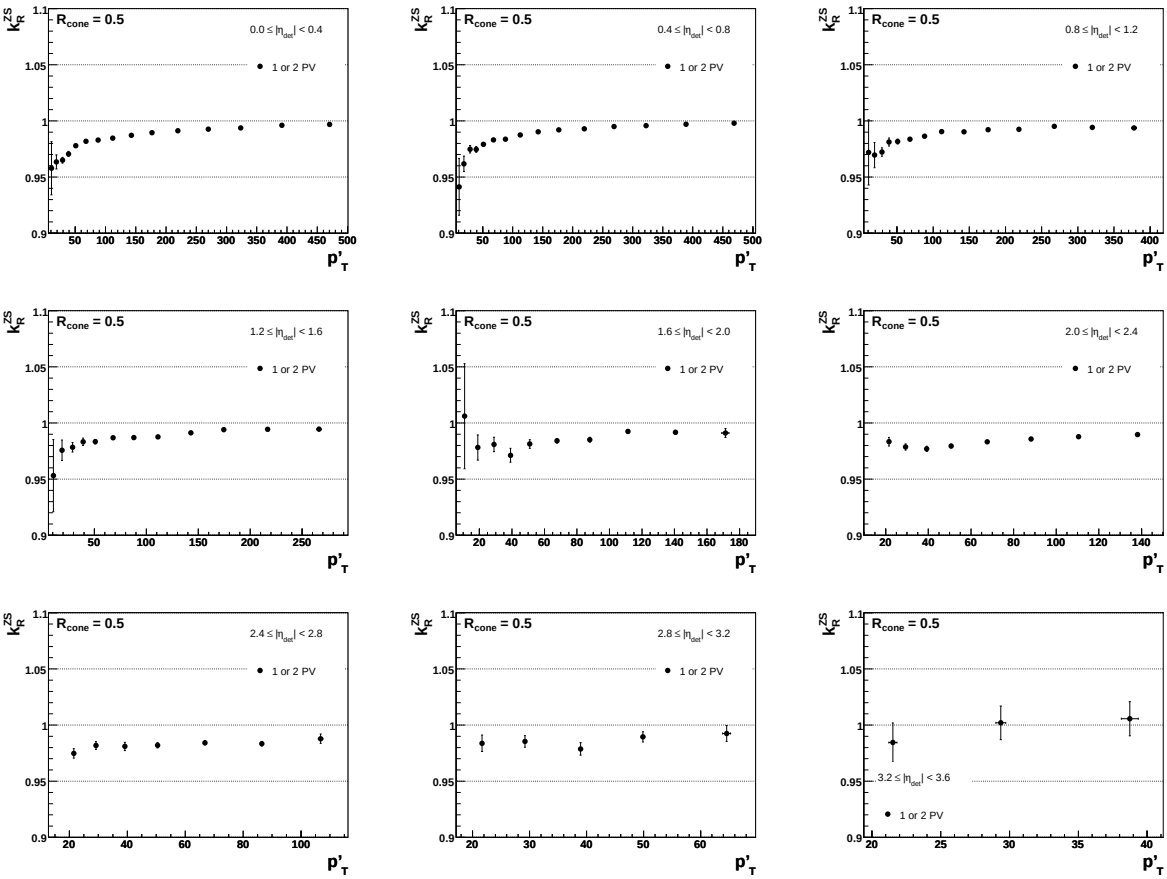

FIG. 160: $k_{\mathrm{R}}^{\mathrm{ZS}}$ correction factor vs p'_T for $\mathcal{R}_{\mathrm{cone}} = 0.5$ jets in the suppressed ZB overlay case. Different plots correspond to different $\left|\eta_{\mathrm{jet}}^{\mathrm{det}}\right|$ bins.

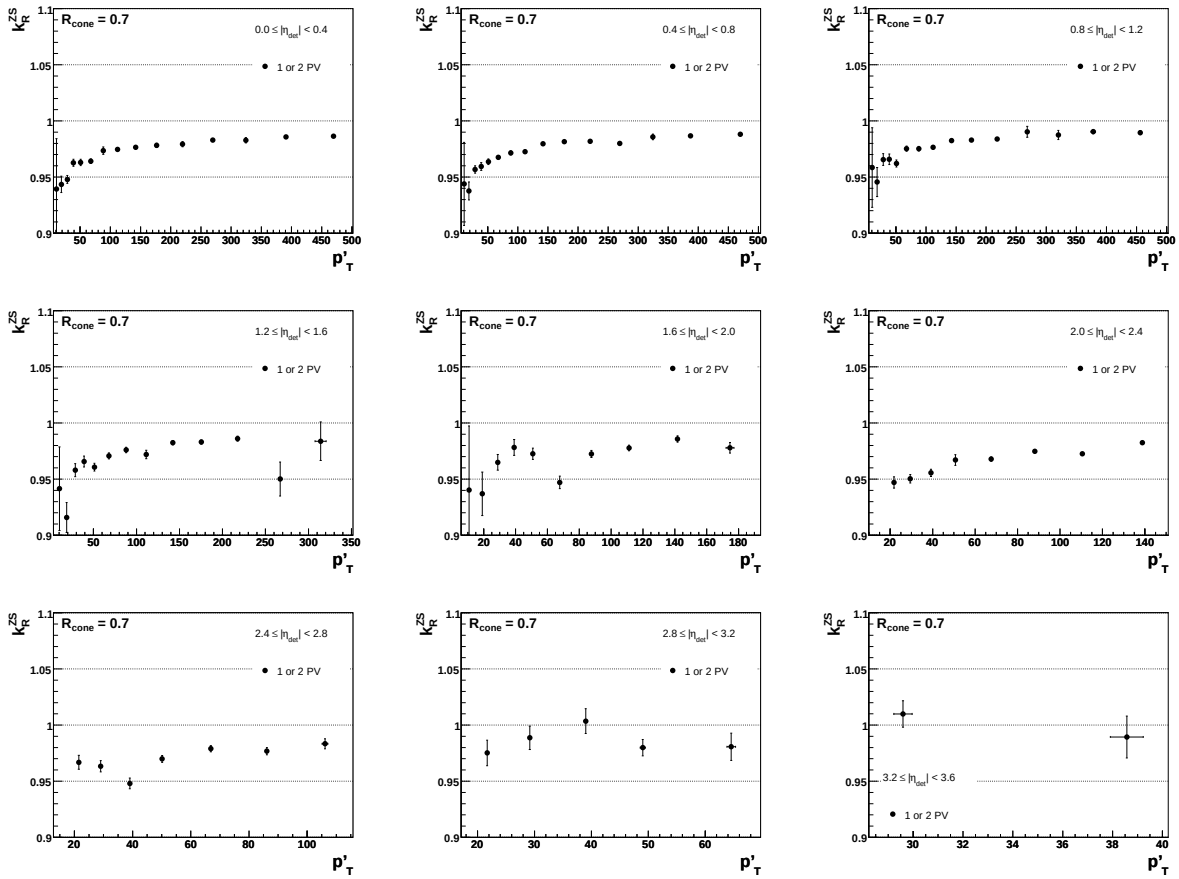

FIG. 161: $k_{\mathrm{R}}^{\mathrm{ZS}}$ correction factor vs p'_T for $\mathcal{R}_{\mathrm{cone}} = 0.7$ jets in the unsuppressed ZB overlay case. Different plots correspond to different $\left|\eta_{\mathrm{jet}}^{\mathrm{det}}\right|$ bins.

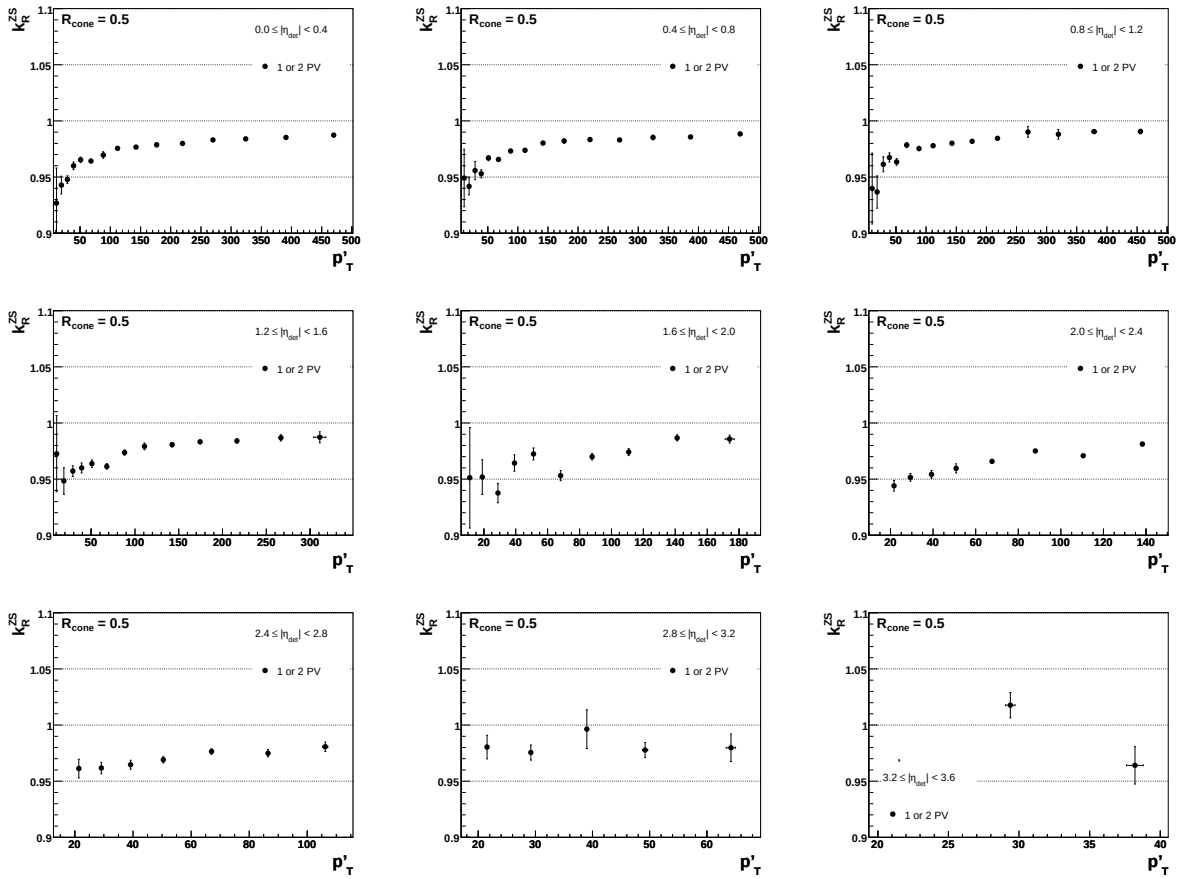

FIG. 162: $k_{\mathrm{R}}^{\mathrm{ZS}}$ correction factor vs p'_T for $\mathcal{R}_{\mathrm{cone}} = 0.5$ jets in the unsuppressed ZB overlay case. Different plots correspond to different $\left|\eta_{\mathrm{jet}}^{\mathrm{det}}\right|$ bins.

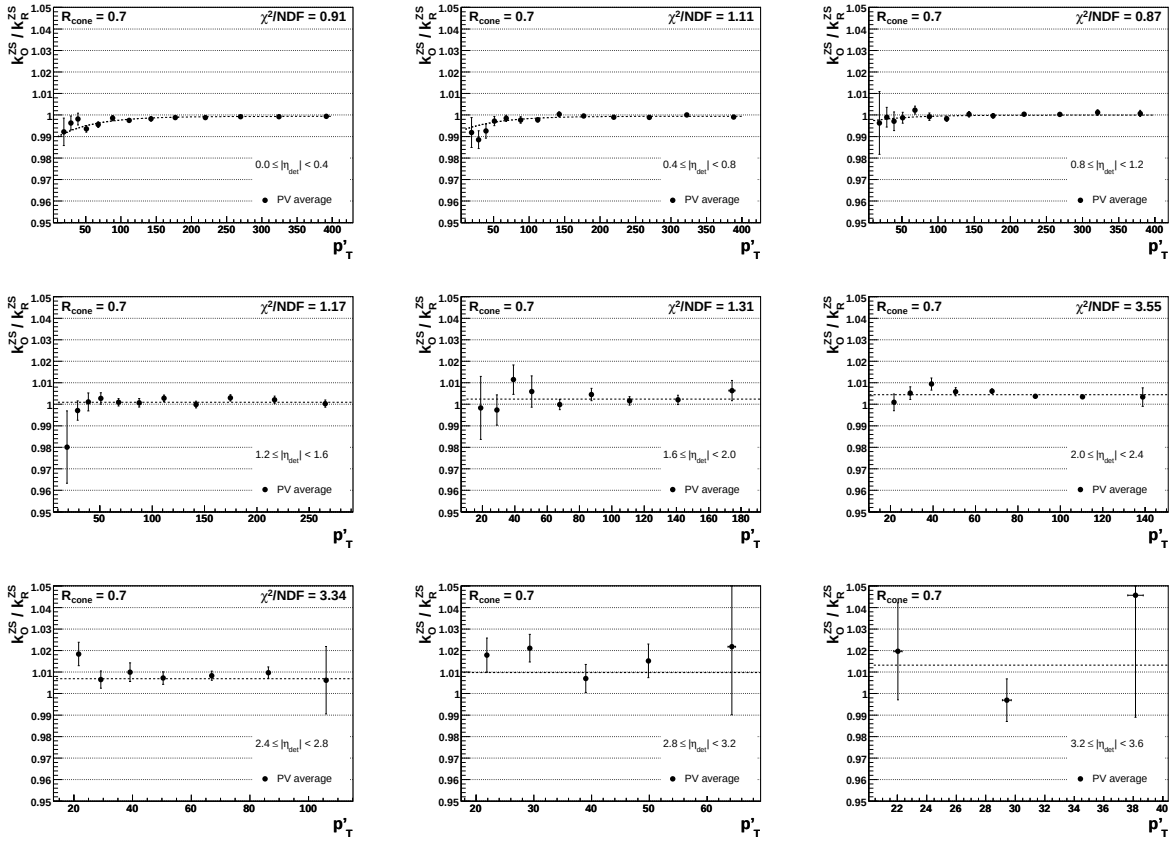

FIG. 163: $k_{\mathrm{O}}^{\mathrm{ZS}}/k_{\mathrm{R}}^{\mathrm{ZS}}$ correction factor vs p'_T for $\mathcal{R}_{\mathrm{cone}} = 0.7$ jets in the suppressed ZB overlay case. Different plots correspond to different $\left|\eta_{\mathrm{jet}}^{\mathrm{det}}\right|$ bins.

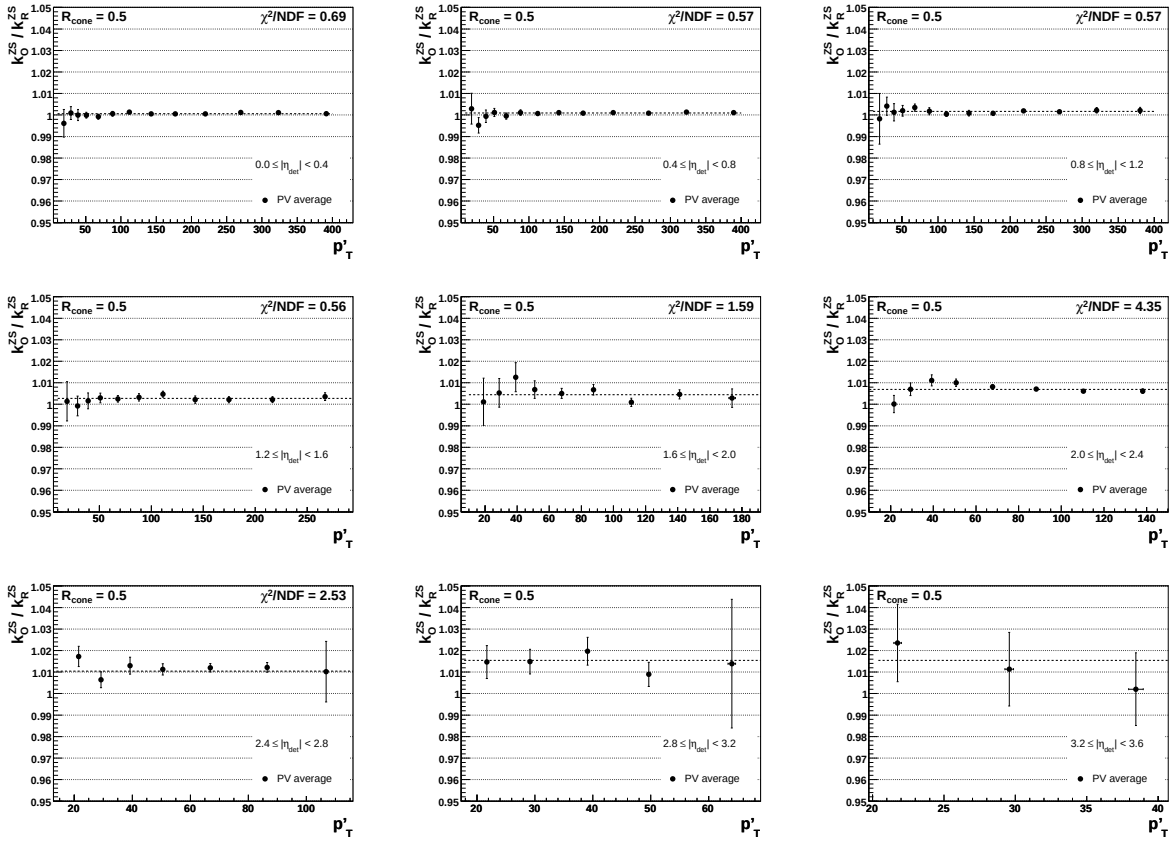

FIG. 164: $k_{\mathrm{O}}^{\mathrm{ZS}}/k_{\mathrm{R}}^{\mathrm{ZS}}$ correction factor vs p'_T for $\mathcal{R}_{\mathrm{cone}} = 0.5$ jets in the suppressed ZB overlay case. Different plots correspond to different $\left|\eta_{\mathrm{jet}}^{\mathrm{det}}\right|$ bins.

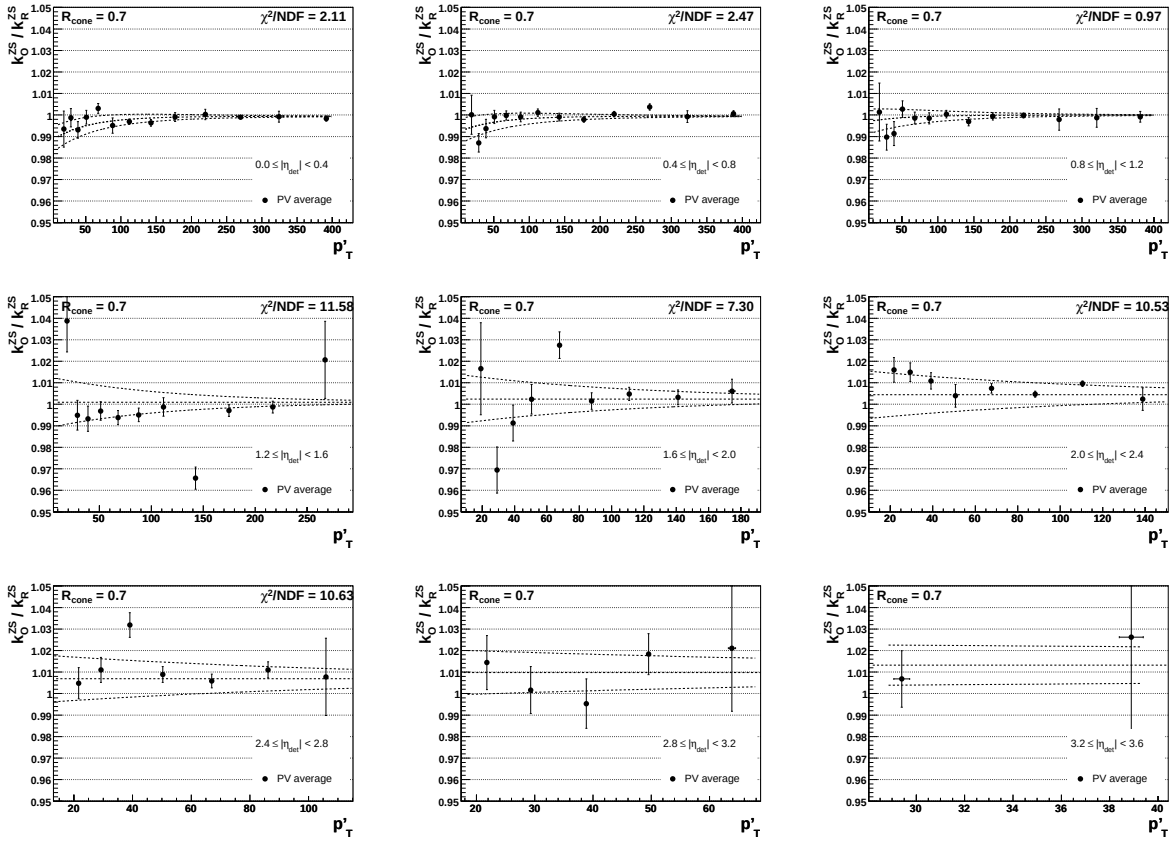

FIG. 165: $k_{\mathrm{O}}^{\mathrm{ZS}}/k_{\mathrm{R}}^{\mathrm{ZS}}$ correction factor vs p'_T for $\mathcal{R}_{\mathrm{cone}} = 0.7$ jets in the unsuppressed ZB overlay case. Different plots correspond to different $\left|\eta_{\mathrm{jet}}^{\mathrm{det}}\right|$ bins.The central dashed line shown represents the suppressed ZB overlay fit, and the two outer dashed lines represent the systematic uncertainty assigned due to the fact of using the suppressed ZB overlay fit.

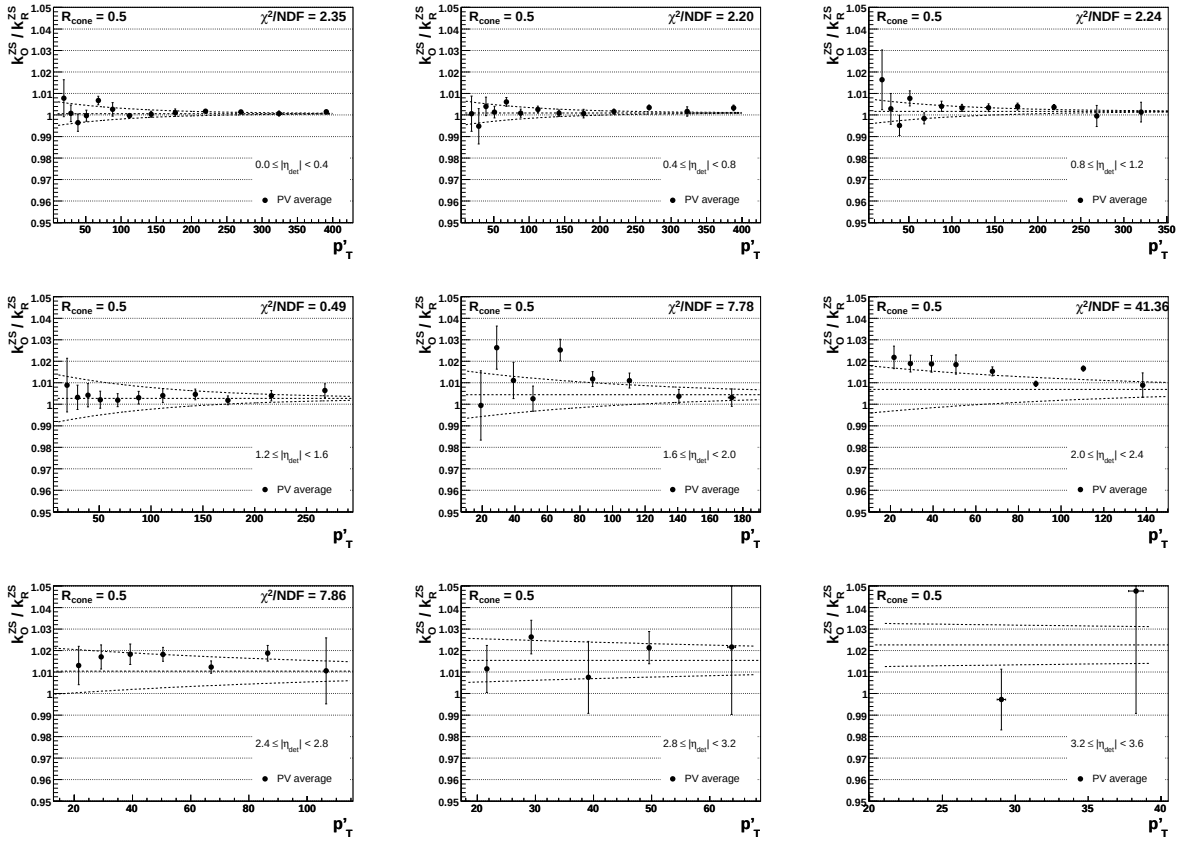

FIG. 166: $k_{\mathrm{O}}^{\mathrm{ZS}}/k_{\mathrm{R}}^{\mathrm{ZS}}$ correction factor vs p'_T for $\mathcal{R}_{\mathrm{cone}} = 0.5$ jets in the unsuppressed ZB overlay case. Different plots correspond to different $\left|\eta_{\mathrm{jet}}^{\mathrm{det}}\right|$ bins.The central dashed line shown represents the suppressed ZB overlay fit, and the two outer dashed lines represent the systematic uncertainty assigned due to the fact of using the suppressed ZB overlay fit.

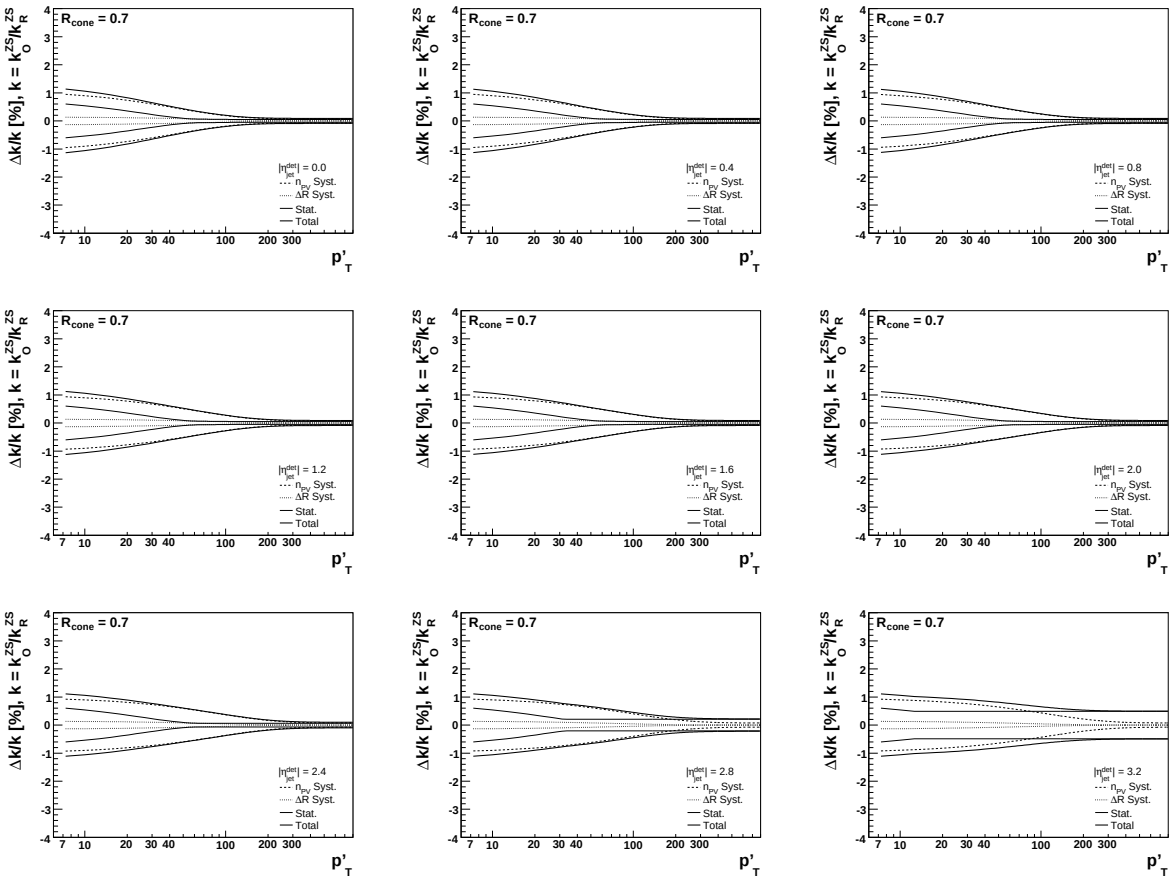

FIG. 167: Relative uncertainties on the $k_{\mathrm{O}}^{\mathrm{ZS}}/k_{\mathrm{R}}^{\mathrm{ZS}}$ correction factor vs p'_T for $\mathcal{R}_{\mathrm{cone}} = 0.7$ jets in the suppressed ZB overlay case. Different plots correspond to different values of $\eta_{\mathrm{jet}}^{\mathrm{det}}$.

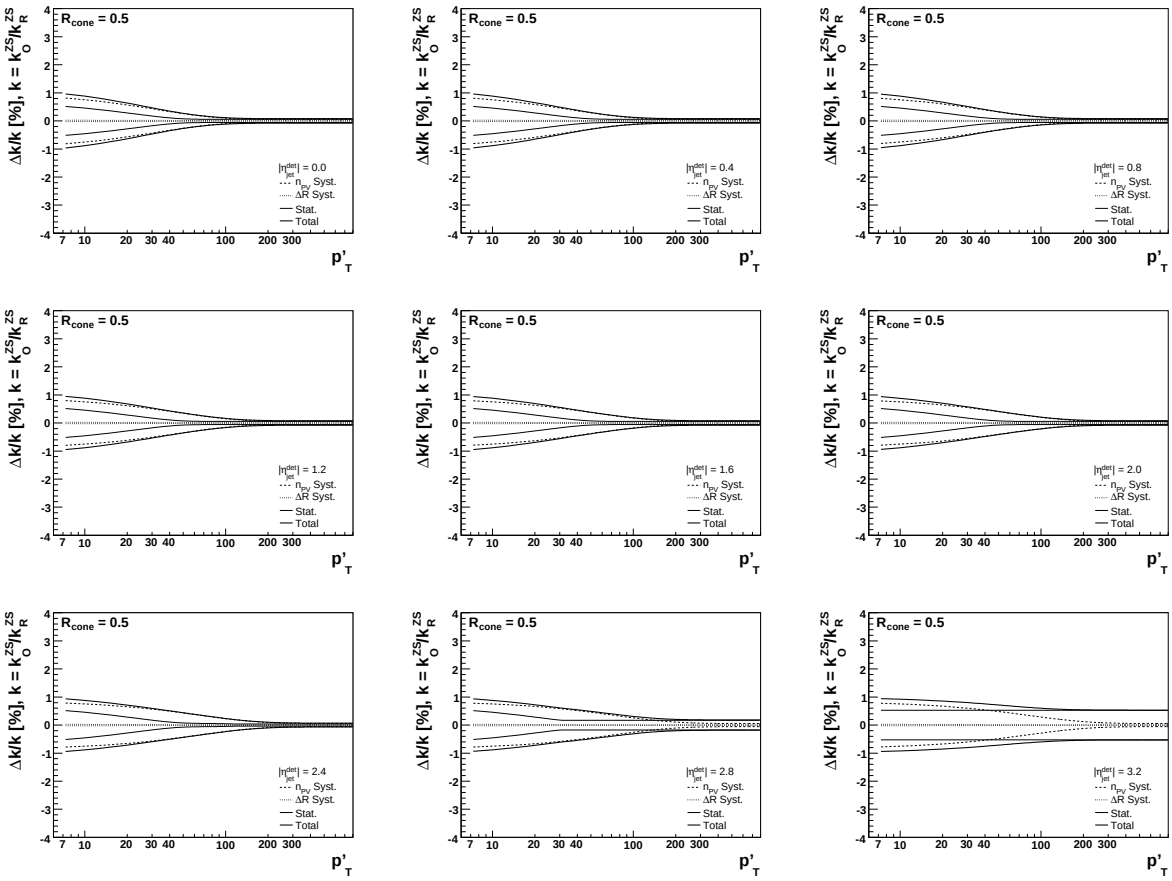

FIG. 168: Relative uncertainties on the $k_{\mathrm{O}}^{\mathrm{ZS}}/k_{\mathrm{R}}^{\mathrm{ZS}}$ correction factor vs p'_T for $\mathcal{R}_{\mathrm{cone}} = 0.5$ jets in the suppressed ZB overlay case. Different plots correspond to different values of $\eta_{\mathrm{jet}}^{\mathrm{det}}$.

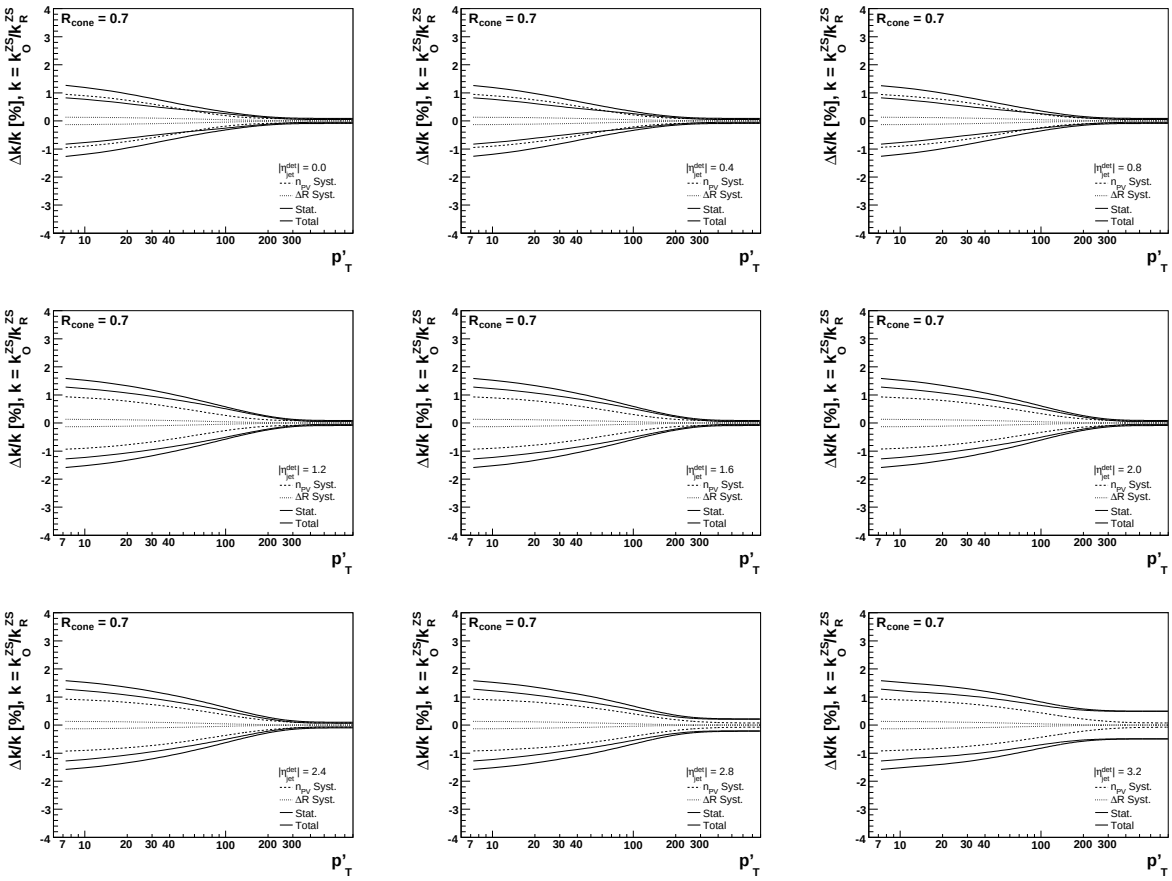

FIG. 169: Relative uncertainties on the $k_{\mathrm{O}}^{\mathrm{ZS}}/k_{\mathrm{R}}^{\mathrm{ZS}}$ correction factor vs p'_T for $\mathcal{R}_{\mathrm{cone}} = 0.7$ jets in the unsuppressed ZB overlay case. Different plots correspond to different values of $\eta_{\mathrm{jet}}^{\mathrm{det}}$.

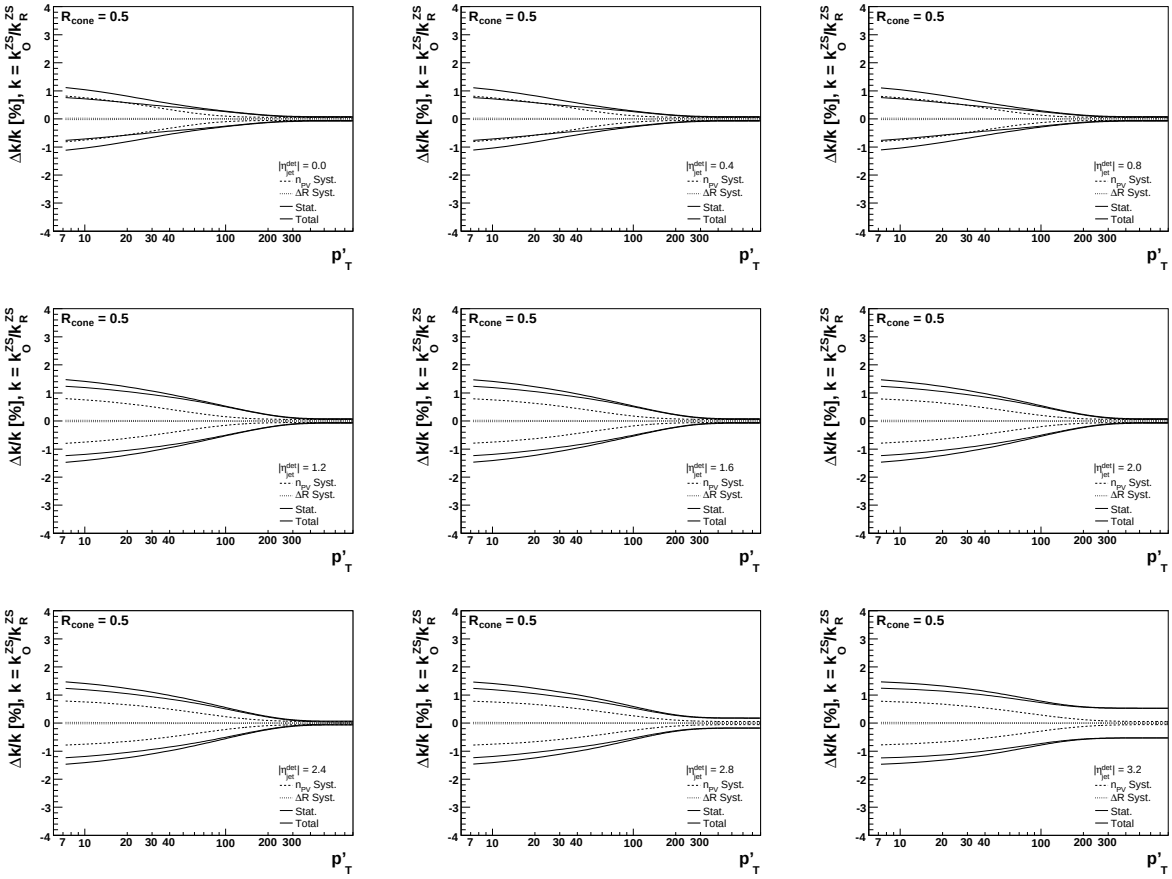

FIG. 170: Relative uncertainties on the $k_{\mathrm{O}}^{\mathrm{ZS}}/k_{\mathrm{R}}^{\mathrm{ZS}}$ correction factor vs p'_T for $\mathcal{R}_{\mathrm{cone}} = 0.5$ jets in the unsuppressed ZB overlay case. Different plots correspond to different values of $\eta_{\mathrm{jet}}^{\mathrm{det}}$.

2. Topology Bias Correction

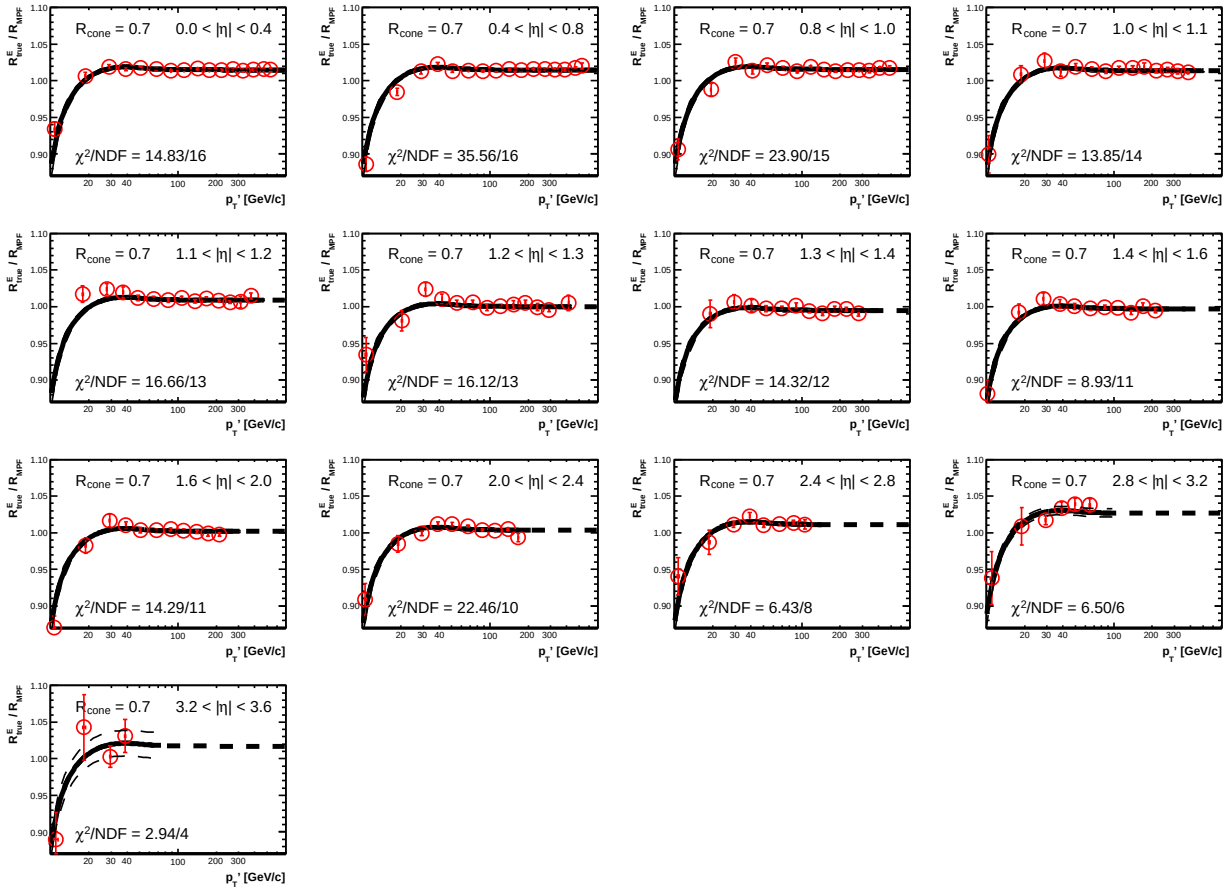

FIG. 171: Topology bias correction for $\mathcal{R}_{\rm cone} = 0.7$ jets.

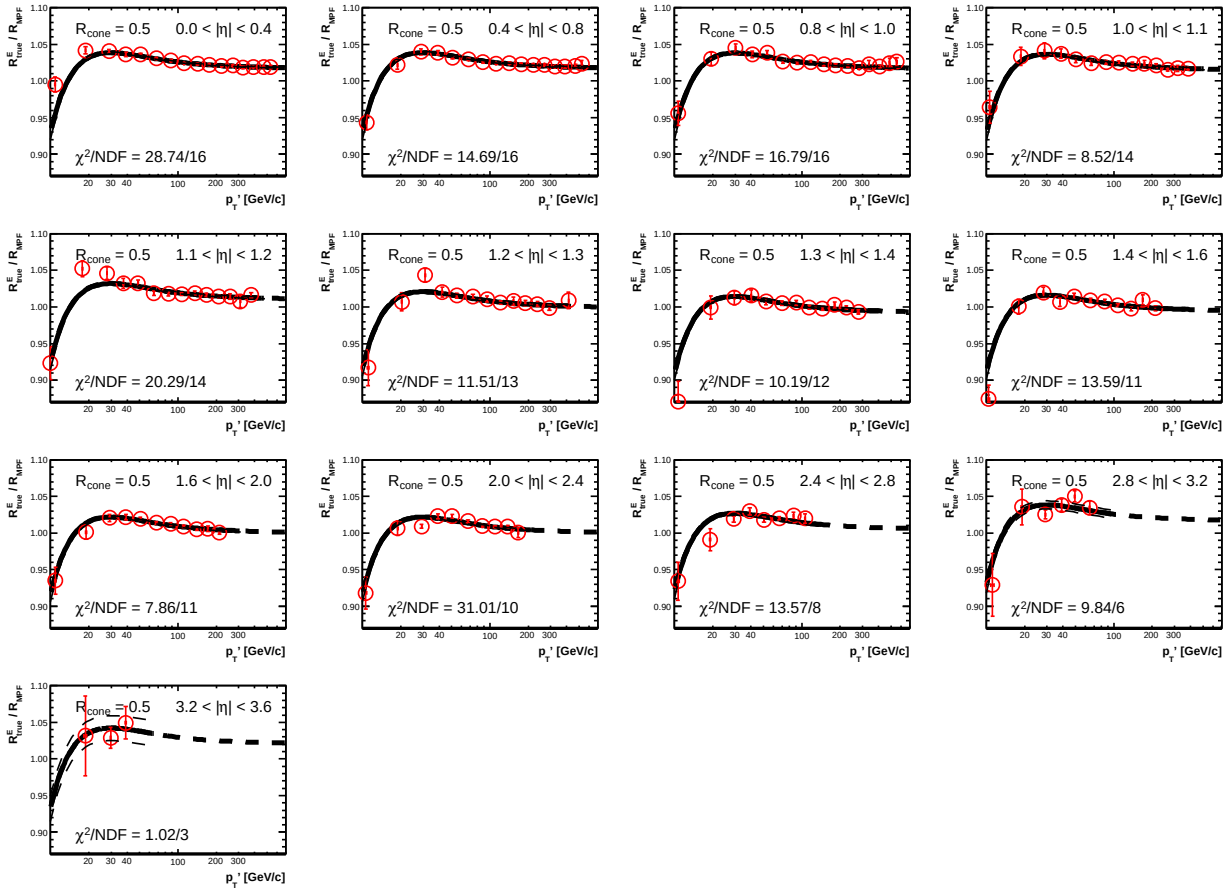

FIG. 172: Topology bias correction for $\mathcal{R}_{\rm cone} = 0.5$ jets.

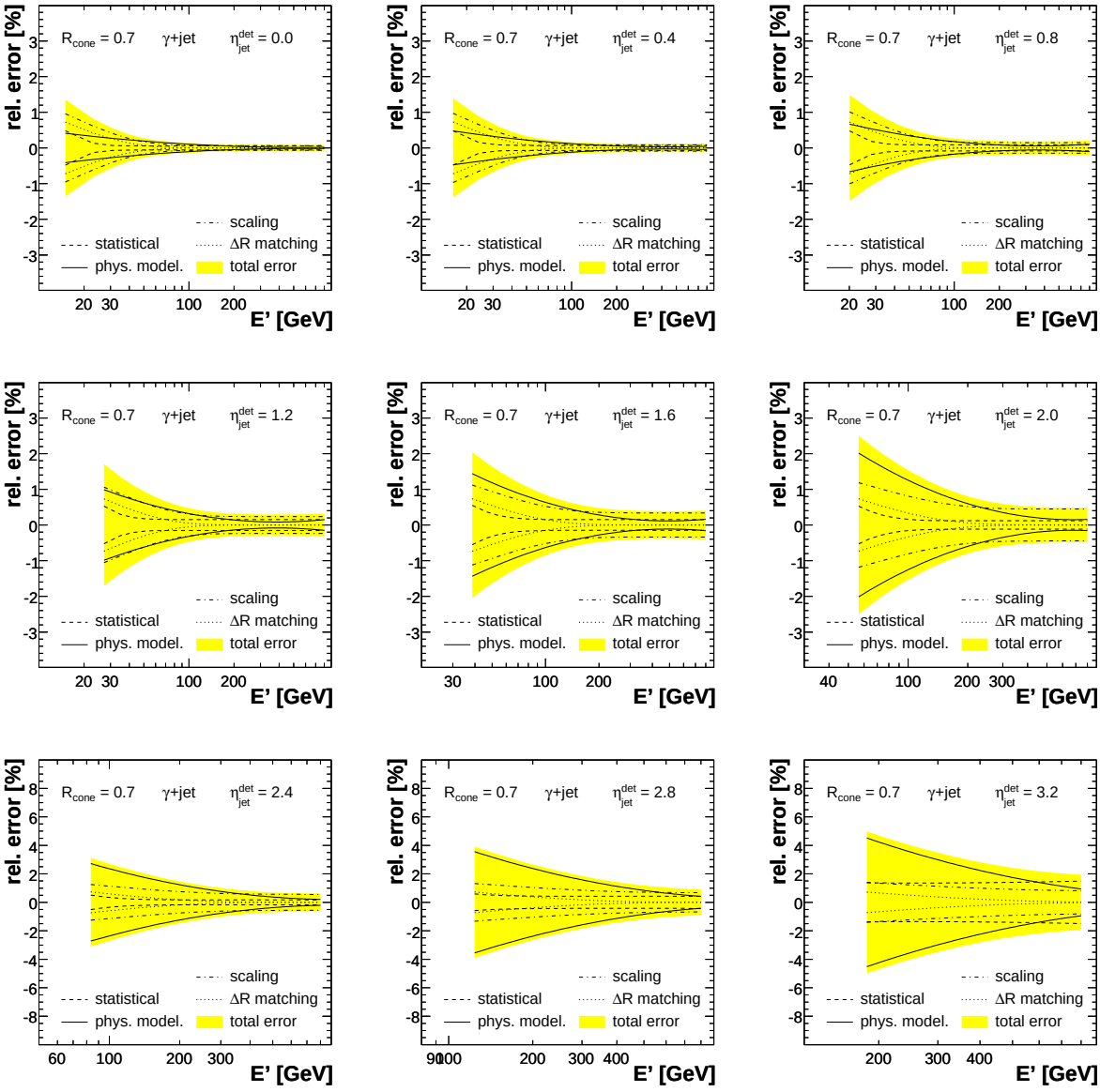

FIG. 173: Relative uncertainties on the $k_{\mathrm{R}}^{\mathrm{topo}}$ correction factor vs p'_T for $\mathcal{R}_{\mathrm{cone}} = 0.7$ jets. Different plots correspond to different values of $\eta_{\mathrm{jet}}^{\mathrm{det}}$.

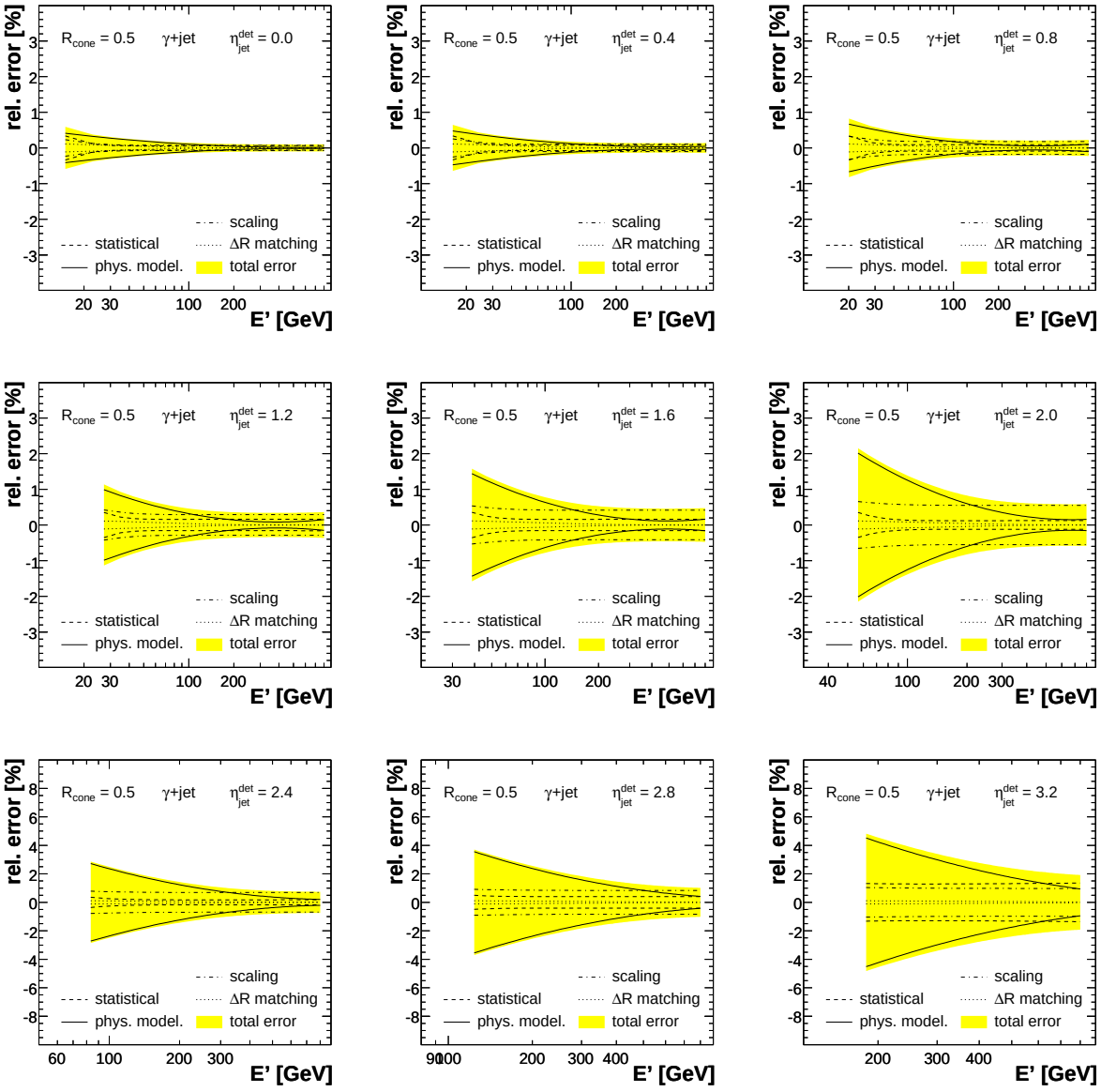

FIG. 174: Relative uncertainties on the $k_{\mathrm{R}}^{\mathrm{topo}}$ correction factor vs p'_T for $\mathcal{R}_{\mathrm{cone}} = 0.5$ jets. Different plots correspond to different values of $\eta_{\mathrm{jet}}^{\mathrm{det}}$.

a. *Systematic Uncertainty from Single Pion Response Scaling*

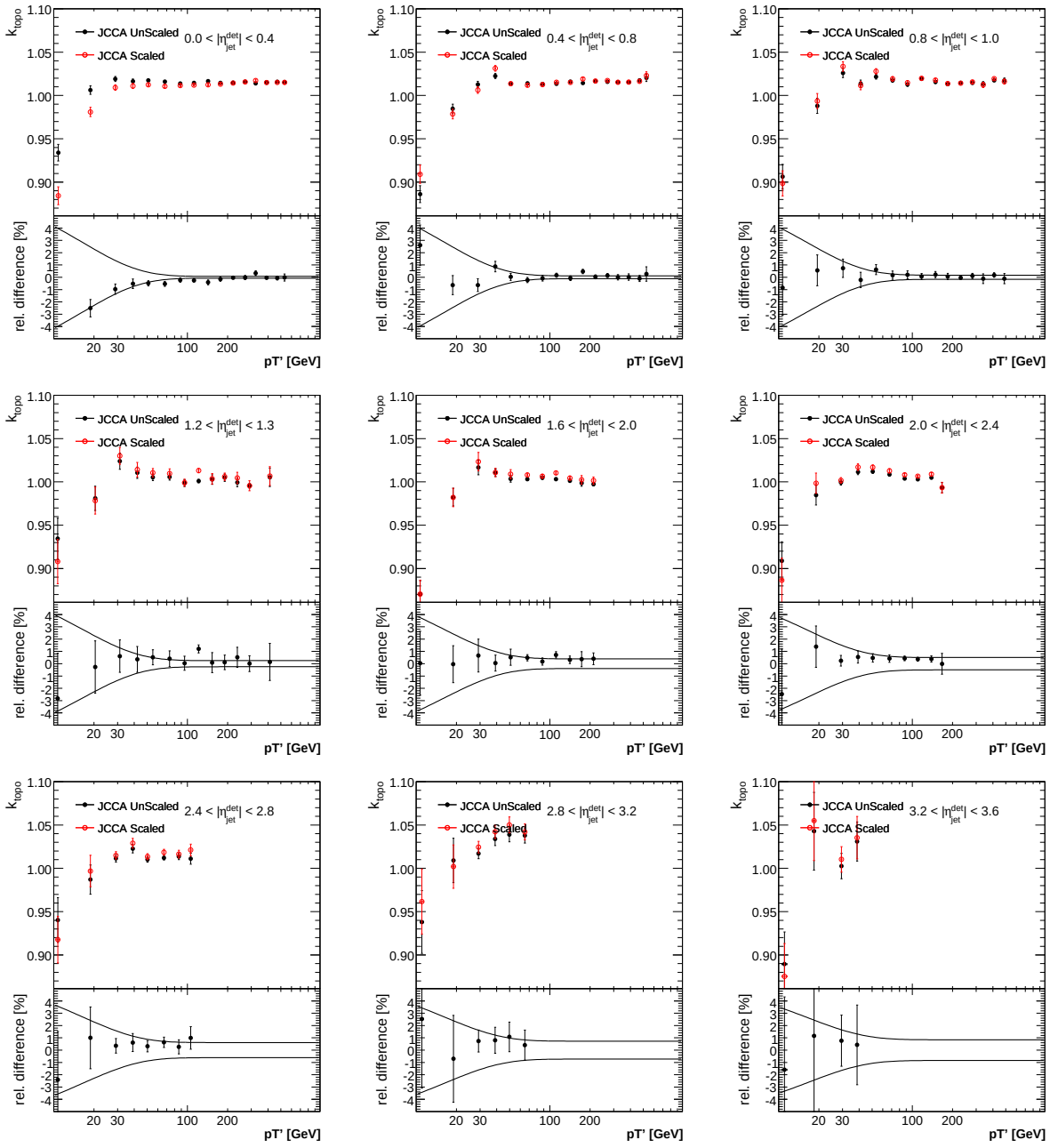

FIG. 175: Comparison of the topology bias correction for $\mathcal{R}_{\text{cone}} = 0.7$ jets between the standard γ+jet MC and the γ+jet MC with a scaled single pion response. The bottom plots present the relative difference, which will be used to assign a systematic uncertainty.

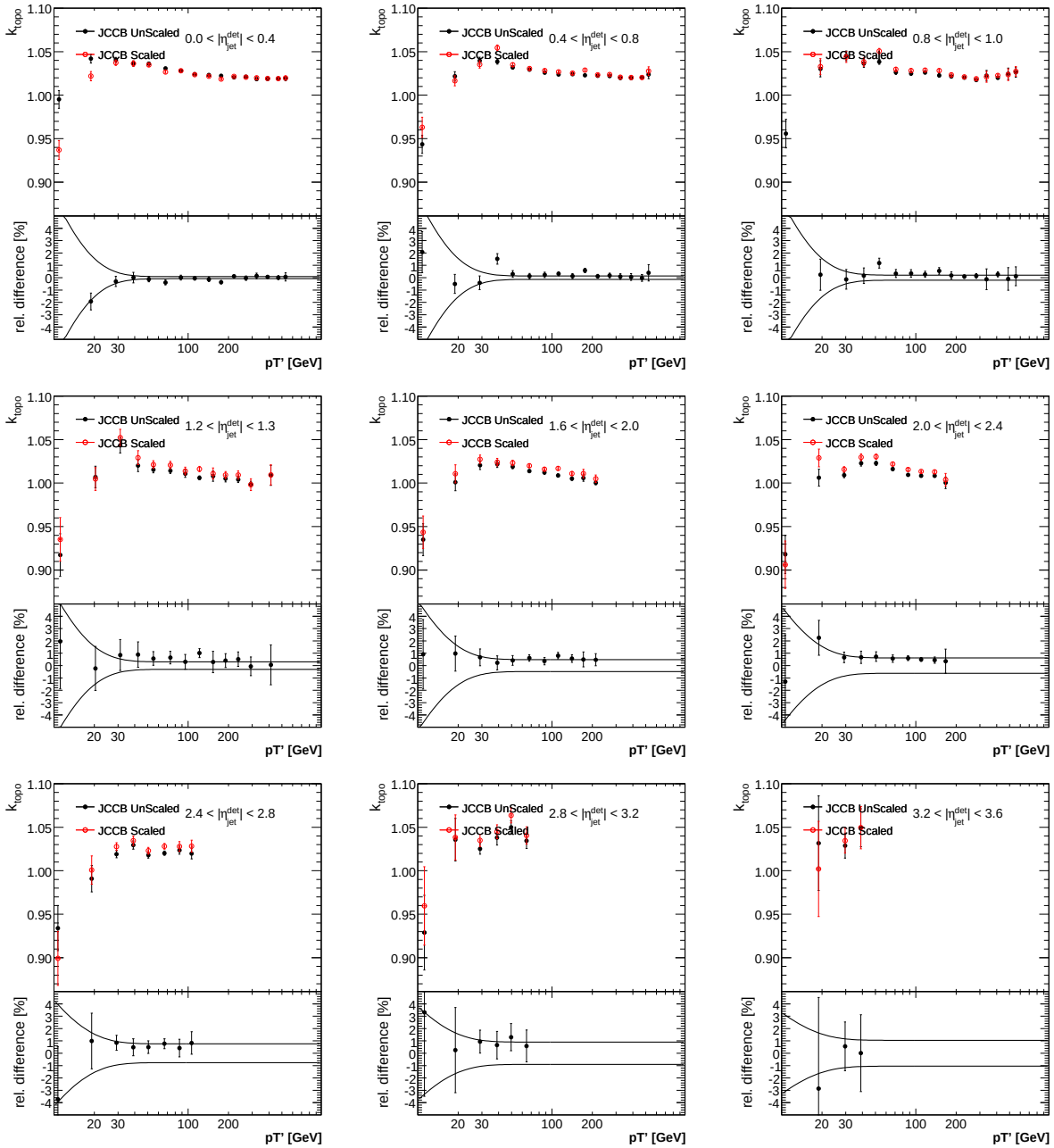

FIG. 176: Comparison of the topology bias correction for $\mathcal{R}_{\text{cone}} = 0.5$ jets between the standard γ+jet MC and the γ+jet MC with a scaled single pion response. The bottom plots present the relative difference, which will be used to assign a systematic uncertainty.

b. Systematic Uncertainty from Physics Modeling

The transverse momentum balance in γ+jet can be mainly spoiled by parton showering from hard scatter partons (initial and final state radiation) or by additional soft radiation caused by parton spectator interactions (soft underlying event). Contributions from the two processes cannot be calculated exactly from the QCD Lagrangian and they must be modeled. Two general purpose MC event generators, PYTHIA and HERWIG [5], were used for the topology bias study. Both generators incorporate the leading order matrix elements for the simulated hard process followed by the leading-log approximation of partonic shower. Soft underlying event (SUE) as well hadronization are modeled in a different way.

We used three sets of PYTHIA parameters, so called Tune A, Tune B and Tune DWT. Tune A and B were tuned to the CDF Run I data [9]. Tune A allows for more initial state radiation (`PARP(67)=4`) than Tune B (`PARP(67)=1`). Consequently, the contribution of soft underlying event is smaller in Tune A than in Tune B. CDF data slightly favor Tune A which is used as a default setting for full MC simulation of DØ detector response. DØ Run II data on dijet azimuthal decorrelations [17] show lack of initial state radiation (ISR) in Tune B while there is too much radiation in Tune A. Data prefers `PARP(67)` to be about 2.5, which has been implemented in Tune DWT. The default setting of HERWIG provides good description of the dijet azimuthal decorrelation data which indicates that initial state radiation is modeled very well. On the other hand it does not describe the CDF Run I data because its soft underlying event model was not tuned to the Tevatron energies.

Ideally, we would have used full MC simulations of the DØ detector. This would be very time consuming however. Rather then this we run particle level MC and we scale down individual particle 4-momenta by their response which was parametrized using input from full MC. In particular, we distinguish electron, photon meson ($\pi^{\pm}$), and baryon (protons and neutrons) responses. Neutrinos, muons, and charged particles with $p_T < 300$MeV have no response. Also particles with $|\eta| > 4.2$ are ignored. Using particle scaled 4-momenta, we recompute missing E_T and we reconstruct "detector" level jets. On such γ + jet MC sample, we then apply the relevant events selection criteria from the response measurement as described in Sect. 8.1. As can be seen in Fig. 177, the response in this fast parametrized MC agrees within 2% with the response observed in data. Since the fast MC is used only for evaluating the systematics rather than for obtaining the correction itself, we consider this level of agreement satisfactory.

The true jet response and MPF response are computed event by event. The ratio of the two quantities, which defines the topology bias correction (see Eq. 28) is shown in Fig. 178 for the three different PYTHIA tunes, in different jet rapidity bins.

Previous studies showed that PYTHIA and HERWIG give significantly different topology bias correction, even for the central rapidity jets. In order to understand those differences,we studied individual sources of topology bias in more detail in case of PYTHIA Tune A. In the case of central jets, the dominant bias is due to soft underlying event, whereas the effect of initial state radiation is negligible (see Fig. 179). In the forward region, the influence of initial state radiation increases and it becomes eventually as large as the effect of soft underlying event. The soft underlying event can explain the whole topology bias in the case of central rapidity jets. This is not true in the forward region where neither combined effect of ISR and SUE does not bring the correction to one. In this region, the final state radiation and the effect of limited calorimeter coverage have to be taken into account in order to explain the whole size of the topology bias (see Fig. 180).

To evaluate the systematics, we considered only PYTHIA. As was shown above, the SUE

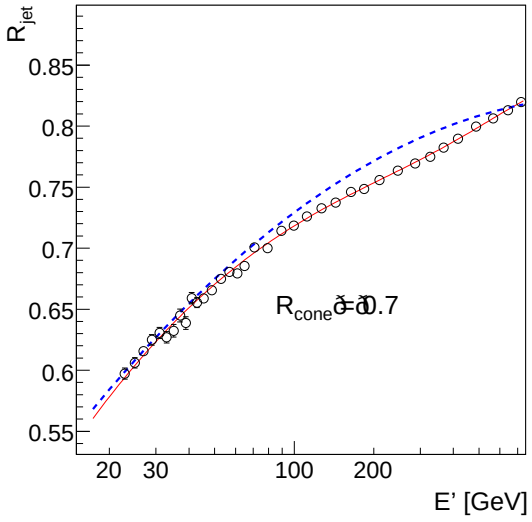

FIG. 177: Cone 0.7 jet response (open circles and solid line) in fast MC with parametrized single particle response. Response is compared with response in data represented by the quadratic log fit Eq. 23 (dashed line).

model is crucial for the description of the topology bias and it is known that HERWIG does not describe the CDF Run I data well. We took the maximum difference with respect to PYTHIA Tune A as the systematic uncertainty. This is shown as the dashed lines in the bottom plots in Fig. 178.

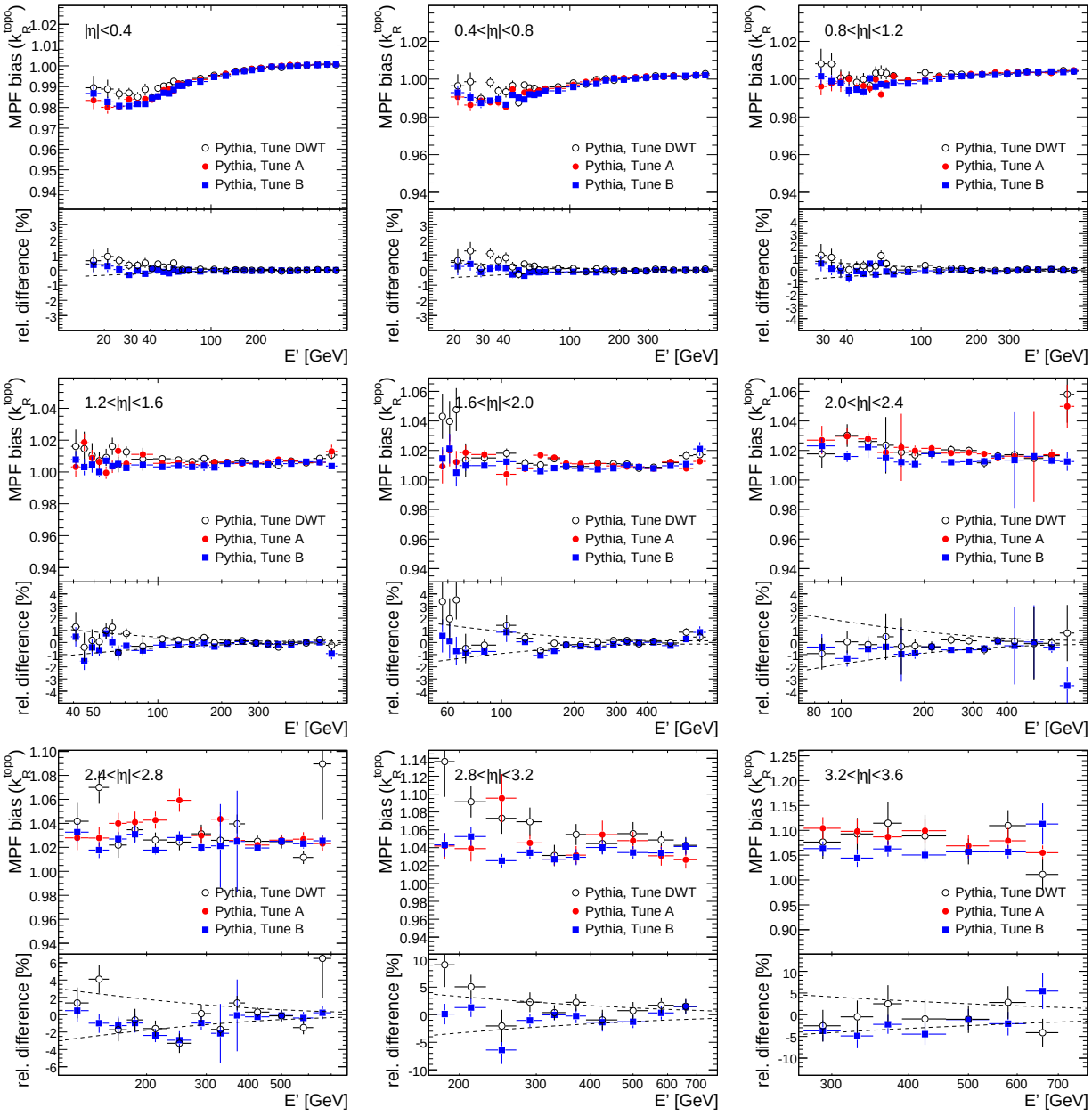

FIG. 178: Comparison of the topology bias correction for the three different PYTHIA tunes, in different jet rapidity bins. The bottom plots present the relative difference with respect to PYTHIA Tune A. The dashed line represent the assigned systematic uncertainty.

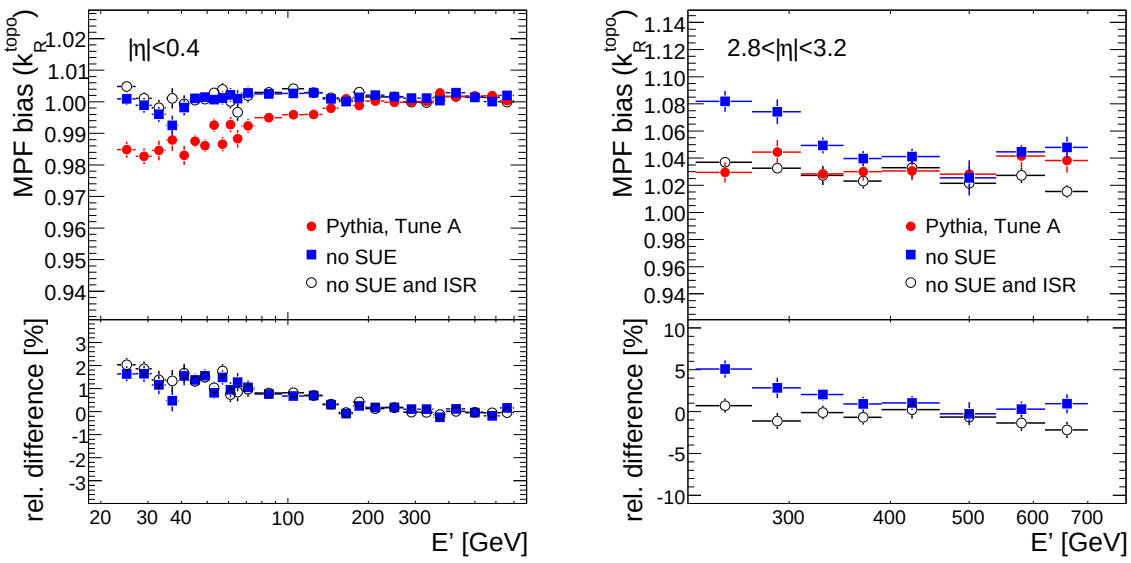

FIG. 179: Dependence of the topology bias on the soft underlying event (SUE) and initial state radiation (ISR) for PYTHIA Tune A.

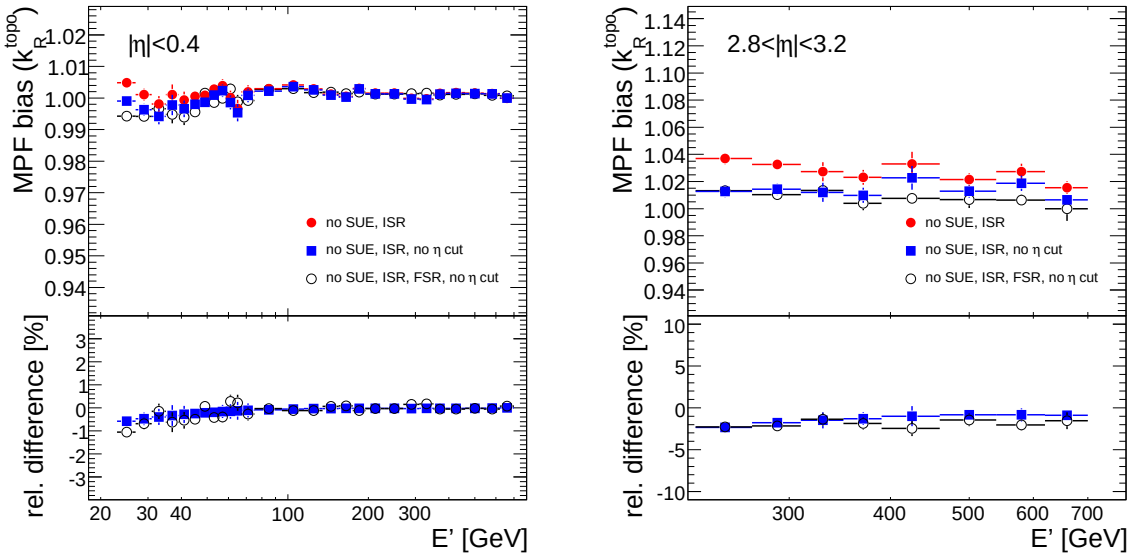

FIG. 180: Dependence of the topology bias on the limited calorimeter coverage (all particles, even with $|\eta| > 4.2$, taken into account) and final state radiation (FSR) for PYTHIA Tune A.

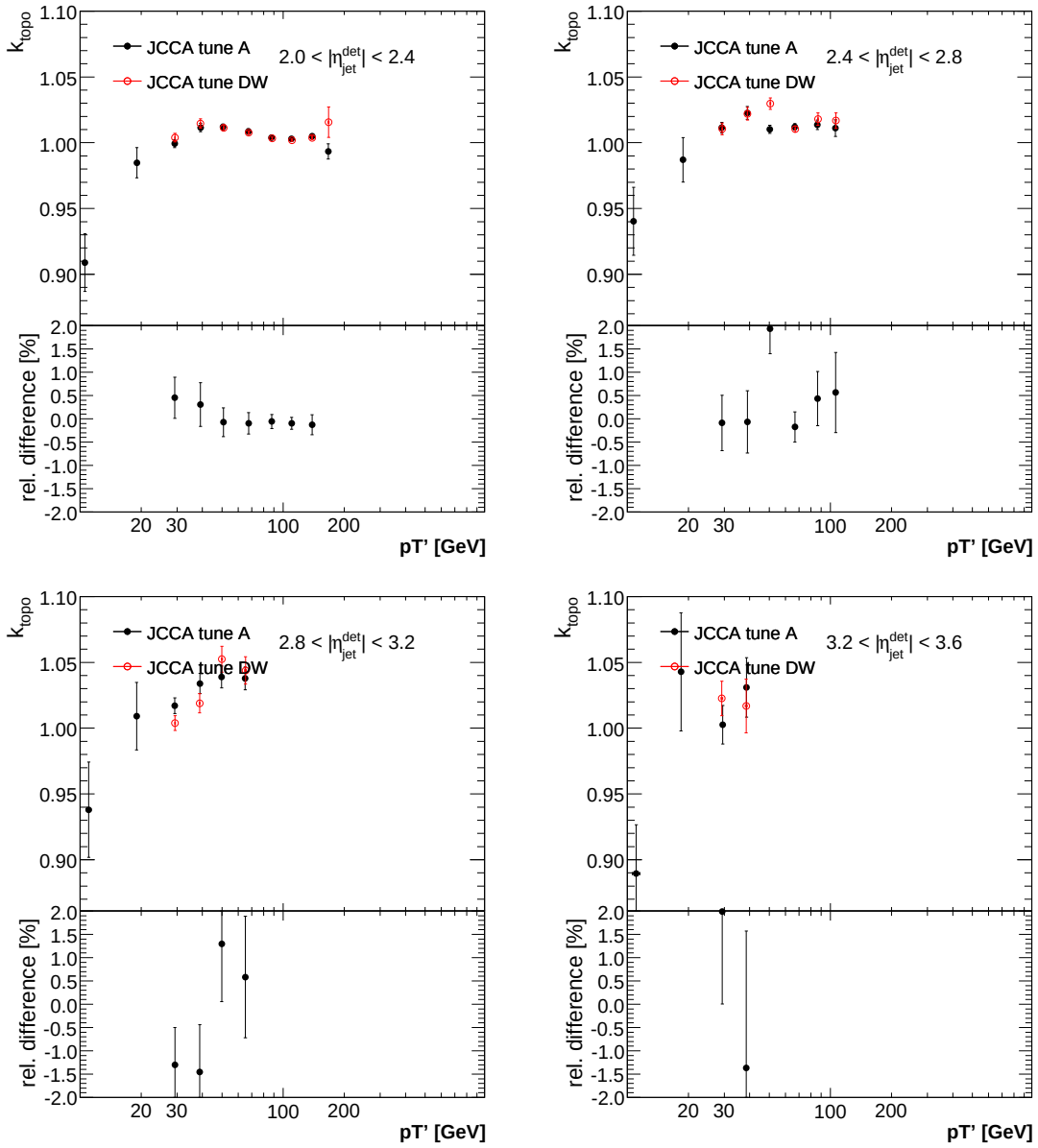

FIG. 181: Comparison of the topology bias correction for $\mathcal{R}_{\text{cone}} = 0.7$ jets between fully simulated samples of Tune A and Tune DW γ+jet MC. The bottom plots present the relative difference, along with the assigned systematic uncertainty (solid curve).

APPENDIX G: SHOWERING CORRECTION

1. Examples of Particle-Jet and Not-Particle-Jet Templates

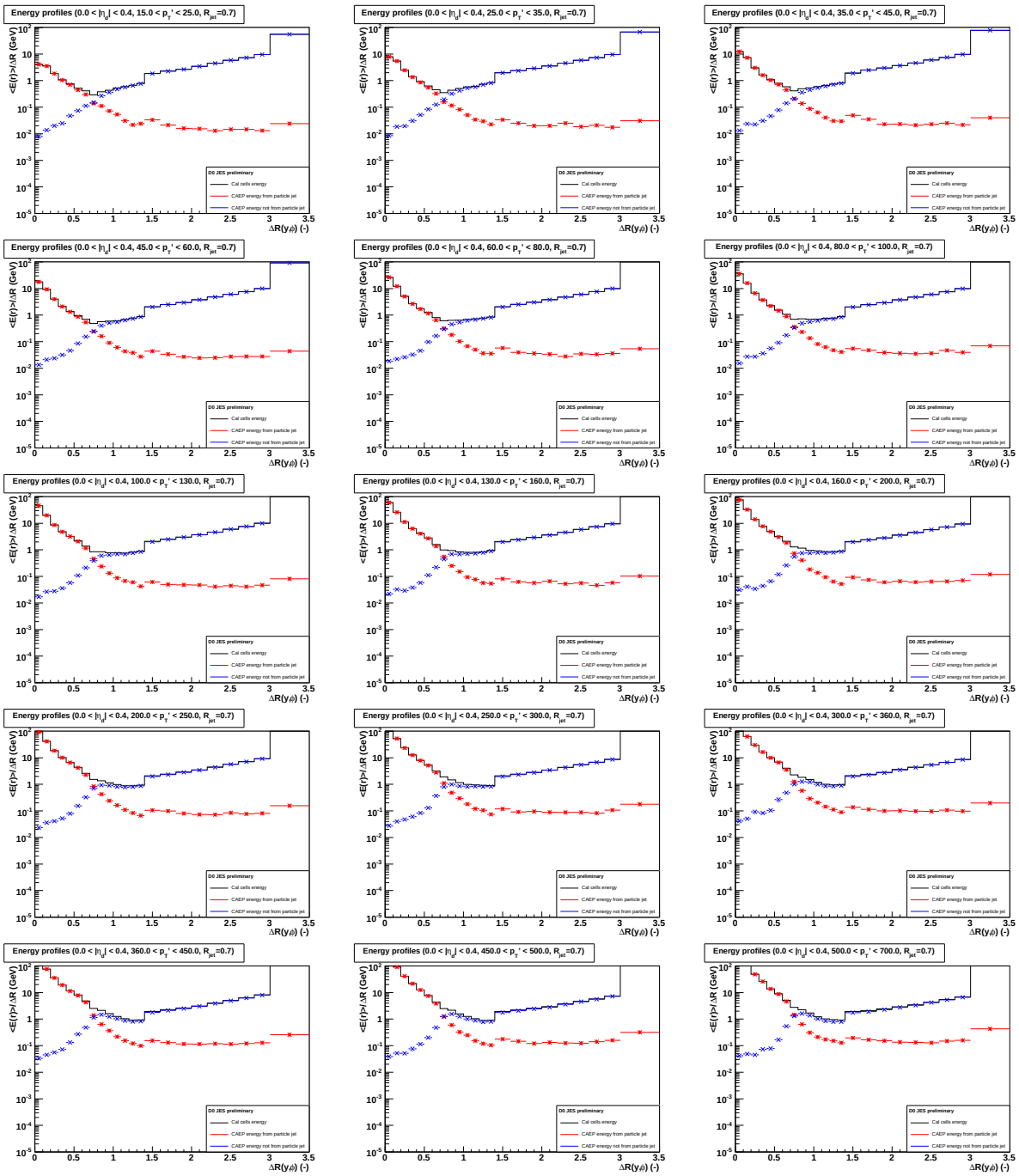

FIG. 182: Examples of particle-jet and not-particle-jet profiles for $\mathcal{R}_{\rm cone} = 0.7$ jets with $\left|\eta_{\rm jet}^{\rm det}\right| < 0.4$ and for different p'_T bins.

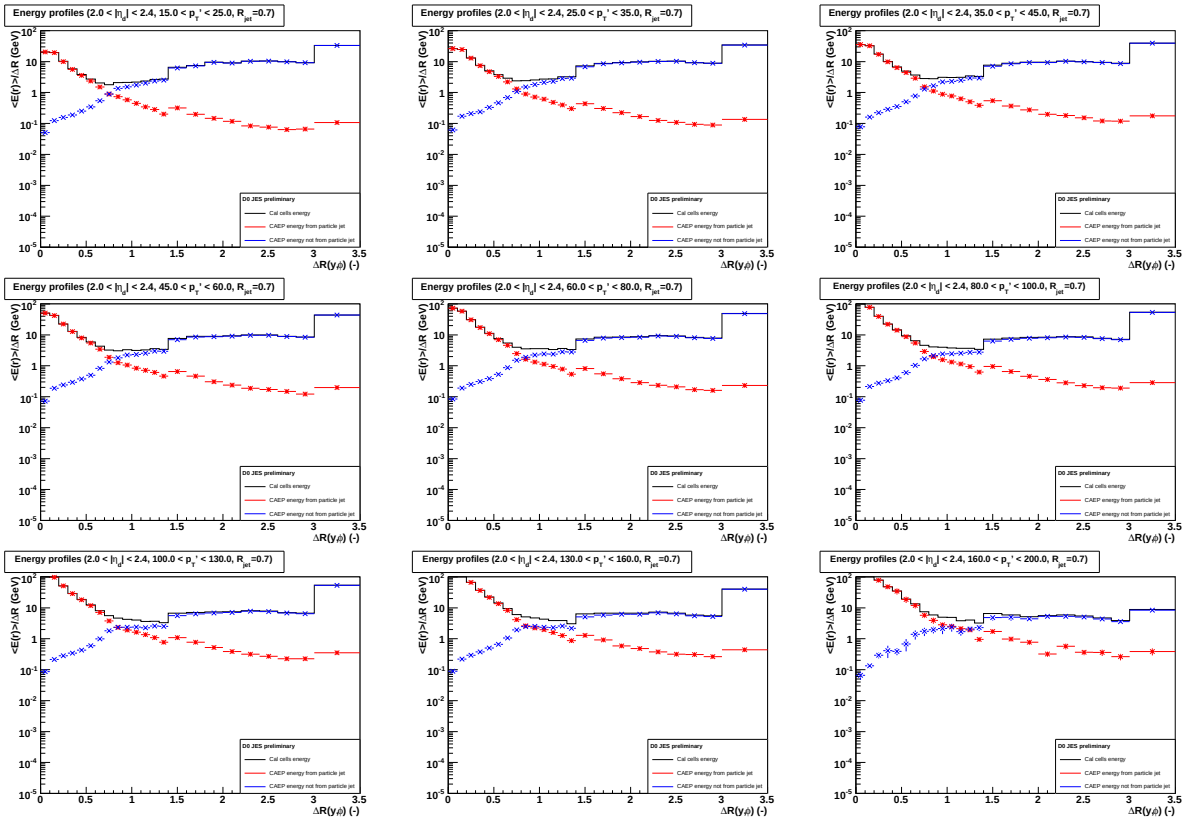

FIG. 183: Examples of particle-jet and not-particle-jet profiles for $\mathcal{R}_{\rm cone} = 0.7$ jets with $2.0 < \left|\eta^{\rm det}_{\rm jet}\right| < 2.4$ and for different p'_T bins.

2. Examples of Offset Templates

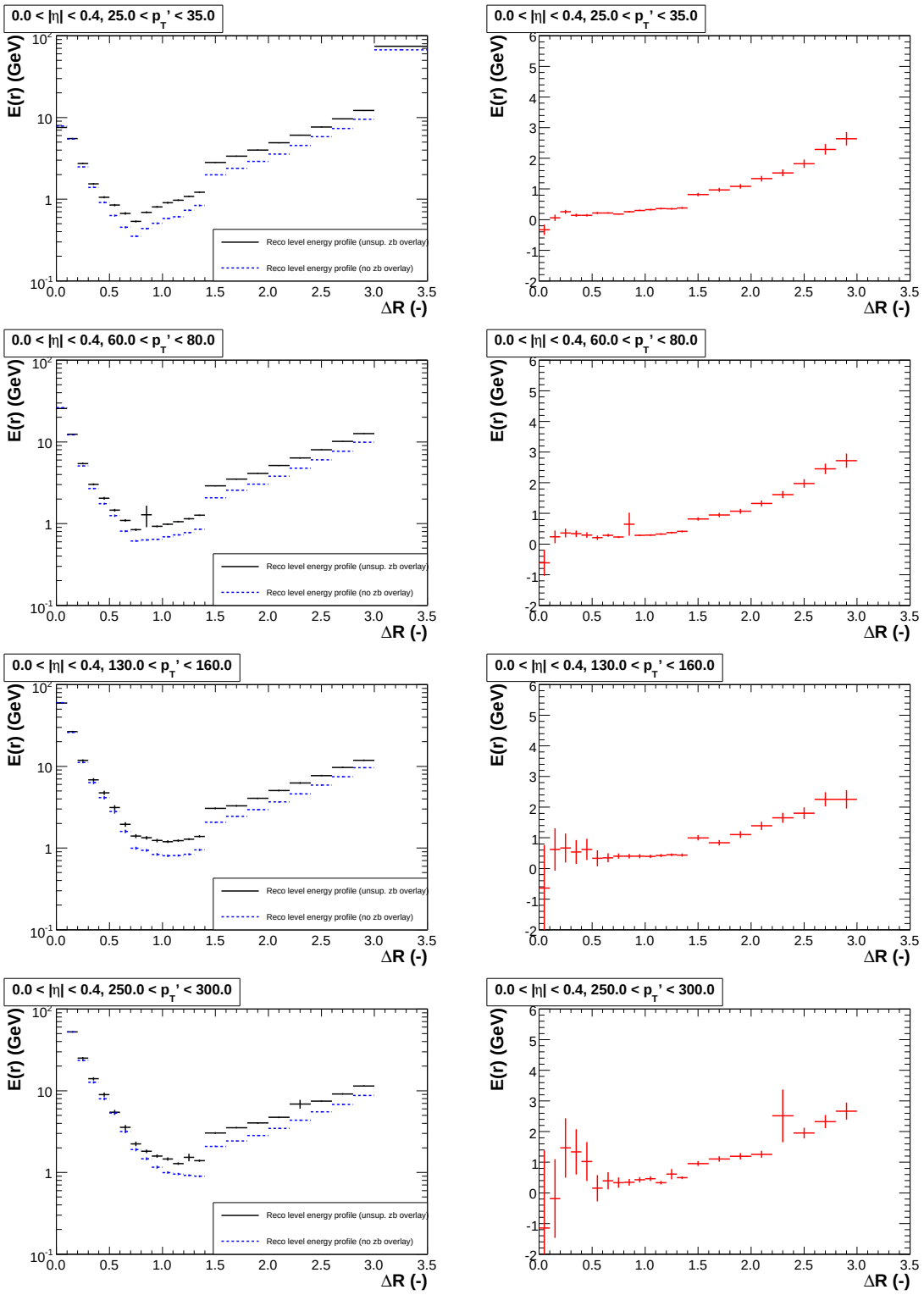

FIG. 184: Right column: examples of true offset profiles for $\mathcal{R}_{\text{cone}} = 0.7$ jets with $\left|\eta_{\text{jet}}^{\text{det}}\right| < 0.4$ and for different p'_T bins. Plots in the right column correspond to the two profiles, γ+jet MC with unsuppressed ZB overlay and without ZB overlay, which are subtracted in order to obtain the true offset profile.

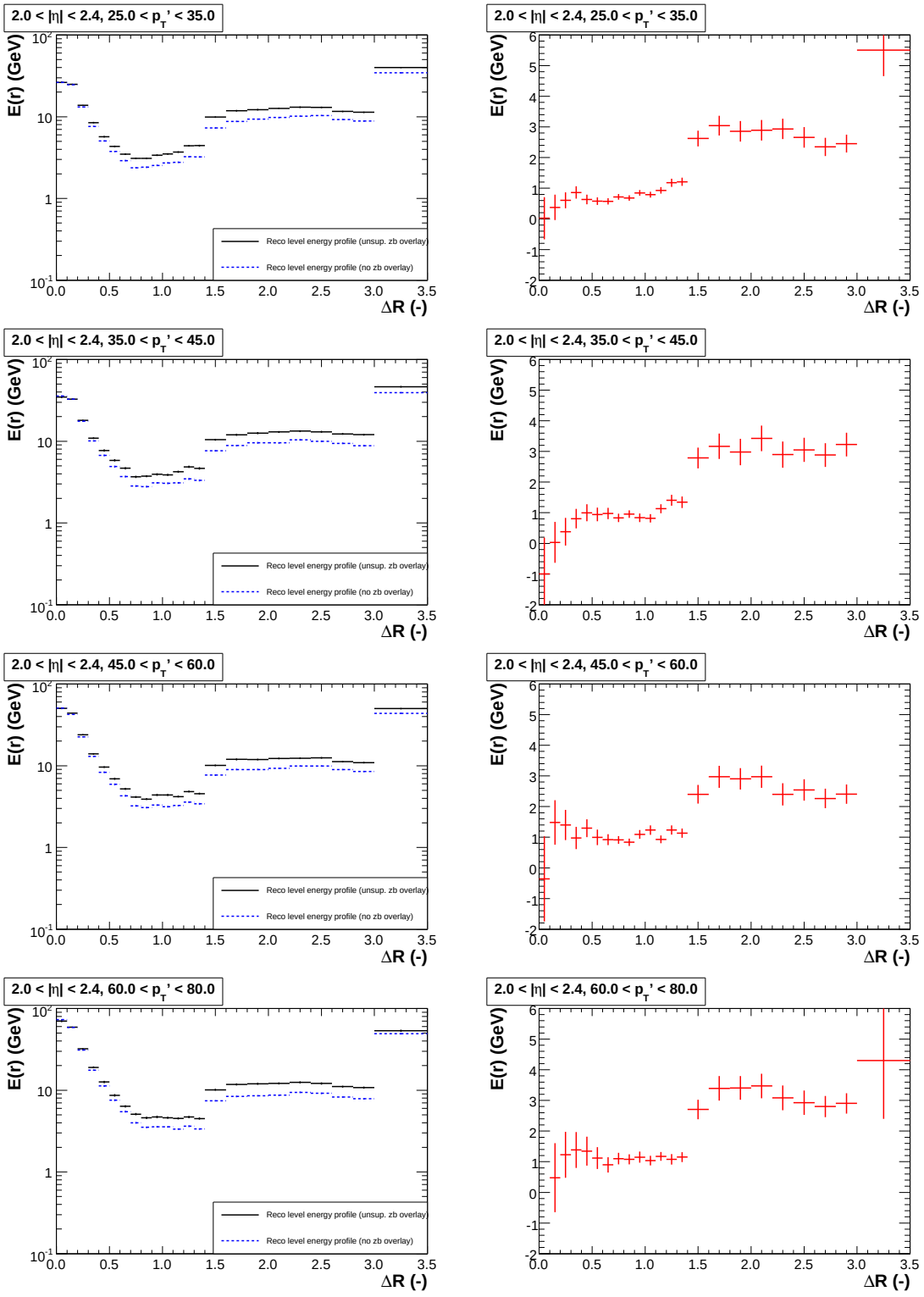

FIG. 185: Right column: examples of true offset profiles for $\mathcal{R}_{\text{cone}} = 0.7$ jets with $2.0 < \left|\eta_{\text{jet}}^{\text{det}}\right| < 2.4$ and for different p'_T bins. Plots in the right column correspond to the two profiles, γ+jet MC with unsuppressed ZB overlay and without ZB overlay, which are subtracted in order to obtain the true offset profile.

3. Examples of Template Fits in MC

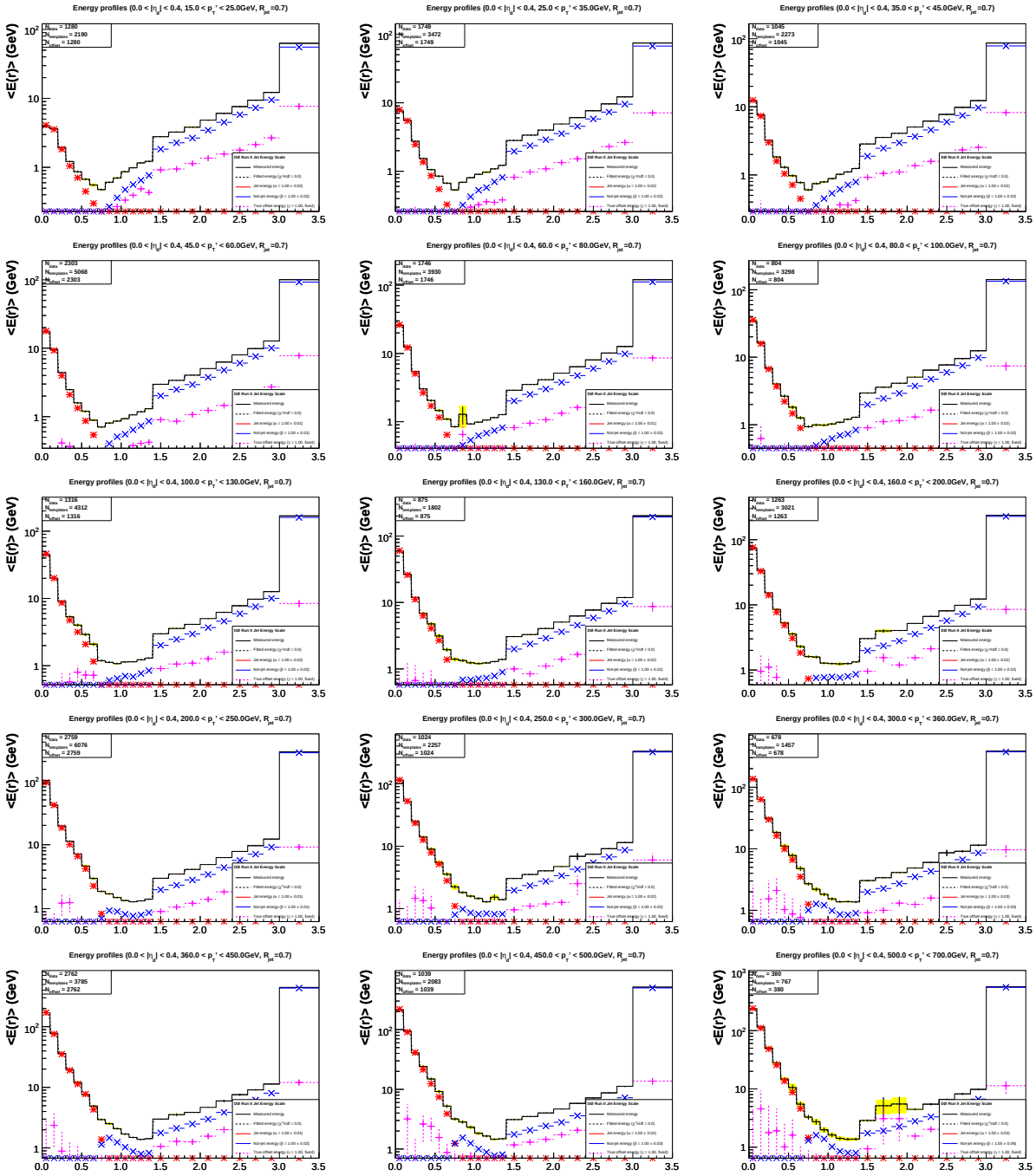

FIG. 186: Examples of template fits for $\mathcal{R}_{\text{cone}} = 0.7$ jets with $\left|\eta_{\text{jet}}^{\text{det}}\right| < 0.4$ in γ+jet MC with unsuppressed ZB overlay. The black points represent the measurements whereas the rest of colored points correspond to the three different templates: particle-jet (red), not-particle-jet (blue) and offset (purple). The solid histogram represents the fitted linear combination of the three templates to the measurements.

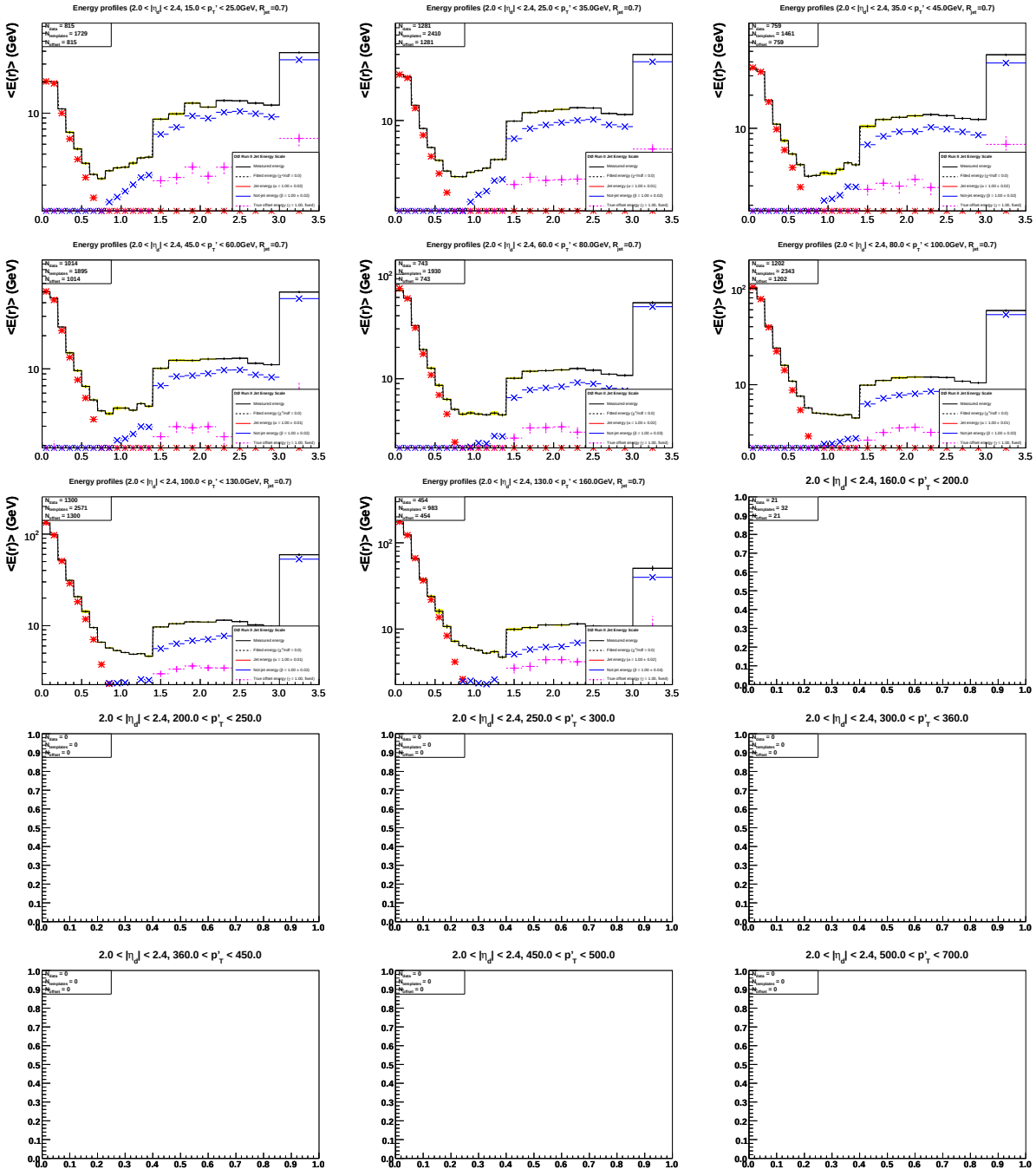

FIG. 187: Examples of template fits for $\mathcal{R}_{\text{cone}} = 0.7$ jets with $2.0 < \left|\eta_{\text{jet}}^{\text{det}}\right| < 2.4$ in γ+jet MC with unsuppressed ZB overlay. The black points represent the measurements whereas the rest of colored points correspond to the three different templates: particle-jet (red), not-particle-jet (blue) and offset (purple). The solid histogram represents the fitted linear combination of the three templates to the measurements.

4. Showering Calibration

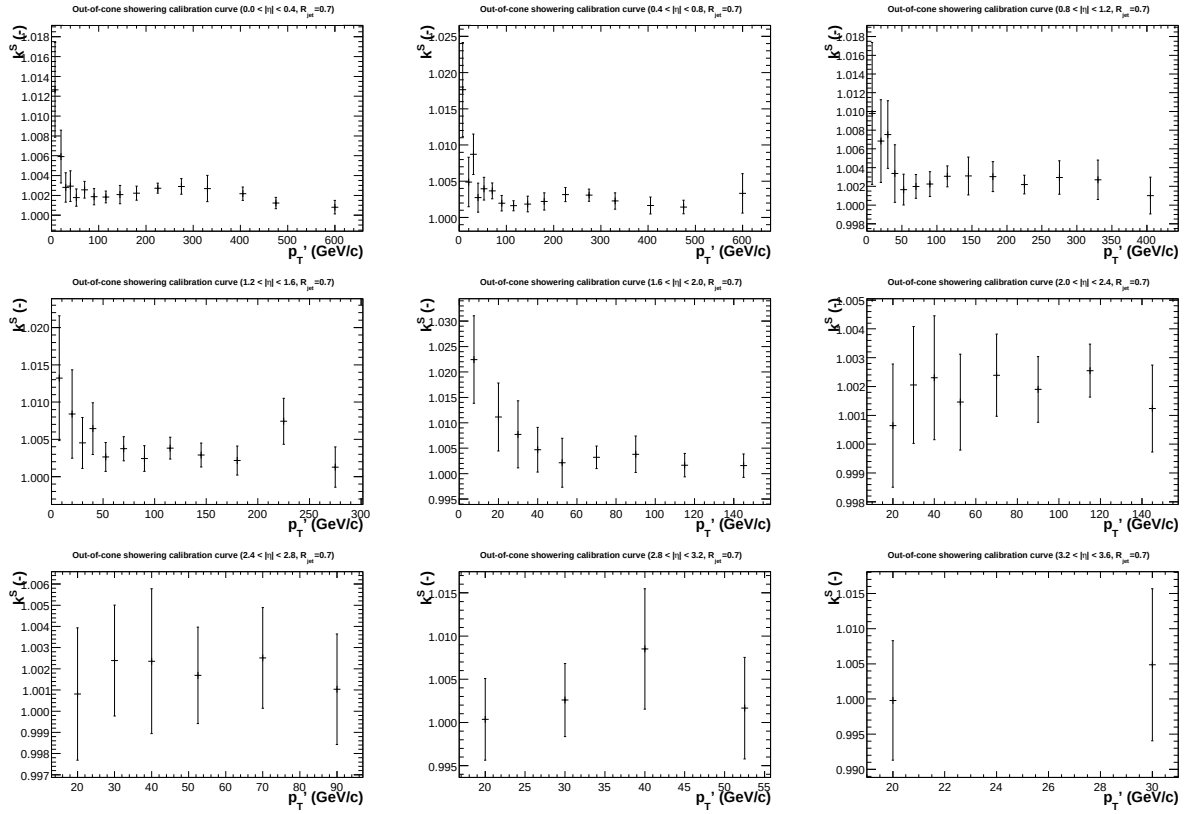

FIG. 188: Calibration factors for the estimated showering correction for $\mathcal{R}_{\text{cone}} = 0.7$ jets in different $\left|\eta_{\text{jet}}^{\text{det}}\right|$ regions and as a function of p_T'.

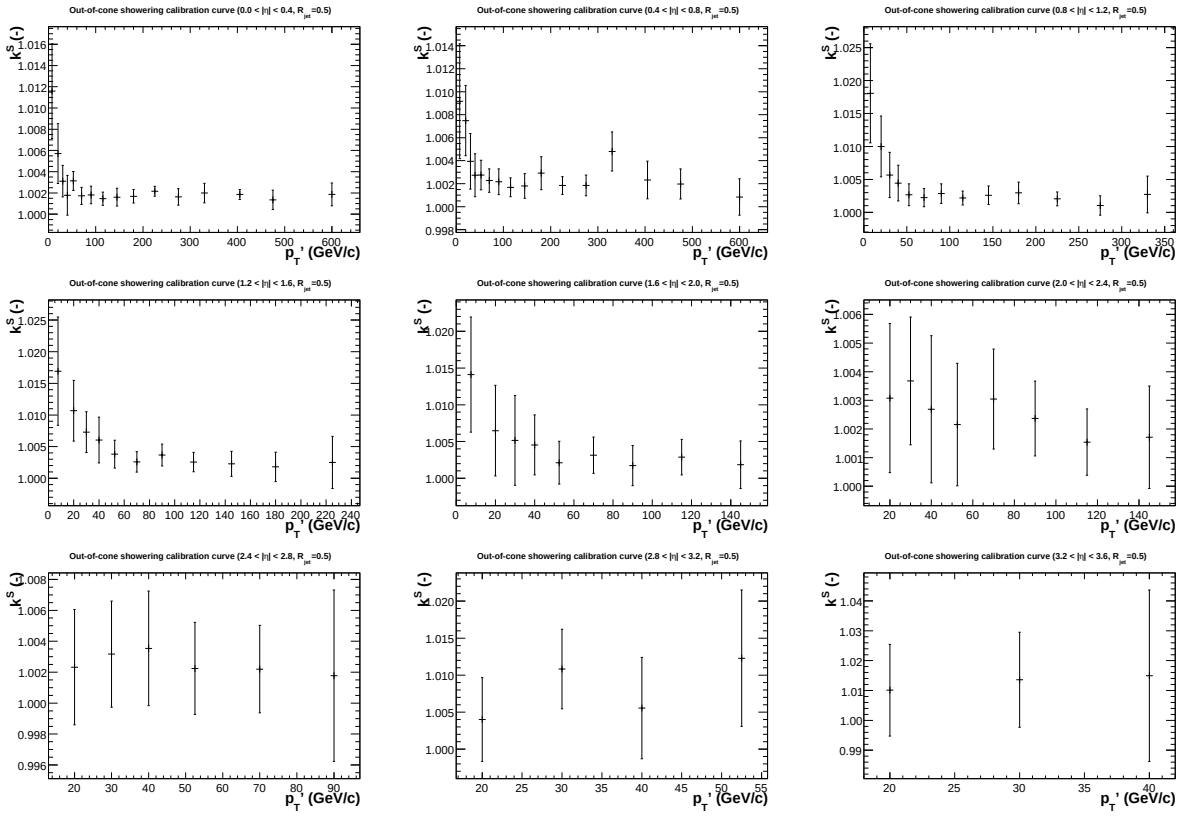

FIG. 189: Calibration factors for the estimated showering correction for $\mathcal{R}_{\text{cone}} = 0.5$ jets in different $\left|\eta_{\text{jet}}^{\text{det}}\right|$ regions and as a function of p_T'.

5. Examples of Template Fits in Data

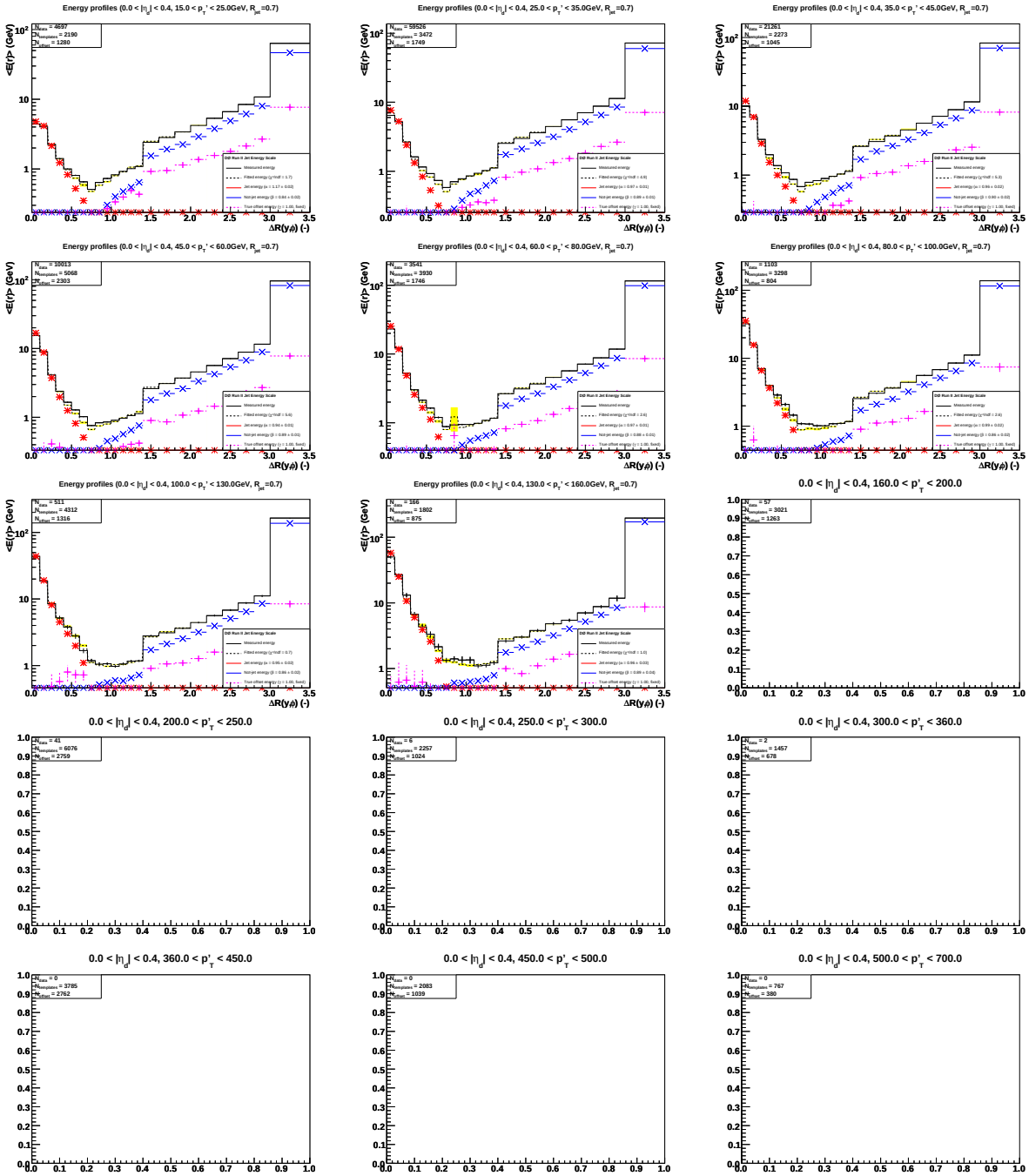

FIG. 190: Examples of template fits for $\mathcal{R}_{\text{cone}} = 0.7$ jets with $\left|\eta_{\text{jet}}^{\text{det}}\right| < 0.4$ in γ+jet data. The black points represent the measurements whereas the rest of colored points correspond to the three different templates: particle-jet (red), not-particle-jet (blue) and offset (purple). The solid histogram represents the fitted linear combination of the three templates to the measurements.

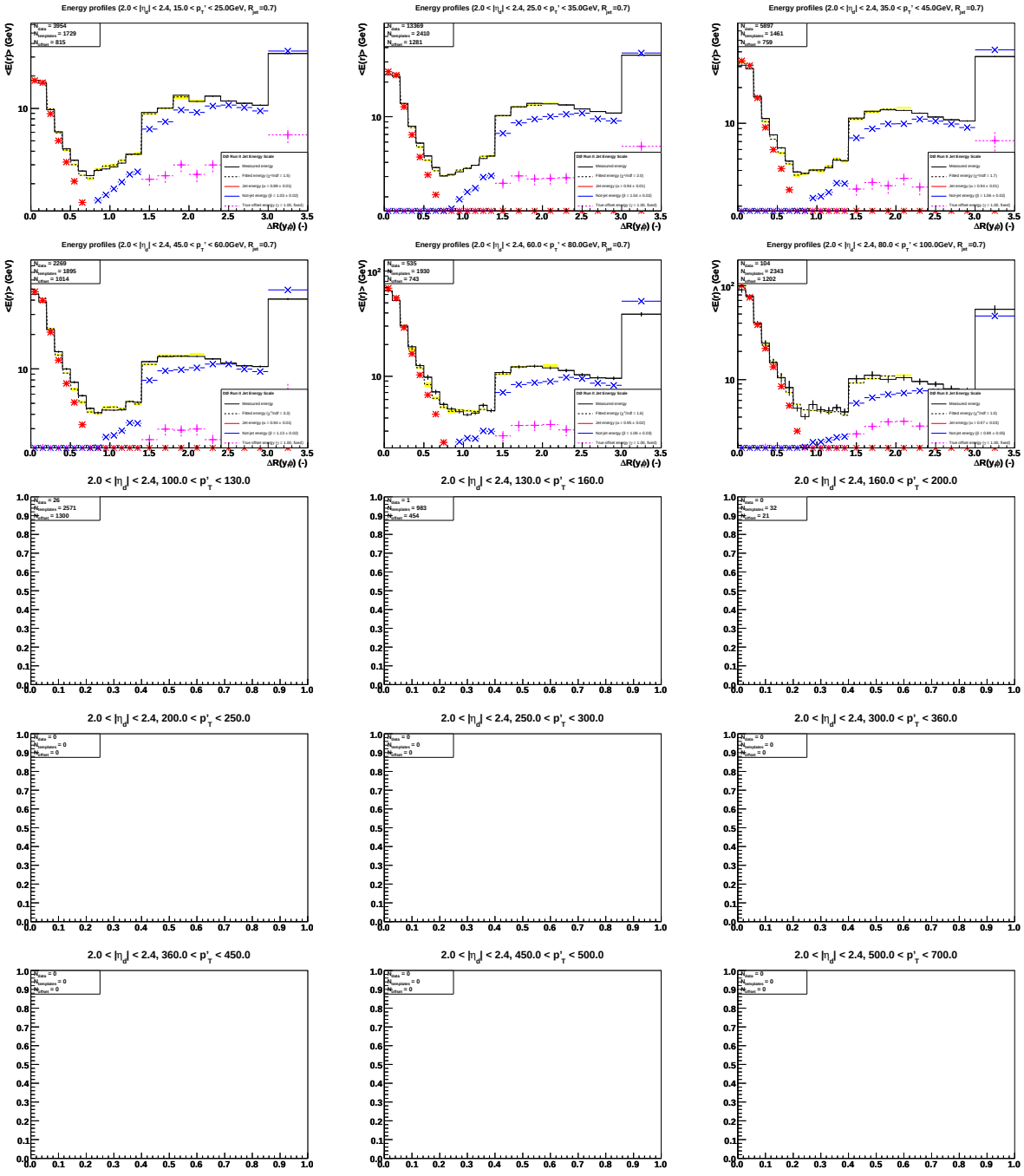

FIG. 191: Examples of template fits for $\mathcal{R}_{\text{cone}} = 0.7$ jets with $2.0 < \left|\eta_{\text{jet}}^{\text{det}}\right| < 2.4$ in γ+jet data. The black points represent the measurements whereas the rest of colored points correspond to the three different templates: particle-jet (red), not-particle-jet (blue) and offset (purple). The solid histogram represents the fitted linear combination of the three templates to the measurements.

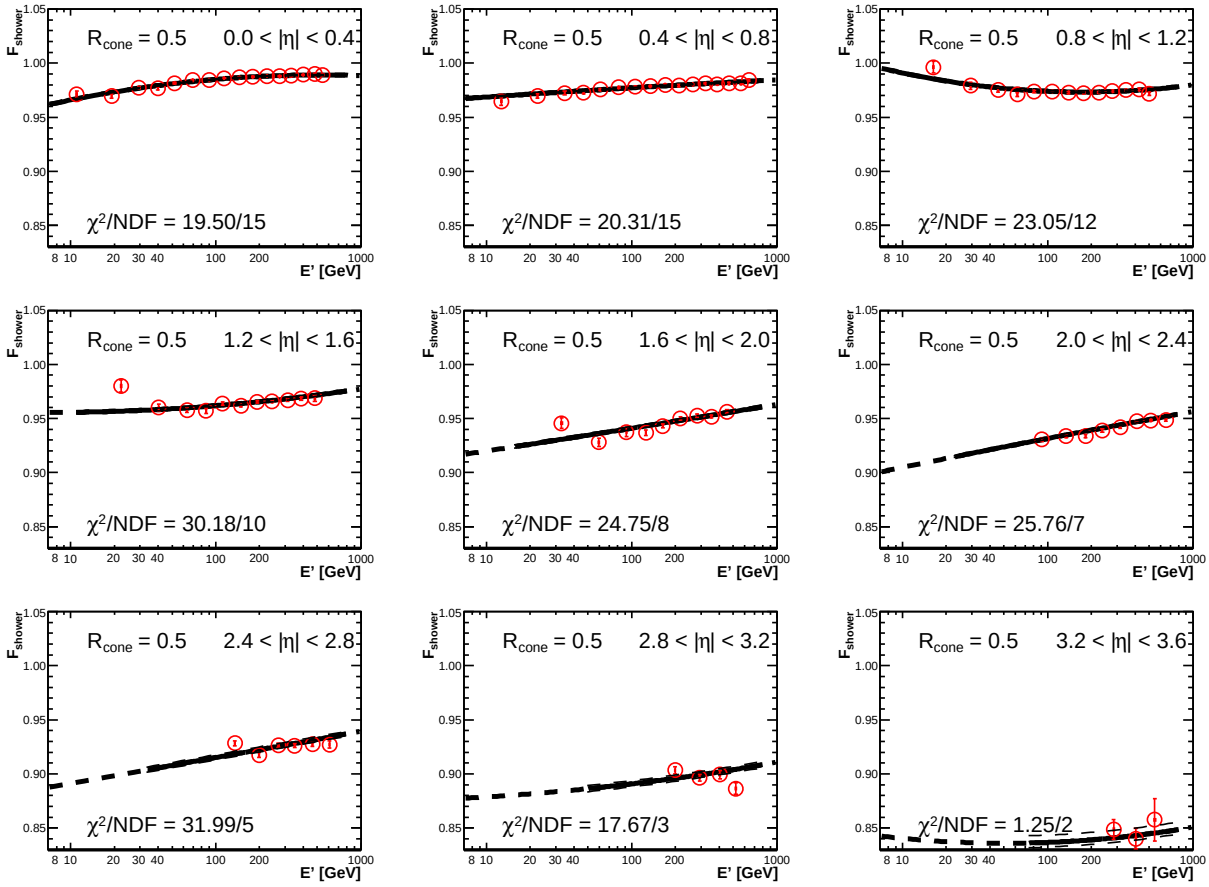

FIG. 192: Showering correction for $\mathcal{R}_{\rm cone} = 0.5$ jets in MC, as a function of p'_T and for different $\eta^{\rm det}_{\rm jet}$ bins. The solid line represents the result of a smooth parameterization of the correction as a function of $(p'_T, \eta^{\rm det}_{\rm jet})$.

7. Showering Correction in Data

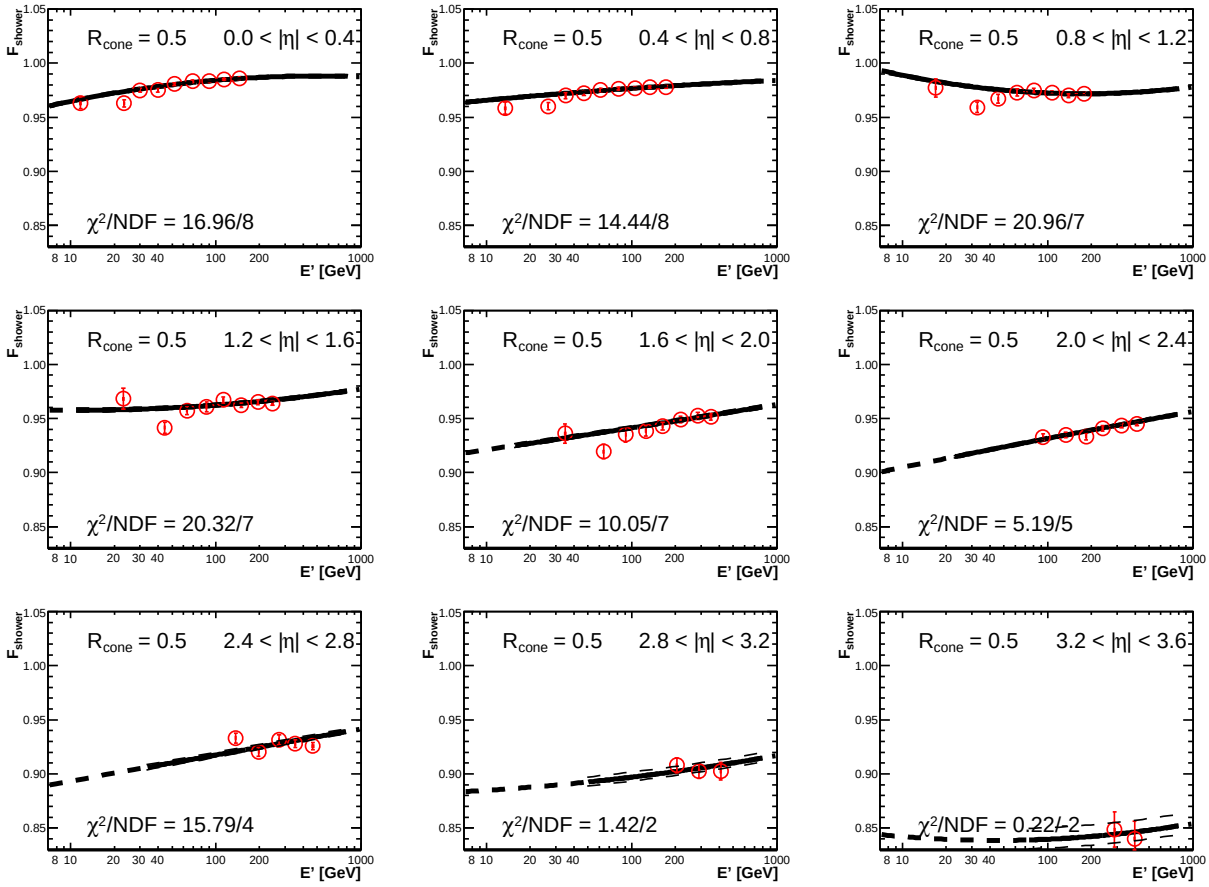

FIG. 193: Showering correction for $\mathcal{R}_{\rm cone} = 0.5$ jets in data, as a function of p'_T and for different $\eta^{\rm det}_{\rm jet}$ bins. The solid line represents the result of a smooth parameterization of the correction as a function of $(p'_T, \eta^{\rm det}_{\rm jet})$.

8. Systematic Checks

This section presents a summary of the studies performed to try to understand the source and impact of the imperfect agreement between data and fitted profiles. The main disagreement is observed for relatively central jets ($\left|\eta_{\rm jet}^{\rm det}\right| < 0.4$ and $0.4 < \left|\eta_{\rm jet}^{\rm det}\right| < 0.8$) with $p'_T < 100$ GeV. See Fig. 194 for an example of a poor and a good quality fit. The χ^2/ndf of the template fit as a function of p'_T is shown in Fig. 195 for $\mathcal{R}_{\rm cone} = 0.7$ jets in different $\left|\eta_{\rm jet}^{\rm det}\right|$ bins.

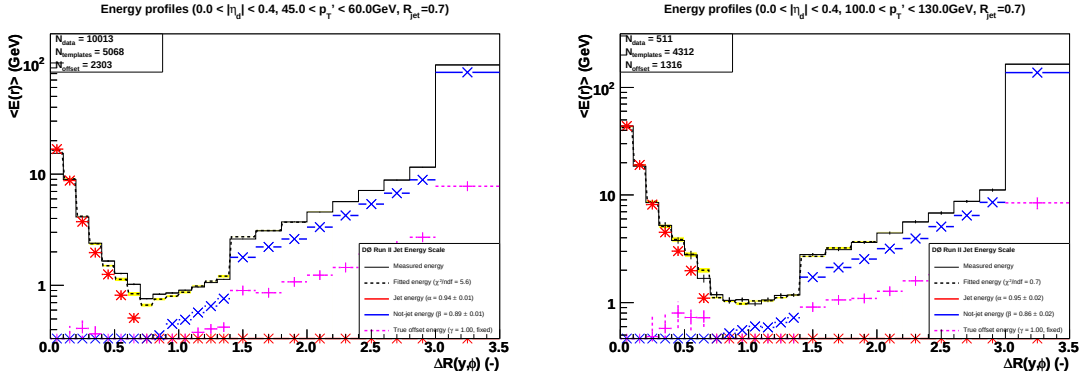

FIG. 194: Examples of template fits for $\mathcal{R}_{\rm cone} = 0.7$ jets with $\left|\eta_{\rm jet}^{\rm det}\right| < 0.4$ in γ+jet data: a poor quality fit at low p'_T (left) and a better quality fit at higher p'_T (right). The black points represent the measurements whereas the rest of colored points correspond to the three different templates: particle-jet (red), not-particle-jet (blue) and offset (purple). The solid histogram represents the fitted linear combination of the three templates to the measurements.

A different way to visualize the discrepancy is by comparing the ratio of integrals (up to $\mathcal{R}_{\rm cone}$) of the energy profile. Fig. 196 presents the ratio of integrals (data/fitted profiles) as a function of p'_T for $\mathcal{R}_{\rm cone} = 0.7$ jets in different $\left|\eta_{\rm jet}^{\rm det}\right|$ bins. If one mentally excludes the low E_T biased region ($p'_T < 30$ GeV) and takes into account the sizable statistical uncertainties, the largest systematic deviations are observed in the $\left|\eta_{\rm jet}^{\rm det}\right| < 0.4$ region (up to $\sim 4\%$ at $p'_T \sim 40$ GeV), followed by $\sim 1-2\%$ effects elsewhere. It is interesting to note that the largest discrepancy between data and fitted templates occurs near $\mathcal{R}_{\rm cone}$, where zero-suppression effects are expected to be largest. Also, most clearly seen in the $\left|\eta_{\rm jet}^{\rm det}\right| < 0.4$ bin, there is an indication for the discrepancy to become smaller with increasing p'_T.

It should pointed out that a $X\%$ discrepancy in the integrals does not directly translate into a $X\%$ bias in the showering correction. This can be better understood by recalling the definition of the showering correction (see Eq. 60), which we reproduce here:

$$\hat{S}_{\rm jet} = \frac{\hat{\alpha} E_{\rm ptclj}^{{\rm meas}(\Delta\mathcal{R}<\mathcal{R}_{\rm cone}),{\rm MC}} + \hat{\beta} E_{\rm not-ptclj}^{{\rm meas}(\Delta\mathcal{R}<\mathcal{R}_{\rm cone}),{\rm MC}}}{\hat{\alpha} E_{\rm ptclj}^{{\rm meas},{\rm MC}}}, \qquad \text{(G1)}$$

i.e. it is the ratio of visible energy up to $\mathcal{R}_{\rm cone}$ from both the particle-jet and not-particle-jet to the total visible energy (up to infinity) from the particle-jet. These integrals are in absence of offset energy, are predicted by the MC and scaled by the fitted α and β coefficients. (Please remember that the offset subtraction is effectively accomplished via the incorporation of the true offset profile in the fit.) As it can be appreciated, typical simulation inaccuracies will likely affect both numerator and denominator, leading to a partial cancellation. For instance, if the particle-jet profile in data is slightly narrower than in the simulation near

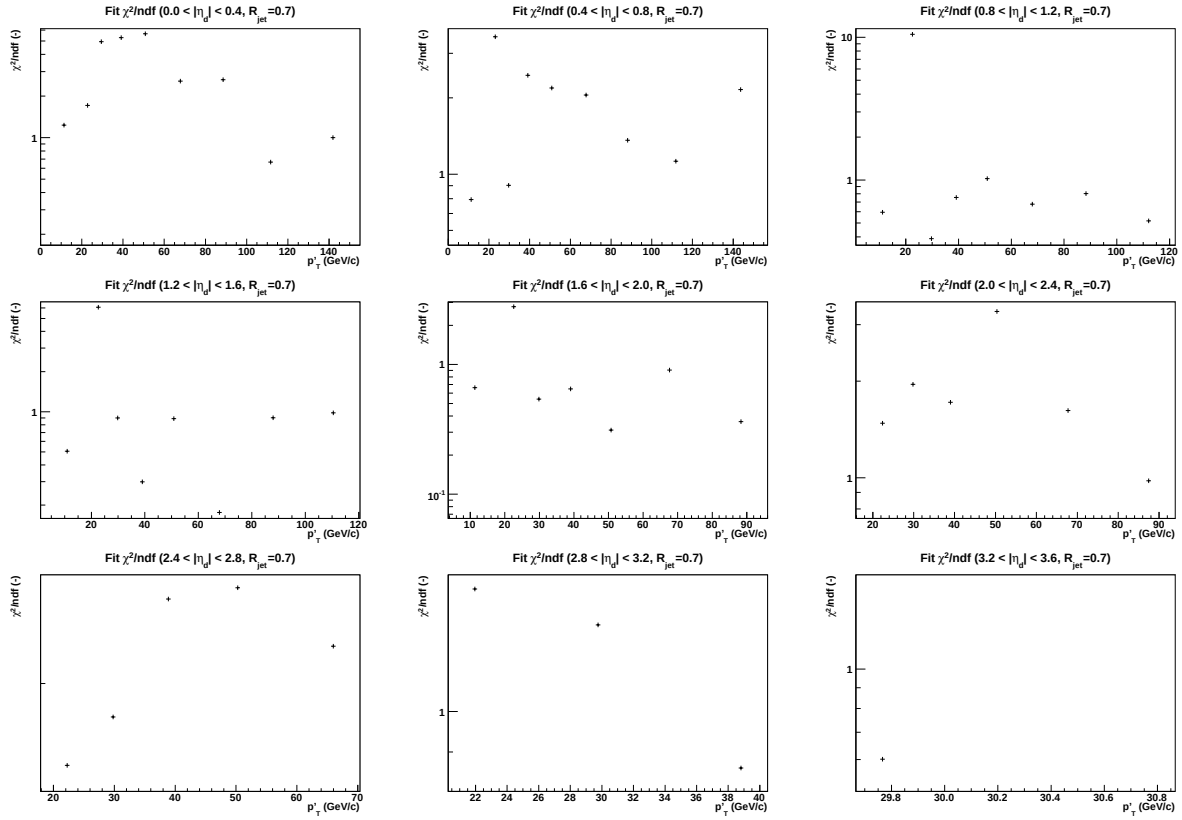

FIG. 195: χ^2/ndf as a function of p'_T from the template fit to data $\mathcal{R}_{\rm cone} = 0.7$ jets in different $\left|\eta^{\rm det}_{\rm jet}\right|$ regions.

the jet core (e.g. because of a higher fraction of π^0s during the jet fragmentation), the data and fitted profile integrals up to $\mathcal{R}_{\rm cone}$ will differ roughly by the fractional contribution of that excess energy, whereas showering would be essentially unaffected as it basically cancels in the ratio. Similar partial cancellations occur in the case of differences between data and MC in single pion response (see e.g. Fig. 209), zero supression effects near $\mathcal{R}_{\rm cone}$, etc, where both particle-jet and not-particle-jet contributions can be affected by a similar amount.

In order to determine what kind of systematic uncertainty should be assigned, a number of studies have been performed trying to identify a likely cause for the discrepancy. Here we just present a summary of these studies (see Ref. [23] for a detailed discussion, including a more complete set of plots):

- offset profile: since the offset profile is effectively obtained from data via the zero bias overlay, it is unlikely this is the responsible. This has been verified by performing the template fit for events with exactly one primary vertex, where the offset contribution (already subdominant) is further reduced by $\sim 30-40\%$ as compared to the default selection ($1 \leq n_{\rm PV} \leq 2$). As expected, no significant difference neither on the showering correction nor on the goodness of fit is observed. An artificial way to improve the goodness of fit would be by scaling the offset profile by a factor $\sim 1.3-1.5$. Scaling the offset profile by 1.3 has typically a $\leq 0.5\%$ effect on showering. However, given the above test with $n_{\rm PV} = 1$ and the fact that the offset is actually determined from data, this cannot really be justified. We tentatively conclude that offset modeling is not really responsible for the discrepancy.

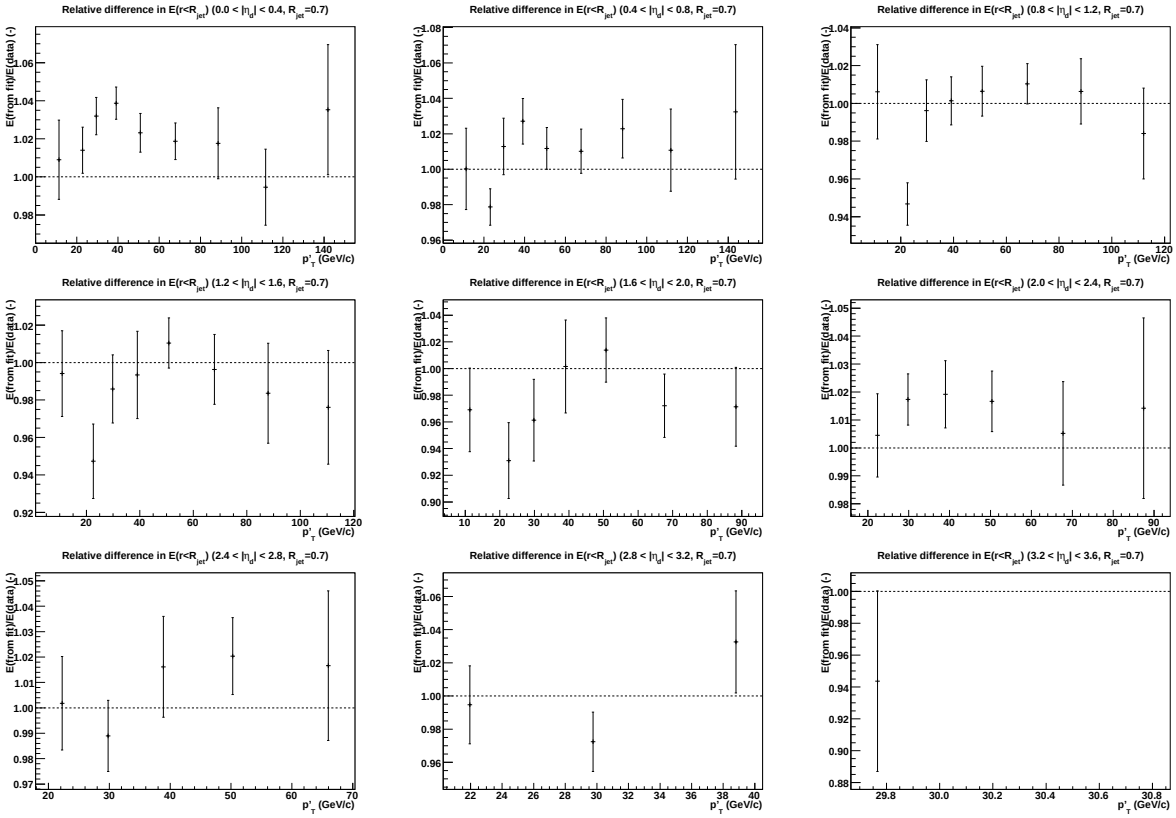

FIG. 196: Ratio of integrals of the energy profiles up to $\mathcal{R}_{\rm cone}$ between the data and fitted profile for $\mathcal{R}_{\rm cone} = 0.7$ jets as a function of p'_T and in different $\left|\eta^{\rm det}_{\rm jet}\right|$ regions.

- dijet background: the gluon-dominated jets from the dijet background contamination are wider than the quark-dominated jets in γ+jets (see Fig. 11 in Ref. [23]), and therefore expected to lead to a similar discrepancy to the one observed. This is checked by fitting profiles resulting from mixing γ+jet and EM+jet MC in the expected proportions, with templates obtained in pure γ+jet MC. This is complete analogy with what is being done in data. Fig. 197 compares the resulting ratio of integrals as a function of p'_T for $\mathcal{R}_{\rm cone} = 0.7$ jets in different $\left|\eta^{\rm det}_{\rm jet}\right|$ bins. Despite the limited EM+jet MC statistics, there are indications that such ratio has a similar trend to the one observed in data, in particular for $\left|\eta^{\rm det}_{\rm jet}\right| < 0.4$: i.e. the ratio is larger than one at low p'_T and decreases towards one as the sample purity increases. However, the systematic uncertainty in showering due to the dijet background has been evaluated and it is found to be rather small (see Appendix G10). We therefore conclude that the background contamination could be responsible for at least half of the observed discrepancy.

- slices in the jet profile: in order to investigate the possibility of the discrepancy being caused by instrumental problems or the modeling of the underlying event, we have compared data and MC in η or ϕ slices of the jet profile, built by considering only a subset of towers requiring either $\Delta\eta(\text{jet}, \text{tower}) < 0.1$ (η-slice) or $\Delta\phi(\text{jet}, \text{tower}) < 0.1$ (ϕ-slice). For a jet with $\left|\eta^{\rm det}_{\rm jet}\right|$ <0.4, the η-slices consider only towers in a ϕ-ring contained in CC, therefore being insensitive to instrumental problems in the ICR or the modeling of the underlying event near the beam axis. Therefore, it probes the shape of the particle-jet profile and also the energy in the photon hemisphere. On the

other hand, the ϕ-slice has an increased sensitivity to the modeling of the underlying event as a function of η, as well as material effects from particles entering the solenoid at large incident angle (in the case of the η-slice, even particles with large $\Delta\mathcal{R}$ with respect to the jet axis enter the solenoid at $\sim 90^{\circ}$). Examples of slices are shown in Fig. 198 for $\mathcal{R}_{\rm cone} = 0.7$ jets with $45 < p'_T < 60$ GeV in three different $\left|\eta^{\rm det}_{\rm jet}\right|$ regions. These slice tests contain plenty of information. Unfortunately, due to time/manpower limitations it is not currently possible to carry out this study beyond a "qualitative check". The tentative conclusion is that both particle-jet and not-particle-jet profiles appear reasonably well described and no obvious instrumental effects are observed which could explain the discrepancy.

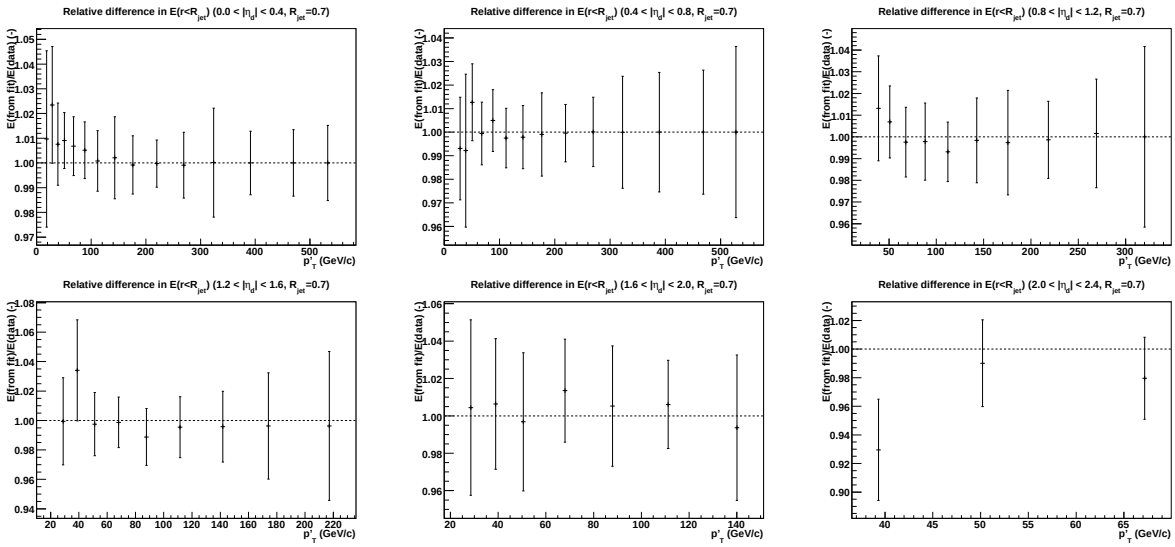

FIG. 197: Ratio of integrals of the energy profiles up to $\mathcal{R}_{\rm cone}$ between the mixture MC and fitted profile for $\mathcal{R}_{\rm cone} = 0.7$ jets as a function of p'_T and in different $\left|\eta^{\rm det}_{\rm jet}\right|$ regions.

From the above studies, the tentative conclusion is that a significant fraction of the discrepancy might be caused by the dijet background contamination, for which a somewhat conservative systematic uncertainty has already been assigned (see e.g. Fig. 205). However, it is possible that part of the discrepancy is caused by some other imperfections in the simulation, which are very difficult to evaluate. Given these limitation, we adopt a more pragmatic approach and try to assess what would be the impact on showering by "forcing a perfect fit" in the $[\mathcal{R}_{\rm cone} - 0.2, 1.0]$ $\Delta\mathcal{R}$ range, believed to be the most sensitive region to effects such as zero-suppression, shower development in the calorimeter, material description, etc. "Forcing a perfect fit" means that the fit is performed excluding the $[\mathcal{R}_{\rm cone} - 0.2, 1.0]$ $\Delta\mathcal{R}$ range and that the actual energy measured in that region needs to be assigned in a physical way to the particle-jet and not-particle-jet templates (it is assumed that the offset profile is not the source of the problem). Since very likely any inaccuracies in the simulation would affect both templates, a well-motivated assignment of the excess energy is based on the expected fraction of energy from either the particle-jet or not-particle-jet profiles in each $\Delta\mathcal{R}$ bin. Therefore, the showering fraction is computed exactly as in Eq. 60, with the following modifications:

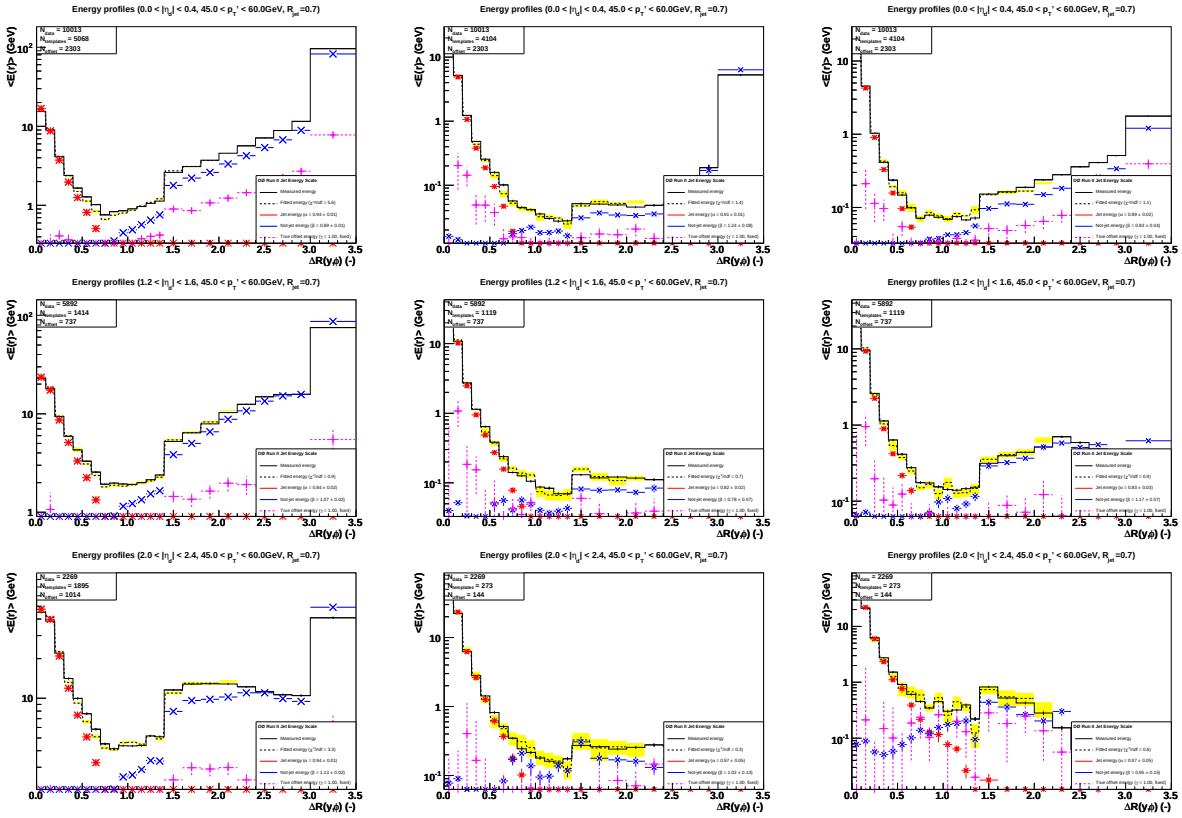

FIG. 198: Fitted energy profiles in data for $\mathcal{R}_{\text{cone}} = 0.7$ jets with $45 < p'_T < 60$ GeV in different detector regions: $\left|\eta^{\text{det}}_{\text{jet}}\right| < 0.4$ (top), $1.2 < \left|\eta^{\text{det}}_{\text{jet}}\right| < 1.6$ (middle) and $2.0 < \left|\eta^{\text{det}}_{\text{jet}}\right| < 2.4$ (bottom). Compared in different columns: nominal profile (left), η-slice (center) and ϕ-slice (rigth).

$$
\begin{aligned}
E^{\text{meas}(\Delta\mathcal{R}<\mathcal{R}_{\text{cone}}),\text{MC}}_{\text{ptclj}} &= \sum_{0\leq\Delta\mathcal{R}_i\leq\mathcal{R}_{\text{cone}}} E^{\text{meas,MC}}_{\text{ptclj,i}}\kappa_i, \\
E^{\text{meas,MC}}_{\text{ptclj}} &= \sum_{0\leq\Delta\mathcal{R}_i<\infty} E^{\text{meas,MC}}_{\text{ptclj,i}}\kappa_i, \\
E^{\text{meas}(\Delta\mathcal{R}<\mathcal{R}_{\text{cone}}),\text{MC}}_{\text{not-ptclj}} &= \sum_{0\leq\Delta\mathcal{R}_i\leq\mathcal{R}_{\text{cone}}} E^{\text{meas,MC}}_{\text{notptclj,i}}\kappa_i,
\end{aligned}
\tag{G2}
$$

with

$$
\kappa_i = \begin{cases} \frac{E^{\text{data}}_{\text{i}} - E^{\text{offset}}_{\text{i}}}{\hat{\alpha}E^{\text{meas,MC}}_{\text{ptclj,i}} + \hat{\beta}E^{\text{meas,MC}}_{\text{not-ptclj,i}}} & (\Delta\mathcal{R}_i \in [\mathcal{R}_{\text{cone}} - 0.2, 1.0]) \\ 1 & (\Delta\mathcal{R}_i \notin [\mathcal{R}_{\text{cone}} - 0.2, 1.0]) \end{cases}
\tag{G3}
$$

where $\hat{\alpha}, \hat{\beta}$ are the estimated scale factors from the template fit excluding the $[\mathcal{R}_{\text{cone}} - 0.2, 1.0]$ $\Delta\mathcal{R}$ range. Fig. 199 compares the original to forced fit profiles for $\mathcal{R}_{\text{cone}} = 0.7$ jets in data with $45 < p'_T < 60$ GeV in different detector regions. As a result of this procedure, an improved agreement (although not necessarily perfect) of the ratio of integrals is also obtained, as shown in Fig. 200. Finally, a comparison between the extracted showering correction using the original and the forced fit is given in Figs. 201 and 201, respectively for

$\mathcal{R}_{\rm cone} = 0.7$ and 0.5 jets. As it can be appreciated, the difference is typically $< 0.4\%$, which is conservatively taken as an additional systematic uncertainty.

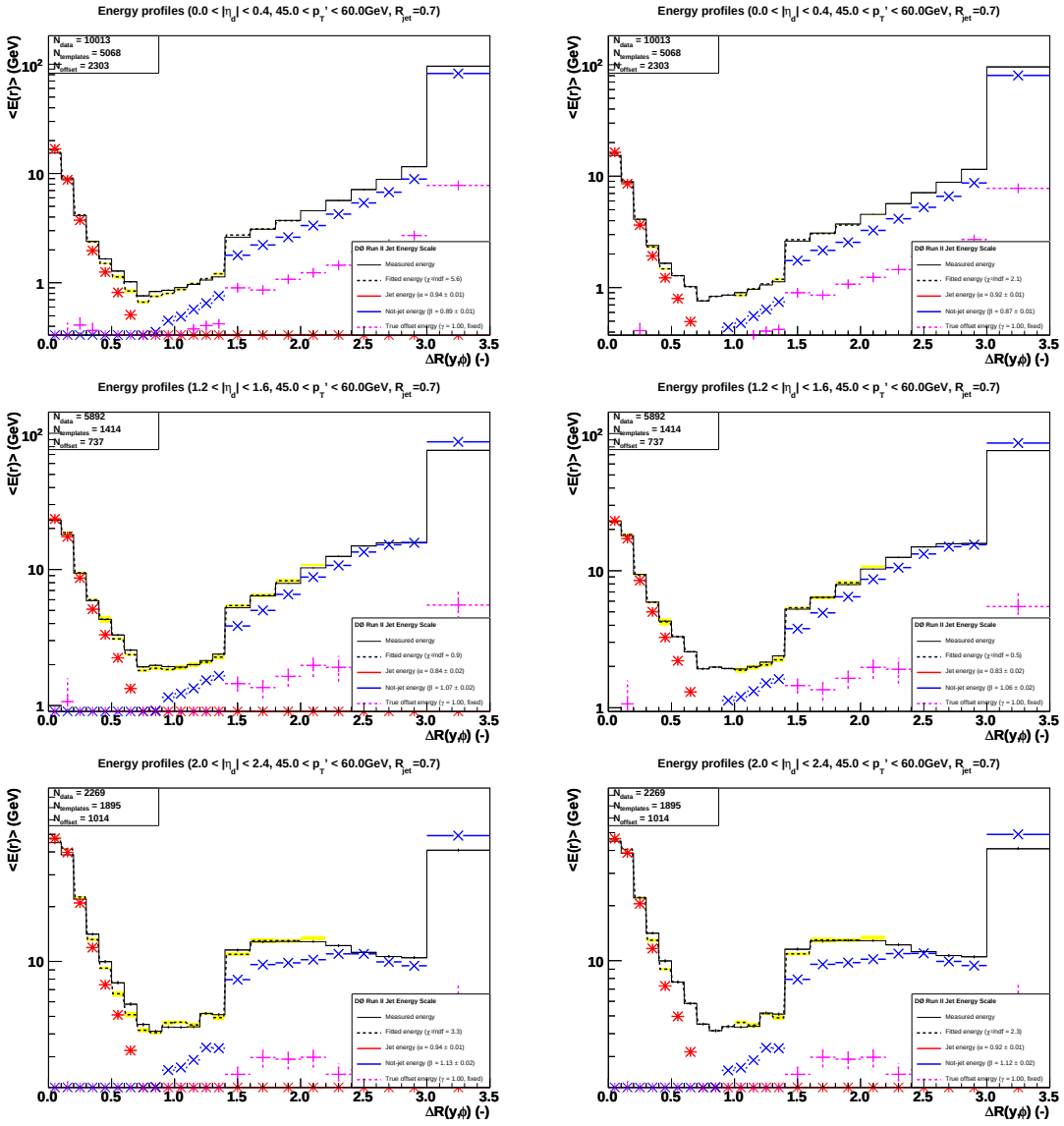

FIG. 199: Fitted energy profiles in data for $\mathcal{R}_{\rm cone} = 0.7$ jets with $45 < p'_T < 60$ GeV in different detector regions: $\left|\eta^{\rm det}_{\rm jet}\right| < 0.4$ (top), $1.2 < \left|\eta^{\rm det}_{\rm jet}\right| < 1.6$ (middle) and $2.0 < \left|\eta^{\rm det}_{\rm jet}\right| < 2.4$ (bottom). Compared in different columns: original fit (left), forced fit (rigth).

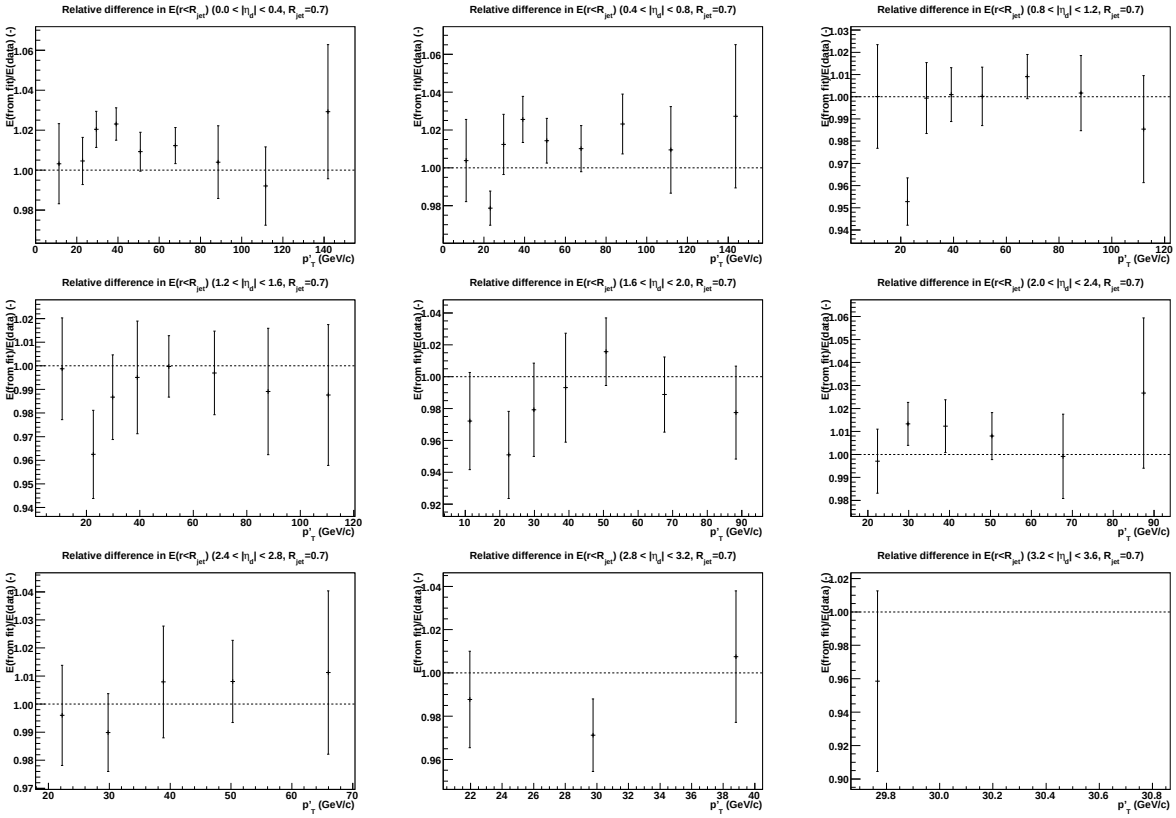

FIG. 200: Ratio of integrals of the energy profiles up to $\mathcal{R}_{\rm cone}$ between the data and fitted profile for $\mathcal{R}_{\rm cone} = 0.7$ jets as a function of p'_T and in different $\left|\eta_{\rm jet}^{\rm det}\right|$ regions.

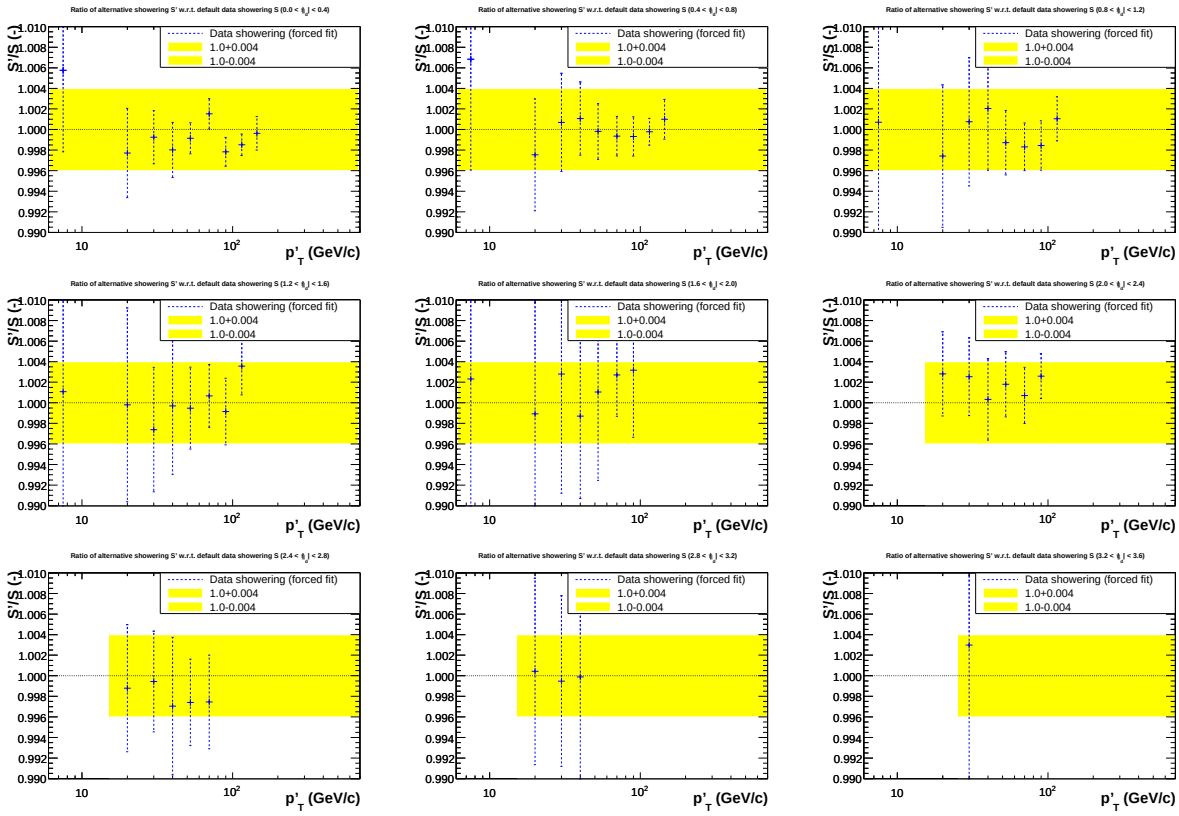

FIG. 201: Ratio of showering corrections extracted using the forced fit versus the original fit for $\mathcal{R}_{\text{cone}} = 0.7$ jets in data. The ratio is shown as a function of p'_T in different $\left|\eta^{\text{det}}_{\text{jet}}\right|$ bins. The yellow band represents the conservative 0.4% systematic uncertainty assigned.

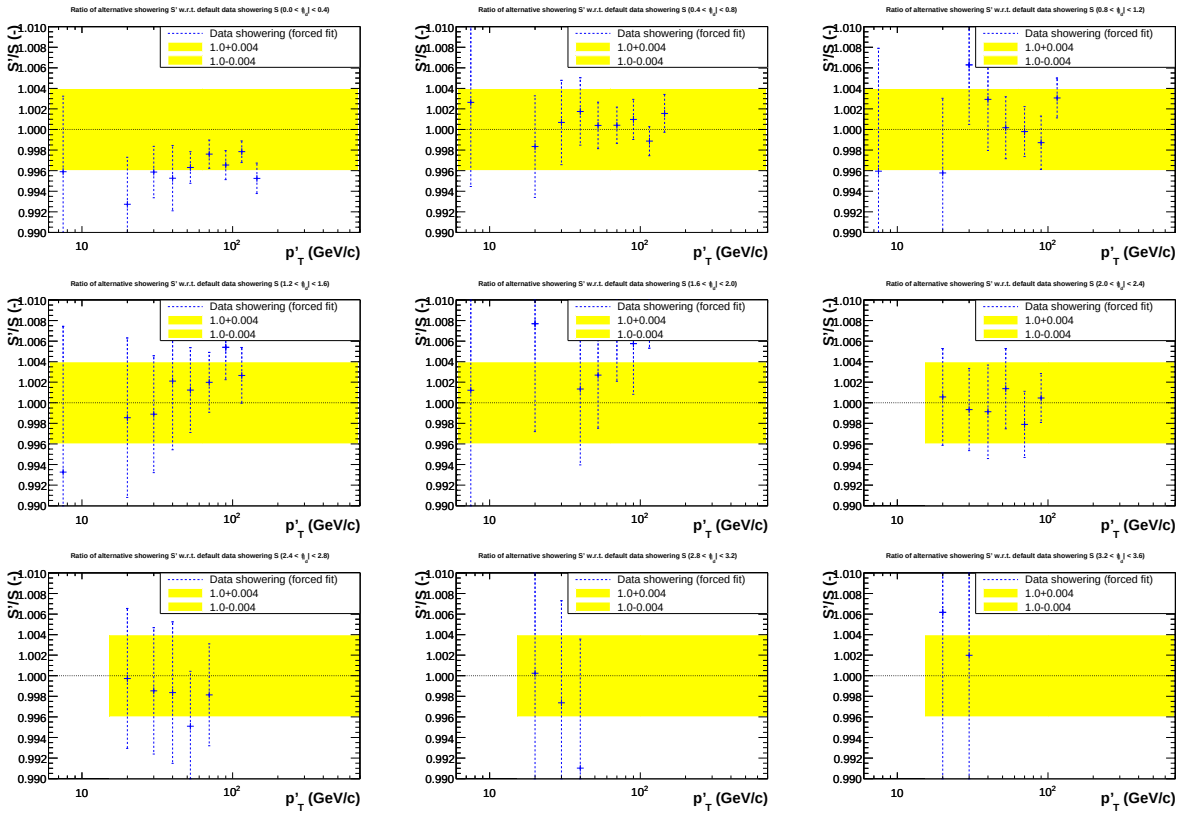

FIG. 202: Ratio of showering corrections extracted using the forced fit versus the original fit for $\mathcal{R}_{\text{cone}} = 0.5$ jets in data. The ratio is shown as a function of p'_T in different $\left|\eta^{\text{det}}_{\text{jet}}\right|$ bins. The yellow band represents the conservative 0.4% systematic uncertainty assigned.

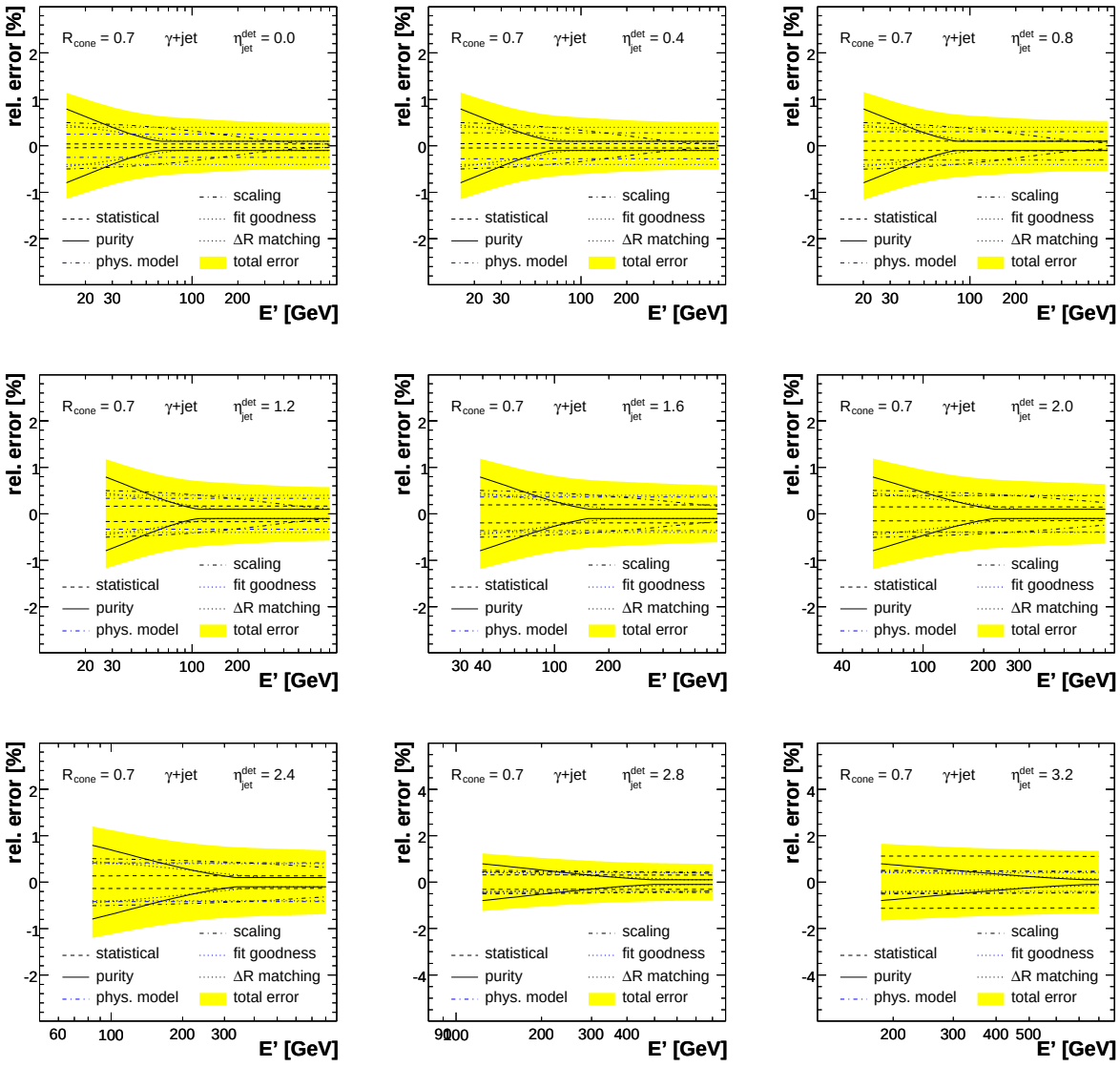

FIG. 203: Relative uncertainties on the showering correction vs p'_T for $\mathcal{R}_{\rm cone} = 0.7$ jets in data. Different plots correspond to different values of $\eta^{\rm det}_{\rm jet}$.

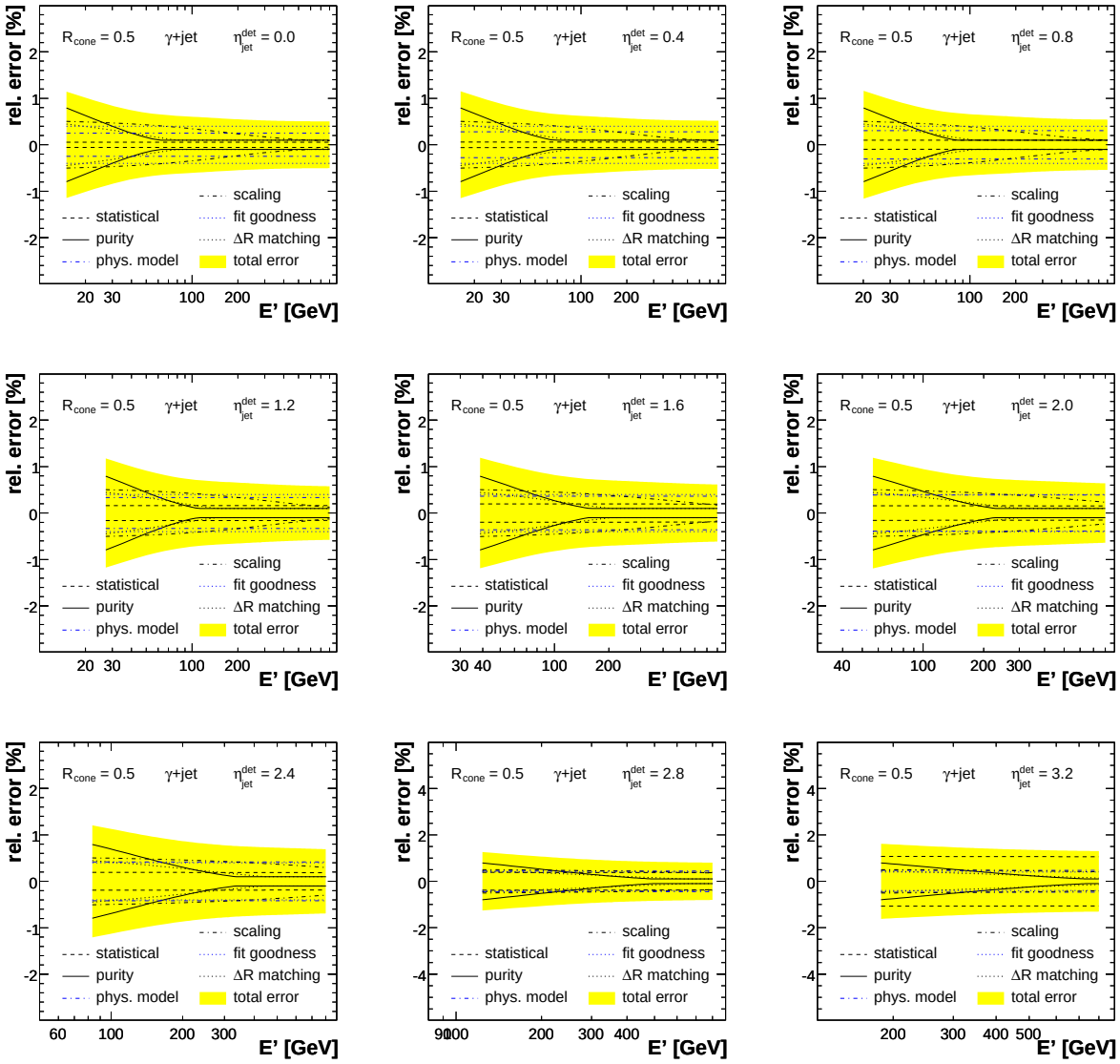

FIG. 204: Relative uncertainties on the showering correction vs p'_T for $\mathcal{R}_{\rm cone} = 0.5$ jets in data. Different plots correspond to different values of $\eta^{\rm det}_{\rm jet}$.

10. Systematic uncertainty from Dijet Background Contamination

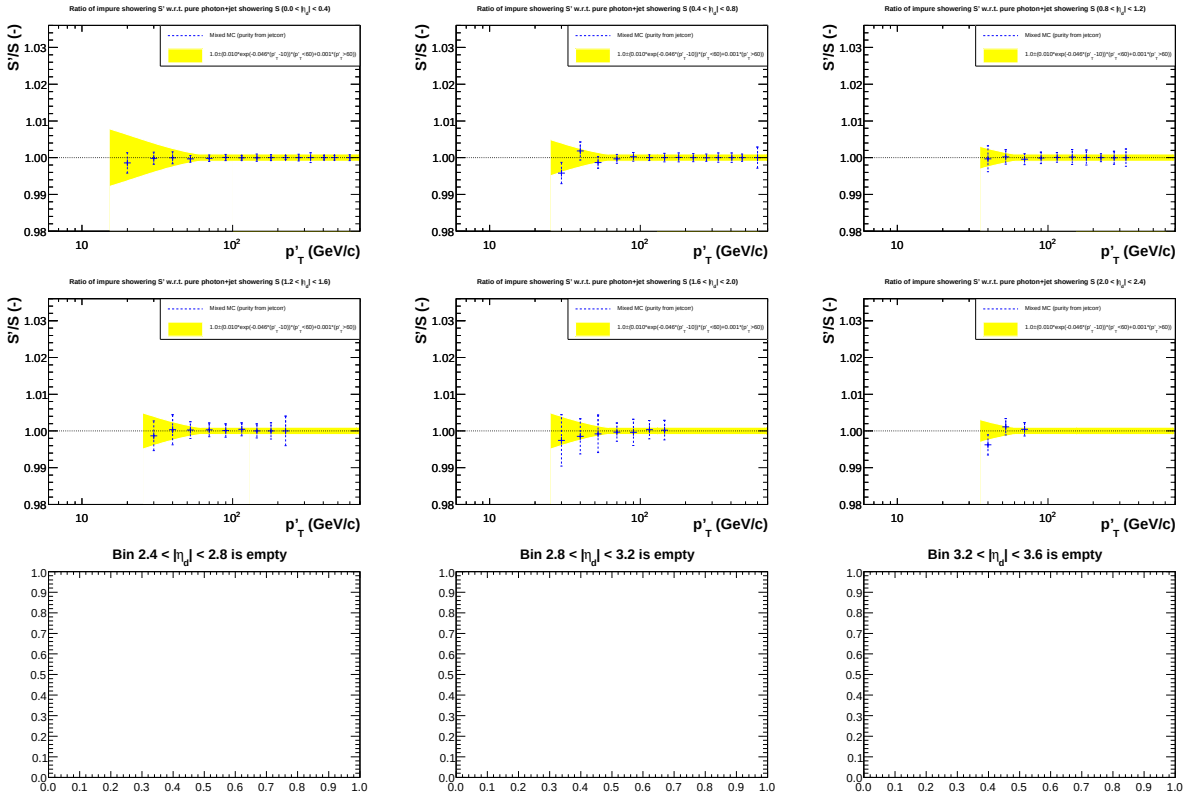

FIG. 205: Comparison of the templated-based showering corrections for $\mathcal{R}_{\rm cone} = 0.7$ jets obtained in pure γ+jet MC and from γ+jet plus EM+jet MC mixed according to the expected sample purity in data. Shown is the relative difference with respect to nominal (pure γ+jet MC). The yellow band illustrates the assigned systematic uncertainty.

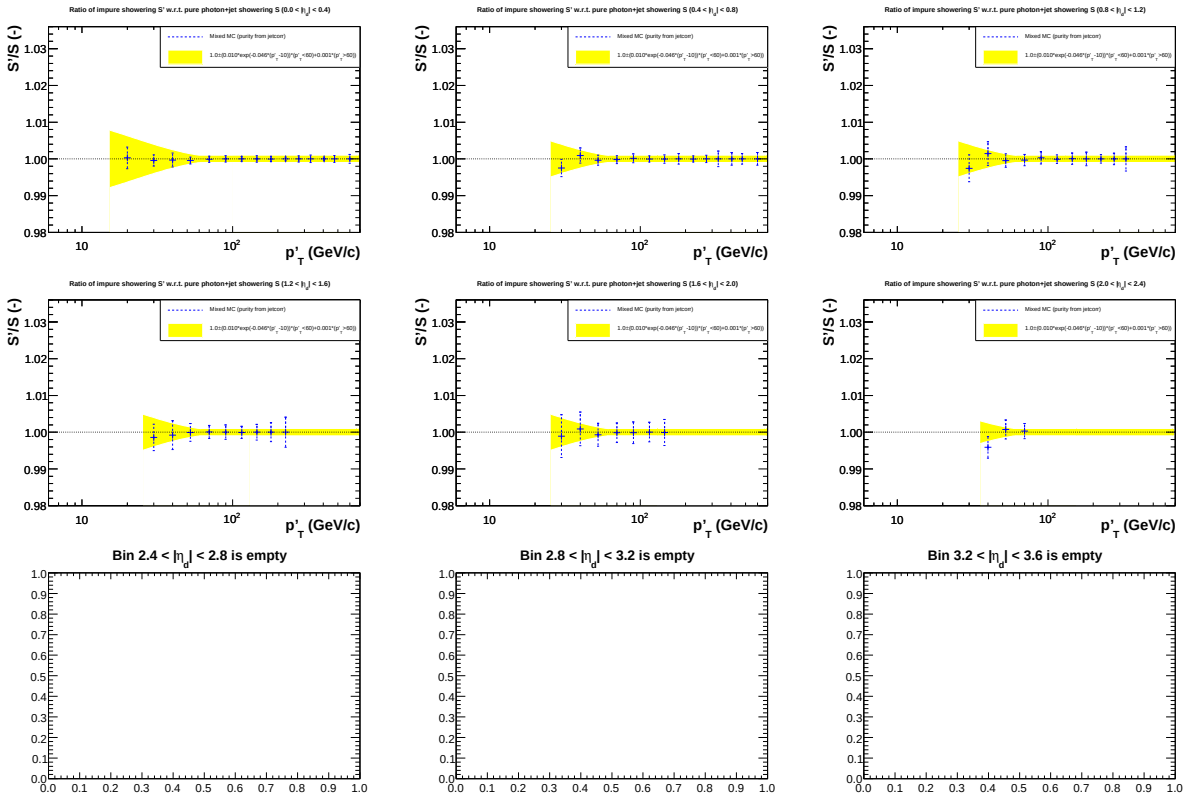

FIG. 206: Comparison of the templated-based showering corrections for $\mathcal{R}_{\rm cone} = 0.5$ jets obtained in pure γ+jet MC and from γ+jet plus EM+jet MC mixed according to the expected sample purity in data. Shown is the relative difference with respect to nominal (pure γ+jet MC). The yellow band illustrates the assigned systematic uncertainty.

11. Systematic uncertainty from $\Delta\mathcal{R}$ Matching

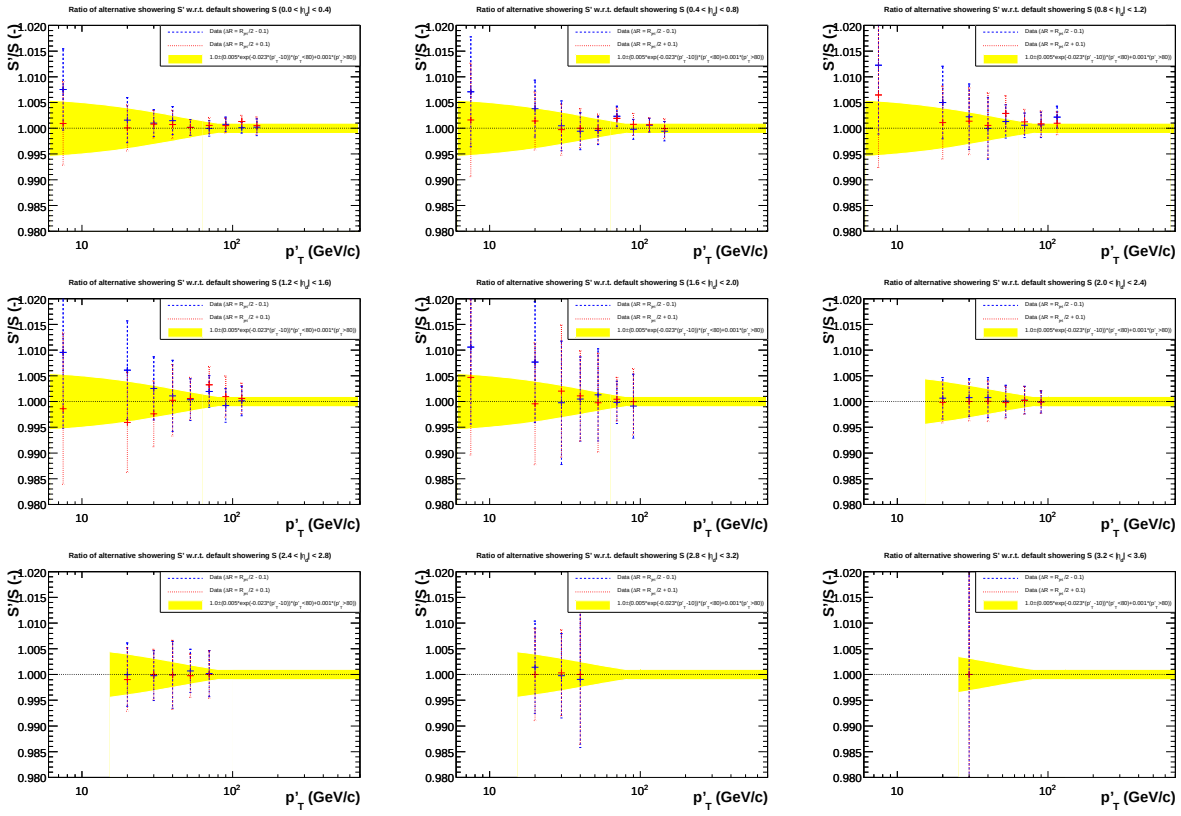

FIG. 207: Comparison of the templated-based showering corrections for $\mathcal{R}_{\rm cone} = 0.7$ jets obtained in pure γ+jet MC for different choice of the $\Delta\mathcal{R}$ matching between the particle and reconstructed jets. Shown is the relative difference with respect to nominal ($\Delta\mathcal{R} = \mathcal{R}_{\rm cone}$). The yellow band illustrates the assigned systematic uncertainty.

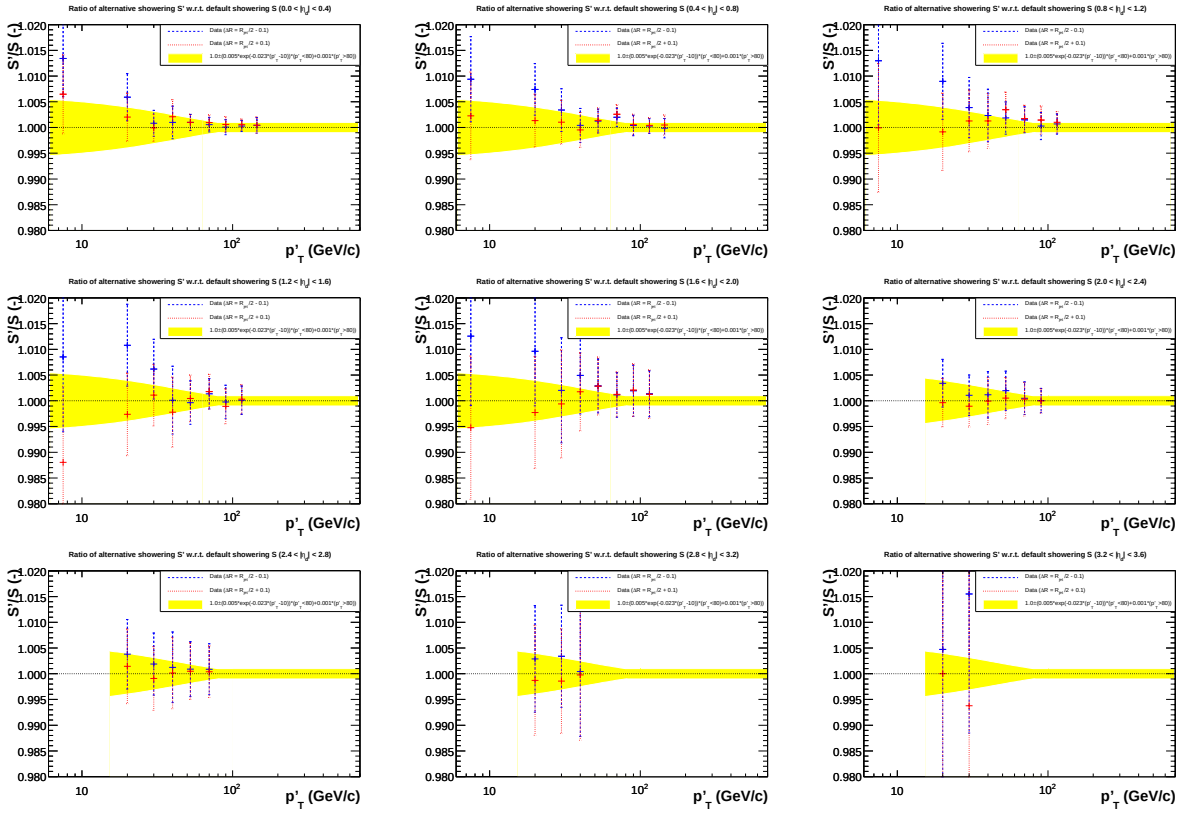

FIG. 208: Comparison of the templated-based showering corrections for $\mathcal{R}_{\rm cone} = 0.5$ jets obtained in pure γ+jet MC for different choice of the $\Delta\mathcal{R}$ matching between the particle and reconstructed jets. Shown is the relative difference with respect to nominal ($\Delta\mathcal{R} = \mathcal{R}_{\rm cone}$). The yellow band illustrates the assigned systematic uncertainty.

12. Systematic uncertainty from Single Pion Response Scaling

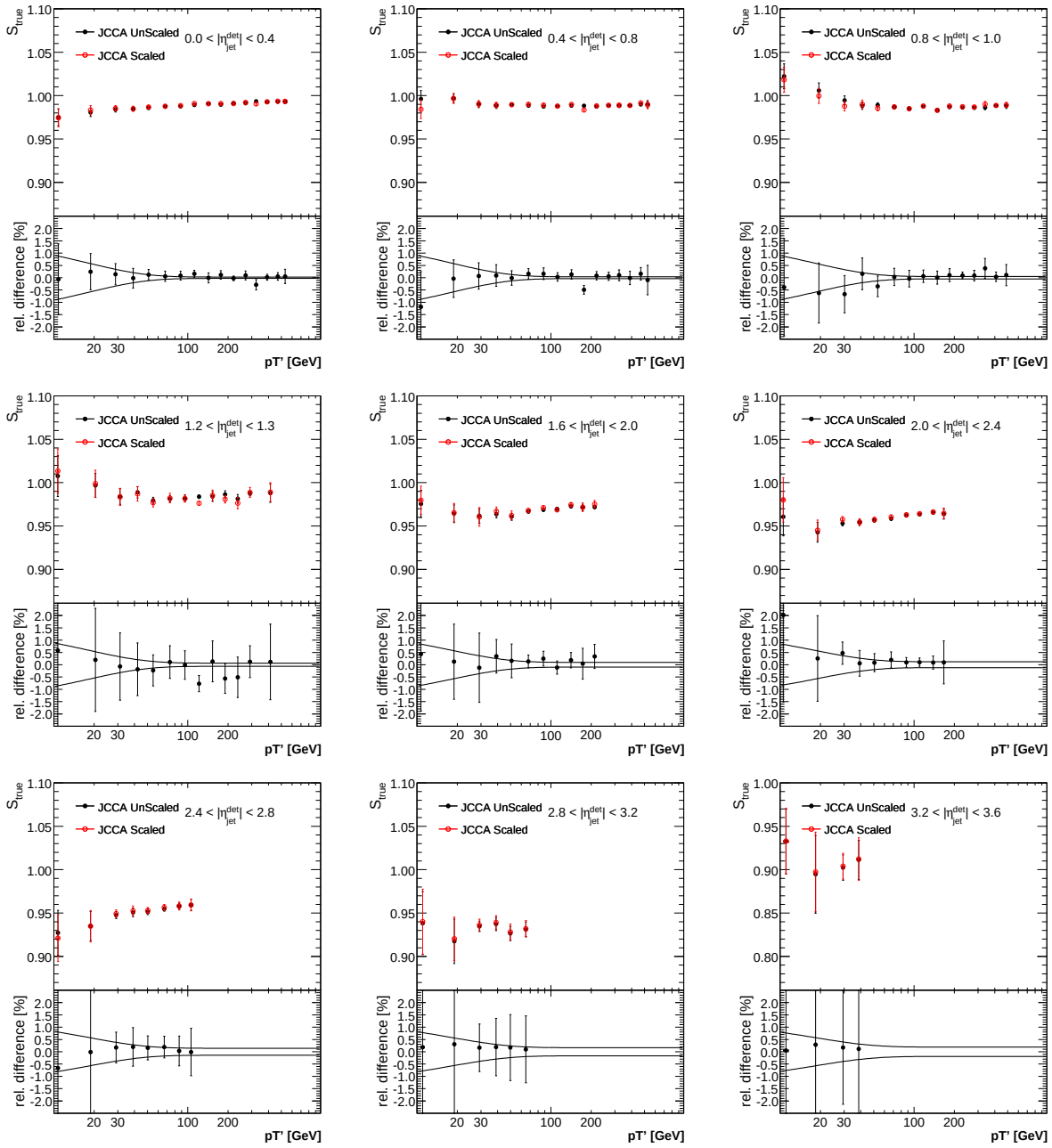

FIG. 209: Comparison of the true showering correction for $\mathcal{R}_{\text{cone}} = 0.7$ jets between the standard γ+jet MC and the γ+jet MC with a scaled single pion response. The bottom plots present the relative difference, along with the assigned systematic uncertainty (solid curve).

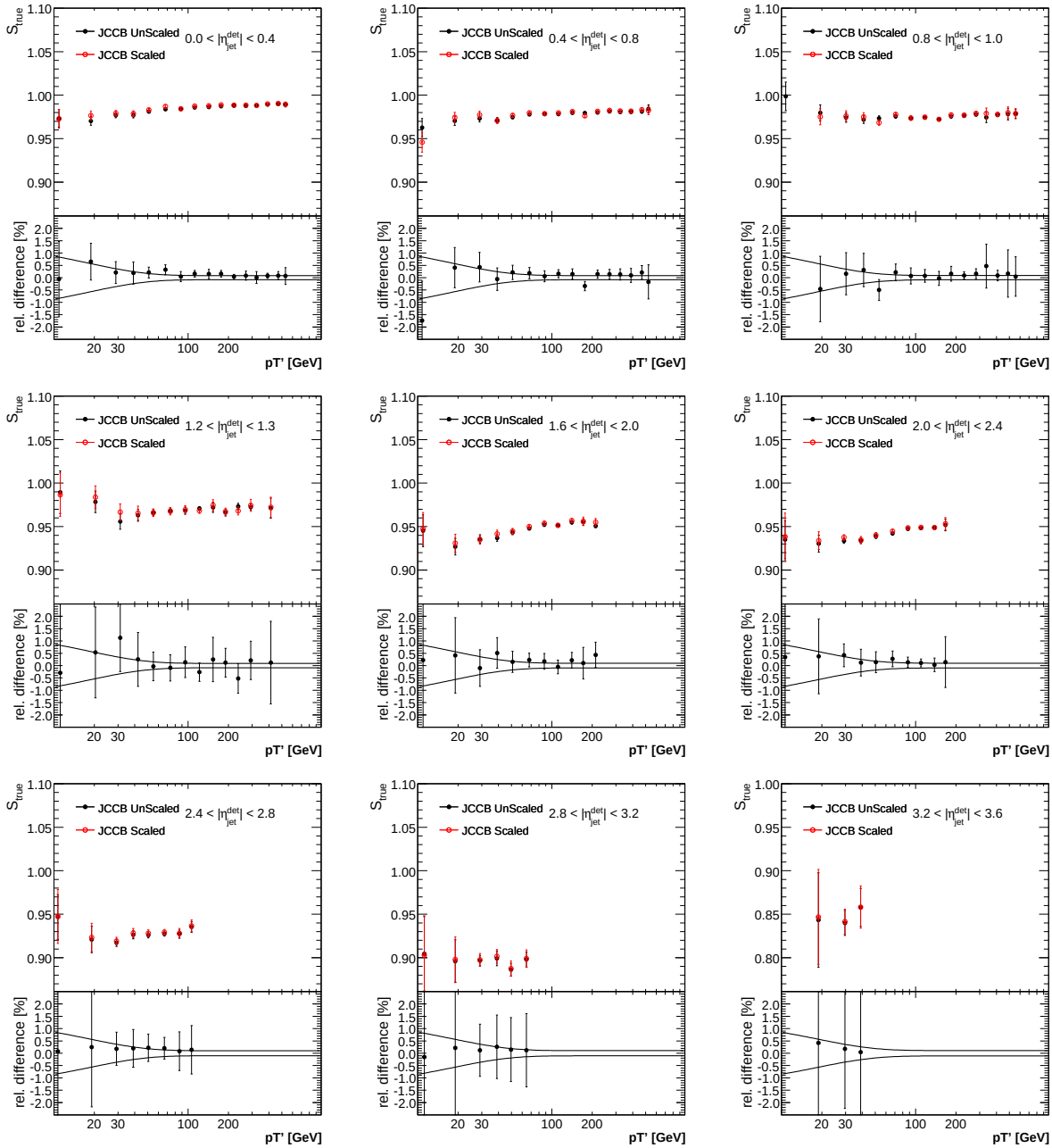

FIG. 210: Comparison of the true showering correction for $\mathcal{R}_{\text{cone}} = 0.5$ jets between the standard γ+jet MC and the γ+jet MC with a scaled single pion response. The bottom plots present the relative difference, along with the assigned systematic uncertainty (solid curve).

13. Systematic uncertainty from Physics Model

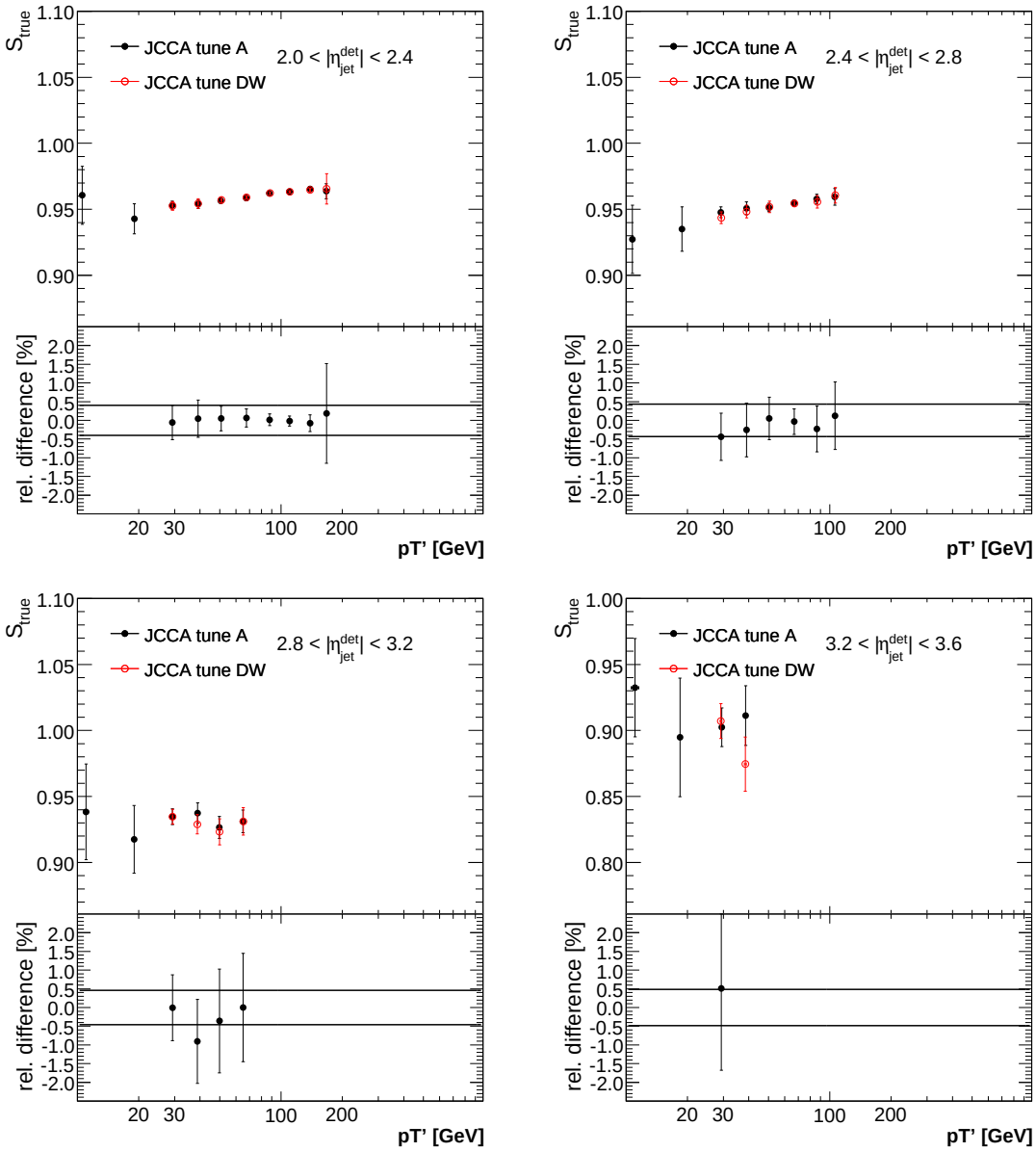

FIG. 211: Comparison of the true showering correction for $\mathcal{R}_{\text{cone}} = 0.7$ jets between γ+jet Tune A and Tune DW MC. The bottom plots present the relative difference, along with the assigned systematic uncertainty (solid curve).

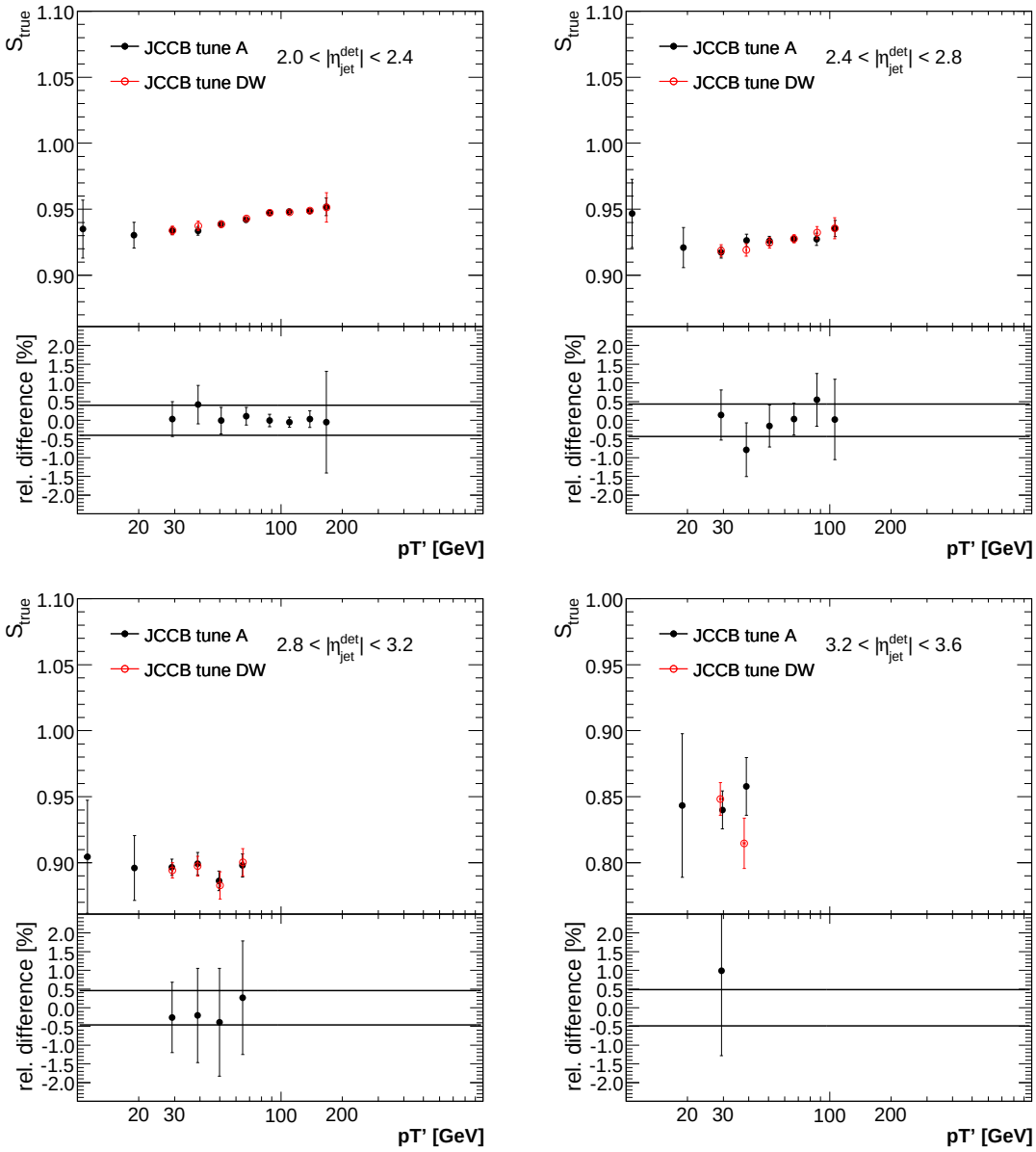

FIG. 212: Comparison of the true showering correction for $\mathcal{R}_{\rm cone} = 0.5$ jets between γ+jet Tune A and Tune DW MC. The bottom plots present the relative difference, along with the assigned systematic uncertainty (solid curve).

APPENDIX H: QCD-SPECIFIC CORRECTIONS

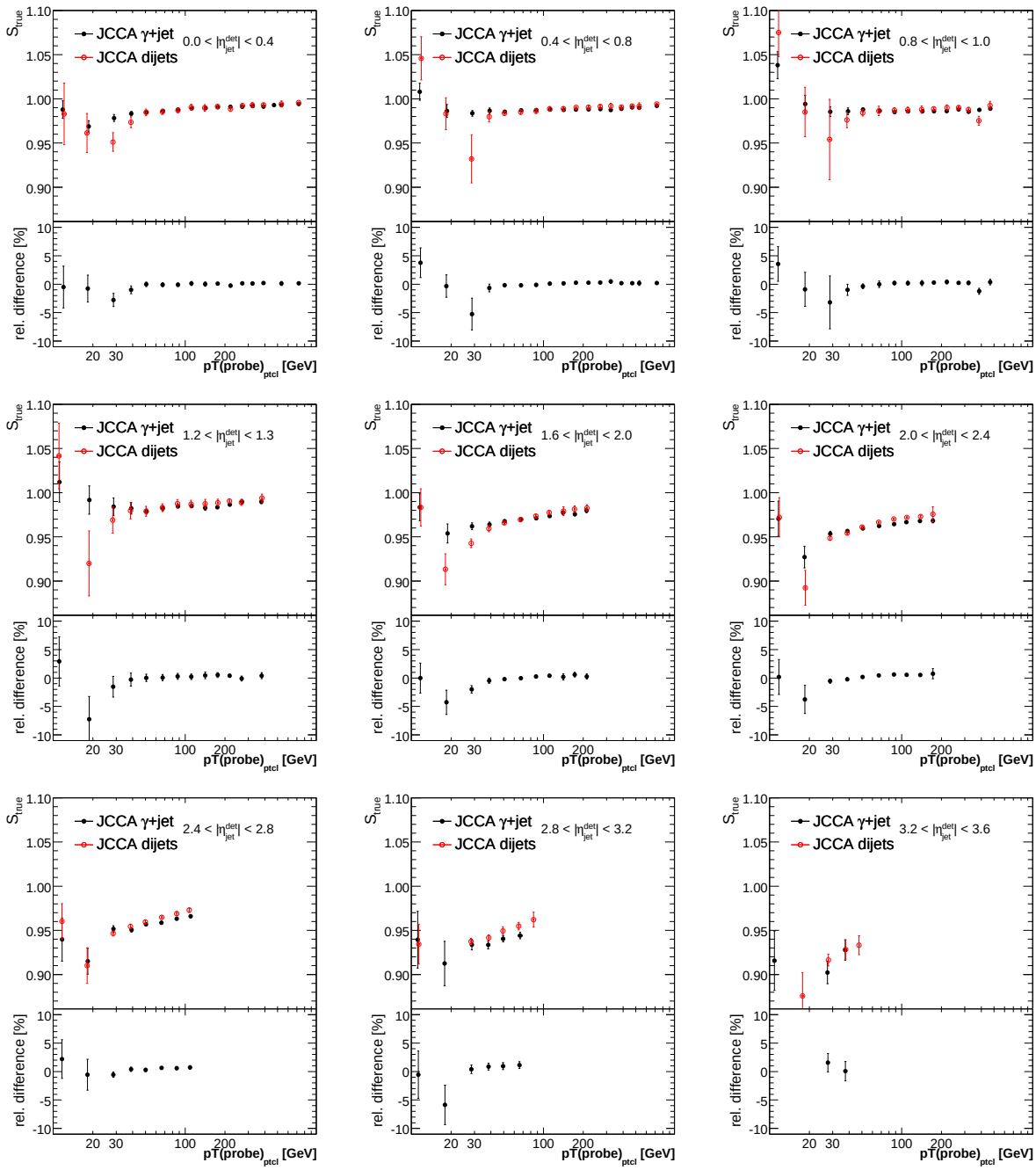

FIG. 213: Comparison of the true showering correction for $\mathcal{R}_{\text{cone}} = 0.7$ jets between γ+jet and QCD dijet events in MC. The bottom plots present the relative difference.

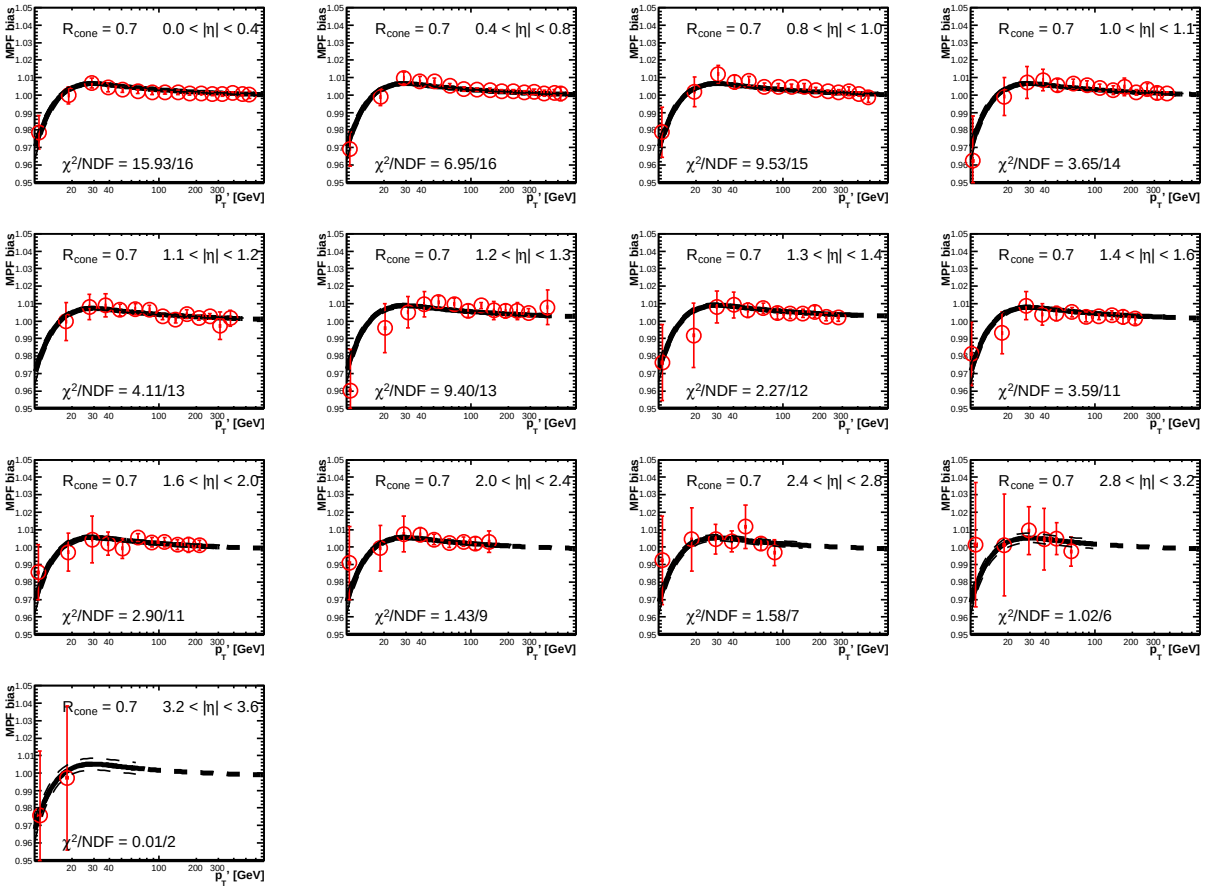

FIG. 214: p_T-based topology bias correction for $\mathcal{R}_{\rm cone} = 0.7$ jets.

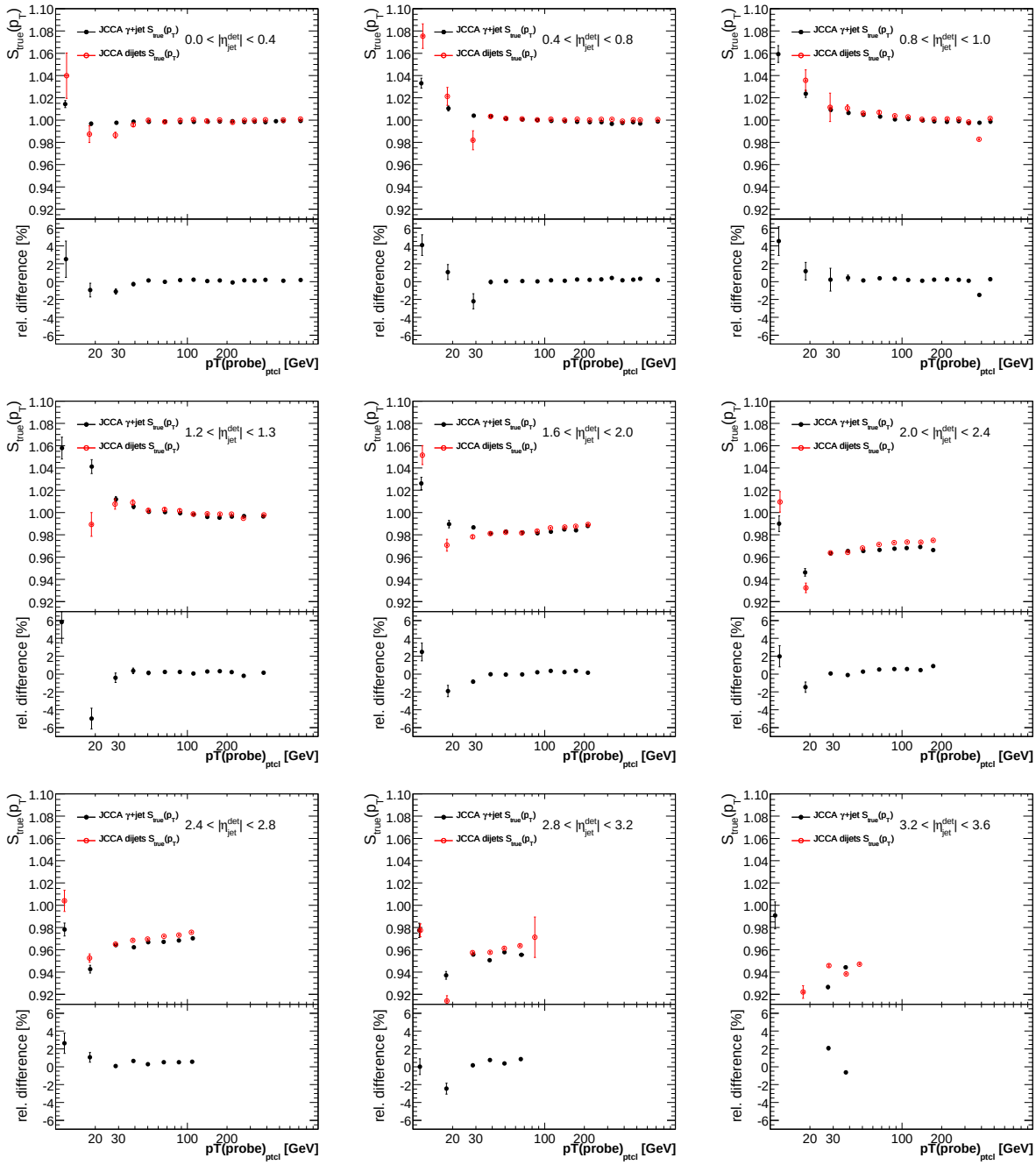

FIG. 215: Comparison of the true showering correction to p_T for $\mathcal{R}_{\rm cone} = 0.7$ jets between γ+jet and QCD dijet events in MC. The bottom plots present the relative difference.

APPENDIX I: CLOSURE TESTS

1. Direct Closure Tests in MC using a Consistent Selection

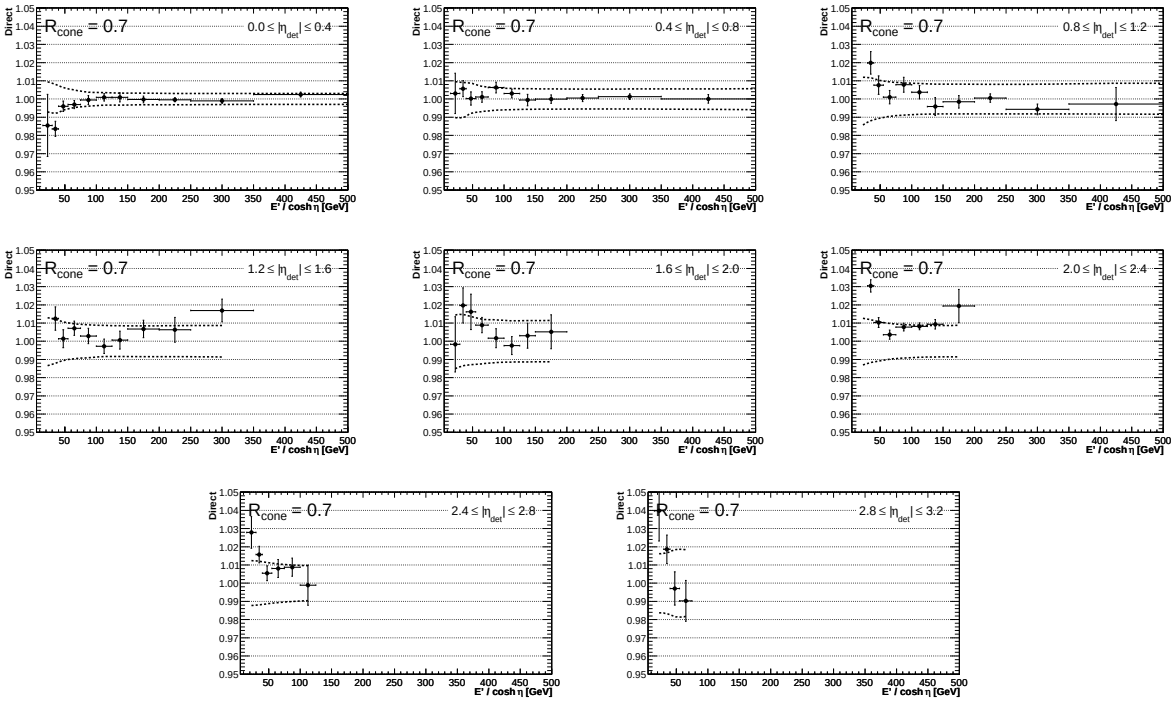

FIG. 216: Closure test for $\mathcal{R}_{\rm cone} = 0.7$ jets in MC as a function of p'_T and in different $\left|\eta^{\rm det}_{\rm jet}\right|$ bins. The points correspond to the value of the direct closure variable (see Eq. 76) and the dashed line represents the total jet energy scale uncertainty.

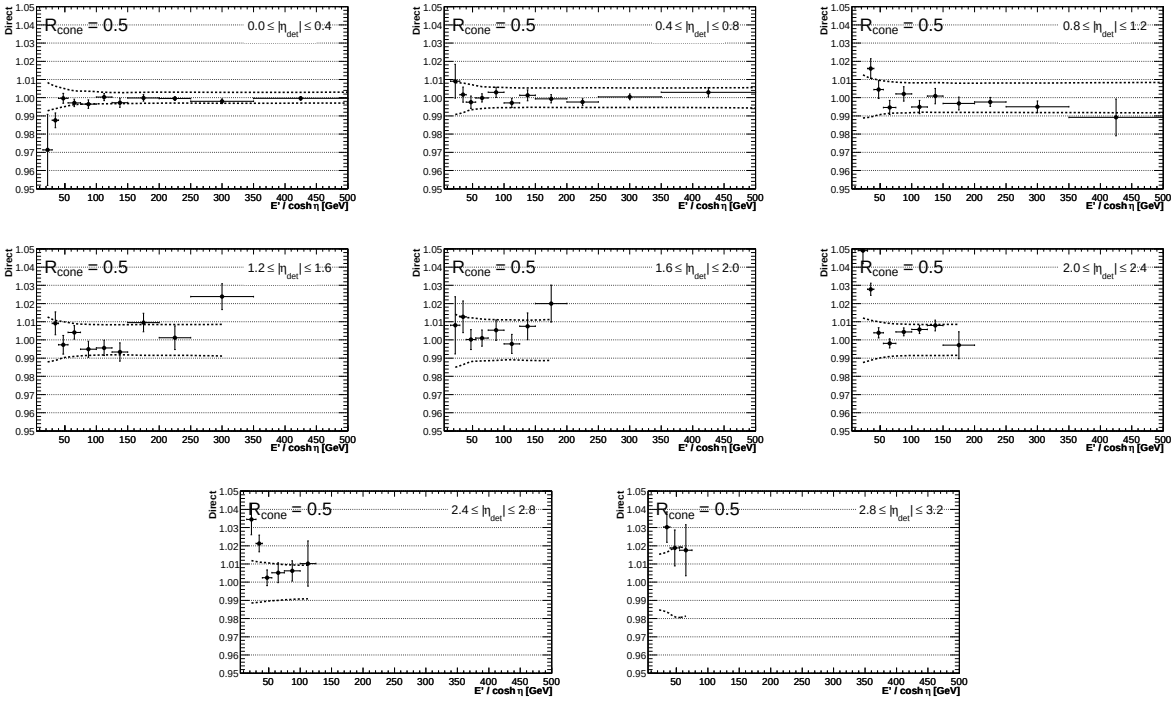

FIG. 217: Closure test for $\mathcal{R}_{\text{cone}} = 0.5$ jets in MC as a function of p'_T and in different $\left|\eta_{\text{jet}}^{\text{det}}\right|$ bins. The points correspond to the value of the direct closure variable (see Eq. 76) and the dashed line represents the total jet energy scale uncertainty.

2. $\Delta\mathcal{R}$ Matching Systematic in Direct Closure Tests in MC

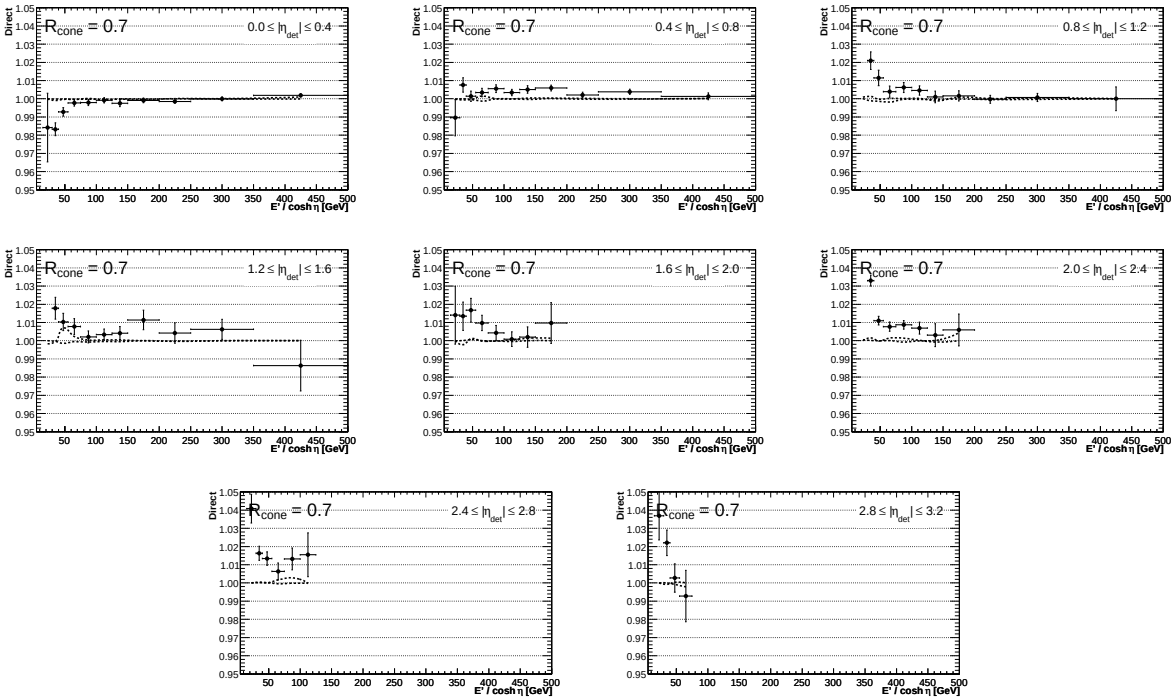

FIG. 218: Closure test for $\mathcal{R}_{\text{cone}} = 0.7$ jets in MC as a function of p'_T and in different $\left|\eta^{\text{det}}_{\text{jet}}\right|$ bins. The points correspond to the value of the direct closure variable (see Eq. 76) and the dashed line represents the uncertainty band resulting from varying the reconstructed-to-particle jet matching criterion by $\Delta\mathcal{R} = \mathcal{R}_{\text{cone}}/2 \pm 0.1$.

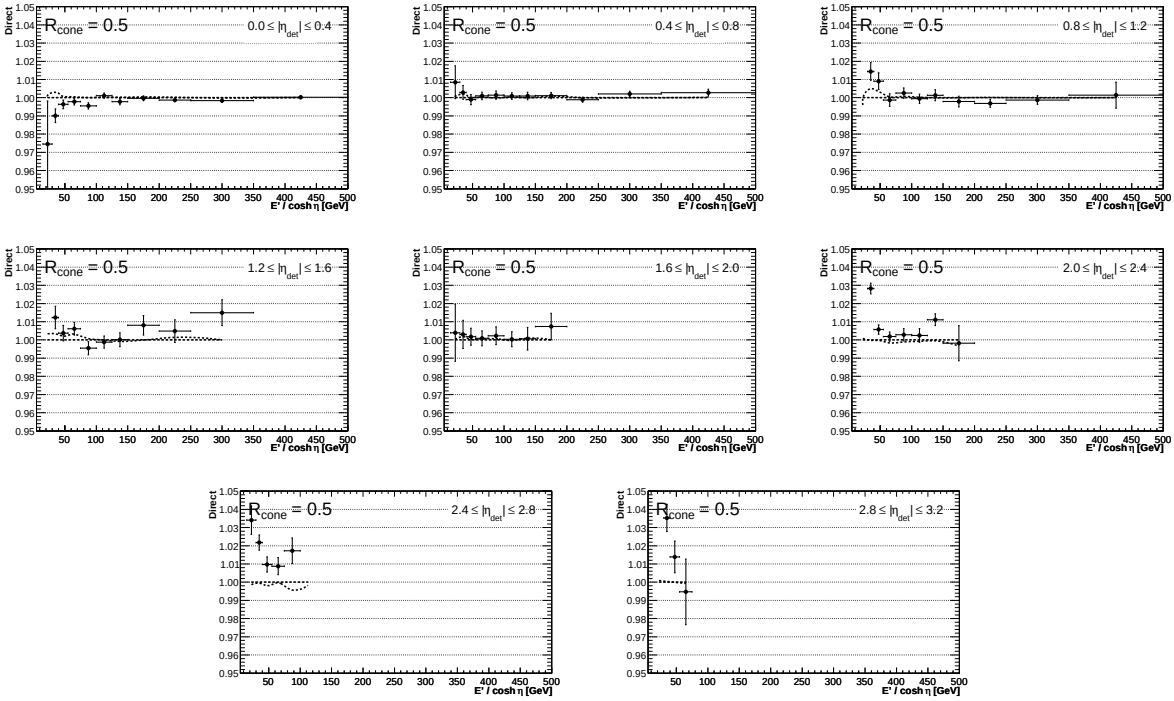

FIG. 219: Closure test for $\mathcal{R}_{\rm cone} = 0.5$ jets in MC as a function of p'_T and in different $\left|\eta^{\rm det}_{\rm jet}\right|$ bins. The points correspond to the value of the direct closure variable (see Eq. 76) and the dashed line represents the uncertainty band resulting from varying the reconstructed-to-particle jet matching criterion by $\Delta\mathcal{R} = \mathcal{R}_{\rm cone}/2 \pm 0.1$.

3. Residual Miscalibration of the QCD Dijet Background

Jet energy scale corrections in data and MC are designed to correct jets from pure γ+jet events back to the particle level:

$$E_{\text{jet}}^{\text{corr}(\gamma+\text{jet})} = k_{\text{JES}}^{(\gamma+\text{jet})} E_{\text{jet}}^{\text{meas}(\gamma+\text{jet})} = E_{\text{jet}}^{\text{ptcl}(\gamma+\text{jet})} \tag{I1}$$

However, the selected γ+jet sample in data is actually a mixture of signal γ+jet and QCD dijet background events. Therefore, the average uncorrected jet energy in a given E' bin can be expressed as:

$$E_{\text{jet}}^{\text{meas,Data}} = \rho E_{\text{jet}}^{\text{meas}(\gamma+\text{jet}),\text{Data}} + (1-\rho) E_{\text{jet}}^{\text{meas(dijet)},\text{Data}}, \tag{I2}$$

where ρ is the sample purity, and $E_{\text{jet}}^{\text{meas}(\gamma+\text{jet})}$ and $E_{\text{jet}}^{\text{meas(dijet)}}$ are, respectively, the measured jet energies from γ+jet signal and QCD dijet background. After jet energy scale correction, the corrected jet energy in data is given by:

$$E_{\text{jet}}^{\text{corr,Data}} = k_{\text{JES}}^{(\gamma+\text{jet}),\text{Data}} E_{\text{jet}}^{\text{meas,Data}} = \rho E_{\text{jet}}^{\text{ptcl}(\gamma+\text{jet})} + (1-\rho) E_{\text{jet}}^{\text{ptcl}(\gamma+\text{jet})} \frac{E_{\text{jet}}^{\text{meas(dijet)},\text{Data}}}{E_{\text{jet}}^{\text{meas}(\gamma+\text{jet}),\text{Data}}}. \tag{I3}$$

A similar expresion can be obtained for the corrected jet energy in mixture MC:

$$E_{\text{jet}}^{\text{corr,MC}} = k_{\text{JES}}^{(\gamma+\text{jet}),\text{MC}} E_{\text{jet}}^{\text{meas,MC}} = \rho E_{\text{jet}}^{\text{ptcl}(\gamma+\text{jet})} + (1-\rho) E_{\text{jet}}^{\text{ptcl}(\gamma+\text{jet})} \frac{E_{\text{jet}}^{\text{meas(dijet)},\text{MC}}}{E_{\text{jet}}^{\text{meas}(\gamma+\text{jet}),\text{MC}}}. \tag{I4}$$

As it can be appreciated, by definition the subset of γ+jet events would be properly intercalibrated between data and MC. However, the subsect of QCD dijet events could remain miscalibrated unless the following condition is satisfied:

$$\frac{E_{\text{jet}}^{\text{meas(dijet)},\text{Data}}}{E_{\text{jet}}^{\text{meas}(\gamma+\text{jet}),\text{Data}}} = \frac{E_{\text{jet}}^{\text{meas(dijet)},\text{MC}}}{E_{\text{jet}}^{\text{meas}(\gamma+\text{jet}),\text{MC}}}. \tag{I5}$$

Unfortunately, the above is not guaranteed because MC does not reproduce the single pion response in data. The size of the effect can be estimated in MC through the following procedure:

1. Consider γ+jet MC events using the nominal γ+jet selection.
2. Due to the limited statistics of the QCD dijet (γ-like) MC, consider instead inclusive QCD dijet events using the nominal dijet selection. Assume the probe jet has a similar flavor composition as the jet in fake γ+jet events. This is expected since the fragmentation of each of the jets is largely uncorrelated.
3. In both cases, match the probe jet with a particle jet.
4. In a given bin of particle-jet p_T, make the ratio of measured probe jet p_T between γ+jet and QCD dijet: $p_{T,\text{jet}}^{\text{meas}(\gamma+\text{jet}),\text{MC}} / p_{T,\text{jet}}^{\text{meas}(\gamma+\text{jet}),\text{MC}}$.
5. Repeat the above steps but after adjusting the cell energies assigned to hadrons with the scaling factor required to match jet response in γ+jet events between data and MC (see Sect. 8.3.1). The resulting ratio of measured jet p_T is denoted as $p_{T,\text{jet}}^{\text{meas}(\gamma+\text{jet}),\text{Data}} / p_{T,\text{jet}}^{\text{meas}(\gamma+\text{jet}),\text{Data}}$ since it is expected to be close to that in data.

Figure 220 presents a comparison of both ratios, as well as the relative difference (Δ),

$$\Delta \equiv \frac{p_{T,\mathrm{jet}}^{\mathrm{meas}(\gamma+\mathrm{jet}),\mathrm{Data}}/p_{T,\mathrm{jet}}^{\mathrm{meas}(\gamma+\mathrm{jet}),\mathrm{Data}}}{p_{T,\mathrm{jet}}^{\mathrm{meas}(\gamma+\mathrm{jet}),\mathrm{MC}}/p_{T,\mathrm{jet}}^{\mathrm{meas}(\gamma+\mathrm{jet}),\mathrm{MC}}} - 1, \tag{I6}$$

as a function of the particle-jet p_T in different $\left|\eta_{\mathrm{jet}}^{\mathrm{det}}\right|$ bins. As it can be appreciated, the largest miscalibration between data and MC is expected for central jets at low p_T (owing to the softer energy spectrum of hadrons), whereas the difference for forward jets is very small. A parameterization of Δ is used to correct the measured jet energy in the QCD dijet (γ-like) MC employed for closure tests in data as follows:

$$E_{\mathrm{jet}}^{\mathrm{meas}(\mathrm{dijet}),\mathrm{MC}} \rightarrow \frac{E_{\mathrm{jet}}^{\mathrm{meas}(\mathrm{dijet}),\mathrm{MC}}}{1+\Delta}. \tag{I7}$$

(In principle, the correction required should be based on ratios of energies, instead of p_Ts. Nevertheless, it has been verified they are numerically almost identical.)

After this correction, provided the γ+jet energy calibration works properly (i.e. $E_{\mathrm{jet}}^{\mathrm{corr}(\gamma+\mathrm{jet}),\mathrm{Data}} = E_{\mathrm{jet}}^{\mathrm{corr}(\gamma+\mathrm{jet}),\mathrm{MC}}$), it is expected that $E_{\mathrm{jet}}^{\mathrm{corr},\mathrm{Data}} = E_{\mathrm{jet}}^{\mathrm{corr},\mathrm{MC}}$ in the mixture sample as well.

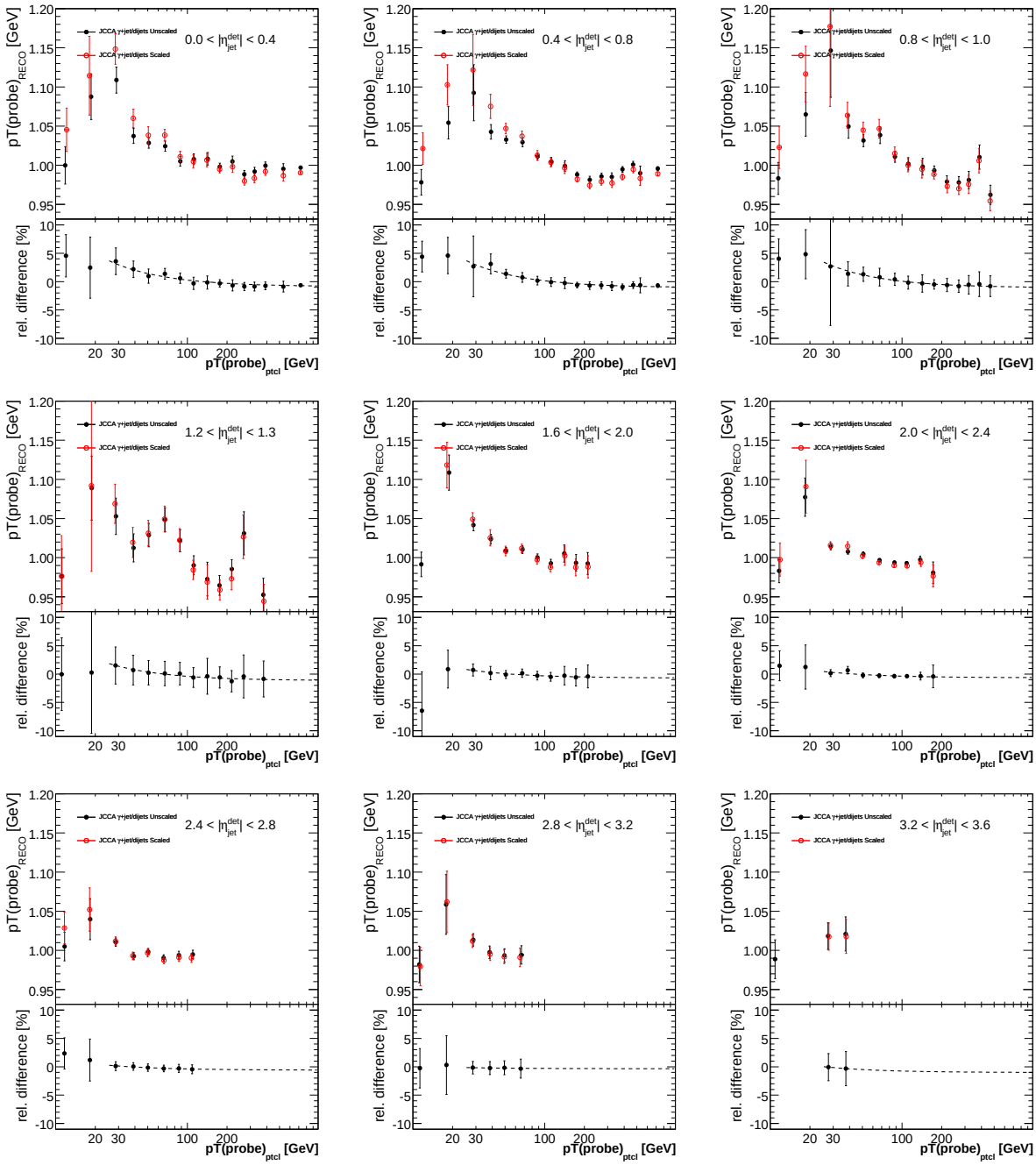

FIG. 220: Ratio of the measured probe jet p_T between γ+jet and QCD dijet events, as a function of particle-jet p_T in different $\left|\eta_{\text{jet}}^{\text{det}}\right|$ bins. This ratio is shown separately in two different scenarios: default MC (black) and MC using a scaled single pion response (red). The relative difference between both ratios, along with its parameterization (dashed curve), is shown in the bottom panels.

4. Data vs Different MCs

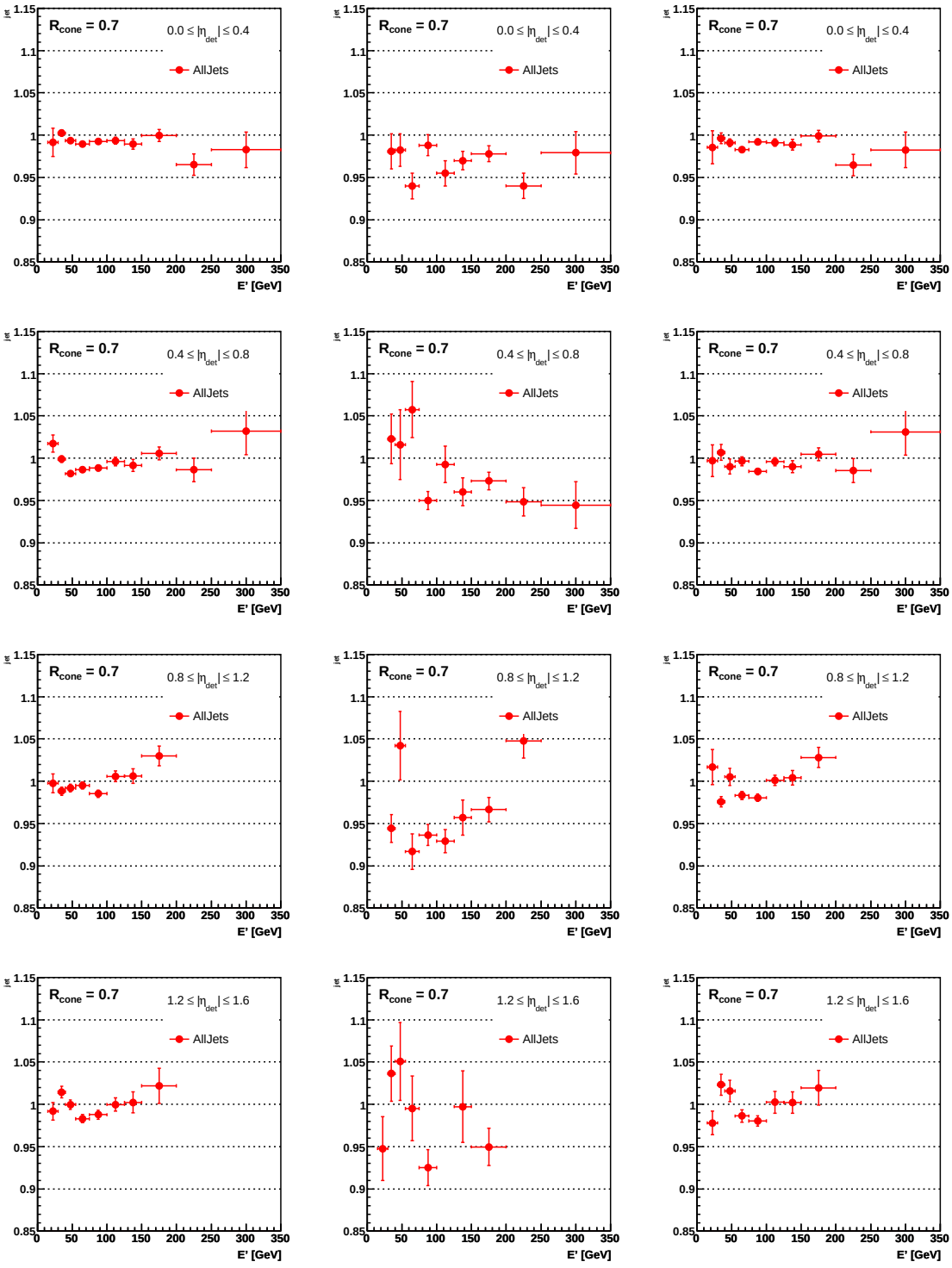

FIG. 221: Relative data-to-MC closure test for $\mathcal{R}_{\text{cone}} = 0.7$ jets as a function of p'_T and in different $\left|\eta^{\text{det}}_{\text{jet}}\right|$ bins. Different rows correspond to different MC scenarios: γ+jet signal (left), QCD dijet (γ-like) background (middle) and mixture (right). Only measurements based on at least 25 equivalent events are displayed.

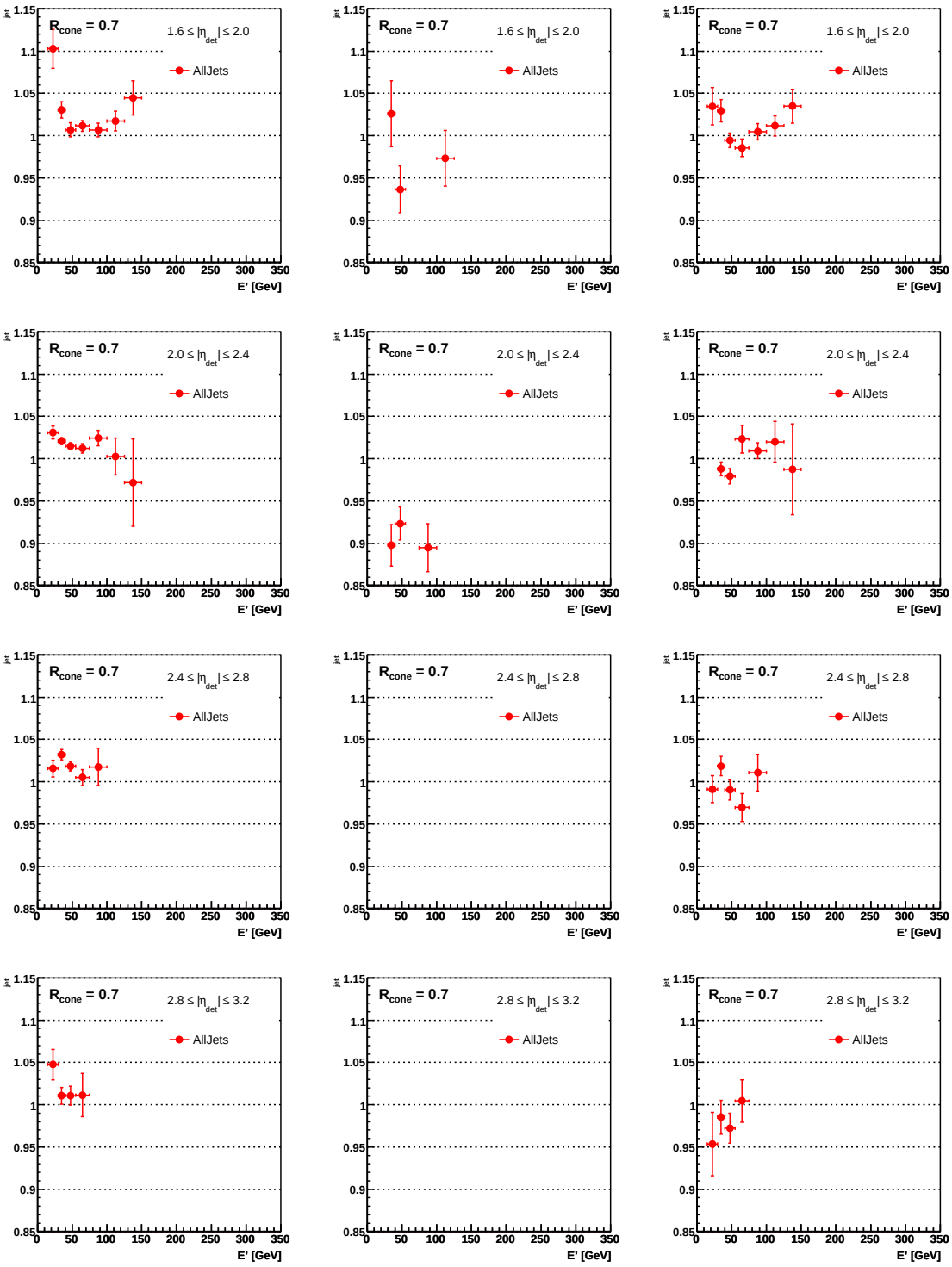

FIG. 222: Relative data-to-MC closure test for $\mathcal{R}_{\text{cone}} = 0.7$ jets as a function of p'_T and in different $\left|\eta_{\text{jet}}^{\text{det}}\right|$ bins. Different rows correspond to different MC scenarios: γ+jet signal (left), QCD dijet (γ-like) background (middle) and mixture (right). Only measurements based on at least 25 equivalent events are displayed.

5. ΔS in Data vs MC mixture

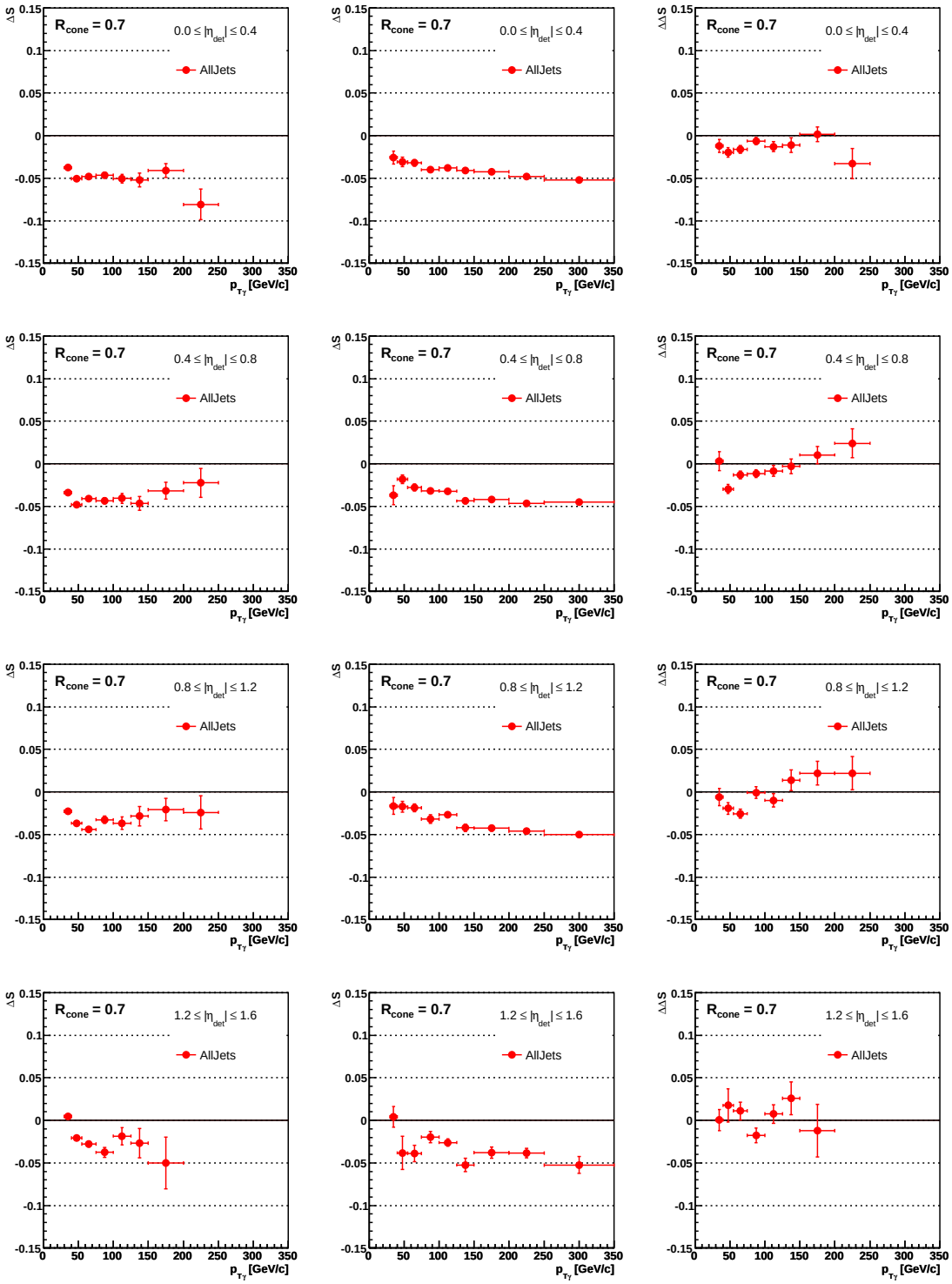

FIG. 223: ΔS in γ+jet events as a function of $p_{T\gamma}^{\mathrm{meas}}$ for $\mathcal{R}_{\mathrm{cone}} = 0.7$ jets in different $\left|\eta_{\mathrm{jet}}^{\mathrm{det}}\right|$ bins. Different columns show the result in data (left), mixed MC (center) and difference between data and mixed MC (right). Only measurements based on at least 25 equivalent events are displayed.

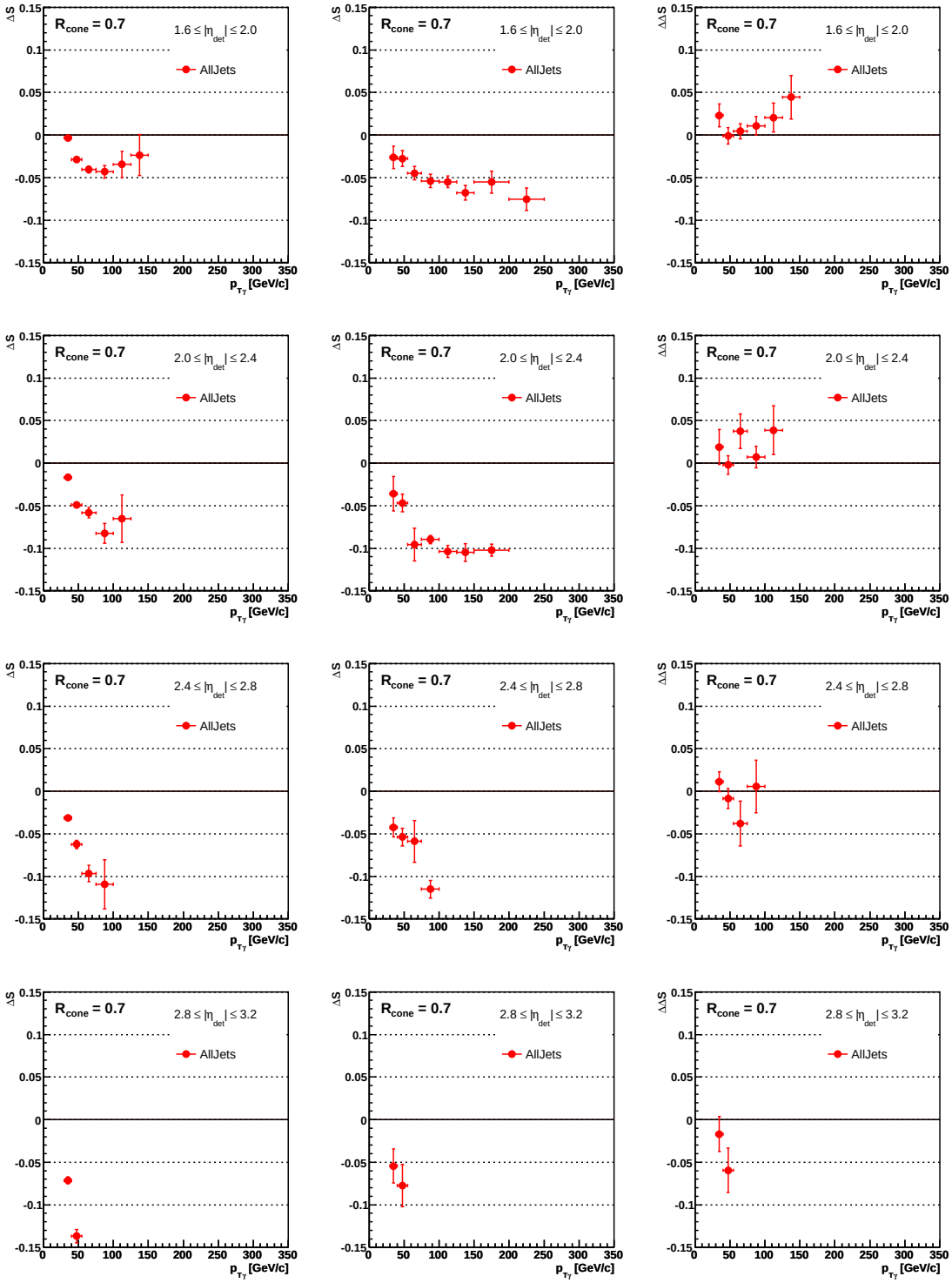

FIG. 224: ΔS in γ+jet events as a function of $p_{T\gamma}^{\mathrm{meas}}$ for $\mathcal{R}_{\mathrm{cone}} = 0.7$ jets in different $\left|\eta_{\mathrm{jet}}^{\mathrm{det}}\right|$ bins. Different columns show the result in data (left), mixed MC (center) and difference between data and mixed MC (right). Only measurements based on at least 25 equivalent events are displayed.

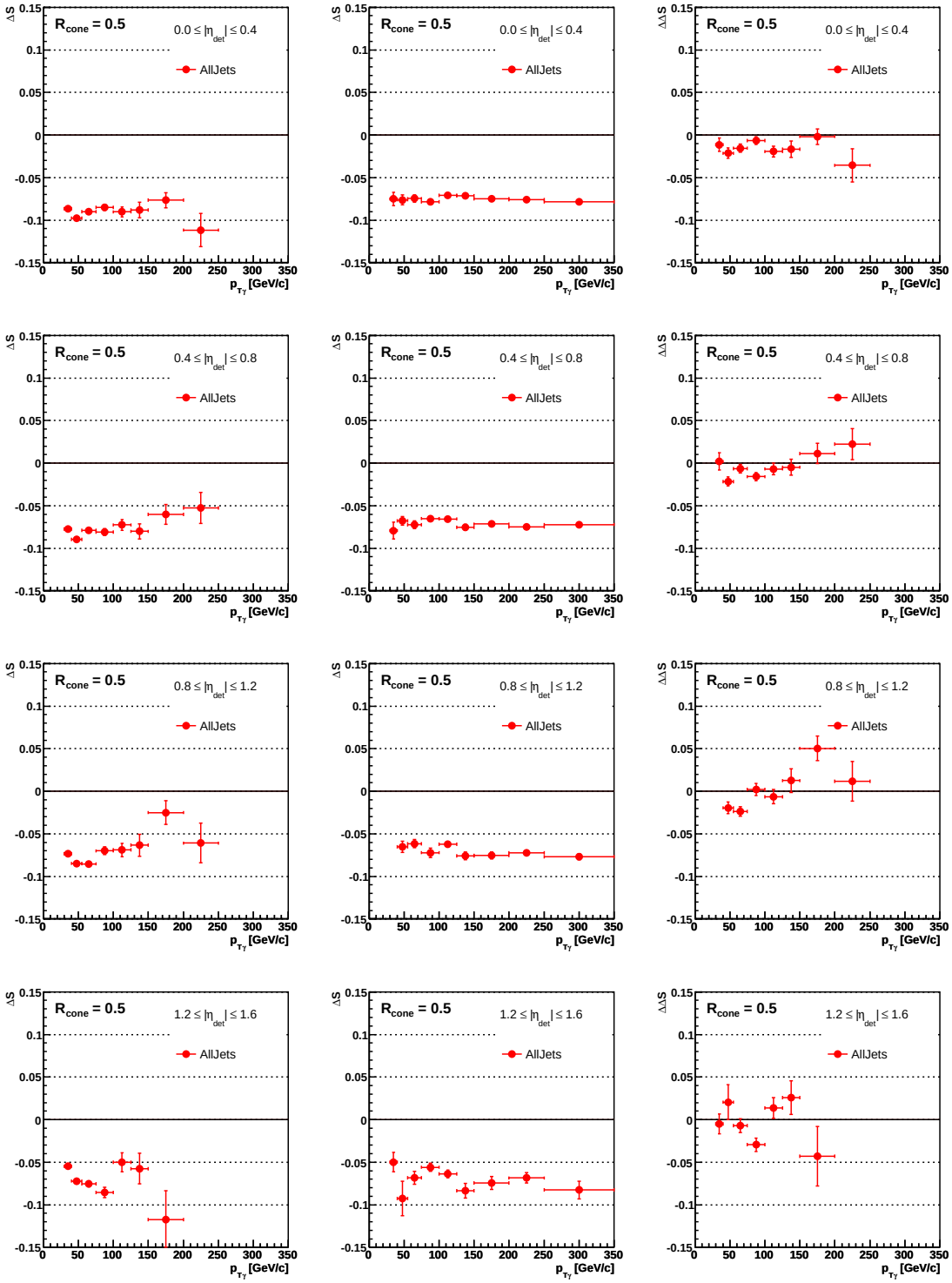

FIG. 225: ΔS in γ+jet events as a function of $p_{T\gamma}^{\mathrm{meas}}$ for $\mathcal{R}_{\mathrm{cone}} = 0.5$ jets in different $\left|\eta_{\mathrm{jet}}^{\mathrm{det}}\right|$ bins. Different columns show the result in data (left), mixed MC (center) and difference between data and mixed MC (right). Only measurements based on at least 25 equivalent events are displayed.

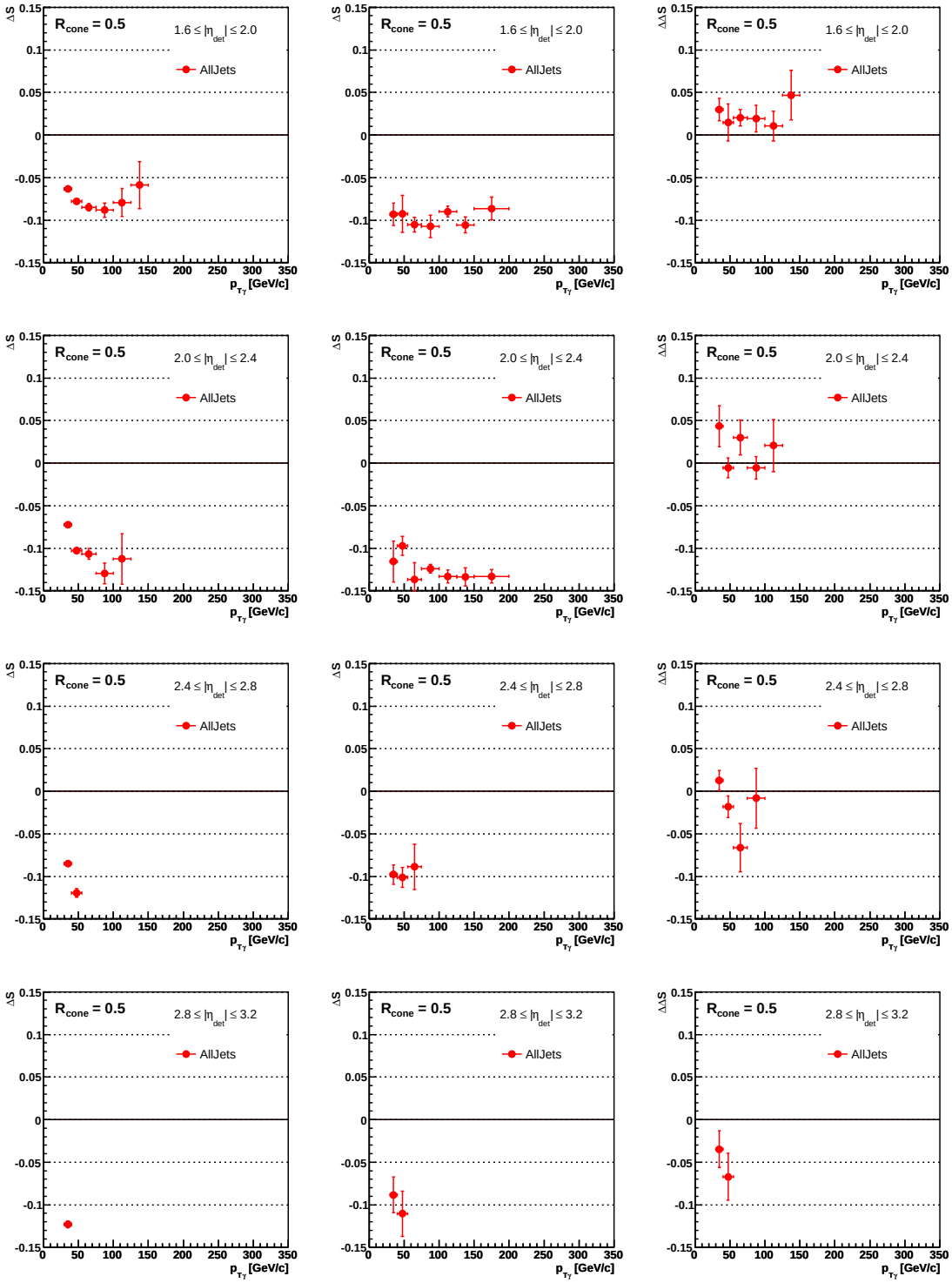

FIG. 226: ΔS in γ+jet events as a function of $p_{T\gamma}^{\mathrm{meas}}$ for $\mathcal{R}_{\mathrm{cone}} = 0.5$ jets in different $\left|\eta_{\mathrm{jet}}^{\mathrm{det}}\right|$ bins. Different columns show the result in data (left), mixed MC (center) and difference between data and mixed MC (right). Only measurements based on at least 25 equivalent events are displayed.

[1] R. E. Kalman, J. Bas. Eng. **82** D, 35 (1960); R. E. Kalman and R. S. Brucy, J. Bas. Eng. **83** D, 95 (1961); P. Billoir, Nucl. Instrum. Meth. A **225**, 352 (1984).
[2] U. Bassler and G. Bernardi, DØ Note 4124, March 2003;
U. Bassler, G. Bernardi, S. Trincaz-Duvoid and J.-R. Vlimant, DØ Note 4146, May 2003;
U. Bassler, E. Busato and J.-R. Vlimant, DØ Note 4335, January 2004.
[3] We use the iterative, seed-based cone algorithm including midpoints, as described on p. 47 in G. C. Blazey *et al.*, in Proceedings of the Workshop: *"QCD and Weak Boson Physics in Run II",* edited by U. Baur, R. K. Ellis, and D. Zeppenfeld, FERMILAB-PUB-00-297 (2000).
[4] T. Sjostrand *et al.*, Computer Physics Commun. **135**, 238 (2001).
[5] G. Corcella *et al.*, JHEP **0101**, 010 (2001) [hep-ph/0011363]; hep-ph/0210213
[6] J. Pumplin *et al.*, JHEP **0207**, 012 (2002) [arXiv:hep-ph/0201195].
[7] D. Bandurin, DØ Note 4672, August 2005.
[8] D. Bandurin, Private Communication.
[9] R. Field and R. Craig Group, arXiv:hep-ph/0510198.
[10] R. Brun and F. Carminati, CERN Program Library, Long Writeup W5013 (1993).
[11] R. Wigmans, *Calorimetry: Energy Measurement in Particle Physics*, Clarendon, Oxford (2000).
[12] F. Abe *et al.* [CDF Collaboration], Phys. Rev. Lett. **69**, 2896 (1992).
[13] A. Kupčo, C. Royon, M. Voutilainen and M. Wobisch, DØ Note 4751, March 2005.
[14] M. Voutilainen, DØ Note in preparation.
[15] V. M. Abazov *et al.* [D0 Collaboration], Phys. Lett. B **639**, 151 (2006) [arXiv:hep-ex/0511054].
[16] D. E. Groom, Nucl. Instrum. Meth. A **572**, 633 (2007) [arXiv:physics/0605164].
[17] V. M. Abazov *et al.* [DØ Collaboration], Phys. Rev. Lett. **94** (2005) 221801 [arXiv:hep-ex/0409040].
[18] D. Acosta *et al.*, CMS Note 2006-067 (2006).
[19] J. Stark, presentation at the "All DØ Meeting", June 9, 2006:
`http://www-d0.hef.kun.nl//fullAgenda.php?ida=a061060&fid=51`
[20] J. Stark, presentation at the "MC Summit", June 20, 2006:
`http://www-d0.hef.kun.nl//fullAgenda.php?ida=a061101&fid=47`
[21] J. Stark, presentation at the "W Mass Meeting", January 24, 2007:
`http://www-d0.hef.kun.nl//fullAgenda.php?ida=a07120&fid=75`
[22] D. Bandurin, DØ Note 4974, February 2006.
[23] J. Hegeman, DØ Note in progress. Most up-to-date version:
`http://www-d0.fnal.gov/phys_id/jes/d0_private/cb_material/p17_final/d0_note_5383_v1.2.ps`
[24] D. Acosta *et al.* [CDF Collaboration], Phys. Rev. D **71**, 112002 (2005) [arXiv:hep-ex/0505013].